University of Engineering and Technology   Institute of Mechanics

Proceedings of
the International Conference on
Engineering Mechanics and Automation
- ICEMA 2010

**The 5 Anniversary of the Faculty of Engineering Mechanics and Automation,
University of Engineering and Technology, Vietnam National University, Hanoi
July 1-2, 2010, Hanoi, Vietnam**

PUBLISHING HOUSE FOR SCIENCE AND TECHNOLOGY

On the occasion of the Fifth Anniversary of the Faculty of Engineering Mechanics and Automation, University of Engineering and Technology, Vietnam National University, Hanoi, the International Conference on Engineering Mechanics and Automation (ICEMA2010) will be organised at University of Engineering and Technology on July 1-2, 2010.

The aim of the conference is to provide an international forum for scientific researchers in the technologies and applications of Engineering Mechanics and Automation. The Conference also aims to provide a chance for exchange of experiences and international collaboration in these fields. The scope of the conference includes, but not limited to, the following topics:

- Fundamental Problems of Fluid Mechanics
- Mechanics with Climate Change and Environment
- Industrial and Environmental Fluid Mechanics
- River and Sea Dynamics
- Fundamental Problems of Mechanics of Solids
- Mechanics of Composite Materials and Structures.
- Fracture Mechanics and Fatigue
- Mechanics of Soil, Rocks and Porous Medium
- Technical Diagnostics
- Linear and Nonlinear Oscillations
- Dynamics of Multibody Systems
- Nonlinear Dynamics and Chaos
- Mechanics of Machines and Mechanism
- Computational Mechanics
- Industrial Automation
- CAD/CAM/CNC Systems
- Control Strategies and Algorithms
- Design Automation
- Intelligent Systems
- Machine Tools and Machinery
- Manufacturing Process Control
- Mechatronics Engineering
- Rapid Prototyping

Steering Committee

Chairman: **Nguyen Ngoc Binh**

Nguyen Dong Anh, Bui Huy Duong, Duong Ngoc Hai, Nguyen Van Hieu, Nguyen Hoa Thinh

Program Committee

Chairman: **Nguyen Cao Menh**

Dao Huy Bich, Guy Bonnet (France), Ngo Huy Can, Truong Huu Chi, Dao Van Dung, D. Dufresne (France), Nguyen Kim Dan (France) Nguyen Van Diep, Nguyen Dinh Duc, Huann-Ming Chou (Taiwan), Cao The Huynh, Le Xuan Huynh, Nguyen Van Khang, Chun-Gon Kim (Korea), Nguyen Tien Khiem, Ku-Chin Lin (Taiwan), Dang Van Ky (France), P. Le Tallec (France), D.J. Lee (Korea), Hoang Xuan Luong, Dinh Van Manh, M. H. Maitournam (France), Yoshihiro Ootao (Japan), Nguyen Van Pho, Dinh Van Phong, Pobedrya B.E. (Russia), Vu Duy Quang, Do Sanh, Nguyen Quoc Son, Pham Manh Thang, Tran Ich Thinh, Bui Dinh Tri, Nguyen The Truyen, Pham Anh Tuan, Masayuki Yamaguchi (Japan)

Organising Committee

Chairman: **Nguyen Dinh Duc**

Vice Chairman: **Pham Manh Thang, Bui Dinh Tri, Tran Duong Tri**

Dang The Ba, Vu Anh Dung, Chun-Gon Kim, Nguyen Thi Viet Lien, Dao Nhu Mai, Hoang Nam Nhat

Secretariat

Chairman: **Dao Nhu Mai**

Nguyen Viet Anh, Nguyen Thi Viet Lien, Phan Thi Cam Ly, Hoang Van Tung

Optimal hedge-algebras-based controller:
Design and application to structural active fuzzy control

Hai-Le Bui[a,], Duc-Trung Tran[b] and Nhu-Lan Vu[c]

[a] *Hanoi University of Technology, No. 1 Dai Co Viet Street – Hanoi – Vietnam, lebh79@gmail.com.*
[b] *Hanoi University of Technology, No. 1 Dai Co Viet Street – Hanoi – Vietnam,
tranductrung-vl@mail.hut.edu.vn.*
[c] *Institute of Information Technology, No. 18 Hoang Quoc Viet Road – Hanoi – Vietnam,
vnlan@ioit.ac.vn.*

Abstract

Vibration causes noise, environmental pollution, human fatigue and injury. In addition, it results in structural fatigue, lowering the strength and safety of the structure, and reducing the accuracy and reliability of the equipment in the system. In this paper, three controllers including OHAFC (optimal hedge-algebras-based fuzzy controller), FCHA (hedge-algebras-based fuzzy controller) and FC (conventional fuzzy controller) are designed. Our attention is paid to reduce vibration amplitude of a cantilever beam subjected to a concentrated harmonic force at its free tip by using a suitable control moment. Simulation results are exposed to illustrate the effect of OHAFC in comparison with HAFC and FC.

Key Words: cantilever beam, fuzzy control, hedge algebras, genetic algorithm.

1. Introduction

Vibration occurs in most machines, structures, and dynamic systems. Vibration can be found in daily life as well as in engineering structures. Vibration results in structural fatigue, lowering the strength and safety of the structure, and reducing the accuracy and reliability of the equipment in the system. Thus, in order to ensure the safety of the structure, and increase the reliability and durability of the equipment, reducing vibration in the system in the process of designing the structure becomes an important issue (Teng et al., 2000).

Depending on the control methods, vibration control in the structure can be divided into two categories, namely, passive control and active control (Preumont and Nihon, 2008). The idea of passive structural control is energy absorption, so as to reduce displacement in the structure. Recent development of control theory and technique has brought vibration control from passive to active and the active control method has become more effective in use.

Fuzzy set theory introduced by Zadeh in 1965 has provided a mathematical tool useful for modelling uncertain (imprecise) and vague data and been presented in many real situations. Recently, many researches on

active fuzzy control of vibrating structures have been done. We mention the works of Darus and Tokhi (2005), Guclu and Yazici (2008), Teng et al. (2000), Wang and Lin (2007) and Wenzhong et al. (2004).

Hedge algebras (HAs) introduced and investigated since 1987 (Ho, 2007; Ho and Nam, 2002; Ho et al., 1999; Ho and Long, 2007; Ho and Lan, 2006; Ho et al., 2006; Ho et al., 2008; Ho and Wechler, 1990; Ho and Wechler, 1992) can be considered as a mathematical order-based structure of terms-domains, the ordering relation of which is induced by the meaning of linguistic terms in these domain. It is shown that each terms-domain has its own order relation induced by the meaning of terms, called semantically ordering relation. Many interesting semantic properties of terms can be formulated in terms of this relation and some of these can be taken to form an axioms system of hedge algebras. These algebras form an algebraic foundation to study a kind of fuzzy logic, called linguistic-valued logic and provide a good mathematical tool to define and investigate the concept of fuzziness of vague terms and the quantification problem and some approximate reasoning methods.

The HAFC, a new fuzzy control algorithm, does not require fuzzy sets to provide the semantics of the linguistic terms used in the fuzzy rule system rather the semantics is obtained through the sematically quantifying mappings (SQMs). In the algebraic approach, the design of an HAFC leads to the determination of the parameter of SQMs, which are the fuzziness measure of primary terms and linguistic hedges occurring in the fuzzy model.

In this paper, applications of HAs and GA in active fuzzy control of a cantilever beam will be presented with three above mentioned controllers to compare their control effect.

2. The cantilever beam

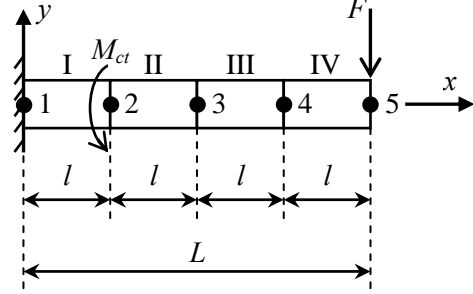We consider a cantilever beam shown in Figure 1.

Figure 1. The cantilever beam

This beam of length L is subjected to an external force $F = F_0\sin\omega t$ at its free tip. E and ρ are the elastic modulus and the mass density of beam material, respectively. The frictional damping and structural damping constants are denoted by α_1 and α_2, respectively. The length of each element is denoted by l. The width and height of the rectangular cross-section are denoted by b and h, respectively. The finite element model (FEM) of the beam includes five nodes (1, 2, 3, 4 and 5) and four elements (I, II, III and IV). Each node has two degrees of freedom (DOF) including: transverse displacement v and slope ϕ. A controllable moment M_{ct} is applied at node 2.

The elemental stiffness matrix (K_e) and mass matrix (M_e) are given by (Rao, 2004):

$$K_e = \frac{EI}{l^3}\begin{bmatrix} 12 & 6l & -12 & 6l \\ 6l & 4l^2 & -6l & 2l^2 \\ -12 & -6l & 12 & -6l \\ 6l & 2l^2 & -6l & 4l^2 \end{bmatrix} \qquad (1)$$

$$M_e = \frac{\rho Al}{420}\begin{bmatrix} 156 & 22l & 54 & -13l \\ 22l & 4l^2 & 13l & -3l^2 \\ 54 & 13l & 156 & -22l \\ -13l & -3l^2 & -22l & 4l^2 \end{bmatrix} \qquad (2)$$

Where, $A = b \times h$ is the cross-sectional area and $I = b \times h^3/12$ is the inertial moment of the cross-sectional area.

The dynamic equation of the cantilever beam is given by:

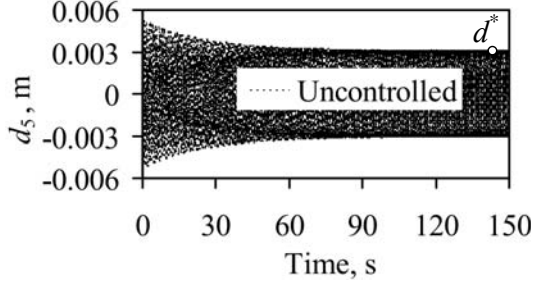$$\mathbf{M\ddot{q}} + \mathbf{C\dot{q}} + \mathbf{Kq} = \mathbf{F} \qquad (3)$$

Figure 2. Uncontrolled displacement – d_5.

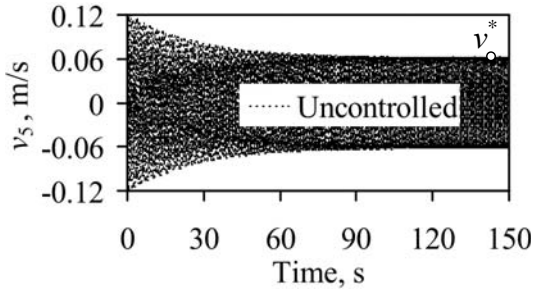Figure 3. Uncontrolled velocity – v_5.

Where **M**, **C** and **K** are global mass, damping and sfiffness matrices, respectively. **C** = α_1**M** + α_2**K**. **F** (containing F and M_{ct}) and **q** are the global vectors of displacement and load, respectively.

The following numerical values are used for simulations (Bandyopadhyay et. al., 2007): $L = 0.3$ m, $b = 0.03$ m, $h = 0.5$ mm, $E = 193.06$ GPa, $\rho = 8030$ kg/m^3, $\alpha_1 = 0.001$, $\alpha_2 = 0.0001$, $F_0 = 0.01$ N and $\omega = 20$ rad/s.

Thus, uncontrolled displacement (d_5) and velocity (v_5) at node 5 (free tip) are shown in Figure 2 and 3, respectively.

3. HAs–based fuzzy controller (HAFC) and Optimal HAFC (OHAFC)

In this section, the basic concepts of FCHA and OFCHA are summarized based on Ho (2007), Ho and Nam (2002), Ho et al. (1999), Ho and Long (2007), Ho and Lan (2006), Ho et al. (2006), Ho et al. (2008), Ho and Wechler (1990), Ho and Wechler (1992).

3.1. Algebraic structure of term-domains

In above reference documents, term-domains of linguistic variables equipped with a semantics-based ordering relation become algebraic structures, called hedge algebras (HAs), and they form an algebraic approach to the approximate reasoning problem. The algebraic approach to term-domains of linguistic variables is to discover algebraic structure of term-domains induced by the natural term meaning. For instance, by the term meaning we can observe that *extremely small < very small < small < approximately small < little small < big < very big < extremely big* ... So, we have a new viewpoint: term-domains can be modelled by a poset (partially ordered set), a semantics-based order structure.

Next, we explain how we can find out this structure.

Consider TRUTH as a linguistic variable and let X be its term-set. Assume that its linguistic hedges used to express the TRUTH are *Extremely*, *Very*, *Approximately*, *Little*, which for short are denoted correspondingly by E, V, A and L, and its primary terms are *false* and *true*. Then, $X =\{$*true*, *V true*, *E true*, *EA true*, *A true*, *LA true*, *L true*, *L false*, *false*, *A false*, *V false*, *E false* ...$\} \cup \{$**0**, **W**, **1**$\}$ is a term-domain of TRUTH, where **0**, **W** and **1** are specific constants called *absolutely false*, *neutral* and *absolutely true*, respectively.

A term-domain X can be ordered based on the following observation:

- *Each primary term has a sign which expresses a semantic tendency*. For instance, *true* has a tendency of "going up", called *positive* one, and it is denoted by c^+, while *false* has a tendency of "going down", called *negative* one, denoted by c^-. In general, we always have $c^+ \geq c^-$, semantically.

- Each hedge has also a *sign*. It is *positive* if it increases the semantic tendency of the primary terms and *negative*, if it decreases this tendency. For instance, V is *positive* with respect to both primary terms, while L has a reverse effect and hence it is *negative*. Denote by H^- the set of all negative hedges and by H^+ the set of all positive ones of TRUTH.

The term-set X can be considered as an abstract algebra $AX = (X, G, C, H, \leq)$, where $G = \{c^-, c^+\}$, $C = \{0, W, 1\}$, $H = H^+ \cup H^-$ and $\leq$ is a partially ordering relation on X. The ordering relation $\leq$ presents semantic qualitative properties of X, such as:

- $hx > x$ if $kx < x$, $\forall h \in H^+$, $k \in H^-$;
- If $h < k$ then $(hx > x \Rightarrow kx > x)$ & $(x > hx \Rightarrow hx > kx)$;
- If $\exists x$ ($x < hx < khx$ or $x > hx > khx$) then $\forall y$ $\{(y<hy \Rightarrow y<hy<khy)$ & $(hy<y \Rightarrow khy<hy<y)\}$;
- If $\exists x$ ($x < khx < hx$ or $x > khx > hx$) then $\forall y$ $\{(y<hy \Rightarrow y<khy<hy)$ & $(hy<y \Rightarrow hy<khy<y)\}$.

3.2. Fuzziness Measure of Vague Terms and Hedges of Term-Domains

The fuzzy inference model often simulates the dependency between two physical variables, namely, linguistic values occurring in the fuzzy model present values of physical variables in a line. This comment suggests us to establish a quantifying mapping from a linguistic domain into a line.

Definition 1. $f: X \to [0, 1]$ is called the semantically quantifying mapping of X if $\forall h, k \in H^+$ or $h, k \in H^-$, and $x, y \in X$:
$$\frac{|f(hx) - f(x)|}{|f(kx) - f(x)|} = \frac{|f(hy) - f(y)|}{|f(ky) - f(y)|}.$$

From the HA viewpoint, we have a visual way to define fuzziness of a linguistic value by the size of set $H(x)$ as follow: the fuzziness measure of x can be measured by the diameter of $f(H(x)) \subseteq [0, 1]$ (Figure 4).
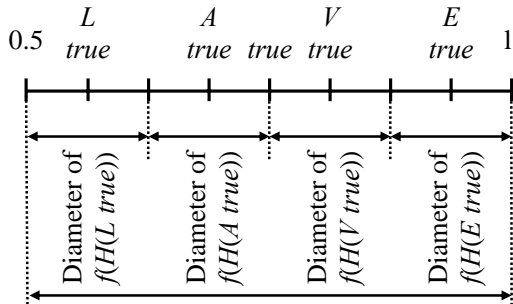

Figure 4. Diameter of $f(H(true))$

Definition 2. An *fm*: $X \to [0, 1]$ is said to be a fuzziness measure of terms in X if:

(*fm1*) $fm(c^-)+fm(c^+) = 1$ and $\sum_{h \in H} fm(hu) = fm(u)$, for $\forall u \in X$;

(*fm2*) for the constants 0, W and 1, $fm(0) = fm(W) = fm(1) = 0$;

(*fm3*) for $\forall x, y \in X$, $\forall h \in H$, $\frac{fm(hx)}{fm(x)} = \frac{fm(hy)}{fm(y)}$, this proportion does not depend on specific elements, called *fuzziness measure of the hedge h* and denoted by $\mu(h)$.

The condition (*fm1*) means that the primary terms and hedges under consideration are complete for modelling the semantics of the whole real interval of a physical variable. That is, except the primary terms and hedges under consideration, there are no more primary terms and hedges. (*fm2*) is intuitively evident. (*fm3*) seems also to be natural in the sense that applying a hedge h to different vague concepts, the relative modification effect of h is the same, i.e. this proportion does not depend on terms they apply to.

To formulate the following proposition, we assume that $H^- = \{h_{-1}, ..., h_{-q}\}$, where $h_{-1} < h_{-2} < ...< h_{-q}$, $H^+ = \{h_1,..., h_p\}$, where $h_1< h_2 < ...< h_p$. Then, the following properties can follow immediately from Definition 2.

Proposition 1. *For each fuzziness measure fm on X, we have*:

i) $fm(hx) = \mu(h)fm(x)$, *for every* $x \in X$;

ii) $fm(c^-) + fm(c^+) = 1$;

iii) $\sum_{-q \leq i \leq p, i \neq 0} fm(h_i c) = fm(c)$, $c \in \{c^-, c^+\}$;

iv) $\sum_{-q \leq i \leq p, i \neq 0} fm(h_i x) = fm(x)$;

v) $\sum_{-q \leq i \leq -1} \mu(h_i) = \alpha$ *and* $\sum_{1 \leq i \leq p} \mu(h_i) = \beta$ where $\alpha, \beta > 0$ *and* $\alpha + \beta = 1$.

3.3. Quantification of Term-Domains of a Linguistic Variable

Definition 3. A function Sign: $X \to \{-1, 0, 1\}$ is a mapping which is defined recursively as follows, for $h, h' \in H$ and $c \in \{c^-, c^+\}$:

i) $\text{Sign}(c^-) = -1$, $\text{Sign}(c^+) = +1$;

ii) $\text{Sign}(hc) = -\text{Sign}(c)$, if h is negative w.r.t. c; $\text{Sign}(hc) = +\text{Sign}(c)$, if h is positive w.r.t. c;

iii) $\text{Sign}(h'hx) = -\text{Sign}(hx)$, if $h'hx \neq hx$ and h' is negative w.r.t. h; $\text{Sign}(h'hx) = +\text{Sign}(hx)$, if $h'hx \neq hx$ and h' is positive w.r.t. h;

iv) $\text{Sign}(h'hx) = 0$ if $h'hx = hx$.

Definition 4. Let *fm* be a fuzziness measure on X. A mapping $\varphi: X \to [0,1]$, which is induced by *fm* on X, is defined as follows:

i) $\varphi(W) = \theta = fm(c^-)$, $\varphi(c^-) = \theta - \alpha fm(c^-) = \beta fm(c^-)$, $\varphi(c^+) = \theta + \alpha fm(c^+)$;

ii) $\varphi(h_j x) = \varphi(x) + \text{Sign}(h_j x)\{\sum_{i=\text{Sign}(j)}^{j} fm(h_i x) - \omega(h_j x) fm(h_j x)\}$,

where $j \in \{j: -q \leq j \leq p \ \& \ j \neq 0\} = [-q^\wedge p]$ and

$\omega(h_j x) = \dfrac{1}{2}[1 + \text{Sign}(h_j x)\text{Sign}(h_p h_j x)(\beta - \alpha)]$.

By Proposition 1, it can be seen that the mapping φ is completely defined by $(p+q)$ free parameters: one parameter of the fuzziness measure of a primary term and $(p+q-1)$ parameters of the fuzziness measure of hedges.

3.4. Example

Consider a hedge algebra $AX = (X, G, C, H, \leq)$, where $G = \{small, large\}$; $C = \{\mathbf{0}, W, \mathbf{1}\}$; $H^- = \{Little\} = \{h_{-1}\}$; $q = 1$; $H^+ = \{Very\} = \{h_1\}$; $p = 1$; $\theta = 0.5$; $\alpha = 0.5$; $\beta = 0.5$. Hence,

$\mu(Very) = 0.5$; $\mu(Little) = 0.5$;

$fm(small) = 0.5$; $fm(large) = 0.5$;

$\varphi(small) = \theta - \alpha fm(small) = 0.5 - 0.5 \times 0.5 = 0.25$;

$\varphi(Very\ small) = \varphi(small) + \text{Sign}(Very\ small) \times (fm(Very\ small) - 0.5fm(Very\ small)) = 0.25 + (-1) \times 0.5 \times 0.5 \times 0.5 = 0.125$;

$\varphi(Little\ small) = \varphi(small) + \text{Sign}(Little\ small) \times (fm(Little\ small) - 0.5fm(Little\ small)) = 0.25 + (+1) \times 0.5 \times 0.5 \times 0.5 = 0.375$;

$\varphi(large) = \theta + \alpha fm(large) = 0.5 + 0.5 \times 0.5 = 0.75$;

$\varphi(Very\ large) = \varphi(large) + \text{Sign}(Very\ large) \times (fm(Very\ large) - 0.5fm(Very\ large)) = 0.75 + (+1) \times 0.5 \times 0.5 \times 0.5 = 0.875$;

$\varphi(Little\ large) = \varphi(large) + \text{Sign}(Little\ large) \times (fm(Little\ large) - 0.5fm(Little\ large)) = 0.75 + (-1) \times 0.5 \times 0.5 \times 0.5 = 0.625$.

3.5. Optimal FCHA

The main aim of a control problem is to regulate the controlled object into its stable state or to minimize a goal function defined on the *whole* controlled process. In order to find the optimal parameters for designing a fuzzy controller, we have to examine *an optimal problem for the whole controlled process*.

(1) *Determine the control problem*: Suppose that we have a fuzzy control problem of an application for which we can determine the following factors:

- A fuzzy rule-base with linguistic descriptions, which represents an expert knowledge of the application domain for defining the state and control action values of the controlled object in every control cycles;

- Establish a discrete control model, equations (3), which defines the computation relationship between numeric-valued states of the controlled object and numeric-valued control action in each control cycle;

- A criterion for evaluating the effectiveness of the control method: Goal function $g(x_1, \ldots, x_m)$, where $x_1, x_2, \ldots, x_m$ and u can be computed by formulas defined by the established control model.

(2) *Construct an optimal control algorithm based on HAs*: This step consists of the following tasks:

- Considering parameters of the fuzziness measure of a primary term and hedges as design variables and determining their intervals;

- Constructing a Fitness-Algorithm to evaluate the fitness level of the parameters for GA based on the calculation of the state

values of the controlled object and the control action.

- Optimizing the parameters using GA. In this paper a GA is used as the search algorithm and based on the code of Chipperfield et. al. (1994).

4. Fuzzy controllers of the cantilever beam

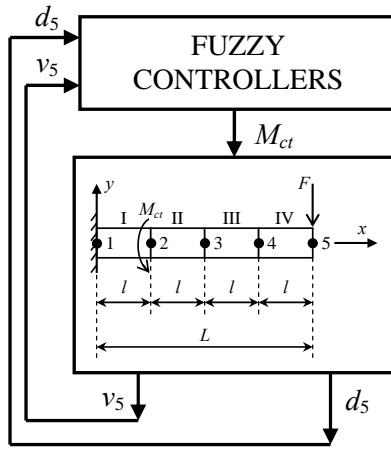The fuzzy controllers are based on the closed-loop fuzzy system shown in Figure 5.

Figure 5. Fuzzy controllers of the beam

Where, M_{ct} is determined by above-mentioned controllers, d_5 and v_5 are determined by equation (3).

The goal of controllers is to reduce vibration amplitude at the cantilever beam's free tip.

It is assumed that the universes of discourse of two state variables are $-d^* \leq d_5 \leq d^*$; $-v^* \leq v_5 \leq v^*$ (see Figure 2 and 3) and of the control moment is -0.002 Nm $\leq M_{ct} \leq 0.002$ Nm.

In the following parts of this section, the authors will present establishing steps of the controllers.

4.1. Conventional fuzzy controller (FC) of the beam

In this subsection, FC of the beam is established (establishing steps of a FC could refer in Mandal, 2006) using Mamdani's

inference and centroid defuzzification method with nine control rules.

4.1.1. Constructing the membership functions

Three membership functions for d_5 and v_5 in their intervals are established with values negative (N), zero (Z) and positive (P) as shown in Figure 6 and 7.

Then, five membership functions for M_{ct} in its interval are established with values negative big (NB), negative (N), zero (Z), positive (P) and positive big (PB) as shown in Figure 8.
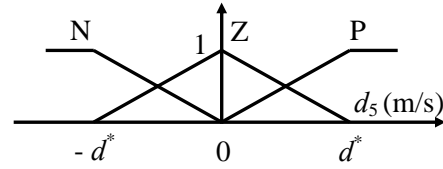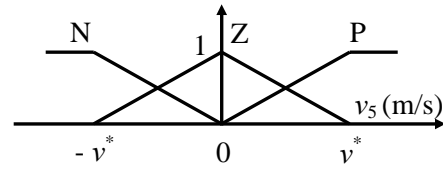

Figure 6. Membership functions for d_5
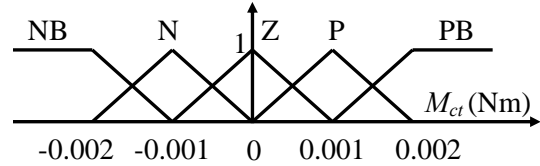

Figure 7. Membership functions for v_5

Figure 8. Membership functions for M_{ct}

4.1.2. Constructing rule base

The fuzzy associative memory table (FAM table) is established as shown in Table. 1.

Table 1. FAM table.

d_5	v_5		
	N	Z	P
N	PB	P	Z
Z	P	Z	N
P	Z	N	NB

4.2. Hedge-algebras-based fuzzy controller (HAFC) of the beam

In FC, the FAM table is formulated in Table 1. The linguistic labels in Table 1 have to be transformed into the new ones given in Table 2, that are suitable to describe linguistically reference domains of [0, 1] and can be modeled by suitable HAs. The HAs of the state variables d_5 and v_5 are $AX_i = (x_i, G, C, H, \leq)$, where $x_i = d_5$ or v_5, $G = \{small, large\}$, $C = \{0, W, 1\}$, $H = \{H, H^+\} = \{Little, Very\}$, and the HA of the control variable $AM = (M_{ct}, G, C, H, \leq)$ with the same sets G, C and H as for d_5 and v_5, however, their terms describe different quantitative semantics based on different real reference domains.

The semantically quantifying mappings (SQMs) φ are determined and shown in Table 3 (see subsection 3.4). Like this, we have the SAM (semantic associative memory) table with semantically quantifying mappings (d_5 and v_5 are replaced with d_{5s} and v_{5s}, respectively) as shown in Table 4.

Table 2. Linguistic transformation

NB	N	Z	P	PB
Very small	*small*	*W*	*large*	*Very large*

Table 3. Parameters of SQMs

Very small	*small*	*W*	*large*	*Very large*
0.125	0.25	0.5	0.75	0.875

Table 4. SAM table.

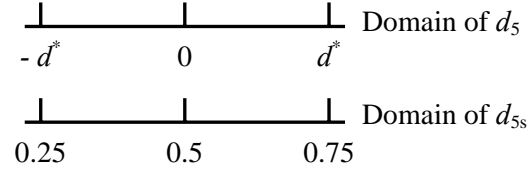| d_{5s}	v_{5s}		
	small: 0.25	*W*: 0.5	*large*: 0.75
small: 0.25	*Very large*: 0.875	*large*: 0.75	*W*: 0.5
W: 0.5	*large*: 0.75	*W*: 0.5	*small*: 0.25
large: 0.75	*W*: 0.5	*small*: 0.25	*Very small*: 0.125

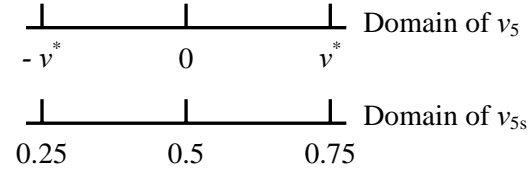

Figure 9. Transformation: d_5 to d_{5s}

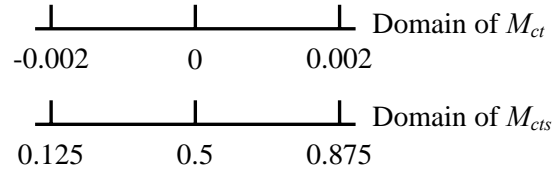Figure 10. Transformation: v_5 to v_{5s}
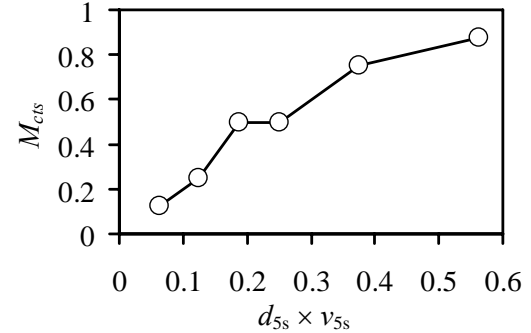

Figure 11. Transformation: M_{ct} to M_{cts}

Figure 12. Quantifying Semantic Curve

The semantization for each linguistic variable are defined by the transformations given in Figure 9-11 (M_{ct} is replaced with M_{cts}). The new terminology "semantization" was defined and accepted in Ho et al. (2008).

The Quantifying Semantic Curve (QSC) is linearly established through the points that present the control rules occurring in Table 4 as shown in Figure 12.

4.3. Optimal HAFC (OHAFC) of the beam

The parameters of the fuzziness measure of a primary term and hedges are now considered as design variables and their intervals are determined as follow:

$\theta = [0.4 \div 0.6]$; $\alpha = [0.4 \div 0.6]$.
The goal function g is defined as follow:

$$g = \sum_{i=0}^{n} \left[\frac{d_5^2(i)}{(d^*)^2} + \frac{v_5^2(i)}{(v^*)^2} \right] = \min \qquad (4)$$

Where, n is the number of control cycles.

The parameters using GA are determined as follow (Chipperfield et. al., 1994): number of individuals per subpopulations: 20; number of generations: 200; recombination probability: 0.8; number of variables: 2; fidelity of solution: 20.

5. Results and discussion

The results include: the optimal QSC of OFCHA, the displacemnt d_5 and velocity v_5 obtained from the fuzzy controllers.

The optimal QSC of OFCHA is shown in Figure 13. The difference between the optimal QSC (Figure 13) and the initial QSC (Figure 12) demonstrates that we can search different values of θ and α to obtained reasonable parameters for an HAFC.

The displacement and velocity at the free tip of the cantilever beam are shown in Figures 14 and 16, respectively. From the figures, we realize that by using fuzzy controllers the structural displacement and velocity output responses have the effect of suppressing vibration. As indicated in these figures, the effects of suppressing structural vibration from the proposed method (OHAFC and HAFC) are more efficient than the conventional control method (FC).
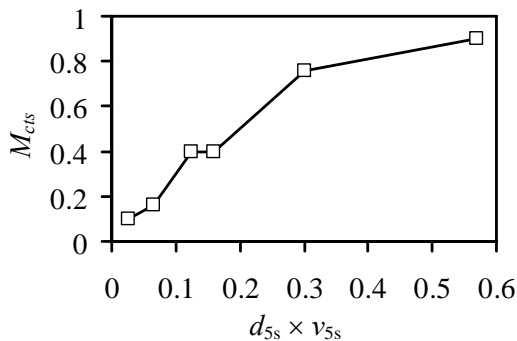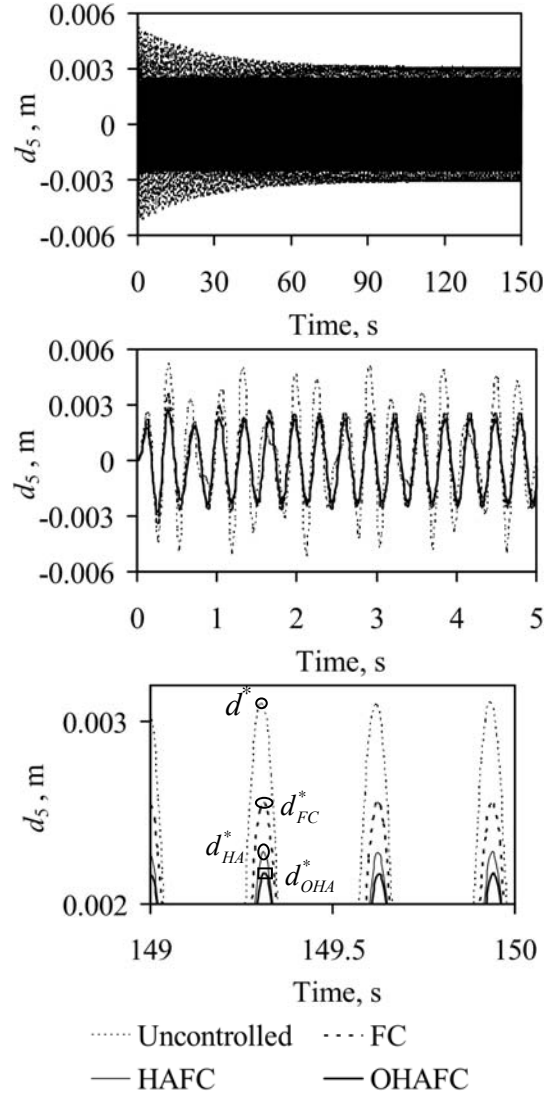

Figure 13. The optimal QSC of OFCHA
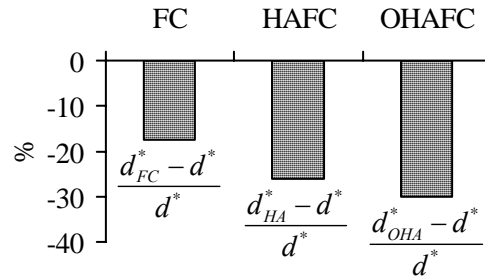

Figure 14. Displacement – d_5.

Figure 15. Variations of the vibration amplitudes of the beam's free tip, %.

The variations of the vibration and velocity amplitudes of the beam's free tip are shown in Figure 15 and 17, respectively.
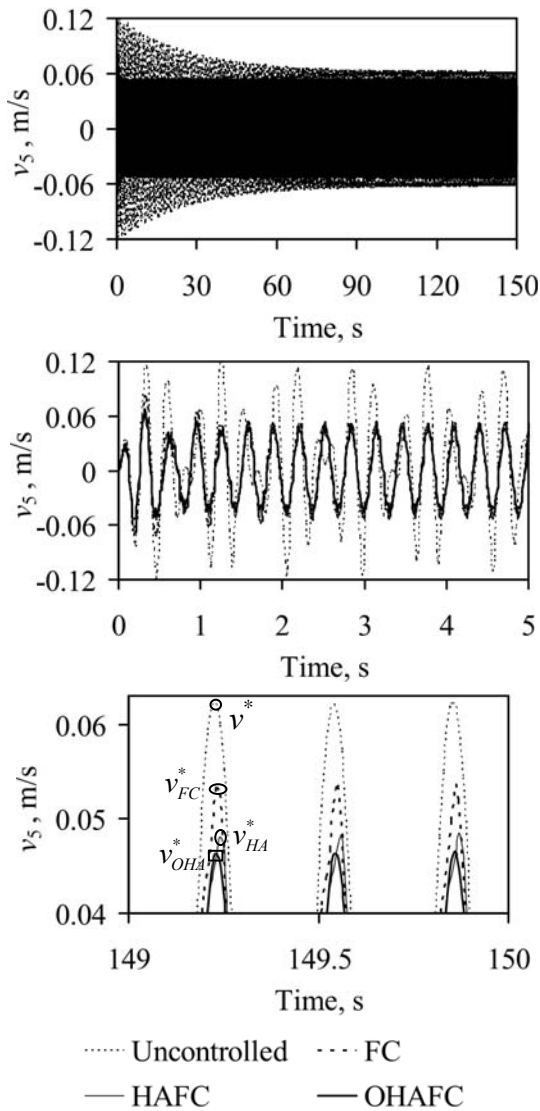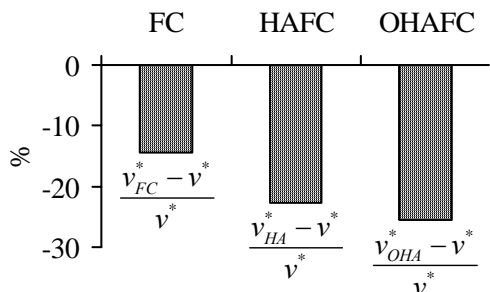
Figure 16. Velocity – v_5.

Figure 17. Variations of the velocity amplitudes of the beam's free tip, %.

It is seen that, the displacement and velocity amplitudes of the beam's free tip are reduce about 17% (FC), 26% (HAFC) and 14% (FC), 23% (HAFC), respectively. The above meaning values should be cared when selecting a controller for structural active control.

6. Conclusions

In the present work, new fuzzy controllers based on HAs are applied for active control of a cantilever beam subjected to a concentrated harmonic force at its free tip. The main results are summarized as follows:

The algebraic approach to term-domains of linguistic variables is quite different from the fuzzy sets one in the representation of the meaning of linguistic terms and the methodology of solving the fuzzy multiple conditional reasoning problems. It allows linearly establishing the Quantifying Semantic Curve through the points corresponding to the control rules. Hence, the defuzzification method of the HAFC is very simple. The semantic order is always guaranteed.

It is clear that the OHAFC and HAFC are simpler, more effective and more understandable in comparison with the FC.

In fuzzy logic, many important concepts like fuzzy set, T-norm, S-norm, intersection, union, complement, composition… are used in approximate reasoning. This is an advantage for the process of flexible reasoning, but there are too many factors such as shape and number of membership functions, defuzzification method,… influencing the precision of the reasoning process and it is difficult to optimize. Those are subjective factors that cause error in determining the values of control process. Meanwhile, approximate reasoning based on hedge algebras, from the beginning, does not use fuzzy set concept and its precision is obviously not influenced by this concept. Therefore, the method based on hedge algebras does not need to determine shape and number of membership function, neither does it need to solve defuzzification problem.

Besides, in calculation, while there is a large number of membership functions, the volume of calculation based on fuzzy control increases quickly, meanwhile the volume of calculation based on hedge algebras does not increase much with very simple calculation. With these above advantages, it is definitely possible to use hedge algebras theory for many different controlling problems.

References

Bandyopadhyay, B., T. C. Manjunath, and M. Umapathy (2007). *Modelling, Control and Implementation of Smart Structures.* Springer, Berlin, Germany.

Chapra, S. C., and R. P. Canale (2006). *Numerical Methods for Engineers.* McGraw-Hill, New York, USA.

Chipperfield, A., P. Fleming, H. Pohlheim, and C. Fonseca (1994). *Genetic Algorithm Toolbox.* Department of Automatic Control and Systems Engineering, the University of Sheffield, UK.

Darus, I. Z. M., and M. O. Tokhi (2005). Soft computing-based active vibration control of a flexible structure. *Engineering Applications of Artificial Intelligence*, 18, pp. 93 – 114.

Guclu, R., and H. Yazici (2008). Vibration control of a structure with ATMD against earthquake using fuzzy logic controllers. *Journal of Sound and Vibration*, 318, pp. 36 – 49.

Ho, N. C. (2007). A topological completion of refined hedge algebras and a model of fuzziness of linguistic terms and hedges. *Fuzzy Sets and Systems*, 158, pp. 436 – 451.

Ho, N. C., and H. V. Nam (2002). An algebraic approach to linguistic hedges in Zadeh's fuzzy logic. *Fuzzy Sets and Systems*, 129, pp. 229 – 254.

Ho, N. C., H. V. Nam, T. D. Khang, and N. H. Chau (1999). Hedge algebras, linguistic-valued logic and their application to fuzzy reasoning. *Internat. J. Uncertainty fuzziness knowledge-based systems*, 7 (4), pp. 347 – 361.

Ho, N. C. and N. V. Long (2007). Fuzziness measure on complete hedge algebras and quantifying semantics of terms in linear hedge algebras. *Fuzzy Sets and Systems*, 158, pp. 452 – 471.

Ho, N. C., and V.N. Lan (2006). Hedge Algebras: An algebraic approach to domain of linguistic variables and their applications. *ASEAN Journal on SCIENCE & TECHNOLOGY FOR DEVELOPMENT Vol 23, N1&2 June 2006.*

Ho N.C., V. N. Lan, and L. X. Viet (2006). An Interpolative reasoning method based on hedge algebras and its application to problem of fuzzy control. *Proceedings of the 10th WSEAS International on Computers, Vouliagmeni, Athens, Greece, July 13-15*, pp. 526 – 534.

Ho, N. C., V. N. Lan, and L. X. Viet (2008). Optimal hedge-algebras-based controller: Design and application. *Fuzzy Sets and Systems*, 159, pp. 968 – 989.

Ho, N. C. and W. Wechler (1990). Hedge algebras: An algebraic approach to structure of sets linguistic truth values. *Fuzzy Set and Systems*, 35, pp. 281 – 293.

Ho, N. C. and W. Wechler (1992). Extended hedge algebras and their application to fuzzy logic. *Fuzzy Set and Systems*, 52, pp. 259 – 281.

Mandal A. K. (2006). *Introduction to Control Engineering.* New Age International (P) Ltd., Publishers, New Delhi.

Preumont, A., and K. S. Nihon (2008). *Active Control of Structures.* JohnWiley & Sons, UK.

Rao, S. S. (2004). *The finite element method in engineering.* Elsevier Science & Technology Books

Teng, T. L., C. P. Peng, and C. Chuang (2000). A study on the application of fuzzy theory to structural active control. *Comput. Methods Appl. Mech. Engrg*, 189, pp. 439 – 448.

Wang, A. P., and Y. H. Lin (2007). Vibration control of a tall building subjected to earthquake excitation. *Journal of Sound and Vibration*, 299, pp. 757 – 773.

Wenzhong, Q., S. Jincai, and Q. Yang (2004). Active control of vibration using a fuzzy control method. *Journal of Sound and Vibration*, 275, pp. 917 – 930.

Coupled Field Simulation
of Magnetic-Mechanical Structures for AFM

Dung C.T.P[1], Tan T.D[1], Long N.T[1]

[1] *Faculty of Electronic and Telecommunication, Hanoi University of Engineering and Technology*
Tel: +84-4-37547709, E-mail address: dungctp@vnu.edu.vn

Abstract

In this paper, design and simulation of two types of cantilever are presented. For the mechanical cantilever, we have designed it using rectangular and triangular structures, which shown the effect of geometry on resonant frequencies and force constant. For the magnetic force driven cantilever, we propose a mechanical model with Ni plate controlled by solenoid coil. We have analyzed some properties such as the effect of Ni plate on the resonant frequencies, the dependence of force on the electric current I and number of solenoid loops N. This is important information for designing more complex MEMS structure in which the mechanical and magneto electric interaction need to be included.

Key Words: are given here

1. Introduction

One of the important instruments of micro/nano technology is Atomic Force Microscope (AFM). This is equipment which allows to record the surface image and to analyze the materials from nano- to atom-size. Moreover, AFM is used to investigate various interactions between a surface sample and the tip of a probe such as atomic interaction, friction, magnetic, electrostatic and attractive (adhesive) forces etc.

This article aims at designing and modeling of the cantilevers using for AFM. This is important and necessary step before fabrication of the cantilever. We have applied the finite element method (FEM) with the ANSYS software for designing and modeling the cantilevers. Out of general silicon cantilever working in air, we focus here on design special mechanical cantilevers used in gaseous and liquid media and the cantilever which is exited by magnetic force that allows operating in the liquid medium and is suitable for studying biological samples.

2. Comprehensive design

As mentioned above, the design and simulation of two types of cantilever have been realized in this work.

The first type is a Si-based mechanical cantilever (see Fig. 1) which operates in two modes: contact mode and half-contact mode. In the half-contact mode, the compulsory oscillation of the cantilever is stimulated by a piezo-actuator located at the end of the cantilever. This cantilever is designed with different geometric structures, namely the rectangular and triangular ones, and different resonant frequencies. In this design, we have focused on the two resonant frequencies regions: 300-600 kHz, the high frequency region suitable for measurements in gaseous media, and the 10-100 kHz, the low frequency region suitable for measurements in liquid media.
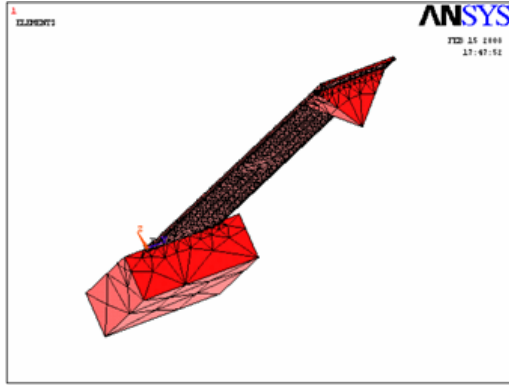

Fig. 1: The designed rectangular cantilever with the dimensions w: L=250μm, W=35μm, and T=1,3μm after split gird lines

Our calculation showed that the resonant frequencies of the cantilever are inversely proportional to its length L and proportional to its width W and height T (see the details in Tab. 1). Based on these results the optimal configurations for the cantilevers having the required resonant frequencies (in this case in the 150-300 kHz and 10-20 kHz regions) can be chosen.

The second type of cantilever is that which is driven by a magnetostatic force. The design of this type aims at the AFM measurements in liquid media, which require the electric insulation of the cantilever as well as the large force to resist the oscillation loss in liquid media.

Table 1: Dependence of resonant frequencies on L, W, T of a rectangular cantilever

L (μm)	W (μm)	T (μm)	Resonant frequencies (KHz)	L (μm)	W (μm)	T (μm)	Resonant frequencies (KHz)
80	35	1.7	243,420	130	35	1.7	95,411
80	35	2	303,490	130	35	2	118,020
80	35	2.3	365,960	130	35	2.3	141,800
100	35	1.7	156,780	350	35	1	7,721
100	35	2	195,306	350	35	1.3	10,839
100	35	2.3	235,200	250	35	1.3	19,970
100	35	2.5	262,530	250	30	1.3	19,955
100	35	2.7	290,310	250	25	1.3	19,932

In this case, the cantilever consists of a Si cantilever coated with a ferromagnetic layer. The cantilever is stimulated to oscillate by an alternating magnetic field produced by a solenoid coil. This system allows controlling the cantilever in half-contact mode in the liquid media. Its structure consists of two parts:

i/ The cantilever is a silicon one coated with a ferromagnetic layer such as Ni or Ni-Fe (see Fig. 2).
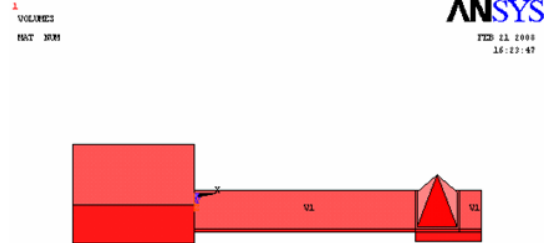

Fig. 2. Model of the Si- cantilever coated with a ferromagnetic layer

ii/ The magnetic coils is designed based on the solenoid coil structure (see Fig. 3)
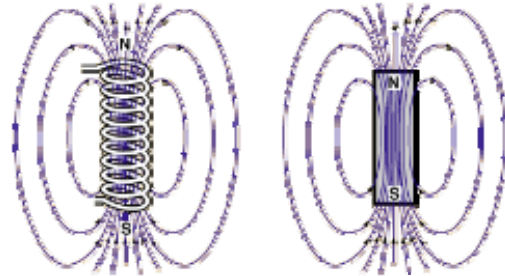

Fig. 3 Principle structure of the exiting coil and its equivalent magnetic circuit

Force constant for this type of cantilever has also been considered to calculate its resonant frequencies. As applying a Fz force along the z axis on the cantilever end, the cantilever will deflect a distance of Δ at its end. This force constant k is specified as k = F_z/Δ. Some simulation results of this model are presented in Figs. 4-7.
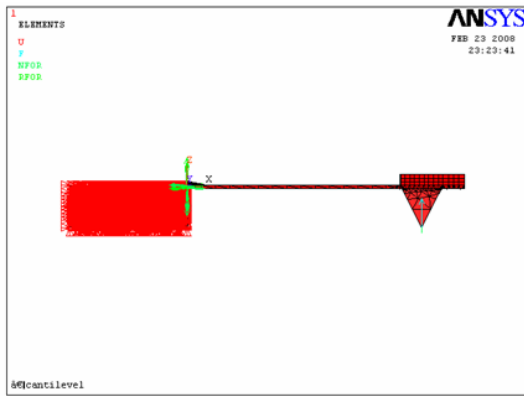

Fig. 4: Simulation of the force applied on the cantilever
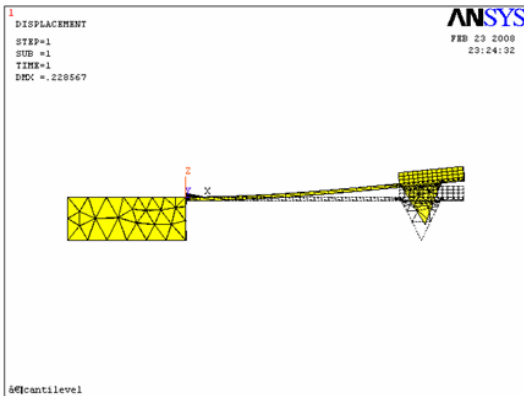

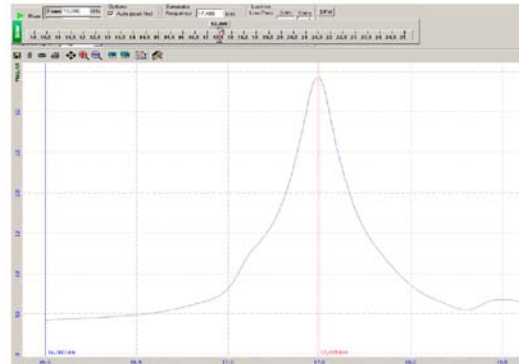Fig. 5: Simulation of the moving of the cantilever under an applied force

Fig. 6: The resonant frequency of the designed AFM system
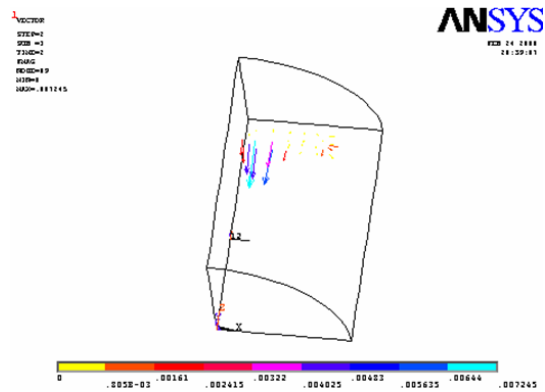
Fig. 6: Effect the magnetic force F applied on the cantilever with N= 500 circle, I = 15 mA

3. ConclusionS

In this paper, design and simulation of two types of cantilever are presented. For the mechanical cantilever, the rectangular and triangular structures have been considered, which has shown the effect of geometry on resonant frequencies and force constant. For the magnetic force driven cantilever, we have proposed a model with the Ni plate controlled by the solenoid coil. For this structure, we have also analyzed some properties such as the effect of Ni plate on the resonant frequencies, the dependence of force on the electric current I and number of solenoid loops N. This information is important for designing more complex MEMS structure in which the mechanical

and magneto electric interaction need to be included.

Ackowledgements

References

Fullin, E. Gobet, J. Tilmans, H.A.C. Bergqvist, J., "A new basic technology for magnetic micro-actuators", MEMS 98, 1998, pp. 143-147.

Jack William Judy, "Batch - Fabricated Ferromagnetic Micro-actuators with Silicon Flexures", Doctor of Philosophy Thesis in Electrical Engineering, University of California - Berkeley, 1996.

Electromagnetic Field Fundamentals, ANSYS Documents.

Dina Kudasheva, General concept and defining characteristics of AFM, http://www.geocities.com.

International Conference on
Engineering Mechanics and
Automation (ICEMA 2010)
Hanoi, July 1-2, 2010

Mechanical Analysis of a Sensing Microgripper

T. Chu Duc[a], T.D. Nguyen[b], D.D. Nguyen[a]

[a] University of Engineering and Technology, Vietnam National University, Hanoi, Vietnam
[b] National University of Civil Engineering, Hanoi, Vietnam

Abstract

A novel design of sensing microgripper based on silicon-polymer electrothermal actuator and piezoresistive force-sensing cantilever beam was presented in [1]. The actuator consists of a silicon comb structure with the aluminum heater on the top and the filled polymer in between the comb finger. The sensor consists of a silicon cantilever with the sensing piezoresistors on the top. The measured microgripper jaw displacement is up to 32 µm at the applied voltage of 4.5 V. The maximum average temperature change is 177 °C. The output voltage of the piezoresistive sensing cantilever is up to 49 mV at the jaw displacement of 32 µm.

This paper presents mechanical analysis for above developed devices based on the finite element simulation and also classical mechanical theory. These devices can be optimized not only on the displacement but also the output force. This proposed sensing microgripper can potentially be used in automatic manipulation system in microassembly, living cell handling, minimally invasive surgery and micro robotics.

Key Words: Direct displacement method, Electrothermal actuator, Microgripper, Sensing microgripper,

1. Introduction

When manipulating microobjects, the dexterity, accuracy and speed are considerably improved when the force on the objects can be sensed and controlled in real-time [2]. The development of such miniaturized manipulators is of great interest for operating on living cells, minimally invasive surgery (MIS), microrobotics and microassembly.

This paper presents mechanical analysis for a novel design, which is presented in [1] based on the finite element simulation and also classical mechanics theory. The devices can be optimized not only on the displacement but also the output force.

2. Sensing microgripper design and operations

Ref [1] presents the design and operations principle of the sensing microgripper based on electrothermal silicon-polymer actuator and piezoresistive force sensing cantilever beam. In Figs. 1 and 2 schematic drawing of the sensing microgripper is shown. The structure is based on the combination of a silicon-polymer electrothermal microactuators and piezoresistive lateral force-sensing cantilever beams. When the electrothermal actuator is activated the microgripper's arm and also the sensing cantilever are bent. This causes a difference in the longitudinal stress on the opposite

sides of the cantilever. This changes the resistance values of the sensing piezoresistors on the cantilever. The displacement of the microgripper jaws can be monitored by the output voltage of the Wheatstone bridge of the piezoresistive sensing cantilever beam. The contact force between the microgripper jaws and clamped object is then determines based on displacement and stiffness of microgripper arm [1].
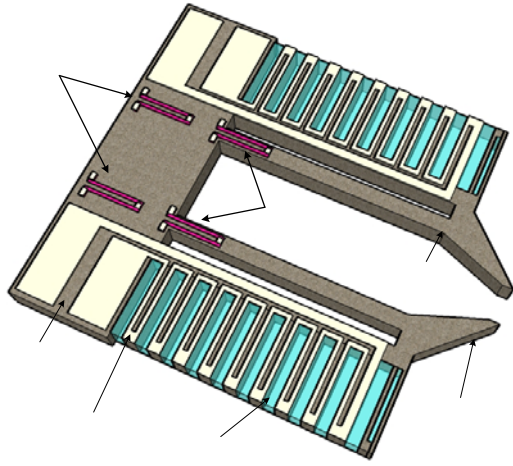

Figure 1. Schematic drawing of the sensing microgripper.
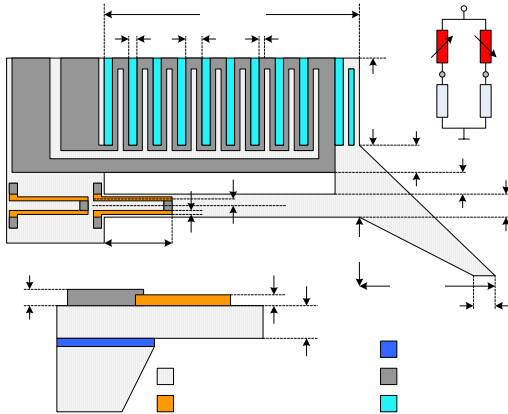

Figure 2. Front-side view and cross-side view of a sensing microgripper arm with geometry symbols and parameters.

The microgripper is designed for normal opened operating mode. Each actuator has a silicon comb finger structure with the aluminum metal heater on top. A thin layer of silicon nitride is employed as the electrical isolation between the aluminum structure and the silicon substrate. Each actuator consists of silicon comb fingers with SU8 polymer layers in between. When the heater is activated, the generated heat is efficiently transferred to the surrounding polymer through the deep silicon comb finger structure that has a large interface area with the polymer layer. The polymer layers expand along the lateral direction causing bending displacement of the actuator arm.

The force sensor design is based on the lateral force-sensing piezoresistive cantilever beam. The four piezoresistors are located on the cantilever beam structure and connected to create a Wheatstone bridge (see Figs. 1 and 2). The piezoresistors are aligned along the [110] direction in the (001) crystal plane of the silicon wafer. The resistor pair located on the cantilever are stress sensing resistors. When the electrothermal actuator is activated the cantilever beam is bent parallel to the wafer surface. Therefore, the differential change of resistance occurs on the two resistors R_{S1} and R_{S2} (see Fig. 2). The resistance change of the piezoresistors depends on the displacement u of the tip of the cantilever beam.

TABLE I. Geometry of the sensing microgripper design

Parameters	Symbol	Value	Unit
Actuator/Cantilever length	L	390	µm
Actuator/Cantilever thickness	T	30	µm
Silicon finger width	H_{Si}	6	µm
SU-8 layer width	H_{SU8}	3	µm
Aluminum heater width	H_{Al}	2	µm
Comb finger width	W_{comb}	75	µm
Silicon bone structure width	W_{bone}	10	µm
Gap between actuator and sensing cantilever	W_{gap}	22	µm
Cantilever width	W_{can}	12	µm
Microgripper jaw length	L_{jaw}	100	µm
Microgripper jaw width	W_{jaw}	28	µm
Tip width	W_{tip}	20	µm
Distance between two jaws	d_{int}	40	µm

The operation principle of the sensing microgripper based on silicon-polymer electrothermal actuator and piezoresistive force sensing cantilever is thoroughly understood using mechanical analysis. It is essential to know the linear expansion of the silicon-polymer stack in order to find the

mechanical deflection and stiffness of the sensing actuator.

3. Thermomechanical finite element modeling

To simulate the performance of the proposed sensing microgripper, a finite element modeling software COMSOL (Comsol Inc.) is used. The related material properties are assumed to be temperature independent. The three-dimensional (3D) thermo-mechanical model is used to determine the steady-state temperature distribution within the actuator and sensing cantilever structures. The thermal expansion and resulting actuator displacement is computed based on the temperature results.

The actuator is modeled in air. The silicon comb structure acts as the heat source and the heat sinks to the rest of the gripper arm. The substrate is assumed to be thermally grounded and thus the temperature of the device anchors is fixed and equal to the ambient temperature. The heat dissipation through convection and radiation to the ambience can be neglected in comparison with the heat losses due to conduction to the actuator anchors when the working temperature is below 500 K [3-5].

Figs. 3 and 4 show the steady-state temperature profile in the actuator and sensing cantilever when the microgripper jaws displacement is 25 µm at the applied voltage of 4.5 V. The maximum temperature change of 195 °C in the actuator occurs approximately at 300 µm far from the anchor along its longitudinal axis. The temperature in the cantilever changes linearly from ambient temperature at the anchor point to 189 °C at its tip. The simulated temperature at the microgripper jaws is 190 °C.
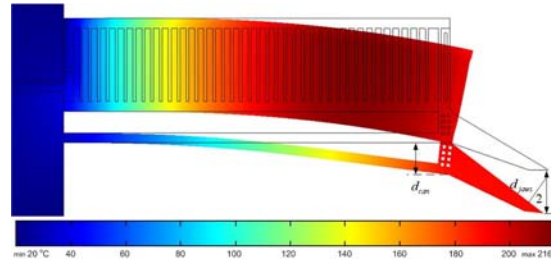

Figure 3. The modeled thermal profile and deformed shape of the actuator and sensing cantilever at the applied voltage of 4.5 V.
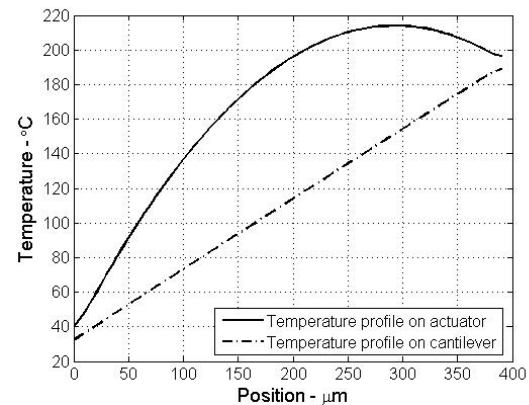

Figure 4. The steady-state thermal profile on actuator and cantilever.

The average working temperature in the electrothermal actuator is estimated by the above simulated temperature at the middle point of all comb fingers. Fig. 5 shows the simulated microgripper jaws displacement versus the average temperature change and also the maximum temperature change. The maximum displacement of the two microgripper jaws d_{jaws} is 25 µm at the average temperature change of 150 °C corresponding to a maximum temperature change of 195 °C (see Fig. 4). The displacement of the sensing cantilever d_{can} is also simulated and shown in Fig. 5. The maximum sensing cantilever tip displacement is 9.3 µm when the microgripper jaws displacement is 25 µm (see Figs. 1 and 5). The initial gap between the two jaws of the microgripper is designed to be 40 µm. Therefore, this proposed sensing microgripper is expected to be

capable of grasping microobjects with a diameter of 15 to 40 µm.

The simulated static lateral stiffness K_l of the sensing microgripper arm is 1.8 kN/m. This value is obtained by using a mechanical model with the external lateral load at the microgripper jaws. The maximum output force of this microgripper is calculated through the maximum displacement of a microgripper arm and its stiffness of 22.5 mN.
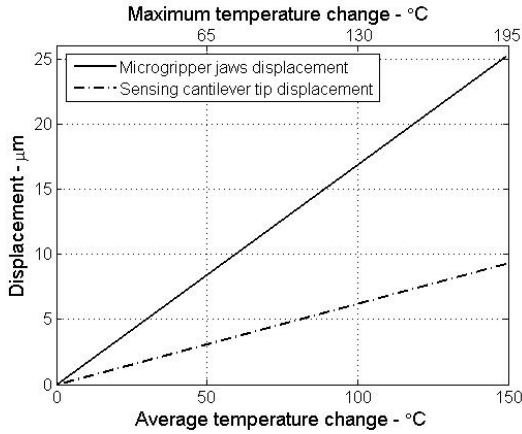

Figure 5. The simulated microgripper jaws displacement and the cantilever tip displacement versus the average working temperature change and maximum temperature change.

4. Mechanical analysis of sensing microgripper

A simplified structure which is used to analyse the sensing microgripper under the change of temperature is shown in Fig. 6. Here, lines *AB*, *CD* and *EF* denote beam elements representative of silicon-polymer stack, silicon bone, and silicon sensing layers, respectively. Those beam elements are fixed on one end, and connected together by a rigid beam *BDF* on the other end. Denote E_{ij}, A_{ij} and I_{ij} to be Young's modulus of material, cross-section area and moment of inertia of cross-section for the beam *ij*, respectively.

The silicon-polymer stack beam *AB* length increases when a power is applied. The performance of the silicon-polymer stack is analyzed based on the hydrostatic

pressure due to constraint effect [6]. Note that for the beam AB, equivalent values of the above parameters are adopted on [1, 6].

In this calculation, it is assumed that the change of average temperature on elements *AB* and *CD* is *ΔT*.
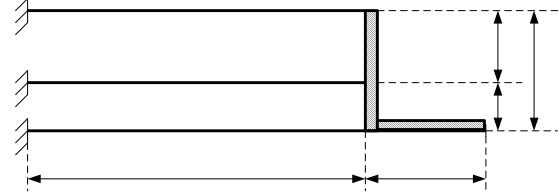
Figure 6. Frame structure to analyse the sensing microgripper

4.1. Sensing microgripper displacement analysis

Fig. 7 shows the deformation of the structure under the change of temperature in beams *AB* and *CD*. In the figure, Z_1 and Z_2 denote the unknown rotation and vertical deflection of the rigid beam *BDF*. Here, it is assumed that the axial expansion of elements *EF* is neglected.
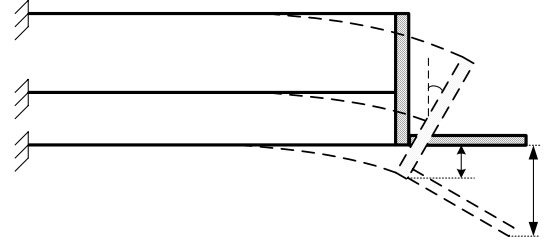
Figure 7. Deformation of the structure

In order to calculate the displacement and the output force at the jaw tip of the sensing micro gripper, the direct displacement method is used. Under the change of temperature *ΔT*, the governing equation for the system is given by :

$$\mathbf{K}\mathbf{Z}(T) = \mathbf{R}(T) \qquad (1)$$

where

$$\mathbf{K} = \begin{bmatrix} r_{11} & r_{12} \\ r_{21} & r_{22} \end{bmatrix}; \ \mathbf{Z}(T) = \begin{Bmatrix} Z_1(T) \\ Z_2(T) \end{Bmatrix}; \text{ and } \mathbf{R}(T) = \begin{Bmatrix} R_1(T) \\ R_2(T) \end{Bmatrix} \ (2)$$

denote stiffness matrix of the structure, displacement vector and output force vector, respectively. To determine stiffness coefficients, unit displacements are applied. Diagrams of bending moments in structural elements are performed in Figs. 8 and 9 for the cases of $Z_1=1$ and $Z_2=1$.

Figure 8. Diagram of the bending moment due to $Z_1=1$

Figure 9. Diagram of the bending moment due to $Z_2=1$

Axial forces in elements *AB* and *CD* under the applied unit displacement $Z_1=1$ are given by

$$\overline{N}_1^{AB} = \frac{\Delta L_{AB} E_{AB} A_{AB}}{L} = \frac{h E_{AB} A_{AB}}{L},$$
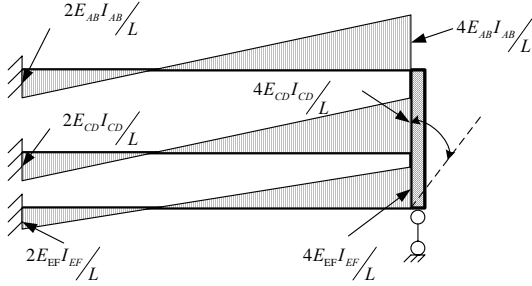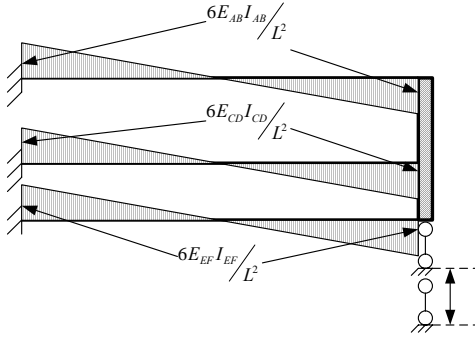$$\overline{N}_1^{CD} = \frac{\Delta L_{CD} E_{CD} A_{CD}}{L} = \frac{h_2 E_{CD} A_{CD}}{L} \quad (3)$$

Note that axial forces in elements *AB* and *CD* due to $Z_2=1$ are zeros. Based on conditions for static equilibrium of the structure, stiffness coefficients are given by :

$$r_{11} = \frac{4E_{AB}I_{AB}}{L} + \frac{4E_{CD}I_{CD}}{L} + \frac{4E_{EF}I_{EF}}{L} + \frac{h^2 E_{AB}A_{AB}}{L} + \frac{h_2^2 E_{CD}A_{CD}}{L},$$
$$r_{22} = \frac{12E_{AB}I_{AB}}{L^3} + \frac{12E_{CD}I_{CD}}{L^3} + \frac{12E_{EF}I_{EF}}{L^3},$$
$$r_{12} = r_{21} = -\left(\frac{6E_{AB}I_{AB}}{L^2} + \frac{6E_{CD}I_{CD}}{L^2} + \frac{6E_{EF}I_{EF}}{L^2}\right)$$
$$(5)$$

Components $R_1(T)$ and $R_2(T)$ of the force vector are calculated based on axial forces on elements *AB* and *CD* due to the change of temperature ΔT. We have

$$R_1(T) = \alpha_1 \Delta T E_{AB} A_{AB} h + \alpha_2 \Delta T E_{CD} A_{CD} h_2,$$
$$R_2(T) = 0 \quad (6)$$

Solving the equation (1), we yield

$$Z_1(T) = \frac{r_{22} R_1(T)}{\det K}; \ Z_2(T) = -\frac{r_{12} R_1(T)}{\det K} \quad (7)$$

where det $K = r_{11}r_{22} - (r_{12})^2$. Vertical displacement $y(T)$ of the microgripper jaw tip under the change of temperature is therefore given by

$$y(T) = Z_1(T)L_{Jaw} + Z_2(T) = \frac{R_1(T)}{\det K}\left(r_{22}L_{jaw} - r_{12}\right) \quad (8)$$

4.2. Sensing microgripper output force analysis

The structure shown in Fig. 10 is adopted to estimate the contact force between the microgripper jaw and the manipulating object.
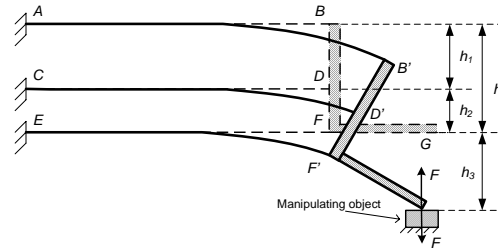

Figure 10. Structure for solving the output force

The unknown force *F* is calculated from the following condition

$$y(T) + y(F) = h_3 \quad (9)$$

where $y(F)$ denotes the vertical displacement due to the reaction force *F*. Similar to the above procedure, the governing equation for solving the displacement $y(F)$ is given by

$$\mathbf{KZ}(F) = \mathbf{R}(F) \qquad (10)$$

where

$$R_1(F) = -FL_{jaw}; \quad R_2(F) = -F$$

Solving the equation (10), we yield

$$Z_1(F) = \frac{1}{\det K}\{r_{22}R_1(F) - r_{12}R_2(F)\},$$

$$Z_2(F) = -\frac{1}{\det K}\{r_{12}R_1(F) - r_{11}R_2(F)\}$$

The vertical displacement of the jaw tip due to the reaction F is given by :

$$y(F) = Z_1(F)L_{Jaw} + Z_2(F)$$

$$= \frac{1}{\det K}\{[r_{22}R_1(F) - r_{12}R_2(F)]L_{jaw} + R_2(F)r_{11} - R_1(F)r_{12}\}$$

Taking the above result in to equation (9), we obtain the value of gripping force

$$F = \frac{R_1(T)(r_{22}L_{jaw} - r_{12}) - h_3 \det K}{r_{11} - 2r_{12}L_{jaw} + r_{22}(L_{jaw})^2} \qquad (13)$$

5. Fabrication

The realized sensing microgripper is shown in Fig. 11. The device is 490 µm long, 350 µm wide, 30 µm thick and with a 40 µm gap between the two jaws. The piezoresistive force sensing cantilever is 390 µm long, 10 µm wide with four piezoresistors on the surface [see Fig. 11(b)]. The fabrication process is based on the DIMES bipolar process and the silicon-polymer actuator process described in [1, 7].

The processes separately developed for the sensor and the actuator part of the system are CMOS compatible and thus can be easily combined as shown in Fig. 12. The first part [Figs. 12(a)-(c)] is essentially the process used for the sensor fabrication. The process for the actuator is then implemented [Figs. 12(d)-(f)] and due to the above mentioned compatibility does not have any negative effect on the sensor functioning.
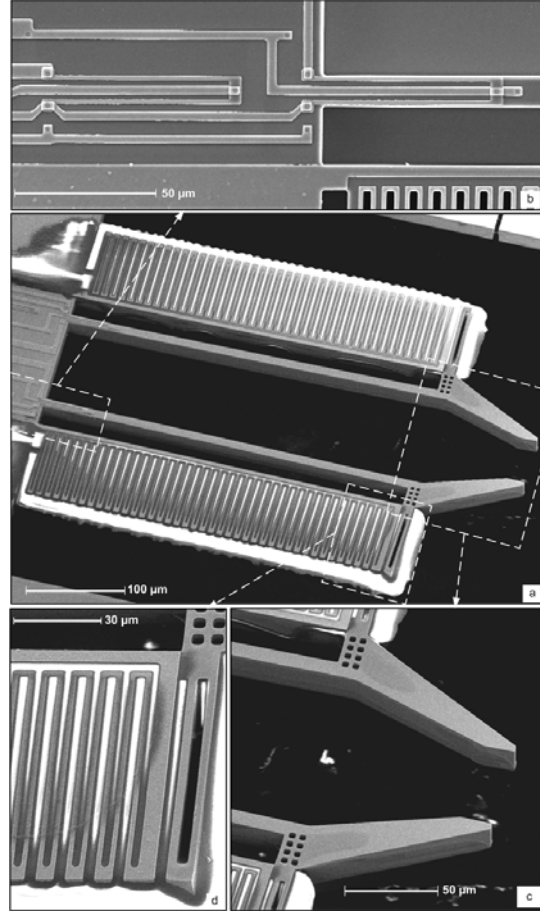

Figure 11. SEM picture of (a) the sensing microgripper and close-ups of (b) the piezoresistors; (c) the jaws, and (d) a section of the thermal actuator.
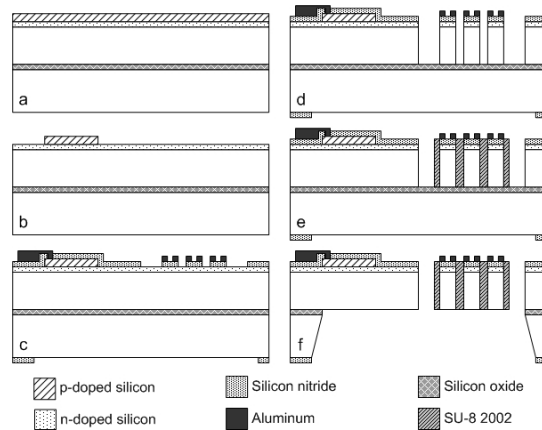

Figure 12. Schematic view of the sensing microgripper fabrication process.

6. Measurement Results

Fig. 13 shows the displacement response of the microgripper jaws in air when a dc voltage is applied on the electrothermal actuator. This measured movement is the total change between the two microgripper jaws position when both arms are activated. The measurement error is estimated to be ±1.5 µm. The measured results meet the simulated value within 7.5 %. A maximum movement of 32 µm is measured at a 4.5 V applied voltage. Therefore, this microgripper is capable of manipulating a microobject with a diameter between 8 and 40 µm.
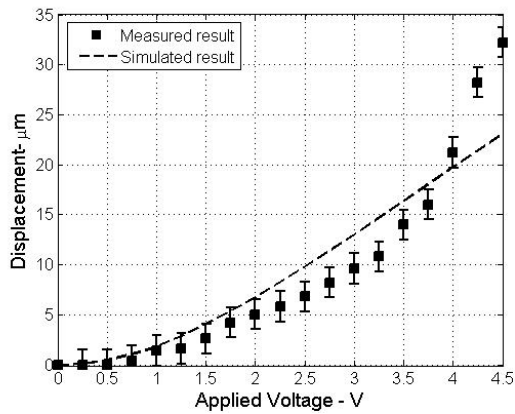
Figure 13. The simulated and measured sensing microgripper jaws displacement versus applied voltage. The maximum measured displacement is 32 µm at 4.5 V.
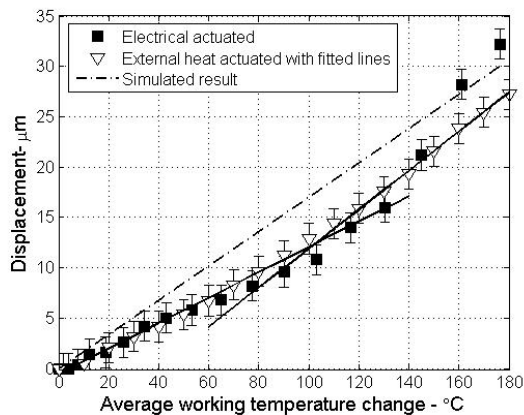
Figure 14. The simulated and measured sensing microgripper jaws displacement versus average working temperature.

The results of the thermal characterization are also shown in Fig. 14. The values obtained with the external heat mode meet the electrical and simulated ones within 7 % and 5 %, respectively. It indicates once again that the aluminum deposition process behaves as expected and the average working temperature of the actuator can be well estimated from the resistance change of the aluminum heater.

Fig. 15 shows the diagrams of the vertical displacement of the microgripper jaws versus the change of temperature. Here, the glass transition temperature of SU8 is 120 °C. The temperature expansion coefficients of SU8 on glass phase and rubber phase are 50 and 150.7 ppm, respectively.

Figs. 14 and 15 shows that the simulated and mechanical analysis results are meet the experimental measurement of the fabricated devices.
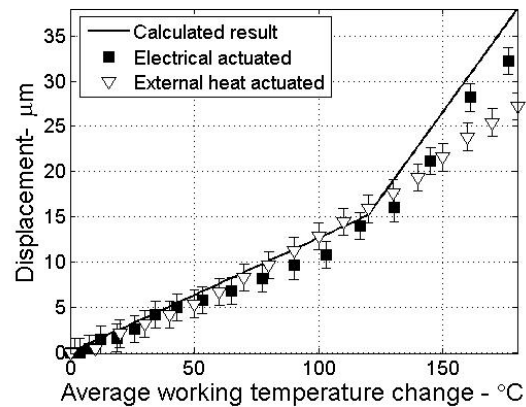
Figure 15. Sensing microgripper jaw displacement versus average working temperature

7. Conclusions

A novel sensing microgripper with dimensions of 490 µm long, 350 µm wide and 30 µm thick is presented which can be used to grasp an object with a diameter between 8 and 40 µm. It provides a jaws displacement up to 32 µm at only 4.5 V applied voltage, with a maximum average working temperature change of 176 °C.

The operation principle of the sensing microgripper based on silicon-polymer electrothermal actuator and piezoresistive force sensing cantilever is investigated based on FEM tool and classical mechanics analysis. The simulated and analysis results are met the experimental measurement. This simulation and analysis can be used for optimizing the mechanical structure of the design. Therefore, the characteristics of this sensing microgripper are such that manipulation of small objects will be more efficient, more accurate and with less fatigue than currently available grippers due to its large jaws displacement and force sensing sensitivity.

REFERENCES

[1] T. Chu Duc, G.K. Lau, J.F. Creemer, P.M. Sarro, "Electrothermal microgripper with large jaws displacement and integrated force sensors," J. Microelectromech. Syst., vol. 17, no. 6, pp. 1546-1555 2008.

[2] M.C. Carrozza, P. Dario, L. P. S. Jay, "Micromechanics in surgery", Transactions of the Institute of Measurement and Control, vol. 25, no. 4, pp. 309-327, 2003.

[3] N.D. Mankame, G.K. Ananthasuresh, "Comprehensive thermal modelling and characterization of an electro-thermal-compliant microactuator", J. Micromech. Microeng. vol. 11, pp. 452-462, 2001.

[4] Q.A. Huang, N.K.S. Lee, "Analysis and design of polysiliocn thermal flexure actuator", J. Micromech. Microeng. vol. 9, pp. 64-70, 1999.

[5] N. Chronis, L.P. Lee, "Electrothermally activated SU-8 microgripper for single cell manipulation in solution", J. MEMS, vol. 14, no. 4, pp. 857-863, 2005.

[6] T. Chu Duc, G.K. Lau, P.M. Sarro, "Polymer constraint effect for electrothermal bimorph microactuators", Appl. Phys. Lett., vol. 91, no. 10, pp. 101902-3, 2007.

[7] T. Chu Duc, J.F. Creemer, P.M. Sarro, "Lateral nano-Newton force-sensing piezoresistive cantilever for microparticle handling", J. Micromech. Microeng. vol. 16, pp. 102-106, 2006.

Development and Characterization of a Fiber Optic Accelerometer

Chun-Gon Kim [a,], Yeon-Gwan Lee [b], Byeong-Wook Jang [c]

[a] Dept. of Aerospace Engineering, KAIST
335 Gwahangno, Yuseong-gu, Daejeon, Korea, cgkim@kaist.ac.kr
[b] Dept. of Aerospace Engineering, KAIST
335 Gwahangno, Yuseong-gu, Daejeon, Korea, yeongwan@kaist.ac.kr
[c] Dept. of Aerospace Engineering, KAIST
335 Gwahangno, Yuseong-gu, Daejeon, Korea, jangbw@kaist.ac.kr

Abstract

Most accelerometers are composed of a mass, a spring, and a damper. The acceleration can be quantified from an equation of dynamic motion expressed in terms of the relative moving displacement. Therefore, if the moving displacement of a seismic mass is inferred from the output signals of a single-degree-of-freedom system, the acceleration can theoretically be obtained by a deformation response factor expressed in the relation between relative displacement and excited acceleration. A reflective grating panel-fiber optic sensor can measure the relative displacement by the movement of a grating panel attached to the seismic mass. The present study is part of an ongoing work to develop grating panel- fiber optic sensors for application in civil engineering. In order to fabricate an adequate probe based on the aforementioned sensing principle, microscopic rotation (< 0.007 degree) should be prevented for stable reflectivity. Therefore, this paper describes the optimum design of a mass-spring structure that features a large linear motion range of the leaf spring without rotation of the seismic mass. Finite element analyses were carried out for a *m-k* model of reflective grating-fiber optic sensor probe. The leaf springs were employed for strict linear motion and parametric studies on the design of the leaf spring were conducted. In order to lend flexibility to the leaf spring, it is divided into N equal parts (N= 3, 4, 5). Parametric studies were also carried out on the length of the seismic mass, the arm width, and the length of the leaf spring, as well as moment balancing design. Through comparison of the FEA results, the optimal design of the leaf spring was determined over the measurement range of acceleration and frequency within the linear elastic region of the leaf spring. Finally, the fabricated accelerometer was successfully tested at 13.5Hz excitation.

Key Words: Leaf Spring, Finite Element Analysis, Relative Moving Displacement, Accelerometer

1. Introduction

Single degree of freedom (SDOF) systems have been widely adapted in sensing probes for the measurement of acceleration, earthquake events, and tilt angles [1-4]. Particularly, a cantilever design was widely adapted as a spring. Because the minor lateral mode or rotation of the seismic mass

are typically permitted for normal operation in conventional capacitance and magnetic based sensor. However, under a sensing principle where a reflected signal from a reflective material of an object is exploited, microscopic rotation and lateral mode should be prevented for normal operation. In this regard, most SDOF systems in sensing probes required strict SDOF motion for high accuracy.

For enhancing the reliability of this sensing principle, advanced *m-k* model is necessary to ensure safe operation without lateral mode and rotation of proof mass. To this end, a leaf plate may be employed as a spring. A leaf spring which embedded a hole at center is particularly useful for providing linear motion of seismic mass. The hole is helpful to support the mass for strict linear motion. To apply this model, an optimal pattern for the leaf spring should be constructed through a parametric study.

This paper describes the optimum design of a mass-spring structure that features a large range of linear motion of the leaf spring and no rotation of the seismic mass. Static and dynamic analyses were conducted for optimal leaf spring pattern and predicting the probe performance. A leaf spring was employed for strict single degree of motion, and parametric studies on the design of the leaf spring were conducted. First, in order to provide flexibility to the leaf spring, it is divided into N equal parts (N= 3, 4, 5). Parametric studies were then carried out on the length of the seismic mass, the arm width, and the length of the leaf spring, as well as the moment balancing design. Through a comparison of the FEA results, the optimal design of the leaf spring was determined over the measurement range of acceleration and frequency within the linear elastic region of the leaf spring. Finally, the best pattern for the leaf spring was developed using commercial software, ABAQUS 6.7. The results of the FEA were applied to a fabrication design of leaf spring. After

assembly of fabricated each components, acceleration test was implemented.

2. Finite Element Analysis (FEA)

This study was conducted to determine an adaptable sensor structure that has a minimal torsion effect and lateral mode and to improve the linear range to provide a wide measurement window.

2.1. Description of FEA model

Figure 1 shows the configuration of the finite element (FE) analytical model (63,813 nodes and 54,559 elements) of a m-k system that includes a grating panel that induces variation of the reflected light. The sensing probe is composed of two leaf springs (element type S4R), a seismic mass (element type C3D8R), and the grating panel (element type S4R).

Using this m-k model, finite element analyses were performed to determine the optimal design for the sensing probe of the reflecting grating-optical fiber sensor.
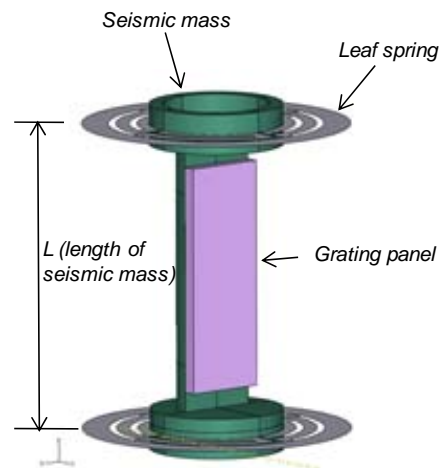

Figure 1. Configuration of detailed m-k model at the FE model

2.2. Description of parameters

The leaf spring has a circular shape, as shown in Fig. 2. Control variables were an external radius of 10mm and an internal radius of 5mm. The leaf spring was divided

into N equal parts to lend flexibility to the spring (N= 3, 4, 5). The length of the seismic mass, L, was varied with the aim of providing a larger measurement frequency range and reduced rotation of the seismic mass. The arm width of the leaf spring, W, and the gap between each part, G, were considered for adaptable spring stiffness, minimizing torsion, and maximizing the range of linear motion. In addition, a moment balancing design, that is, positive moments offset negative moments, was employed to minimize rotation of the seismic mass. Two strategies in particular were adopted for the structural configuration: reversing the direction of the top and bottom leaf springs and employing the moment-offsetting design in each leaf spring. Lastly, the arm length of the leaf spring was varied with the aim of obtaining greater sensitivity and a larger linear motion range within the linear elastic region of the leaf spring, as shown in Table 1.

Table 1 Description of design parameters

Parameter	Objective	Method
N (number of equal parts at one leaf spring)	Flexibility	Leaf spring is divided into N equal parts (N=3,4,5)
L (length of the seismic mass)	Larger measurement frequency range (high natural frequency)	Mass length is reduced
W (arm width of leaf spring)	Adaptable spring stiffness	Minimize the torsion effect and maximize the linear motion range
G (gap between the parts)		
AL (arm length)	Higher sensitivity and larger linear motion range within linear elastic region of leaf spring	Arm length varied. AL was defined the number of arm line.
Moment balancing	Prevent microscopic rotation (< 0.007 °)	Reverse direction of the top and bottom leaf spring in each leaf spring, moment-offsetting
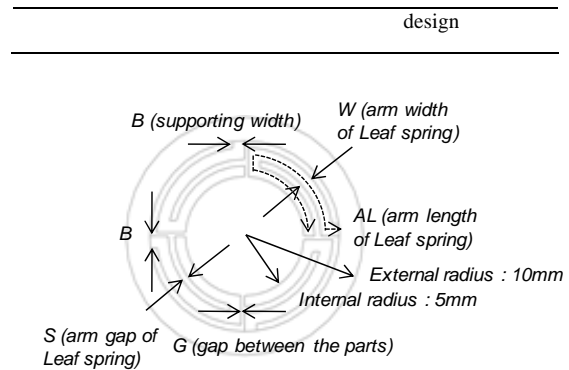
Figure 2. Schematic illustration of detailed parameters at the leaf spring

2.3. Conditions of FEA

The materials of the seismic mass, leaf spring, and grating panel were assumed to be aluminum (7075), copper beryllium alloy (C17200), and quartz, respectively. Table 2 shows the material properties applied in the FEA.

Table 2 Material properties used for FEA

	Aluminum (7075)	Copper Beryllium Alloy (C17200)	Quartz (Fused)
Poisson's ratio	0.33	0.30	0.17
Young's modulus(Gpa)	71.7	127.5	74
Density(kg/m^3)	2810	8250	2200

2.4. Static and dynamic analysis

Verification models for the effects of the aforementioned parameters were designed. Figure 3 describes the eight FE models for verification of N, AL, and moment balancing. The results of the eight model designs were provided in Figure 4. Figure 4 (a) shows the F-S curve of the leaf spring and Figure 4 (b) shows the rotation angle of the seismic mass.

(a) TR   (b) FO   (c) FO-1   (d) FO-2

(e) FO-4   (f) FI   (g) FO-7   (h) FO-11
Figure 3. The FEA models
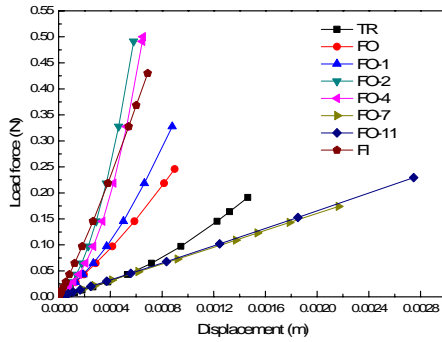
(a) F-S curve
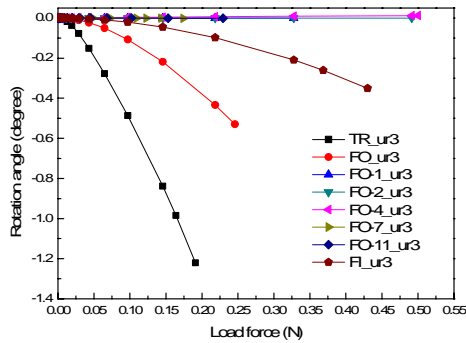
(b) Rotation angle of seismic mass
Figure 4. The FEA result from
nonlinear static analysis

In terms of the linear motion range and sensitivity, models FO-7 and FO-11, shown in Figs. 3 (g) and (h), respectively, provided the best performance due to their low spring coefficient (0.080 and 0.083 [N/mm]). Consequently, the pattern of FO-11 is the best thanks to its rotation angle of 0.00049 [degrees] within the linear elastic region of the leaf spring.

2.5. Summary of FEA results

The evaluation criteria were lateral mode and rotation angle, range of linear motion, and frequency. The results of the FE analysis within the linear elastic range of the leaf spring are summarized in Fig. 5.
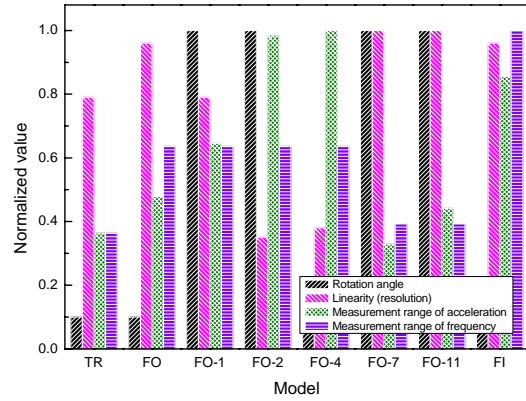
Figure 5. Summary of FEA results based on
four criteria

It was found that the moment balancing design of FO-2 should be employed. In addition, to obtain larger linear motion and high sensitivity, the AL should be controlled according to the designs of FO-7 or FO-11.

3. Acceleration test

3.1. Acceleration test setup

The basic configuration of an acceleration transducer is a mass-spring system housed in a sensor case to cause a seismic mass effect. To evaluate the acceleration, a prototype sensor was fabricated, as shown in Fig. 6. The sensor case is attached to a vibrating component whose motion is inferred from the relative motion between the mass and the sensor case. Based on this design concept, an acceleration test was performed. Before the test, the natural frequency and damping ratio of the sensor head were measured by a fast Fourier transform (FFT) and the logarithmic decrement method under natural oscillation. The sensor head specifications are shown in Table 3.

Table 3. Specifications of sensor head

Natural frequency (*Hz*)	13.5
Damping ratio	0.002246
Grating period (μm)	400
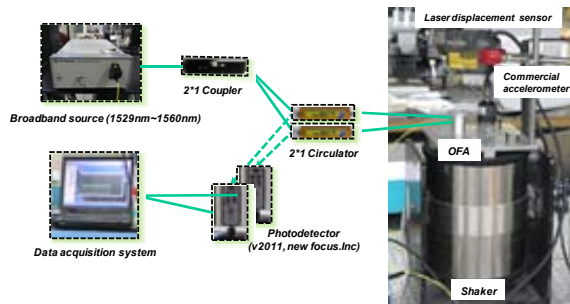
Figure 6. Configuration of the experimental setup

In the experiment, an EDFA (Erbium doped fiber amplifier, 1529 *nm*~1560 *nm*) was used as a light source. The beam reflection on the grating panel is coupled into two optical fibers fixed on the sensor case. Reflective light intensity was measured using the photo detector.

The light intensity signals at the two observing points are periodic sine wave functions of displacement with a phase difference in the quadrature with respect to each other. Hence, through signal processing, the measured relative displacement can be converted into the sensor's acceleration.

3.2. Estimation of acceleration

From the results of the acceleration test, a method of estimating the acceleration using grating panel-optical fiber sensor is suggested. Figure 7 shows the acceleration versus time at an excitation of 13.5Hz, produced via a shaker (VTS100, VTS Co.). The obtained data from optical fiber sensor

(OFA) was compared with the commercial accelerometer (393B12, PCB Co.), as shown in the bottom graph. Thus, the proposed reflection type grating panel-optical fiber sensor shows possibility of an accelerometer through calibrations.
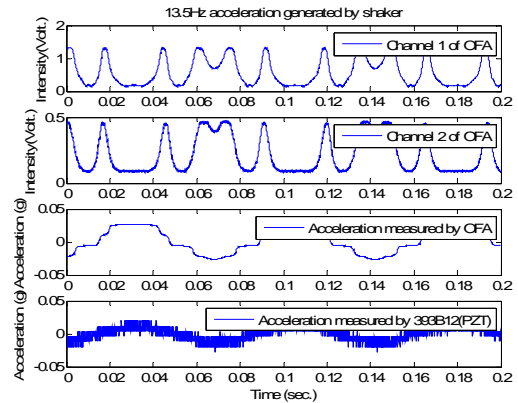
Figure 7. Comparison of a commercial accelerometer and novel reflection type optical fiber accelerometer

4. Summary

This paper presents the optimal design of a novel fiber optic sensor structure composed of a leaf spring and seismic mass. Ultimately, this m-k model is intended for application to grating panel- fiber optic sensors to monitor the acceleration of civil engineering structures. The reflected optical signal of the sensor is influenced by the motion of the seismic mass. Therefore, the parameters of AL, N, and moment balancing were studied via a FEA. Through static and dynamic analyses, specifications of a virtual accelerometer with a leaf spring pattern were inferred. Based on the results of the FEA, the optimum design of the leaf spring pattern was determined in terms of providing maximal sensitivity to motion of the reflective grating and realizing a reflective grating-fiber optic sensor. From the acceleration test, the possibility of estimating acceleration using the grating panel-optical fiber sensor was verified at 13.5 Hz excitation. Using the proposed sensor system it was demonstrated that the output signals

reflected by the grating panel could be used for an accelerometer.

Acknowledgements

5. References

1.   Wu Zhaoxia, Song Aijuan, Yan Dongmei, Li Zhiquan, "Distributed FBG Accelerometer based on signal Reconstruction," *Proc. of SPIE*, Vol. 7127, 712704, 2008.

2.   M. D. Todd, G. A. Johnson, B. A. Althouse, and S. T. Vohra, "Flexural beam-based fiber bragg grating Accelerometers," *IEEE photonics technology letters*, Vol.10, No.11, Nov. 1998.

3.   C. Z.shi, N. Zeng, H. L. Ho, C. C. chan, M. Zhang, W. Jin, Y.B. Liao, "Cantilever optical vibrometer using fiber bragg grating," *Opt. Eng.* 42(11) 3179-3181, Nov. 2003

4.   D H Kim, "A fiber-optic tiltmeter system based on the moiré-fringe effect," *Measurement Science and Technology*, 20, 2, 025203, 2009.

Mô hình, mô phỏng tính toán hệ thống chuyển đổi năng lượng sóng biển dạng phao nổi

Đặng Thế Ba[1], Đinh Văn Mạnh[2] và Phạm Thị Minh Hạnh[2]

*[1]Trường Đại học Công nghệ, Đại học Quốc gia Hà Nội, 144 Xuân Thủy, Cầu Giấy, Hà Nội;
email:badt@vnu.edu.vn
[2]Viện Cơ học, 264 Đội Cấn, Ba Đình, Hà Nội*

Tóm tắt:

Nhu cầu phát triển năng lượng tái tạo là một thực tế, trong đó có nguồn năng lượng sóng biển. Báo cáo trình bày một số kết quả ban đầu về nghiên cứu chuyển đổi năng lượng sóng biển. Từ các nghiên cứu tham khảo về tiềm năng năng lượng sóng biển Việt Nam và tìm hiểu phân tích một số nguyên lý chuyển đổi năng lượng sóng, mô hình, mô phỏng tính toán hệ thống chuyển đổi năng lượng sóng biển dạng phao nổi đã được lựa chọn nghiên cứu xây dựng. Mô hình mô phỏng quá trình chuyển đổi năng lượng sóng thông qua tác dụng gây ra chuyển động đứng của phao và cơ cấu chuyển đổi trong phao đã được xây dựng. Chương trình tinh đã được xây dựng và sử dụng để tính toán khảo sát một số tính năng quan trọng của thiết bị. Khả năng chuyển đổi năng lượng sóng cho một số cấu hình phao và điều kiện sóng cũng đã được tính toán. Các kết quả tính toán và chương trình có thể sử dụng làm cơ sở cho tính toán thiết kế, chế tạo các thiết bị thử nghiệm và phát triển tiếp theo.

Từ khoá: năng lượng sóng, chuyển đổi năng lượng sóng, mô phỏng phao chuyển đổi năng lượng sóng

1. Giới thiệu

Năng lượng truyền thống hiện đang tăng về giá cả và cạn kiệt về nguồn cung. Nghiên cứu sử dụng năng lượng mới, tái tạo là tất yếu, đã và đang được quan tâm và phát triển mạnh trên thế giới.

Các nghiên cứu về năng lượng sóng đang được tiến hành ở nhiều hướng: Nghiên cứu đánh giá tiềm năng năng lượng sóng tại các khu vực; Nghiên cứu lý thuyết, thực nghiệm, thử nghiệm chuyển đổi năng lượng sóng.

Các nghiên cứu chuyển đổi năng lượng sóng hiện đang được phát triển mạnh trên thế giới với nhiều loại nguyên lý được đề xuất. Tuy nhiên đa phần vẫn đang ở giai đoạn thử nghiệm [3,4].

Ở nước ta, nghiên cứu sử dụng năng lượng cũng đã bắt đầu được quan tâm. Đã có một số nghiên cứu về tiềm năng năng lượng sóng cũng như nghiên cứu chế tạo thiết bị được thực hiện [1]. Kết quả nghiên cứu tiềm năng cho thấy nguồn năng lượng này ở nước ta cũng không thực sự lớn, chỉ có một số khu vực ngoài khơi biển Miền Trung có tiềm năng đáng kể để khai thác. Tuy nhiên bờ biển

nước ta dài, nhu cầu sử dụng điện cho những hoạt động ven biển, trên biển và hải đảo là rất lớn trong khi nguồn cấp từ đất liền thì gặp nhiều khó khăn. Vì vậy nghiên cứu sử dụng nguồn năng lượng sóng cũng như năng lượng biển là thực dự có ý nghĩa. Các nghiên cứu chuyển đổi năng lượng sóng cũng đã được thực hiện bởi một vài dự án tại Viện công nghệ giao thông [2]; Viện Cơ Khí. Tuy nhiên các nghiên cứu này chỉ mới dừng ở việc thử nghiệm chế tạo theo các mẫu đã có sẵn mà chưa có những nghiên cứu tính toán đầy đủ.

Báo cáo này trình bày nghiên cứu bước đầu về tính toán mô phỏng thiết bị chuyển đổi năng lượng sóng dạng phao. Thiết bị dạng này có ưu điểm là cơ động, khắc phục được nhiều khó khăn kỹ thuật so với các thiết bị dạng khác. Những kết quả mô phỏng là tiền đề tốt cho cho tính toán thiết kế, chế tạo thử nghiệm trong các bước tiếp theo.

2. Năng lượng sóng và chuyển đổi

2.1 Năng lượng sóng

Các tính toán [3] chỉ ra rằng nguồn năng lượng nhận được từ sóng biển là rất lớn và tổng năng lượng sóng có thể lên tới 2.5 terawat. Tuy nhiên mật độ của nó thì phân bố khác nhau ở các vùng khác nhau. Ở những vùng biển gần xích đạo có mật độ nhỏ, cỡ 10-20kW/m (trên một mét đỉnh sóng). Những vùng biển ở gần hai cực có mật độ lớn hơn, cỡ 60-80kW/m [3] (trong đó các quốc gia có tiềm năng lớn như Ai-len, Thổ-Nhĩ-Kỳ, Ca-na-đa...). Với hiểu biết và công nghệ hiện tại, tổng năng lượng sóng có thể khai thác được vào khoảng 0.5 TW (tiêu thụ năng lượng thế giới năm 2009 khoảng 15 TW).

Ở nước ta, các nghiên cứu khảo sát cho thấy [1], tiềm năng năng lượng sóng khoảng vài chục kW/m. Khu vực biển nam Trung bộ là có tiềm năng nhất, mật độ trung bình năm khoảng 40kW/m. Các khu vực khác tiềm năng không lớn lắm, trung bình từ 10-20 kW/m. Về mặt thời gian, phân bố năng lượng sóng không đều theo các tháng. Khu vực biển miền Trung, năng lượng sóng trung bình theo tháng bé nhất chỉ khoảng 5-10 kW/m. Trong khi tháng lớn nhất có khi đến 100kW/m. Đây cũng là một trong những khó khăn trong việc khai thác sử dụng năng lượng sóng ở nước ta. Khu vực tiềm năng nhất ở nước ta là ngoài khơi tỉnh Bình Thuận.

2.2 Chuyển đổi năng lượng sóng

Qua nghiên cứu nguyên tắc hoạt động của các loại thiết bị chuyển đổi năng lượng sóng đã và đang được phát triển trên thế giới, có thể nhận thấy một nguyên tắc cơ bản như sau: Thiết bị chuyển đổi năng lượng sóng thường có bốn bộ phận chính sau:

– Bộ phận ổn định với chuyển động tương đối của sóng biển.

– Bộ phận chịu tác động của sóng, nó được nối với bộ phận ổn định qua bộ phận thu năng lượng sóng. Bộ phận chịu tác động của sóng phải có khả năng chuyển động cùng với chuyển động của sóng và bị ràng buộc với bộ phận thu năng lượng sóng.

– Bộ phận thu năng lượng sóng chuyển đổi năng lượng thu được từ bộ phận chuyển động thành các dạng năng lượng có thể sử dụng hoặc chuyển tải được.

– Bộ phận lưu trữ hoặc chuyển tải và đưa vào sử dụng năng lượng sóng.

Sơ đồ nguyên lý của một số loại của một số thiết bị chuyển đổi năng lượng sóng mô tả trên Hình 1.

Tuỳ thuộc vào mục đích, điều kiện sóng, vị trí lắp đặt mà các bộ phận có cấu tạo khác nhau và sử dụng các nguyên lý hoạt động khác nhau. Tuy nhiên loại thiết bị dạng phao nổi tỏ ra có ưu điểm hơn cả do tính cơ động trong lắp đặt, đơn giản trong yêu cầu một công trình biển, sử dụng nguyên lý hoạt động đơn giản…

a) b)

c) d)
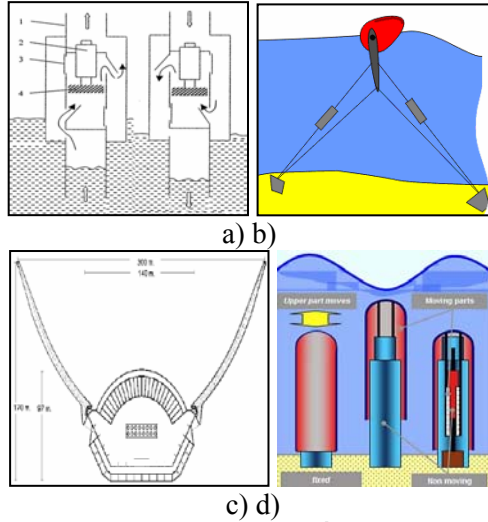
a)Dao động cột nước trong ống; b)Dao động phao; c)Đập nước nổi; d)Co bóp theo áp lực

Hình 1. Một số nguyên lý cơ bản

3. Mô hình và tính toán mô phỏng thiết bị chuyển đổi năng lượng dạng phao nổi

3.1 Cấu tạo và nguyên lý

Cấu tạo cơ bản của thiết bị mô tả trong Hình 2, gồm các bộ phận chính sau:

− Phao nổi bên trong chứa tổ hợp phát điện.

− Tổ hợp phát điện gồm các bình chứa áp lực, đường ống, turbine, máy phát.

− Phao được nối cứng với một lồng hình trụ phía dưới, mở hai đầu. Dưới tác dụng của sóng phao và lồng sẽ chuyển động cùng nhau.

− Đĩa thu năng năng lượng dạng piston nằm giữa lồng, chuyển động dọc lồng.
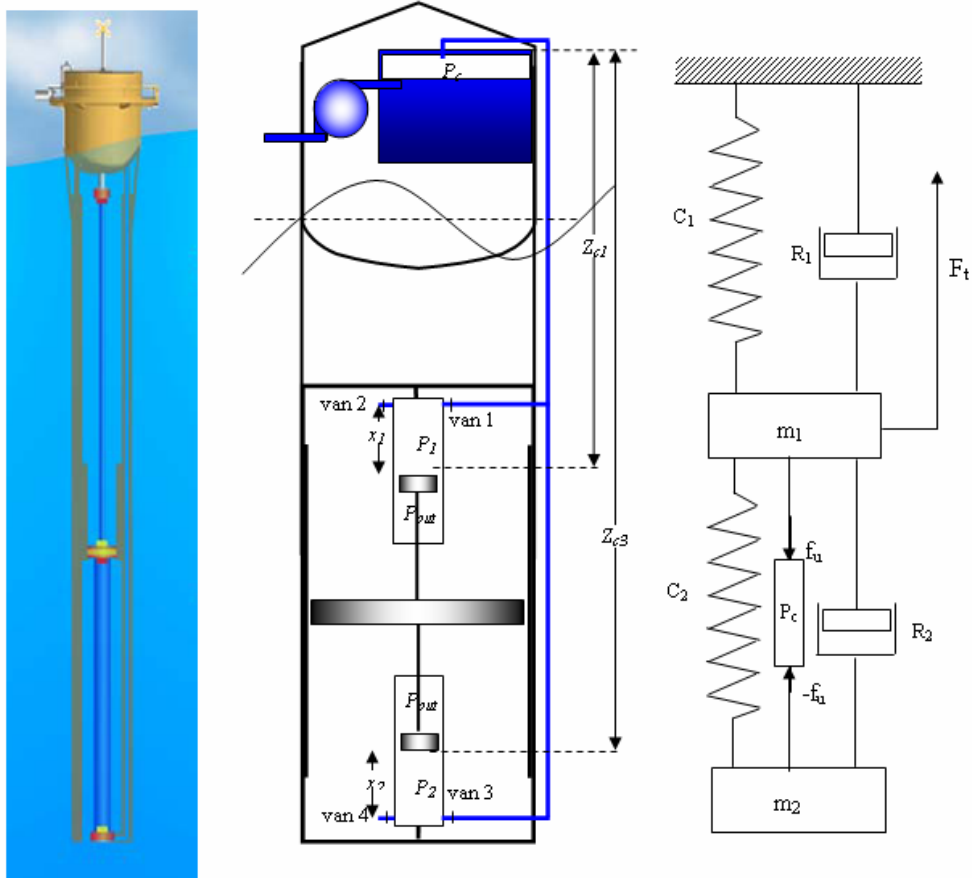
Hình 2: Sơ đồ cấu tạo và mô hình hoá hệ thống

− Hai bơm thể tích hoạt động ngược chiều nhau 1 và 2. Một đầu bơm nối với đĩa, đầu kia nối với lồng, chuyển động tương đối của đĩa và lồng sẽ làm hai bơm này

hoạt động để cấp nước cho bình chứa áp lực.

– Hệ thống ống dẫn để dẫn nước từ bơm lên bể nước áp lực và ngược lại.

– Bể tích nước áp lực chứa một phần nước và phần trên là khí. Do khí có tính nén được nên được sử dụng như là công cụ điều áp làm cho dòng chảy qua turbine được ổn định hơn.

– Turbine phát điện sử dụng nguồn nước áp lực trong bình áp.

– Các hệ thống điều khiển như điều khiển van cấp nước turbine, điều chỉnh ổn áp…

Thiết bị sẽ làm việc như sau: Dưới tác dụng của thành phần lực theo chiều đứng của sóng biển, phao sẽ chuyển động lên xuống cùng với lồng hình trụ nối cứng với phao. Trong trong khi dưới tác dụng lên đĩa, đã được thiết kế sao cho chu kỳ chuyển động của đĩa lệch pha với chuyển động của lồng, kéo 2 bơm chuyển động và đẩy nước vào bình chứa áp lực qua van 1 và 2 (ở 2 nửa chu kỳ, quá trình hút của bơm này là quá trình đẩy của bơm kia), nước áp lực sau đó được xả cấp cho turbine để phát điện. Điện được điều chỉnh ổn định tương ứng theo nhu cầu sử dụng.

Để hệ thống hoạt động hiệu quả, các thông số cấu tạo của thiết bị cần được tính toán và lựa chọn một cách tối ưu, trong đó hệ thống thủy động lực học cấp nước vào bình áp lực đóng vai trò quan trọng.

3.2 Mô hình hoá và mô phỏng

a) Sóng biển

Sóng biển thực rất phức tạp, để đơn giản, ở đây chỉ sử dụng các kết quả của lý thuyết sóng tuyến tính trong vùng có độ sâu lớn. Khi đó phương trình sóng có thể viết dạng:

$$\eta(t) = \eta_a \cos(\omega t - kx) \qquad (1)$$

Trong đó $\eta(t)$ là độ cao sóng, η_a là biên độ, ω là tần số sóng, k là số sóng.

b)Chuyển động của phao nổi

Thiết bị được thiết kế để thu năng lượng do chuyển động lên xuống (heavy) của phao dưới tác động của sóng. Vùng đặt thiết bị có độ sâu đủ lớn, neo ổn định và chuyển động lên xuống theo chu kỳ sóng, nên chỉ xét chuyển động theo phương thẳng đứng của hệ thống.

Đối với phao nổi, kích thước nhỏ (bán kính <0,2 bước sóng), phương trình chuyển động của thành phần thẳng đứng có dạng:

$$m_{b1}\ddot{s}_b(t) = F_{e,b}(t) + F_{r,b}(t) + F_{b,b}(t)$$
$$+ F_{b,v}(t) + F_{b,f}(t) + F_{b,u}(t) \ (2)$$
$$+ F_{f,db}(t)$$

Trong đó m_{b1} là khối lượng của phao, $\ddot{s}_b(t)$ là gia tốc chuyển dịch đứng của phao, $F_{e,b}(t)$ là lực kích thích theo chiều đứng của sóng tới, $F_{r,b}(t)$ là lực theo chiều đứng do sóng phát xạ, $F_{b,b}(t)$ là tổng lực đẩy thủy tĩnh và lực trọng trường, $F_{b,v}(t)$ là lực cản nhớt, $F_{b,f}(t)$ là lực ma sát, $F_{b,u}(t)$ là lực ngoài do cơ cấu thu năng lượng nối với phao, $F_{f,db}(t)$ là lực ma sát do cơ cấu hoạt động của đĩa trong lồng phao.

Trong trường hợp phao có cấu tạo hình trụ tròn, đường kính $2r$, chiều dài không kể đáy $2l$, trong đó phần chìm dưới mặt nước khi tĩnh là l, khối lượng m_{b1}, phần đáy có cấu tạo nửa hình cầu bán kính r, tiết diện phao là S_{wb}. Biểu thức các lực có thể viết cụ thể như sau [11]:

– Lực tác động theo chiều đứng của sóng vào phao:

$$F_{e,b}(t) = \exp(-kl)\kappa_{33}\rho g S_{wb}\eta_a \cos(\omega t) \ (3)$$

– Lực sóng tán xạ $F_{r,b}$ có dạng:

$$F_{r,b} = -m_{33}\ddot{s}_b(t) - R_{33}\dot{s}_b(t) \qquad (4)$$

– Lực thuỷ tĩnh có dạng:

$$F_{b,b} = -S_{b,b}s_b(t) \qquad (5)$$

– Lực cản của nước:

$$F_{b,f} + F_{b,v} = -(R_{b,f} + R_{b,v})\dot{s}_b(t)$$
$$- 0.5 C_B \rho A_B |\dot{s}_b(t)|\dot{s}_b(t) \qquad (6)$$

trong đó khối lượng kèm của phao, $m_{33} = (2\pi/3)r^3\rho\mu_{33}$; μ_{33} là hệ số khối lượng kèm không thứ nguyên phụ thuộc vào số sóng, bán kính phao, độ dài phao và độ sâu của nước biển; Hệ số lực cản kèm, $R_{33} = \exp(-2kl)\omega\rho(2\pi/3)a^3\varepsilon_{33}$; ε_{33} là hệ số cản kèm không thứ nguyên Havelock phụ thuộc vào số sóng và bán kính phao; κ_{33} là hệ số lực kích thích không thứ nguyên của sóng tới; Hệ số lực nâng, $S_{b,b} = \pi\rho g r^2$, $R_{b,f}$ là hệ số cản ma sát nước lên lồng, $R_{b,v}$ là hệ số cản nhớt lên lồng phao, $R_{b,s} = 0.5 C_B \rho A_B |\dot{s}_b(t)|$ là hệ số cản lên thiết diện lồng, C_B là hệ số, A_B diện tích thiết diện thành lồng [11].

– Áp lực của bơm lên lồng:

$$F_{b,u} = -A_p[(P_1 - P_{out1}) + (P_2 - P_{out2})] \quad (7)$$

– Lực do 2 lò xo của 2 bơm 1 và 2 tác động lên phao

$$F_c = -2c(s_b(t) - s_d(t)) \quad (8)$$

trong đó $s_d(t)$ là chuyển dịch của đĩa

– Lực ma sát của đĩa lên lồng phao

$$F_{f,bd} = -R_{d,b}(\dot{s}_b(t) - \dot{s}_d(t)) \quad (9)$$

– Lực nâng thực tác dụng lên phao ở thời điểm cân bằng là hiệu của lực nâng lên phao và trọng lượng của phao (cả lồng):

$$F_{m,b} = g(\rho V_b - m_{b1}) \quad (10)$$

trong đó V_b là thể tích chìm dưới mặt nước của phao khi ở vị trí cân bằng, m tổng khối lượng của phao và cơ cấu nối cứng với phao. Lực này cân bằng với lực nâng tác dụng lên đĩa (và các cơ cấu nối cứng với đĩa).

Thay biểu thức các lực (3)-(10) vào phương trình (2), phương trình chuyển động của phao viết được:

$$m_b \ddot{s}_b(t) + R_b \dot{s}_b(t) + (S_b + 2c)s_b(t) =$$
$$F_{e,b}(t) + R_{d,b}\dot{s}_d(t) + 2cs_d(t) \quad (11)$$
$$- A_p[(P_1 - P_{out1}) + (P_2 - P_{out2})]$$

trong đó $m_b = m_{b1} + m_{33}$ là tổng khối lượng phao và khối lượng kèm, $R_b = R_{33} + R_{b,f} + R_{b,v} + R_{b,s} + R_{d,b}$ là tổng hệ số lực

cản lên phao, $F_{e,b}(t)$ là lực tác động của sóng lên phao, $\dot{s}_d(t)$ là vận tốc của đĩa.

c) Chuyển động của đĩa trong lồng

Đĩa chuyển động trong lồng của phao, nối với phao qua các bơm. Phương trình chuyển động của đĩa cũng có dạng tương tự như phương trình (11) với ký hiệu chỉ số dưới là chữ d thay vì chữ b. Các lực tác dụng lên đĩa gồm:

– Lực tác dụng của phao lên đĩa thông qua hai bơm

$$F_{d,u} = A_p[(P_1 - P_{out1}) + (P_2 - P_{out2})] \quad (12)$$

– Lực khối lượng kèm

$$F_{m,d} = m_{21}\ddot{s}_b(t) \quad (13)$$

– Lực ma sát lên thành lồng của phao và của xylanh trong bơm 1 và 2

$$F_{f,bd} = -R_{d,b}(\dot{s}_d(t) - \dot{s}_b(t)) \quad (14)$$

– Lực do 2 lò xo của 2 bơm 1 và 2

$$F_c = 2c(s_b(t) - s_d(t)) \quad (15)$$

– Lực cản nhớt của nước lên đĩa có dạng [11]

$$F_{drag,d} = -0.5 C_D \rho A_D |\dot{s}_d(t)|\dot{s}_d(t) \quad (16)$$

– Lực nâng tác dụng lên đĩa

$$F_{d,b} = -S_{d,b}s_d(t) \quad (17)$$

trong đó $S_{d,b} = \pi\rho g r_d^2 - m_d$

Ở trạng thái cân bằng, đĩa được treo ổn định với lực nổi của phao

$$F_{m,d} = -g(\rho V_b - m_b)$$

Cuối cùng phương trình chuyển động của đĩa viết được ở dạng:

$$(m_d + m_{21,d})\ddot{s}_d(t) + R_{d,b}\dot{s}_d(t) + 2cs_d(t) = \\ F_{drag,d} + F_{u,d} + R_{d,b}\dot{s}_b(t) + 2cs_b(t) \quad (18)$$

trong đó c là độ cứng của lò xo trong bơm ống 1 và 2.

d) Dòng chảy trong các bơm

– Quá trình hút trong bơm 1 [8, 9, 10]

$$\frac{P_1}{\gamma} = \frac{P_{11}}{\gamma} - [z_{h11} + \frac{v_{xl}^2}{2g} + \sum h_{w11} + h_{qt11}] \quad (19)$$

– Quá trình đẩy trong bơm 1

$$\frac{P_1}{\gamma} = \frac{P_c}{\gamma} + [z_{c1} + \frac{v_{xl}^2}{2g} + \sum h_{w12} + h_{qt12}] \quad (20)$$

– Quá trình hút trong bơm 2

$$\frac{P_2}{\gamma} = \frac{P_{21}}{\gamma} - [z_{h21} + \frac{v_{xl}^2}{2g} + \sum h_{w21} + h_{qt21}] \quad (21)$$

– Quá trình đẩy trong bơm 2

$$\frac{P_2}{\gamma} = \frac{P_c}{\gamma} + [z_{c3} + \frac{v_{xl}^2}{2g} + \sum h_{w22} + h_{qt22}] \quad (22)$$

trong đó P_1, P_2 là áp suất trong buồng bơm 1 và 2 tương ứng, P_{11} và P_{21} là áp suất nước tại phía ngoài van hút 2 và 4, z_{c1} và z_{c3} là độ cao của bình chứa so với van 1 và van 3, z_{h11} và z_{h21} là độ cao từ mặt piston 1 và 2 đến mặt ngoài van hút 2 và 4 tương ứng, P_c là áp suất trong bình tích nước áp lực, v_{xl} là vận tốc chuyển động tương đối của xylanh, $\sum h_{wij}$ là tổn thất dọc ống (bao gồm tổn thất cục bộ qua van và tổn thất dọc đường). h_{qt} là tổn thất quán tính.

Đối với các tổn thất dọc đường, có thể tính được như sau [8, 9, 10]:

$$\sum h_{11} = h_{van2} \; ; \; \sum h_{12} = h_{van1} + h_{ong1} \; ;$$
$$\sum h_{21} = h_{van4} \; ; \; \sum h_{22} = h_{van3} + h_{ong2}$$

– Tổn thất cục bộ qua van 1 (van hút bơm 1)

$$h_{van1} = \zeta \frac{v_{xl1}^2 D_{xl}^4}{2gD^4} \quad (23)$$

– Tổn thất cục bộ qua van 2 (van đẩy bơm 1)

$$h_{van2} = \zeta \frac{v_{xl1}^2 D_{xl}^4}{2gD^4} \quad (24)$$

– Tổn thất cục bộ qua van 3 (van hút bơm 2)

$$h_{van3} = \zeta \frac{v_{xl2}^2 D_{xl}^4}{2gD^4} \quad (25)$$

– Tổn thất cục bộ qua van 4 (van đẩy bơm 2)

$$h_{van4} = \zeta \frac{v_{xl2}^2 D_{xl}^4}{2gD^4} \quad (26)$$

– Tổn thất dọc ống 1 (chảy từ sau van 2 lên bể chứa áp lực)

$$h_{ong1} = \lambda_t \frac{v_{xl}^2 D_{xl}^4}{2gD^4} \frac{l_1}{D} \quad (27)$$

– Tổn thất dọc ống 2 (chảy từ sau van 4 vào bể chứa áp lực)

$$h_{ong2} = \lambda_t \frac{v_{xl}^2 D_{xl}^4}{2gD^4} \frac{l_2}{D} \quad (28)$$

– Tổn thất cục bộ qua van 5 (vào bình)

$$h_{van5} = \zeta \frac{v_{xl}^2 D_{xl}^4}{2gD^4} \quad (29)$$

Tương tự các tổn thất quán tính được tính như sau :

– Tổn thất quán tính trong bơm 1

$$h_{qt11} = \frac{1}{g}(\frac{A_{p1}}{A_1}l_1 + x_1)(\ddot{s}_b(t) - \ddot{s}_d(t)) \quad (30)$$

– Tổn thất quán tính trong bơm 2

$$h_{qt21} = \frac{1}{g}(\frac{A_{p2}}{A_2}l_2 + x_2)(\ddot{s}_b(t) - \ddot{s}_d(t)) \quad (31)$$

trong đó v_{xl1} và v_{xl2} là vận tốc xylanh trong bơm 1 và 2 tương ứng; D là đường kính ống; D_{xl} đường kính xy lanh; λ_l hệ số trở lực đường ống; l_1 và l_2 là độ dài đường ống 1 và 2 tương ứng; ζ là hệ số trở lực qua van; A_{p1}, A_{p2} là thiết diện bơm 1 và 2; A_1, A_2 là thiết diện ống 1 và 2; x_1, x_2 là vị trí của piston tính từ vị trí xuất phát phía van xả, g là gia tốc trọng trường.

e) Áp suất bình chứa

Bình chứa được cấu tạo là một hình trụ độ cao l_t, bán kính r_t. Ban đầu có mực nước đến vòi ra turbine độ cao h_t. Khi nước được bơm vào bình và dâng lên quá độ cao đặt van xả vào turbine lúc đó nước mới được mở để cấp vào turbine.

Bộ phận điều khiển sẽ được sử dụng để điều chỉnh giữ ổn định ở áp suất trung bình P_c. Như vậy lưu lượng trung bình qua turbine bằng lưu lượng trung bình do 2 bơm cấp theo thời gian. Dòng chảy vào bình được xác định là Q do bơm, với áp suất giả định không đổi P_c. Giá trị P_c xác định để cấu hình đạt hiệu quả chuyển đổi cao nhất.

f) Dòng chảy và năng lượng qua turbine

– Cột áp turbine

$$H = (Z_t + \frac{P_c}{\gamma} + \frac{v_{t1}^2}{2g}) - (Z_{t2} + \frac{P_a}{\gamma} + \frac{v_{t2}^2}{2g}) \quad (32)$$

– Lưu lượng qua turbine

$$v_{t1} = v_{t2}\frac{A_2}{A_1} \quad (33)$$

– Công suất turbine

$$N_{tb} = \eta_{tb}9.81QH \quad (34)$$

trong đó Z_{t1} là độ cao của đầu vào turbine, Z_{t2} là độ cao đầu ra turbine, v_{t1} và v_{t2} là vận tốc nước tại đầu vào và đầu ra của turbine, P_c là áp suất ở đầu vào turbine và là áp suất bình chứa, P_a là áp suất không khí, $Q = v_{t2}A_2$ là lưu lượng xả nước qua turbine A_1 và A_2 là diện tích mặt cắt ống trước và sau turbine, N_{tb} công suất turbine, η_{tb} là hiệu suất turbine, h_{wt} tổng tổn thất dọc ống vào và ra turbine.

g) Hệ phương trình chuyển động

Sau khi đưa hết các biểu thức lực vào các phương trình mô tả chuyển động của phao và đĩa, hệ phương trình chuyển động được viết lại như sau (2 trạng thái được phân biệt bởi chuyển động tương đối giữa phao và đĩa):

– Quá trình hút trong bơm 1, đẩy trong bơm 2

$$m_b\ddot{s}_b(t) + (R_b + R_{d,b})\dot{s}_b(t) + (S_b + 2c)s_b(t)$$
$$= F_{e,b}(t) + 2cs_d(t) + R_{d,b}\dot{s}_d(t) - A_p(P_c + \rho g z_c) \quad (35)$$
$$- A_p\rho[(\dot{s}_b(t) - \dot{s}_d(t))^2 + (\frac{3\xi}{2} + \lambda\frac{l_2}{D})\frac{D_{xl}^4}{D^4})$$
$$+ (\frac{A_{p1}}{A_p}l_2 + 2l_0)(\ddot{s}_b(t) - \ddot{s}_d(t))]$$

$$(m_d + m_{21,d})\ddot{s}_d(t) + R_{d,b}\dot{s}_d(t) + 2cs_d(t)$$
$$= F_{drag,d} + R_{d,b}\dot{s}_b(t) + 2cs_b(t)$$
$$+ A_p(P_c + \rho g z_c)$$
$$+ A_p\rho[(\dot{s}_b(t) - \dot{s}_d(t))^2(1 \quad (36)$$
$$+ (\frac{3\xi}{2} + \lambda\frac{l_2}{D})\frac{D_{xl}^4}{D^4})$$
$$+ (\frac{A_{p1}}{A_p}l_2 + 2l_0)(\ddot{s}_b(t) - \ddot{s}_d(t))]$$

– Quá trình đẩy trong bơm 1, hút trong bơm 2

$$m_b\ddot{s}_b(t) + (R_b + R_{d,b})\dot{s}_b(t) + (S_b + 2c)s_b(t)$$
$$= F_{e,b}(t) + 2cs_d(t) - A_p(P_c + \rho g z_c)$$
$$- A_p\rho[(\dot{s}_b(t) - \dot{s}_d(t))^2(1 \quad (37)$$
$$+ (\frac{3\xi}{2} + \lambda\frac{l_1}{D})\frac{D_{xl}^4}{D^4})$$
$$+ (\frac{A_{p1}}{A_p}l_1 + 2l_0)(\ddot{s}_b(t) - \ddot{s}_d(t))]$$

$$(m_d + m_{21,d})\ddot{s}_d(t) + R_{d,b}\dot{s}_d(t) + 2cs_d(t)$$
$$= F_{drag} + R_{d,b}\dot{s}_b(t) + 2cs_b(t)$$
$$+ A_p(P_c + \rho g z_c)$$
$$+ A_p\rho[(\dot{s}_b(t) - \dot{s}_d(t))^2(1 \quad (38)$$
$$+ (\frac{3\xi}{2} + \lambda\frac{l_1}{D})\frac{D_{xl}^4}{D^4})$$
$$+ (\frac{A_{p1}}{A_p}l_1 + 2l_0)(\ddot{s}_b(t) - \ddot{s}_d(t))]$$

– Sắp xếp lại thuận tiện hơn ở dạng:

$$M_1\ddot{s}_b(t) + M_2\ddot{s}_d(t) = G_b(t) \quad (39)$$
$$M_3\ddot{s}_b(t) + M_4\ddot{s}_d(t) = G_d(t) \quad (40)$$

trong đó

$$M_1 = m_b + \rho(A_{p1}l_2 + 2A_pl_0);$$
$$M_2 = -\rho(A_{p1}l_2 + 2A_pl_0))$$
$$M_3 = -\rho(A_{p1}l_2 + 2A_pl_0);$$
$$M_4 = m_d + m_{21,d} + \rho(A_{p1}l_2 + 2A_pl_0)$$

$$G_b(t) = -(R_b + R_{d,b})\dot{s}_b(t)$$
$$- A_p \rho (1 + \frac{D_{xl}^4}{D^4}(\frac{3\xi}{2} + \lambda \frac{l_2}{D}))(\dot{s}_b(t) - \dot{s}_d(t))^2$$
$$- (S_b + 2c)s_b(t) + F_{e,b}(t) + 2cs_d(t)$$
$$+ R_{d,b}\dot{s}_d(t) - A_p(P_c + \rho g z_c)$$

$$G_d(t) = -R_{d,b}\dot{s}_d(t)$$
$$+ A_p \rho (1 + \frac{D_{xl}^4}{D^4}(\frac{3\xi}{2} + \lambda \frac{l_2}{D}))(\dot{s}_b(t) - \dot{s}_d(t))^2$$
$$- 2cs_d(t) + R_{d,b}\dot{s}_b(t) + 2cs_b(t)$$
$$+ A_p(P_c + \rho g z_c)$$

Các phương trình chuyển động có thể viết lại ở dạng hệ phương trình trạng thái như sau:

$$\dot{s}_b(t) = u_b(t) \qquad (41)$$

$$\dot{u}_b(t) = G_b(t)\frac{1}{M_1}(1 - \frac{M_2 M_3}{M_1 M_4})^{-1}$$
$$- G_d(t)\frac{M_2}{M_1 M_4}(1 - \frac{M_3 M_2}{M_4 M_1})^{-1} \qquad (42)$$

$$\dot{s}_d(t) = u_d(t) \qquad (43)$$

$$\dot{u}_d(t) = -G_b(t)\frac{M_3}{M_1 M_4}(1 - \frac{M_2 M_3}{M_1 M_4})^{-1}$$
$$+ G_d(t)\frac{1}{M_4}(1 - \frac{M_2 M_3}{M_1 M_4})^{-1} \qquad (44)$$

Hệ phương trình này được giải số bằng công cụ lập trình Matlab, trong đó tham số đầu vào cần xác định gồm: điều kiện sóng; kích thước hình học của các bộ phận của phao, lồng, bơm và hệ đường ống; áp suất bình.

3.3 Một số kết quả tính toán khảo sát

Các phương trình trong hệ (44) được giải số bằng chương trình viết trên Matlab. Sau khi đã kiểm tra thử nghiệm với bài toán tuyến tính, chương trình đã được sử dụng để tính toán khảo sát cho một số cấu hình phao và hệ thống cũng như các điều kiện sóng khác nhau. Các kết quả khảo sát này là cơ sở tốt cho những cho tính toán thiết kế chế tạo một hệ cụ thể.

Các thông số cơ bản ban đầu của hệ thống được cho như trong Bảng 1.

Bảng 1. Các thông số cơ bản hệ thống

Tham số	Giá trị	Đơn vị
Biên độ sóng	1.0	m
Chu kỳ sóng	7	s
Bán kính phao	0.15	m
Độ dài phao	1.0	m
Khối lượng phao	146.0	kg
Bán kính đĩa	0.15	m
Mật độ đĩa	1030	kg/m³
Chiều dài lồng	3.0	m
Bán kính bơm	0.025	m
Độ cứng lò xo bơm	1.0	N/m
Bán kính ống dẫn	0.012	m

Các kết quả tính toán trình bày trong các Hình 3 và 4.
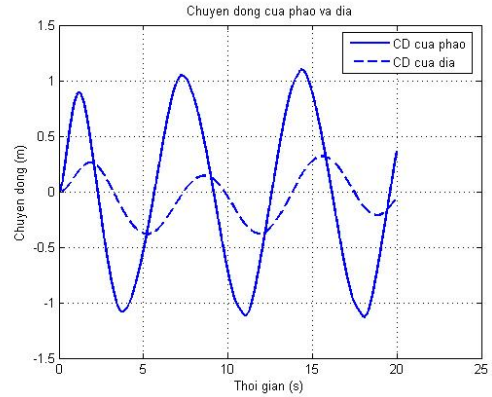
Hình 3. Chuyển động của phao và đĩa
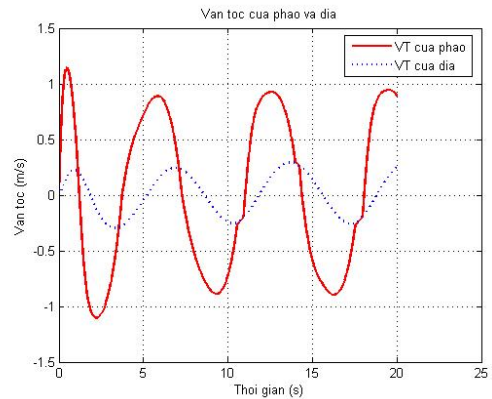
Hình 4. Vận tốc của phao và đĩa

Hình 3 cho thấy chuyển động của phao và đĩa có sự lệch pha nhất định. Điều đó khẳng định sự dịch chuyển của bơm để cấp nước

lên bình chứa. Hình 4 mô tả vận tốc tương ứng của phao và đĩa. Vì phao và đĩa được nối với nhau qua bơm nên sự khác nhau về vận tốc cho thấy một phần động năng đã được sử dụng để chuyển thành thế năng của nước trong bình chứa. Tuy nhiên trong một chu kỳ có những khoảng thời gian lực tác động của phao vào đĩa nhỏ hơn áp lực thiết lập trong bình chứa, vì vậy cả phao và đĩa chuyển động với cùng vận tốc và trong giai đoạn này nước không được bơm vào bình.

Các kết quả khảo sát năng lượng thu được từ thiết bị theo các điều kiện sóng khác nhau cho trong Bảng 2, trong đó năng lượng tính bằng watt. Từ bảng này có thể thấy với kích thước phao 0.3m, và khi sóng có biên độ 0.5m chu kỳ 5 giây thì năng lượng thu được khoảng 18watt, có thể đủ cung cấp cho một đèn tín hiệu trên biển. Với cùng một biên độ sóng và cấu hình phao cố định, thì sóng có chu kỳ khác nhau năng lượng thu được cũng khác nhau. Tuy nhiên chỉ có một sóng có chu kỳ mà dao động sóng và dao động phao ở gần mức cộng hưởng nhất thì năng lượng thu được là lớn nhất.

Bảng 2. Năng lượng chuyển đổi (w) theo điều kiện sóng

Chu kỳ T(s)	Biên độ sóng - η_a	
	0.5 m	1 m
3	17.54	29.43
4	21.30	39.94
5	18.71	34.26
6	11.10	26.62
7	5.12	18.10
8	0.93	12.82
9	--	9.26

Các kết quả khảo sát khả năng chuyển đổi năng lượng cho sóng biên độ 1m chu kỳ 7s đối với kích thước phao khác nhau cho trên Bảng 3. Công suất chuyển đổi trong bảng đạt được khi coi hiệu suất turbine là 100%. Từ kết quả tính toán có thể nhận thấy nếu phao có kích thước đủ lớn, năng lượng thu được là rất đáng kể. Trong một vùng biển có điều kiện sóng biên độ 1m, việc lắp đặt vài chục phao có thể cung cấp điện đủ năng lượng cho

dân cư của một xã hoặc một đảo. Từ kết quả trong bảng cũng cho thấy với một điều kiện sóng nhất định, kích thước phao càng lớn năng lượng thu được càng lớn. Tuy nhiên khi tăng kích thước thì cũng không được vượt qua giới hạn 0.2 lần bước sóng ví đây là điều kiện áp dụng cho mô hình tác động của sóng lên phao nổi.

Bảng 3. Năng lượng chuyển đổi theo kích thước phao

KL Phao (Kg)	ĐK Phao (m)	Cột áp Turbine (m)	Công suất (w)	Công suất sóng (w)
146	0.3	1.9	18.10	81.9
404	0.5	2.8	78.79	338.5
1617	1.0	5.8	669.62	1174.6

4. Kết luận

Theo nguyên lý cơ bản của các thiết bị chuyển đổi năng lượng sóng và tham khảo các cấu hình đã và đang được nghiên cứu trên thế giới và với mục đích nghiên cứu khảo sát một loại thiết bị khả thi trong chế tạo cũng như lắp đặt, các tác giả đã đề xuất một cấu tạo nguyên lý cho một thiết bị chuyển đổi năng lượng dạng phao nổi.

Trên cơ sở cấu tạo nguyên lý đã thiết lập mô hình mô phỏng hoạt động của thiết bị. Các phương trình của mô hình đã được giải số bằng công cụ Matlab. Chương trình đã được tính toán kiểm tra với bài toán tuyến tính, sau đó sử dụng để tính toán mô phỏng cho hệ phi tuyến đầy đủ.

Các kết quả tính toán khả năng chuyển đổi năng lượng sóng với các kích thước phao và điều kiện sóng khác nhau cũng đã được thực hiện. Các kết quả cho thấy khả năng chuyển đổi và sử dụng năng lượng sóng là hiện thực. Chương trình có thể sử dụng cho tính toán thiết kế ở giai đoạn tiếp theo là thiết kế, chế tạo và thử nghiệm.

Tài liệu tham khảo

1. Đỗ Ngọc Quỳnh và cộng sự (2003). Nghiên cứu đánh giá tiềm năng sử dụng năng lượng biển ở Việt Nam. Báo cáo tổng kết đề tài cấp Viện Khoa học và Công Nghệ Viêt Nam, Viện Cơ học, Viện khoa học và Công nghệ Việt Nam, Hà Nội.

2. Nguyễn Hữu Nhật và cộng sự (2002). Nghiên cứu sử dụng năng lượng sóng biển làm nguồn chiếu sáng phao tín hiệu hoạt động ngoài khơi biển Việt Nam. Báo cáo tổng kết đề tài cấp Bộ Giao thông Vận tải, Viện Công nghệ Giao thông Vận tải, Hà Nội.

3. United Kingdom Department of Trade and Industry's New and Renewable Energy Programme. (2003). Wave and Marine current enegy.

4. Brooke, J. (2003). Wave Energy Conversion. Elsevier Ocean Engineering, New York.

5. Eidsmoen, H. (1996). Simulation of a slack-moored heaving-buoy wave-energy converter with phase control. Norwegian University of Science and Technology N-7034 Trondheim Norway.

6. Eidsmoen, H. (1995). Hydrodynamic parameters for a two-body axisymmetric system. Applied Ocean Research. 17 (2). 103-115.

7. Cummins, W. E. (1962). The Impulse Response Function and Ship Motions. Schiffstechnik. 9. 101-109.

8. Chung, J. S. and Kim, M. H. (1995). Added Mass and Damping on an Oscillating Surface-Piercing Column with a Horizontal Cylinder: Square Cross Sections, International Journal of Offshore and Polar Engineering. 5 (3). 119

9. Falnes, J. (2002). Ocean Waves and Oscillating Systems: Linear Interactions Including Wave-Energy Extraction. Cambridge University Press.

10. Finnemore, E. J. and Franzini, J. B. (2002). Fluid Mechanics with Engineering Applications (10th Edit.), Mc Graw Hill.

11. Hoàng Bá Chư, Trương Ngọc Tuấn, (2005). Sổ tay thuỷ khí động lực học ứng dụng, Nhà xuất bản khoa học và kỹ thuật.

12. Kixelep, P.G. và cộng sự, (1982). Sổ tay tính toán thủy lực (dịch từ tiếng Nga). Nhà xuất bản Nông nghiệp, Hà nội.

13. Brian, D. H. and Daniel, T. V. (2007). Essential Matlab for Engineers and Scientists, Elsevier Pub., New York.

14. http://appsl. Eere.Energy.gov/consumer/renewableenergy/ocean/

15. http://www.technologystudent.com.energy1.tidal7.htm

16. http://www.anwsite.wavep.htm

Data Assimilation for the River Flood Routing
- Muskingum Model

Dang The Ba, Nguyen Van Tu and Nguyen Van Điep

Faculty of Engineering Mechanics and Automation
University of Engineering and Technology, Vietnam National University
144 Xuan-Thuy, Cau-Giay, Hanoi, Email:badt@vnu.edu.vn

Abstract:

Muskingum model has been widely used for modeling the river flood routing. However, there are some difficulties in forecast operations for a system because of determining model's parameters and inaccuracy in input data. In this paper, Muskingum model was developed for the flood routing in a system of rivers; for determining model's parameters, Variational Data Assimilation method was applied; to improve the model's results from the leak or inaccuracy of the input data, it were updated and corrected by Kaman Filter with the help of observed data in downstream. Model was used in some test cases and shown the good results. It was also tested with a real river system – Lo Gam. The results showed that the flood routing forecasts from the model in 24, 48 and 72 hours is agreeable to that happened in the river at Tuyen Quang.

Key Words: *Variatinal Data Assimilation, Muskingum model, Kalman filter, river flood routing*

1. Introduction

The determination of accurate data for hydraulic model is always encountered difficulties affecting the accuracy of forecasting results. On the other hand, with the development of monitoring technologies, data of the stream in river are increasingly diverse and highly reliable. So the development and application of data assimilation methods to incorporate scientifically between simulation models and monitoring data to get results more accurate prediction of stream in river hydraulic flow, Hydrology is the current trend in the world.

The application of data assimilation methods for simulation models of flow in rivers can be implemented in four stages of the calculation process:

- ***Input updating:*** In fact, the input such as boundary conditions, initial conditions, lateral discharge... are very difficult to identify accurately. Therefore, the assimilatoin of monitoring data at the stations and simulation results to correct all of these parameters is essential and significantly improve the forcast results [1,2,3]

- Model's parameters identification: In the hydraulic models, parameters such as roughness, slope, cross-sectional area ... are

very difficult to Identify directly. So the data assimilation is a effective method to determine them appropriately.

- *Updating the state variables:* Due to errors from the input data and simplifying assumptions of the model, simulation results often contain certain errors compared to reality. The use of measured data for updating and corecting the simulation results also significantly improve forecasting results [1,2,3,5].

- *Updating the model's outputs:* Outputs of the model are understood as the values of derivatives of state variables that are used in actual forecasting. The Kalman filter methods are usually used for updating and correctingt the model's output variables from oserved data. From there to help improve forecasting results [5,6,8,9].

The paper presents a development of data assimilation for the Muskingum model - River flood routing model. In this development, data assimilation has been developed for the two calculation process. The first is variational data assimilation for identification model parameters and the second is linear Kalman filter for correcting and updating the model's output - water elevation along the river .

The model have been implemented for a real river - Lo Gam system and shown good results.

2. The Muskingum model

Muskingum is an effective computational model of flood flow in a reach of river (McCarthy, 1938). In this model, the water storage S of a reach of river is represented by the function of inflow and outflow, I and O.

- The equation of the model can be written in the following form:

$$S = K[xI + (1-x)O] \qquad (1)$$

Where K and x are called the Muskingum coefficients (was first developed by the U.S.

Army Corps of Engineers in connection with the flood control schemes in the Muskingum River Basin, Ohio), K is a storage constant having the dimension of time and x is a dimensionless constant for a reach of the river. In natural river, x ranges from 0.1 to 0.5. The Eq. (1) in most flood flows approaches a straight line. Trial values of x are assumed and plots of 'S vs. [xI + (1 − x) O]' are in the form of storage loops; for a particular value of x, the plot is a straight line and the slope of the line gives K. After determining the values of K and x, the outflow O from the reach may be obtained by combining with conservation equation:

$$I = O + \Delta S \qquad (2)$$

Selecting a short time interval Δt, called calculation time step, and subindex 1 and 2 represent for start and end point. Equation (2) can be rewritten as follow:

$$\left(\frac{I_1 + I_2}{2}\right)t - \left(\frac{O_1 + O_2}{2}\right)\Delta t = S_2 - S_1 \qquad (3)$$

and equation (1) can be rewritten as:

$$S_2 - S_1 = K\left[x(I_2 - I_1) + (1-x)(O_2 - O_1)\right] \qquad (4)$$

Combining the two equations (3) and (4) and then simplifying we'll obtain the equation of outflow of a reach as follow:

$$O_2 = C_0 I_2 + C_1 I_1 + C_2 O_1 \qquad (5)$$

where:

$$C_0 = -\frac{Kx - 0.5\Delta t}{K - Kx + 0.5\Delta t} \qquad (5.a)$$

$$C_1 = \frac{Kx + 0.5\Delta t}{K - Kx + 0.5\Delta t} \qquad (5.b)$$

$$C_2 = \frac{K - Kx - 0.5\Delta t}{K - Kx + 0.5\Delta t} \qquad (5.c)$$

Combining of the equations 5a, 5b, 5c we get the following equation:

$$C_0 + C_1 + C_2 = 1$$

The routing period – simulation time step, Δt should be less than the time of travel for the flood wave through the reach, otherwise it is possible that the wave crest may pass completely through the reach during the routing period. Usually the routing period is taken as about 1/3 to 1/4 of the flood wave travel time through the reach. If there is lateral inflow, it should be added to *I* or *O* accordingly as it enters at the upstream or downstream end of the reach. In another cases, the lateral inflow may be divided into two portions, a portion to each *I* and *O*.

Muskingum method has advantages as simple, easily tested and applied in practice. Muskingum method has advantages as simple calculation, easily tested and applied in practice. Problems encountered when using it is the determination of the parameters K and x for each reach of a river section.

3. Variational Data Assimilation for Model's Parameters Identification

Application of Variational data assimilation [2, 3] for parameters identifying of Muskingum model in a river system can be proposed briefly as follows:

The equation of model can be rearranged in the control equation as follows

$$\begin{cases} \partial_t y(k,t) + A(k, y(k,t)) = 0 \\ y_{|t=0} = y_0 \end{cases} \tag{6}$$

In which, outflow of each reach denoted by the state variable vector, y. The parameters K and x is denoted by control parameter vector, k. Observed water flow at stations are denoted by y_{obs}.

The parameters of the model can be found by minimizing the objective function *J(k, yo)* that it is squared deviation between calculated results *y* and the observed data *y_{obs}*.

$$J(k, y_0) = \frac{1}{2} \int_0^T \|y(k,t) - y_{obs}\|^2 dt \tag{10}$$

To minimize the objective function *J(k, y₀)*, we can use optimization methods. In this methods, the methods using the objective function gradient is used extensively and effectively for nonlinear problems. The results in this paper was implemented by using the algorithm L-BSGF-B [2]. The next problem is how to compute effectively the objective function gradient.

Based on the variational method, Ledimet and colleagues have developed an efficient method to determine the objective function gradient by using the conjugate variable, $\tilde{y}$, of the state variable, *y* [12]. The results of this method is obtained a system of equations to determine the objective function gradient. Equations are written as follows, *ΔJ*:

$$\begin{cases} \partial_t y(t) + A(k, y(k,t)) = 0 \\ \partial_t \tilde{y}(t) - \left[\dfrac{\partial A}{\partial y}\right]^T \tilde{y}(t) = Cy(t) - y_{obs}(t) \\ y(0) = y_0 \\ \tilde{y}(T) = 0 \\ \nabla J = \int_0^T \left[\dfrac{\partial A}{\partial k}\right]^T \tilde{y}(t) dt \end{cases} \tag{11}$$

The process of objective function gradient is implemented as follows: Intergrate model's equation for the entire time period [0, T] to get values of *y*. Then intergrating the adjoint equations in the corresponding time period [T, 0] to get $\tilde{y}$. From y and $\tilde{y}$, the objective function gradient is calculated by last expression of (11).

However, by using numerical solver for conjugation equations of $\tilde{y}$, we always get incorrect values of the objective function gradient because of the discrete process always generate errors. The best way to calculate $\tilde{y}$ and the objective function gradient is to use the model's code. In this paper, the code for calculating $\tilde{y}$ and the objective function gradient is build by using TAPENAD tool [10].

Thus, by applying the variational data assimilation method, a algorithm and a program for Muskingum model's parameters identification was developed. The program consists of four modules: A forward module for computing the outflow of reachs, *y*; A backward module for computing the conjugate value of outflow, $\tilde{y}$; A module for computing the gradient of the objective function; A minimizing module for identification the values of K and x coefficients.

The program can be used for two purposes: identfying model's parameters and flood routing forecasting.

4. Kalman filter for correcting and updating simulation result

When using computer models for forecasting, the results often contain errors, compared with reality. The expected result is more suitable if the results is always being updated and corrected with the observed data. To improve flood forecasting results in Muskingum model, Kalman filter method has been applied. The algorithm is briefly presented as follows:

The model's equation should be rewritten in the control equations form as follows:

$$Q_k = AQ_{k-1} + BU_k \qquad (12)$$

And use symbol X to represent Q, equation (12) become a standart form of a control system:

$$X_k = AX_{k-1} + BU_k + W_{k-1} \qquad (13)$$

For the observed data, Z (flow or water elevation), we can have the following form:

$$Z_k = HX_k + v_k \qquad (14)$$

The steps of Kalman filter method for Muskinggum model as follows:

1. At the initial time step, outflow of reachs are known as the initial condition,

X_0^a. The posteriori error covariance matrix is set to unit matrix, $P_0^a = [\delta_{ij}]$.

2. Solving Muskingum equation to obtain the predicted state estimate for outflow of reachs X_k^f and calculatinhg the predicted estimate covariance matrix, P_k^f :

$$X_k^f = AX_{k-1}^a + BU_k$$
$$P_k^f = AP_{k-1}^a A^T + Q \qquad (14)$$

3. Coputing the Kalman gain, *K*

$$K_k = P_k^f H^T (HP_k^f H^T + R)^{-1} \qquad (15)$$

4. Updating observed data to correct predicted result X_k^a and computing the posteriori error covariance matrix for next step, P_k^a

$$X_k^a = K_k(Z_k - HX_k^f)$$
$$P_k^a = (I - K_k H)P_k^f \qquad (16)$$

5. Go back to step 2 to continue for next time step

Base on the algorithm presented above, a computing module for correcting and updating the model's results was built. Some test cases were implemented and it shown good results [1, 5].

5. Program and Teste Case

On the basis of two modules were developed as described above, a program for riveˋ flood routing was built. In addition to the computing module, the program has been developed the graphic user friendly interface to facilitate operational use in practice.

The program can be used in two functions: Automatically indentification the parameters of the model according to historical observation data and forcasting calculation that the observed data is updated daily.

The program was used for a test case - the Red River system, flowing from the Hoa

Binh, Yen Bai and Tuyen Quang to Hanoi. The study system is schematised as in Fig. 1.
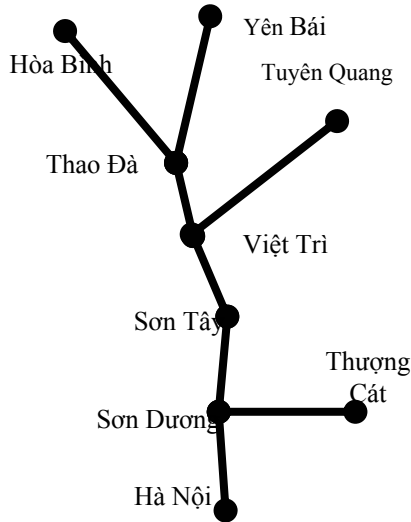

Figure 1: The Red River system diagram

The system is modeled by eight reachs. Computation time is three months (July to September) in flood season of the year 2007. The data for the calculation include the inflow at the upper boundaries at Hoa Binh, Yen Bai, Tuyen Quang, observed water level in Sontay and Hanoi stations.

From the observed data, the parameters of model are determined by using variational assimilation algorithm shown in table 1.

Table 1. Parameter for Muskingum model

	1	2	3	4	5	6	7	8
K	58.0	20.2	160.0	15.3	160.0	1.7	1.0	3.9
x	0.2	0.2	0.4	0.2	0.5	0.2	0.2	0.2

After determining parameters, predicting and correcting process is implemented by using computation program for forecasting the river flood routing in river system. The short-term forecast was implemented for 1h, 12h, 24h, 36h, 48h, 60h and 72h.

The results of water level forecast for each hour are presented on Figure 2 and 3. Figure 2 is a comparison between the forecasted water levels with measured data in Son Tay station; Figure 3 is a comparison

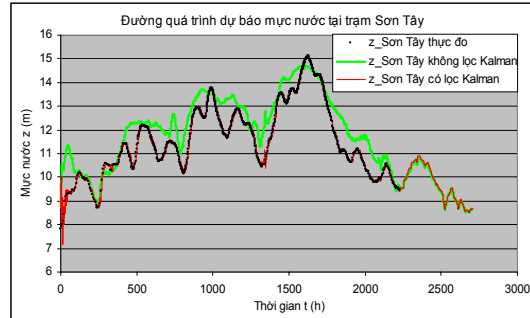between the forecasted water level with the data measured at Hanoi station.

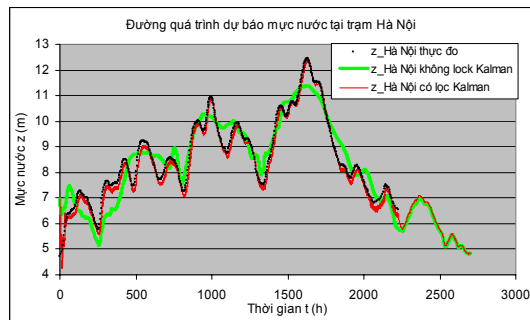Figure 2: Comparation between water levels in Sontay station

Figure 3: Comparation between water levels in Hanoi station

Comparison shown computed result is well suitable with observed data.

In the another cases, the forecasting for 12h, 24, 36h, 48 and 72h also shown the good results. An example of forecasted results at SonTay station presented in Table 2.

Table 2. Forecasted results at Sontay station

Time for Forecating (h)	Forecated Z(m)	Observed Z(m)	Error (%)
12	13.66	13.63	0.22
24	13.89	13.73	1.17
36	14.13	13.68	3.29
48	14.24	13.57	4.94
60	14.38	13.73	4.73
72	14.51	14.07	3.13

Table 3. Short-term forecast in Hanoi

Time for Forecasting (h)	Forecasted Z(m)	Observed Z(m)	Error (%)
12	10.11	10.59	4.53
24	10.42	10.74	2.98
36	10.68	10.76	0.74
48	10.85	10.65	1.88
60	10.97	10.72	2.33
72	11.12	11.00	1.09

6. Conclusion

Based on the Muskingum model, a model for forecasting flood routing in the river system has been built

In order to identify parameters of model, variational data assimilation method is developed and applied. The results permit to determine parameters of model rapidly and reliably. It ensures ability to apply in real forecasting operation.

In forecasting computation process, observed data is usually updated base on development and application of Kalman filter algorithm. Its purpose is to use observed data and produce forecasting that tend to be closer to the true values of the measurements and their associated calculated values.

Base on the developed modules, software with graphical user friendly interface have developed which is ready for end-user in real forecasting operation.

A test case for the real system have been implemented and shown the good results.

The advantages of this model are: It is simple in using; it doesn't needs the geometric information like cross section, slope, roughness...

References

1. Dang The Ba, Nguyen Van Tu, Nguyen Van Diep "An *Application of Kalman Filter to Compute the Flood Flow in River system"* proceeding of National Conference on Fluid Mechanics, 07/2009.

2. Dang The Ba, Doan Viet Phan, " Variational Data Assimilation to Identify Parameter of The Flood Flow Model in River, A paper in National Conference on Fluid Mechanics, 07/2009.

3. F.X. Le Dimet, W. Castaings and B. Vieux, *"Data Assimilation in Hydrology : Variational Approach"*, Laboratoire Jean-Kuntzmann, Université de Grenoble and INRIA, Grenoble, France.

4. F.X. Le Dimet, I.M. Navon and Dacian N. Daescu, *"Second Order Informationin Data Assimilation"* August21, 2001

5. Geir Evensen, *"The ensemble Kalman filter: theoretical formulation and practical implementation"*, Ocean Dynamics, 53, 343-367, 2003.

6. Henrik Madsen, Claus Skotner, *"Adaptive state updating in real-time river flow forecasting – a combined filtering and error forecasting procedure"*, J. of Hydrology, 308 (2005), 302-312.

7. J. Blum , F.X Le Dimet and I. Michael Navon, *"Data Assimilation for Geophysical Fluids"*, Computational Methods for the Atmosphere and the Oceans, Volume 14: Special Volume (Handbook of Numerical Analysis), Elsevier Science Ltd, New York, 2008

8. J. C. Refsgaard, Dan Rosbjerg, Lars M. Marcussen, *"Application of the Kalman filter to real time operation and to uncertainty analyses in hydrological modelling"*, Proceedings of the Hamburg Symposium on Scientific Procedures Applied to the Planning, Design and Management of Water Resources Systems, 1983.

9. Jean-Philippe Drecourt, *"Kalman filtering in hydrological modelling"*, DAIHM Technical Report 2003-1.

10. Project Tropics, *"A.D. Tool TAPENADE"*, INRIA Sophia-Antipolis, France, 2008.

11. Y. H. Lee and V. P. Singh. *Tank model using Kalman filter.* J. of Hydrological Engineering, pp. 344-349, 1999.

12. Yeou-Koung Tung *"River Flood Routing by Nonlinear Muskingum Method"* Journal Article 1985 WWRC-85-48, Journal of Hydraulic Engineering, Volume 111.

Return Period Curves of Storm Tide for Sea Dike Design and Upgrade in the Quangninh – Quangnam Coastal Zone of Vietnam

Dinh Van Manh[a], Le Nhu Nga[b], Nguyen Thi Viet Lien[c]

Institute of Mechanics, 264 Doi Can Str., Ba Dinh, Hanoi, Vietnam
[a] dvmanh@imech.ac.vn, [b] lnnga@imech.ac.vn, [c] nvlien@imech.ac.vn

Abstract

Vietnam faces to the South China Sea with the coastline of more than 3000 km. Tide regime along the coastal zone are rather complicated, diurnal tide with the range of about 4.5m in the north, mixed tide with range of only several decades cm in the middle and semi-diurnal with range of about 5 m in the south. On the other hand, yearly in average there are 4, 5 typhoons land on and influence to the coast. In history, a lot of typhoons caused serious surges (higher than 3.5m) and damaged sea dike system and many buildings in the coastal zone. These two phenomena are mainly affected to sea level height in the Vietnam coast.

In the Quangninh – Quangnam marine area, tide and typhoon surges have been considered in many projects and research programs. However, the obtained results on these phenomena are not very appropriate to apply to sea dike design. In this study, on the basis of historical data of typhoons, sea levels observed at tide gauges, statistical models are used in order to produce distribution laws of typhoon parameters (time, location of typhoon center, depression, maximum wind speed etc.), and then a huge number of typhoon tracks with their parameters are created by Monte Carlo procedure. Next, hydrodynamic models are applied to calculate astronomical tide levels and typhoon surge characteristics. Finally, returned period curves (exceedance probability) of storm surge plus tide at points in distance of about 10km along the coast are produced. These curves are appropriate to use as the boundary condition in the sea dike design.

Key Words: tide, storm surge, storm tide, return period.

1. Introduction

Vietnam faces to the South China Sea with the coastline of more than 3000 km. Tide regime along the coastal zone are rather complicated, diurnal tide with the range of about 4.5m in the north, mixed tide with range of only several decades cm in the middle and semi-diurnal with range of about 5 m in the south. On the other hand, yearly in average there are 4, 5 typhoons land on and

influence to the coast. In history, a lot of typhoons caused serious surges (higher than 3.5m) and damaged sea dike system and many buildings in the coastal zone. These two phenomena are mainly affected to sea level height in the Vietnam coast.

In order to protect the long coastal zone, a sea dike system had been built year after year. At present, in the face of downgrading of the sea dike system as well as willing to have more safety protection system, the advanced techniques in sea dike design in the world, such as in the Netherlands, China, are considered to apply. However, these techniques require many parameters and information on ground soil, hydrodynamics, in which the returned period of specific sea level height is an important parameter.

In the Quangninh – Quangnam marine area as well as in the whole Vietnam marine region, tide and typhoon surges have been considered in many projects and research programs. However, the obtained results on these phenomena are not very appropriate to apply to sea dike design. In order to support the sea level characteristics for sea dike design and upgrade, in this study, numerical models are applied to calculate astronomical tide levels and typhoon surge characteristics. Firstly, on the basis of historical data of typhoons, sea levels observed at tide gauges. Secondly, by using statistical models, distribution laws of typhoon parameters (time, location of typhoon center, depression, maximum wind speed …) are produced, and then a large number of artificial typhoon tracks with their parameters are created by the Monte Carlo procedure. Thirdly, hydrodynamic models are calibrated and validated for tide and storm surge simulations, and then applied to calculate astronomical tide in period of 19 year and surges caused by the artificial typhoons. Finally, returned period curves (exceedance probability) of storm surge plus tide at points in distance of about 10km along the coast are produced. These curves are appropriate to

use as the boundary condition in the sea dike design.

2. Data collection and analysis

- *Historical typhoon data*: All typhoons with their parameters acted in the South China Sea and landed on Vietnam coast are collected. The typhoon parameters are time, typhoon center's location, speed and direction of center movement, air pressure depression at center, maximum wind speed and its radius from the center and landed point. From 1951 to 2007, there are 313 typhoons occurred in the study area (in annual average, about 6 typhoons per year) as shown Fig. 1.
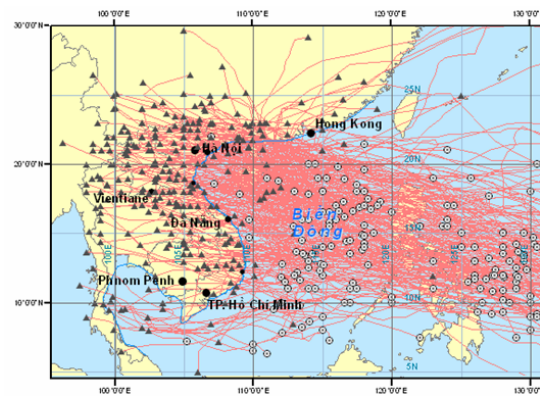

Fig. 1: Tracks of typhoons affected to Vietnam coast from 1951 to 2007.

- *Sea level data:* Hourly sea levels at 28 stations along the coast from Quangninh to Quangnam provinces (sea Fig.2) in different time periods are collected, namely, for 5 years from 2003 to 2007 at all stations; for 5 or 7 days surrounding the landed day of 132 selected typhoons. Furthermore, the in situ maximum surge data of 17 typhoons measured just after their landing.

- *Harmonic constant analysis*: The sea level data for 5 years at stations are used to analyze the harmonic constants of over 30 tidal constituents by using the least square method (Nguyen Van Moi et al., 2004). However, on the basis of the obtained results, only 10 tidal constituents with the significant amplitudes are selected for numerical

verification and astronomical tide calculation later. They are 4 diurnal tides (K_1, O_1, P_1, Q_1), 4 semi-diurnal (M_2, S_2, N_2, K_2) and 2 long periods (annual and semi-annual) Sa, Ssa.
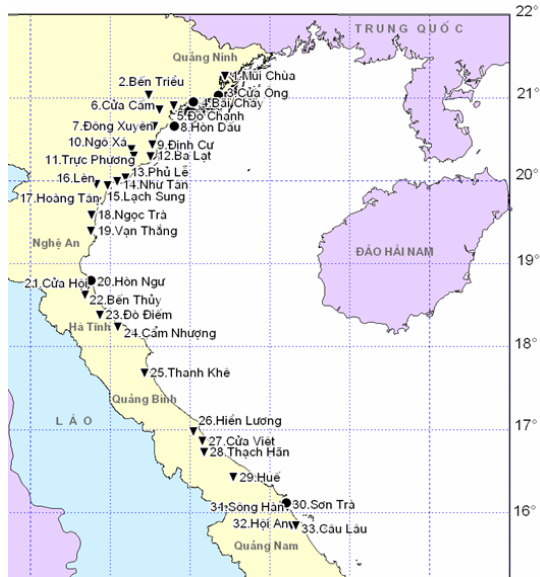

Fig. 2: Locations of tide gauges.

- *Strom surge extraction*: Typhoon surges ζ_S are obtained by elimination of astronomical tide ζ_T from measured sea level data ζ_O as following:

$$\zeta_S = \zeta_O - \zeta_T \tag{1}$$

In which, astronomical tide specified by

$$\zeta_T = A_0 + \sum_{i=1}^{n} f_i H_i \cos\left[q_i t + (V_o + u) - g_i\right] \tag{2}$$

Where, A_0 is a reference to mean the sea level; q_i, H_i, g_i – angle velocity, amplitude and phase of the ith tidal constituent, respectively; f_i, V_0 and u – astronomical parameters.
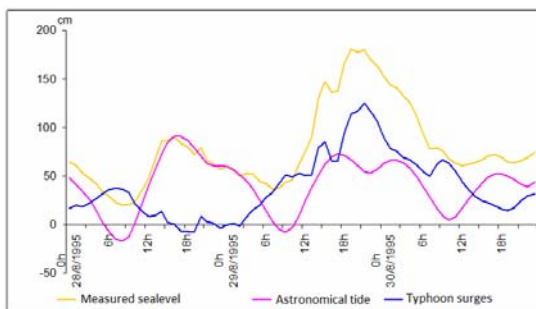

Fig. 3: Surges (green line) due to typhoon Lois-8/1995 at Dinhcu station.

As an example, in Fig. 3, the typhoon surges (green line) from the 28th to 30th August, 1995 at Dinhcu station are extracted by subtracting the astronomical tide values (red line) from measured sea levels. In this case, the highest of typhoon surges is about 120cm.

- *Probability distribution functions of typhoon parameters:* In order to generate artificial typhoons by the Monte Carlo Procedure, on the basis of the historical typhoon data set, the probability distribution functions of the following parameters are specified: landing point (λ), landing time and date (hour, day, month, year), speed (V_f) and direction (θ) of typhoon center, air pressure depression (P_{min}) at the center. Several of obtained distribution functions are presented in Figs 4 and 5.
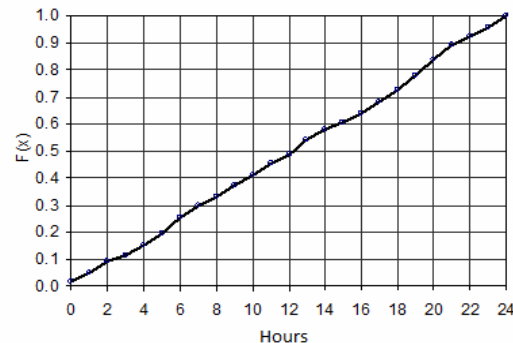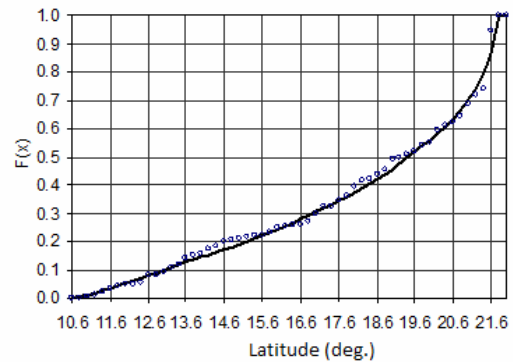

Fig. 4: Probability distribution function of landing points (λ) and time (h).
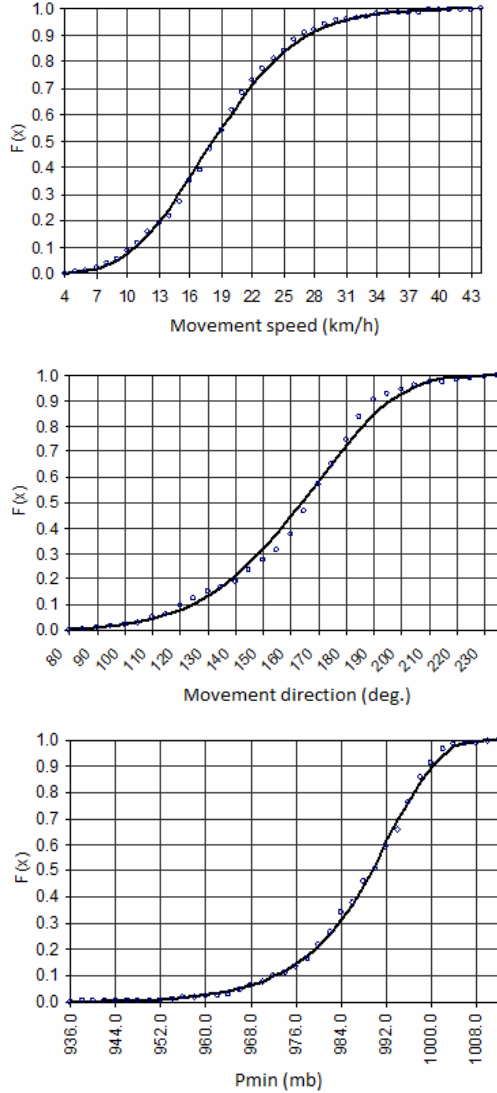
Fig. 5: Probability distribution function of movement speed (V_f) and direction (θ) and air pressure depression (P_{min}).

The statistic analysis results point out that the correlation coefficients (Table 1) between parameters are small; the highest value is the relation of month and landing point. It means that the typhoon parameters are quite independent except the landing location and the month, typhoon landing location changing from the Northern part to the Southern part from the beginning to the ending of the season is quite dominant [3]. Furthermore, the distribution function of landing time shows that typhoons are able to

land on the coast at any time, it results in the astronomical tide oscillation and typhoon surges can be considered as two independent random processes.

Table 1: Correlation coefficients of typhoon parameters.

| | (θ) | (V_f) | (P_{min}) | λ | Landing time | | |
					hour	day	month
V_f	0.15						
P_{min}	-0.01	-0.20					
λ	0.01	0.10	-0.17				
hour	0.08	-0.07	0.01	0.05			
day	0.07	-0.09	0.06	0.02	0.00		
month	0.24	0.01	0.06	-0.32	-0.05	-0.22	
year	-0.12	-0.09	-0.08	-0.05	0.09	0.06	-0.05

- *Bathymetry data:* Depth values for numerical models of the study area are extracted from the bathymetry maps: scale of 1/1,000,000 for the whole South China Sea, 1/50.000 or 1/25,000 for the coastal zones of Vietnam. The overall depth of the study area is shown in Fig. 3.
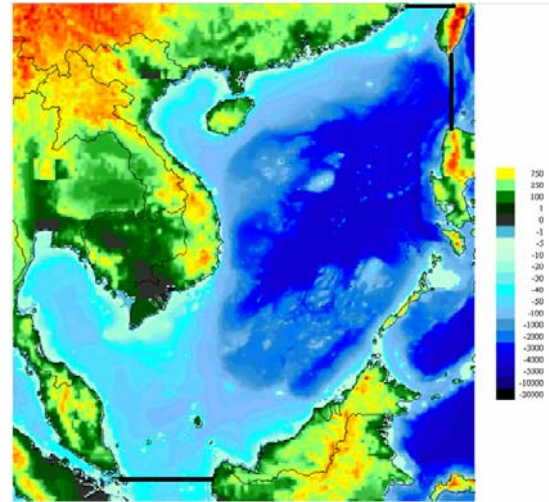
3. Numerical model Setup

Fig. 6: Overall depth (m) and modeling extent.

In order to simulate tide oscillation and typhoon surges in the study area, the software TSIM2001 for 2D hydrodynamic calculation is applied. This software is developed on the basis of the 2D nonlinear shallow water equations, finite difference

method with the ADI scheme (Pham Van Ninh, 1998).

Modeling extent is limited from 99.0 to 121.0°E and from 1.3 to 24.5°N, and covered by a regular grid of 1/12 degrees. Open boundaries are shown by bold black lines in Fig. 6.
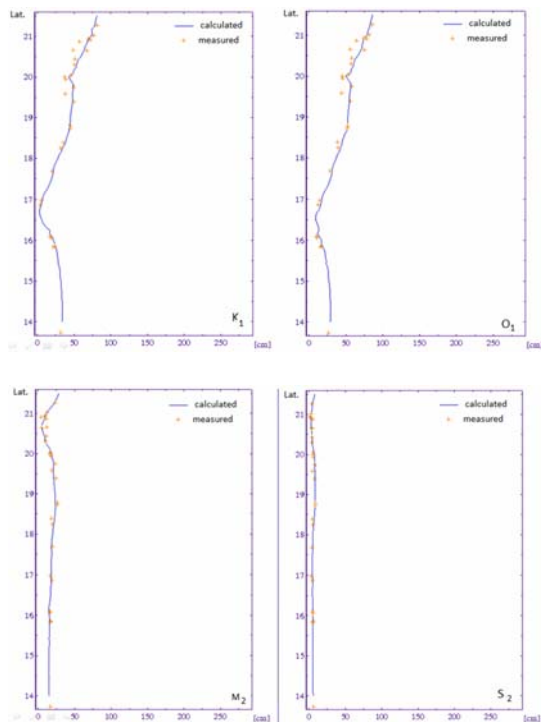

Fig. 7: Calculated (solid line) and observed (+) amplitude of K_1, O_1, M_2 and S_2 tides.
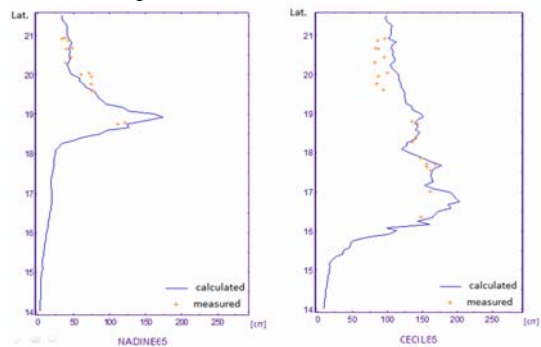

Fig. 8: Calculated (solid line) and observed (+) maximum surges caused by Nadine-65 and Cecil-85 typhoons along the coast.

It is necessary to calibrate the numerical model before calculating astronomical tide and typhoon surges. In fact, tide and typhoon surges take place simultaneously and their interaction is nonlinear, however, this phenomenon is not very significant (Pham Van Ninh, 1998). Therefore, in order to reduce calculation time in the later section, tide and typhoon surges are calibrated and validated separately.
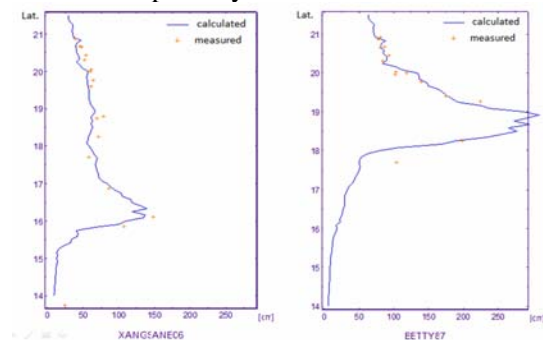

Fig. 9: Calculated (solid line) and observed (+) maximum surges caused by Xangsane-06 and Betty-87 typhoons along the coast.

Firstly, harmonic constants of 10 tidal constituents at stations along the coast from Quangninh to Quangnam are exploited for the model calibration. The obtained calculated results point out that the model can simulate rather well tide level distribution in the study area, as shown in Fig. 7.

Secondly, 99 typhoons, which caused the maximum surges greater than 50cm along the coast, are selected for model calibration (70 cases) and validation (29 cases). For each selected typhoon, only the maximum surge values at every station are considered to compare with the calculated ones. For example, Figs 8 and 9 are comparisons of calculated and measured maximum surges along the coast. In general, the numerical model is verified acceptably to simulate typhoon surges in the study area.

4. Calculation of astronomical tide levels

Hourly astronomical tide levels at the coastal points (as shown in Fig. 10) are calculated by

using the formulae (2) for 19 year, from 1990 to 2008. The calculated harmonic constants (amplitude H_i and phase g_i) of 10 tidal constituents are obtained from the numerical model after calibration. Mathematically, in 19-year period, all situations of astronomical tide are revealable. These tide levels will be combined with typhoon surge values to build returned period (and exceedance probability) curves.
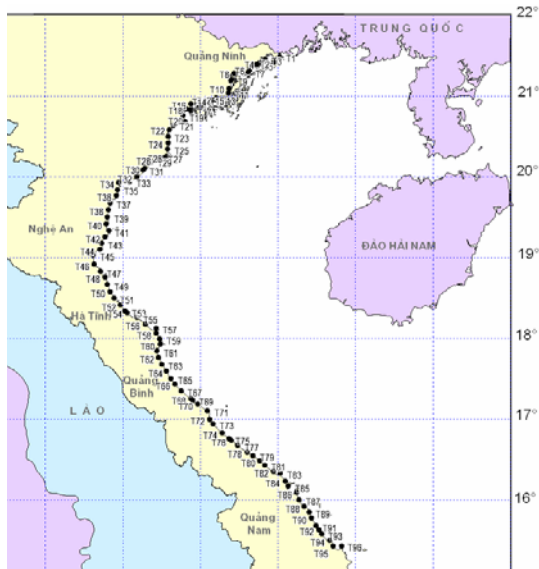

Fig. 10: Coastal points where returned period curves built.

5. Calculation of artificial typhoon's surges

It is clear that only 57 years data of typhoon parameters and surges are too short for revealing characteristics of typhoon surges in the study area, therefore it is necessary to consider methods to enlarge data set. On the basis of probability distribution functions obtained in Section 2, the Monte Carlo procedure is applied to create 5,490 artificial typhoons, equivalently for 1,000 year data (about 5.49 typhoons per year) *[6]*.

Then the numerical model is used for calculating surges caused by these typhoons. The results are to obtain maximum surges of each artificial typhoon at every coastal point (at each point, there are 5,490 surge values).

These surge values will be combined with tide levels obtained in Section 4 to build returned period (and exceedance probability) curves *[5]*.

6. Returned period curves

As mentioned before, tide and typhoon supposed are two natural independent phenomena. A typhoon can hit the coast at any tidal moment of high or low or in between. Therefore, a typhoon surge can combine incidentally any tide level.

At each point, a mathematical accumulative function of storm surge was created based on 1,000-year artificial storm surge data set; and an accumulative distribution of tide was built based on 19-year calculated astronomical tide level (as shown in Fig. 11).
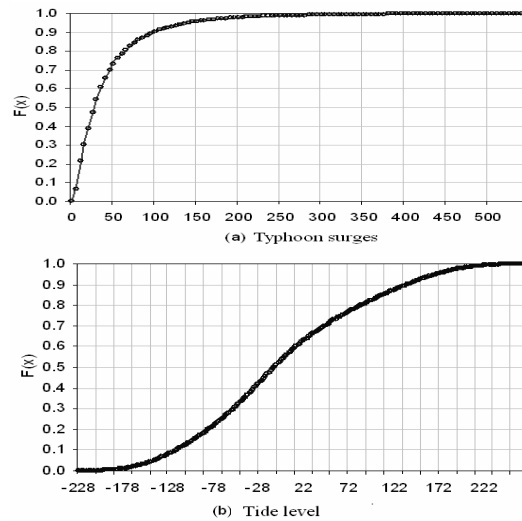
Fig. 11: Typhoon surge (a) and tide level accumulative function (108°10'E, 21°30'N).

Then the combination schema of tide and typhoon surge is showed on the Fig. 12.

In order to have high certainty combined water level (storm surge plus tide) at 100 and 200 year return periods, 54,900 combined data (equivalent to 10,000 years of typhoon) is created based on the below equation (3).

$$\{H_{Cb}\}_i = \{H_S\}_j + \{H_T\}_k \tag{3}$$

where, H_{Cb} is combined water level, H_S – storm surge, H_T – tidal water level, $i=1$ to 54,900, $j=1$ to 5,490, $k=1$ to 55,200.
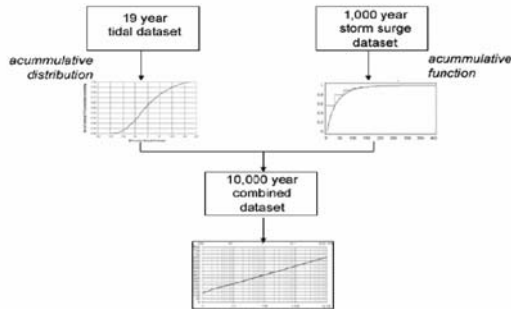

Fig. 12: Combination schema of typhoon surge and tide level.

Storm surge is estimated randomly based on its accumulative function equation (4) *[2, 4]*:

$$H_B = inv(F(P_{H_B})) \qquad (4)$$

where, F is accumulative function, P_{HB} - accumulative probability, identified randomly in between 0 and 1 uniformly, *inv* – inverted function of F.

Tidal water level was picked up directly from its accumulative distribution by using the Piecewise linear method and accumulative probability P was identified randomly in between 0 and 1 uniformly. For example, tidal water level at P of 0.77 is 53cm, as shown in Fig 13.
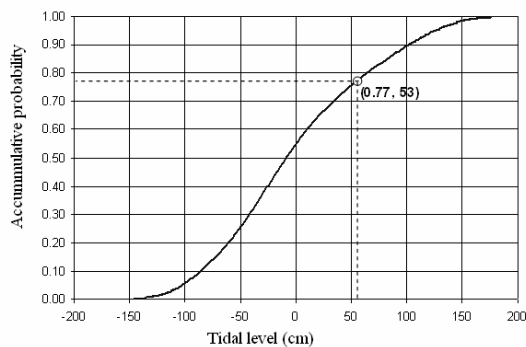

Fig. 13: Piecewise linear method used for picking up tidal level from its accumulative distribution P.

Return period and Annual exceedance probability were calculated based on Equation 5 [2, 4]:

$$T_{rH_{Cb}} = \frac{Rank_{H_{Cb}}}{L}, \quad P = \frac{1}{T_{rH_{Cb}}}$$

where, T_{rHcb} is return period of H_{TB} in year, $Rank_{Hcb}$ – rank of H_{Cb} ($Rank_{Hcb}=1$ for Max$\{H_{Cb}\}$, $Rank_{Hcb}=48,900$ for Min$\{H_{Cb}\}$), L – length of data in year, P – annual exceedence probability in percentage.

In the study area, at all 96 coastal points, storm (surge plus) tide exceedance probability and return period curves are created. An example of the curve is showed in Fig. 14.
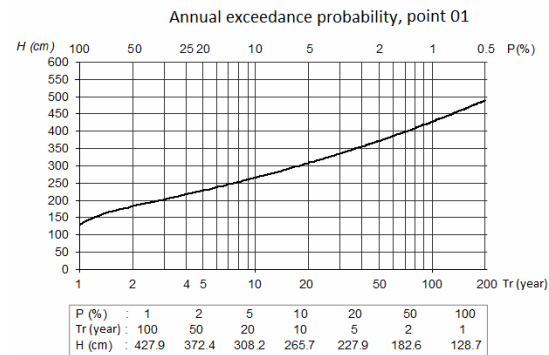
Fig. 14: Returned period curve of storm tide at point 01.

7. Conclusions

On the basis of the data on typhoon parameters and sea water levels mearured at tide gauges from 1951 to 2007 in the South China Sea, specially in the coast zone from Quangninh to Quangnam Provinces, as well as applying various models in statistic, hydrodynamics, the returned period curves (and annual exceedance probability) of storm surge plus tide at 96 points in distance of about 10km along the coast are produced. These curves are appropriate to use as the boundary condition in the design of sea dike as well as of other coastal constructions.

Reference

[1] Pham Van Ninh and et al. (1998*). The typhoon surges in Vietnam: the Regime Characteristics and Prediction. Proceedings of the 5th Asian Science and Technology Week, Hanoi.*

[2] Le Van Thao and et al. (2000). *Storms and Tropical Depressions Disaster Study*. Disaster Management Unit, UNDP Project VIE/97/002.

[3] Federal Emergency Management Agency (FEMA) (2005). *Final Draft Guidelines for Coastal Flood Hazard Analysis and Mapping for the Pacific Coast of the United States*. FEMA Study.

[4] Wang, S. Y. and et al. (2007). *Combined Total Storm Tide Frequency Restudy for Dog Island in Franklin Country*. Florida, Florida Department of Environmental Protection, Bureau of Beaches and Coastal Systems.

[5] Dinh Van Manh and et al. (2009*). A numerical model for calculating tide and typhoon surges in the coastal zone from Quangninh to Quangnam*. Proceedings of the National Conference on Fluid Mechanics.

[6] Le Nhu Nga and Dinh Van Manh (2009*). Artificial Typhoon for calculating typhoon surge characteristics in the coastal zone from Quangninh to Quangnam*. Proceedings of the National Conference on Fluid Mechanics.

[7] Nguyen Van Moi and et al. (2004), Some problems on tide analysis and prediction, proceeding of National Conference on Fluid Mechanics.

Bending ofThree Phase Composite Plate wth Creep Effect

Dinh Khac Minh[a], Pham VanThu[b] and Nguyen Dinh Duc[c]

[a] *Shipbuilding Science and Technology Institute, Hanoi, Vietnam*
[b] *Vietnam Maritime University, Haiphong, Vietnam*
[c] *University of Engineering and Technology, Vietnam National University, Hanoi*

Abstract.

Nowadays three phase composite materials are widely used in the shipbuilding industry. When reinforced with fiber and particle, the physical and mechanical properties of polymer composite materials are improved. This paper reports the bending analysis of three phase composite plate with epoxy matrix, reinforced glass fiber and titanium oxide particles including creep effect when shear stress is taken into account. The obtained results show that creep strains lead to compression in the composite material. Introducing reinforced fibers and particles reduces the plate's deflection, when increasing the stretch coefficient allows the calculation of creep deflection during a long loading period.

Key words: *bending, three phase composite, plate, creep*

1.Introduction

When a structure is loaded by periodic constant loads or thermal loads, it will have not only elastic strain but also creep strain.

The creep phenomenon was firstly considered in the 1920s in the analysis for metal under high thermal load. Then it has been strongly developed since the 1950s-1960s until present. Beside theoretical results, experimental evidences were found proving the existence of creep strain and its effect on the material's strain [1,2,4,5]. In the research of creep, functional of time is often used. Let $v(\tau)$, in which $\tau \in (-\infty, t]$ is a physico-mechanical process, then creep is considered as a functional of $v(\tau)$ [1]. The expression in the cases of viscoelasticity and elastoplasticity is as follow:

$$U = \overset{t}{\underset{-\infty}{F}}(v) \qquad (1)$$

The functional F can be linear or nonlinear. When F is linear, (1) can be rewritten as [1]:

$$u(t) = v(t) + \lambda \int_{-\infty}^{t} K(t, \tau) v(\tau) d\tau \qquad (2)$$

If $v(t)$ is a periodic function or in other words, the following condition for $v(t)$ to be

a periodic function K of variable *(t-τ)* is satisfied [1]:

$$K(t,\tau) = K(t-\tau) \tag{3}$$

In (2), the lower limit of the integral is -∞, but in fact, any history of F starts from a certain point: the beginning of materials manufacturing, or the beginning of loading process. So that (3) can be rewritten as:

$$u = v + \lambda \int_0^t K(t-\tau)v(\tau)d\tau \tag{4}$$

In the simplest case (one dimension), the stress-strain nonlinear relationship can be expressed as [2,5]:

$$\varepsilon(t) = C_1 \int_0^t K_{11}(t-\tau)\sigma(\tau)d\tau$$
$$+ C_2 \int_0^t \int_0^t K_{22}(t-\tau_1, t-\tau_2)\sigma(\tau_1)\sigma(\tau_2)d\tau_1 d\tau_2 +$$
$$+ C_3 \int_0^t \int_0^t \int_0^\tau K_{33}(t-\tau_1, t-\tau_2, t-\tau_3)\sigma(\tau_1)\sigma(\tau_2)\sigma(\tau_3)d\tau_1 d\tau_2 d\tau_3 + \dots$$

$$\tag{5}$$

In the tensor form [8]

$$\varepsilon_{ij}(t) = C_{ijkl} \int_0^t K_{11}(t-\tau)\sigma_{kl}(\tau)d\tau +$$
$$C_{ijklop} \int_0^t \int_0^t K_{22}(t-\tau_1, t-\tau_2)\sigma_{kl}(\tau_1)\sigma_{op}(\tau_2)d\tau_1 d\tau_2 +$$
$$+ C_{ijkloprs} \int_0^t \int_0^t \int_0^t K_{33}(t-\tau_1, t-\tau_2, t-\tau_3)\sigma_{kl}(\tau_1)\sigma_{op}(\tau_2)\sigma_{rs}(\tau_3)d\tau_1 d\tau_2 d\tau_3 + \dots$$

$$\tag{6}$$

The multiple term in (6) has the following form [8,10]:

$$K_{nn}(t-\tau_1, t-\tau_2, \dots, t-\tau_n)$$
$$= K_{nn}^*(t-\tau_1)K_{nn}^*(t-\tau_2)\dots K_{nn}^*(t-\tau_n) \tag{7}$$

In the case of anisotropic materials, in general the stress-strain relationship is as follow [3,4,10,11]:

$$\varepsilon_{ij}(t) = \sigma_{kl}B_{ijkl} + \int_0^t \sigma_{kl}(t)K_{ijkl}(t-\tau)d\tau \tag{8}$$

Equation (8) is Hooke law for viscoelastic environment. Here the B_{ijkl} and K_{ijkl} *(t-τ)* are obtained from experiment.

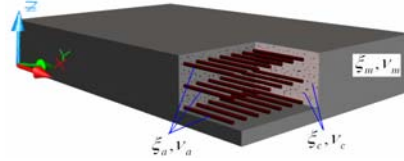Consider a plate made of 3-phase composite (Fig.1)

Figure 1. Three phase composite plate.

Experimental results [1-4] show that creep strain is notable only under the action of shear stress, then (8) can be written in the following form:

$$\begin{cases} \sigma_{11} = A_{11}\varepsilon_{11} + A_{12}\varepsilon_{22} \\ \sigma_{22} = A_{22}\varepsilon_{22} + A_{12}\varepsilon_{11} \\ \sigma_{12} = A_{66}\varepsilon_{12} - \int_0^t \widetilde{A}_{66}(t-\theta)\varepsilon_{12}(\theta)d\theta \end{cases} \tag{9}$$

The function $\widetilde{A}_{66}(t-\theta)$ stands for the creep property of the material and can be determined from experiment and normally expressed as [2]:

$$\widetilde{A}_{66}(t-\theta) = \frac{1}{n}A_{66}^* e^{-\frac{t-\theta}{n}} \tag{10}$$

Here A_{66}^* and *n* are obtained from experiment; *n* is the stretch coefficient of the material.

2.Bending equation considering creep effect.

2.1. Analytical research

The research of the effect of each phase (fiber, particle) on the bending of 3-phase composite plate is done in [13]. [14] investigates the bending of 3-phase composite plate when shear effect is taken into account. In the making of bending

equation, the plate's bending moment is determined as below [2,13,14]:

$$M_x = -\left(D_x \frac{\partial^2 w}{\partial x^2} + D_1 \frac{\partial^2 w}{\partial y^2} \right);$$

$$M_y = -\left(D_y \frac{\partial^2 w}{\partial y^2} + D_1 \frac{\partial^2 w}{\partial x^2} \right)$$

Creep appears in the expression of twist moment:

$$
\begin{aligned}
H &= \int_{-0,5h}^{0,5h} z\sigma_{12} dz \\
&= \int_{-0,5h}^{0,5h} \left[A_{66}\varepsilon_{12} - \int_0^t \widetilde{A}_{66}(t-\theta)\varepsilon_{12}(\theta) \right] z dz \\
&= -2A_{66}\frac{\partial^2 w}{\partial x \partial y}\frac{h^3}{12} + 2\frac{h^3}{12}\int_0^t \widetilde{A}_{66}(t-\theta)\frac{\partial^2 w}{\partial x \partial y} d\theta
\end{aligned}
\tag{11}
$$

where:

$$D_x = \frac{h^3}{12}A_{11}; \; D_1 = \frac{h^3}{12}A_{12}; \; D_y = \frac{h^3}{12}A_{22};$$

$$D_{xy} = \frac{h^3}{12}A_{66} \; A_{11} = \frac{E_{11}}{1-v_{12}v_{23}}; \; A_{22} = \frac{E_{22}}{1-v_{12}v_{23}};$$

$$A_{12} = \frac{E_{11}v_{23}}{1-v_{12}v_{23}} = \frac{E_{22}v_{12}}{1-v_{12}v_{23}}; \; A_{66} = G_{12} \tag{12}$$

In (12), the elastic modules of 3-phase composite is completely determined as in [12].

Introduce (11) and (12) into equilibrium equation:

$$\frac{\partial^2 M_x}{\partial x^2} + \frac{\partial^2 M_y}{\partial y^2} + 2\frac{\partial^2 H}{\partial x \partial y} = -q$$

We get the plate's deflection equation when creep strain is taken into account:

$$
\begin{aligned}
D_x \frac{\partial^4 w}{\partial x^4} &+ D_y \frac{\partial^4 w}{\partial y^4} + 2(D_1 + D_{xy})\frac{\partial^4 w}{\partial x^2 \partial y^2} - \\
&- 2B\int_0^t \widetilde{A}_{66}(t-\theta)\frac{\partial^4 w}{\partial x^2 \partial y^2} d\theta = q
\end{aligned}
\tag{13}
$$

here: $B = \dfrac{h^3}{12}$

For a rectangular plate of size $a \times b$, free boundary condition (Fig.2) bearing constant load:

$$q = q_0 \sin\frac{\pi x}{a}\sin\frac{\pi y}{b} \tag{14}$$

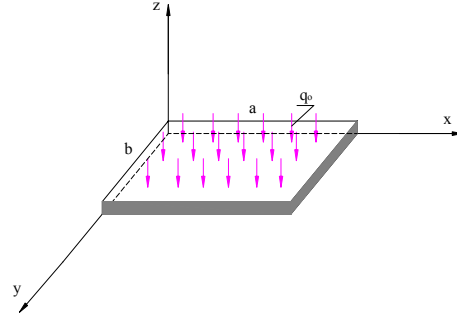Figure 2. Rectangular plate, free boundary condition bearing constant bending load.

The root of equation (13) is:

$$w(t) = c(t)\sin\frac{\pi x}{a}\sin\frac{\pi y}{b} \tag{15}$$

From the boundary conditions:

$$\begin{cases} x = 0; w = 0; y = 0; w = 0; \\ x = a; w = 0; y = b; w = 0; \end{cases} \tag{16}$$

Considering the following relationship:

$$\frac{\partial^2 w(t)}{\partial x^2} = -\left(\frac{\pi}{a}\right)^2 w(t); \frac{\partial^2 w(t)}{\partial y^2} = -\left(\frac{\pi}{b}\right)^2 w(t)$$

$$\frac{\partial^4 w(t)}{\partial x^4} = \left(\frac{\pi}{a}\right)^4 w(t); \frac{\partial^4 w(t)}{\partial y^4} = \left(\frac{\pi}{b}\right)^4 w(t); \tag{17}$$

$$\frac{\partial^4 w(t)}{\partial x^2 \partial y^2} = \frac{\pi^4}{a^2 b^2} w(t)$$

Introduce (14), (15) and (17) into (13), we get the equation for the deflection $c(t)$ of the plate's central point, which is a function of time t:

$$
\begin{aligned}
D_x &\left(\frac{\pi}{a}\right)^4 c(t) + D_y \left(\frac{\pi}{b}\right)^4 c(t) \\
&+ 2(D_1 + D_{xy})\frac{\pi^4}{a^2 b^2} c(t) \\
&- 2B\frac{\pi^4}{a^2 b^2}\int \widetilde{A}_{66}(t-\theta)c(\theta)d\theta = q_0
\end{aligned}
\tag{18}
$$

In abbreviate form:

$$D \cdot c(t)) - \widetilde{D} \int_0^t \widetilde{A}_{66}(t-\theta)c(\theta)d\theta = q_0 \quad (19)$$

with

$$\begin{cases} D = D_x \left(\dfrac{\pi}{a}\right)^4 + D_y \left(\dfrac{\pi}{6}\right)^4 + 2(D_1 + D_{xy})\dfrac{\pi^4}{a^2 b^2} \quad (20) \\ \widetilde{D} = 2B\dfrac{\pi^4}{a^2 b^2} \end{cases}$$

To solve equation (18) we need to know the form of $\widetilde{A}_{66}(t-\theta)$. Introduce (10) into (19) we get:

$$D \cdot c(t) - \widetilde{D}A_{66}^* \frac{1}{n}\int_0^t e^{-\frac{t-\theta}{n}} c(\theta)d\theta = q_0 \quad (21)$$

Notice that the term under integral in (21) has the form:

$$\frac{d}{dt}\int_0^t e^{-\frac{t-\theta}{n}} c(\theta)d\theta = -\frac{1}{n}\int_0^t e^{-\frac{t-\theta}{n}} c(\theta)d\theta + c(t) \quad (22)$$

Differentiate both the two sides of (21) with respect to t:

$$D\dot{c}(t) + \widetilde{D}A_{66}^* \frac{1}{n^2}\int_0^t e^{-\frac{t-\theta}{n}} c(\theta)d\theta - \frac{1}{n}\widetilde{D}A_{66}^* c(t) = 0$$

$$(23)$$

From (21) and (23) we have:

$$nD\dot{c}(t) + \left(D - \widetilde{D}A_{66}^*\right)c(t) - q_0 = 0 \quad (24)$$

The condition for initial elasticity:

$$c_0 = c(t=0) = \frac{q_0}{D}$$

$$= \frac{q_0}{D_x \left(\dfrac{\pi}{a}\right)^4 + D_y \left(\dfrac{\pi}{b}\right)^4 + 2(D_1 + D_{xy})\dfrac{\pi^4}{a^2 b^2}} \quad (25)$$

The root of equation (24) can be expressed as:

$$c(t) = \frac{q}{D - \widetilde{D}A_{66}^*} + \left(\frac{q_0}{D} - \frac{q_0}{D - \widetilde{D}A_{66}^*}\right)e^{-\frac{D-\widetilde{D}A_{66}^*}{D}\frac{t}{n}}$$

$$(26)$$

2.2. Numerical research

Consider a 3-phase composite plate having the following properties:

Polymer epoxy matrix	$E_m = 2.75\,GP_a$	$\nu_m = 0.35$
Glass fiber	$E_a = 72.38\,GP_a$	$\nu_a = 0.2$
Titanium dioxide particle	$E_c = 147\,GP_a$	$\nu_c = 0.21$

The deflection $c(t)$ is expressed in (73) corresponding to each of the following cases

	Case 1	Case 2
Titanium dioxide volume ratio ξ_c	0.2	0.3
Glass fiber volume ratio ξ_a	0.1 0.2 0.3 0.4	0.1 0.2 0.3 0.4
Considering time t	1000, 5000, 10000, 50000, 100000 hours	

A_{66}^* and n are given the values 200 and 10^6, respectively.

The results for the plate's deflection caused by creep are provided in Table 1,2,3,4 below (the value of deflection is equal the given value in the table multiplied by load q_0):

Table 1. Creep displacement (mm) of 2-phase polymer composite (without added particle).

$\xi_c = 0$; $n = 10^6$

	t = 1000	t = 5000	t = 10000	t = 50000	t = 100000
$\xi_a = 0$	1.4968	1.4911	1.4839	1.4277	1.3604
$\xi_a = 0,1$	0.0363	0.0362	0.0360	0.0346	0.0329
$\xi_a = 0,2$	0.0013	0.0013	0.0013	0.0012	0.0012
$\xi_a = 0,3$	2.0680e-5	2.0597e-5	2.0494e-5	1.9691e-5	1.8731e-5
$\xi_a = 0,4$	4.2996e-5	4.2824e-5	4.2610e-5	4.0940e-5	3.8944e-5

Table 2. Creep displacement (mm) of 3-phase polymer composite (particle volume ratio is 10%).

$\xi_c = 0{,}1$; $n=10^6$

	t = 1000	t = 5000	t = 10000	t = 50000	t = 100000
$\xi_a = 0$	1.0293	1.0253	1.0203	0.9814	0.9349
$\xi_a = 0{,}1$	0.0577	0.0574	0.0572	0.0549	0.0523
$\xi_a = 0{,}2$	0.0085	0.0084	0.0084	0.0081	0.0077
$\xi_a = 0{,}3$	0.0026	0.0026	0.0026	0.0025	0.0024
$\xi_a = 0{,}4$	0.0018	0.0018	0.0018	0.0017	0.0016

Table 3. Creep displacement (mm) of 3-phase polymer composite (particle volume ratio is 20%).

$\xi_c = 0{,}2$; $n=10^6$

	t = 1000	t = 5000	t = 10000	t = 50000	t = 100000
$\xi_a = 0$	- 0.7109	- 0.7081	- 0.7047	- 0.6777	- 0.6454
$\xi_a = 0{,}1$	- 0.0732	- 0.0729	- 0.0725	- 0.0697	- 0.0663
$\xi_a = 0{,}2$	- 0.0178	- 0.0178	- 0.0177	- 0.0170	- 0.0162
$\xi_a = 0{,}3$	- 0.0076	- 0.0076	- 0.0075	- 0.0072	- 0.0069
$\xi_a = 0{,}4$	- 0.0051	- 0.0051	- 0.0050	- 0.0048	- 0.0046

Table 4. Creep displacement (mm) of 3-phase polymer composite (particle volume ratio is 30%).

$\xi_c = 0{,}3$; $n=10^6$

	t = 1000	t = 5000	t = 10000	t = 50000	t = 100000
$\xi_a = 0$	- 0.4898	- 0.4878	- 0.4855	- 0.4668	- 0.4445
$\xi_a = 0{,}1$	- 0.0816	- 0.0813	- 0.0808	- 0.0777	- 0.0739
$\xi_a = 0{,}2$	- 0.0268	- 0.0267	- 0.0266	- 0.0256	- 0.0243
$\xi_a = 0{,}3$	- 0.0133	- 0.0133	- 0.0132	- 0.0127	- 0.0121
$\xi_a = 0{,}4$	- 0.0089	- 0.0088	- 0.0088	- 0.0085	- 0.0080

Conclusions

In this paper we've researched the bending of a 3-phase composite plate when creep is taken into account. The deflection equation was obtained for a composite plate having creep effect.

From the analysis for a 3-phase composite plate consisting of polymer matrix, glass fiber and titanium dioxide, the following conclusion can be archived:

- The creep strain of the 3-phase composite plate considered in this research is not notable.

- The creep strain causes to shrink plate. It means that sad bending displacement of plate reduces.

- Changing in the volume ratios of the fiber and particle component can lead to change in the creep strain of the plate in bending.

- The creep stain of plate will reduces if the volume ratios of the fiber component in composite increases.
- For assumed 3 phase composite plate, the creep strain will increase if the volume ratios of titanium oxide particle are increased.

Acknowledgment

References

1. Rabotnov IY.N. Mechanics of deformed solid bodies, Moscow, "Nauka", 1998

2. Malmeiter A.K, Tamyz V.P, Teterc G.A. Strength of polymers and composite materials. Riga, "Zinatie" 1980

3. Iliushin A.A., Pobedrya B. E. The basis of Mathematical theory for thermovisco elastics ,Moscow, "Nauka", 1970

4. Rabonov Yu. N. The creep of element structural, Moscow, "Nauka", 1966

5. Rjanhixin A.R. Theory of creep, Moscow, "Ctroi" Publiser, 1968

6. Iliushin A.A, Ogibalov P.M. Theory of viscoelastic and method of parameters. J. Mechanics of polymers, 1966, N2, p.190-196.

7. Kregerc A.F. J.Mechanics of polymers, 1970, N1. P.34-42

8. Grin A., Adkinc D. The nonlinear theory of continum mechanics, 1985, Moscow, "MIR".

9. Soldatov M.M., J. Mechanics of polymers, 1967, N5, p.921-926.

10. Rozovxki M.I., J. Physics of solids, 1955, Vol.25, N13, p.2339-2354.

11. Xalganhik P.L., J. Mechanics of solid bodies, 1973, N4, p.149-159.

12. Dinh Khac Minh, Pham Van Thu. The mechanical behaviour of 3-phase composite reinforced with fibers and particles. Proceeding of National Mechanics Conference, Hanoi 2009.

13. Dinh Khac Minh, Pham Van Thu. The bending analysis of 3-phase composite plate. Journal of Transportation and Vehicle, 7-2009.

14. Nguyen Dinh Duc, Dinh Khac Minh. Beending analysis of three-phase polymer composite plates reinforced by glass fibers and Titanium oxide particles. J. Computational Materials Sciencs (In Press), available online 10 May 2010

Chế độ thủy triều vùng biển Tây Nam Việt Nam

Đỗ Ngọc Quỳnh[a], Nguyễn Thị Việt Liên[b], Đinh Văn Mạnh[c],
Đặng Song Hà[d]

Viện Cơ học, 264 Đội Cấn, Ba Đình, Hà Nội
[a]*dnquynh@imech.ac.vn*, [b]*nvlien@imech.ac.vn*, [c]*dvmanh@imech.ac.vn*, [d]*riversong2104@yahoo.com*

Abstract

In the Southwest marine area of Vietnam, the tide regime is rather complicated. However, this phenomenon has not been paid attention well because the tide range is not so large, furthermore, tide gauge stations as well as the measured tide data are very limited, so results on tide modeling are still modest and in almost these studies only 4 major tidal constituents are considered.

In order to understand more the tide phenomenon in this area, the well-known software MIKE21 has been applied using the tide data observed at the tide gauges as well as from recent field surveys for boundary conditions and model verification. Furthermore, 8 tidal constituents (K_1, O_1, P_1, Q_1, M_2, S_2, K_2, N_2) are taken into account. In the result, the major tidal characteristics are reproduced after the software is calibrated and validated carefully.

Key Words: tide, numerical modeling, MIKE21

1. Mở đầu

Thủy triều trong Vịnh Thái Lan nói chung và vùng biển Tây Nam nói riêng (hình 1) thường được các tác giả trong ngoài nước nghiên cứu như là một bộ phận của Biển Đông. Vì vậy, độ phân giải không gian còn nhiều hạn chế. Trong bài báo này trình bày kết quả nghiên cứu thủy triều vùng biển Tây Nam với lưới tính mịn, cho phép tính đến sự thay đổi chi tiết của đường bờ và địa hình đáy biển cho 8 sóng triều thành phần, bao gồm các sóng K_1, O_1, P_1, Q_1, M_2, S_2, K_2 và N_2. Công cụ tính toán là phần mềm MIKE21

– tính toán thủy lực và môi trường biển được phát triển bởi Viện Thủy lực Đan Mạch (DHI) (Mike21, 2005).

2. Thiết lập mô hình số trị

2.1 Số liệu đầu vào

Để áp dụng MIKE21 tính toán thủy triều vùng biển Tây Nam Việt Nam đã sử dụng các số liệu sau:

- Bản đồ địa hình của Hải quân Nhân dân năm 1982 tỉ lệ 1/100.000 cho vùng ven biển Tây Nam và tỷ lệ 1/1.000.000 cho vùng còn lại của vịnh Thái Lan. Các bản đồ này được

số hóa bằng công nghệ GIS, sau đó chuyển đổi sang khuôn dạng của phần mềm Surfer để xử lý tạo file độ sâu cho mô hình.
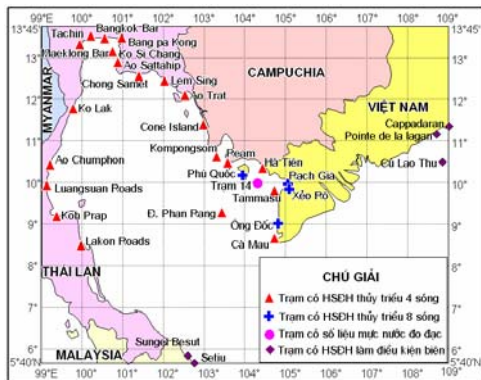

Hình 1. Vị trí vùng nghiên cứu

- Số liệu hằng số điều hòa 4 sóng triều chính (K_1, O_1, M_2, S_2) của Đề tài cấp Nhà nước KT.03.03: "Thủy triều Biển Đông và sự dâng lên của mực nước biển ven bờ Việt Nam" (hình 2).

- Số liệu hằng số điều hòa 8 sóng triều (K_1, O_1, M_2, S_2, N_2, K_2, P_1, Q_1) được phân tích từ chuỗi số liệu mực nước 5 năm (2004-2008) tại các trạm hải văn Ông Đốc, Xẻo Rô, Rạch Giá, Phú Quốc (hình 2) (Đề tài KC.09.02/06-10).
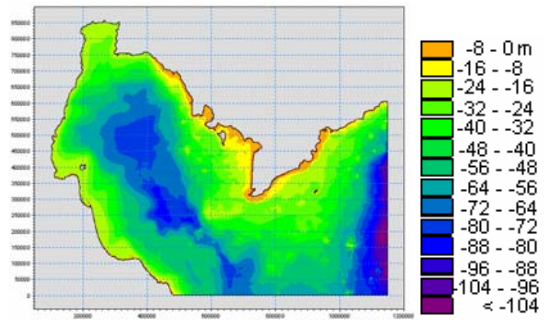
- Số liệu đo mực nước 7 ngày tại vị trí (104°20E, 10°00'N) (Trạm 14) từ 19/9 đến 22/9/2007 và từ 10/3 đến 17/3/2009 (hình 2) của Đề tài KC.09.02/06-10.

Hình 2. Vị trí các điểm có số liệu hằng số điều hòa thủy triều

2.2 Lưới tính

Đã thiết lập lưới tính có kích thước 2km x 2km trên toàn vùng nghiên cứu (545 x 435 lưới) và nội suy độ sâu miền tính (hình 3).
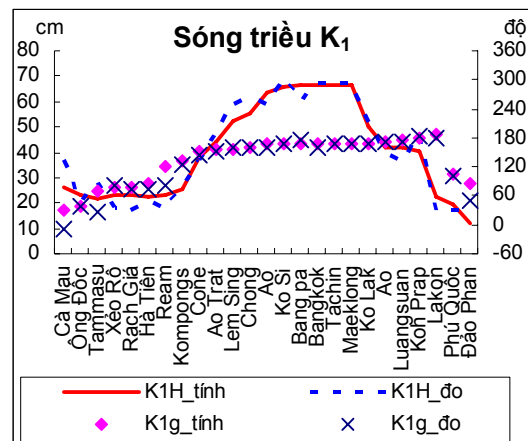

Hình 3. Độ sâu miền tính

Điều kiện biên được nội suy từ các hằng số điều hòa tại các trạm hải văn (hình 2).

## 3. Hiệu chỉnh và kiểm tra mô hình

Trước hết, mô hình được hiệu chỉnh về biên độ và pha cho 8 sóng triều (K_1, O_1, P_1, Q_1, M_2, S_2, K_2, N_2). Các hình 4-11 là so sánh hằng số điều hòa của từng sóng triều giữa kết quả tính toán và giá trị phân tích từ số liệu thực đo.

Hình 4. So sánh kết quả tính toán và thực đo hằng số điều hòa sóng triều K_1
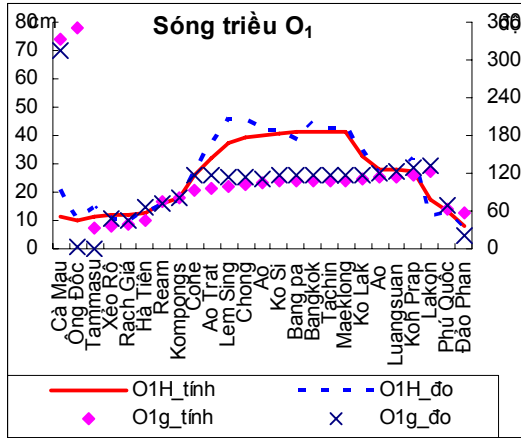
Hình 5. So sánh kết quả tính toán và thực đo
hằng số điều hòa sóng triều O_1
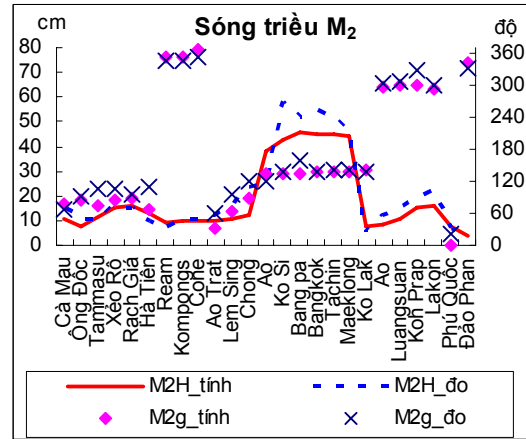
Hình 8. So sánh kết quả tính toán và thực đo
hằng số điều hòa sóng triều M_2

Hình 6. So sánh kết quả tính toán và thực đo
hằng số điều hòa sóng triều P_1

Hình 9. So sánh kết quả tính toán và thực đo
hằng số điều hòa sóng triều S_2

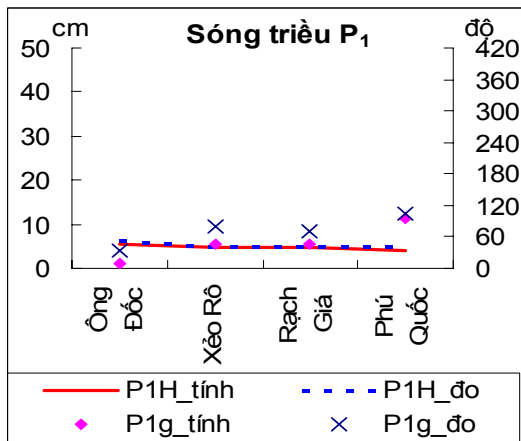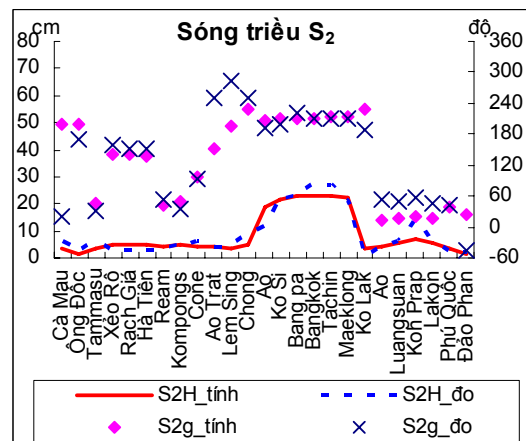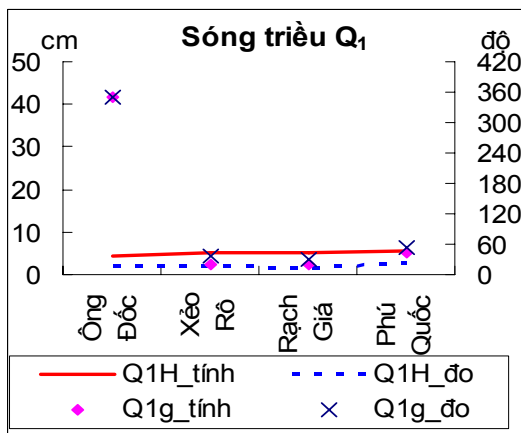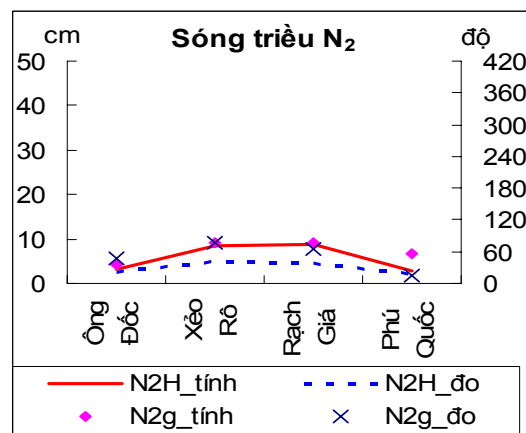Hình 7. So sánh kết quả tính toán và thực đo
hằng số điều hòa sóng triều Q_1

Hình 10. So sánh kết quả tính toán và thực đo
hằng số điều hòa sóng triều N_2
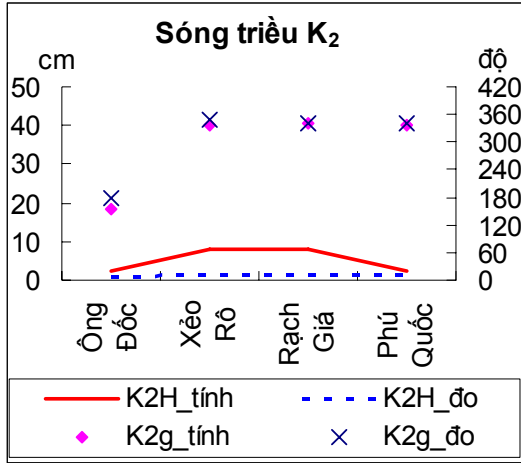
Hình 11. So sánh kết quả tính toán và thực đo
hằng số điều hòa sóng triều K_2

Sau khi mô hình MIKE21 đã được hiệu chỉnh về biên độ và pha của từng sóng triều, đã sử dụng số liệu đo đạc mực nước tại trạm 14 vào tháng 9/2007 và tháng 3/2009 để kiểm tra mô hình. Các hình 12 và 13 là kết quả kiểm tra mô hình này.

Kết quả so sánh chỉ ra rằng mô hình MIKE21 đã được hiệu chỉnh và kiểm tra tốt, có thể sử dụng để mô tả các đặc trưng về dao động thủy triều trong khu vực nghiên cứu với độ chính xác chấp nhận được.
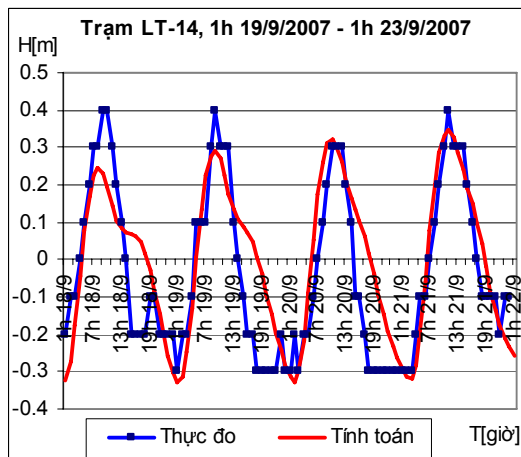
Hình 12. So sánh kết quả tính toán và thực đo
mực nước từ 1h 19/9 đến 1h 23/9/2007

Hình 13. So sánh kết quả tính toán và thực đo
mực nước từ 19h 10/3 đến 14h 14/3/2009

4. Tính hằng số điều hòa thủy triều

Sau khi được hiệu chỉnh và kiểm tra khá tốt, mô hình MIKE21 được sử dụng để tính hằng số điều hòa của 8 sóng triều là K_1, O_1, P_1, Q_1, M_2, S_2, N_2, K_2 trong vùng nghiên cứu. Các hình 14-21 là các bức tranh phân bố đẳng biên độ và pha của từng sóng triều vùng biển Tây Nam.
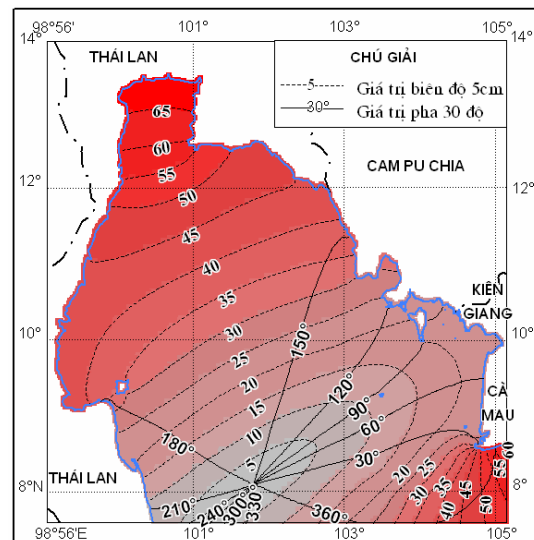
Hình 14. Phân bố biên độ và pha sóng K_1
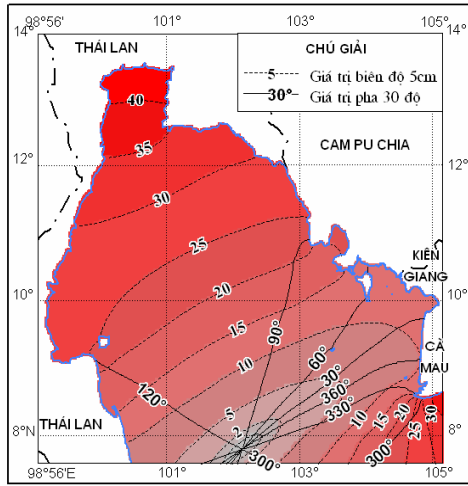
Hình 15. Phân bố biên độ và pha sóng O_1
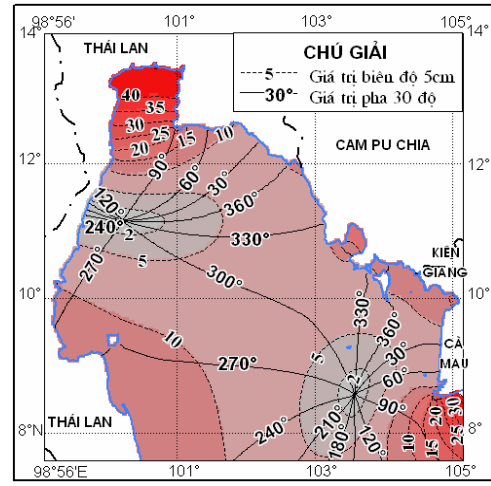
Hình 18. Phân bố biên độ và pha sóng M_2
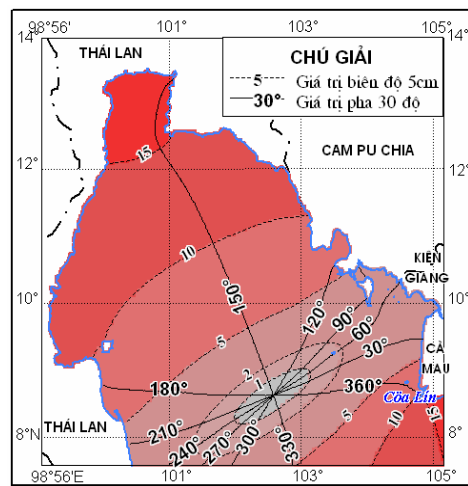
Hình 16. Phân bố biên độ và pha sóng P_1
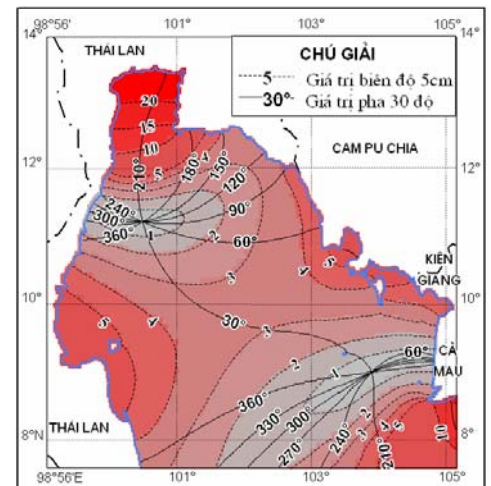
Hình 19. Phân bố biên độ và pha sóng S_2
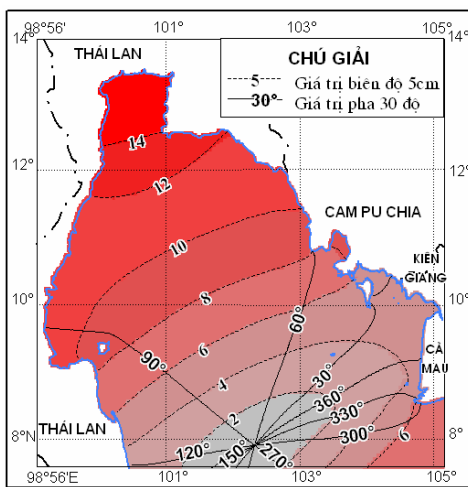
Hình 17. Phân bố biên độ và pha sóng Q_1
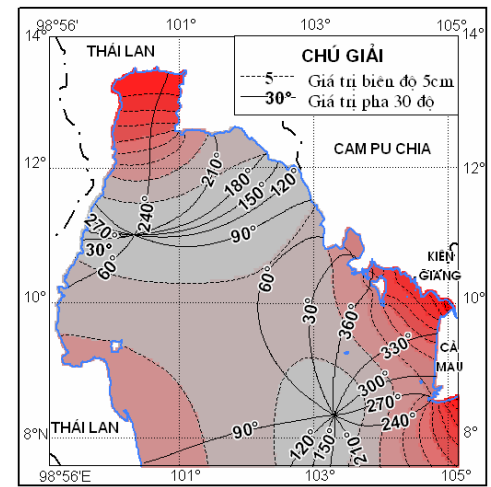
Hình 20. Phân bố biên độ và pha sóng N_2
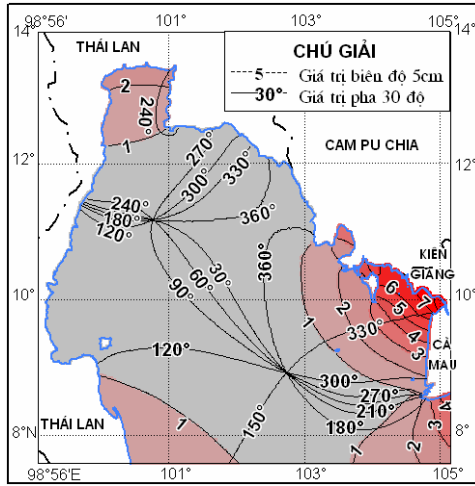
Hình 21. Phân bố biên độ và pha sóng K_2

Nhận xét

Trước hết có thể nhận thấy rằng, các bản đồ phân bố này về xu thế chung là thống nhất với các bản đồ được xây dựng theo kết quả tính toán cho toàn Biển Đông với độ phân giải thô hơn. Tuy nhiên, các kết quả tính toán với độ phân giải cao hơn trong khuôn khổ Đề tài này đã đưa ra những bản đồ phân bố chi tiết hơn, định lượng tốt hơn cho vùng nghiên cứu và có thể tìm thấy những đặc điểm mà những bản đồ phân bố thô hơn không phát hiện được.

a) Các sóng chu kỳ ngày (O_1, K_1, P_1, Q_1)

Bản đồ phân bố đẳng biên độ và đồng pha của các sóng triều chu kỳ ngày này có những nét tương đối giống nhau, chỉ có khác nhau chút ít về giá trị đại lượng và hình dạng phân bố các đường đồng mức (xem hình vẽ 14-17).

- Sóng O1: Đây là sóng nhật triều có tên gọi Mặt trăng chính, có chu kỳ 25,819 giờ, tốc độ góc là 13,943 độ/giờ. Bản đồ phân bố pha chỉ ra rằng, sóng có một điểm vô triều trong vịnh Thái Lan tại tọa độ 7°50'06"N, 102°07'48"E. Điểm vô triều này gần giữa cửa Vịnh, trên đường thẳng nối mũi Cà Mau (Việt Nam) với cảng Kota Baharu (Malaysia). Trong các bản đồ phân bố thủy triều Biển Đông của nhóm Đỗ Ngọc Quỳnh, Nguyễn Thị Việt Liên (Đề tài KT.03.03, 1996) hay của Yanagi T., T. Takao and A.

Morimoto (1997) xây dựng trên cơ sở tài liệu đo đạc vệ tinh đều có một điểm vô triều này nằm ở phía cửa vịnh Thái Lan, nhưng các tọa độ có xê dịch đi. Quanh điểm vô triều đã chỉ ra ở trên, sóng O_1 lan truyền ngược chiều kim đồng hồ. Đây là đặc điểm rất phổ biến tại các biển thuộc Bắc Bán cầu trên thế giới. Theo sự giải thích của Talor (1920), đây là kết quả của sự giao thoa của sóng tới và sóng phản xạ Kevin. Như vậy, quy luật chung này cũng đúng cho sóng nhật triều trong vịnh Thái Lan. Trong vùng biển ven bờ Tây Nam Việt Nam, giá trị pha theo quy luật chung vừa nhận xét ở trên, cũng được tăng dần trong khoảng 300-330° ở khu vực mũi Cà Mau lên 360° ở khu vực cửa Sông Đốc, rồi đạt 30° ở vùng Rạch Giá và tăng lên đến 60° ở khu vực Phú Quốc, Hà Tiên. Nghĩa là sóng nhật triều O_1 truyền từ vùng mũi Cà Mau lên vùng Hà Tiên, Phú Quốc sẽ chậm pha khoảng 6 giờ. Về biên độ sóng O_1, phân bố tăng dần từ điểm vô triều hướng đi các phía. Các đường đẳng biên độ tạo thành dải song song cắt ngang Vịnh và tăng dần giá trị từ cửa Vịnh lên phía đỉnh Vịnh. Ở khu vực đỉnh Vịnh (vùng Bangkok), giá trị biên độ sóng O_1 cỡ 40cm và lớn hơn. Ở vùng biển ven bờ Tây Nam Việt Nam, biên độ sóng O_1 khoảng 10-15cm.

- Sóng K_1: Là sóng nhật triều có tên gọi Mặt trăng - Mặt trời, có chu kỳ 23,934 giờ và tốc độ góc 15,041 độ/giờ. Bức tranh phân bố các đường đồng pha và đẳng biên độ cũng tương tự như sóng O1. Sóng K_1 cũng có một điểm vô triều phân bố ở vùng cửa Vịnh, tại tọa độ 8°07'08"N, 101°47'47"E. Sự chuyển pha quanh điểm vô triều cũng xảy ra ngược chiều kim đồng hồ. Tương ứng giá trị pha của K_1 vùng ven bờ Tây Nam Việt Nam biến đổi từ 0-30° ở khu vực mũi Cà Mau tới 60° ở vùnh Rạch Giá và 90° ở vùng Hà Tiên, Phú Quốc. Sóng truyền từ vùng mũi Cà Mau lên vùng Hà Tiên, Phú Quốc sẽ chậm pha khoảng 6 giờ. Về biên độ, sóng K_1 lớn hơn gấp 2 lần so với sóng O_1. Ở đỉnh Vịnh, giá trị biên độ sóng K_1 cỡ 70cm, ở vùng biển ven bờ Tây Nam Việt Nam, biên độ sóng K_1 đạt 25-30cm.

- Sóng P_1: Sóng nhật triều có tên gọi Mặt trời chính, có chu kỳ 24,066 giờ và tốc độ góc 14,959 độ/giờ. Bức tranh phân bố các đường đồng pha và đẳng biên độ cũng tương tự như các sóng ở trên. Sóng P_1 cũng có một điểm vô triều ở vùng giữa cửa Vịnh nhưng nằm sâu vào phía Vịnh hơn, tại tọa độ $8^o40'55''N$, $102^o34'48''E$. Sự chuyển pha quanh điểm vô triều cũng xảy ra ngược chiều kim đồng hồ. Tương ứng giá trị pha của P_1 vùng ven bờ Tây Nam Việt Nam biến đổi từ 0° ở khu vực mũi Cà Mau đến 90° ở vùng Hà Tiên, Phú Quốc. Sóng truyền từ vùng mũi Cà Mau lên vùng Hà Tiên, Phú Quốc sẽ chậm pha khoảng 6 giờ. Biên độ sóng P_1 nhỏ hơn hẳn so với K_1 và O_1. Tại vùng đỉnh Vịnh, biên độ sóng P_1 chỉ đạt khoảng 15-20cm. Ở vùng ven bờ Tây Nam Việt Nam, giá trị biên độ sóng P_1 khoảng 5-10cm.

- Sóng Q_1: Sóng nhật triều có tên gọi Ellip Mặt trăng lớn, có chu kỳ 26,868 giờ và tốc độ góc 13,399 độ/giờ. Bản đồ phân bố các đường đồng pha và đẳng biên độ cũng tương tự như các sóng nhật triều đã nói ở trên. Sóng Q_1 cũng có một điểm vô triều ở vùng giữa cửa Vịnh, tại tọa độ $7^o57'29''N$, $102^o19'44''E$, gần với điểm vô triều của các sóng O_1 và K_1. Biến đổi pha quanh điểm vô triều cũng xảy ra ngược chiều kim đồng hồ như quy luật chung. Tương ứng giá trị pha của sóng Q_1 trong vùng ven biển Tây Nam Việt Nam biến đổi từ $300-330^o$ ở vùng mũi Cà Mau đến 30° ở vùng Hà Tiên, Phú Quốc. Sóng truyền từ vùng mũi Cà Mau lên vùng Hà Tiên, Phú Quốc sẽ chậm pha khoảng 4 đến 6 giờ. Biên độ sóng Q_1 nhỏ hơn sóng P_1 một chút. Tại vùng đỉnh Vịnh, biên độ sóng Q_1 khoảng 14-15cm. Ở vùng ven bờ Tây Nam Việt Nam, giá trị biên độ Q_1 khoảng 4-6cm.

b) Các sóng chu kỳ nửa ngày (M_2, S_2, N_2, K_2)

Các sóng chu kỳ nửa ngày trong vịnh Thái Lan nhỏ hơn đáng kể so với các sóng chu kỳ ngày. Sự phân bố các đường đồng pha và đẳng biên độ nhìn chung cũng phức tạp và đa dạng hơn. Chúng chỉ có một số nét chung như cùng tồn tại hai điểm vô triều ở các khu vực giống nhau và giá trị biên độ đều nhỏ ở hầu như phần lớn không gian Vịnh. Tuy nhiên khi xem xét chi tiết chúng lại có những điểm không giống nhau (xem các hình vẽ 18-21).

- Sóng M_2: Sóng bán nhật triều có tên gọi Mặt trăng chính có chu kỳ 12,420 giờ và tốc độ góc 28,984 độ/giờ. Theo bản đồ đồng pha, sóng triều M_2 có hai điểm vô triều: một ở cửa Vịnh và một ở bên trong vịnh Thái Lan, tại các tọa độ $8^o37'34''N$, $103^o34'30''E$ và $11^o10'52''N$, $100^o08'42''E$. Trong bản đồ phân bố sóng triều M_2 cho toàn Biển Đông của Fang (1986) cũng chỉ ra tồn tại hai điểm vô triều trong vịnh Thái Lan, bản đồ tính toán của Đỗ Ngọc Quỳnh và Nguyễn Thị Việt Liên (Đề tài KT.03.03, 1996) và bản đồ xây dựng theo tài liệu vệ tinh của T. Yanagi và T. Takao (1997) cũng chỉ ra một điểm vô triều ở cửa Vịnh và một điểm ảo phía trong Vịnh. Vị trí các điểm vô triều theo các tác giả khác nhau có chút ít xê dịch. Tuy nhiên điểm vô triều ở vị trí gần cửa Vịnh theo các tính toán khác nhau là khá gần nhau. Một điều rất thú vị đều thống nhất giữa các bản đồ là sự biến đổi pha quanh điểm vô triều ở khu vực cửa Vịnh đều xảy ra theo chiều kim đồng hồ. Như đã nói ở phần phân tích sóng triều O_1 rằng, theo quy luật chung ở hầu hết các biển thuộc Bắc Bán cầu, sự biến đổi pha quanh điểm vô triều đều xảy ra ngược chiều kim đồng hồ và Taylor (1920) đã giải thích hiện tượng này. Trong dữ liệu khoa học biển của thế giới cũng đã đưa ra trường hợp đặc biệt không theo quy luật chung: đó là tại biển Hắc Hải, biến đổi pha của sóng bán nhật triều quanh điểm vô triều xảy ra theo chiều kim đồng hồ. Sterneck (1922) đã giải thích hiện tượng này là do tác động của hai loại lực kích động theo hướng đông - tây và hướng nam - bắc trong quá trình hình thành thủy triều ở biển này. Sau khi phát hiện ra hiện tượng biến đổi pha của các sóng bán nhật triều M_2, S_2 tại vịnh Thái Lan T.Yanagi, T.Takao (1998) đã tính toán và giải thích hiện tượng trái quy luật chung này là do sự tác động của các dao động theo chu kỳ riêng tồn tại trong Vịnh. Những nghiên cứu cần phải tiếp tục

tiến hành để làm rõ hơn cơ chế đặc biệt của hiện tượng này. Như vậy, trong khuôn khổ tính toán của Đề tài này đã chỉ ra được sóng M_2 tồn tại hai điểm vô triều trong vịnh Thái Lan, trong đó điểm vô triều ở cửa Vịnh có biến đổi pha theo chiều kim đồng hồ là ngược quy luật, còn điểm bên trong Vịnh thì biến đổi pha vẫn ngược chiều kim đồng hồ như thông thường. Vấn đề này gợi mở để tiếp tục có những nghiên cứu sâu sắc hơn về bản chất và cơ chế của hiện tượng. Như vậy, do sự tồn tại của hai điểm vô triều và vận hành biến đổi pha do chúng chi phối mà phân bố pha của sóng M_2 trong vịnh Thái Lan khá phức tạp và phân chia ra thành các vùng biến đổi khác nhau. Từ vùng mũi Cà Mau lên Hà Tiên, Phú Quốc giá trị pha của M_2 giảm dần, có nghĩa thời gian xảy ra thủy triều ở Hà Tiên, Phú Quốc sẽ sớm hơn so với khu vực Cà Mau chứ không chậm pha như trường hợp các sóng nhật triều. Về biến đổi biên độ sóng M_2, có thể thấy biên độ lớn nhất tập trung ở vùng đỉnh Vịnh và vùng phía đông Nam Bộ (Việt Nam). Khu vực đỉnh Vịnh (vùng Bangkok, Thái Lan) biên độ M_2 có thể đạt 40-45cm. Vùng ven bờ Tây Nam Việt Nam biên độ M_2 khoảng 5-15cm.

- Sóng S_2: Sóng bán nhật triều có tên gọi Mặt trời chính có chu kỳ đúng 12 giờ và tốc độ góc 30 độ/giờ. Các bản đồ phân bố gần giống với sóng M_2, nhưng biên độ nhỏ hơn, chỉ bằng nửa M_2. Sóng S_2 cũng tồn tại hai điểm vô triều trong vịnh Thái Lan. Một ở phía cửa Vịnh, gần bờ Việt Nam, biến đổi pha ở đây cũng theo chiều kim đồng hồ như sóng M_2. Một nằm phía trong Vịnh, biến đổi pha ở điểm này xảy ra ngược chiều kim đồng hồ như sóng M_2 và tuân theo quy luật thông thường. Một đặc điểm thấy rất rõ trong biến đổi pha của sóng S_2 là tạo thành những dải rộng hẹp khác nhau. Trong các dải không gian hẹp, pha biến đổi rất nhanh. Ngược lại, ở những dải không gian rộng pha biến đổi rất chậm. Chẳng hạn, ở vùng biển ven bờ Tây Nam Việt Nam có một dải phía bắc cửa Sông Đốc, pha biến đổi rất nhanh từ 60° đến 150°. Sau đó đi lên phía Hà Tiên hay xuống phía mũi Cà Mau thì pha biến đổi chậm đi rất

nhiều. Biên độ sóng S_2 ở khu vực đỉnh Vịnh đạt 20-25cm, ở phía bờ Tây Nam Việt Nam khá nhỏ, chỉ khoảng 1-5cm.

- Sóng N_2: Sóng bán nhật triều có tên gọi Ellip Mặt trăng lớn, có chu kỳ 12,658 giờ và tốc độ góc 28,880 độ/giờ. Sóng triều N_2 cũng có hai điểm vô triều ở các vị trí gần giống với các vị trí của sóng M_2 và S_2. Tọa độ của các điểm vô triều N_2 là $8^o22'51''$N, $103^o18'10''$E và $11^o02'02''$N, $100^o16'37''$E. Khác với các sóng M_2 và S_2, biến đổi pha của sóng N_2 quanh hai điểm vô triều này đều theo quy luật ngược chiều kim đồng hồ. Biến đổi pha của N_2 cũng đều đặn hơn, không tạo thành các dải biến đổi quá nhanh và quá chậm như trường hợp của sóng S_2 đã nói ở trên. Giá trị pha sóng N_2 biến đổi từ 240°-270° vùng mũi Cà Mau đến 350°-360° vùng Hà Tiên, Phú Quốc, nghĩa là sóng triều N_2 truyền từ mũi Cà Mau lên Hà Tiên, Phú Quốc sẽ chậm pha khoảng 3 giờ. Biên độ sóng N_2 khá nhỏ, ở vùng đỉnh Vịnh cỡ 8-9cm, ở phía bờ Tây Nam Việt Nam biến đổi từ 3-8cm.

- Sóng K_2: Sóng bán nhật triều có tên gọi Mặt trăng - Mặt trời, có chu kỳ 11,967 giờ và tốc độ góc 30,082 độ/giờ. Sóng K_2 cũng có hai điểm vô triều trong vịnh Thái Lan. Vị trí của chúng cũng lân cận với các điểm vô triều của các sóng bán nhật triều khác. Tọa độ của các điểm vô triều là $8^o58'16''$N, $102^o43'19''$E và $11^o13'01''$N, $100^o43'23''$E. Biến đổi pha của sóng K_2 quanh điểm vô triều cũng khác hẳn so với các sóng bán nhật triều khác. Nghĩa là tại điểm gần cửa Vịnh, biến đổi pha ngược chiều kim đồng hồ như quy luật thông thường, nhưng ở điểm bên trong Vịnh lại biến đổi theo chiều kim đồng hồ như trường hợp ngược quy luật. Rõ ràng sự biến đổi pha của các sóng bán nhật triều trong vịnh Thái Lan là rất phức tạp, không theo quy luật thông thường. Đặc điểm này cần thiết phải nghiên cứu sâu sắc hơn trong tương lai. Biên độ sóng K_2 trong toàn Vịnh rất nhỏ, chỉ cỡ 1-2cm. Vùng biên độ lớn chỉ tập trung xung quanh vùng Kiên Giang, ở đây biên độ K_2 cỡ 6-7cm.

5. Phân vùng chế độ thủy triều

Sau khi tính hằng số điều hòa 4 sóng triều chính K_1, O_1, M_2, S_2 đã tiến hành phân loại chế độ thủy triều và dòng triều vùng ven bờ Tây Nam theo chỉ số Vander- Stock (Duvanhin, 1960) như sau:

$$F_H = \frac{H_{K_1} + H_{O_1}}{H_{M_2} + H_{S_2}}$$

với Hx là biên độ thủy triều của các sóng triều tương ứng K_1, O_1, M_2, S_2,

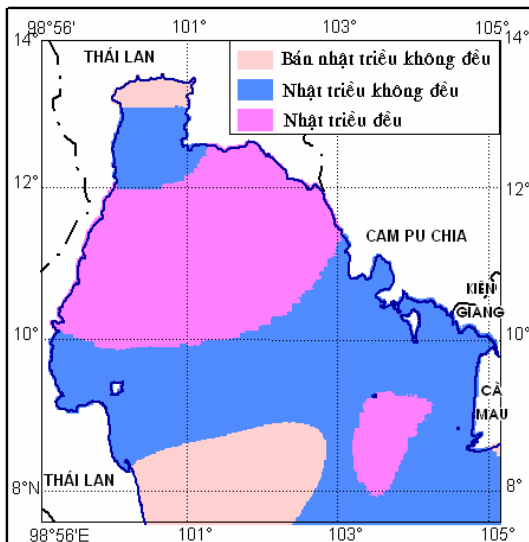Chế độ thủy triều và dòng triều phụ thuộc vào giá trị F_H sau:

$F_H = 0{,}0 \div 0{,}25$: Chế độ bán nhật triều đều

$F_H = 0{,}25 \div 1{,}5$: Chế độ bán nhật triều không đều

$F_H = 1{,}50 \div 3{,}0$: Chế độ nhật triều không đều

$F_H > 3{,}0$: Chế độ nhật triều đều

Đã tính toán và đưa ra các bản đồ phân bố chế độ thủy triều (hình 22).

Hình 22. Chế độ thủy triều vùng biển Tây Nam

Nhận xét

Từ hình 22 có thể thấy rằng chế độ thủy triều vịnh Thái Lan thuộc về chế độ nhật triều là chủ yếu. Nghĩa là đại đa số không gian Vịnh mang chế độ nhật triều không đều và nhật triều đều, chỉ có một phạm vi nhỏ ở đỉnh Vịnh có chế độ bán nhật triều không đều. Vùng biển phía Tây Nam Việt Nam mang chế độ nhật triều không đều. Hàng ngày thường có một lần triều lên và một lần triều xuống. Trong một tháng có khoảng 2-3 ngày có 2 lần triều lên và 2 lần triều xuống xảy ra trong thời kỳ nước kém (biên độ thủy triều nhỏ).

6. Tính mực triều thiên văn cao nhất và thấp nhất

Chế độ thủy triều thường có chu kỳ thiên văn gần 19 năm. Vì vậy để có mực triều thiên văn cao nhất và thấp nhất sẽ tính thủy triều từng giờ tại từng điểm trong vùng quan tâm trong suốt 19 năm, rồi sẽ chọn giá trị cao nhất và thấp nhất. Chu kỳ 19 năm được chọn ở đây là những năm 1991-2009. Mực nước triều được xem là tổng hợp từ các sóng triều thành phần dạng hình sin đơn giản với biên độ và chu kỳ khác nhau.

Công thức tính mực triều tổng hợp từ các sóng thành phần có dạng sau:

$$z_t = A_o + \sum_{i=1}^{n} f_i H_i \cos(\sigma_i t + (V_o + u)_i - g_i)$$

trong đó: z_t là độ cao mực triều tại thời điểm t; A_o - độ cao mực nước trung bình so với số không trạm hoặc không độ sâu; n - số sóng triều thành phần; f_i - hệ số suy giảm biên độ (tham số thiên văn biên độ); $(V_o + u)_i$ - pha ban đầu của sóng thành phần trên kinh tuyến Greenwich (tham số thiên văn pha); σ_i - vận tốc góc của sóng thành phần thứ i; H_i, g_i - hằng số điều hòa biên độ và pha của sóng thành phần thứ i.

Các sóng được chọn để đưa vào tính toán cho vùng biển ven bờ biển Tây Nam là K_1, O_1, P_1, Q_1, M_2, S_2, N_2, K_2 (n=8). Các tham số thiên văn f_i và $(V_o + u)_i$ của 8 sóng này được tính theo các công thức trong công trình của Duvanhin, 1960. Độ cao mực nước trung bình (A_o) cho vùng biển Tây Nam lấy theo trạm Hà Tiên (A_o=76cm).

Kết quả tính toán được đưa ra trên hình 23 và 24.
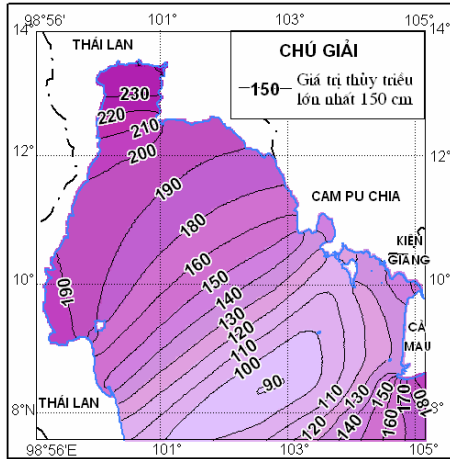
Hình 23. Phân bố mực triều thiên văn lớn nhất
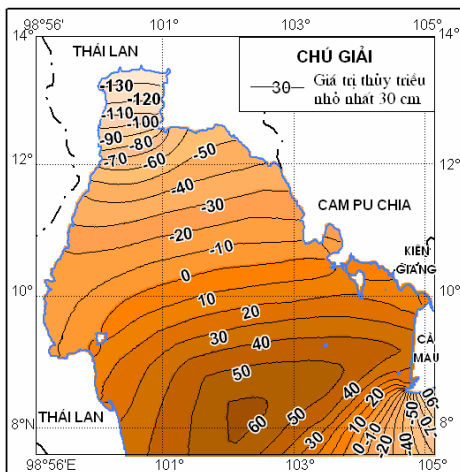
Hình 24. Phân bố mực triều thiên văn nhỏ nhất

Nhận xét

Có thể thấy giá trị thủy triều cực đại sẽ nhỏ nhất ở vùng ngoài khơi gần cửa Vịnh (khoảng 90cm) và tăng dần lên phía đỉnh Vịnh, ở đây đạt trên 230cm. Vùng bờ phía Tây Nam Việt Nam từ Cà Mau đến Hà Tiên đạt khoảng 140-150cm. Giá trị thủy triều cực tiểu sẽ có giá trị lớn nhất ở ngoài khơi gần cửa Vịnh (khoảng 60cm) và giảm dần lên phía đỉnh Vịnh, ở đây hạ xuống dưới 130cm. Vùng bờ phía Tây Nam Việt Nam từ Cà Mau đến Hà Tiên, giá trị thủy triều cực tiểu giảm xuống đến 10-20cm. Như vậy cũng chứng tỏ rằng vùng ngoài khơi gần cửa Vịnh dao động thủy triều có biên độ nhỏ và dao động thủy triều lớn nhất tăng dần lên phía bắc, lớn nhất ở khu vực đỉnh Vịnh.

Kết luận

Mô hình MIKE21 đã được hiệu chỉnh và kiểm tra khá tốt và được sử dụng để nghiên cứu hằng số điều hòa 8 sóng triều thành phần (K_1, O_1, P_1, Q_1, M_2, S_2, K_2, N_2). Các bức tranh phân bố biên độ và pha của các sóng triều phù hợp với kết quả của các tác giả trong ngoài nước nghiên cứu bằng các phương pháp khác nhau. Với những tính toán cho lưới tính chi tiết, các kết quả về phân vùng chế độ thủy triều và giá trị cực trị của mực triều thiên văn là tài liệu cần thiết, phục vụ cho các hoạt động phát triển kinh tế - xã hội, an ninh quốc phòng trên vùng biển này.

Tài liệu tham khảo

Báo cáo kết quả thực hiện đề tài: "Thủy triều Biển Đông và sự dâng lên của mực nước biển ven bờ Việt Nam", mã số KT.03.03 (1996). Hà Nội.

Báo cáo kết quả thực hiện đề tài: "Nghiên cứu các điều kiện tự nhiên và môi trường vùng biển Tây Nam, phục vụ phát triển kinh tế và bảo vệ an ninh chủ quyền quốc gia", mã số KC.09.02/06-10 (2010). Viện Cơ học, Hà Nội.

Duvanhin A. I (1960). *Thủy triều trong biển*. Nhà xuất bản Khí tượng Thủy văn. Lêningrad (tiếng Nga).

Fang G. (1986). *Tide and tidal current charts for the marginal seas adjacent to China. Chinese Journal of Oceanology and Limnology 4*, No.1, pp.1-16.

Mike 21 & MIKE3 Flow Model FM (2005). DHI Water & Environment.

Taylor G. I. (1920). *Tidal Oscillations in the gulfs and rectangular basins*. Proc. Lond. Math. Soc., 20, 148-181.

Yanagi T. and T. Takao (1997). *A numerical experiment on the tide and tidal current in the South China Sea*. 9th JECSS-PAMS Proccedings.

Yanagi T., T. Takao and A. Morimoto (1997). *Co-tidal and co-range charts in the South China Sea derived from the satellite altimetry data*. La mer, 35, 85-94.

Yanagi T. and T. Takao (1998). *Clockwise phase propagation of semi-diurnal tides in the Gulf of Thailand*. J. of Ocenography, vol.54.

Research and Design Energy Storage Control Model in the Conversion from Ocean Waves into Electricity

Manh Hoang Van[a] and Thang Pham Manh[b]

[a] Mechatronics engineer, Faculty of Engineering Mechanics and Automation, University of Engineering and Technology, Vietnam National University, Ha Noi, manhhv87@vnu.edu.vn.
[b] Lecturer, Faculty of Engineering Mechanics and Automation, University of Engineering and Technology, Vietnam National University, Ha Noi, thangpm@vnu.edu.vn.

Abstract

Nowadays, energy is one of proplems that gets the attention from all countries over the world. Beside the classical energy sources such as: thermoelectric, hydroelectric, there is a new energy source that have been attracted in recent years. That is ocean waves energy. This paper presents the research and design of Energy Storage Control Model (ESCM) that converted ocean wave energy into electrical energy. This model consists of a wave energy converter (WEC) that used to transform ocean wave energy into electrical energy, rectifier, voltage stabilizer, and an embedded controller. The converted energy is stored in a Lead-Acid Battery (12V, 5AH). This charge process is controlled by the microcontroller of Microchip, PIC16F877A.

Key Words: *energy storage control model (ESCM), water energy converter (WEC), lead-acid battery charger, microcontroller, fly-back converter.*

1. INTRODUCTION

The electricity demand today for industries as well as daily life is increasing. The traditional energy sources are being exploited to the utmost and the diminishing status. Moreover, the amount of CO_2 generated in the process of using resources that have caused the pollution of living environment. Challenge that put the pressure on all the countries is find renewable energy sources. It is a necessary and urgent task. A form of renewable energy has been researched that use energy from ocean waves.

Ocean wave energy is renewable energy resources that are available in nature. Using ocean wave energy will reduce environmental pollution compared with energy from the fuel. Ocean wave energy is endless because there are up to 70% of earth face is covered byte water.

To use wave energy, an energy storage system is required to store the electrical energy is converted from wave energy. System model is shown in Figure 1.

As known, it's inconvenient to create wave in the laboratory and the cost of

creating wave, wave energy conversion module using water from a reservoir flows down to rotate blade of turbine (if using actual wave of the final results of the tuner as well as to make the turbine rotating blades). The blade turbine is connected to a rotor of electric motor. This rotor rotates along with the rotation of blade. When the rotor rotates, it generates an alternate current. This alternate current will be rectified into direct current to charge for a lead-acid battery.

The DC voltage after rectifying will be applied to a module that controls the lead-acid's charge process. The charge controller module obtains a DC/DC converter and a microcontroller (PIC16F877A).
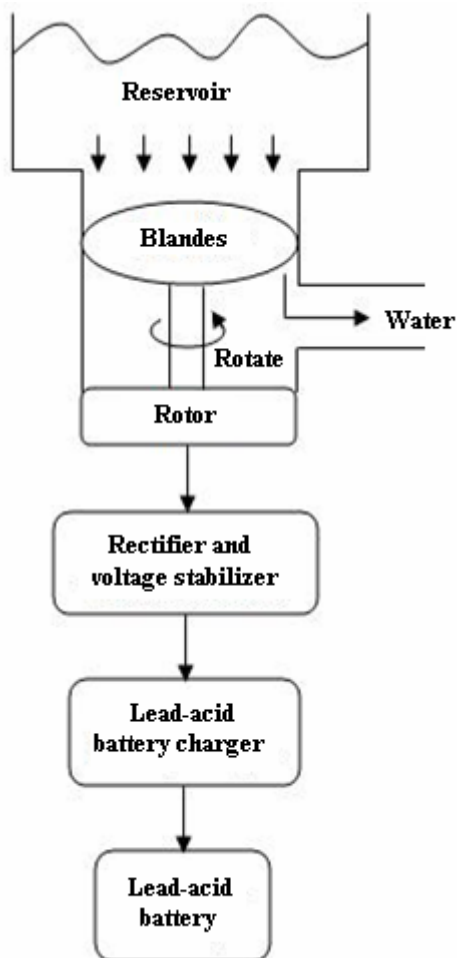
Figure 1: Model of energy storage system

2. HARDWARE DESIGN

2.1. Ocean wave energy converter into AC current

There are a lot of wave energy converters to convert wave energy into electricity such as: turbine type, buoy type. Each type has its advantages and disadvantages. In this system model, oscillation water column (OWC) wave energy converter is used. This device uses the Kaplan turbine to rotate the rotor of electric motor and it has parameters: AC Voltage 220V, Oscillating current 2.5 - 10A, Frequency 50Hz, and Power 300W.

2.2. Rectifier and voltage stabilizer module

Rectifier and voltage stabilizer module is used to convert AC current that created by wave energy converter into DC current. This is a Fly-back converter that is designed employing IC UC3842 of Fairchild Semiconductor. It is an integrated pulse width modulator (PWM) designed with both these objectives in mind. This IC provides designers an inexpensive controller with which they can obtain all the performance advantages of current mode operation.

Without varying the ramp oscillator frequency with load, only a constant frequency converter is possible and this is the basis of line current mode converter circuit. Duty cycle is a function of load demand up to the limit imposed by the internal duty cycle clamp and, beyond this, output voltage decreases with increased output current demand.

The characteristics of rectifier and voltage stabilizer are:
- Input voltage: 85V-265V/AC.
- Frequency: 50 Hz – 63 Hz.
- Output: 19V-5A/DC.
- Efficiency: 80%

Figure 2 shows the topology of a Fly-back circuit. Input of this circuit is DC voltage that is rectified by bridge rectifier circuit. A fast switching MOSFET (S) is used with fast dynamic control over switch duty ratio (ratio

Research and Design Energy Storage Control Model in the Conversion from Ocean Waves into Electricity

of ON time to switching time-period) to maintain the desired output voltage. The transformer is used for voltage isolation as well as for better matching between input and output voltage and current requirements.

Figure 2: Fly-back converter

Figure 3: Principle diagram of rectifier and voltage stabilizer module
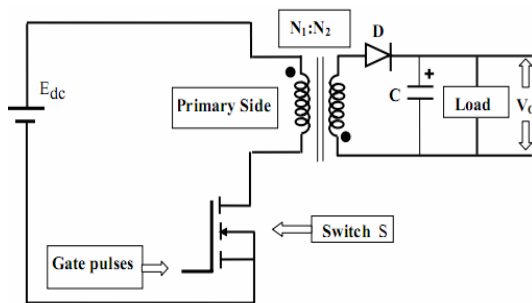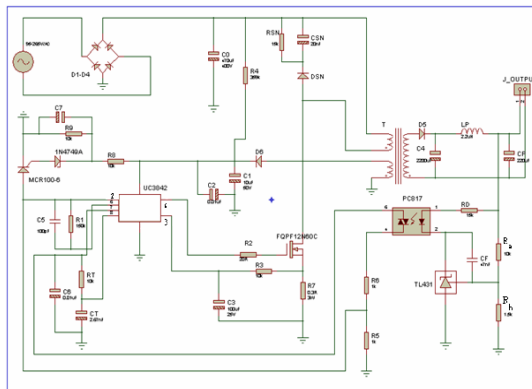
When switch S is on, the primary winding of the transformer is connected to the input supply with its dotted end connected to the positive side. At this time, the diode 'D' connected in series with the secondary winding gets reverse biased due to the induced voltage in the secondary. Thus with the turning on of switch 'S', primary winding is able to carry current but current in the secondary winding is blocked due to the reverse biased diode. The flux established in the transformer core and linking the windings

is entirely due to the primary winding current.

When S turns "off" the primary current stops, all winding voltages reverse by Fly-back action, and the output diodes and secondary windings now conduct current. Therefore, the primary and secondary windings in the Fly-back "transformer" conduct current at different times.

2.3. Battery charger module

The PIC16F877A comes with the onboard PWMs are useful for controlling charge control circuit, while the Analog-to-Digital converter (ADC) can monitor the charge state to prevent overcharge. The charger is designed to charge a sealed lead-acid battery (12V, 5AH); however, the charge parameters are easily modified to work with different lead – acid batteries.

This design uses a constant current, allowing the voltage to rise until the battery voltage reaches a full charge. The charge current is then turn off to prevent overcharging. This allow a high initial charge to quickly bring the battery to a full charge and a low maintenance charge current as needed to maintain the full charge.

The PI controller and Buck converter control the charger current to the battery. When PI controller senses that the charge current is too high, PWM output will pull the gate of the MOSFET (Q_1) low, turning off the current from the power supply and allows current to flow through D_2. The Buck converter (L_1, C_2 and D_2) takes over and modulates the current to the battery at a controlled rate. When PI controller senses the charge current is too low, it turns on, allowing current from power supply to flow through Q_1. The Buck converter now increases current at controlled rate.

The component values for inductor and output capacitance chosen based on the operating parameters of the system.

The inductor value (L):

$$L = \left(V_{IN_{max}} - V_{Out}\right) \cdot \frac{\frac{V_{Out}}{V_{IN_{max}}} \cdot 1}{f_{SW} \cdot 1}$$

Where:

$V_{IN_{max}}$ = Maximum input voltage

V_{Out} = Output voltage

f_{SW} = Buck converter switching frequency

LIR = Inductor-current ratio

$I_{Out_{max}}$ = Maximum output current

The output capacitance (C_{Out}) is chosen such that:

$$C_{Out} = L \frac{I_{Peak}^2}{(\Delta V + V_{Out})^2 - V_{Out}^2}$$

$$\Delta V = \sqrt{V_{Out}^2 + L \frac{I_{Peak}^2}{C_{Out}}} - V_{Out}$$

$$I_{Peak} = I_{Out_{max}} + \frac{\Delta I_{inductor}}{2}$$

$$\Delta I_{inductor} = LIR \cdot I_{Out_{max}}$$

Where:

V_{Out} = Output voltage

I_{peak} = Peak current through the inductor

ΔV = Output – voltage overshoot
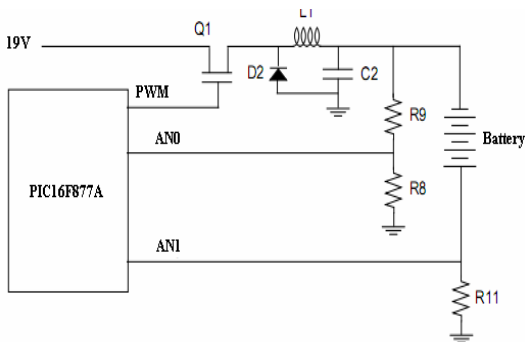
Figure 4: Buck converter
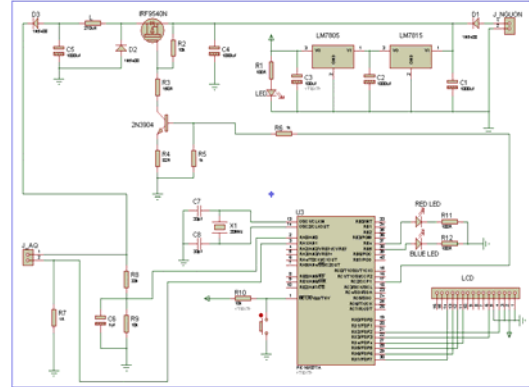
Figure 5: Principle diagram of lead-acid battery charger module

3. ALGORITHM

The controller starts by measuring the voltage on the battery to determine the initial charge rate (high, low, or off). Next, it sets up the PI controller to control and monitor the constant current charge.

With charge at a high rate (1A for this batter) until the voltage of battery is above the high limit (13.8V). The charge current is the cut off, allowing the battery voltage to decay until it descends past the low limit (12.5V). A low current charge (500mA) is then applied to again bring the battery voltage up past the high limit. The drift down/trickle charge cycle repeats.
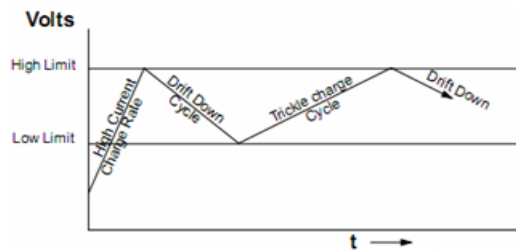
Figure 6: Charging strategy

Research and Design Energy Storage Control Model in the Conversion from Ocean Waves into Electricity
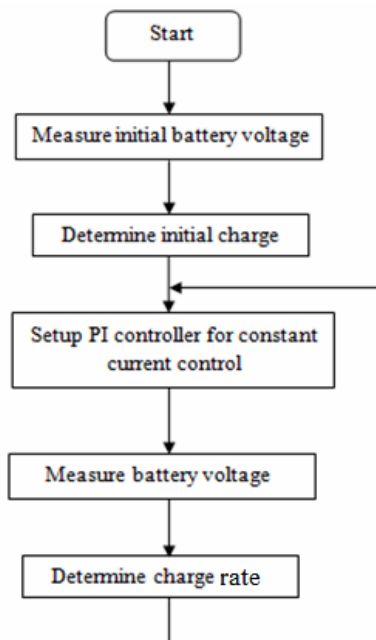
Figure 7: Controller flow chart Results

4. RESULTS

The system hardware is successful designed. Furthermore, lead-acid battery charger has been built and test with results as follows.

When the programmable voltage reference was set to supply the fast charge current of 1A, the actual charge current is 1.06mA. When the programmable voltage reference was set to supply 500mA trickle current, the actual output was measured to be as high as 485mA.

Take about 4 to 6 hours to full charge.
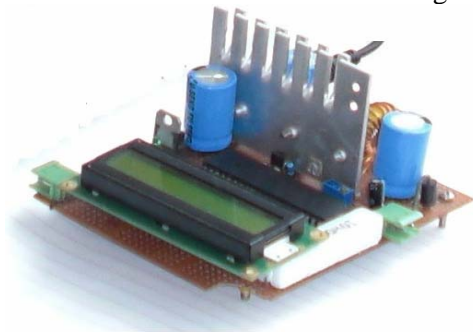
Figure 8: Battery charger

5. CONCLUSION

This article presented the research and design energy storage control model in the conversion from ocean wave into electricity (ESCM). All of the tests were implemented in laboratory but they can be improved to apply in daily life. Battery charging algorithm can be improved to obtain a larger efficiency and more flexibility.

6. REFERENCES

[1] Abraham I. Pressman, Keith H.Billings, Taylor Morey. SWITCHING POWER SUPPLY DESIGN, Third Edition, 2009, p117 – 160.

[2] Battery Charger for SLA, NiCd, NiMH and Li-Ion Batteries. ATMEL AVR450, p1 – 42.

[3] Dan Bulter. Lead-Acid Battery Charger Implementation Using PIC14C000. Microchip AN626, 01/18/2002, p1 – 31.

[4] Donald Schelle and Jorge Castorena. Buck-Converter Design Demystified. Power Electronics Technology, June 2006, p1 – 6.

[5] Intelligent Battery Charger Reference Design. Microchip PICREF-2, p1 – 65.

[6] Jenifer Vinning. Ocean Wave Energy Convertion, December 2005, p11 – 18

[7] Stephen Bowling. A Digital Constant Current Power Led Driver. Microchip AN1138, 10/05/07, p1 – 10.

[8] Stephen Bowling. Buck-Boost LED Driver Using the PIC16F785 MCU. Microchip AN1047, 07/21/06, p1 – 10.

[9] Application Note AN4137 Design Guidelines for Off – line Fly back Converter Using Fairchild Power Switch (FPS[TM]). Fairchild Semiconductor, 2003, p1 – 20.

[10] Application Note AN4140 Transformer Design Consideration for off-line Flyback Converters using Fairchild Power Switch (FPS[TM]), Fairchild Semiconductor, 3/24/04, p1 – 9.

Development of Intelligent Dynamic Encoding Algorithm for Searches (iDEAS) for Reliable Global Optimization

Jo-Hwan Kim[a], Man-Seok Kim[b], Min-Goo Choi[c], and Jong-Wook Kim[d]

[a] *Dong-A University, Hadan-2-dong, Saha-gu, Busan, Korea (kimhades@hotmail.com)*
[b] *Dong-A University, Hadan-2-dong, Saha-gu, Busan, Korea (luhyoun@nate.com)*
[c] *Dong-A University, Hadan-2-dong, Saha-gu, Busan, Korea (choimk@hotmail.com)*
[d] *Dong-A University, Hadan-2-dong, Saha-gu, Busan, Korea (kjwook@dau.ac.kr)*

Abstract

This paper proposes a method of measuring irregularity of cost landscape as a preliminary study for developing intelligent dynamic encoding algorithm for searches (iDEAS), which is a fast global optimization method of engineering problems. Since 2002, the DEAS group including eDEAS, uDEAS, and mDEAS has been successively developed with top-class search results by which it is acknowledged as one of the cutting-edge metaheuristics. The proposed measure of search status and irregularity will provide useful information for intelligent transformation of DEAS structure, which is validated through two benchmark functions.

Key Words: cost landscape, global optimization, DEAS, search intelligence, function optimization

1. Introduction

Dynamic encoding algorithm for searches (DEAS) is a computational optimization method group which do not require a derivative equation of objective function to be minimized or maximized (Kim et al. 2004, Kim et al. 2007, Kim et al. 2008, Kim et al. 2009). DEAS uses a binary string as a genotype for a certain real value like genetic algorithm (GA), while it differs from GA in that the binary strings constitute a binary matrix and its column is gradually expanded as local search progresses.

From the viewpoint of neighborhood cardinality, DEAS can be classified into exhaustive DEAS (eDEAS), univariate DEAS (uDEAS), and modular DEAS; eDEAS generates approximately 2^n neighboring matrices (Kim et al., 2004), whereas uDEAS produces about $2n$ matrices for an n-th order problem (Kim et al. 2008). mDEAS is a hybridized version of eDEAS and uDEAS, and thus its cardinality is much less than eDEAS with higher reliability than uDEAS (Kim et al. 2009).

This paper provides an analytic approach for comprehending current search status and cost landscape in the framework of template patterns. As mentioned above, eDEAS is a

thorough search method at the cost of exponentially increasing cardinality. The rich information attained in running eDEAS is beneficial for analyzing the cost function property, which can endow transformation to the other types of DEAS in an intelligent way. In this context, all the diagonal pairs are investigated in terms of several patterns for inference of cost function shape.

2. DEAS

2.1. Global search

DEAS series are global optimization methods that possess global and local search strategies. As the global search strategy, DEAS adopts the multistart method where local search is iterated from random points scattered over a search space. After conducting a finite number of local searches from selected random points, DEAS attains a global minimum that is the best local minimum found so far. Since DEAS uses binary representation, i.e., search space is divided by finite grids, a random initial point is one of the intersection points of the grids. Therefore initial points should be checked if they were previously evaluated to avoid unnecessary cost evaluation. To this end, the routine named HISTORY CHECK is easily implemented in DEAS by concatenating all the rows in initial variable matrices into one string, storing them in memory, and comparing them with former strings (Kim et al., 2004). The global optimization performance of HISTORY CHECK is quite strong despite code simplicity.

2.2. Local search

The local search strategy in DEAS comprises bisectional search (BSS) and unidirectional search (UDS). BSS is derived from the property that insertion of 0 (or 1) right to LSB of a binary number leads to decrease (or increase) of transformed real values from that of the original binary number. This phenomenon is adopted for
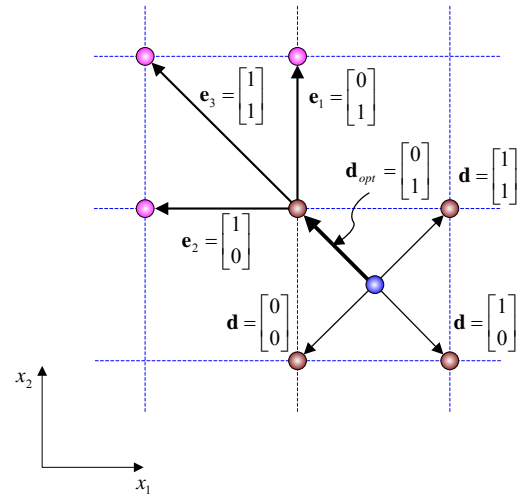
Figure 1. BSS and UDS of eDEAS in two-dimensional search space

local search; in the case the cost computed with a 0-added string is smaller than the cost of a 1-added string, one can obtain a better approximation of a local minimum by adding 0 to the current string as a result. However, the in-depth search of BSS should be balanced with UDS by extending it along an optimal BSS direction while maintaining string length.

For UDS, the simple operations of increment addition (INC) and decrement subtraction (DEC) for a binary string are carried out until a better optimum is located. An example of UDS, which is started from 01 and preceded by BSS, is

$$011 \overset{UDS(1)}{\rightarrow} 100 \overset{UDS(2)}{\rightarrow} 101 \overset{UDS(3)}{\rightarrow} \cdots$$

In this case, BSS finds that INC is promising. In terms of directions, BSS searches vertically, while UDS searches horizontally.

Fig. 1 shows how to make neighboring points in BSS and UDS of eDEAS in two-dimensional search space. In BSS, $4(=2^2)$ direction vectors **d** yields 4 neighboring points, and 0 and 1 denote decrease and increase from the parent point located in center position, respectively. Likewise, in UDS extension vectors **e** play

Table 1. Category of cost relation patterns (L: linear, P: peak, F: flat, U: up, D: down)

Name	Pattern	Name	Pattern
LU (1)		LD (2)	
PU (3)		PD (4)	
FU (5)		FD (6)	
UF (7)		DF (8)	
FF (9)			

the role to extend the current search along the best BSS direction $\mathbf{d}_{opt}$. This paper deals with manipulation of only direction vectors for measuring landscape ruggedness.

3. Cost Pattern Analysis

In general, most local optimization methods including DEAS accept the best or the first point among the neighborhood points for code simplicity. However, they contain useful information on the landscape of cost function around the incumbent point.

From the viewpoint of DEAS, eDEAS is suitable for a rugged cost function, while uDEAS is compatible for a smooth cost function. In Kim et al. (2007), ruggedness had been attempted to be measured by checking irregular behaviors of BSS and UDS in one-dimension. However, it is somewhat complicated to extend the measure to multi-dimensional cases.

This paper proposes a new diagonal cost pattern analysis (DCPA) to measure ruggedness of cost landscape as a preliminary study for iDEAS. Diagonal cost pattern is made of three BSS points; a left-

hand child point(Y^l), a right-hand child point(Y^r), and its parent point(X). The number of all possible combination of diagonal cost patterns is nine as shown in Table 1.

For ease of comprehension, two diagonals in Fig. 1 are used for DCPA; from a point with $\mathbf{d} = \begin{bmatrix} 0 & 0 \end{bmatrix}^T$ to the one with $\mathbf{d} = \begin{bmatrix} 1 & 1 \end{bmatrix}^T$ (D1), and from a point with $\mathbf{d} = \begin{bmatrix} 0 & 1 \end{bmatrix}^T$ to the one with $\mathbf{d} = \begin{bmatrix} 1 & 0 \end{bmatrix}^T$ (D2). Considering that 0 and 1 in direction vectors represent opposite directions with each other, a counter point of a diagonal is made of a complementary direction vector. In general, BSS in n-dimensional space produces 2^{n-1} diagonals in terms of direction vectors as shown in Table 2.

Fig. 2 shows five categories of cost diagonal patterns selected for comprehension of the relation between cost landscape and constituent diagonals. Fig. 2(a) represents the condition that x_1 has dominance, whereas Fig. 2(b) corresponds to the case x_2 is dominant. Owing to the single variable dominance, it is obvious that uDEAS is more appropriate with much less computation time.
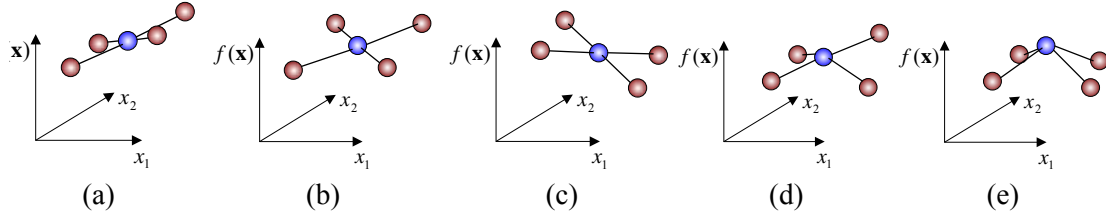
Figure 2. Categories of diagonal cost patterns

Table 2. End points of cost diagonals represented by direction vectors

Direction vector	Encoded number		Direction vector	Encoded number
$00\cdots00$	0		$11\cdots11$	2^n-1
$00\cdots01$	1	$\Leftrightarrow$	$11\cdots10$	2^n-2
$\vdots$	$\vdots$		$\vdots$	$\vdots$
$01\cdots11$	$2^{n-1}-1$		$10\cdots00$	2^{n-1}

In Fig. 2(c), there's no single-variable dependency in cost patterns. However, overall shape is flat, and thus uDEAS might be able to perform equally. Fig. 2(d) has irregular patterns in two diagonals and Fig. 2(e) has a peak at a BSS parent point, both of which have no apparent dominant direction. Therefore, as this condition happens, eDEAS will search a better child point more robustly.

In terms of the cost pattern classifications in Table 1, Fig. 2(a) has two diagonal patterns LU and LU for D1 and D2, respectively. In the same manner, Fig. 2(b) and Fig. 2(c) have diagonal patterns of LU-LD, and LD-LD, respectively. As shown in the figures, overall cost landscapes of the three cases are smooth with some slopes. On the other hand, the peaky patterns of Fig. 2(d) and Fig. 2(e) have the diagonal pattern of LU-PU and PU-PU, respectively, which contain at least one PU or PD pattern.

From the above expressions in terms of patterns, it can be postulated that a rugged cost function will have peaky patterns more often than smooth patterns. It implies that a smooth function will have a sequence of lower pattern number combinations during eDEAS. To validate the proposed measure of landscape ruggedness, two representative cost functions are employed and their sequences are compared in the present work.

4. Experiment

The first test function is a biased unimodal function written as

$$f_{BU}(x) = 100x_1^2 + x_2^2, \quad -2 \le x_1, x_2 \le 2. \quad (1)$$

The second test function is six-hump camel-back function expressed as

$$f_{CA}(x) = 4x_1^2 - 2.1x_1^4 + \frac{1}{3}x_1^6 + x_1x_2 - 4x_2^2 + 4x_2^4, \quad (2)$$
$$-5 \le x_1, x_2 \le 5.$$

Table 3 shows diagonal pattern numbers of the two functions in terms of BSS row lengths. For the smooth and biased function f_{BU}, diagonal numbers are almost 2 (LD), while a more complicated function f_{CA} yields diagonal pattern 4 (PD) many times. When D1 and D2 are equally 4 (PD) as shown in the sixth and tenth row lengths of the f_{CA} results, it implies that the current BSS fails to find a better child point than the incumbent parent point, which happens with a rugged cost function. On the other hand, if a BSS has a pattern which contains at least one LU or LD, it produces an improved point irrespective of cost ruggedness. Therefore in

Table 3. Cost patterns of two test functions (RL: row length, 1: LU, 2: LD, 3: PU, 4: PD)

Func.		f_{BU}								f_{CA}							
Init. Matrix		$[00]^T$		$[01]^T$		$[10]^T$		$[11]^T$		$[00]^T$		$[01]^T$		$[10]^T$		$[11]^T$	
Diag.		D1	D2	D1	D2	D1	D2	D1	D2	D1	D2	D1	D2	D1	D2	D1	D2
	2	2	2	2	2	1	1	1	1	2	4	4	2	4	1	1	4
	3	2	2	2	2	2	2	2	2	2	1	2	1	2	1	2	1
	4	2	2	2	2	2	2	2	2	2	4	2	4	2	4	2	4
	5	2	2	2	2	2	2	2	2	1	2	1	2	1	2	1	2
R	6	2	2	2	2	2	2	2	2	4	2	4	2	4	2	4	2
L	7	2	2	2	2	2	2	2	2	4	4	4	4	4	4	4	4
	8	2	2	2	2	2	2	2	2	1	2	1	2	1	2	1	2
	9	2	2	2	2	2	2	2	2	4	2	4	2	4	2	4	2
	10	2	2	2	2	2	2	2	2	4	4	4	4	4	4	4	4

this paper we propose a ratio of pattern 4 as a ruggedness measure. For f_{BU} , ratio of pattern 4 is 0%, and for f_{CA} 44%. The relation between the ratio and the cost-landscape will be testified with various functions, and the database will be used for intelligent transformation to a proper DEAS type automatically during search.

5. Conclusion

The present study aims at measuring ruggedness of cost landscape in the current search for eDEAS. A concept of diagonal cost pattern is newly proposed for the measure, which is straightforward and easy to extract at BSS. Relation between the proposed measure and cost landscape is validated through two test functions. After collection of database with more test functions, intelligent DEAS will be devised by transforming DEAS structures between search. The advanced version of DEAS will be applied to on-line trajectory generation for humanoid walking and moving.

Acknowledgement

References

J. -W. Kim, and S. W. Kim (2004). Numerical method for global optimization: dynamic encoding algorithm for searches. *IEE Proc.-Control Theory and Appl.*, 151(5), pp. 661−668.

J. -W. Kim, Y. Park, T. Kim, and S. W. Kim (2007). Extraction of shape information of cost functionc using dynamic encoding algorithm for searches (DEAS). *Journal of Control, Automation, and Systems Engineering*, 13(8), pp. 790−797.

J. -W. Kim, T. Kim, Y. Park, and S. W. Kim (2008). On-load motor parameter identification using univariate dynamic encoding algorithm for searches, *IEEE Trans. Energy Conversion*, 23(3), pp. 804−813.

E. Kim, J. Kim, and J. -W. Kim (2009). Development of modular DEAS (mDEAS) and its application to optimal trajectory generation of biped walking, *Trans. KIEE*, 58(2), pp. 382−390.

Design Autopilot Software for Helicopter
on Flight Motionless and Vertical Take off - Landing

Lã Hải Dũng[a], **Trần Quốc Cường**[b] and **Đặng Ngọc Thanh**[c]

[a] *Military Technical Institute, lahaidung@gmail.com*
[b] *Military Technical Institute, cuong208@gmail.com*
[c] *Military Technical Academy, thanhgialam@yahoo.com*

Abstract

The helicopter is a vehicle, which can fly motionless, vertical, front, back and vertical take off-landing without runway. It is used popularly in security, defence and national economy. The aerodynamics and control of helicopter is different from the aircraft. This article presents researches into design autopilot software for helicopter on flight motionless and vertical take off - landing.

1. Introduction

Helicopter is a kind of plane, which have outstanding features including the ability to hover, climb and land vertically and fly in various directions and climb and land without runways. As a result, it has a wide range of applications in defense and economy.

The rotary mainly produces lift and controlling helicopter so the characteristics of aerodynamics and dynamics and the controlling of helicopters are different from other ordinary planes.

The study and design autopilot software for helicopters without pilots is very complicated. A flowering, climbing, and descending vertically are basic flying modes of helicopters. The article presents the study of design programming autopilot software for those flying modes.

2. The forces and moments affecting when helicopters climbing and descending vertically

For conventional helicopters, which have one main rotor and tail rotor, the forces and moment acting on them when hovering, climbing and descending are in fig 1 [1].

The main rotor thrust T, which is perpendicular to the rotating surface of the rotor blades, is divided into two parts T_y and T_z, which are vertical and horizontal respectively. The magnitude of them depends on the height of the flight, the geometric characteristics of the main rotor, angle speed w and blade pitch angle φ, and it is determined by the controlling angle θ (controlling blade pitch angle and the power of engine).
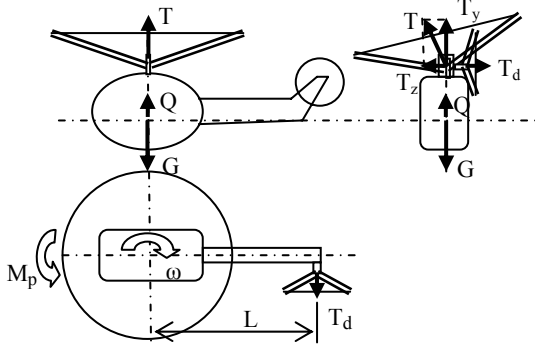
Figure 1. The forces and moments affecting
when helicopters hovering

- The weight G of helicopter;
- The tail rotor thrust T_d

- Opposing moment M_p produced by the
wash plate is opposite to the rotary direction.

When helicopter climb and descend
vertically there is a reaction force Q. This
force is opposite to the helicopter motion.

In blade element theory [3] the blade are
divided into n parts follow its radius, main
rotor thrust T is:

$$T = N \int_0^R \frac{\rho(\omega r)^2}{2} c_y^\alpha \alpha b dr \qquad (1)$$

In which:

      N- means the number of blade;

      ρ- absolute density of air;

      r- radius of blade section;

      C_y^α -coefficient list of main blades

by angle of attack;

ω- the speed of main rotor blade;

α- the angle of attack of blade
section on the blade pitch angle φ,

flapping angle and the flap
coefficient k;

b- the length of the section profil of
the blade;

      R- radius of blade .

Therefore, at different altitude levels due
to the different density of air. The collective

levels need to be controlled in different
positions so that T_y is equal to the weight G.

When the blade rotates, it pushes the air
down and creating sensory flow with the
velocity of flight patch angle

$$V_i = \sqrt{\frac{T}{2\rho A}} \qquad (2)$$

with A= $2\pi R^2$ - the area of circular flat plate.

At this point, the velocity of each blade
section is:

$$U = \sqrt{(V_i + V_y)^2 + (\omega r)^2} \qquad (3)$$

Angle of resultant velocity:

$$\phi = \arcsin\left(\frac{V_i + V_y}{U}\right) \qquad (4)$$

The angle of attack at each blade section is:

$$\alpha = \varphi - \varphi_x - k.\beta - \phi \qquad (5)$$

At this point, the lift and drag force acting on
it:

$$dL = \frac{\rho U^2}{2} c_y^\alpha \alpha b r$$
$$dX = \frac{\rho U^2}{2} c_x b r \qquad (6)$$

The main rotor thrust of each blade section
is:

$$dT = dL \cos\phi - dX \sin\phi \qquad (7)$$

The operation mode of rotor blade is
characterized by the coefficient:

$$\mu = \frac{V_i + V_y}{\omega R} \qquad (8)$$

The coefficient for the ratio between
aerodynamic lift and flapping enteric of
blade is:

$$\gamma = \frac{\rho c_y^\alpha b R^4}{I_\beta} \qquad (9)$$

with I_β - inertial moment of blade.

At this point, the average flap angle of the
blade is:

$$a_0 = \int_0^R ((\alpha + \phi)\bar{r}^2 - \bar{r}\mu)\bar{r}\gamma / 2 \qquad (10)$$

of which: $\bar{r} = \dfrac{r}{R}$ - relative diameter of blade section.

And flapping angle of the blade according to angle of azimuth in blade rotation:

$$\beta(\psi) = a_0 + a_1 \cos\psi + b_1 \sin\psi \qquad (11)$$

with: ψ - angle of azimuth in blade rotation;

a_1 - Tilt angle of T vector tilt forward in comparison with main rotor (in hover, vertical climb and descent, this parameter is zero);

b_1 - the tilt angle of T vector. These angles depend on the tilt angles of the tilt disk, the control signal from periodic changing cyclic stick.

The opposing moment M_p produced by the main rotor blade is calculated by the formula:

$$M_p = N \int_0^R dX dr \qquad (12)$$

The vertical drag force acting on helicopter is:

$$Q = \frac{\rho c_{xt} V_y^2}{2} S \qquad (13)$$

Where c_{xt}: coefficient of vertical drag force;

S- the vertical area of helicopter .

The calculation of the tail rotor thrust T_d is the same as with main rotor. The only difference is there is only control parameter, which is blade pitch angle.

When helicopter hover the equation of its force and moment is:

$$\left. \begin{array}{l} T_y = G \\ T_z = T_d \\ M_p = T_d.L_d \end{array} \right\} \qquad (14)$$

When helicopter climbs and descend vertically, equation of its motion is [2]:

$$\left. \begin{array}{l} \dfrac{dV_y}{dt} = (T_y + Q - G)/m \\[2mm] T_z - T_d = 0 \\[2mm] M_p - T_d.L_d = 0 \\[2mm] \dfrac{dH}{dt} = V_y \end{array} \right\} \qquad (15)$$

Where:

V_y - velocity of vertical climb and descent;

H - flight height;

M - helicopter weight.

From the formulas (1) to (13), it is absolutely possible to identify the parameters needed to solve equations (14) and (15).

3. Design autopilot software for helicopter to hover, climbs descend vertically

When hovering, climbing and descending vertically, the autopilot system of helicopter require the devices in the following diagram (figure 2)

It can be seen that, in order to control helicopter we need:

- Sensors to measure the height (H), V_y vertical velocity, rotor speed of helicopter around the vertical shaft ω_y, the rotary speed of the engine ω .

- The programs to give off control signal:

+ The helicopter does not sign around vertical shaft: $\omega_{yct} = 0$;

+ The rotary speed of main rotor is constant: $\omega_{ct} = const$;

+ The required height H_{ct}.

- Computers: analyze the real time parameters from sensors and programs to produce control signal servo.

- Servo control:

+ Servo ω_{dc} - control the position of collective level to maintain rotation of main rotor;

+ Servo θ - control blade pitch of main rotor to maintain the altitude;

Lã Hải Dũng et al

+ Servo θ_d - control blade pitch of tail blades to stop the helicopter from spinning around the vertical shaft.
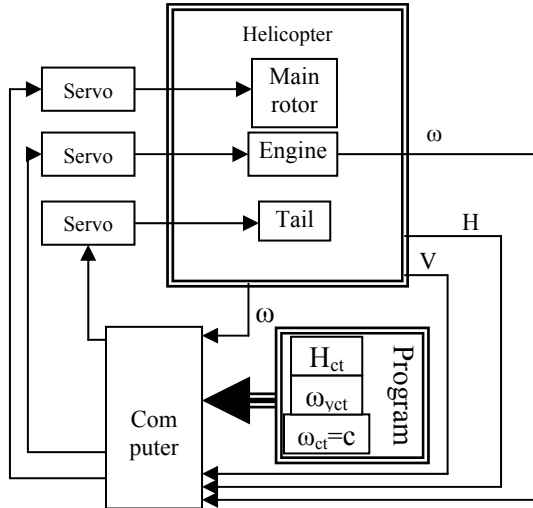

Figure 2. The control system in vertical

The autopilot algorithm in flight mode is:

$$\left.\begin{array}{l}\theta = k_H\left(H_{ct} - H\right) + k_{Vy}V_y \\ \alpha_{dc} = k_{\omega dc}\left(\omega_{ct} - \omega\right) \\ \theta_d = k_{\theta d}\omega_y\end{array}\right\} \quad (16)$$

Where $k_H,\ldots, k_{\theta d}$ are control coefficients.

In order to be able to calculate the above control coefficients is the experimental methods are often used with the simulation of different stages in computer [4]. The helicopter motion is simulated by the equations (15) with the calculations of parameters using formulas (1)-(13).

4. Some results

4.1 The object of the calculation

Simulating the calculation and design an algorithm for autopilot in computer for one type of helicopter "X60SE" with the following parameters (table 1) [5].

By the simulation the control circles of this type of helicopter with the use of experiments, the obtained results with necessary values as follow:

$$k_H = 0,137 ; k_{Vy} = 0,02 ;$$
$$k_{\omega dc} = 0,105; k_d = 0,26 .$$

Table 1: The X60SE helicopter parameters

Quantity	Symbol	Metric unit
Weight	m = 8,2	kg
Blades of main rotor	N = 2	
The number of fins of tail	$N_d = 2$	
Empirical constant in expression for induced velocity	k = 0,2	-
The rotary speed	ω = 167	rad/s
Radius of main rotor blade	R = 0,775	m
The curve blade of main rotor blade	b = 0,058	m
The coefficient of list basing on the angle of attack of the blades of main rotor blade	$c_y^\alpha = 5,5$	1/rad
The opposing force coefficient of main rotor blade	$c_{x0} = 0,025$	-
Flapping inertial moment of main rotor blade	$I_\beta = 0,038$	kg.m^2
Radius of tail fin	$R_d = 0,13$	m
The curve blade of tail fin	$b_d = 0,029$	m
The coefficient of list basing on the angle of attack of the blades of tail rotor	$c_{yd}^\alpha = 5,0$	1/rad
The coefficient of the blades of tail rotor	$c_{xdd} = 0,024$	-
The ratio transmission rate between tail fin and main rotor	$n_t = 4,66$	-
Power	$N_{dc} = 2000$	w
Vertical area	S = 0,15	m^2

4.2 Result for hover mode

The analysis show that at different altitudes different the blades pitch angle control is required to maintain the hover. This results in different flapping angles of

the main rotor blade. Fig 3 illustrates that the variations of the blade pitch angle and flapping angles of the main rotor blades at depends on the changes in altitude.
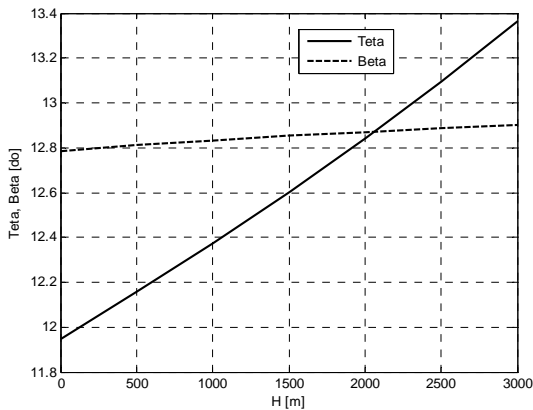

Figure 3. The dependence blades pitch angles and flapping angles of the main rotor blade an altitude.

As can be seen from the graph, when the altitude increases the airflow decreases. Therefore, the equilibrium between the drag force of main rotor blade and the weight can only be obtained retained when the common blade pitch angle is increased. The angle of blade sections of main rotor blade is increased. This results in constant lift of blade elements at different altitude. The flapping angle of the blades of the main rotor blade is identified by the equilibrium moments between airflow force, weight, opposing force, inertia in flapping flat plate around its horizontal hinge. This is because the altitude is higher, the opposing flap force decreases and this leads to the rise in flapping angles. However, due to the small influence opposing flap force on flap motion, the increase in flapping angle is minimal.

As can be seen on the graph (fig 4), when blade pitch angle grows, the drag force and flapping angle of blades increase. This calculation analysis enables us to maximum use of blade pitch angle and the engine capacity.
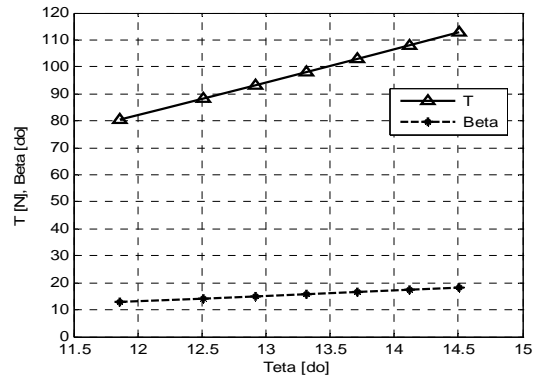
Figure 4. The dependence main rotor thrust and flapping angle of main rotor blade follow blades pitch angle

4.3 Results for vertical climb and descent

First, the reactions of helicopter need to be calculated with different blade pitch angles. When the blade pitch angle is varied to the time (fig. 5) the changes in helicopter motion parameters are illustrated in figure 6-9.
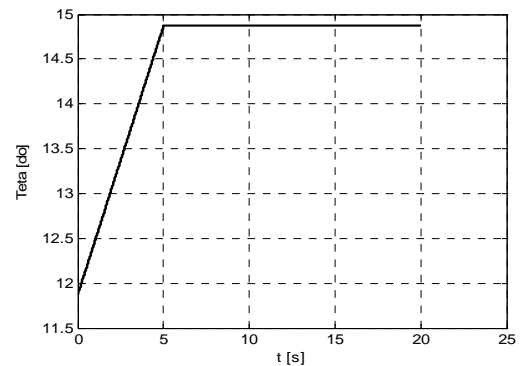
Figure 5. Control rule of blade pitch angles
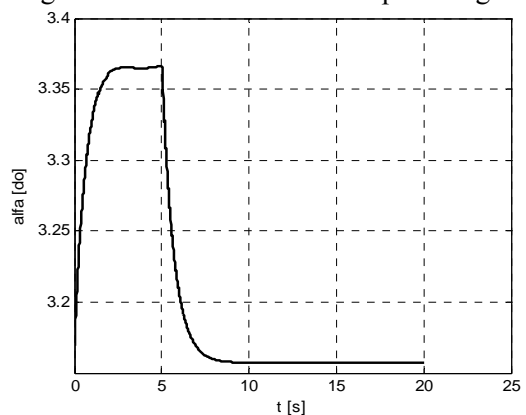
Figure 6. Variations in attack angles $\bar{r}$ =0,7
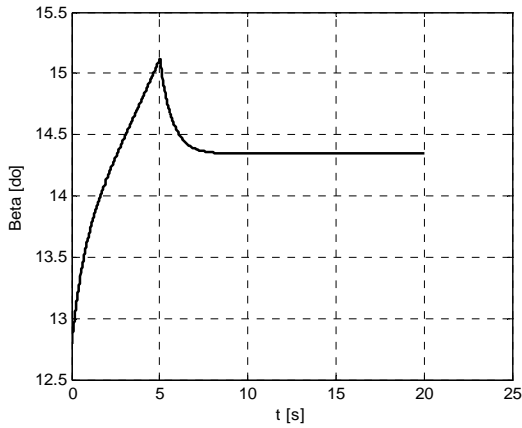
Figure 7. Variations in flapping angles.
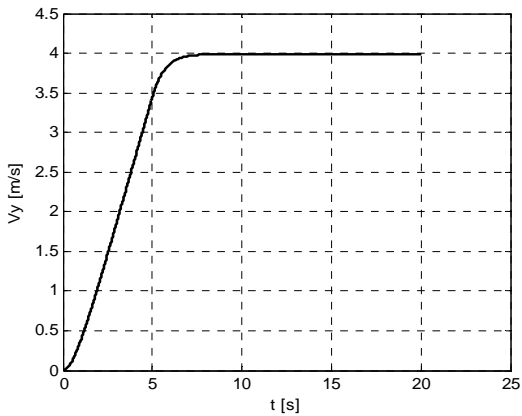
Figure 8. Variations in vertical velocity
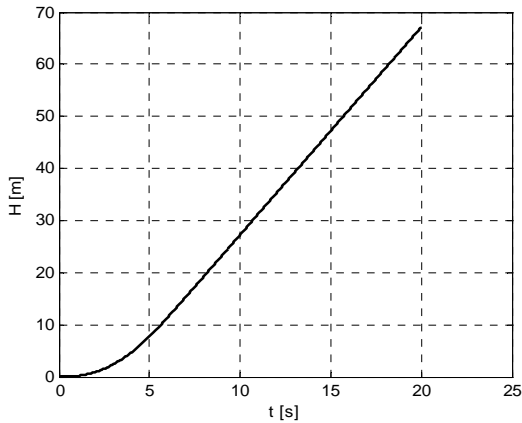
Figure 9. Variations in altitude

These results serve as basic for identifying and adjusting the control coefficient basing on default equations. The values of the program and the helicopter altitude controlled as shown in fig 10.
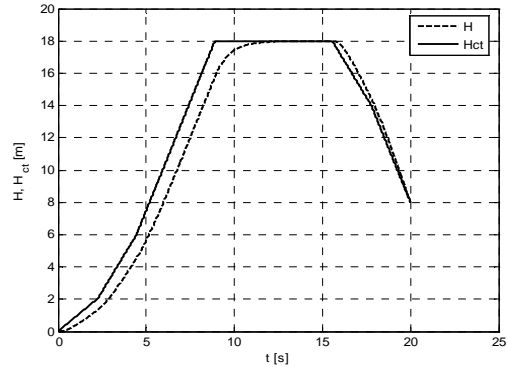
Figure 10. The altitude in the program and the real altitude when controlled

In order to obtain the above control program, the common blade pitch angle is controlled as illustrated in fig 11 and the speed of vertical climb and descent is shown in fig 12.
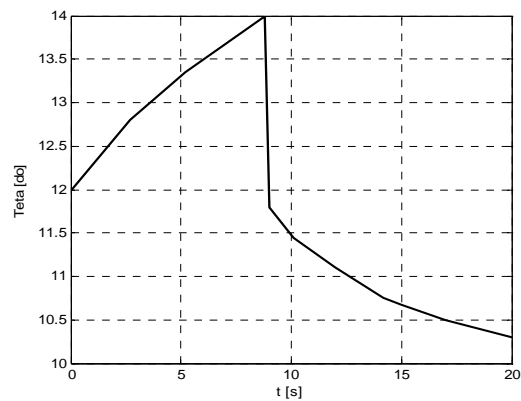
Figure 11. Variations in the blade pitch angle
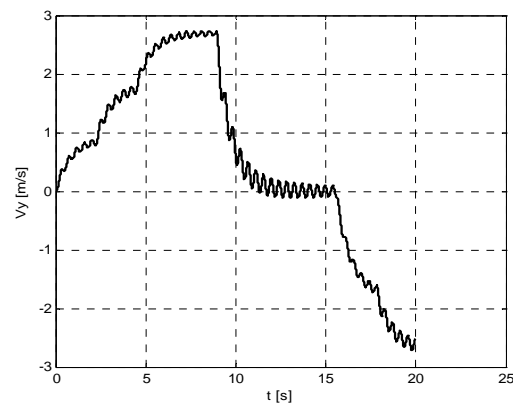
Figure 12. Variations in climb and descending speed.

5. Conclusion

The obtained results and control coefficients show that the autopilot software has controlled the helicopter correctly. The altitude tolerance is less than 1m and the controlling delay is less than 0.7s.

In control process, variations of parameters agree by physical rules.

This software can use research into aerodynamic flight, stability and control characters of helicopter and bring in computer for auto control helicopter vertical climb and descent.

6. References

[1]. Lã Hải Dũng, *Các hệ thống máy bay*, Học viện Không quân, Hà Nội, 2000.

[2]. Đỗ Minh Khai, Lã Hải Dũng, *Kết cấu và độ bền máy bay*, Học viện Không quân, Hà Nội, 2000.

[3]. Lã Hải Dũng, *Xác định góc đón điều khiển và hệ số bù vẫy của trực thăng*, Hội nghị Tự động và Khí cụ bay toàn quốc, Hà nội, 2005.

[4]. Nguyễn Đức Cương, *Mô hình hoá và mô phỏng khí cụ bay tự động*, Trung tâm KHKT&CN QS, Hà Nội, 2002.

[5]. Miniature Aircraft USA, Orlando, Fla, *X-Cell. 60 graphite SE Helicopter Kit Instruction Manual*, 1999.

Application of the Stochastic Regulated Linearization for Nonlinear System with Gaussian Colored Noise External Excitation

La Duc Viet[a], Nguyen Ba Nghi[b] and Phan Thi Tra My[c]

[a] PhD, Institute of Mechanics, 264 Doi Can, Ha Noi, ldviet@imech.ac.vn
[b] Msc, Institute of Mechanics, 264 Doi Can, Ha Noi, nbnghi@imech.ac.vn
[c] Bsc, Institute of Mechanics, 264 Doi Can, Ha Noi, pttmy@imech.ac.vn

Abstract

Instead of simplifying the nonlinear expression as usual, the regulated linearization technique presented in this paper replace the nonlinear term by higher order terms. By taking into account the higher order statistics, the technique has more of a possibility to capture the behavior of the system in case of large nonlinearity. In this paper, the formulation of regulated linearization is presented for nonlinear oscillator subjected to Gaussian colored noise excitation. The results are checked on Duffing oscillator and Van der Pol oscillator. In all oscillators, the results show that the regulated linearization can reduce significantly the errors in comparison with conventional linearization.

Key Words: Stochastic linearization, Colored noise

1. Introduction

The nonlinearity and uncertainty usually appear in many engineering problems. In general, the stochastic nonlinear systems are not exactly solvable. The linearization method is probably the most commonly used technique for nonlinear stochastic analysis. It has remained surprisingly popular tool over many years because of its simplicity. The method is based on replacing the original nonlinear system by a linear one, which is equivalent to the original one in some probabilistic sense. Because the probabilistic measures of discrepancy between the nonlinear and linear systems are numerous,

the linearization method covers many different approaches, which can be referenced in several review publications, for instance [1,2,3].

Anh and Di Paola [4] suggested new realization of the stochastic linearization that appears to be extremely unusual at the first glance. Instead of simplifying the nonlinear expression, the authors, suggested to seemingly first complicate it by replacing it by higher order terms. These higher order terms then were replaced by the linear approximation, in several steps, with a regulated coefficient. Recently, Elishakoff [5] extended the regulated linearization technique to two step regulation. The extension showed considerable improvement

of the results in the Lutes and Sarkani oscillator, especially in case of large nonlinearity.

However, the regulated linearization technique mentioned above just has been demonstrated for mechanical systems subjected to white noise excitation. In reality, the oscillators are often subjected to non-white or colored random excitations. In this paper, we derive the formulation of regulated linearization technique for nonlinear system under colored noise external excitation. The regulated linearization, then, is demonstrated by simulation of Duffing oscilator.

2. The Formulation of Regulated Linearization

We study the following nonlinear random vibration problem:

$$\ddot{x} + 2\zeta\omega_0\dot{x} + \omega_0^2 x + g(x,\dot{x}) = f(t) \quad (1)$$

where $x(t)$ is the displacement, $\dot{x}$ is the velocity, $\ddot{x}$ is the acceleration of a single degree of freedom system, ζ is the damping ratio, ω_0 is the natural frequency, $f(t)$ is the random excitation, $g(x,\dot{x})$ is a nonlinear function. In this paper, for simplicity, we consider the nonlinear function describes nonlinear spring force as:

$$g(x,\dot{x}) = \sum_{i=1}^{n} a_i |x|^{\alpha_{1i}} |\dot{x}|^{\alpha_{2i}} \operatorname{sgn}(x) \quad (2)$$

where a_i ($i=1,..n$) are real numbers, α_{1i}, α_{2i} are positive real numbers and *sgn* denotes the signal function.

2.1. The conventional linearization

The conventional linearization would perform the following replacements of the nonlinear terms by the linear ones:

$$|x|^{\alpha_{1i}} |\dot{x}|^{\alpha_{2i}} \operatorname{sgn}(x) \to \lambda_i x \quad (3)$$

where λ_i ($i=1,2..n$) are linearization coefficients chosen so as to minimize the mean-squared values as:

$$e_1 = \left\langle \left(|x|^{\alpha_{1i}} |\dot{x}|^{\alpha_{2i}} \operatorname{sgn}(x) - \lambda_i x \right)^2 \right\rangle$$

in which $\langle \bullet \rangle$ denotes the expected value. Setting the derivatives of e_1 with respect to λ_i equal to zeros gives:

$$\lambda_i = \left\langle |x|^{\alpha_{1i}+1} |\dot{x}|^{\alpha_{2i}} \right\rangle \Big/ \left\langle |x|^2 \right\rangle \quad (4)$$

Then the scheme (3) of conventional linearization is written as:

$$|x|^{\alpha_{1i}} |\dot{x}|^{\alpha_{2i}} \operatorname{sgn}(x) \to \frac{\left\langle |x|^{\alpha_{1i}+1} |\dot{x}|^{\alpha_{2i}} \right\rangle}{\left\langle |x|^2 \right\rangle} x \quad (5)$$

2.2. The regulated linearization

Anh and Di Paola [4] suggested a stochastic linearization technique that appears to be extremely unusual. The non-linear terms are first replaced by higher-order nonlinear ones. After that, the higher-order nonlinear terms are replaced by the original non-linear terms but with regulated coefficient. The last step is followed by the conventional replacement. The scheme of the process can be expressed as:

$$|x|^{\alpha_{1i}} |\dot{x}|^{\alpha_{2i}} \operatorname{sgn}(x)$$
$$\to c_i |x|^{2\alpha_{1i}-1} |\dot{x}|^{2\alpha_{2i}} \operatorname{sgn}(x) \quad (6)$$
$$\to r_i |x|^{\alpha_{1i}} |\dot{x}|^{\alpha_{2i}} \operatorname{sgn}(x) \to r_i \lambda_i x$$

The coefficients c_i ($i=1,2..n$) are chosen to minimize the following errors:

$$e_2 = \Bigg\langle \Bigg(|x|^{\alpha_{1i}} |\dot{x}|^{\alpha_{2i}} \operatorname{sgn}(x) - $$
$$c_i |x|^{2\alpha_{1i}-1} |\dot{x}|^{2\alpha_{2i}} \operatorname{sgn}(x) \Bigg)^2 \Bigg\rangle$$

Setting the derivatives of e_2 with respect to c_i equal to zeros gives the following result:

$$c_i = \frac{\left\langle |x|^{3\alpha_{1i}-1} |\dot{x}|^{3\alpha_{2i}} \right\rangle}{\left\langle |x|^{4\alpha_{1i}-2} |\dot{x}|^{4\alpha_{2i}} \right\rangle} \tag{7}$$

The coefficients r_i ($i=1,2..n$) are chosen to minimize the following errors:

$$e_3 = \left\langle \left(c_i |x|^{2\alpha_{1i}-1} |\dot{x}|^{2\alpha_{2i}} \operatorname{sgn}(x) \right. \right.$$

$$\left. \left. -r_i |x|^{\alpha_{1i}} |\dot{x}|^{\alpha_{2i}} \operatorname{sgn}(x) \right) \right\rangle$$

Analogously, the results are obtained as:

$$r_i = c_i \frac{\left\langle |x|^{3\alpha_{1i}-1} |\dot{x}|^{3\alpha_{2i}} \right\rangle}{\left\langle |x|^{2\alpha_{1i}} |\dot{x}|^{2\alpha_{2i}} \right\rangle} \tag{8}$$

Combining (4), (7), (8), the scheme (6) can be reduced as:

$$|x|^{\alpha_{1i}} |\dot{x}|^{\alpha_{2i}} \operatorname{sgn}(x) \rightarrow$$

$$\frac{\left\langle |x|^{3\alpha_{1i}-1} |\dot{x}|^{3\alpha_{2i}} \right\rangle^2 \left\langle |x|^{\alpha_{1i}+1} |\dot{x}|^{\alpha_{2i}} \right\rangle}{\left\langle |x|^{4\alpha_{1i}-2} |\dot{x}|^{4\alpha_{2i}} \right\rangle \left\langle |x|^{2\alpha_{1i}} |\dot{x}|^{2\alpha_{2i}} \right\rangle \left\langle |x|^2 \right\rangle} x \tag{9}$$

In summary, we can combine (2), (5), (9) to linearize the nonlinear function $g(x,\dot{x})$ as:

$$g(x,\dot{x}) \rightarrow k_e x \tag{10}$$

where

$$k_e = \sum_{i=1}^{n} \gamma_i \frac{\left\langle |x|^{\alpha_{1i}+1} |\dot{x}|^{\alpha_{2i}} \right\rangle}{\left\langle |x|^2 \right\rangle} \tag{11}$$

in which γ_i ($i=1,..n$) are regulated coefficient defined by:

$$\gamma_i = 1 \quad \textit{with conventional linearization}$$

$$\gamma_i = \frac{\left\langle |x|^{3\alpha_{1i}-1} |\dot{x}|^{3\alpha_{2i}} \right\rangle^2}{\left\langle |x|^{4\alpha_{1i}-2} |\dot{x}|^{4\alpha_{2i}} \right\rangle \left\langle |x|^{2\alpha_{1i}} |\dot{x}|^{2\alpha_{2i}} \right\rangle}$$

$$\textit{with regulated linearization}$$

$$\tag{12}$$

In the next sections, the linearizations will be applied to the oscillator excited by filtered white noise excitation.

3. The Case of Filtered White Noise Excitation

The white noise process is a mathematical idealization and is physically impossible. In reality, the oscillators are often subject to non-white or colored random excitations. Many random excitations can be modeled as the output of a dynamic system subject to a Gaussian white noise excitation. In other words, random excitations can be viewed as the filtered white noise process. Let the excitation $f(t)$ be a Gaussian colored noise treated as an output of a linear filter subjected to Gaussian white noise, i.e:

$$f = b^T \eta$$
$$\dot{\eta}(t) = A\eta(t) + \dot{\xi}(t) \tag{13}$$

in which $\eta(t)$ and b are m-dimensional vector, A is a $m \times m$ constant matrix, $\dot{\xi}(t)$ is a stationary Gaussian white noise with covariance matrix W. Using the linearization expressed by (10), the linearized equation of (1) can be written in state space as:

$$\dot{z}(t) = \tilde{A}z(t) + H\dot{\xi}(t) \tag{14}$$

in which

$$z = \begin{bmatrix} x \\ \dot{x} \\ \eta \end{bmatrix}; H = \begin{bmatrix} \mathbf{0} \\ \mathbf{0} \\ I_m \end{bmatrix}; \tag{15}$$

$$\tilde{A} = \begin{bmatrix} 0 & 1 & \mathbf{0} \\ -k_e - \omega_0^2 & -2\zeta\omega_0 & b^T \\ \mathbf{0} & \mathbf{0} & A \end{bmatrix}$$

where I_m denotes the $m \times m$ identity matrix and $\mathbf{0}$ denotes the null matrix with appropriate dimensions. The expected values of responses then can be found by many techniques for linear systems [6]. Because the equivalent stiffness k_e depends on the expected values of response as shown in (11) , we obtain simultaneous equations to solve the linearized responses.

4. Application to The Duffing Oscillator

4.1. The linearization coefficients

Consider the Duffing oscillator:

$$\ddot{x} + 2\zeta\omega_0\dot{x} + \omega_0^2 x\left(1 + \varepsilon x^2\right) = f(t) \quad (16)$$

where ζ is the damping ratio, ω_0 is the natural frequency and ε is the nonlinear parameter. Using the following transformation:

$$\tilde{x} = x\sqrt{\varepsilon}, \qquad \tilde{f} = f\sqrt{\varepsilon}$$

We can normalize equation (16) as:

$$\ddot{\tilde{x}} + 2\zeta\omega_0\dot{\tilde{x}} + \omega_0^2\tilde{x}\left(1 + \tilde{x}^2\right) = \tilde{f}(t) \quad (17)$$

It is noted that, from Eq (17), the level of nonlinearity is expressed by mean squared value of $\tilde{x}$. When $\left\langle \tilde{x}^2 \right\rangle \square \ 1$, the nonlinearity is small and conversely. For simplicity, we omit the tilde notation and the following standard form of the Duffing oscillator is considered:

$$\ddot{x} + 2\zeta\omega_0\dot{x} + \omega_0^2 x + \omega_0^2 x^3 = f(t) \quad (18)$$

The nonlinear function now has the form of the expression (2)

$$g(x,\dot{x}) = 2\zeta\omega_0\dot{x} + \omega_0^2 x + \omega_0^2 x^3$$

$$= \sum_{i=1}^{n} a_i |x|^{\alpha_{1i}} |\dot{x}|^{\alpha_{2i}} \,\mathrm{sgn}(x)$$

in which

$$n = 1, a_1 = \omega_0^2, \alpha_{11} = 3, \alpha_{21} = 0.$$

Substituting above values into (11), (12) gives:

$$k_e = \gamma \frac{\left\langle x^4 \right\rangle}{\left\langle x^2 \right\rangle}$$

$$\gamma = \begin{bmatrix} 1 & \textit{with conventional linearization} \\ \dfrac{\left\langle x^8 \right\rangle^2}{\left\langle x^{10} \right\rangle \left\langle x^6 \right\rangle} & \textit{with} \\ & \textit{regulated linearization} \end{bmatrix}$$

By using the following expression [6]:

$$\left\langle |x|^a \right\rangle = \sqrt{\frac{\left(2\left\langle x^2 \right\rangle\right)^a}{\pi}} \Gamma\left(\frac{a+1}{2}\right)$$

for every real number a, the linearization coefficient is obtained as:

$$k_e = 3\omega_0^2 \gamma \left\langle x^2 \right\rangle;$$

$$\gamma = \begin{bmatrix} 1 & \textit{conventional linearization} \\ 7/9 & \textit{regulated linearization} \end{bmatrix}$$

$$(19)$$

It is noted that the expected value $\left\langle x^2 \right\rangle$ is obtained from linearized system (14). Because the linearized system (14) depends on linearization coefficient k_e, the expected value $\left\langle x^2 \right\rangle$ in general is obtained by an iterative procedure.

4.2. The numerical Simulation

The exact response of nonlinear system in case of colored noise excitation can not be

found in analytical form. The Monte Carlo method is used instead. In simulation, the system parameters are fixed, the colored noise shape parameters are given several values and the autospectral density of the white noise is changed in order to change the level of nonlinearity, which has measured by the mean squared displacement.

a. The first order colored noise case

In this case, the excitation $f(t)$ is an output of a first order linear filter subjected to Gaussian white noise, i.e:

$$\dot{f}(t) = -hf(t) + h\sqrt{S_0}\,\dot{\xi}(t) \qquad (20)$$

in which $\dot{\xi}(t)$ is a Gaussian white noise with unit autospectral density, S_0 is a positive constant, h is a parameter representing the shape of autospectral density curve of colored noise. The filter (20) has form of (13), in which:

$$b = 1, \quad A = -h, \quad W = 2\pi h^2 S_0$$

In simulation, the damping ratio ζ and the natural frequency ω_0 are fixed at the values of 0.5 and 1, respectively. Because the analytical results do not exist, the Monte Carlo method is used. The results are presented for several values of parameter h, which is defined in Eq (20). Let Δ be the percentage error between the linearized response $<x^2>_{lin}$ and the simulated response $<x^2>_{sim}$:

$$\Delta = \frac{\left|<x^2>_{sim} - <x^2>_{lin}\right|}{<x^2>_{sim}} \qquad (21)$$

We plot Δ versus the level of nonlinearity. In Figs 1a-1c, the solid lines and dash lines represent the relative error of regulated linearization and conventional linearization, respectively.
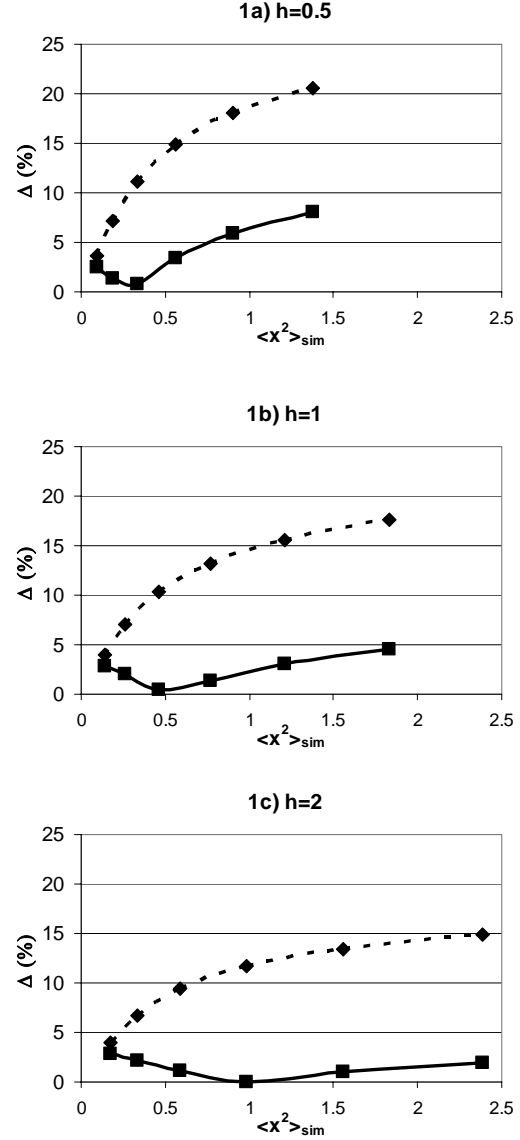
Figure 1a – 1c:
The variations of relative errors in case of first order colored noise excitation

It can be seen that the errors increase when the nonlinearity level increases. Both linearization methods have worse performance when h is small. However, the regulated linearization has much better performance, especially in case of large nonlinearity. The largest error of 20% obtained by conventional linearization can be reduced to about 8% by using regulated linearization.

b. The second order colored noise case

In this case, the excitation $f(t)$ is an output of a second order linear filter subjected to Gaussian white noise, i.e:

$$\ddot{f}(t) = -2h\Omega\dot{f}(t) - \Omega^2 f(t) + \Omega^2\sqrt{S_0}\dot{\xi}(t)$$
(22)

in which $\dot{\xi}(t)$ is a Gaussian white noise with unit autospectral density, S_0 is a positive constant, h and Ω are two parameters representing the shape of autospectral density curve of colored noise. The filter (22) has form of (13), in which

$$b = \begin{bmatrix} 1 \\ 0 \end{bmatrix}; \qquad A = \begin{bmatrix} 0 & 1 \\ -\Omega^2 & -2h\Omega \end{bmatrix};$$

$$W = \begin{bmatrix} 0 & 0 \\ 0 & 2\pi\Omega^4 S_0 \end{bmatrix}$$

The parameters ζ, ω_0 are fixed at the values of 0.5 and 1, respectively. The parameter h defined in (22) is fixed at 0.5. The results are presented for several values of parameter Ω, which is also defined in (22). The relative error Δ defined in (21) is plotted versus the level of nonlinearity. In Figs 2a-2c, the solid lines and dash lines represent the relative error of regulated linearization and conventional linearization, respectively.


2a) $\Omega=0.5$

2b) $\Omega=1$

2c) $\Omega=2$
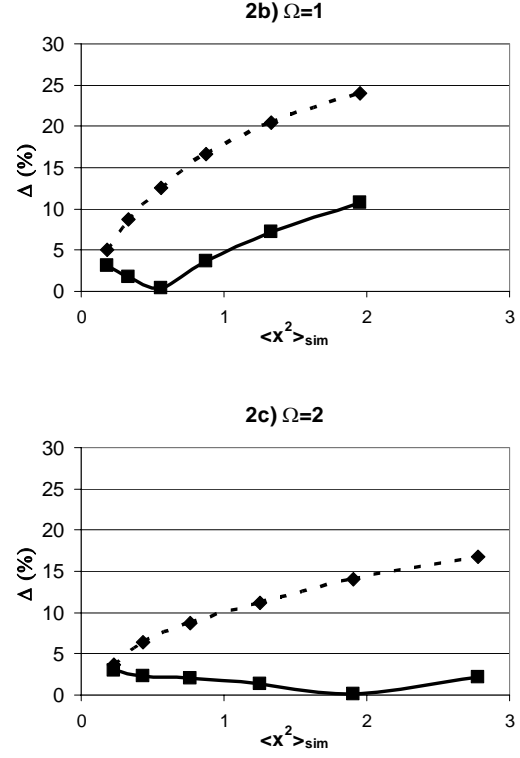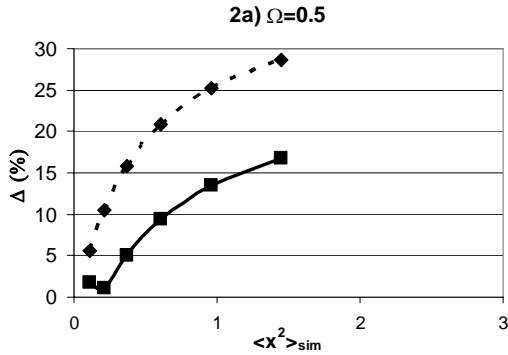
Figure 2a – 2c:
The variations of relative errors in case of second order colored noise excitation

The obtained results are similar to the ones in case of first order colored noise. The error increase when the nonlinearity level increases. Both linearization methods have worse performance when Ω is small. The regulated linearization has much better performance, especially in case of large nonlinearity. The largest error of 29% obtained by conventional linearization can be reduced to about 17% by using regulated linearization.

5. Conclusion

In this study, the regulated linearization technique is presented. By taking into account the higher order statistics, a regulated coefficient is multiplied to the coefficients of conventional linearization. The technique is formulated for nonlinear systems subjected to colored noise excitation.

The applications of the regulated linearization are presented for Duffing oscilator. The results obtained from numerical calculations show that the regulated linearization can produce significant improvement of accuracy in case of large nonlinearity.

6. Acknowledgement

7. References

[1] L. Socha, (2008), *Linearization Methods for Stochastic Dynamic Systems*, Lect.Notes Phys. 730, Springer, Berlin Heidelberg.

[2] Roberts, J. and Spanos, P. (1990), *Random Vibration and Statistical Linearization*, John Wiley and Sons, Chichester.

[3] Proppe, C., Pradlwarter, H., and Schueller, G. (2003), *Equivalent linearization and Monte Carlo simulation in stochastic dynamics*, Probab. Eng. Mech. 18, 1–15.

[4] Anh, N.D., Di Paola, M., (1995), Some Extensions of Gaussian Equivalent Linearization, *International Conference on Nonlinear Stochastic Dynamics*, Hanoi, Vietnam, pp. 5–16.

[5] Elishakoff I., Andriamasy L. and Dolley M., (2009), *Application and extension of the stochastic linearization by Anh and Di Paola*, Acta Mech, 204, 89–98

[6] Lutes, L.D. and Sarkani, S, (2004), *Random Vibration: Analysis of Structural and Mechanical Systems*, Elsevier, Amsterdam.

Frequency Domain versus Time Domain Modal Identifications for Ambient Excited Structures

Le Thai Hoa[a], Yukio Tamura[b], Akihito Yoshida[c] and Nguyen Dong Anh[d]

*[a] Wind Engineering Research Center, Tokyo Polytechnic University, Japan
1583 Iiyama, Atsugi Kanagawa 243-0297, Japan; thle@arch.t-kougei.ac.jp
Hanoi University of Engineering and Technology, Vietnam National University, Hanoi
144 Xuan Thuy, Cau Giay, Hanoi, Vietnam; thle@vnu.edu.vn
[b] Department of Architectural Engineering, Tokyo Polytechnic University, Japan
1583 Iiyama, Atsugi Kanagawa 243-0297, Japan; yukio@arch.t-kougei.ac.jp
[c] Department of Architectural Engineering, Tokyo Polytechnic University, Japan
1583 Iiyama, Atsugi Kanagawa 243-0297, Japan; yoshida@arch.t-kougei.ac.jp
[d] Hanoi University of Engineering and Technology, Vietnam National University, Hanoi
144 Xuan Thuy, Cau Giay, Hanoi, Vietnam; ndanh@imech.ac.vn*

Abstract

Ambient vibration test is one of the most applicable and reliable methods among vibration tests due to recently fast evolvement of measurement, sensor technologies and data processing, and economical benefit as well. Modal identification methods of the ambient vibration structures are output-only identification techniques which have commonly been branched into either the frequency domain or the time domain. Each the frequency domain-based or the time domain-based modal identification methods has its own advantage and limitation. The frequency domain-based modal identification methods or non-parametric identification ones have been widely used for the output-only system identification due to their advantages in estimating natural frequencies high frequency resolution and mode shapes, but they have uncertainty and troublesome in the damping estimation. Inversely, the time domain-based modal identification methods or parametric ones benefit in the damping estimation, but difficulty in parameters. This paper will present theoretical backgrounds of the most modern and recent modal identification methods in the frequency domain and in the time domain such as Frequency Domain Decomposition (FDD) and Stochastic Subspace Identification (SSI). Full-scale ambient measurements of 5-storey steel building have been carried out for the modal parameter estimation. Applicable evaluation of the frequency domain-based and the time domain-based modal identification methods will be also discussed.

Key Words: System identification; Ambient vibration; Output-only identification; Frequency domain; Time domain; Frequency domain decomposition; Stochastic subspace identification

1. Introduction

Full-scale vibration testing is the most reliable method to determine modal parameters of structures (e.g. natural frequencies, damping ratios and mode shapes) which are served as multipurpose uses as model updating and validation, response prediction, structural control and

damage detection of both experimental and operation structures. Generally, the vibration testing can be subdivided depending on types of excitation by two main branches: forced vibration testing including free vibration testing and ambient vibration testing. In the first branch, the structures are excited by shaker or impulse hammer. In case of the free vibration testing, exciting force is suddenly lifted. The forced testing usually involve with measuring both input excitations and output responses. Accordingly, input-output identification methods are used to estimate the modal parameters of structures through indentifying either frequency response function (FRF) or impulse response function (IRF). This testing advantages over deterministic input excitation which can be controlled and optimized to the response of interested vibration modes. However, the forced vibration test requires additional equipments like shaker and accompanying instrumentations, traffic shut-down. Thus it is suitable to conduct this test with small-scaled or medium-scaled structures, however, in cases of structures with flexible, large-scaled and low-ranged, closed natural frequencies, the controlling of input excitation for optimized level of response is often difficult and costly. It is noted that output-only identification with measured responses only also can be applied for the forced vibration testing, but effects of input excitation and harmonics must be eliminated from the output response before the modal parameters extracted. The ambient vibration testing using natural and environmental excitations such as traffic vehicles, human activities, wind and wave… does not require the traffic disturbance, shaker and additional instrumentations, but require highly sensitive sensors and data processing techniques. However, with development of sophisticated sensor technology and identification techniques, the ambient testing has become the most practical and reliable method for the modal parameter identification from multipurpose laboratory experiments and full-scale measurements. Because only the output response can be measured without the input excitations in the ambient testing, thus the output-only identification is applied to estimate the modal parameters (Cunha et al., 2006).

Modal parameter identification or output-only identification of the ambient excited structures is key issue and the most attractive topic for both experimental modal analysis and operational modal analysis. So far, a number of the output-only identification techniques have been developed for MDOF systems, which is often classified into three branches (1) Frequency domain-based methods; and (2) Time domain-based methods. The frequency domain-based modal identification methods, also known non-parametric identification ones have been widely used for the output-only system identification of the ambient vibration structures due to their reliability, effectiveness and advantages in estimating high-resolved natural frequencies and mode shapes. The modern modal identification methods for the ambient testing in the frequency domain are Frequency domain decomposition (FDD) and Enhanced frequency domain decomposition (EFDD). The ambient testing does not require to identify either FRFs or IRFs because the input force cannot be measured. Ambient testing has been successfully applied for many types of civil engineering structures such as bridges (Abdel_Ghaffar and Scanlan, 1985; Siringoringo and Fujino, 2008), buildings and engineering towers (Tamura et al., 2005). However, the ambient testing and the output-only identification contain its shortcomings and uncertainties due to unknown input excitations, input influence, noise disturbances and leakage effect due to the Fourier transform and so on. Moreover, the frequency-domain identification methods are often based on strict hypotheses such as uncorrelated white noise inputs, light damping and effectiveness of decomposition techniques for simplification. Especially,

there is troublesome damping estimation in the frequency domain due to difficulty and unreliability in estimating auto power spectral function and free decay function for each structural mode (Brincker et al., 2001a; Tamura et al., 2005). Just so-called operational deflection shapes or unscaled mode shapes can be obtained from the ambient testing because scaling factor not to be determined due to unknown input forces (Brincker et al., 2001b).

The Stochastic Subspace Identification (SSI) is the powerful and most applicable technique for the output-only identification methods in the time domain, originally presented by Van Overschee and De Moor, 1993. SSI has been branched by either COV-SSI or DATA-SSI due to dealing with covariance matrix (Toeplitz matrix) of the output data or data matrix (Hankel matrix) directly. It is noted that number of parameters such as the number of block rows, the number of system orders and so on must be required for the SSI procedure and carefully selected. Similar to FDD, the theory of SSI is also assumed that excitation forces are Gaussian distributed stochastic broad-band white noises. SSI has applied for estimating modal parameters of variety of structures by some authors such as Peeters and De Reock, 1999; Weng et al., 2008; Reynders and De Roeck, 2008.

This paper presents fundamental theories of the most practical modern identification methods, concretely the Frequency Domain Decomposition and its enhanced version in the frequency domain, and Stochastic Subspace Identification in the time domain. Comparative results will be discussed. Full-scale ambient measurements of 5-storey steel structure have been carried out for the modal parameter identification with emphasis on natural frequencies and damping ratios.

2. Frequency domain-based methods

2.1. Frequency Domain Decomposition

Analysis of the output-only response data is carried out in the frequency domain using well-known FDD technique. The key point of the FDD will be briefly summarized hereafter. Relationship between excitation inputs and output response can be expressed in the frequency domain through the FRF matrix as follows:

$$S_{XX}(\omega) = H(\omega) S_{FF}(\omega) H(\omega)^{*T} \qquad (1)$$

where *, T denote conjugate and transpose operations; $S_{FF}(\omega), S_{XX}(\omega)$: power spectral matrices of inputs and outputs; $H(\omega)$: FRF matrix.

The FRF matrix can be expressed commonly under a form of residues/poles (He and Fu, 2001; Brincker et al., 2001a):

$$H(\omega) = \sum_{i=1}^{N} \left(\frac{a_i}{j\omega - \lambda_i} + \frac{a_i^*}{j\omega - \lambda_i^*} \right) \qquad (2a)$$

$$H(\omega) = \sum_{i=1}^{N} \left(\frac{\gamma_i \phi_i \phi_i^T}{j\omega - \lambda_i} + \frac{\gamma_i^* \phi_i^* \phi_i^{*T}}{j\omega - \lambda_i^*} \right) \qquad (2b)$$

where i, N: index, number of modes; a_i, λ_i: i-th complex residue and complex pole in which $a_i = \gamma_i \phi_i \phi_i^T$ with light damping and $\lambda_i = -\zeta_i \omega_i + j\omega_i \sqrt{1 - \zeta_i^2}$; ω_i, ζ_i: i-th natural frequency and damping ratio; ϕ_i, γ_i: i-th mode shape vector and scaling factor.

If the inputs are uncorrelated white noise inputs, the input power spectral matrix of the inputs is diagonal constant one $S_{FF}(\omega) = diag(c_1, c_2, ... c_N)$ and damping is light, one can obtains the output power spectral matrix at evaluated frequency ω_i decomposed modally as follows:

$$S_{XX}(\omega) = \sum_{i=1}^{N} \left(\frac{d_i \phi_i \phi_i^T}{j\omega - \lambda_i} + \frac{d_i^* \phi_i^* \phi_i^{*T}}{j\omega - \lambda_i^*} \right) \qquad (3)$$

where d_i: i-th scalar constant. Expression of the output power spectral matrix in Eq.(3) is similar one of some matrix decompositions

in the complex domain, thus these can be used to decompose the output power spectral matrix.

The output power spectral matrix has been orthogonally decomposed using the eigenvalue decomposition to obtain spectral eigenvalues and spectral eigenvectors:

$$S_{XX}(\omega) = \Phi(\omega)\Theta(\omega)\Phi(\omega)^{*T} \qquad (4a)$$

$$S_{XX}(\omega) = \sum_{k=1}^{M} \varphi_i(\omega)\theta_1(\omega)\varphi_i(\omega)^{*T} \qquad (4b)$$

where $\Phi(\omega), \Theta(\omega)$: spectral eigenvectors and spectral eigenvalues matrices; k, M: index and number of spectral eigenvectors. Because the eigenvalue decomposition is fast-decaying, thus the output power spectral matrix can be approximated by using the lowest-order spectral eigenvalue and eigenvector as follows:

$$S_{XX}(\omega) \approx \varphi_1(\omega)\theta_1(\omega)\varphi_1(\omega)^{*T} \qquad (5)$$

where $\varphi_1(\omega), \theta_1(\omega)$: the first spectral eigenvector and first spectral eigenvalue.

Due to the first-order spectral eigenvalue and eigenvector are dominant in a term of energy contribution, thus the first spectral eigenvalue contains full information of dominant frequencies to be used for extracting the natural frequencies, whereas the first spectral eigenvector brings information of mode shapes at each dominant frequency. The i-th mode shape can be estimated from the first spectral eigenvector at certain dominant frequencies (ω_i: i-th natural frequency) as follows:

$$\phi_i = \varphi_1(\omega_i) \qquad (6)$$

where ϕ_i: i-th mode shape

2.2. Enhanced Frequency Domain Decomposition

Originally, the damping ratios estimation cannot be carried out by the FDD, but its enhanced version has been developed for this purpose. Enhanced frequency domain decomposition has been developed basing on the frequency domain decomposition for estimating the damping ratios only (Brincker et al., 2001b). As can be seen from Eq.(6) that FDD extracts the mode shape from the first spectral eigenvector at selected natural frequency, thus prior knowledge of the natural frequencies must be required for this identification technique. Accuracy of estimated mode shapes can be evaluated via correlation criteria between estimated mode shapes and analytical mode shapes, moreover, among these criteria Modal Assurance Criterion (MAC) is preferably used:

$$MAC(\%) = \frac{|\phi_E \phi_A^T|^2}{\{\phi_E^T \phi_E\}\{\phi_A^T \phi_A\}} \qquad (7)$$

where ϕ_E, ϕ_A: estimated mode shapes and analytical mode shapes, respectively.

For the damping estimation, the key point here is to identify the auto power spectral density function of the single-DOF generalized coordinate of certain mode from the spectral eigenvalues. Because the first spectral eigenvalue contributes dominantly almost energy of system, thus it is often used to extract the auto power spectral density functions. Searching the auto power spectral function of certain mode from the first eigenvalue is carried out on both sides of value of the natural frequency, and it is terminated until the desirable limit of MAC reached. The remaining values of the auto spectral density function in the calculated frequency range are set to zero. From identified auto power spectral density functions, the damping ratios are obtained via logarithmic decrement technique of free decay functions, of which these free decay functions obtained by converting the auto spectral density function in the frequency domain back to the time domain by inverse fast Fourier transform technique (Brincker et al. 2001b). It is also noted that validation of the natural frequencies can be checked through these free decay functions.

3. Time domain-based methods

3.1. Stochastic Subspace Identification

Consider a discrete-time response stochastic state-space model (Van Overschee and De Moor, 1993)

$$Y_{k+1} = AY_k + w_k \qquad (8a)$$

$$X_k = CY_k + \upsilon_k \qquad (8b)$$

where A, C: system matrices; Y: state vector; X: measurement response; k: index of discrete state; and w, υ: process noise and measurement noise. System matrices A, C containing the system modal parameters will be identified by SSI technique.

All response data are normally represented by the data matrix of the block Hankel matrix, which this is convenient to divide original data into two parts: the past worked as reference basis and the future as processing data. For the reference-based stochastic subspace identification, the Hankel matrix plays a critically important role in the SSI algorithm. Hankel matrix of single response data $X = \{x_0, x_1, \dots x_j, \dots x_N\}^T$ can be formulated here for a brevity:

$$H = \begin{bmatrix} x_0 & x_1 & \dots & x_{j-1} \\ x_1 & x_2 & \dots & x_j \\ \dots \\ x_{i-1} & x_i & \dots & x_{i+j-2} \\ \hline x_i & x_{i+1} & \dots & x_{i+j-1} \\ x_{i+1} & x_{i+2} & \dots & x_{i+j} \\ \dots \\ x_{2i-1} & x_{2i} & \dots & x_{2i+j-1} \end{bmatrix} = \begin{bmatrix} X_p^{ref} \\ \hline X_f \end{bmatrix} (9)$$

where i: a user-defined index; N: number of samples in response data; j: number of columns; and X_p^{ref}, X_f: the past and future parts. To ensure all samples of the output vector X_k populate in the Hankel matrix, the number of j can be equal to N-2i+1 or N=2i+j-1. Thus, dimensions of the matrices are $H \in R^{2Nixj}$, $X_p^{ref} \in R^{Nixj}, X_f \in R^{Nixj}$. If there are M response outputs, do similar way for

the Hankel matrix of each output and organize in column-based format to build up the entire Hankel matrix of all outputs.

The orthogonal projection of the future part on the past one is carried out. This projection is introduced as geometrical tool or conditional mean operation under following formula (Van Overschee and De Moor, 1993):

$$O = \left(X_f / X_p^{ref}\right) = X_f X_p^{ref} \left(X_p^{ref} X_p^{refT}\right)^{-1} X_p^{ref} (10)$$

where /: projection operator; O: orthogonal projection of Hankel matrix.

Because so-called observability matrix is used to identify initial conditions, then the system matrices, but the observability matrix itself can be estimated by factoring the orthogonal projection due to such following steps. Firstly, singular value decomposition (SVD) is applied for the orthogonal projection, the singular values and singular vectors estimated through SVD:

$$O = USV^T = \begin{pmatrix} U_1 & U_2 \end{pmatrix} \begin{pmatrix} S_1 & 0 \\ 0 & S_2 \end{pmatrix} \begin{pmatrix} V_1^T \\ V_2^T \end{pmatrix} \quad (11)$$

where U, V: singular vectors; S: singular values. Here, we organize these singular values, vectors into two groups with indices 1 and 2. Dominant low-order singular values and their associated singular vectors group in U_1, S_1, V_1, whereas the smallest high-order singular values and vectors in U_2, S_2, V_2. Actually, this is approximation, reduced-order model or noise effect reduction, in which the dominant singular values and vectors are used to estimate the system parameters, while the small singular values are neglected, we have:

$$O \approx U_1 S_1 V_1 \qquad (12)$$

where $U_1 \in R^{Nixk}; S_1 \in R^{kxk}; V_1 \in R^{jxk}$; k: number of system order or reduced order.

Secondly, the observability matrix can be estimated from reduced-order model:

$$\Gamma = U_1 S_1^{0.5} \qquad (13)$$

where Γ : observability matrix $\Gamma \in R^{Nixk}$

Finally, the system matrices A, C can be determined from this observability matrix as follows:

$$A = \underline{\Gamma}^{-1}\overline{\Gamma} \qquad (14a)$$

$$C = \hat{\Gamma} \qquad (14b)$$

where $\underline{\Gamma} \in R^{N(i-1)xk}$ denotes Γ without last N rows; $\overline{\Gamma} \in R^{N(i-1)xk}$ denotes Γ without first N rows; and $\hat{\Gamma} \in R^{Nxk}$: first N rows of Γ.

3.2. Modal parameter estimation

The modal parameters then are estimated from the system matrices. Using either SVD or eigenvalue decomposition to decompose the system matrix A as follows:

$$A = \Psi\Lambda\Psi^{*T} \qquad (15)$$

where Λ : diagonal eigenvalue matrix containing complex poles and natural frequencies; and Ψ : eigenvector matrix, containing information of mode shapes.

Concretely, i-th natural frequencies and damping ratios can be determined as following formulae (Weng et al., 2008):

$$\omega_i = \frac{a_i}{2\pi\Delta T} \text{ and } \zeta_i = \frac{b_i}{\sqrt{a_i^2 + b_i^2}} \qquad (16)$$

where $a_i = |\arctan(\text{Im}(\lambda_i)/\text{Re}(\lambda_i))|; b_i = \ln(\lambda_i)$

The i-th mode shape can be estimated from the system matrix C and eigenvectors:

$$\phi_i = C\psi_i \qquad (17)$$

In the SSI method, the all response outputs are arranged firstly to form the Hankel matrix. Second, the orthogonal projection of the Hankel matrix is carried out with reduced-order approximation using the SVD, before to estimate the observability matrix. Third, the system matrices are determined from the observability matrix. Final, the eigenvalue decomposition or SVD is used to decompose the system matrix, and the modal parameters can be identified.

4. Full-scale measurements

Full-scale ambient measurements have been carried out on a 5-storey steel frame at the test site of the Disaster Prevention Research Institute (DPRI), Kyoto University (see Figure 1). Ambient data were recorded at all 5 floor levels and ground as reference, by tri-axial velocity sensors with output velocity signals (VCT Corp., Models UP255S/UP252) with A/D converter, amplifier and laptop computer. All data were sampled for period of 30 minutes per floor (5 minutes per a set-up) with sampling rate of 100Hz. Sensors have been located to capture ambient motions in lateral X-direction and horizontal Y-direction from ground level to 5th floor, see Figure 1 (Kuroiwa and Iemura, 2007).
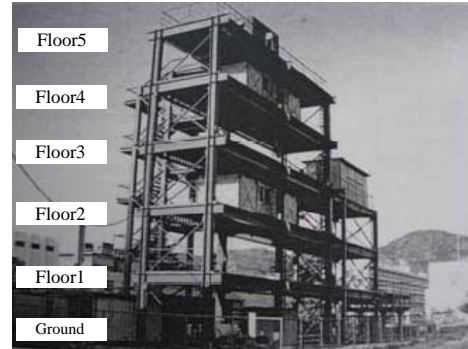

Figure 1. Five-storey steel structure

Only outputs sensors and modal parameters in the X direction have been discussed in this paper. It is noted that all outputs were velocity time series, thus a single integration in the time domain using a trapezoic integration approach has been required to obtain output displacements which are necessary for estimating mode shapes in next steps. A integration drift due to unknown initial condition of the displacements during the time integration have been treated through compensation to be zero-mean output displacements. Integrated output displacements at all floors are shown in Figure 2.
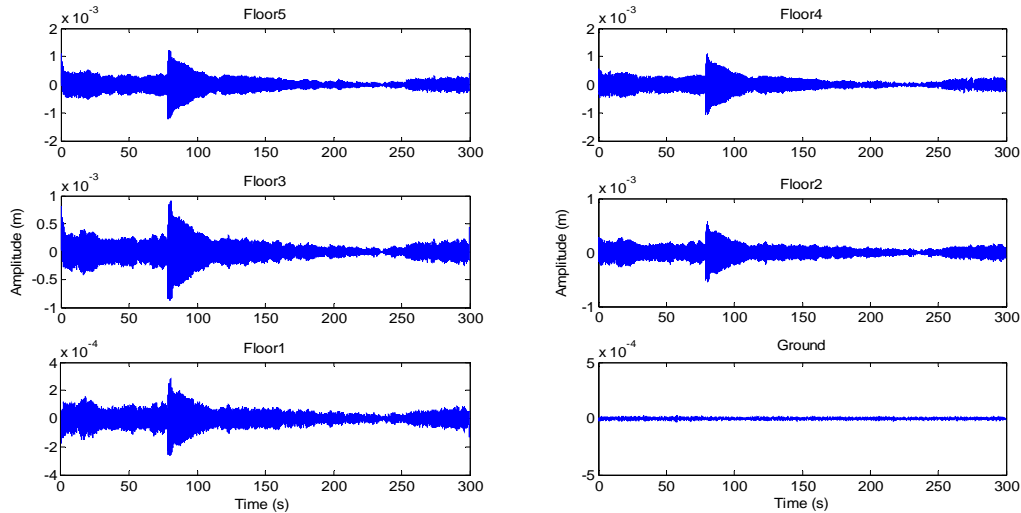
Figure 2. Integrated output displacements

5. Modal parameter estimation

In the traditional way using Peak Picking (PP) technique, the peak frequencies can be extracted from the output series using power spectral analysis, then the mode shapes can be estimated based on values and directions of the power spectral matrix and phase matrix at each frequency peaks. However, this method cannot extract the damping.

Proper Orthogonal Decomposition of the output PSD matrix. All six normalized spectral eigenvalues and first four eigenvectors are shown in Figure 4 and Figure 5. Energy contributions of each spectral eigenvector and its corresponding eigenvalue can be estimated roughly based on its summed eigenvalues on analyzed frequency band (here 0-30Hz bandwidth). Concretely, first four eigenvalues and associated eigenvectors roughly contribute
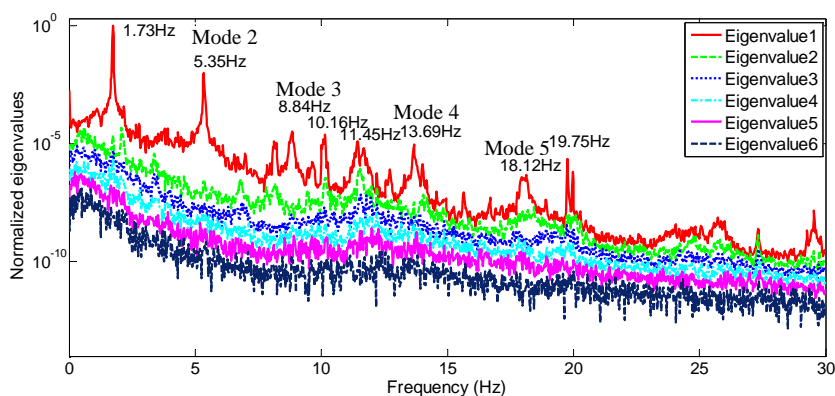

Figure 3. Normalized spectral eigenvalues

The output power spectral density (PSD) matrix has been established from the output displacements $X(t) = \{X_1(t), X_2(t), ... X_M(t)\}^T$ (M: number of sensors). Spectral eigenvalues and eigenvectors have been determined via

99.9%, 0.07%, 0.01%, 0.00% respective to the dynamically structural system. As a results, the first spectral eigenvalues and eigenvectors characterize modal parameters of the structure. Estimated peak frequencies in Figure 4 are compared

with analytical finite element model (FEM) results to identify nutural frequencies associated with order of mode shapes. Bending modes in the X direction corresponding the estimated natural frequencies can be determined via the first spectral eigenvector at these frequencies following the Eq.(6). MAC values of the first five mode shapes evaluated by Eq.(7) are respectively

100%，99.76%，99.8%，98.95% and 99.3%．Thus, there is a good agreement between the FDD-based mode shapes and FE-based ones. First four mode shapes are shown in Figure 5 in comparison between FEM, PP and FDD. There are good agreements in estimated mode shapes between analytical and identification methods
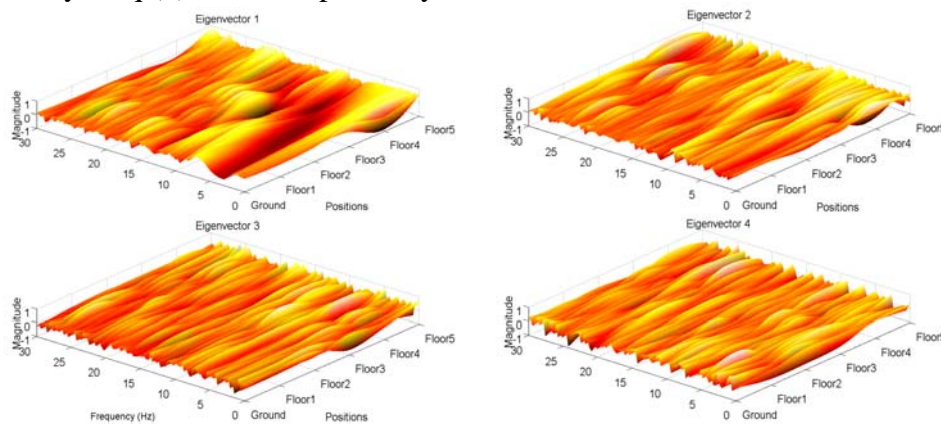

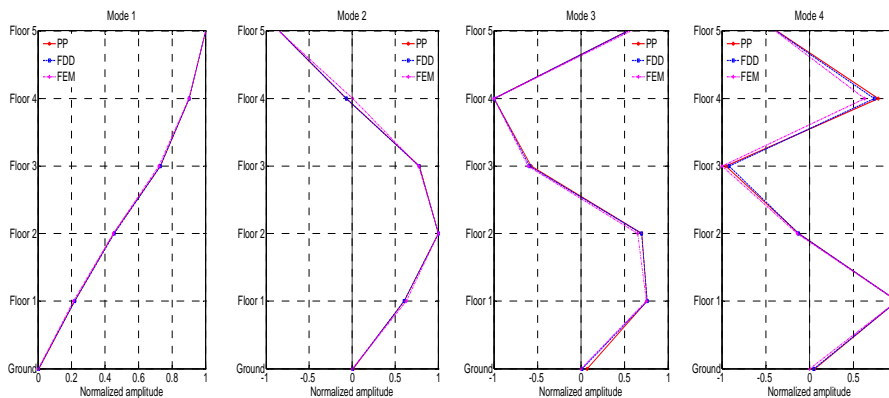Figure 4. First four spectral eigenvectors

Figure 5. First four mode shapes

For the damping extraction, firstly auto power spectral density functions of each mode have been identified in the Enhanced Frequency Domain Decomposition (EFDD) via the MAC value, secondly, the free decay functions corresponding to mode shapes have been identified to be convenient for the logarithmic decrement estimation and damping ratios of each mode. Figure 6 shows the estimated auto spectral density functions

of the first five structural modes at MAC=98%, while Figure 7 indicates the estimated free decay functions of these mode shapes.

Next, modal parameters have been identified using the SSI algorithm in the time domain as presented in the part 4. Number of measured outputs are 6, with N=30000 samples each. In order to build up the stability diagrams, the number of

block rows in Hankel matrix and number of system orders or number of singular values used in reduced-order model have been varies, concretely i=20÷125 with step 10, k=5÷60 step 5. Stability diagram for the frequency at varied k=5÷60 step 5 and i=50 is shown in Figure 8. First five

natural frequencies can be observed in this frequency stability diagram. Apparently, the natural frequencies extracted by SSI are similar to those from FDD. Damping stability diagram is indicated in Figure 9.
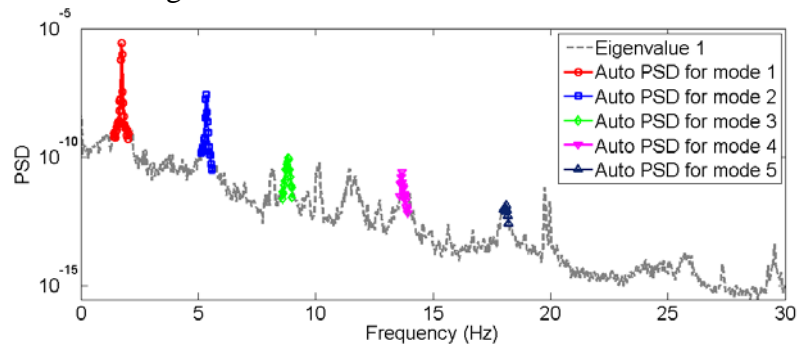

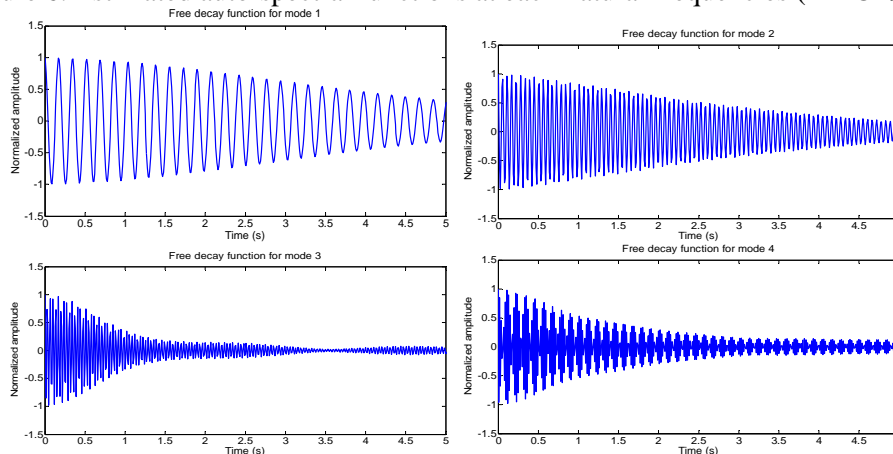Figure 6. Estimated auto-spectral functions at each natural frequencies (MAC=98%)

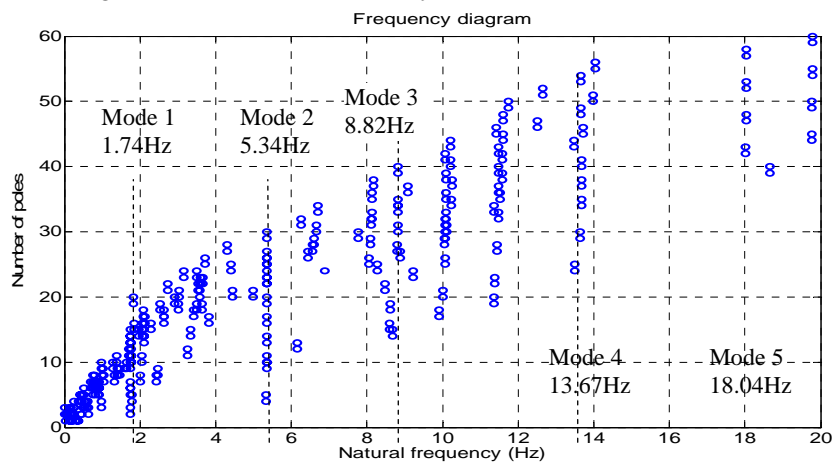Figure 7. Estimated free decay functions of first four modes

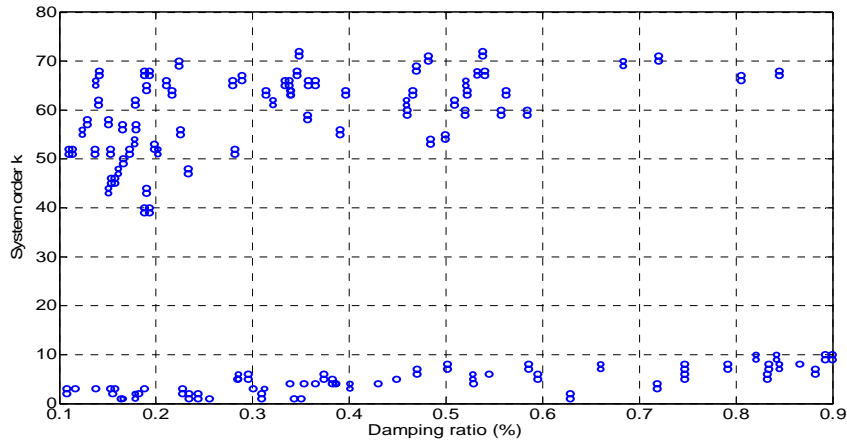Figure 8. Frequency stability diagram

Figure 9. Damping ratio stability diagram

6. Conclusion

Modal parameters identifications of the 5-storey steel structure using FDD and SSI-DATA have been investigated. Identified natural frequencies are well agreement between them and with FEM results. Identified mode shapes also are good fitted between FDD, PP and FEM methods. Damping ratios can be identified from FDD and SSI, however, refined technique should be further investigated for more reliability of the damping estimation.

References

Abdel-Ghaffar, A.M. and Scanlan, R.H. (1985). Ambient vibration studies of Golden Gate bridge: I. Suspension structure. *Engineering Mechanics*, ASCE, 111, 4, pp. 463-482.

Brincker, R., Zhang, L., and Andersen, P. (2001a). Modal identification of output-only systems using frequency domain decomposition. *Smart Materials and Structures*, 10, pp. 441-445.

Brincker, R., Ventura, C.E., and Andersen, P. (2001b). Damping estimation by frequency domain decomposition. *Proc. the 19th Int'l Modal Analysis Conference* (IMAC), pp. 141-146.

Cunha, A., Caerano, E., Magalhaes, F., and Moutinho, C. (2006). From input-output to output-only modal identification of civil engineering structures. *SAMCO Final Report*

He, J. and Fu, Z.F. (2001). *Modal analysis.* Butterworth-Heinemann.

Kuroiwa, T., and Iemura, H. (2007). Comparison of modal identification of output-only systems with simultaneous and non simultaneous monitoring. *Proc. the World Forum on Smart Materials an Smart Structures Technology* (SMSST07), Chongqing & Nanjing, China.

Siringoringo, D.M. and Fujino, Y. (2008). System identification of suspension bridge from ambient vibration response. *Engineering Structures*, 30, pp. 462-477.

Peeters, B. and De Roeck, G. (1999). Reference-based stochastic subspace identification for output-only modal analysis. *Mechanical Systems and Signal Processing*, 13, 6, pp. 855-878.

Tamura, Y., Yoshida, A. and Zhang, L. (2005). Damping in building and estimation techniques. *Proc. the 6th Asia-Pacific Conference on Wind Engineering* (APCWE-VI), Seoul Korea, pp. 193-214.

Van Overschee, P. and De Moor, B. (1993). Subspace algorithms for the stochastic identification problem. *Automatica*, 29,2, pp. 649-660.

Weng, J.H., Loh, C.H., Lynch, J.P., Lu, K.C., Lin, P.Y. and wang, Y. (2008). Output-only modal identification of a cable-stayed bridge using wireless monitoring systems. *Engineering Structures*, 30, pp. 1820-1830.

Output-only System Identification using Wavelet Transform

Le Thai Hoa[a,], Yukio Tamura[b] , Akihito Yoshida[c], Nguyen Dong Anh[d]

[a] *Wind Engineering Research Center, Tokyo Polytechnic University, Japan*
1583 Iiyama, Atsugi Kanagawa 243-0297, Japan; thle@arch.t-kougei.ac.jp
Hanoi University of Engineering and Technology, Vietnam National University, Hanoi
144 Xuan Thuy, Cau Giay, Hanoi, Vietnam; thle@vnu.edu.vn
[b] *Department of Architectural Engineering, Tokyo Polytechnic University, Japan*
1583 Iiyama, Atsugi Kanagawa 243-0297, Japan; yukio@arch.t-kougei.ac.jp
[c] *Department of Architectural Engineering, Tokyo Polytechnic University, Japan*
1583 Iiyama, Atsugi Kanagawa 243-0297, Japan; yoshida@arch.t-kougei.ac.jp
[d] *Hanoi University of Engineering and Technology, Vietnam National University, Hanoi*
144 Xuan Thuy, Cau Giay, Hanoi, Vietnam; ndanh@imech.ac.vn

Abstract

System identification of ambient vibration structures using output-only identification techniques has become a key issue in the structural health monitoring and the assessment of engineering structures. Modal parameters of the ambient vibration structures consist of natural frequencies, mode shapes and modal damping ratios. So far, a number of mathematical models on the output-only identification techniques have been developed and roughly classified by either parametric methods in the time domain or nonparametric ones in the frequency domain. Each identification method in either the time domain or the frequency one has its own advantage and limitation. Parametric methods in the time domain are preferable for estimating modal damping but difficulty in natural frequencies, mode shapes extraction, whereas the nonparametric ones in the frequency domain advantage on natural frequencies, mode shapes extraction, but uncertainty in damping estimation. Most recently, new approach in both time and frequency domains based on Wavelet Transform (WT) has been developed for output-only identification techniques with a new concept of time-frequency identification in the time-frequency plane. This paper will present theoretical bases of the wavelet transform for output-only system identification of the ambient vibration data. Measured data will be applied for identifying natural frequencies and damping ratios. Modified complex Morlet wavelet function will be used for more adaptation on the time and frequency resolutions. Frequency resolution adjustment techniques have been proposed to estimate modal parameters of high-order modes.

Key Words: System identification; Output-only identification; Ambient data; Time Frequency analysis; Wavelet transform; Modified Morlet wavelet

1. Introduction

System identification methods of output-only data have become a key issue in structural health monitoring and assessment of engineering structures. Modal parameters of the ambient vibration structures consist of natural frequencies, mode shapes and damping ratios as well. So far, a number of

mathematical models on the output-only identification techniques have been developed and roughly classified by either parametric methods in the time domain or nonparametric ones in the frequency domain. Each identification method in either the time domain or the frequency one has its own advantage and limitation. Generally, parametric methods in the time domain such as Ibrahim time domain (ITD), Eigensystem realization algorithm (ERA) or Random decrement technique (RDT) are preferable for estimating modal damping but difficulty in natural frequencies, mode shapes extraction, whereas nonparametric methods in the frequency domain like Peak-picking (PP), Frequency domain decomposition (FDD) or Enhanced frequency domain decomposition (EFDD) advantage on natural frequencies, mode shapes extraction, but uncertainty in damping estimation. Recently, new approach based on Wavelet transform (WT) and Hilbert-Huang transform (HHT) have been developed for output-only identification techniques in the concept of time-frequency plane. Preferable advantages of this time-frequency based methods are to estimate the natural frequencies in the frequency slides and the damping ratios in the time slides on the time-frequency plane, especially WT is powerful analyzing tool for processing non-stationary, transient and non-linear inputs and outputs.

Wavelet transforms (WT) has recently developed basing on a convolution operation between a signal and a basic wavelet function which allows to represent in time-scale (frequency) domains, also called as a time-frequency analysis (Daubechies, 1992). The WT advantages to conventional Fourier transform (FT) and its modified version as Short-time Fourier transform (STFT) in analyzing non-stationary, non-linear and intermittent signals with temporo-spectral information and multi-resolution concept. The WT uses the basic wavelet functions (wavelets or mother wavelets), which can dilate (or compress) and translate basing on

two parameters: scale (frequency) and translation (time shift) to apply short windows at low scales (high frequencies) and long windows at high scales (low frequencies). Basing on a discretization manner of the time-scale plane and characteristics of wavelets, the WT can be branched by the continuous wavelet transform (CWT) and the discrete wavelet transform (DWT). Recently, the WT have been applied to extract modal parameters from vibration tests (ex., Staszewski, 1997; Ladies and Gouttebroze, 2002; Slavic et al., 2003; Kijewski and Kareem, 2003). However, the WT applications have recently had some troublesome difficulties and limitation as follows: (1) Analysis of time-frequency resolutions; (2) Extraction of close frequencies; (3) Identification of modal parameters in high-order modes; (4) Reality of practical data with many sources of noises and influence of external excitation; and (5) Time interval and reliability for damping estimation. Normally, the traditional complex Morlet wavelet (Daubechies, 1992; Kijewski and Kareem, 2003), with only parameter of central frequency is mostly used in the WT analysis, however, this traditional wavelet is not convenient to deal with high time-frequency resolutions, close frequency identification problem, and high-mode parameters where sophisticated the analysis of high time-frequency resolutions must be required. Modified complex Morlet wavelet has been discussed by some authors (Ladies and Gouttebroze, 2002; Yan et al., 2006) to give comprehensive approach for time-frequency resolution analysis.

This paper presents theoretical bases of the wavelet transform-based technique for output-only system identification of the ambient vibrated structure with more focused on the time-frequency resolutions for estimating the modal parameters of high-order modes. Practical output data and modified complex Morlet wavelet will be used for the output-only system

identification. Frequency resolution adjustment techniques have been proposed in order to determine the modal parameters of the high-order modes.

2. Wavelet transform

The CWT of given signal x(t) is defined as the convolution operation between signal x(t) and wavelet function $\psi_{\tau,s}(t)$ (Daubechies, 1992):

$$W_\psi^x(\tau, s) = \int_{-\infty}^{\infty} x(t)\psi_{\tau,s}^*(t)dt \qquad (1)$$

where $W_\psi^x(s,\tau)$: CWT coefficients at translation τ and scale s in the time-scale plane; asterisk * means complex conjugate; $\psi_{\tau,s}(t)$: wavelet function at translation τ and scale s of basic wavelet function $\psi(t)$, or mother wavelet:

$$\psi_{\tau,s}(t) = \frac{1}{\sqrt{s}}\psi\left(\frac{t-\tau}{s}\right) \qquad (2)$$

The mother wavelet, or wavelet for brevity, satisfy such following conditions as oscillatory function with fast decay toward zero, zero mean value, normalization and admissibility condition as follows:

$$\int_{-\infty}^{\infty}\psi(t)dt = 0; \quad \int_{-\infty}^{\infty}|\psi(t)|^2\, dt = 1; \qquad (3a)$$

$$C_\psi = \int_{-\infty}^{\infty}\frac{|\hat{\psi}(\omega)|^2}{\omega}d\omega < \infty \qquad (3b)$$

The CWT coefficients can be considered as a correlation coefficient and a measure of similitude between the wavelet and the signal in the time-scale plane. The higher coefficient is, the more the similarity. It is noted that the wavelet scale is not a Fourier frequency, but revealed as an inverse of frequency. Accordingly, a relationship between the Fourier frequency and wavelet scale can be approximated:

$$f_F = \frac{f_c}{s} \qquad (4)$$

where f_F: Fourier frequency; s: wavelet scale; and f_c: central frequency.

3. Modified complex Morlet wavelet

Up to now, the traditional complex Morlet wavelet is commonly used for the CWT analysis, because it contains harmonic components similarly to the Fourier transform. The complex Morlet wavelet and its Fourier transform are given as follows (Kijeweski and Kareem, 2003):

$$\psi(t) = (2\pi)^{-1/2}\exp(i2\pi f_c t)\exp(-t^2/2) \quad (5a)$$

$$\hat{\psi}(sf) = (2\pi)^{-1/2}\exp\left(2\pi^2(sf - f_c)^2\right) \qquad (5b)$$

where $\psi(t), \hat{\psi}(sf)$: complex Morlet wavelet and its Fourier transform coefficient. It is noted that here is only the central frequency as the traditional complex Morlet wavelet.

Modified complex Morlet wavelet is used by Ladies and Gouttebroze, 2002; Yan et al., 2006 as follows:

$$\psi(t) = (\pi f_b)^{-0.5}\exp(j2\pi f_c t)\exp(-t^2/f_b) \quad (6a)$$

$$\hat{\psi}(sf) = \exp(-\pi^2 f_b(sf - f_c)^2) \qquad (6b)$$

where f_b: bandwidth parameter

Investigations on the modified Morlet wavelet with some parameters (f_c and f_b) are shown in Figure 1.

4. Time-frequency resolution analysis

Analysis of the time-frequency resolution is inevitable for the close frequency identification and the high-mode parameter identification using the wavelet transform.

Time-frequency resolution plane of the wavelet transform is shown in Figure 2, in which high frequency resolution and low time resolution are used for low frequency band, and inversely. The Heisenberg's uncertainty principle revealed us that it is impossible to simultaneously obtain optimal time resolution and optimal frequency resolution. Kijewski and Kareem, 2003 discussed the time-frequency resolution for the wavelet transform using the traditional

Morlet wavelet, also suggested for parameter   selection.

Figure 1. Modified Morlet wavelet with some parameters

Wavelet transform

Figure 2. Time-frequency resolution plane

The time and frequency resolutions of the modified Morlet wavelet can be expressed as follows (Yan et al., 2006):

$$\Delta f_\psi = \frac{1}{2\pi\sqrt{f_b}} \quad (7a)$$

$$\Delta t_\psi = \frac{\sqrt{f_b}}{2} \quad (7b)$$

where $\Delta f_\psi, \Delta t_\psi$: frequency resolution and time resolution of the modified Morlet wavelet. Here, relationship between the frequency and time resolutions is $\Delta f_\psi \Delta t_\psi = 1/4\pi$ considered as optimal product, normally we have the relationship $\Delta f_\psi \Delta t_\psi \geq 1/4\pi$.

In the interrelation between the Fourier frequency and the wavelet central frequency, wavelet scale as shown in the Eq.(4), we have $s = f_c/f$, one obtain the resolutions of time and frequency:

$$\Delta f = \frac{\Delta f_\psi}{s} = \frac{f}{2\pi f_c \sqrt{f_b}} \quad (8a)$$

$$\Delta t = s\Delta t_\psi = \frac{f_c\sqrt{f_b}}{2f} \quad (8b)$$

Thus, one can adjust the wavelet central frequency f_c and the bandwidth parameter f_b to obtain the desired frequency resolution and the desired time one at analyzing frequency f.

5. Modal parameters estimation

Consider a linear damped MDOF structure superimposed by N-modes, a response solution of the structure due to ambient external excitation as Gaussian distributed broad-band white noises can be expressed as follows:

$$X(t) = \sum_{j=1}^{N} A_i \exp(-2\pi\zeta_i f_i t)\cos(2\pi f_{di}t + \theta_i) + X_p \quad (9)$$

where N: number of combined modes; i: index of mode; A_i: amplitude of i-th mode; θ_i: phase angle; f_i, ζ_i: undamped frequency and damping ratio of i-th mode;

$f_{di} = f_i\sqrt{1-\zeta_i^2}$: damped natural frequency; X_p : perturbation due to noises and effect of external excitation.

There is no convincing study on the effect of the ambient loading on accuracy of the output-only system identification methods. It is noted that some authors (Ladies and Gouttebroze, 2002; Kijewski and Kareem, 2003 and so on) used the random decrement technique to eliminate the effect of external excitation and estimate impulse responses of structure. However, this technique as conditional correlation function and averaging processing can weaken high spectral components, but low energies in the signal. Normally, effect of perturbation due to noise and external excitation is eliminated.

Substituting Eqs.(9) and (6) into Eq.(1), one can obtain the wavelet transform coefficient (Yan et al., 2006):

$$W_\psi^X(\tau,s) = \frac{\sqrt{s}}{2}\sum_{i=1}^{N} A_i \exp(-2\pi\zeta_i f_i \tau)$$

$$\exp(-\pi^2 f_b (sf_i - f_c)^2)\exp(j(2\pi f_{di}\tau + \theta_i)) \quad (10)$$

Because the wavelet coefficient is localized at certain fixed scale s=s_i, thus only i-th mode associated with the wavelet scale s_i dominantly contributes to Eq.(10), other modes can be negligible. Noting that from Eq.(4) we have $s_i = f_c/f_i$ or $s_i f_i - f_c = 0$, thus the term in Eq.(10) $\exp(-\pi^2 f_b (sf_i - f_c)^2) = 1$. The wavelet coefficient at scale s_i can be rewritten as SDOF system at i-th mode:

$$W_\psi^X(\tau,s_i) = \frac{\sqrt{s_i}}{2} A_i \exp(-2\pi\zeta_i f_i \tau)\exp(j(2\pi f_{di}\tau + \theta_i))$$

$$\quad (11)$$

Substituting time t for translation τ, and expressing Eq.(11) in a form of the Hilbert transform's analytic signal of instantaneous amplitude and instantaneous phase as follows:

$$W_\psi^X(t,s_i) = B_i(t)\exp(j\varphi_i(t)) \quad (12)$$

where $B_i(t), \varphi_i(t)$: instantaneous amplitude and phase, which are determined as:

$$B_i(t) = \frac{\sqrt{s_i}}{2} A_i \exp(-2\pi\zeta_i f_i t) \quad (13a)$$

$$\varphi_i(t) = 2\pi f_{di} t + \theta_i \quad (13b)$$

Logarithmic expression of the instantaneous amplitude, then differentiating logarithmic amplitude, and differentiating the phase angle, one obtains:

$$\frac{d\ln B_i(t)}{dt} = -2\pi\zeta_i f_i \quad (14a)$$

$$\frac{d\varphi_i(t)}{dt} = 2\pi f_i\sqrt{1-\zeta_i^2} \quad (14b)$$

From Eqs.(14a) and (14b), the i-th natural frequency and the i-th damping ratio can be estimated as follows:

$$f_i = \frac{1}{2\pi}\sqrt{\left(\frac{d\ln B_i(t)}{dt}\right)^2 + \left(\frac{d\varphi_i(t)}{dt}\right)^2} \quad (15a)$$

$$\zeta_i = -\frac{1}{2\pi f_i}\frac{d\ln B_i(t)}{dt} \quad (15b)$$

For estimating damping ratios from the wavelet logarithmic amplitude envelope, the linear fitting technique can be applied. Above-discussed wavelet transform-based procedure has been applied for estimating the natural frequencies and the damping ratios of ambient vibrated data of the structure.

6. Results and discussions

Ambient vibration measurements have been carried out on a 5-storey steel structure at the test site of the Disaster Prevention Research Institute (DPRI), Kyoto University. Ambient data were recorded at all 5 floor levels and ground as reference, by tri-axial velocity sensors. Data were sampled on 5-minute records with 100Hz sampling rate (Kuroiwa and Iemura, 2007). Velocity outputs have been integrated to displacements for convenient use. Time series of the integrated displacement at first floor and its power spectral density functions (PSD) are presented in Figure 3. Combined with Finite Element Model (FEM) results, first five bending modes and associated natural frequencies can be identified.
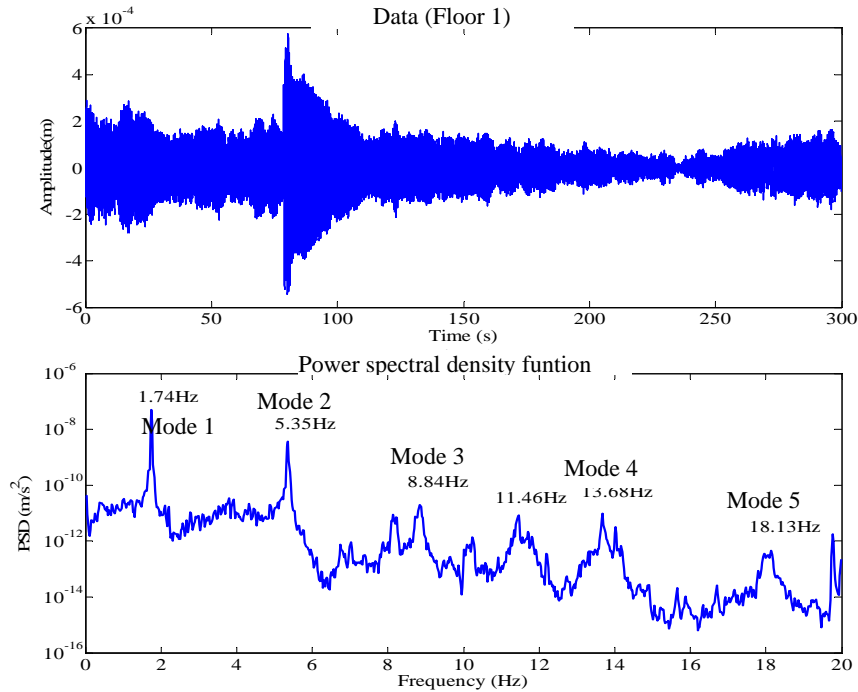
Figure 3. Data and its PSD

Figure 4 shows the wavelet transform coefficient (WTC) of the data on the frequency band 0÷20Hz and the time duration 50÷150seconds, with the central frequency f_c=2 and the bandwidth parameter f_b=20. As can be seen from Figure 4, there are only two frequency peaks observed at 1.73Hz and 5.34Hz, which correspond to two first modes. Frequencies of the high-order modes (the 3rd mode, 4th mode and 5th mode) can be estimated by this WCT. Reason is given here because single frequency resolution has been applied to whole frequency band 0÷20Hz, which is good for low frequency analysis, but not appropriate to higher frequency bands.
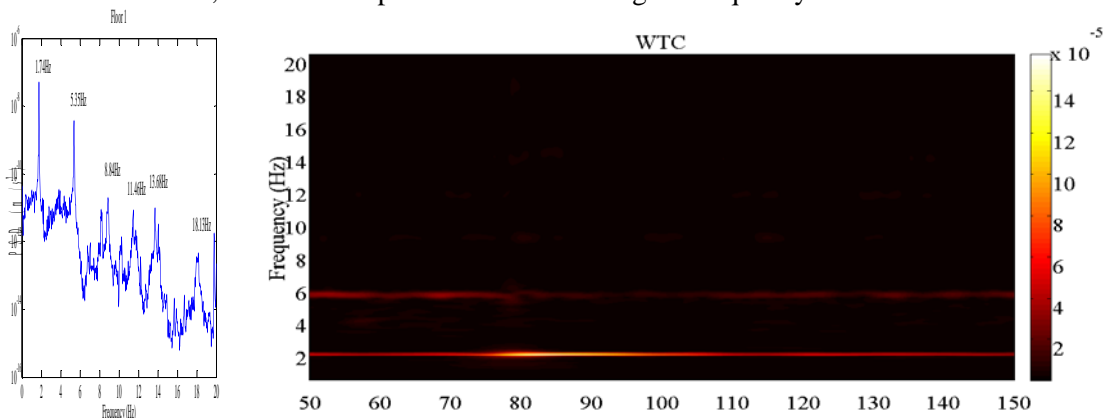
Figure 4. Wavelet transform coefficient (at f_c=2, f_b=20)

In order to identify the modal parameters of higher modes, it is proposed here techniques for frequency resolution adjustment as follows:

1. Bandwidth resolution adjustment: Analyzing frequency band is divided into several bandwidths, and one applies the Morlet wavelet with concrete parameters (f_c, f_b) to each frequency bandwidth.

Here, there are bandwidths of 0÷20Hz such as 0÷5Hz, 5÷10Hz, 8÷12Hz, 12÷16Hz, and 16÷20Hz.

2. Broadband filtering: The data is broadband filtered into several bandwidths. This process remains desired frequency band for the wavelet transform coefficients, other undesired bands can be negligible. Next, the Morlet wavelet with adjusted frequency resolution applies to band-passed components. Here, the broadband filtered components of 0÷20Hz are 0÷3Hz, 3÷6Hz, 6÷12Hz, and 12÷24Hz.

3. Narrowband filtering: Similar to the second technique, the signal is filtered not on broad bandwidths, but on narrow bandwidths, which are close to each natural frequency. This technique is much more localized around natural frequencies, but it requires prior information on these natural frequencies on the signal. Also, this technique eliminates effects of undesired frequencies on the wavelet coefficient analysis. Here, the data is filtered narrow bandwidths of 1÷3Hz; 4÷6Hz; 8÷10Hz; 13÷15Hz, and 17÷19Hz.

Figure 5 shows the wavelet transform coefficients at four frequency bandwidths following the bandwidth resolution adjustment technique. The Morlet wavelet parameters (f_c, f_b) also are associated with the frequency bandwidths. Obviously, all the frequency peaks can be observed at each analyzing bandwidths, even close frequencies can be determined in the bandwidth of 12-16Hz.

Broadband and narrowband components from the original data are shown in Figure 6. The frequency bandwidths also are indicated in each filtered components.

The wavelet transform coefficients of the broadband components and the narrowband ones, as shown in Figure 6 are presented in Figure 7 and Figure 8. As can be seen from the Figures 7 and 8, the natural frequencies, with application of the band-pass filtering are appeared more clearly and visibly than without filtering as in Figure 5. Although the close peak frequencies all can be observed in Figure 6 and Figure 7 at the natural frequency of the 4-th mode.
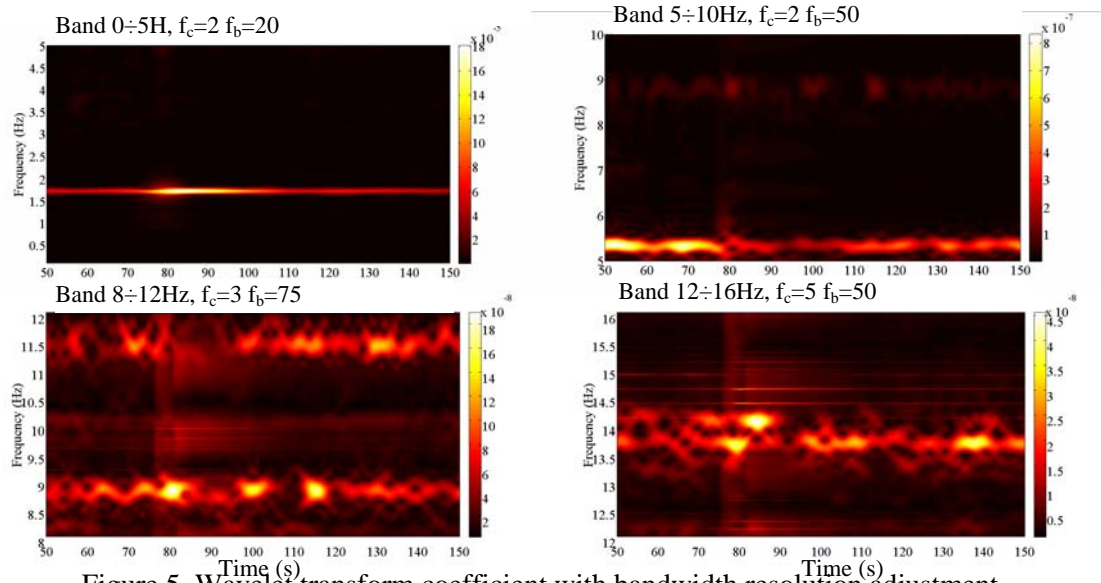

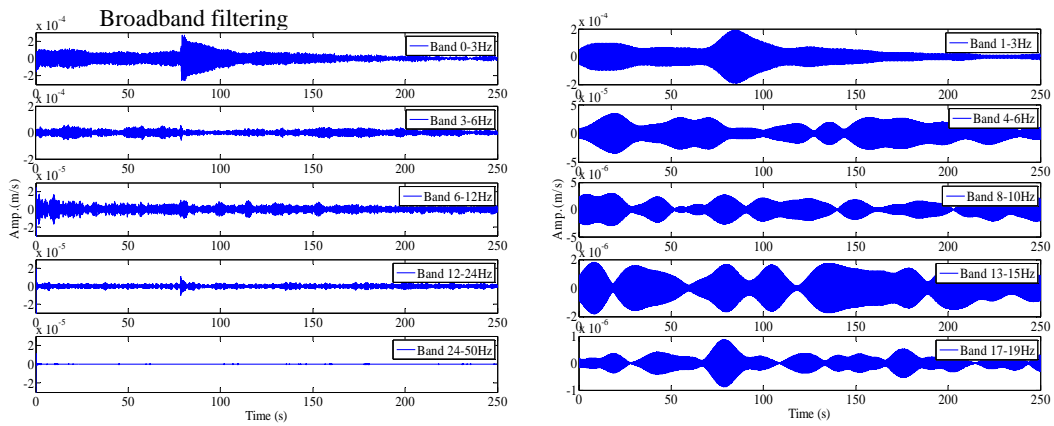Figure 5. Wavelet transform coefficient with bandwidth resolution adjustment

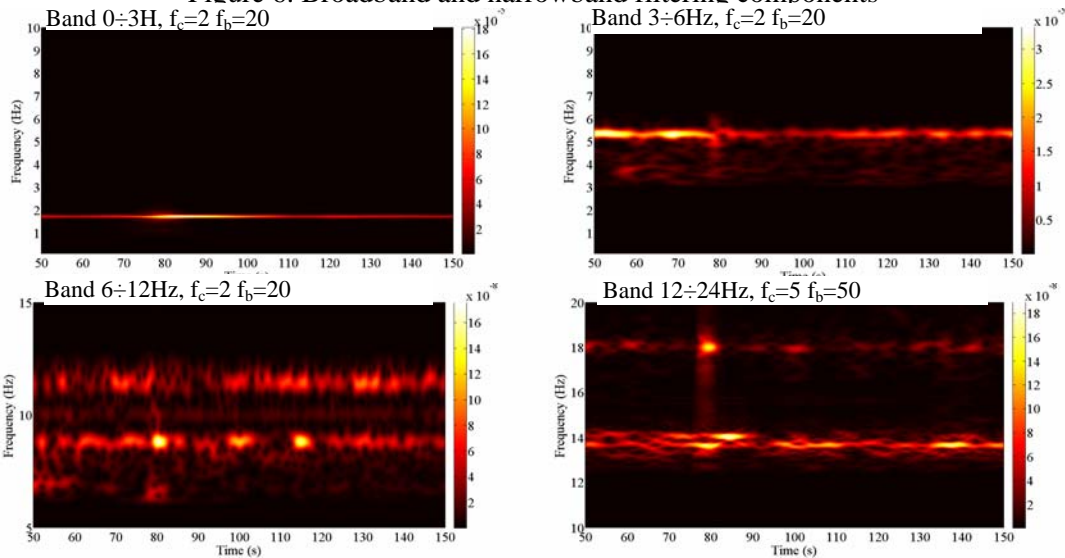Figure 6. Broadband and narrowband filtering components

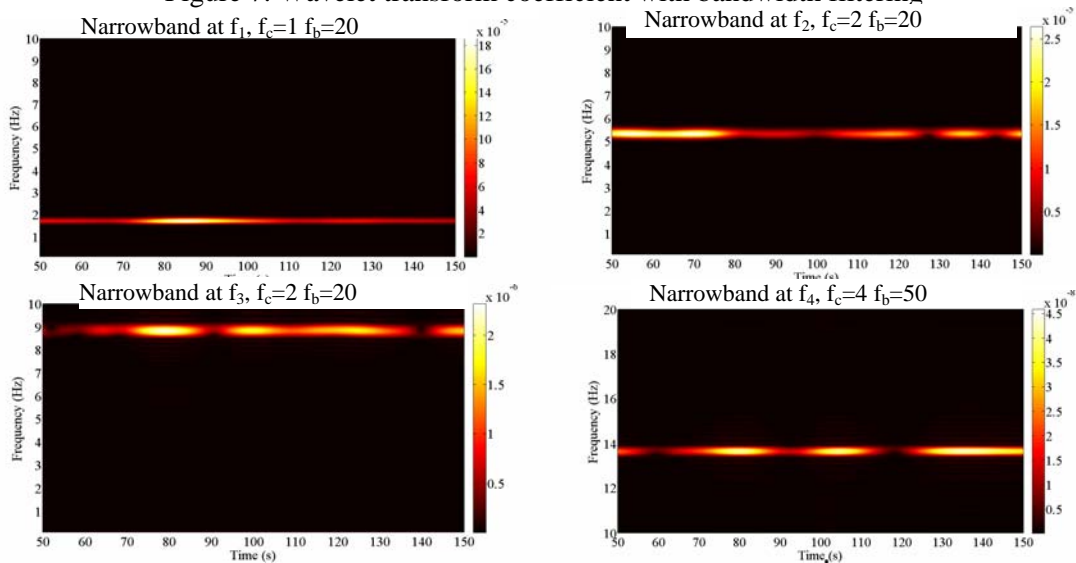Figure 7. Wavelet transform coefficient with bandwidth filtering

Figure 8. Wavelet transform coefficient with narrowband filtering

Figure 9 shows the wavelet logarithmic amplitude envelopes of the wavelet transform coefficients of the narrowband components. The logarithmic decrements can be estimated via the linear least-square fitting technique as red lines shown in the same plots, the damping ratios then are determined. However, the questionable point here is that how is the time duration in the wavelet logarithmic amplitude envelopes selected for estimating the damping ratios. There is no any discussion on this matter, but it is generally agreed that the selection of time duration much influences on accuracy and reliability of identified damping ratios. It argues that some following guidelines should be taken into consideration for damping estimation:

(1) Time duration should start around clear and maximum peak of wavelet transform coefficient.

(2) Short localized time duration should be preferable.
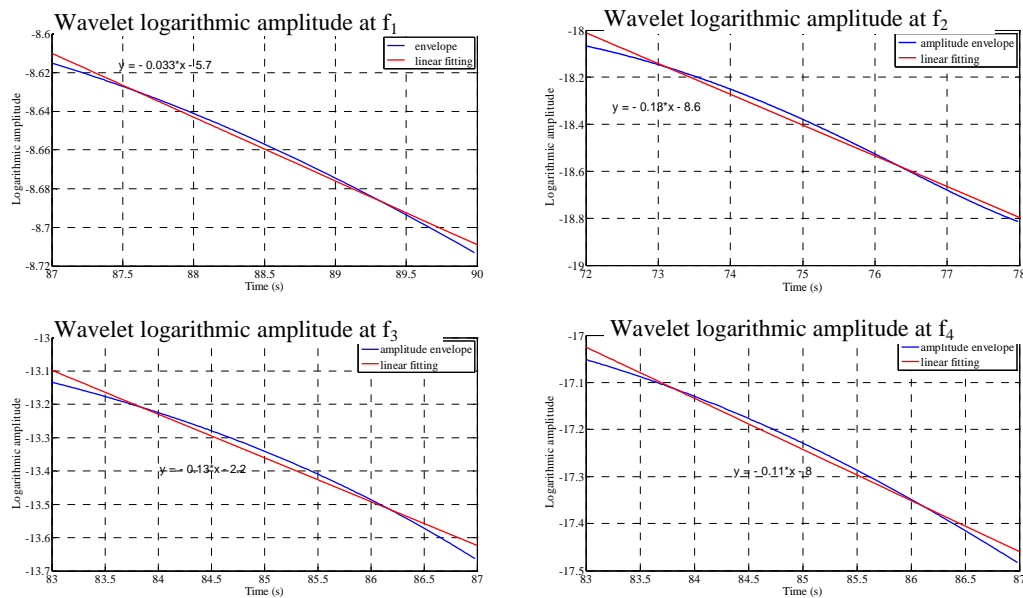

Figure 9. Damping estimation from wavelet logarithmic amplitude envelope

The wavelet transform coefficients are very clear observed when one applies the narrowband filtering (see Figure 8), especially, they are localized in the frequency domain but stretched in the time domain. This characteristic is convenient for estimating the damping ratios.

Results of the natural frequencies and damping ratios extracted from mentioned three techniques are listing this Table 1. There is good agreement observed for the identified natural frequencies between the techniques.

Table 1. Identified natural frequencies (Hz)

	Mode1	Mode2	Mode3	Mode4	Mode5
PSD	1.74	5.35	8.84	13.68	18.13
WT(1)	1.74	5.32	8.81	13.64	18.07
WT(2)	1.73	5.34	8.82	13.59	18
WT(3)	1.73	5.35	8.83	13.64	18.04

Table 2. Identified damping ratios (%)

	Mode1	Mode2	Mode3	Mode4	Mode5
WT(3)	0.52	2.07	2.07	1.75	2.22

Note: WT(1), (2), (3) corresponding to frequency resolution techniques as (1) bandwidth adjustment; (2) broadband filtering; and (3) narrowband filtering

7. Conclusion

Output system identification of ambient data using the wavelet transform has been presented in the paper. Modified Morlet wavelet is more adaptive and appropriate to treat with sophisticated time-frequency resolution analysis. Three frequency resolution techniques have been proposed to estimate the modal parameters of the high-order modes and the close frequency problem. Identified natural frequencies from three techniques are good agreement. However, further investigations on selection of time duration in the wavelet logarithmic amplitude envelopes are required for more reliability and accuracy of the damping estimation.

References

Daubechies, I. (1992). *Ten lectures on wavelets*. CBMS-NSF.

Kijewski, T.L., and Kareem, A. (2003). Wavelet transforms for system identification: considerations for civil engineering applications. *Journal of Computer-aided Civil and Infrastructure Engineering*, 18, pp.341-357.

Kuroiwa, T., and Iemura, H. (2007). Comparison of modal identification of output-only systems with simultaneous and non simultaneous monitoring. *Proc. the World Forum on Smart Materials an Smart Structures Technology* (SMSST07), Chongqing & Nanjing, China.

Ladies, J., and Gouttebroze, S. (2002). Identificationof modal parameters using wavelet transform. *Int'l Journal of Mechanical Science,* 44, pp. 2263-2283.

Meo, M., Zumpano, G., Meng, X., Cosser, E., Roberts, G., and Dodson, A. (2006). Measurement of dynamic properties of a medium span suspension bridge by using the wavelet transform. *Mechanical Systems and Signal Processing*, 20, pp. 1112-1133.

Slavic, J., Simonovski, I., and Boltezar, M. (2003). Damping identification using a continuous wavelet transform: application to real data. *Journal of Sound and Vibration*, 262, pp. 291-307.

Staszewski, W. J. (1997). Identification of damping in MDOF systems using time-scale decomposition. *Journal of Sound and Vibration*, 203, 2, pp. 283-305.

Yan, B.F., Miyamoto, A., and Bruhwiler, E. (2006). Wavelet transform-based modal parameter identification considering uncertainty. *Journal of Sound and Vibration*, 291, pp. 285-301.

Numerical Analysis for Impact Response and Damage of Composite Plates

In Lee[a,] and Eun-Ho Kim[b]

[a] Department of Aerospace Engineering, School of Mechanical, Aerospace and System Engineering, KAIST, 373-1 Guseong-dong, Yuseong-gu, Daejon, Korea, E-mail:inlee@kaist.ac.kr
[b] Department of Aerospace Engineering, School of Mechanical, Aerospace and System Engineering, KAIST, 373-1 Guseong-dong, Yuseong-gu, Daejon, Korea, E-mail:eunhokim@kaist.ac.kr

Abstract

Fiber reinforced composite materials are widely used for various structures especially for aerospace structures because of their high specific stiffness and strength. However, composite materials have low toughness and they are susceptible to damage from impact loading. Especially for low velocity impact, matrix crack and delamination damage mainly appears in the structures. They are hard to be detected in their appearance. These barely visible impact damages can reduce strength of composite structures. Composite plates were fabricated with unidirectional CFRP prepregs and impact tests of composite plates were performed at various impact energies to investigate the impact behaviors and impact damages of composite plates. Damage mode due to low velocity impact depends on the impact energy level. Critical damages always appeared with fiber breakage. C-scan was used to inspect the overall damage areas of composite plates. Cross-sections of damaged plates were inspected with light-microscope to figure out internal damage modes due to low-velocity impact. Numerical analyses of composite plates subjected to low-velocity impact were performed. Damage model of composite material was developed for reliable impact analysis. It is developed based on the continuum damage mechanics and failure criteria of composite material. Progressive damage analyses were performed with the developed damage model. The damage model was implemented in the user material subroutine of commercial finite element analysis program, ABAQUS/explicit. Cohesive zone model was used for delamination damage. Impact analyses of composite plates were performed with ABAQUS/explicit and the developed damage model. Analysis results were compared with the experiment data for the verification of damage model. Impact analysis with the developed damage model predicted the impact behaviors and damage region reasonably.

Key Words: composite plat, impact response, impact damage, damage model, numerical analysis

1. Introduction

Fiber reinforced composite materials are widely used for various structures especially for aerospace structures because of their high specific stiffness and strength. Metal materials are being replaced to composite materials for weight savings of structures. However, composite materials have low toughness and they are susceptible to damage from impact loading. Especially for low velocity impact, even though the impact energy is low, it can induce matrix crack and

delamination in the structure. These internal impact damages are hard to be detected. These barely visible impact damages reduce the strength of the structures. It is well known that delamination can significantly reduce the compressive strength. Low velocity impact with large impact energy can fracture composite structure. Therefore impact damage should be considered in the design of composite structures considering possible impacts during fabrication, operation and repairing process for safety of the structures.

Impact behavior and impact damage of composite structure is very complicated and hard to be predicted. They depend on many parameters such as geometric shape of composite structure and impactor, impact energy, boundary condition, layup-sequence of composite structures and so on.

Analysis technique is required to predict impact behaviors, impact damage and residual strength of composite structures. Finite element analysis method is generally used for structural analysis. For reliable impact analysis of composite structures, reasonable damage criteria and damage model are required to predict the initiation and propagation of impact damage.

Composite material have several damage modes; such as fiber breakage, matrix crack and delamination. Each damage mode appears in different stress or strain condition and affects impact behavior and degradation of residual strength in different way. The initiation of each damage mode should be considered separately with different failure criterion. After the damage initiation, stress distribution around the damage are changed depending on the damage. It should be appropriately considered with the damage model.

Recently, progressive damage analysis is generally used for reasonable impact analysis with damage models based on continuum damage mechanics.

Matzenmiller et al.(1995) proposed Weibull distribution function for the fiber failure mode because strength of a fiber bundle with initial defects follows the Weibull distribution function.

Williams et al.(2001) used the Mazenmiller's model for both fiber failure and marix failure. He used shell element for the impact analysis of composite plate.

Tabiei et al.(2009) also used the Mazenmiller's model for damage model. He used solid element for impact analysis of composite plate.

Shape parameters of Weibull distribution function were usually determined by parametric studies for appropriate analysis (Williams et al., 2001 and Tabiei et al., 2009)

However, the shape parameters can be determined by statistical analysis of strength data obtained from material property tests.

In this research, low velocity impact tests of CFRP composite plates were performed at various impact energies to investigate the impact behaviors and impact damages. Overall damage area including non-visible internal damage was inspected with C-scan. Cross-section of impact specimens were also inspected with light-microscope to figure out internal damage modes.

Damage model for composite material based on Mazenmiller's model was developed and implemented in user material subroutine of commercial FEA program, ABAQUS/explicit. Impact analyses of composite plate were performed with ABAQUS/explicit and the damage model. Analysis results were compared with those of impact test and C-scan.

2. Experiment

2.1. Materials and test procedures

Composite plates were fabricated with carbon/epoxy prepreg CU125NS (HANKUK CARBON Co.). Material properties are represented in Table 1. Lay-up sequence of the plates was $[0^o_2/90^o_2/0^o_2/90^o_2/0^o_2]_s$. Dimension of specimens was 100mm x 100mm x 2mm. Impact tests were performed

with drop weight type impact testing machine INSTRON DYNATUP 9250HV. Steel impactor was used. Its diameter was 1/2 inch and mass was 6.5kg. Impact specimens were clamped with a hydraulic fixing device. Square frame jigs were used to give square boundary condition as shown in Fig 1. Width of the frame was 10mm.

Figure 1. Maximum contact force and Central deflection

Impact tests were performed at a range of impact energy, 5J~40J to investigate both visible and non-visible impact damages. Overall damage area was inspected with C-scan using 10MHz ultrasound. Cross-section of the specimens impacted with 5J and 15J impact energy was inspected with light-microscope to figure out the internal damage modes.

Table 1. Material properties of CU125NS*

Modulus	Strength
E_{11} : 135.4GPa	XT : 2.93 GPa
E_{22}, E_{33} : 9.6GPa	XC : 1.65 GPa
$G_{12} G_{13}$: 4.8GPa	YT : 54.0 MPa
G_{23} : 3.2GPa	YC : 240.0 MPa
$v_{12} v_{13}$: 0.31	S12,S13: 74.0MPa
v_{23} : 0.52	S23 : 65.0MPa

* Choi, I.H. and Hong, C. S.(1994) and Kang, S. – G.(2006)

2.2. Test results

Maximum contact forces and central deflections are represented in terms of impact energy in Fig. 2. Impact energies can be categorized into three levels according to impact damages as shown in Fig. 2 for the composite plates.

The first energy level was lower than 15J in this model. In this range of impact energy, internal damages mainly appeared. Damages were hard to be detected in its appearance. Nondestructive testing methods should be used to detect this kind of internal damage. C-scan image showed large delamination around the impact region. Internal damage was matrix crack and delamination. Fiber damage did not appear. Maximum contact force linearly increased with increasing impact energy in this level of impact energy.

Second energy level was between 15J and 30J. Composite plates were critically damaged with fiber breakage. Contact force was suddenly decreased with fiber damage in contact force history. Impact damages clearly appeared in its appearance. There are large variations in maximum contact force.

Third energy level was larger than 30J. Composite plates were penetrated by the impactor and central deflections abruptly increased in deflection-energy graph of Fig. 2.

Maximum central deflection seems to increase linearly as impact energy increase except for the cases of penetration. The largest damage mode was delamination in low velocity impact. The range of impact energy levels can depend on several parameters; such as geometry of composite structure and impactor, material properties, layup-sequence, boundary condition etc.
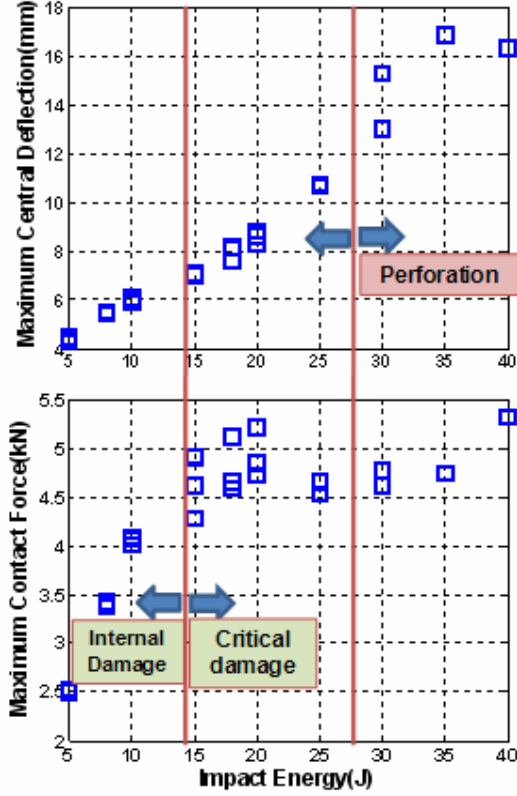
Figure 2. Maximum contact force and
Central deflection

3. Analysis

3.1. Damage model

Damage model of composite material was developed based on Mazenmiller's model and implemented in the user material subroutine of ABAQUS/explicit program.

Mazenmiller et al.(1995) assumed that the progression of fiber damage is following the cumulative Weibull distribution as shown in Eq. (1).

$$\omega = 1 - \exp\left\{ -\frac{1}{me}\left(\frac{E^0 \varepsilon}{X}\right)^m \right\} \tag{1}$$

where m is a shape parameter and X, E^0, ε are strength, initial stiffness, and strain, respectively. Complementary cumulative Weibull distribution function in Eq. (2)

means the ratio of residual properties for damaged materials.

$$d = 1 - \omega \tag{2}$$

It was applied for the fiber crack and two-transverse cracks in in-plane and out-of-plane as shown in the following Equations.

- Fiber crack:

$$d_1^{(n+1)} = \min\left\{ \exp\left[-\frac{1}{m_f e}\left(\frac{E_{11}^0 |\varepsilon_{11}|}{X}\right)^{m_f}\right], d_1^n \right\} \tag{3}$$

- Matrix crack (in-plane):

$$d_2^{(n+1)} = \min\left\{ \exp\left[-\frac{1}{m_m e}\left(\frac{E_{22}^0 |\varepsilon_{22}|}{Y}\right)^{m_m}\right], d_2^n \right\} \tag{4}$$

-Matrix crack (out-of-plane):

$$d_3^{(n+1)} = \min\left\{ \exp\left[-\frac{1}{m_m e}\left(\frac{E_{33}^0 |\varepsilon_{33}|}{Y}\right)^{m_m}\right], d_3^n \right\} \tag{5}$$

where subscript f and m means fiber and matrix respectively. Maximum failure strain criterion is used in this model. Damage of composite material is irreversible process and the ratio of residual properties, d_i, can not increase. The ratios, d_i, was applied to the related material properties to consider the effects of damages. The progression of damage depends on the shape parameter m. Stress-strain curves of composite material in fiber direction are presented in Fig. 3 for several shape parameters. If the shape parameter is large, damage starts early and is slowly progressed. However the strength is not affected by the shape parameter.
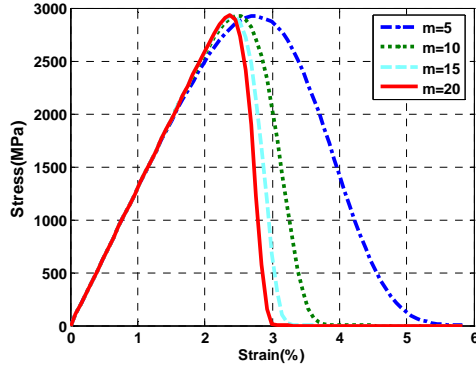
Figure 3. Strain-stress curves at several shape parameters

William et al.(2001) and Tabiei et al.(2009) determine the shape parameter through parametric studies for fiber crack, matrix crack and shear cracks. They suggested 10~20 for fiber crack and 2~6 for matrix crack and shear crack. 20 was used for fiber crack and 5 was used for matrix crack in this research.

Cohesive zone model was used for the delamination (Travesa, 2007). It was applied only between the layers which stacking sequence is changed because Dost et al.(1991) described that no delaminations occur between adjacent layers with the same fiber orientation. The behavior of cohesive element is represented by traction($t_{n,s,t}$)-displacement($\delta_{n,s,t}$) relation as shown in Eq. (6).

$$t = \begin{Bmatrix} t_n \\ t_s \\ t_t \end{Bmatrix} = \begin{bmatrix} K_{nn} & K_{ns} & K_{nt} \\ K_{ns} & K_{ss} & K_{st} \\ K_{nt} & K_{st} & K_{tt} \end{bmatrix} \frac{1}{T_o} \begin{Bmatrix} \delta_n \\ \delta_s \\ \delta_t \end{Bmatrix} \qquad (6)$$

where subscript n, s and t mean normal and two shear mode respectively. T_o means constitutive thickness of cohesive element. Quadratic strain-based failure criterion was used for the initiation of delamination as given in Eq. (7).

$$\left\{\frac{\langle \varepsilon_n \rangle}{\varepsilon_n^o}\right\}^2 + \left\{\frac{\varepsilon_s}{\varepsilon_s^o}\right\}^2 + \left\{\frac{\varepsilon_t}{\varepsilon_t^o}\right\}^2 = 1 \qquad (7)$$

where superscript o means maximum failure strain and $\langle\ \rangle$ is the MacAuley bracket. Benzeggagh-Kenane equation was used for the propagation of the delamination.

Damage model for fiber and matrix crack was implemented in the user material subroutine of ABAQUS/explicit.

3.2. Impact Analysis

Impact analysis was performed with ABAQUS/explicit and the developed damage model. Analysis model was developed based on the impact test model which has four parts; impactor, composite plate and two square frames as shown in Fig. 4. Lower frame was fixed and pressure was applied in the upper surface of the upper frame. Sphere was used for the impactor. Appropriate density was assigned to the sphere for 6.5kg of mass. Mesh size of the composite plate was determined from conversion test. Quad model was used to reduce the computation time.
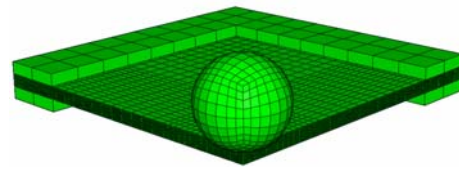

Figure 4. Analysis model

4. Results and Discussion

4.1. Results

The numerical analysis using the developed damage model and cohesive zone model was very effective to predict the impact behavior and the impact damages of composite plates. Contact force histories at 5J and 15J are compared with experiment data as shown in Fig. 5. At 5J of impact

energy, non-visible impact damage mainly appeared inside of the structure. At 15J of impact energy, composite plate was critically damaged and contact force abruptly decreased. Numerical analyses with the developed damage model well estimated the non-visible damages and critical damages at wide range of impact energies. Central deflections were predicted a little smaller than those of experiments but they are also comparable to the experiment data.
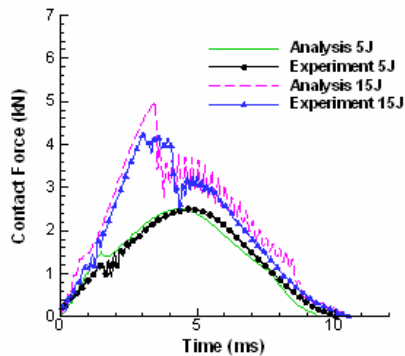

Figure 5. Contact force history

Damage area at 5J was compared with C-scan image in Fig. 6. Overall impact damage is shown in C-scan image around the impact location. Damage area predicted by numerical analysis is overlapped on the C-scan image in Fig. 6. The largest damage area was delamination and the damage area is comparable to C-scan image.
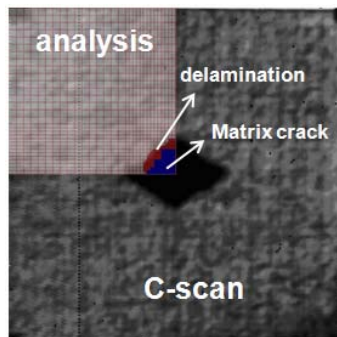
Figure 6. Comparison of damage area at 5J

4.1. Discussion

Impact tests of composite plate were performed at various impact energies and impact damages were inspected with C-scan and light-microscope. The damage model based on maximum failure strain and continuum damage mechanics was developed for impact analysis of composite plates. It was effective to predict the impact behavior and overall impact damage of composite plates at wide range of impact energy except when composite plate was penetrated by impactor.

Acknowledgement

5. References

Williams, K. V. and Vaziri, R. (2001). Application of a damage mechanics model for predicting the impact response of composite materials. *Computers and Structures*, 79, pp.997-1011.

Taibiei, A. and Aminjikarai, S.B. (2009). A strain-rate dependent micro-mechanical model with progressive post-failure behavior for predicting impact response of unidirectional composite lamintes. *Composite Structures*, 88, pp.65-88.

Matzenmiller, A., Lubliner, J. and Taylor, R. L. (1995). A constitutive model for anisotropic damage in fiber-composites. *Mechanics of Materials*, 20(2), pp.125-152.

Travesa, A. T. (2007). *Simulation of delamination in composites under quasi-static and fatigue loading using cohesive zone models*, Doctoral dissertation, University of Girona.

Dost, E. F., Ilcewicz, L. B. and Avery, W. B. (1991). Effects of stacking sequence on impact damage resistance and residual strength for quasi-isotropic laminates. *ASTM STP*, 1110, pp.476-500.

Choi, I. H. and Hong, C. S. (1994). New approach for simple prediction of impact force history on composite laminates. *AIAA journal*, 32, pp.2067-2072.

Kang, S. –G. (2006). *Characteristics of composite materials and application to the cryogenic propellant tank*. Doctoral dissertation, KAIST.

Short natural fiber reinforced polypropylene composites: Effect of coupling agents and fiber loading

F. A. Mirza[a], S. M. Rasel[a], B. S. Kim[b] and J. I. Song[a]

[a] *Department of Mechanical Engineering, Changwon National University, Changwon 641-773, South Korea, e-mail: jisong@changwon.ac.kr*
[b] *Composite Materials Group, Korea Institute of Materials Science, Changwon 641-773, South Korea, e-mail:kbs@kims.re.kr*

Abstract

In recent years, natural fiber reinforced polymeric composites (green composites) have drawn wide attention to get rid of adverse effect on environment by using of artificial fibers. However, certain problems associated with the use of natural fibers, such as the poor compatibility between the fibers and polymeric matrices greatly reduce the potential of natural fibers to be used as reinforcement for polymers. Jute fibers reinforced polypropylene (PP) composites were manufactured by injection molding technique. In order to improve the affinity and adhesion between fibers and matrix during manufacturing, maleic anhydride grafted polypropylene (MAPP) as a coupling agent has been employed. Physical properties such as void contents and water absorption rate were studied. Tensile and flexural tests were carried out to evaluate the composites mechanical properties. Tensile strengths and modulus for jute fiber composites were higher than that of raw PP. In addition, strength and modulus were found to be influenced by the variation of MAPP contents (1%, 2%, and 3%) and by increasing the fibers loading. Like tensile properties, the flexural properties of composites were improved. Scanning electron microscope images of short jute fiber composites shows significant enhancement on the adhesion between the fibers and matrix. In addition, for predicting the mechanical properties of discontinuous short natural fiber composites, numerical simulations were performed using MATLAB software. The predictions were quite similar with the experimental results.

Key Words: Natural fibers, Polymeric matrices, Maleic anhydride grafted polypropylene, Interfacial adhesion, Mechanical properties prediction

1. Introduction

Over the past decade there has been a growing interest in the use of lignocellulosic fibers as reinforcing elements in polymeric matrix [1–5]. The specific properties of this natural product, namely low cost, lightweight, renewable character, high specific strength and modulus, availability in a variety of forms throughout the world, and the possibility to generate energy motivate their association with organic polymers to elaborate composite materials. However, it is well known that different surface properties between the fiber and the matrix, i.e. the former is highly polar and hydrophilic while the latter is, generally, non-polar and

relatively hydrophobic, impose the surface modification of the fibers surface, in order to improve the fiber/polymer compatibility and their interfacial adhesion [6]. Without such a treatment, natural fibers embedded in a polymeric matrix generate unstable interfaces and the stress applied to the fiber/polymer composite is not efficiently transferred from the matrix to the fiber and the beneficial reinforcement effect of the fiber remains underexploited. Likewise, the poor ability of the polymer to wet the fiber hinders the homogeneous dispersion of short fibers within the polymeric matrix [7-11].

The main objective of this study is to manufacture short jute fiber reinforced composites by injection molding technique as followed by the evaluation of their mechanical properties. Maleic anhydride grafted polypropylene was employed to improve the bonding between the fibers and matrix. In addition, fiber surface modification by NaOH was employed for better bonding.

2. Experimental Details

2.1. Materials

Polypropylene (PP) supplied by Honam Petrochemical Corp. (Korea) was used as the matrix. The specific weight and the melting point of PP were 0.95 g/cm^3, and 170°C, respectively. Maleic anhydride grafted polypropylene (MAPP) (Eastman, USA) was used as coupling agent. Jute fibers from Philippine were used as reinforcement. Analytical grade NaOH (98%) from Kudko. Co. (Korea) was used in the treatment of jute fibers.

2.2. Composite Fabrication

Firstly, jute fibers were treated with 2 wt% NaOH for 24hours. Vacuum dried treated jute fibers were chopped into short lengths about 2mm to insure an easy blending. The chopped jute fibers and PP were than compounded with the coupling

agent in a manual mixer. The mixed blends were molded in twin-screw extruder (PRIM TSC 16TC, Thermo Electron Corp.) to form pellets of diameter 1.0mm by using the melt mixing process. After extrusion, the dried pellets were used to make specimens for tensile and 3-point bending test using an injection molding equipment. In addition, the specimens of pure PP were also prepared using the injection molding technique. Tensile test (according to ASTM D 638 Type I) and 3-point bending test (according to ASTM D 790) were carried out using a Universal Testing Machine (RB 301 Unitech M).

3. Results and Discussions

3.1. Void Contents

Table 1 shows the densities and void contents of the jute/PP composites manufactured. After immersion in alkali for 24hrs, the globular pultrusions present in the untreated fiber disappeared but it leads to the formation of a large number of voids. In addition, the use of water as a suspension medium for extruded composite rods during prepregging can absorbs water and causes these voids. However, it was observed that with the increased of MAPP content from 1 to 3%, there was a relative reduction of the void contents.

Table 1. Void contents of composites

Composite	Void, vol%	M_d, g/cm^3	T_d, g/cm^3
1% MAPP	4.08	0.90	0.94
2% MAPP	3.32	0.91	0.94
3% MAPP	1.53	0.92	0.94

3.2. Water Absorptions

The results of the water absorption tests are summarized below in Table 2. It can be observed that the fiber-based composites showed significantly high water absorption

Table 2. Water absorptions of composites

Composite	Void, vol%	M_d, g/cm^3	T_d, g/cm^3
1% MAPP	4.08	0.90	0.94
2% MAPP	3.32	0.91	0.94
3% MAPP	1.53	0.92	0.94

due to the hydrophilic character of jute fibers. However, compared to water absorption of jute fibers, the composites exhibit much lower water absorption values. These much lower values obtained for composites than for fibers themselves are because cellulose fibers are covered by PP layers that slow down the diffusion of water. Moreover, the hydrophilic –OH groups present in the jute fibers react with the acid anhydride group present in MAPP to form ester linkages. This reduces the water absorbing capacity in the jute/PP composites.

3.3. Mechanical Properties

Figure 1 shows the effect of jute fibers and coupling agent on the tensile properties of the reinforced PP. In case of 10 vol. % composites, the addition of 1 wt% MAPP increased the tensile strength of the composites from 20.28MPa to 24.19MPa while in case of 20 vol. % composites; the addition of 1 wt% MAPP increased the tensile strength from 20.28MPa to 26.81MPa. The improvement of mechanical properties by adding MAPP was occurred through a better bonding between cellulosic fiber surfaces and PP was caused by the esterification of the anhydride groups of MAPP with the hydroxyl groups of cellulosic fibers. Because of the fact that jute fiber is lignocellulosic and contains more than 60% cellulose, we assume that a similar chemical bonding occurred between the hydroxyl groups of jute fibers and anhydride groups of MAPP. Moreover, further improvements of the tensile strengths of the composites were

observed by adding MAPP contents from 1% up to 3% for both composites.

Figure 2 shows the tensile modulus of raw PP and jute/PP composites (10 vol. % and 20 vol. %). It was observed that the elastic moduli were remarkably higher than those of raw PP, and they were almost independent of whether coupling agent was added or not even though there are certain increases in the properties by adding MAPP contents. The moduli were determined from the initial slope of the stress-strain curve. At the initial slope, only a very small strain region can be considered, which is practically not influenced by the interface between fiber and matrix. So it was clear that even though
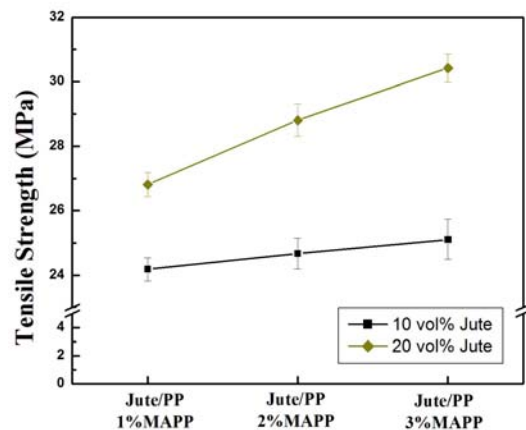

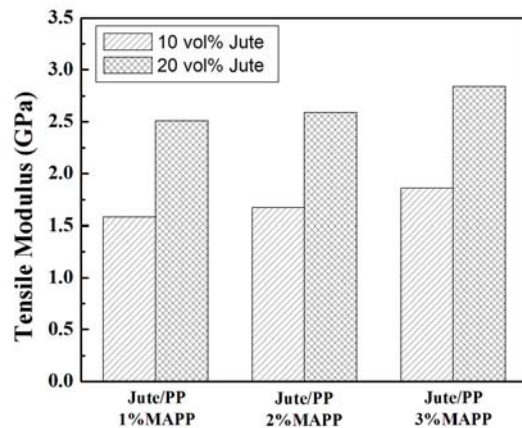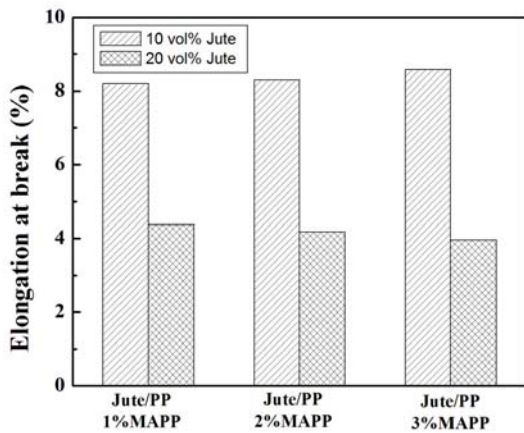Figure 1. Tensile strengths of Jute/PP composites

Figure 2. Tensile modulus of Jute/PP composites

MAPP contents can't affect the modulus of the composites, but due to the improvement of the interfacial adhesion between the fibers and matrix, the moduli were increased remarkably.

Variation of elongation at break of jute fiber composites containing different MAPP contents and fiber loading is shown in Fig. 3. The decreases can be explained by constrained matrix flow in the presence of less-extensible fibers and the effects of internal stress concentrations initiated by fiber-induced microcracks. However, the percentage elongations of break of the jute fibers composites were increased with the increasing of MAPP content from 1% to 3% for 10 vol. % jute fiber composites. Unlike the 10 vol. % composites, the composites containing 20 vol. % shows the reverse trends for the elongation at break. It means the jute fiber inclusion on the composites have better effects on the elongation at break.

The flexural properties of jute/PP composites were also studied. Fig. 4 shows the flexural strength of jute fiber composites containing different MAPP contents and fiber loading. The additions of MAPP content provide a significant effect on the flexural strengths of the composites. The improvement of flexural properties by adding MAPP was occurred through a better bonding between cellulosic fiber surfaces

and PP was caused by the esterification of the anhydride groups of MAPP with the hydroxyl groups of cellulosic fibers. We assume that a similar chemical bonding occurred between the hydroxyl groups of jute fibers and anhydride groups of MAPP.

Figure 5 shows the flexural modulus of jute/PP composites for both 10 vol. % and 20 vol. % jute fiber. It was observed that the flexural moduli were remarkably increased. They were almost independent of whether coupling agent was added or not even though there are certain increases in the properties by adding MAPP contents. The average flexural modulus of 10 vol. % and 20 vol. % composites were 40.34GPa and 48.85GPa, respectively.
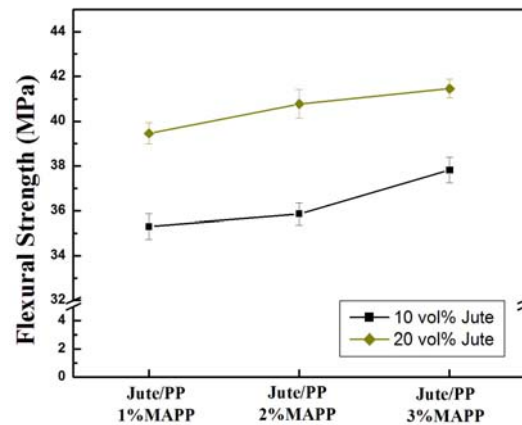

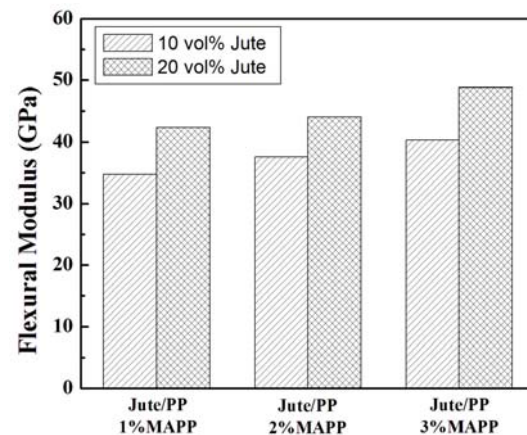Figure 4. Flexural strengths of Jute/PP composites

Figure 3. Elongation at break of Jute/PP composites

Figure 5. Flexural modulus of Jute/PP composites

3.4. Surface Morphology

Figs 6 shows the SEM observations of fractured surface for polypropylene based composites with 10 vol. % jute fibers. After NaOH treatment, their surface seems to be clean, intact and free from any adhering polymer. This is because the cementing material such as the hemi cellulose and a part of lignin were removed from the multi cellular matrix to some extent. The reduced hemi-cellulose contents in the fibers may lead to the improvement of the composites mechanical properties. The fibers are broken off near the surface and do not leave any voids on the fractured surface. However, the fibers were pulling out from the matrix surfaces; a thin layer of polymer matrix was covering the fiber surfaces. This observation gives direct evidence about the adhesion
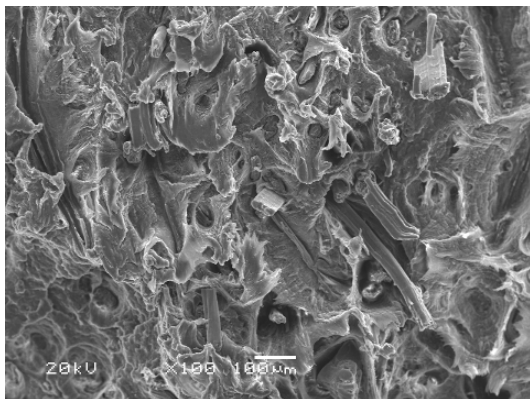
Figure 6. SEM micrographs of fractured surfaces of Jute/PP composites (x100)
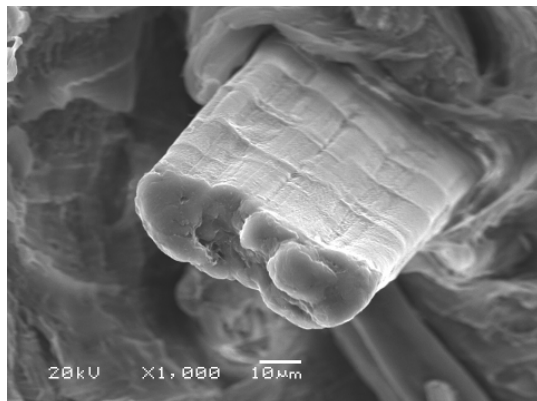
Figure 7. SEM micrographs of fractured surfaces of Jute/PP composites (x1000)

improvement at the interface in the presence of reactive MAPP. It is noticeable that the voids in these natural fiber composites seem to be disappeared. This is also indicates that the adhesion improved.

3.5. Mechanical Properties Prediction

With a view to compare with the experimental results the volume percentage was considered 10 and 20% for the simulation. Halpin-Tsai equations for unidirectional discontinuous fiber lamina were used to predict the individual Young's modulus of the composites in longitudinal direction. The length and diameter of the jute fibers were assumed to 2mm and 0.05mm, respectively. The Poisson's ratio of matrix and fibers were also assumed to be 0.4 and 0.20, respectively. Though experimental results such as the tensile test had been conducted to calculate the Young's modulus of the unidirectional composites, only Young's modulus was be compared with the simulation results. Other properties could not be compared due to the lack of experimental results.

A thin lamina containing randomly oriented discontinuous fiber exhibits planar isotropic behavior. The properties are ideally the same in all directions in the plane of the lamina. As jute fibers were randomly mixed with the matrix, there is no definite or specific fiber alignment can't be distinguished. That's why for jute fiber reinforced composites, it was assumed to the same situation like the thin lamina. Table 3 shows the comparative view from the experimental with simulation results.

It is observed that the results in simulation are less than the actual experimental results. The possible

Table 3. Comparison of Young's modulus of composites

Composite	10 **vol%**	20 **vol%**
Experimental	1.86	2.61
Simulation	1.5	2.36

explanation of the variation in the two results is that, in actual case MAPP had been used to improve the interfacial adhesion between the fibers and matrix. It is the evidence that MAPP has a significant influence on the mechanical properties of the composites. Thus, the using of MAPP as a coupling agent was effective to reinforcement of jute fibers.

4. Conclusions

Jute fiber reinforced polypropylene matrix composites were successfully developed by the injection molding technique. The improvement of tensile strengths, modulus and elongation at break of the composites can be observed. The addition of MAPP contents as coupling agent improved the composite performance by enhancing the adhesion between jute fibers and PP matrix. As the elongations at breaks were reduced in jute fiber polypropylene composites, it can be suitable candidates for strain improvement in hybrid composite systems. Similar to tensile properties, improvement in flexural properties were also significant. The predictions of mechanical properties coincide well with the experimental results.

5. Acknowledgement

6. References

Khondker, O. A., U. S. Ishiaku, A. Nakai, and H. Hamada (2006). A novel processing technique for thermoplastic manufacturing of unidirectional composites reinforced with jute yarns. *Composites: Part A*, 37, pp. 2274-2284.

Abdelmouleh, M., S. Boufi, M. N. Belgacem, and A. Dufresne (2007). Short natural-fibre reinforced polyethylene and natural rubber composites: Effect of silane coupling agents and fibers loading. *Composites Science and Technology*, 67, pp. 1627-1639.

Wulin, Q., E. Takashi, and H. Takahiro (2006). Structure and properties of composites of highly crystalline cellulose with polypropylene: Effects of polypropylene molecular weight. *European Polymer Journal*, 42, pp. 1059-1068.

Andrzej, K. B., and O. Faruk (2006). Injection moulded microcellular wood fiber-polypropylene composites. *Composites: Part A*, 37, pp. 1358-1367.

Mariano, P., C. Donatella, A. Irene, K. Zbigniew, and E. Poirkowska (2006). Functionalization compatibilization and properties of polypropylene composites with Hemp fibers. *Composites Science and Technology*, 66, pp. 2218-2230.

Gatenholm, P., and J. Felix (1993). Wood fiber/polymer composites: fundamental concepts, process, and material options. Madison: Forest Product Society.

Carvalho, L. H., A. L. Leao, F. X. Carvalho, and E. Frollini (1997). Lignocellulosic-plastics composites. Brazil: USP and UNESP, 1997.

Belgacem, M. N., and A. Gandini (2005). The surface modification of cellulose fibers for use as reinforcing elements in composite materials. *Comp Inter*, 24(1-2), pp. 41-75.

Park, J. M., T. Q. Son, S. H. Byung, and K. D. Lawrence (2006). Interfacial evaluation of modified Jute and Hemp fibers/polypropylene (PP)-maleic anhydride polypropylene copolymers (PP-MAPP) composites using micromechanical technique and nondestructive acoustic emission. *Compos Sci Tech*, 66, pp. 2689-2699.

Panthapulakkal, S., M. Sain, and L. Law (2005). Effect of coupling agents on rice husk-filled HDPE extruded profiles. *Polym Int*, 54, pp. 137-142.

Keener, T. J., R. K. Stuart, and T. K. Brown (2004). Maleated coupling agents for natural fiber composites. *Composites Part A*, 35, pp. 357-362.

Some Results about Vibration Reduction by Energy Dissipation Devices

Nguyen Dong Anh

Institute of Mechanic, VAST, ndanh@imech.ac.vn

Abstract

The paper presents shortly some results obtained recently in the study of vibration reduction using energy dissipation devices. The main attention is given to the following problems:
- Design and manufacture of some energy dissipation devices. Test in laboratory to obtain dynamic characteristics.
- Installation of energy dissipation devices into real structures. Test in practice to investigate the effect of vibration reduction.

An example of illustration is taken about the vibration reduction of stayed cables using fluid dampers.

Key Words: energy dissipation devices, vibration reduction, fluid dampers

1. Introduction

In recent years, serious efforts have been undertaken to investigate energy dissipation systems, such as friction, viscous, tuning mass or liquid dampers, which are characterized by a capacity to dissipate energy when subjected to deformation or motion [1,2,11,13-17]. The energy dissipation may be achieved either by converting kinetic energy to heat or by transferring energy among vibration modes. The paper presents shortly some results obtained recently at Institute of Mechanics in the study of vibration reduction using energy dissipation devices.

An example of illustration is taken about the vibration reduction of stayed cables using fluid dampers. When a stayed cable is subjected to moderate external disturbance, a good performance may be expected when connected to linear fluid viscous damper [3-5]. The structure and concept of fluid viscous damper for cable vibration are presented with a comparison of theoretical calculation and experiment for a fluid viscous damper. The damper performance in the cable vibration modes is of particular interest. The dynamics of the cable-damper system depends on the frequency, the location of damper, parameters of the damper. The modal damping ratios and optimal values of parameters of the damper are investigated. The experiments with fluid dampers-cables system are carried out in the Laboratory and on Ben Coc stayed cable bridge in Hatay province, Vietnam.

2. Design and Manufacture of Some Energy Dissipation Devices

The purpose of this study is to outline some principal steps in the problem of design and manufacture of some energy dissipation devices such as linear and nonlinear fluid viscous dampers, turn mass or liquid dampers. Figure 1 shows an offshore structure and its mechanical model in the form of inverted double pendulum.
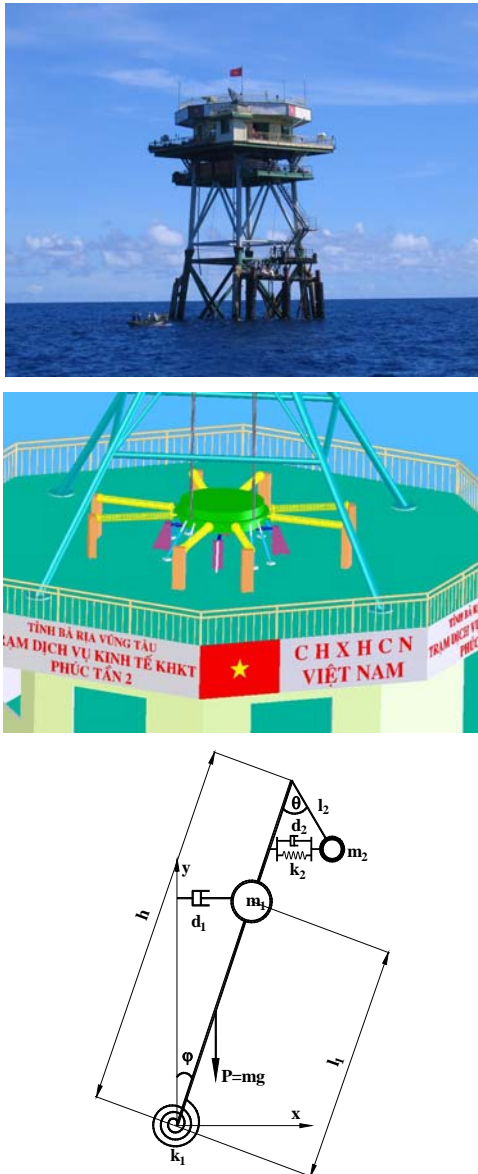

Figure 1. Offshore structure and its mechanical model with TMD

In order to reduce the undesired vibration a turn mass damper (TMD) is considered to

be installed into the offshore structure. The manufacture of TMD model is shown in Figure 2.

Figure 2. TMD experimental model

When a stayed cable is subjected to moderate external disturbance, a good performance may be expected when connected to linear fluid viscous damper. A

fluid viscous damper dissipates energy by forcing a fluid through an orifice causing a damping force. A prototype fluid viscous damper was manufactured in the cooperation with NARIME as shown in Figure 3.

Figure 3. Prototype damper for testing in laboratory

This damper has the following parameters; stroke is 0.05m, diameter of cylinder is 0.04m and the designed damping force is F=0.1939*V (kN/cm/s), where V is the velocity.

3. Test in The Laboratory

3.1. Dynamic characteristics of fluid dampers

In order to check the designed damping force, a test in the laboratory was carried out as shown in Fig. 4.

Figure 4. Test set up in the laboratory

The damper was tested at three frequencies and amplitudes of piston stroke, namely $f_{1,2,3}$ =1, 2, 3 (Hz) and $A_{1,2,3}$ =1.0, 0.85, 0.75 (cm), respectively. The displacements of the piston are $X(t)=A_{1,2,3}*\sin(2\pi f_{1,2,3}t)$. The experimental results in comparison with theoretical calculations regarding the relationship between damping force F and the

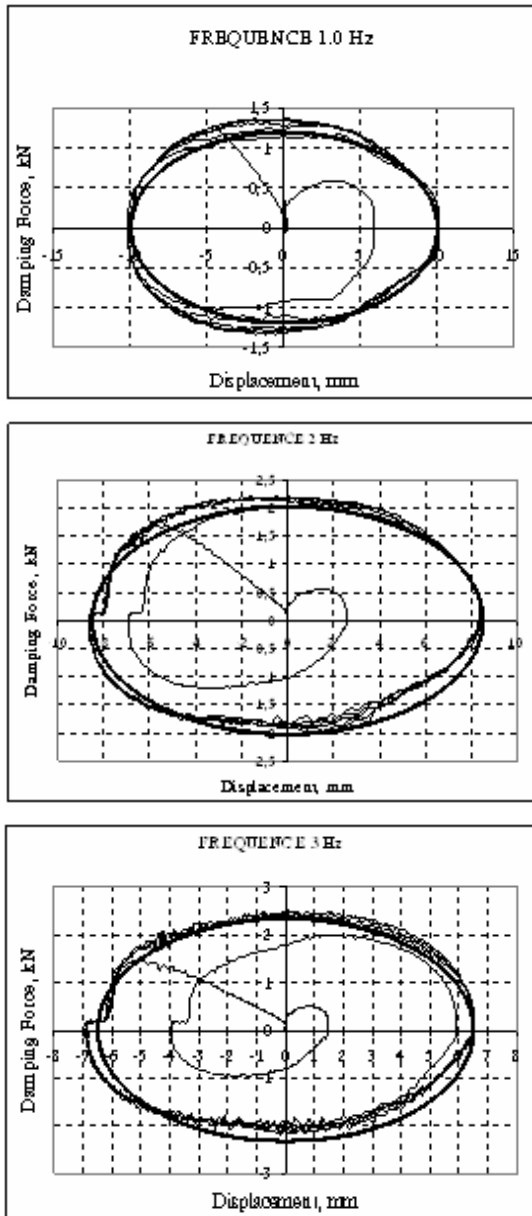displacement of damper at three different frequencies are plotted in Fig. 5.

Figure 5. Loops of damping force/ displacement in testing frequency of 1 Hz, 2 Hz, 3 Hz
(thick lines are theoretical results and thin lines are experimental results)

According to these figures the closed loops of displacement and damping force are ellipses.
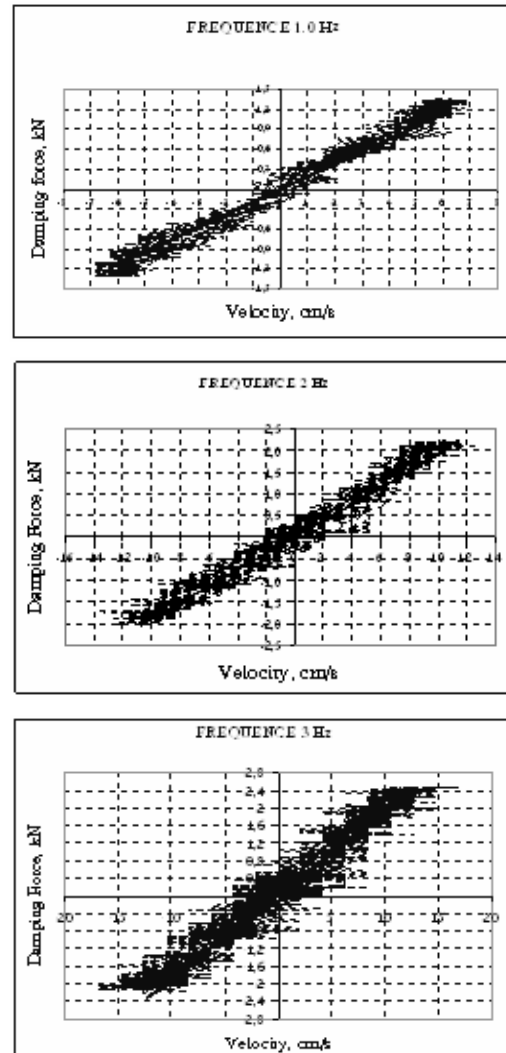

Figure 6. Damping force – Velocity in testing frequency 1 Hz, 2 Hz, 3 Hz.
(thick lines are theoretical results and thin lines are experimental results).

Fig. 6 also shows the experimental results in comparison with theoretical results regarding the relationship between damping force F and velocity V of the damper, where $V(t) = A_{1,2,3} * 2\pi f_{1,2,3} * \cos(2\pi f t)$. This shows that the theoretical and experimental results are in good agreement.

3.2. Cable-Damper experiment in laboratory

In order to check the theoretical result, a experiment of damper-cable system was

carried out in Laboratory for different parameters (damping forces, cable tensions) of damper and cable as shown in Fig. 7.

Figure 7. Damper-cable experiment in the laboratory

The theoretical and experimental results were in reasonable agreement.

4. Damper-Cable System

The free vibration of a taut cable with attached linear viscous damper near the end of the cable was investigated [7] and extended by Krenk [8] who used a complex wave number to obtain an asymptotic solution for the modal damping. A numerical investigation was carried out by Pachero et al. [9] to obtain modal damping estimation curves. It has been being investigated and extended by [10,12]. The effect of the damper depends on its adequate damping coefficient, namely if the damper force is too

large it will act as a support, and if the damper force is too small it will fail to dissipate energy. Within two limits there would be an intermediate optimal tuning of damper corresponding to a maximum modal damping.

4.1. Damping characteristic of a cable with a damper

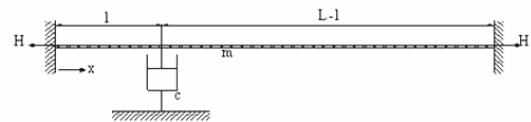A model of a simply supported taut cable with linear viscous damper is shown in Figure 8.

Figure 8. A model of taut cable with a viscous damper

The transverse vibration of the cable-damper system is described by the equation.

$$m\frac{\partial^2 u}{\partial t^2} - H\frac{\partial^2 u}{\partial x^2} = c\frac{\partial u(l,t)}{\partial t}\delta(x-l) \quad (1)$$

where $u(x,t)$ is transverse deflection, m is mass per unit length, H is horizontal cable force, x is coordinate along the cable chord axis, and $\delta(x)$ is the Dirac delta function.

Suppose the damper location is given. In order to investigate the behaviour of modal damping ratios, ξ_i versus θ corresponding to the first three vibration modes (i=1, 2, and 3) are shown in the Figure 9(a) for the interval $\theta = [0,100]$ and for $l/L = 0.05$.
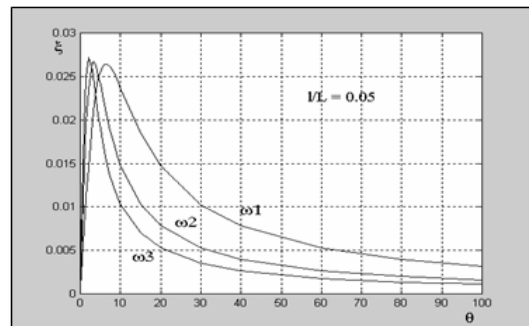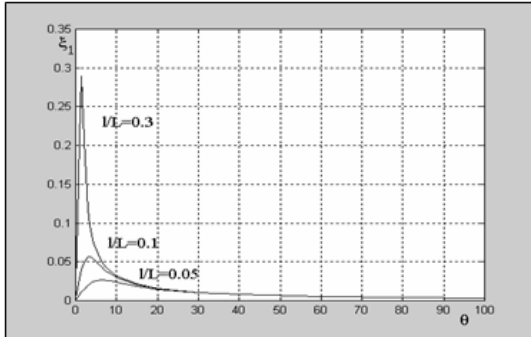

Figure 9(a). Plots of ξ versus θ
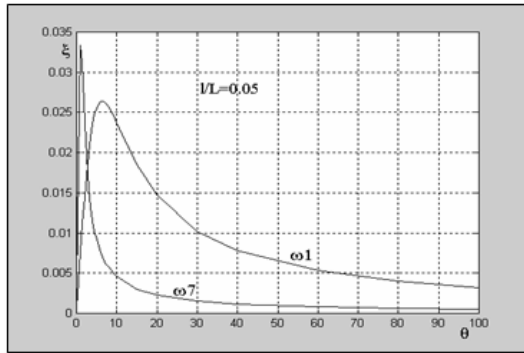
Figure 9(b). Plots of ξ_1 with different l/L

Figure 9(c). Plots of ξ_1 and ξ_7 versus θ

Figure 9(b) depicts three curves of ξ_1 corresponding to three different damper locations: $l/L = 0.05$, 0.1, and 0.3. It is seen that the modal damping ratios increase when θ is increasing. They reach almost the same maximal value but at different values of θ, as shown in Table 1.

Table 1: Maximum modal damping ratios

θ	6.45	3.25	2.25
ξ	ξ_{1max} =0.0264	ξ_{2max} =0.0267	ξ_{3max} =0.0272

Thus, the tuning effect of damper can be clearly seen in the Figures 9(a, b, c). Further, the damping effect is better when the relative distance of damper location is larger. It is obtained in the Figure 9c that the maximum damping ratio is larger for higher frequencies, see also Table 1.
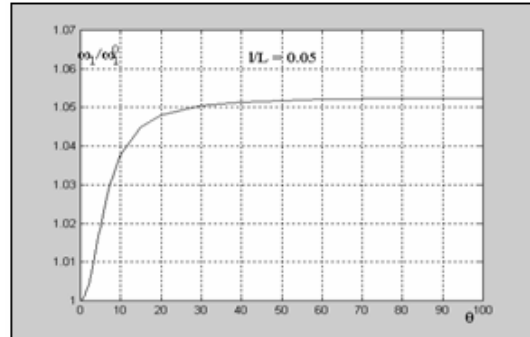

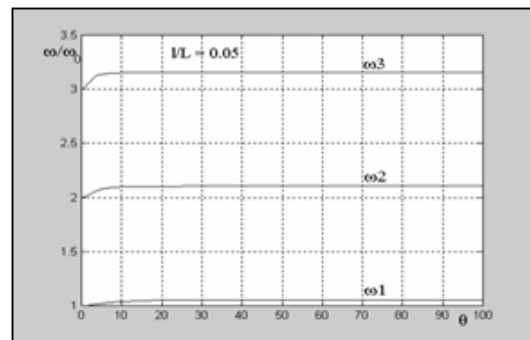Figure 10(a). Plots of non-dimensional damped frequencies ω_1/ω_1^0 versus θ

Figure 10(b). Plots of non-dimensional damped frequencies ω_i/ω_1^0 versus θ

Plots of non-dimensional damped frequencies ω_i/ω_1^0 versus θ are shown in Figures 10(a,b) where ω_1^0 is the undamped fundamental natural frequency.

5. Test in Practice to Investigate The Effect of Vibration Reduction

Ben Coc stayed cable bridge designed by Thang Long Consultant under Thang Long Construction Corporation was built in 2002. The bridge has 3 spans, 4m-width, main girder is made of shape steel I450, cross girder is of I400, cross bracing is of L100x10 and L75x8. Bridge deck is concrete. Design load is H10 (means traffic flow with the trucks weigh 10T, distance 4 m/each, and one heavy truck 13T). Piers are concrete columns, and two towers are steel frames.

Figure 11. Damper-cable experiment in
Ben Coc Bridge

Cable characteristic per a strand: Cross section area-140mm^2, weight/1m-1,37 kg (see Fig.11). Cable acceleration response without and with dampers are shown in Figs. 12 and 13, respectively.
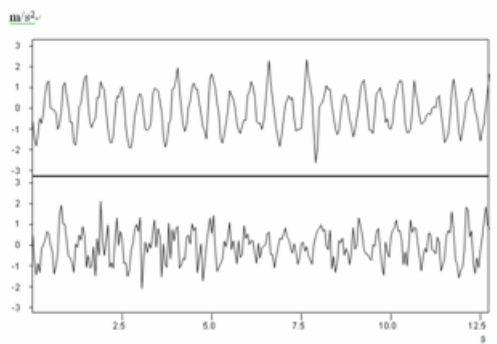

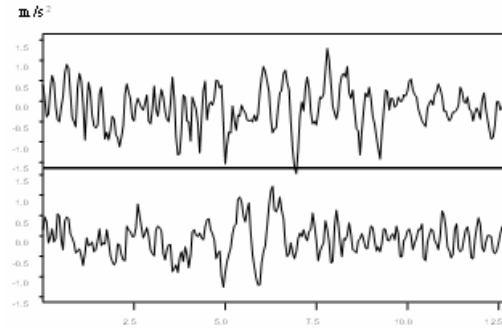Figure 12. Cable acceleration response
without damper

Figure 13. Cable acceleration response
with damper

Table 2. Maximum values of cable acceleration

	Without damper		With damper		Efficiency (%)
	First measurement m/s^2	Second measurement m/s^2	First measurement m/s^2	Second measurement m/s^2	
Cable No 1	2.64	2.59	1.78	1.64	32.58
Cable No 2	2.12	2.08	1.25	1.51	28.77

Vibration reduction of cable acceleration is shown in Table 2. It is seen that the efficiency is about 30%.

6. Conclusion

In recent years, serious efforts have been undertaken to investigate energy dissipation systems, such as friction, viscous, tuning mass or liquid dampers, which are characterized by a capacity to dissipate energy when subjected to deformation or motion. The paper presents shortly some results obtained recently in the study of vibration reduction using energy dissipation devices. The main attention is given to the following problems:

- Design and manufacture of some energy dissipation devices. Test in laboratory to obtain dynamic characteristics
- Installation of energy dissipation devices into real structures. Test in practice to investigate the effect of vibration reduction

An example of illustration is taken about the vibration reduction of stayed cables using fluid dampers. The structure and concept for fluid viscous damper are presented with numerical and experimental comparison for a fluid viscous damper. The experiments with fluid dampers-cables system are carried out in the Laboratory and on Ben Coc stayed cable bridge in Hatay province, Vietnam.

7. Acknowledgement.

8. References

[1] Premont, A. *Vibration control of active structures,* Second Edition, Kluwer, Dordrecht.

[2] Soong T.T (2000). Supplemental energy dissipation: State-of-the-art and state-of-the-practice, *Int. Conf. on Advances in Structural Dynamics*, Eds. Ko J.M. and Xu Y.L, Elsevier, pp. 109 – 120.

[3] D. Lee and D.P. Taylor (2002), Viscous damper development and future trends. *Struct Des Tall Buil* 10 5 , pp. 311 – 320.

[4] D.P. Taylor and M.C. Constantinou (1995). Testing procedures for high-output fluid viscous dampers used in building and bridge structures to dissipate seismic energy. *Shock Vib* 2 5 , pp. 373 – 381.

[5] Pekan, G., Mander, J.B. and Chen, S.S. (1999). Fundamental Considerations for The Design of Nonlinear Viscous Damper, *Earthquake Engineering and Structural Dynamics*, 28, pp. 1405 – 1425.

[6] N. Gluck, A.M. Reinhorn, J. Gluck and R. Levy, (1996). Design of supplemental dampers for control of structures. *J Struct Eng* 122 12, pp. 1394 – 1399.

[7] Kovacs (1981), Zur Frage der Seilschwingungen und der Seildampfung. *Die Bautechnik* 59 10, pp. 325 – 332.

[8] Krenk S, Nielsen R. K,(2001). Vibration of a shallow cable with a viscous damper. *Proceedings of the Royal Society, London, A* 458, pp. 339 – 357.

[9] Pacheco, B. M., Fujino, Y., and Sulekh, A. (1993), Estimation curve for modal damping in stay cables with viscous damper, *J. Struct. Eng.,* 119, N6, pp. 1961 – 1979.

[10] Nguyen Dong Anh, P.X.Khang, Nguyen Cao Thang, T.H.Vinh et al (2006), Vibration Control of Stayed Cables Using Fluid Dampers. *Proceedings of 8th Japan-Korea Seminar on Steel Bridges*, Nagoya , pp. 721-731.

[11] Nguyen Dong Anh, H.Matsuhisa, La Duc Viet, M.Yasuda, Vibration control of an inverted pendulum type structure by passive mass-spring-pendulum dynamic vibration absorber, *Journal of Sound and Vibration* 307, pp. 187-201.

[12] Nguyen Dong Anh, P.X.Khang, Vu Manh Lang, N.N.Long et al (2006), Some results about vibration reduction of stayed cables in Viet Nam, *Proceedings of ITST*, pp. 17-30

[13] Nguyen Dong Anh, Ninh Quang Hai, W.Schiehlen (2006), Application of extended averaged equations to nonlinear vibration analysis, *Proceedings of Nanjing*, China, pp. 147-156.

[14] Nguyen Duc Tinh (2006), The influence of nonlinear terms in mechanical systems having two degrees of freedom, *Vietnam Journal of Mechanics*, vol. 28, No. 3, pp. 155-164.

[15] Nguyen Dong Anh, Ngo Thi Hong Hue, Investigation of high order stochastic differential equations using averaging method*, Vietnam Journal of Mechanics*, Vol. 29, No. 1, pp. 37-46.

[16] Nguyen Dong Anh, Ninh Quang Hai, W.Schiehlen (2007), Nonlinear vibration analysis by an extended averaged approach, *Int. J. Nonlinear Dynamics*, Springer, V.27, N1-3, pp. 235-248.

[17] Nguyen Dong Anh, Luu Xuan Hung (2008), A new improvement for stochastic linearization based on concentrated response zone, *J. Advances in Natural Sciences*, Vol.9, N.1, pp. 9-22

Design of a Rubber Bushing to Reduce Vibration of the Gun Mounted on Vehicle during Shooting

Nguyen Dong Anh[a], Nguyen Xuan Anh[b] and Do Van Diep[c]

[a] *Institute of Mechanics- Hanoi Vietnam, ndanh@imech.ac.vn*
[b] *University of Le Quy Don - Hanoi Vietnam*
[c] *University of Le Quy Don - Hanoi Vietnam, dvdiepvcg@gmail.com*

Abstract

The purpose of this work is to design a rubber bushing to reduce vibration of guns mounted on the vehicle and to improve shooting accuracy. The rubber bushing is intended to be used for changing the magnitude and mode of gun vibrations. Experimental verification of the optimization technique, which minimizes the root mean square (RMS) of gun acceleration frequency response and RMS of the force transmitted frequency response, show that this method can be implemented on linear systems to isolate the guns from harmonic and random excitation. This optimization technique is also applied to select stiffness and damping ratio of rubber bushing. The resulting from half-car gun-vehicle with or without RB model illustrated the effectiveness of the RB.

Key Words: rubber bushing, shooting stability, isolation

1. Introduction

Rubber bushings (RB) are used in a large variety of applications (automotive, buildings and in rotating machines) in order to reduce the transmission of mechanical vibrations from the equipments toward the foundation as well as to improve stability of equipment. The isolation is obtained by inserting a rubber bushing that acts as a link between the source subsystem and the isolated subsystem. There are two quantities generally used to evaluate the effectiveness of an isolation system: the transmissibility and the power transmitted (Rivin, 2003).

Gun vibrations lead to dispersion in the shot patterns. Thus, vibration reduction of a gun due to impulse of shooting should lead to improve accuracy (Bulman et al., 1996) and (Kang et al, 2003). The forces are transmitted to the foundation upon which the guns are installed. If the transmission of vibrations to the foundations is not avoided the adjoining guns also set to vibrate.

To minimize the forces transmitted to the foundation can be mounted on springs or dampers or some other vibration isolation material such as rubber. Vibration isolation is measured in terms of the motion or force transmitted to the foundation. The lesser the force or motion transmitted the greater the

vibration isolation (Tamboli, 1999) and (Jazar et al, 2006).

The aim of this study is the research and design optimization of rubber bushing to reduce vibrations due to gun mounted on the vehicle generation during shooting and to improve shooting accuracy.

2. Passive RB Model

To study the passive 1 DoF rubber bushing, a simple model is constructed. It is composed of a linear spring and damper, as illustrated in Figure 1. In the literature, this model is known as the Kelvin -Voigt model of rubber.
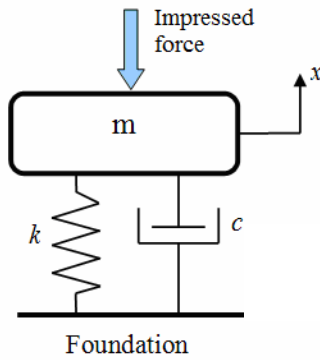

Figure 1. The passive 1 DoF RB model

The governing equation can be determined by considering that the total forcing on the machine is equal to its mass multiplied by its acceleration (Newton's second law):

$$m\ddot{x} + c\dot{x} + kx = F(t) \qquad (1)$$

where $F(t)$ is impressed force generated by the gun during shooting.

The design objectives can now be restated in terms of the above system parameters, the challenge is to find the optimal linear stiffness k and damping c which constrain the displacement of the mass m, measured by the coordinate x, yet minimize the transferred force $F_T(t)$ criteria due to an input force $F(t)$ generated by the gun during

shooting. With this linear model, the principle of superposition permits the study of the two disturbances; base excitation and force excitation, independently. In this study, we only consider force excitation due to shooting.

It is helpful to nondimensionalise Eqn.(1), so that

$$\ddot{x} + 2\zeta\dot{x} + \omega_n^2 x = f(t) \qquad (2)$$

where

$$\zeta = \frac{c}{2m\omega_n}; \quad \omega_n^2 = \frac{k}{m}; \quad f(t) = \frac{F(t)}{m}$$

In the case of forced vibrations, it is defined as the rating force transmitted to impress upon the system. It is a measure of the effectiveness of a rubber bushing.

2.1. Harmonic excitation

For the sake of simplicity, this impressed force such as a harmonic excitation $f(t) = F_0 \cos(\omega t)$.

Response in the form

$$x(t) = X \cos(\omega t + \phi) \qquad (3)$$

where

$$X = \frac{F_0}{k\sqrt{(1-r)^2 + (2\zeta r)^2}} \qquad (4)$$

$$\phi = \tan^{-1}\left(\frac{2\zeta r}{1-r^2}\right) \qquad (5)$$

where $r = \omega / \omega_n$

The forces are transmitted to the foundation through the rubber bushing provided in the system. Thus the forces transmitted to the foundation are the spring force kX and the damping force $c\omega X$. Hence the total force transmitted to the foundation is the vector sum of kX and $c\omega X$.

Force transmitted

$$F_T = \sqrt{(kX)^2 + (c\omega X)^2}$$
$$= kX\sqrt{1 + \left(\frac{c\omega}{k}\right)^2} \qquad (6)$$

Substituting for X from (4)

$$F_T = \frac{F_0\sqrt{1 + (2\zeta r)^2}}{\sqrt{(1-r)^2 + (2\zeta r)^2}} \qquad (7)$$

Transmissibility ratio

$$\phi = \left|\frac{F_T}{F_0}\right| = \frac{\sqrt{1 + (2\zeta r)^2}}{\sqrt{(1-r)^2 + (2\zeta r)^2}} \qquad (8)$$

Relating displacement of the mass X to the input magnitude

$$\gamma = \left|\frac{X}{f}\right| = \frac{1}{\omega_n^2 \sqrt{(1-r)^2 + (2\zeta r)^2}} \qquad (9)$$

A plot of transmissibility ratio is shown in figure given below.
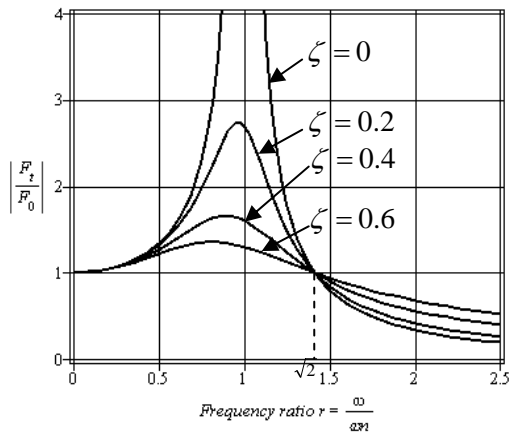

Figure 2. Transmissibility ratio

Figure 2 illustrates the effect of the damping ratio and the cost of increased force transmissibility ratio as the frequency ratio $r > \sqrt{2}$.

Optimum stiffness and damping ratio should be found by examining the response of the system in the frequency range of 0-20 Hz, a critical range for typical mechanical systems (Alkhatib, Jazar and Golnaraghi, 2006). Given a certain damping ratio and stiffness, the performance of the system can be characterized by computing the RMS of the frequency response over a certain bandwidth. According to (Inman, 2001), RMS is a common method of representing a response in the field of vibration. In this case, it is representative of the variance of magnitude of relative motion or acceleration transmissibility – analogous to the weighted average amplitude. The definition of the RMS of function $h(\omega)$ from ω=0-20 Hz is as follows:

$$RMS(h(\omega)) = \sqrt{\frac{1}{40\pi}\int_0^{40\pi} h(\omega)^2 d\omega} \qquad (10)$$

Applying equation (10) to the base excitation, we define

$R = RMS(\phi)$, force transmissibility RMS

$\eta = RMS(\gamma)$, absolute displacement RMS

We obtained a closed form relation for the local minimum RMS of force transmissibility given by (11).

$$\begin{cases} \dfrac{\partial R(\zeta, \omega_n)}{\partial \zeta} = 0 \\ \dfrac{\partial R(\zeta, \omega_n)}{\partial \omega_n} = 0 \end{cases} \qquad (11)$$
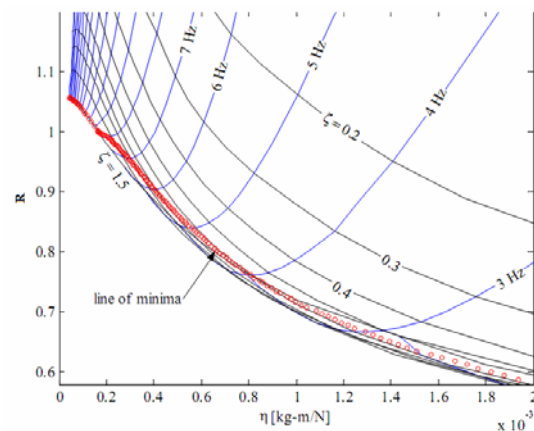

Figure 3. The RMS force transmissibility versus the RMS absolute displacement while harmonic excitation

In case, constant amplitude harmonic force, the RMS of force transmissibility (ϕ) and absolute displacement (γ) are both functions of ζ and ω_n; thus, for a unique pair of ζ and ω_n, a related value of R and η can be found to illustrate the preceding results in the $R - \eta$ plane in Figure 3. Here, the line of minima represents the optimal damping ratio which yields the minimum force transmissibility for a given stiffness or natural frequency.

2.2. Random excitation

Consider the excitation $f(t)$ is a zero mean Gaussian stationary process with the correlation function and spectral density given, respectively, by

$$R_f(t) = \langle f(t)f(t+\tau) \rangle \qquad (12)$$

where $\langle \ \rangle$ denotes the expectation.

$$S_f(\omega) = \frac{1}{2\pi} \int_{-\infty}^{\infty} R_f(\tau)e^{i\omega\tau}d\tau \qquad (13)$$

The mean square value of the transmissibility ratio and relating displacement can then be calculated by the equation

$$\langle \phi^2 \rangle = \int_{-\infty}^{\infty} S_f(\omega)|\phi|^2 d\omega \qquad (14)$$

$$\langle \gamma^2 \rangle = \int_{-\infty}^{\infty} S_f(\omega)|\gamma|^2 d\omega \qquad (15)$$

In order to simplify the analysis of random vibration, we assume that impressed force is excitation as white noise.

Substituting for ϕ from (8) and (9), we have

$$\langle \phi^2 \rangle = S_f \omega_n \int_{-\infty}^{\infty} \frac{1 + (2\zeta r)^2}{(1 - r^2)^2 + (2\zeta r)^2} dr \qquad (16)$$

$$\langle \gamma^2 \rangle = \frac{S_f}{\omega_n^3} \int_{-\infty}^{\infty} \frac{1}{(1 - r)^2 + (2\zeta r)^2} dr \qquad (17)$$

We define the performance measure to be minimized as follow:

$$I_a = \frac{\langle \phi^2 \rangle}{2\pi S_f \omega_n} \qquad (18)$$

The performance measure I_a defined by Eqn.(18) represents the ratio of response (mean square value of transmissibility ratio) of the gun mass m to the excitation with a uniform power spectrum S_f. Parameter $2\pi\omega_n$ of the denominator in Eqn.(18) is used to put the performance measure into dimensionless form, where ω_n is the natural frequency of the gun mass.

Substituting for $< \phi^2 >$ from (14), we have

$$I_a = \frac{1}{2\pi} \int_{-\infty}^{\infty} \frac{1 + (2\zeta r)^2}{(1 - r^2)^2 + (2\zeta r)^2} dr \qquad (19)$$

The definite integral of Eqn.(19) can be evaluated by the method of residues. The performance measure I_a has a minimum value $I_{a\min}$ at a pair certain damping ratio ζ_{opt} and r_{opt} called optimum damping and natural frequency. The optimums ζ_{opt} and r_{opt} are found by the solution of equations:

$$\begin{cases} \dfrac{\partial I_a}{\partial \zeta} = 0 \\ \dfrac{\partial I_a}{\partial r} = 0 \end{cases} \qquad (20)$$

To demonstrate the effectiveness of RB, below presents the survey results on a half-car gun-vehicle model.

3. Effect of a rubber bushing

To assess the effective vibration reducing of RB for the gun mounted on the vehicle, we considered the simple half-car model with RB and without RB.

3.1. Gun-vehicle without RB model

Figure 4 illustrates the half-car model of a gun-vehicle with guns mounted directly on the vehicle body, in which only two degrees of freedom are considered. In this model, the dynamical motion of the vehicle body mounted gun in longitudinal plane is determined. The suspensions are modeled by linear spring in parallel with viscous dampers.
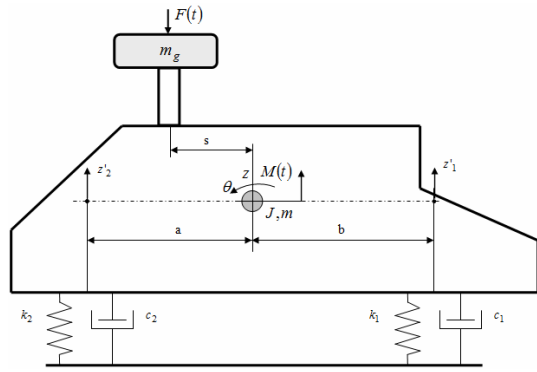

Figure 4. The half gun-vehicle model without RB

The following equations of motion are derived for the model using Newton – Euler method:

$$\begin{cases} (m+m_g)\ddot{z}+k_1 z_1'+k_2 z_2'+c_1 \dot{z}_1'+ \\ \quad + c_2 \dot{z}_2' = F(t) \\ J'\ddot{\theta}+(k_1 z_1'+c_1 \dot{z}_1')a'-(k_2 z_2'+c_2 \dot{z}_2')b' = \\ \quad = F(t)s'+M(t) \end{cases} \quad (21)$$

and the constraints are given by

$$\begin{aligned} z_1' &= z+a'.\sin\theta \approx z+a'.\theta \\ z_2' &= z-b'\sin\theta \approx z-b'.\theta \\ \dot{z}_1' &\approx \dot{z}+a'.\dot{\theta}; \dot{z}_2' \approx \dot{z}-b'.\dot{\theta} \end{aligned} \quad (22)$$

where m is the mass of the vehicle body; m_g is the mass of the gun; J' is the mass moment of inertia for the gun-vehicle body; k_1 and k_2 are the spring stiffness of front/rear suspensions respectively; c_1 and c_2 are the damping coefficients of front/rear suspensions respectively; a' and b' are the

distances of the front/rear suspension locations, with reference to the centre of gravity of the gun-vehicle body; s' is the distances of the gun locations, with reference to the centre of gravity of the gun-vehicle body; z is the vertical displacement of the vehicle body at the centre of gravity; θ is the rotary angle of the vehicle body at the centre of gravity; $F(t)$ and $M(t)$ are the force/moment due to gun generation during shooting respectively.

3.1. Gun-vehicle with RB model

Figure 5 illustrates the half-car model of a gun-vehicle with mounted gun on vehicle through RB, in which three degrees of freedom are considered. The RB is modeled by linear spring k_g in parallel with viscous dampers c_g.
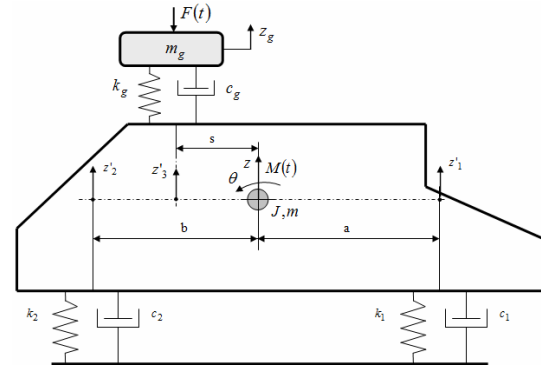

Figure 5. The half gun-vehicle model with RB

$$\begin{cases} m\ddot{z}+k_1 z_1'+k_2 z_2'+c_1 \dot{z}_1'+c_2 \dot{z}_2'- \\ \quad -k_g(z_g-z_3')-c_g(\dot{z}_g-\dot{z}_3')=0 \\ J\ddot{\theta}+(k_1 z_1'+c_1 \dot{z}_1')a-(k_2 z_2'+c_2 \dot{z}_2')b+ \\ \quad +(k_g(z_g-z_3')+c_g(\dot{z}_g-\dot{z}_3'))s=M(t) \\ m_3\ddot{z}_g+k_g(z_g-z_3')+c_g(\dot{z}_g-\dot{z}_3')=F(t) \end{cases} \quad (23)$$

and the constraints are given by

$$\begin{aligned} z_1' &= z+a.\sin\theta \approx z+a.\theta \\ z_2' &= z-b\sin\theta \approx z-b.\theta \\ z_3' &= z-s\sin\theta \approx z-s.\theta \\ \dot{z}_1' &= \dot{z}+a.\dot{\theta}, \dot{z}_2' = \dot{z}-b.\dot{\theta}, \dot{z}_3' = \dot{z}-s.\dot{\theta} \end{aligned} \quad (24)$$

where J is the mass moment of inertia for the vehicle body; a and b are the distances of the front/rear suspension locations, with reference to the centre of gravity of the vehicle body; s is the distances of the gun locations, with reference to the centre of gravity of the vehicle body; z_g is the vertical displacement of the gun. Other symbols same as in Eqns.(21).

Displacement equation of the gun and rotation of vehicle body are derived by solving the differential equation system Eqns.(21) or Eqns.(23) for the force and moment due to gun generation during shooting.

The displacement-time diagram and the rotation angle-time diagram for PKT machine gun mounted on the BRDM-2 wheeled armoured fighting vehicle in single round burst firing condition presented on the Figures 6, 7 and in 6-rounds burst firing condition presented on the Figure 8, 9.
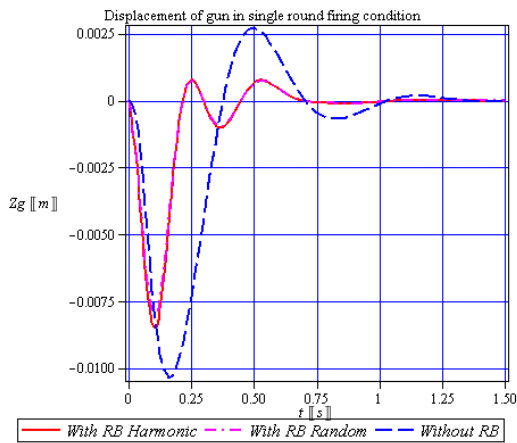

Figure 6. The displacement in single-round burst firing condition, with and without RB

It can be seen from the Figure 6,7 that the response of the displacement of vehicle with RB when harmonic input or white noise input is used is compared to the response of the vehicle without RB. The result of the vehicle with RB is not significantly better than the result of the gun-vehicle without RB. The gun-body displacement is 0.008m with RB versus 0.012m without RB and the rotation of the gun-vehicle is 0.0033rad with RB versus 0.0028rad without RB.
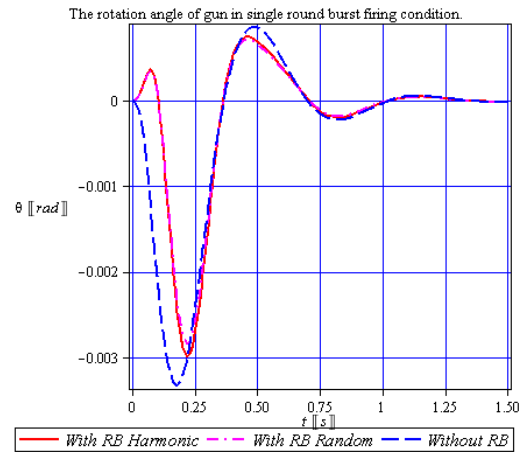

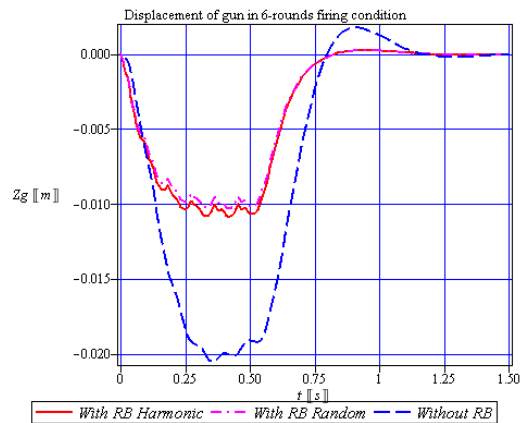Figure 7. The rotation angle in single-round burst firing condition, with and without RB

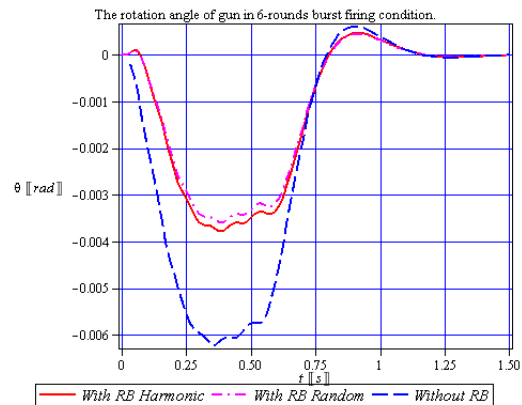Figure 8. The displacement in 6-rounds burst firing condition, with and without RB

Figure 9. The rotation angle in 6-rounds burst firing condition, with and without RB

However, It can be seen from the Figure 8,9 that the displacement and the rotation of the gun mounted on the vehicle had a very strong reduction. Therefore, the shooting accuracy is improved. These examples showed that RB is very effective to improve shooting accuracy. The displacement of the gun-body is 0.011m with RB versus 0.0158m without RB (decreased about 25%) and the rotation angle of the gun-vehicle is 0.0032rad with RB versus 0.0057rad without RB (decreased about 45%).

Effective vibration reducing of the RBs are designed by harmonic excitation input and random excitation input are almost similar.

2. Conclusion

The dynamic response of a rubber bushing to transient excitations has been theoretically and experimentally analyzed. We had to investigate the development of rubber bushing to improve shooting accuracy of the gun mounted on vehicle. Finally, the comparison effectiveness with RB and without RB when gun mounted on a vehicle in single-round and six-rounds burst firing. A feature work may develop an active bushing.

3. References

Bulman, D.N. (1996), The effects of vehicle and barrel motion on the accuracy of a repeat fire small cannon. In Proceedings of the Eighth U.S. Army Symposium on Gun Dynamics, Newport, Rhode Island, 14(16), pp. 1-12.

Inman, D. J. (2001), Engineering vibration, (2nd ed.). Upper Saddle River, N.J.:Prentice Hall.

Jazar, G. N., Alkhatib, R., Golnaraghi, M. F.(2006), Root mean square optimization criterion for vibration behaviour of linear quarter car using analytical methods, Vehicle System Dynamics, 44(6), pp. 477-512.

Kang, X.Z., Ma, C.M, Wei, X.D (2003). Modeling theory of gun system. Defense Industry Publishing Co, Beijing.

Lin, Y., Luo, W. and Zhang, Y.M. (1990), New Method for the Optimization of a Vibration Isolation System, Journal of Vibration, Acoustics, Stress, and Reliability in Design, 112,(3), pp. 413-416.

Peleg, K. (1979), Frequency response of non-linear single degree-of-freedom systems. Int. J. Mech. Sci. 21, pp. 75–84.

Rivin, E. I. (2003), *Passive Vibration Isolation*, ASME Press.

Tamboli, J. A., Joshi, S. G. (1999), Optimal Design of a Passive Suspension System of a Vehicle Subjected to Actual Random Road Excitations, Journal of Sound and Vibration, 219(2): pp. 193-205.

Continuous element for vibration analysis of laminated composite beams and plates

Nguyen Manh Cuong, Tran Ich Thinh, Dang Tien Dai, Dinh Gia Ninh
Hanoi University of Science and Technology, Vietnam

Abstract

This paper presents a new numerical method: Continous Element Method (CEM) for vibration analysis of laminated composite beams and plates taking into account the shear deflection effects. Natural frequencies of composite beams and thick composite plates subjected to different boundary conditions obtained with this kind of formulation are in close agreement with finite element solutions. The main advantage is the reduction of the size of the model thus allowing high precision in the results for a large frequency range and a reduced time of computing. Numerical examples of different types of laminated composite beams and plates confirm the advantage of this method.

Key Words: Continuous element method, Dynamic stiffness matrix, Laminated composite, Composite beam, Composite plate, Dynamic transfer matrix, Vibration analysis

1. Introduction

The Continuous Element Method (CEM) is a highly efficient way to analyse harmonic responses of structures made up of many simple elements. It is based on the dynamic stiffness matrix $[K(\omega)]$, which gives exact relations between forces and displacements at the ends of a structural element [1]. In the case of straight beam assemblies, exact solutions of the equations of motion according to Euler–Bernoulli assumptions or the Rayleigh and Timoshenko theories have been used to develop the dynamic stiffness matrices [1], [4], [6], [11], [12]. The calculation of the dynamic stiffness matrix for curved beams is based on an integration of the equations of motion [5]. With the same approach, a metal axisymmetric cylindrical shell element with shear effects has been developed [3]. Metal plate's continuous elements are also developed [7]. For this kind of elements, the solution of the equations of motion is theoretically unattainable. Nevertheless, a dynamic stiffness matrix has been built from series expansion for plate of Mindlin [3]

The composite beam and plate members have been increasingly used over the past few decades in the fields of aerospace, civil and mechanical engineering due to their excellent engineering features. The increased use of laminated composite beams and plates requires a better understanding of vibration characteristics of these structures.

The main objective of this paper, therefore, is to obtain the dynamic stiffness

matrix in order to determine natural frequencies for symmetric laminated beams and for anti-symmetric angle-ply laminated plates which take into account both the rotatory inertia and shear deformations effects.

2. Theory of laminated composite

Consider a plate of total thickness h composed of N orthotropic layers. The principal material coordinates $\left(x_1^k, x_2^k, x_3^k\right)$ of the kth lamina oriented at an angle θ_k to the laminate coordinate x.

2.1. Lamina reduced stiffnesses

The plane stress-reduced stiffness are calculated from the engineering constants of the kth layer:

$$Q_{11} = \frac{E_1}{1 - \upsilon_{12}\upsilon_{21}}, \quad Q_{12} = \frac{\upsilon_{12}E_2}{1 - \upsilon_{12}\upsilon_{21}},$$

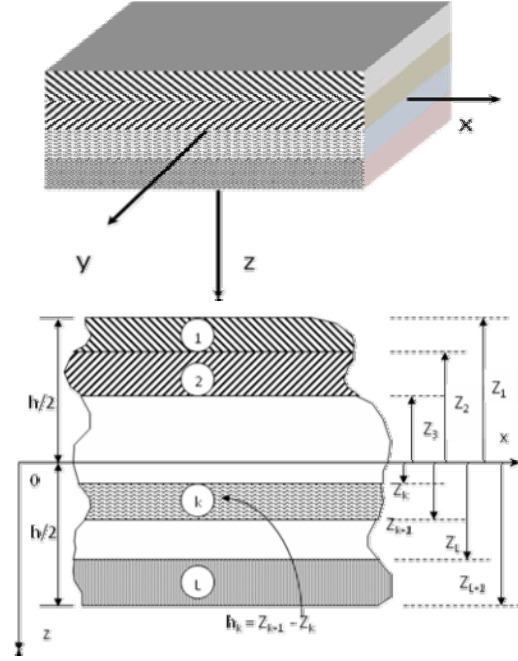$$Q_{22} = \frac{E_2}{1 - \upsilon_{12}\upsilon_{21}}, Q_{66} = G_{12}, Q_{44} = G_{23}, Q_{55} = G_{13} \tag{2.1.1}$$

Fig. 1 Coordinate system and layer numbering for a laminated plate.

These coefficients are modified for the laminate coordinates (x,y,z) as:

$$\overline{Q_{11}} = Q_{11}\cos^4\theta + 2(Q_{12} + 2Q_{66})\sin^2\theta\cos^2\theta + Q_{22}\sin^4\theta$$

$$\overline{Q_{12}} = (Q_{11} + Q_{22} - 4Q_{66})\sin^2\theta\cos^2\theta + Q_{12}(\sin^4\theta + \cos^4\theta)$$

$$\overline{Q_{22}} = Q_{11}\sin^4\theta + 2(Q_{12} + 2Q_{66})\sin^2\theta\cos^2\theta + Q_{22}\cos^4\theta$$

$$\overline{Q_{16}} = (Q_{11} - Q_{12} - 2Q_{66})\sin\theta\cos^3\theta + (Q_{12} - Q_{22} + 2Q_{66})\sin^3\theta\cos\theta$$

$$\overline{Q_{26}} = (Q_{11} - Q_{12} - 2Q_{66})\sin^3\theta\cos\theta + (Q_{12} - Q_{22} + 2Q_{66})\sin\theta\cos^3\theta$$

$$\overline{Q_{66}} = (Q_{11} + Q_{22} - 2Q_{12} - 2Q_{66})\sin^2\theta\cos^2\theta + Q_{66}(\sin^4\theta + \cos^4\theta)$$

$$\overline{Q_{44}} = Q_{44}\cos^2\theta + Q_{55}\sin^2\theta$$

$$\overline{Q_{45}} = (Q_{55} - Q_{44})\sin\theta\cos\theta$$

$$\overline{Q_{55}} = Q_{55}\cos^2\theta + Q_{44}\sin^2\theta \tag{2.1.2}$$

2.2. Laminate Constitutive Equations

The constitutive equations of the laminate can be expressed in terms of strains as follows

$$\begin{Bmatrix} N_{xx} \\ N_{yy} \\ N_{xy} \\ M_{xx} \\ M_{yy} \\ M_{xy} \end{Bmatrix} = \begin{bmatrix} A_{11} & A_{12} & A_{16} & B_{11} & B_{12} & B_{16} \\ A_{12} & A_{22} & A_{26} & B_{12} & B_{22} & B_{26} \\ A_{16} & A_{26} & A_{66} & B_{16} & B_{26} & B_{66} \\ B_{11} & B_{12} & B_{16} & D_{11} & D_{12} & D_{16} \\ B_{12} & B_{22} & B_{26} & D_{12} & D_{22} & D_{26} \\ B_{16} & B_{26} & B_{66} & D_{16} & D_{26} & D_{66} \end{bmatrix} \begin{Bmatrix} \varepsilon_{xx}^{(0)} \\ \varepsilon_{yy}^{(0)} \\ \gamma_{xy}^{(0)} \\ \varepsilon_{xx}^{(1)} \\ \varepsilon_{yy}^{(1)} \\ \gamma_{xy}^{(1)} \end{Bmatrix}$$

$$, \begin{Bmatrix} Q_y \\ Q_x \end{Bmatrix} = \kappa \begin{bmatrix} A_{44} & A_{45} \\ A_{45} & A_{55} \end{bmatrix} \begin{Bmatrix} \dfrac{\partial w_0}{\partial y} + \varphi_y \\ \dfrac{\partial w_0}{\partial y} + \varphi_x \end{Bmatrix}$$

where:
$$A_{ij} = \sum_{k=1}^{N} \overline{Q}_{ij}^{(k)} \left(z_{k+1} - z_k \right),$$

$$(A_{44}, A_{45}, A_{55})$$
$$= \sum_{k=1}^{N} \left(\overline{Q}_{44}^{(k)}, \overline{Q}_{45}^{(k)}, \overline{Q}_{55}^{(k)} \right)(z_{k+1} - z_k)$$

$$B_{ij} = \frac{1}{2} \sum_{k=1}^{N} \overline{Q}_{ij}^{(k)} \left(z_{k+1}^2 - z_k^2 \right),$$

$$D_{ij} = \frac{1}{3} \sum_{k=1}^{N} \overline{Q}_{ij}^{(k)} \left(z_{k+1}^3 - z_k^3 \right) \qquad (2.2.2)$$

A_{ij}: Extensional stiffnesses, B_{ij}: Bending-extentional stiffnesses, D_{ij}: Bending-stiffnesses

3. Continuous element method for vibration analysis of laminated composite beams

3.1. Governing equations

In this research, the bending vibration of symmetrically laminated beams is examined using the Classical Laminated Plate Theory (CLPT) [11]. Assume that: $M_{yy} = M_{xy} = 0$ and the laminated beam under consideration is long enough to make the effects of the Poisson ratio and shear coupling on the deflection negligible. Then the transverse deflection will be a function of coordinate x (along the length of the beam) and time t: $w_0 = w_0(x,t)$
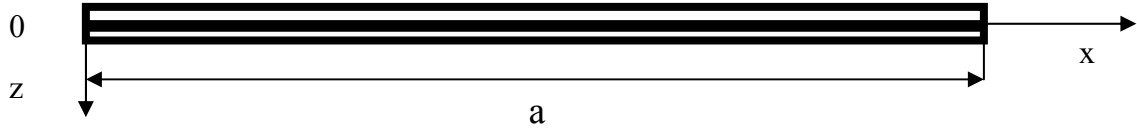

Fig.2 Geometry of a laminated composite beam.

The equation of motion for symmetrically laminated long beams can be written as [11]:

$$-\frac{\partial^2}{\partial x^2}\left(E_{xx}^b I_{yy} \frac{\partial^2 w_0}{\partial x^2} \right) = \hat{I}_0 \frac{\partial^2 w_0}{\partial t^2} - \hat{I}_2 \frac{\partial^4 w_0}{\partial x^2 \partial t^2}$$
$$(3.1.1)$$

Here: $D_{11}^* = \left(D_{22}D_{66} - D_{26}D_{26} \right)/\det(D)$

$$M = bM_{xx}, \quad Q = bQ_x, \quad E_{xx}^b = \frac{12}{h^3 D_{11}^*} = \frac{b}{I_{yy}D_{11}^*}, \quad I_{yy} = \frac{bh^3}{12}$$
$$(3.1.2)$$

$$M(x) = -E_{xx}^b I_{yy} \frac{\partial^2 w_0}{\partial x^2} \quad Q = \frac{\partial M}{\partial x}$$

$$\varphi = \frac{\partial w_0}{\partial x}$$

$$\hat{I}_0 = bI_0, \quad \hat{I}_2 = bI_2, \quad I_i = b \int_{-h/2}^{h/2} \rho(z)^i dz \quad (i = 0,1,2)$$

where b is the width and h is the total thickness of the laminate.

The boundary conditions are of the forms:

+ Clamped:

$$w_0 = \frac{dw_0}{dx} = 0$$

+ *Free:*

$$Q = \frac{dM}{dx} = 0 \qquad M = 0$$
$$(3.1.3)$$

+ *Simply supported:*

$$w_0 = 0 \qquad\qquad M = 0$$

3.2. Analytical solution for vibration of symmetrical laminated beams

For natural vibration, the solution is assumed to be periodic:

$$w_0(x,t) = W(x)e^{i\omega t} \qquad i = \sqrt{-1}$$
(3.2.1)

By introducing (3.2.1), the governing equation (3.1.1) reduces to:

$$E_{xx}^b I_{yy} \frac{d^4 W}{dx^4} = \omega^2 \hat{I}_0 W - \omega^2 \hat{I}_2 \frac{d^2 W}{dx^2}$$
(3.2.2)

Equation (3.2.2) has the general form:

$$p \frac{d^4 W}{dx^4} + q \frac{d^2 W}{dx^2} - rW = 0$$
(3.2.3)

where:

$$p = E_{xx}^b I_{yy}, \qquad q = \omega^2 \hat{I}_2, \qquad r = \omega^2 \hat{I}_0$$

$$\begin{Bmatrix} W_{(x=0)} \\ W_{(x=a)} \\ \varphi_{(x=0)} \\ \varphi_{(x=a)} \end{Bmatrix} = \begin{bmatrix} 0 & 1 & 0 & 1 \\ \sin(\lambda a) & \cos(\lambda a) & \sinh(\mu a) & \cosh(\mu a) \\ \lambda & 0 & \mu & 0 \\ \lambda \cos(\lambda a) & -\lambda \sin(\lambda a) & \mu \cosh(\mu a) & \mu \sinh(\mu a) \end{bmatrix} \begin{Bmatrix} c_1 \\ c_2 \\ c_3 \\ c_4 \end{Bmatrix} = [A] \begin{Bmatrix} c_1 \\ c_2 \\ c_3 \\ c_4 \end{Bmatrix}$$
(3.3.1)

Secondly, another relation between the vector of resultant forces and moments and the vector of constants will be constructed:

$$\begin{Bmatrix} Q_{(x=0)} \\ Q_{(x=a)} \\ M_{(x=0)} \\ M_{(x=a)} \end{Bmatrix} = -\frac{1}{D_{11}^*} \begin{bmatrix} -\lambda^3 & 0 & \mu^3 & 0 \\ -\lambda^3 \cos(\lambda a) & \lambda^3 \sin(\lambda a) & \mu^3 \cosh(\mu a) & \mu^3 \sinh(\mu a) \\ 0 & -\lambda^2 & 0 & \mu^2 \\ -\lambda^2 \sin(\lambda a) & -\lambda^2 \cos(\lambda a) & \mu^2 \sinh(\mu a) & \mu^2 \cosh(\mu a) \end{bmatrix} \begin{Bmatrix} c_1 \\ c_2 \\ c_3 \\ c_4 \end{Bmatrix} = [B] \begin{Bmatrix} c_1 \\ c_2 \\ c_3 \\ c_4 \end{Bmatrix}$$
(3.3.2)

By eliminating the constants' vector, the dynamic stiffness matrix will be determined as:

$$[K(\omega)] = [B][A]^{-1}$$
(3.3.3)

Based on [K(ω)], the natural frequencies of the laminated composite beam will be calculated. This matrix relates the vector of forces and moments resultant of one end to the vector of displacements of the other end of the beam.

The general solution of (3.2.3) is:

$$W(x) = c_1 \sin \lambda x + c_2 \cos \lambda x + c_3 \sinh \mu x + c_4 \cosh \mu x$$
(3.2.4)

With:

$$\lambda = \sqrt{\frac{1}{2p}\left(q + \sqrt{q^2 + 4qr}\right)}, \qquad \mu = \sqrt{\frac{1}{2p}\left(-q + \sqrt{q^2 + 4qr}\right)}$$
(3.2.5)

where c_1, c_2, c_3 and c_4 are constants, which are to be determined using the boundary conditions.

3.3. Dynamic stiffness matrix [K(ω)]

In order to construct the dynamic stiffness matrix [K(ω)], first the bending displacements and rotation angles have to be expressed at the two ends of the beam (x=0 and x=a). Then, the relation between the displacement vector and the vector of constants is written in the matrix form as:

$$\begin{Bmatrix} Q_{(x=0)} \\ Q_{(x=a)} \\ M_{(x=0)} \\ M_{(x=a)} \end{Bmatrix} = [K(\omega)] \begin{Bmatrix} W_{(x=0)} \\ W_{(x=a)} \\ \varphi_{(x=0)} \\ \varphi_{(x=a)} \end{Bmatrix}$$
(3.3.4)

4. Continuous element method for vibration analysis of laminated composite plates

4.1. Strong formulation

Let consider a rectangular anti-symmetric angle-ply plate with two opposite edges simply supported while the remaining edges have any combination of free, clamped and simply supported boundary conditions. Fig. 4.1.1. describes the coordinates system, dimensions and displacements of plate.
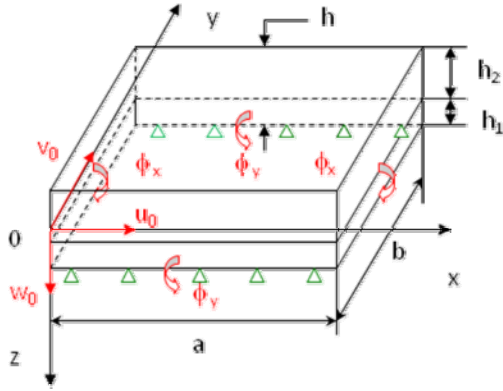

Fig. 3 An anti-symmetric angle-ply plate with two opposite edges simply supported.

The plate's model of Continuous Element Method will be constructed using the First Order Shear Deformation Theory (FSDT) [11]. The laminates exhibit twisting-extensional coupling, and the differential equations associated with the FSDT take the form:

$$\frac{\partial N_{xx}}{\partial x} + \frac{\partial N_{xy}}{\partial y} = I_0 \frac{\partial^2 u_0}{\partial t^2},$$

$$\frac{\partial M_{xx}}{\partial x} + \frac{\partial M_{xy}}{\partial y} - Q_x = I_2 \frac{\partial^2 \phi_x}{\partial t^2}$$

$$\frac{\partial N_{xy}}{\partial x} + \frac{\partial N_{yy}}{\partial y} = I_0 \frac{\partial^2 v_0}{\partial t^2}, \qquad (4.1.1)$$

$$\frac{\partial M_{xy}}{\partial x} + \frac{\partial M_{yy}}{\partial y} - Q_y = I_2 \frac{\partial^2 \phi_y}{\partial t^2}$$

$$\frac{\partial Q_x}{\partial x} + \frac{\partial Q_y}{\partial y} = I_0 \frac{\partial^2 w_0}{\partial t^2}$$

where the stress resultants can be expressed in terms of displacements by:

$$N_{xx} = A_{11} \frac{\partial u_0}{\partial x} + A_{12} \frac{\partial v_0}{\partial y} + B_{16}(\frac{\partial \phi_x}{\partial y} + \frac{\partial \phi_y}{\partial x})$$

$$N_{yy} = A_{12} \frac{\partial u_0}{\partial x} + A_{22} \frac{\partial v_0}{\partial y} + B_{26}(\frac{\partial \phi_x}{\partial y} + \frac{\partial \phi_y}{\partial x})$$

$$N_{xy} = A_{66}(\frac{\partial u_0}{\partial y} + \frac{\partial v_0}{\partial x}) + B_{16} \frac{\partial \phi_x}{\partial x} + B_{26} \frac{\partial \phi_y}{\partial y}$$

$$M_{yy} = B_{26}(\frac{\partial u_0}{\partial y} + \frac{\partial v_0}{\partial x}) + D_{12} \frac{\partial \phi_x}{\partial x} + D_{22} \frac{\partial \phi_y}{\partial y}$$

$$Q_x = \kappa A_{55} \frac{\partial w_0}{\partial x} + \phi_x \quad Q_y = \kappa A_{44} \frac{\partial w_0}{\partial y} + \phi_y$$

$$M_{xx} = B_{16}(\frac{\partial u_0}{\partial y} + \frac{\partial v_0}{\partial x}) + D_{11} \frac{\partial \phi_x}{\partial x} + D_{12} \frac{\partial \phi_y}{\partial y}$$

$$M_{xy} = B_{16} \frac{\partial u_0}{\partial x} + B_{26} \frac{\partial v_0}{\partial x} + D_{66}(\frac{\partial \phi_x}{\partial y} + \frac{\partial \phi_y}{\partial x})$$

$$(4.1.2)$$

where k is the shear correction coefficient (k=5/6).

The different boundary conditions are defined by:

- Simply supported (SS) at edges y=0, b:

$$v_0 = w_0 = \phi_x = M_{yy} = N_{xy} = 0 \qquad (4.1.3)$$

- Simply supported (SS) at edges y=0, a:

$$u_0 = w_0 = \phi_y = M_{xx} = N_{xy} = 0 \qquad (4.1.4)$$

- Free (F) at edges x = 0, a:

$$N_{xx} = N_{xy} = Q_x = M_{xx} = M_{xy} = 0 \qquad (4.1.5)$$

- Clamped (C) at edges x = 0, a:

$$u_0 = v_0 = w_0 = \phi_x = \phi_y = 0 \qquad (4.1.6)$$

For applying the Lévy type solution procedure, the following representation is used:

$$u_o(x, y) = \sum_{m=1}^{\infty} u_m(x) \cos \alpha y$$

$$N_{xx}(x, y) = \sum_{m=1}^{\infty} N_{xxm}(x) \sin \alpha y$$

$$v_o(x, y) = \sum_{m=1}^{\infty} v_m(x) \sin \alpha y$$

$$N_{xy}(x, y) = \sum_{m=1}^{\infty} N_{xym}(x) \sin \alpha y$$

$$w_o(x, y) = \sum_{m=1}^{\infty} w_m(x) \sin \alpha y$$

$$Q_x(x, y) = \sum_{m=1}^{\infty} Q_{xm}(x) \sin \alpha y$$

$$(4.1.7)$$

$$\phi_x(x, y) = \sum_{m=1}^{\infty} \varphi_{xm}(x) \sin \alpha y$$

$$M_{xx}(x, y) = \sum_{m=1}^{\infty} M_{xxm}(x) \sin \alpha y$$

$$\phi_y(x, y) = \sum_{m=1}^{\infty} \varphi_{ym}(x) \cos \alpha y$$

$$M_{xy}(x, y) = \sum_{m=1}^{\infty} M_{xym}(x) \cos \alpha y$$

where: $\alpha = m\pi/b$

The vector $\{y\}_m^T = \{u_m, v_m, w_m, \varphi_{xm}, \varphi_{ym}, N_{xxm}, N_{xym}, Q_{xm}, M_{xxm}, M_{xym}\}^T$ is called state-solution vector.

First, the forces and moments resultant N_{yy}, Q_y, M_{yy} will be expressed as functions of the state-solution vector. Then, by replacing (4.1.7) in equations (4.1.1) and (4.1.2), a system of ordinary differential equations in the x-coordinate, after some elementary algebraic manipulation, can be expressed as:

$$\frac{du_m}{dx} = J_1 N_{xxm} - J_2 M_{xym}$$
$$+ (B_{26} J_2 - A_{12} J_1) v_m \alpha$$

$$\frac{dv_m}{dx} = J_4 N_{xym} - J_5 M_{xxm}$$
$$- (D_{12} J_5 - B_{26} J_4) \varphi_{ym} u_m \alpha^2$$

$$\frac{dw_m}{dx} = \frac{Q_{xm}}{KA_{55}} - \varphi_{xm}$$

$$\frac{d\varphi_{xm}}{dx} = -J_5 N_{xym} + J_6 M_{xxm}$$
$$+ (D_{12} J_6 - B_{26} J_5) \varphi_{ym} \alpha$$

$$\frac{d\varphi_{ym}}{dx} = -J_2 N_{xxm} + J_3 M_{xym}$$
$$- (B_{26} J_3 - A_{12} J_2) v_m \alpha - \varphi_{xm} \alpha$$

$$\frac{dN_{xxm}}{dx} = -I_o \omega^2 u_m - N_{xym} \alpha$$

$$\frac{dN_{xym}}{dx} = -I_o \omega^2 v_m + (A_{12} J_1 - B_{26} J_2) N_{xx} \alpha$$
$$+ (2 A_{12} B_{26} J_2 - J_1 A_{12}^2 - B_{26}^2 J_3$$
$$+ A_{22} A_{11} J_1 - A_{12} B_{16} J_2) v_m \alpha^2$$
$$+ J_2 (A_{11} - A_{12}) M_{xym} \alpha$$

$$(4.1.8)$$

$$\frac{dQ_{xm}}{dx} = -I_o \omega^2 w_m + \alpha^2 k A_{44} w_m$$
$$+ k A_{44} \alpha \varphi_{yxm}$$

$$\frac{dM_{xxm}}{dx} = -I_2 \omega^2 \varphi_{xm} + Q_{xm} + \alpha M_{xym}$$

$$\frac{dM_{xym}}{dx} = [-I_2 \omega^2 + (2 J_5 B_{26} D_{12} -$$
$$B_{26} J_4 - J_6 D_{12} A_{12} + D_{22}) \alpha^2$$
$$+ k A_{44}] \varphi_{ym} + k A_{44} \alpha w_m$$
$$+ \alpha (D_{12} J_5 - B_{26} J_4) N_{xym}$$
$$+ \alpha (B_{26} J_5 - D_{12} J_6) M_{xxm}$$

With:

$$J_1 = \frac{D_{66}}{A_{11} D_{66} - B_{16}^2} , \quad J_2 = \frac{B_{16}}{A_{11} D_{66} - B_{16}^2},$$

$$J_3 = \frac{A_{11}}{A_{11} D_{66} - B_{16}^2} , \quad J_4 = \frac{D_{11}}{A_{66} D_{11} - B_{16}^2},$$

$$J_5 = \frac{B_{16}}{A_{66} D_{11} - B_{16}^2} , \quad J_6 = \frac{A_{66}}{A_{66} D_{11} - B_{16}^2}.$$

$$(4.1.9)$$

Equation (4.1.8) is written in the matrix form for each mode *m*:

$$\frac{d\{y\}_m}{dx} = [A]_m \{y\}_m \qquad (4.1.10)$$

where $[A]_m$ is a 10x10 matrix.

A formal solution of equation (4.1.10) is given by:

$$\{y\}_m = C e^{[A]_m} \qquad (4.1.11)$$

Here C is the constant calculated from the boundary conditions.

4.2. Dynamic transfer matrix, dynamic stiffness matrix [K(ω)]

The state vector solution will be expressed at the two edges of the plate: x = 0 and x = a, yields:

At x=0 : $\{y(0)\}_m = C e^{[A]_m 0}$ (4.2.1)

At x=a : $\{y(a)\}_m = Ce^{[A]_m a}$ (4.2.2)

The elimination of C from (4.2.1) and (4.2.2) gives:

$$\{y(a)\}_m = e^{[A]_m a}\{y(0)\}_m \qquad (4.2.3)$$

The dynamic transfer matrix $[T]_m$ is given by:

$$[T]_m = e^{[A]_m a} \qquad (4.2.4)$$

Then $[T]_m$ is separated into four blocks:

$$[T]_m = \begin{bmatrix} T_{11} & T_{12} \\ T_{21} & T_{22} \end{bmatrix} \qquad (4.2.5)$$

Finally, the dynamic stiffness matrix $[K(\omega)]_m$ is determined by:

$$[K(\omega)]_m = \begin{bmatrix} -T_{12}^{-1}T_{11} & T_{12}^{-1} \\ T_{21} - T_{22}T_{12}^{-1}T_{11} & T_{22}T_{12}^{-1} \end{bmatrix}_m$$
(4.2.6)

For the determination of the natural frequencies, the determinant of the dynamic stiffness matrix $[K(\omega)]_m$ must be set to zero.

5. Numerical results

In order to validate the continuous element method, various examples will be presented for vibration analysis of laminated beams and plates. Beams and plates are calculated using tree materials with following properties:

Table 1. Materials used for the validation of CEM.

Material	E_1 (GPa)	E_2 (GPa)	ν_{12}	G_{12} (GPa)	G_{23} (GPa)	G_{13} (GPa)	ρ (Kg/m³)
Mat. 1	$25E_2$	6.895	0.25	$0.5E_2$	$0.2E_2$	$0.5E_2$	1300.00
Mat. 2	144.8	9.65	0.3	4.14	3.45	4.14	1389.23
Mat. 3	$40E_2$	9.65	0.25	$0.6E_2$	$0.5E_2$	$0.6E_2$	1389.23

5.1. Vibration analysis of symmetrical laminated composite beam

First, the solution by this method is compared to the analytical solutions of Reddy [11] (Tab. 2) for different lamination schemes, the results are very closes (error under 3%). Material 1 is used, h = 0.016 m, b = 0.8 m, a/h = 100.

Secondly, the natural frequencies of clamped-clamped AS4/3501(0°/90°)$_s$ Graphite/Epoxy beams calculated by Finite Element (ANSYS) using SHELL99 element and by Continuous Element Method are

shown in Tab. 3. Here, Mat 2 is used, b = 0.8 m, L = 20×b, h = 0.01 m.

The computing time of natural frequencies for clamped-clamped AS4/3501(0°/90°)$_s$ Graphite/Epoxy beams is presented in Tab. 4.

The natural frequencies of free-free (0°/90°)$_s$ laminated Graphite/Epoxy beams and the computing time are shown in Tab. 5 and Tab. 6 respectively.

The natural frequencies of free-free (45°/-45°)$_s$ laminated Graphite/Epoxy beams and the computing time are shown in Tab. 7 and Tab. 8 respectively. The material is Mat 1, b = 0.8 m, L = 20×b, h = 0.01 m.

Table 2. Nondimentionalized fundamental frequencies of clamped-clamped laminated beams, $\overline{\omega} = \omega a^2 \sqrt{I_0 / E_2 h^3}$.

Laminate	Reddy[11]	CEM (1 element)	Error
$(0/90^0)_s$	5.455	**5.398**	1.05%
$(90^0/0)_s$	2.326	**2.256**	3.00%
$(45^0/-45^0)_s$	1.535	**1.534**	0.07%

Table 3. Natural frequencies of clamped-clamped (0°/90°)ₛ Graphite/Epoxy beams (Hz).

Mode	ANSYS (20×1)	ANSYS (640×1)	CEM (1 element)	Error
1	7.1372	7.1897	7.3211	1.81%
2	9.4869	9.5703	9.7085	1.42%
3	15.194	15.348	15.9155	3.90%
…..	…..	…..	…..	…..
225	-	1359.8	1360	0.02%
226	-	-	1377	-
227	-	1385.8	1394	0.60%
228	-	1411.9	1411	0.06%
229	-	-	1428	-
230	-	-	1445	-
231	-	1464.7	1462	0.18%

Table 4. Computing time for clamped-clamped (0°/90°)ₛ laminated Graphite/Epoxy beams.

ANSYS (20×1)	ANSYS (640×1)	CEM (1 element)
1 s	10 s	3 s

Table 5. Natural frequencies of free-free (0°/90°)ₛ laminated Graphite/Epoxy beams (Hz).

Mode	ANSYS (20×1)	ANSYS (640×1)	CEM (1 element)	Error
1	7.1372	7.1897	7.3211	1.81%
2	9.4869	9.5703	9.7085	1.42%
3	15.194	15.348	15.9155	3.9%
…..	…..	…..	…..	…..
228	-	1411.9	1411	0.06%
229	-	-	1428	-
230	-	-	1445	-
231	-	1464.7	1462	0.18%

Table 6. Computing time for free-free laminated (0°/90°)ₛ Graphite/Epoxy beams.

ANSYS (20×1)	ANSYS (640×1)	CEM (1 element)
3 s	12 s	4 s

Table 7. Natural frequencies of free-free (45°/-45°/-45°/45°) laminated beams (Hz).

Mode	ANSYS (20×1)	ANSYS (640×1)	Continuous element	Error
1	7.628	7.1276	7.3021	2.40%
2	9.307	8.4210	8.7535	3.80%
3	10.034	9.8172	10.1859	3.60%
4	11.303	11.329	11.6183	2.40%
…	…	…	…	…
63	-	779.25	770.469	1.13%

64	-	-	783.202	-
65	-	-	799.117	-
66	-	814.352	808.663	0.70%

Table 8. Computing time for free-free (45°/-45°/-45°/45°) laminated beam.

ANSYS (20×1)	ANSYS (640×1)	CEM (1 element)
1 s	8 s	2 s

The natural frequencies of the beam depend on the lamination scheme and boundary conditions. Results obtained by Continuous element method are close agreement to those obtained by Reddy [11] and by Finite Element method in low frequencies. Differences are remarked at the medium and high frequencies (Table 3, 5, 7). In this domain, the precision of the finite element model depends on the meshing of the structure meanwhile the continuous element method works without difficulties. By using the minimum of meshing (only one element in this case), the gain in computing time and in data storage of the continuous element method is important.

5.2. Vibration analysis of anti-symmetric laminated plate with two opposite edges simply supported

Based on the dynamic stiffness matrix $[K(\omega)]$, examples of the supported-free-supported-free (SFSF) plates with different materials, angles and number of layers are presented in order to validate the continuous element method. Results obtained are compared to those of Reddy [11] (Mat. 3 is used, $h_1 = h_2 = 0.0127$m, a/h = 10).

Table 9. Nondimentionalized fundamental frequencies of SFSF (θ/-θ) laminated plate, $\overline{\omega} = \omega a^2 \sqrt{\rho/E_2}/h$.

θ^o	Number of layers	Reddy [11]	Frequency	Errors (%)
30	2	FSDT	6.95	5.82
		CLPT	7.58	2.71
		CEM (m=1÷3)	**7.38**	
45	2	FSDT	4.76	0.42
		CLPT	5.12	7.11
		CEM (m=1÷3)	**4.77**	
60	2	FSDT	3.33	1.83
		CLPT	3.47	6.12
		CEM (m=1÷3)	**3.27**	

Then, results will be compared to the calculations by Finite Element Method (ANSYS) using the SHELL99 element.

Table 10 and Table 11 show the natural frequencies and the computing time of the SFSF (45°/-45°) laminated plate with following properties: Mat. 2, $h_1 = h_2 = 0.0127$ m, h/a=0.1

Natural frequencies and calculating time for SFSF (45°/-45°/45°/-45°) laminated plate are presented in Table 12 and Table 13 respectively. Mat. 2 is used, $h_1 = h_2 = h_3 = h_4 = 0.00635$ m, h/a=0.1

Throughs different cases, the advantages of the continuous element method are confirmed. From the analytical solution of

plate's differential equations and Lévy series, the responses obtained are more accuracy. Vibration modes are found (Table 10, mode 229, 230 or Table 12, Mode 11) by Continuous Element method but not by the Finite Element one. By using only one continuous element of plate, the calculating times are also reduced, especially for medium or high frequencies.

Table 10. Natural frequencies of SFSF (45°/-45°) laminated composite plate (Hz)

Mode	ANSYS (20×20)	ANSYS (100×100)	CEM (m=1÷3)	Error
1	1338.8	1337.8	1386.24	3.62%
2	3313.9	3310.4	3315.68	0.16%
3	5822.4	5808.1	5798.49	0.17%
…	...	...	…	…
10	8645.3	8597.8	8604.55	0.08%
11	-	-	9365.63	-
12	-	-	10092.3	-
13	11752	11634	11609.5	0.22%

Table 11. Computing time for SFSF (45°/-45°) laminated plate.

ANSYS (20×20)	ANSYS (100×100)	CEM (m=1÷3)
20 s	6950 s	15 s

Table 12. Natural frequencies of SFSF (45°/-45°/45°/-45°) laminated plate (Hz)

Mode	ANSYS (10 x10)	ANSYS (20 x20)	CE (m=1÷3) Errors
1	1610.4	1609.0	1601 0.5%
2	3836.6	3832.8	3852 0.5%
3	4285.3	4285.2	4305 0.5%
4	4805.9	4805.8	5051 4.85%
...	.....	…..	..... …..
10	9548.4	9501.8	9479 0.24%
11	…..	…...	10366 …..
12	12719	12594	12540 0.43%

Table 13. Computing time for SFSF (45°/-45°/45°/-45°) laminated plate.

ANSYS (20×20)	ANSYS (100×100)	CEM (m=1÷3)
25 s	7280 s	18 s

6. Conclusions

An efficient approach to investigate the vibration of laminated composite beams and plates is presented. The continuous element method has been successfuly used to develop the dynamic stiffness matrix for symmetric laminated beams and anti-symmetric angle-ply laminated plates taking into account

rotatory inertia and shear deflection effects. Natural frequencies obtained with this kind of formulation are in close agreement with finite element solutions and with analytical methods. The main advantage is the reduction of the size of the model thus allowing high precision in the results for a large frequency range. The next research concerns the introduction of coupling effects with fluid or other kinds of structural elements such as laminated composite shells or structures with stiffnesses.

Acknowledgements

References

1. Clough RW, Penzien J. Dynamic of structures. New-York: McGraw-Hill; 1975.

2. Casimir J. B., Nguyen Manh Cuong, Thick shells of revolution: Derivation of the dynamic stiffness matrix of continuous elements and application to a tested cylinder, Computers & structures 2007, vol. 85, n°23-24, pp. 1845-1857.

3. Nguyen Manh Cuong, Eléments Continus de plaques et coques avec prise en compte du cisaillement transverse. Application à l'interaction fluide-structure, Thèse de Doctorat, Université Paris VI, 2003.

4. Banerjee JR, Williams FW, Coupled bending-torsional dynamic stiffness matrix for Timoshenko beam elements, Comput Struct 1992;42:301–10.

5. Casimir JB, Duforet C, Vinh T, Dynamic behaviour of structures in large frequency range by continuous element methods. J. Sound Vib 2003;267:1085–106.

6. Lunden R, Akesson B, Damped second order Rayleigh Timoshenko beam vibrationin space –an exact complex dynamic member stiffness matrix". Int J Numer Methods Eng 1983;19:431–49.

7. Casimir J B, Kevorkian S, Vinh T. The dynamic stiffness matrix of two-dimensional elements – application to Kirchhoff's plate continuous elements. J. Sound Vib 2005;287:571–89.

8. K. M. LiewY. Q. Huang and J. N. Reddy. Vibration analysis of symmetrically laminated plates based on FSDT using the moving least squares differential quadrature method. Computer Methods in Applied Mechanics and Engineering 2003,192, 19, 2203-2222.

9. Leung AYT, Dynamic stiffness and substructures. New-York: Springer; 1993.

10. Li Jun, Hua Hongxing, Shen Rongying. Dynamic stiffness analysis for free vibrations of axially loaded laminated composite beams. Composite Structures 84; 2008, 87–98.

11. J.N. Reddy. Mechanics of laminated composite plates and shells. Theory and Analysis. Second Edition. CRC Press, 2004.

12. Kim NI, Kim MY. Exact dynamic stiffness matrix of non-symmetric thin-walled curved beams subjected to initial axial force. J. Sound Vib 2005;284(3–5):851–78.

13. Lee U, Spectral element method in structural dynamics, Incheon, Korea: Inha University Press; 2004.

14. Le Sourne H. Devéloppement d'Elements Continus de coques axisymetriques et de coudes. Thèse de Doctorat, Université de Nantes, 1998

Van Leer's Scheme for the Two-Dimensional Shallow Water Equation with Variable Topography using Unstructured Mesh

Nguyen Thanh Don[a] and Hoang Van Lai[b]

Institute of Mechanics, Vietnam Academy of Science and Technology
Email:[a] thanhdon@hotmail.com; [b] hvlai@imech.ac.vn

Abstract

In this paper, the well-known upwind scheme of Van Leer for hyperbolic equations are programmed and tested to solve the two dimensional Saint Venant (or shallow water) equations. We consider unstructured meshes and Van Leer's well-known upwind scheme to obtain a suitable result in point of view practice. The source term involving the gradient of topography is upwind in a similar way as the flux term. The resulting schemes are compared in term of *conservation property*. For the time discretization we consider both explicit and implicit schemes. Finally we present the numerical schemes. Finally we present the numerical result for some well know test case.

This paper is accomplished due to assistances of Prof. DARTUS Denis, Prof. Jerome Monnier, Prof. J.P Villa. Thank them very much for their devotion.

Key-words: Shallow water equations, topography variable, upwind schemes, unstructured meshes

1. Introduction:

Conservation laws with source terms often have steady states in which the flux gradients are nonzero but exactly balanced by the source terms. If the difficulties concern to aspect partially conservative of the system is now totally resolve - It appear another question more recurrent the: notion of equilibrium and well balanced scheme schema. This is the main subject of majority of publications devoted to Saint-Venant in the last ten years. This question is related to the presence in the system Saint-Venant, a topographic source term has already proposed in the late 80s and was resolved in the mid 90s to the notion of equilibrium and well balanced scheme schema. Many numerical methods (e.g., fractional step methods) have difficulty preserving such steady states and cannot accurately calculate small perturbations of such states. So many researches have been realized to overcome this problem.

In 1993, Bermudez and Vazquez, who work in Spain, Europe proposed a method to make compatible the discretization of the terms of flux and source terms in case linear. From a classical scheme of Roe, it is to extend the concept of up winding source terms in the projecting the eigenvectors of the Jacobean matrix of the flow. They get together for the preservation of the balance water at rest. This work has been extended to

two-dimensional case and the method has been applied to the treatment of friction term.

At same time, on the other side of the Atlantic, in USA, R.J. LeVeque has also researched the issue of numerical treatment of source terms in hyperbolic conservation laws for many years. From 1990, he was interested in the case of conservation laws scalar in the presence of chemical reactions and showed that the methods classics were not satisfactory in the presence of stiff source terms. His interest in the Saint-Venant equations is more recent. Following the work done in homogeneous, he proposed an adaptation to non-homogeneous case: the expression of flux, the conventional variables means cell are replaced by variables reconstructed so as to preserve the equilibrium. This leads to modified Riemann problems at the cell edges in which the jump now corresponds to perturbations from the steady state. His research for the general case where function flux is non linear

It is surprised that although two auteurs in difference place developed their own difference approached method but they obtained the same result in case linear.

2. Godunov method

This paper deals with the numerical solution of 1D Shallow Water Equations for channels with variable depth and width. These equations for channels of rectangular cross-section are a couple of conservation laws linking the depth h and the discharge q, which in condensate form read as follows

$$\frac{\partial W}{\partial t} + \frac{\partial}{\partial x} F(W) = G(x, W) \tag{1}$$

where $W = \begin{pmatrix} h \\ hu \end{pmatrix} = \begin{pmatrix} h \\ q \end{pmatrix}$ is the unknown,

while F is the flux function

$$F(W) = \begin{pmatrix} q \\ \dfrac{q^2}{h} + \dfrac{1}{2} gh^2 \end{pmatrix} \tag{2}$$

Also G is the source term that arises due to variable depth of channel. This is define by

$$G(x, W) = \begin{pmatrix} 0 \\ gh \dfrac{\partial Z}{\partial x} \end{pmatrix} \tag{3}$$

where Z is a function which describes the bottom of the channel.

Let $W_i \equiv W_i^n$ denote cell averages at time t_n and let $\overline{W}_i \equiv W_i^{n+1}$ be the updated cell averages at time t_{n+1}. (We suppress superscripts since all the methods discussed are one-step methods and other superscripts will be needed below). Godunov's method for the homogeneous conservation law (2) is derived by viewing the data at time t_n as defining a piecewise constant function with value W_i in the i th cell and jump discontinuities at the cell interfaces $x_{i-1/2}$, as shown in Fig. 1a. Solving the Riemann problems at the interfaces gives rise to waves propagating in the x-t plane, as indicated in Fig. 1b.

(a)

(b)
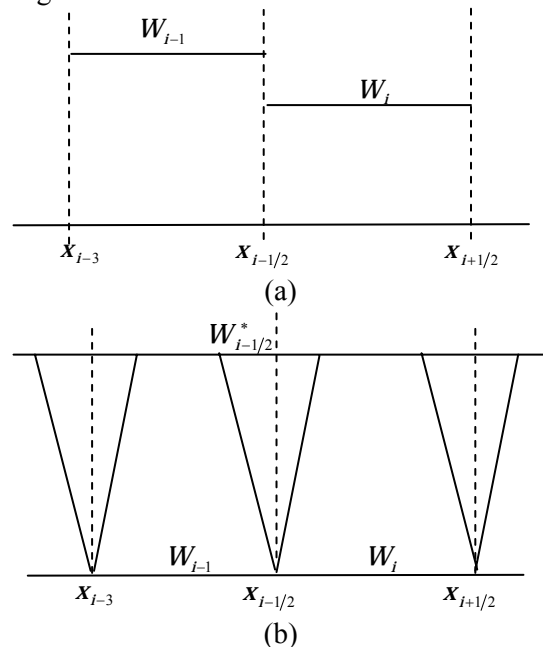
Figure. 1. (a) Data in two adjacent grid cells, viewed as defining a piecewise constant function for Godunov's method. (b) Structure of the solution to the resulting Riemann problems, as seen in the x-t plane.

If $W_{i-1/2}^*$ denotes the value of the Riemann solution along the interface $x_{i-1/2}$ for $t > t_n$, then Godunov's method can be written as

$$\overline{W}_i = W_i - \frac{\Delta t}{\Delta x}\left(F\left(W_{i+1/2}^*\right) - F\left(W_{i-1/2}^*\right)\right)$$
$$+ \Delta t G(W_{i-1/2}^*, W_{i+1/2}^*) \qquad (4)$$
$$= W_i - \frac{\Delta t}{\Delta x}\left(A^+\Delta W_{i-1/2} - A^-\Delta W_{i+1/2}\right)$$
$$+ \Delta t G(W_{i-1/2}^*, W_{i+1/2}^*)$$

where G is the numerical source term and the function φ, the numerical flux, the notation of flux splitting is used for flux differences

$$A^+\Delta W_{i-1/2} = F(W_i) - F\left(W_{i-1/2}^*\right)$$
$$A^-\Delta W_{i+1/2} = F\left(W_{i+1/2}^*\right) - F(W_i) \qquad (5)$$

Note, however, that the notation has been modified here to use $i-1/2$ as the index for the interface between cells *i-1* and *i* (rather than using *i* for this index). In this paper it will be important to make distinctions between edge values and cell-centered values.

Solving the Riemann problem at $x_{i-1/2}$ gives a flux difference splitting

$$F(W_i) - F(W_{i-1}) = A^-\Delta W_{i-1/2} + A^+\Delta W_{i-1/2} \ (6)$$

The right-going portion $A^+\Delta W_{i-1/2}$ modifies the cell average W_i while the left-going portion $A^-\Delta W_{i-1/2}$ modifies the cell average W_{i-1}.

Often this splitting is accomplished by decomposing the jump $W_i - W_{i-1}$ into a set of waves $W_{i-1/2}^p$ propagating with speeds $\lambda_{i-1/2}^p$, for $p = 1,2,...,M_W$, where M_W is the number of waves (typically equal to the dimension of the system). Then we have

$$W_i - W_{i-1} = \sum_{p=1}^{M_w} W_{i-1/2}^p \qquad (7)$$

While the Rankine–Hugoniot condition across each wave results in

$$F(W_i) - F(W_{i-1}) = \sum_{p=1}^{M_W} \lambda_{i-1/2}^p . W_{i-1/2}^p$$

The simplest example is a constant coefficient linear system, $F(W) = A.W$ in which case the waves are eigenvectors of *A* with the wave speeds being the corresponding eigenvalues. For a nonlinear system such as the shallow water equations, the physical waves are typically shocks or rarefaction waves, but a Roe and Van Leer linearization are used so that the waves and speeds are eigenvectors of an average Jacobian matrix $A_{i-1/2}$ determined by Q_{i-1} and Q_i. The flux difference splitting is then given by:

$$A^-\Delta W_{i-1/2} = \sum_{p=1}^{M_W} \left(\lambda_{i-1/2}^p\right)^- . W_{i-1/2}^p$$

$$A^+\Delta W_{i-1/2} = \sum_{p=1}^{M_W} \left(\lambda_{i-1/2}^p\right)^+ . W_{i-1/2}^p$$

where, $\lambda^+ = \max(\lambda,0)$, $\lambda^- = \min(\lambda,0)$. Only this flux difference splitting is needed for Godunov's method, but the individual waves and speeds, coupled with nonlinear limiters, are used further to define second-order correction terms in the high-resolution methods

The flux function F can be written as F (W) = A (W) W, matrix A is diagonalizable if h > 0, concretely $A = X\Lambda X^{-1}$, where

$$\Lambda = \begin{pmatrix} \lambda_1 & 0 \\ 0 & \lambda_2 \end{pmatrix}, \lambda_1 = \frac{q}{h} - \sqrt{gh},$$

$$\lambda_2 = \frac{q}{h} - \sqrt{gh}, X = \begin{pmatrix} 1 & 1 \\ \lambda_1 & \lambda_2 \end{pmatrix} \qquad (8)$$

This naturally yields the flux decomposition $F(W) = F^+(W) + F^-(W)$ where

$$F^{\pm}(W) = A^{\pm}(W).W,$$

with $A^{\pm}(W) = X.\Lambda^{\pm}.\Lambda$ (9)

and $\Lambda^+ = \begin{pmatrix} \max(\lambda_1,0) & 0 \\ 0 & \max(\lambda_2,0) \end{pmatrix}$,

$$\Lambda^- = \begin{pmatrix} \min(\lambda_1,0) & 0 \\ 0 & \min(\lambda_2,0) \end{pmatrix} \quad (10)$$

In accordance with this decomposition, the flux-splitting schemes are built from numerical flux functions of the form

$$\varphi(U,V) = \varphi^+(U,V) + \varphi^-(U,V) \quad (11)$$

with

$$\varphi^+(U,V) = B_1(U,V).U,$$

$$\varphi^-(U,V) = B_2(U,V).V \quad (10)$$

where B_1 and B_2 are 2×2 matrices that should be specified for each actual scheme. φ^+ and φ^- respectively represent up winding to the left and to the right.

A consistent scheme for the homogeneous equation is obtained if B1 and B2 verify

$$F^+(W) = B_1(W,W)W,$$

$$F^-(W) = B_2(W,W)W \quad (12)$$

The schemes of Steger-Warming and Vijayasundaram, are defined respectively by $B_1(U, V) = A^+(U)$, $B_2(U, V) = A^-(V)$ and $B_1(U, V) = A^+((U + V)/2)$, $B_2(U, V) = A^-((U +V)/2)$.

3. Treatment term source of Bermudez and Vazquez.

In this section we construct the numerical source function associated to the schemes. The construction of G must reflect an up winding of the source term according to the construction of the numerical flux function. In this case, matrices of re-scaling must be introduced, with the aim of achieving the condition of enhanced consistency.

Following this idea we start from the following expression:

$$G = A \cdot A^{-1}G = \left(\frac{A}{2} + \frac{|A|}{2} + \frac{A}{2} - \frac{|A|}{2} \right) \cdot A^{-1} \cdot G$$

$$= \underbrace{\frac{1}{2}\left(G + |A| \cdot A^{-1}G\right)}_{G_L} + \underbrace{\frac{1}{2}\left(G - |A| \cdot A^{-1}G\right)}_{G_R}$$

(13)

For the sake of brevity we only define the numerical source functions corresponding to:

$$G(x_{i-1}, x_i, x_{i+1}, W_{i-1}, W_i, W_{i+1})$$
$$= \frac{1}{2}\left(G_{i,L} + G_{i,UL}\right) + \frac{1}{2}\left(G_{i,R} + G_{i,UR}\right) \quad (14)$$

with the following definition for $(G)_{i,L}$, $(G)_{i,R}$, $(G)_{i,UL}$ and $(G)_{i,UR}$.

$$G_{i,L} = \begin{pmatrix} 0 \\ g\frac{(h_{i-1} + h_i)}{2} \cdot \frac{(Z_i - Z_{i-1})}{\Delta x} \end{pmatrix},$$

$$G_{i,R} = \begin{pmatrix} 0 \\ g\frac{(h_i + h_{i+1})}{2} \cdot \frac{(Z_{i+1} - Z_i)}{\Delta x} \end{pmatrix} \quad (17)$$

We define $(G)_{i,UL}$ and $(G)_{i,UR}$ as

$$G_{i,UL} = \frac{1}{\Delta x}\left[A(W_{i-1/2})|A^{-1}(W_{i-1/2}) \right.$$
$$\left. \begin{pmatrix} 0 \\ g\frac{(h_{i-1} + h_i)}{2} \cdot (Z_i - Z_{i-1}) \end{pmatrix} \right] \quad (18)$$

$$G_{i,UR} = \frac{1}{\Delta x}\left[A(W_{i+1/2})|A^{-1}(W_{i+1/2}) \right.$$
$$\left. \begin{pmatrix} 0 \\ g\frac{(h_i + h_{i-1})}{2} \cdot (Z_{i+1} - Z_i) \end{pmatrix} \right] \quad (19)$$

Beside this definition for $(G)_{i,L}$, $(G)_{i,R}$, $(G)_{i,UL}$ and $(G)_{i,UR}$, we have also some definition of Steger Warming and Vijayasundaram.

Steger Warming:

$$G_{i,L} = \left(\begin{matrix} 0 \\ g\dfrac{(h_{i-1}+h_i)}{2}.\dfrac{(Z_i - Z_{i-1})}{\Delta x} \end{matrix} \right),$$

$$G_{i,R} = \left(\begin{matrix} 0 \\ g\dfrac{(h_i+h_{i+1})}{2}.\dfrac{(Z_{i+1} - Z_i)}{\Delta x} \end{matrix} \right) \qquad (15)$$

We define $(G)_{i,UL}$ and $(G)_{i,UR}$ by

$$G_{i,UL} = \frac{1}{\Delta x}\left[|A(W_i)|A^{-1}\left(\frac{W_{i-1}+W_i}{2}\right)\left(g\frac{\overset{0}{(h_{i-1}+h_i)}}{2}.Z_i\right) - \right.$$

$$\left. - |A(W_{i-1})|A^{-1}\left(\frac{W_{i-1}+W_i}{2}\right)\left(g\frac{\overset{0}{(h_{i-1}+h_i)}}{2}.Z_{i-1}\right)\right]$$

$$(16)$$

$$G_{i,UR} = \frac{1}{\Delta x}\left[|A(W_{i+1})|A^{-1}\left(\frac{W_i+W_{i+1}}{2}\right)\left(g\frac{\overset{0}{(h_i+h_{i+1})}}{2}.Z_{i+1}\right) \right.$$

$$\left. - |A(W_i)|A^{-1}\left(\frac{W_i+W_{i+1}}{2}\right)\left(g\frac{\overset{0}{(h_i+h_{i+1})}}{2}.Z_i\right)\right]$$

$$(17)$$

Vijayasundaram:

$$G_{i,L} = \left(\begin{matrix} 0 \\ g\dfrac{(h_{i-1}+h_i)}{2}.\dfrac{(Z_i - Z_{i-1})}{\Delta x} \end{matrix} \right),$$

$$G_{i,R} = \left(\begin{matrix} 0 \\ g\dfrac{(h_i+h_{i+1})}{2}.\dfrac{(Z_{i+1} - Z_i)}{\Delta x} \end{matrix} \right) \ (17)$$

where by $h_{j+1/2}$ represent $(h_j + h_{j+1})/2$. We define $(G)_{i,UL}$ and $(G)_{i,UR}$ as

$$G_{i,UL} = \frac{1}{\Delta x}\left[A(W_{i-1/2})\,A^{-1}(W_{i-1/2}) \right.$$

$$\left. \left(g\frac{\overset{0}{(h_{i-1}+h_i)}}{2}.(Z_i - Z_{i-1})\right)\right] \qquad (18)$$

$$G_{i,UR} = \frac{1}{\Delta x}\left[A(W_{i+1/2})\,A^{-1}(W_{i+1/2}) \right.$$

$$\left. \left(g\frac{\overset{0}{(h_i+h_{i-1})}}{2}.(Z_{i+1} - Z_i)\right)\right] \qquad (19)$$

4. Treatment source term of R. J. Leveque

Godunov's method and the wave-propagation algorithm are based on viewing the finite volume cell average in each time step as defining a piecewise constant function with constant value W_i in the i th grid cell. Solving the Riemann problem between W_{i-1} and W_i at a cell interface gives a set of waves which affect both of the cell averages over the next time step.

The basic idea explored here is to introduce a new discontinuity in the center of each grid cell at the start of each time step, with value W_i^- on the left half of the cell and W_i^+ on the right half. These values are chosen so that

$$\frac{1}{2}\left(W_i^- + W_i^+\right) = W_i \qquad (20)$$

and also, if possible, that

$$F\left(W_i^-\right) - F\left(W_i^+\right) = \psi\left(W_i, x_i\right)\Delta x \qquad (21)$$

The condition (20) guarantees that the cell average is unchanged by the modification, while (21), if satisfied, means that the waves resulting from solving the Riemann problem at this new discontinuity will exactly cancel the effect of the source term in this cell. Hence it is not necessary to solve this newly introduced Riemann problem or deal with the resulting waves in the algorithm, nor is it necessary to apply the source term any longer. By ignoring both, we respect the steady state balance inherent in the equations. (Note that (5) is a discrete version of $F(W)_x = \psi$)

We must still solve Riemann problems at the cell interfaces, but these are now between modified states W_i^- and W_{i-1}^+ rather than between W_i and W_{i-1} (see Fig. 2). If the solution is quasi-steady then $W_{i-1}^+ \approx W_i^-$

(whereas W_i and W_{i-1} might have had a large jump between them if the steady state solution has rapid spatial variation, leading to "strong" waves in the Riemann solution). By solving the Riemann problem between W_i^- and W_{i-1}^+ we are working directly with the perturbations from steady state, as desired. The resulting "weak" waves modify the cell averages by small amounts corresponding directly to the dynamic perturbations, rather than making larger changes based on strong waves which must later be undone by the source terms. By contrast, in a fractional step approach the limiters are applied to the strong waves coming from the original data, and if these are rapidly varying then the limiting procedure can lead to a complete corruption of the small amplitude perturbations of interest.

In this paper the shallow water equations (in one and two dimensions) will be used as an example. The shallow water equations have the advantage of being a relatively simple system where the ideas are easy to explain and interpret physically. With this example it is also possible to put in any reasonable bottom topography and have a physically meaningful test problem, which is not the case with gravitational source terms, for example, where only certain forms of the source term make sense. Hence the approach can be subjected to a wider variety of tests. The shallow water equations with bottom topography are also extremely important in their own right.

Modifications for source terms.

Now suppose we replace the constant value W_i in Fig. 1 by two values W_i^- and W_i^+ with a jump at the cell center, as shown in Fig. 2a. If W_i^+ and W_i^- are chosen as

$$
\begin{aligned}
W_i^- &= W_i - \delta_i \\
W_i^+ &= W_i + \delta_i
\end{aligned}
\tag{22}
$$

for some vector δ_i, then (4) will be satisfied and total mass will be preserved. If we now apply the idea of Godunov's method, advancing forward in time for this piecewise constant data, we obtain the x-t structure shown in Fig. 2b.

(a)

(b)
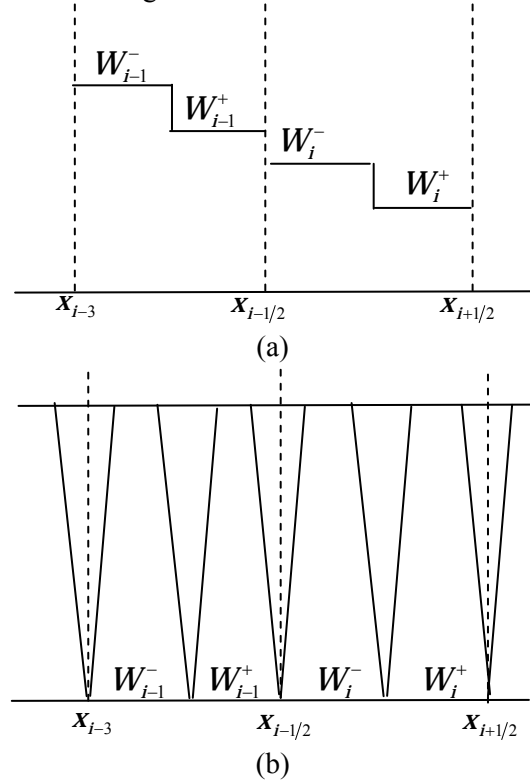
Figure 2. (a) The same data in two adjacent grid cells as in Fig. 1, after introducing a jump – in the center of each grid cell for the quasi-steady method. (b) Structure of the solution to the resulting Riemann problems, as seen in the x-t plane.

In addition to the Riemann problems at the cell edges, there is a Riemann problem to be solved at the cell center which also leads to a set of waves. For a sufficiently small time step Δt (small enough that the Courant number is less than 1/2), the waves remain entirely within the i th cell. The cell average is now updated by the incoming waves from each cell edge, as before, and also by all the waves from the Riemann problem at the cell center, since they all remain in this cell. As a result, we do not need to actually solve this Riemann problem to split the flux difference

$F\left(W_i^+\right) - F\left(W_i^-\right)$ into left-going and right-going pieces, since both will be used to update the cell average. If we now denote the flux difference splitting at the cell interfaces by $A^+\Delta\widetilde{Q}_{i-1/2}$ (incoming waves from the left edge, arising from solving the Riemann problem between Q_{i-1}^+ and Q_i^- $A^+\Delta\widetilde{Q}_{i+1/2}$ (incoming waves from the right edge), then the full update formula is now

$$\overline{W}_i = W_i - \frac{\Delta t}{\Delta x}\left(A^+\Delta\widetilde{W}_{i-1/2} - A^-\Delta\widetilde{W}_{i+1/2}\right)$$
$$- \frac{\Delta t}{\Delta x}\left(F\left(W_i^+\right) - F\left(W_i^-\right)\right)$$

$$(23)$$

The tildes on $A^+\Delta\widetilde{W}_{i-1/2}$ and $A^-\Delta\widetilde{W}_{i-1/2}$ serve as a reminder that the flux-difference splitting is now based on modified data W_{i-1}^+ and W_i^-

Now suppose there is a source term $\psi(q, x)$ in the equation, giving (1). Then a simple first order unsplit method results from taking the Godunov update (11) and also adding in $\Delta t.\psi(Q_i, x_i)$ the source contribution over time Δt. Adding this to (11) results in

$$\overline{W}_i = W_i - \frac{\Delta t}{\Delta x}\left(A^+\Delta\widetilde{W}_{i-1/2} - A^-\Delta\widetilde{W}_{i+1/2}\right)$$
$$- \Delta t.\left(\psi(Q_i, x_i) - \frac{1}{\Delta x}\left(F\left(W_i^+\right) - F\left(W_i^-\right)\right)\right)$$

$$(24)$$

If we can choose δ_i in (10) so that (5) is satisfied, then the final term here drops out and we have a method that looks identical to the original Godunov method (6), but with the flux difference splitting $A^\pm\Delta\widetilde{W}_{i-1/2}$ determined by solving the Riemann problems with data W_{i-1}^+ and W_i^- used rather than the original flux-difference splitting $A^\pm\Delta W_{i-1/2}$ based on W_{i-1} and W_i.

Linear systems

First consider the linear hyperbolic system with a (possibly nonlinear) source term,

$$W_t + AW_x = \psi \quad (25)$$

We assume that ψ is a smooth function of q and also that A is nonsingular. Then any steady state solution is smooth and satisfies

$$W_x = A^{-1}\psi \quad\quad\quad (26)$$

together with appropriate boundary conditions.

When A is nonsingular, the condition (5) can always be satisfied in each grid cell for the system (13). Given a state W_i we need to find δ_i so that $W_i^- = W_i - \delta_i$, $W_i^+ = W_i + \delta_i$ satisfy

$$A\left(W_i^+ - W_i^-\right) = \Delta x.\psi$$

where $\psi_i = \psi(W_i, x_i)$; which leads to

$$\delta_i = \frac{\Delta x}{2} A^{-1}\psi_i \quad\quad\quad (27)$$

For the linear system, the Riemann problem can be explicitly solved in terms of the eigenstructure of A. Let

$$A = R\Lambda R^{-1}$$

where $\Lambda = diag\left(\lambda^p\right)$ is the matrix of eigenvectors and

$$R = \left[r^1 \mid r^2 \mid ... \mid r^m\right]$$

is the matrix of right eigenvectors, $A.r^p = \lambda^p.r^p$.
Let $\lambda^+ = \max(\lambda, 0)$, $\lambda^- = \min(\lambda, 0)$ and set

$$\Lambda^\pm = diag\left(\left(\lambda^p\right)^\pm\right)$$
$$A^\pm = R.\Lambda^\pm.R^{-1}$$

$$(28)$$

so that $A = A^+ + A^-$ gives a splitting of A into pieces with nonnegative eigenvalues and pieces with non positive eigenvalues, respectively.

For the homogeneous problem with $\psi \equiv 0$, Godunov's method reduces to

$$\overline{W}_i = W_i$$
$$- \frac{\Delta t}{\Delta x}\left(A^+(W_i - W_{i-1}) + A^-(W_{i+1} - W_i)\right)$$

This is simply the upwind method. The waves $W_{i-1/2}^p$ are eigenvectors of A

Now suppose there is a source term and we choose δ_i as in (15) so that this source term is exactly cancelled. Godunov's method as extended in Section 2 then becomes

$$\overline{W}_i = W_i$$
$$- \frac{\Delta t}{\Delta x}\left(A^+(W_i^- - W_{i-1}^+) + A^-(W_{i+1}^- - W_i^+)\right)$$

Using $W_i^\pm = W_i \pm \delta_i$ in this expression and rearranging terms shows that

$$\overline{W}_i = W_i$$
$$- \frac{\Delta t}{\Delta x}\left(A^+(W_i - W_{i-1}) + A^-(W_{i+1} - W_i)\right) \quad (29)$$
$$+ \Delta t\left(A^+ A^{-1}\psi_{i-1/2} + A^+ A^{-1}\psi_{i+1/2}\right)$$

where $\psi_{i-1/2} = \frac{1}{2}\left(\psi_{i-1} + \psi_i\right)$

If $\psi = gh\frac{\partial Z}{\partial x}$ then

$$\psi_{i-1/2} = \frac{1}{2}\left(g(h_{i-1} + h_i).\frac{Z_i - Z_{i-1}}{\Delta x}\right)$$

exactly similar to the treatment of Bermudez and Vazquez.

Hence, for the linear system, this method is equivalent to applying the upwind method to the original data but with a first order approximation to the source term also included. Note that

$$A^+ A^{-1} + A^- A^{-1} = \left(A^+ + A^-\right)A^{-1} = I$$

so that the final term in (18) does give a consistent approximation to $\Delta t\psi_i$. This term can also be interpreted as follows: $\psi_{i-1/2}$ is

an approximation to the source term at $x_{i-1/2}$, which is split into two pieces $A^- A^{-1}\psi_{i-1/2}$ and $A^+ A^{-1}\psi_{i-1/2}$ (which sum to $\psi_{i-1/2}$). The first piece is used to modify W_{i-1} while the latter modifies W_i. This amounts to projecting $\psi_{i-1/2}$ onto the right-going characteristics to compute the portion updating W_i and onto the left-going characteristics to compute the portion updating W_{i-1}. This approach is often used for source terms even for nonlinear problems, in which case the eigenstructure of the Roe matrix at $x_{i-1/2}$ might be used to split $\psi_{i-1/2}$, for example.

Quasi-steady flow

There are other steady states besides the stationary state with u=0, consisting of steady flow in which the momentum m is constant in x but nonzero. There are several different regimes of such flow, depending on the bottom topography and the free stream Froude number $Fr = u/\sqrt{gh}$ (analogous to the Mach number in compressible gas dynamics). If the free stream Froude number is sufficiently small then the flow is entirely sub critical .Fr<1 everywhere), while if the free stream Froude number is sufficiently large then the flow is entirely supercritical .Fr>1 everywhere). In both these cases the solution is smooth and the quasi-steady method proposed here appears to work just as well as for the stationary steady state.

Case matrix A is singular

For intermediate free stream Froude numbers, the flow can be Tran critical with transitions where Fr passes through 1, and hence one of the eigenvalues $u \pm \sqrt{gh}$ of the Jacobian passes through 0. Referring back to the case of a linear system discussed in Section 4, this would correspond to a singular matrix A. Note that in this case there

exist vectors [q] for which A[q]=0, which means the Rankine–Hugoniot conditions can be satisfied with speed 0. It is only in this singular case that the steady state solution can contain a stationary shock. Figure 5

shows one such case, in which the free stream Froude number is less than one but the flow accelerates to a supercritical value over the hump and then decelerates through a shock wave on the lee side of the ridge.
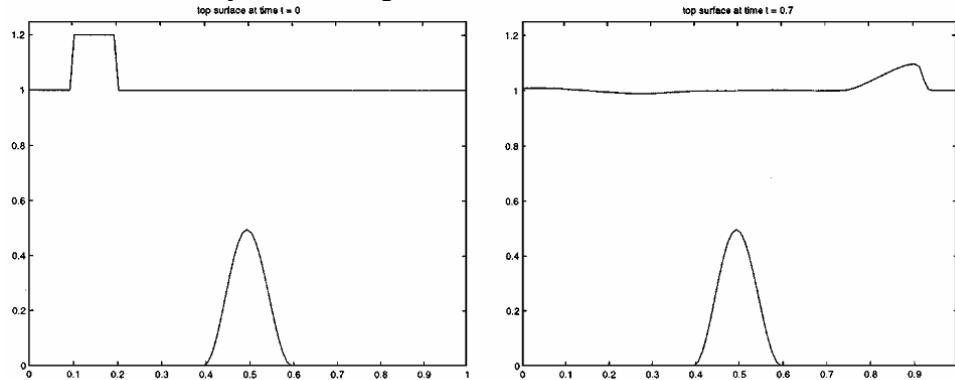
Figure 3. Bottom topography and top surface for the one-dimensional shallow water equations of the case ε=0.2. At time t=0.7 the right-going portion of the pulse has moved past the hump.
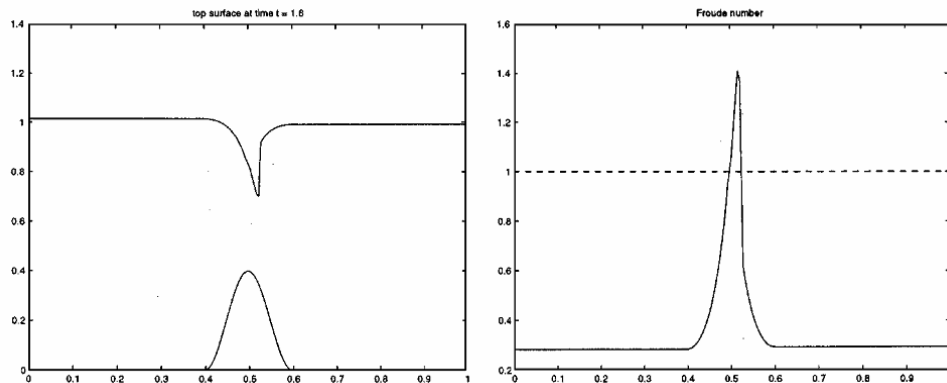
FIG. 4. Trans critical flow over a ridge, where the Froude number passes through 1 and the steady state solution contains a shock wave. Values are computed with the quasi-steady method after obtaining an initial approximation with a fractional step method

Recalling the expression (27) for δ_i in the case of a linear system, it might be expected that difficulties can arise in solving for the required δ_i in the trans critical case. The solution shown in Fig.4 was computed by starting with impulsive initial data h(x,0)=1-B(x) and u=03 and marching forward in time. At the time when the shock first forms, non convergence of the Newton iteration was observed when using the quasi-steady method as described above.

Instead of using the quasi-steady method from the start, the fractional step method or

other method should be used until after the shock formed and an approximate steady state was reached, at which point the quasi-steady method could be successfully used without further difficulty (in spite of the singularity of the Jacobian). It is not surprising that the fractional step or other approach is more robust than the quasi-steady approach for data that are not close to steady state.

Once an approximate steady state is reached, the quasi-steady method appears to work well in many, though not all, trans critical cases. This requires further study, and

the trans critical case is mentioned here primarily as a caution to potential users of this approach.

5. First numerical test

Water at rest: The first test is the water at rest with a variable topography. We check if the finite volume solver is "well balanced" or not. That means that it must preserves at least water at rest solutions. The test is totally satisfactory.
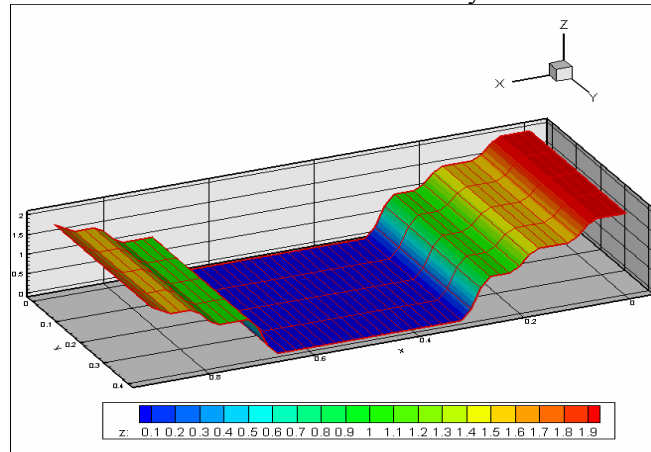
Figure 5. The topography variable of the test water at rest.

6. Conclusions:

The quasi-steady wave-propagation method introduced here allows one to accurately incorporate source terms into high-resolution Godunov methods for a certain class of problems. In particular, if the solution is close to a steady state in which the source terms balance the flux gradient, then this approach results in Riemann solvers and limiters being applied to small jumps at cell interfaces corresponding to the deviation from steady state, rather than to larger deviations within the steady state. This results in excellent resolution of the propagation of small perturbations.

For source term problems where the solution is far from steady state, this quasi-steady approach is probably not appropriate. The present method also has some difficulties in the case of transcritical steady states, where the steady state includes a shock across which the Jacobian is singular.

References

[1] A. Bermudez, A. Dervieux, J. A. Desideri, M. E. Vazquez Cendon, Upwind schemes for the two-dimensional shallow water equations with variable depth using unstructured meshes. Comput. Methods Appl. Mech. Eng. 155,49(1998)

[2] R.J. LeVeque Balancing Source Terms and Flux Gradients in High-Resolution Godunov Methods : The Quasi-Steady Wave-Propagation Algorithm. J. Comput. Phys. 146, 346-365 (1998).

[3] E F. Toro. Shock-Capturing Methods for Free-Surface Shalow Flows. Springer (1999).

[4] E.D. Fernandez-Nieto, D. Bresch, J. Monnier, A consistent intermediate wave speed for a well-balanced HLLC solver. Comptes Rendus de l Académie des Sciences - Series I - Mathematics 346, 795-800 (2008).

[5] Emmanuel Audusse , Modelisation hyperbolique et analyse numerique pour les ecoulements en eaux peu profondes. Ph.D.Thesis L'Universite Pierre et Marie Curie Paris VI, 2004

[6] J.G. Zhou, D.M. Causon, C.G. Mingham, and D. M. Ingram. The Surface Gradient Method for the Treatment of Source Terms in the Sallow-Water Equations. J. Comput. Phys., Vol. 168 pp. 1-25 (2001)

Buckling and Postbuckling of Functionally Graded Cylindrical Shells Subjected to Mechanical and Thermal Loads

Nguyen Dinh Duc[a], Hoang **Van Tung** [b]

[a] *University of Engineering and Technology,*
Vietnam National University, Ha Noi, Viet Nam.
[b] *Faculty of Civil Engineering, Hanoi Architectural University, Ha Noi, Viet Nam*

Abstract

This paper presents an analytical approach to investigate the buckling and postbuckling of functionally graded cylindrical shells under axial compressive and thermal loads. Material properties are assumed to be temperature-independent, and graded in the thickness direction according to a simple power law distribution in terms of the volume fraction of constituents. Equilibrium and compatibility equations for cylindrical shells are derived by using the classical shell theory with both geometrical nonlinearity in von Karman-Donnell sense and initial geometrical imperfection are taken into consideration. The resulting equations are then solved by Galerkin method to determine closed-form expressions of buckling loads and postbuckling load-deflection curves. Stability analysis for a simply supported cylindrical shell show the effects of material and geometric parameters, buckling mode and imperfection on the behavior of the shell.

Keywords: *Functionally graded material, classical shell theory, Postbuckling, Cylindrical shell*

1. Introduction

In recent years, Functionally Graded Materials (FGMs) which named by a group of material scientists in Japan in 1984, have attracted much interest as high performance heat resistant materials for aircraft, space vehicles and other engineering applications. Functionally graded materials are composite materials, which are microscopically inhomogeneous, and the mechanical properties vary smoothly and continuously from one surface to the other. It is this continuous change that results in gradient properties in functionally graded materials. Typically, these materials are made from a mixture of metal and ceramic or a combination of different metals. Unlike fiber-matrix composite which have a strong mismatch of mechanical properties across the interface of two discrete materials bonded together and may result in debonding at high temperature, functionally graded materials have the advantage of being able to withstand very high temperature environments and extremely large temperature gradients, while maintaining their structural integrity. The ceramic material provides high temperature resistance

due to its low thermal conduction and expansion coefficients while the ductile metal component prevents fracture due to thermal stresses. Furthermore, a mixture of ceramic and metal with a continuously varying volume fraction can be easily manufactured.

The generation of this type of material poses many problems for material and mechanics scientists, especially researchers on structures made of functionally graded materials such as FGM plates and shells. Eslami and his co-workers [2-5] used an analytical approach to investigate the linear buckling of FGM rectangular plates under mechanical and thermal loads. They employed the classical plate theory [2, 3] and higher order shear deformation theory [4, 5] and adjacent equilibrium criterion basing on assumption of small deflection to derive closed-form expressions of critical loadings of simply supported FGM plates. Then these studies were extended for imperfect FGM plates under mechanical and thermal loads [7, 8]. Lanhe [6] also studied thermal buckling of a a simply supported moderately thick rectangular FGM plate by using the first order shear deformation theory. Na and Kim [9] used the finite element method with 18 node solid element to analyze thermomechanical buckling for functionally graded composite plates including metal, FGM and ceramic layers. Linear stability of FGM cylindrical shells under thermal loads has been reported by Shashiah and Eslami [11] and Lanhe et al. [12] by making use of analytical approaches. Postbuckling behavior of FGM rectanglular plates under various kinds of loading such as mechanical, thermal and electric loads has been treated in studies [13-18]. In addition, the postbuckling behavior of FGM cylindrical shells has been investigated in works [19-24].

In this report, buckling and postbuckling behaviors of FGM cylindrical shells subjected to axial compression and thermal loads are investigated by an analytical approach. Material properties of constituents are assumed to be temperature independent and effective properties of FGM shell are graded in the thickness direction according to a simple power law distribution in terms of volume fractions of constituents. Equilibrium and compatibility equations are established within the framework of classical shell theory taking into account geometrical nonlinearity in von Karman-Donnell sense and initial geometrical imperfection. Explicit expressions of buckling loads and postbucking paths are determined by Galerkin method and stability analysis of simply supported FGM shells is carried out to show the effects of material and geometrical properties, buckling and imperfection on the behavior of shells.

2. Functionally graded cylindrical shells

Consider a functionally graded circular shell of radius of cavature R, thickness h and length L as shown in Fig. 1. The shell is made of a mixture of ceramics and metals and is defined in coordinate system (x, θ, z), where x and θ are in the axial and circumferential directions of the shell, respectively, and z is perpendicular to the middle surface and points inwards ($-h/2 \leq z \leq h/2$). Suppose that the material composition of the shell varies smoothly along the thickness in such a way that the inner surface is ceramic-rich and the outer surface is metal-rich by following a simple power law in terms of the volume fractions of the constituents as

$$V_c(z) = \left(\frac{2z+h}{2h}\right)^k \quad , \quad V_m(z) = 1 - V_c(z) \quad (1)$$

where V_c and V_m are the volume fractions of ceramic and metal constituents, respectively, and volume fraction index k is a nonnegative number ($0 \leq k < \infty$).
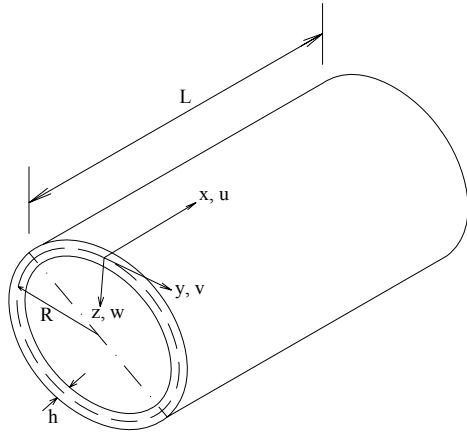
Figure. 1. Configuration and the coordinate system of the FGM cylindrical shell

We assume that the effective properties P_{eff} of functionally graded shell, such as the modulus of elasticity E and the coefficient of thermal expansion α change in the thickness direction z and can be determined by the linear rule of mixture as

$$P_{eff}(z) = \text{Pr}_c V_c(z) + \text{Pr}_m V_m(z) , \qquad (2)$$

where Pr denotes a temperature-independent material property, and subscripts m and c stand for the metal and ceramic constituents, respectively.

From Eqs. (1) and (2) the effective properties of FGM cylindrical shell can be written as follows in which Poisson ratio ν is assumed to be constant.

$$[E(z), \alpha(z)] = [E_m, \alpha_m],$$
$$+[E_{cm}, \alpha_{cm}]\left(\frac{2z+h}{2h}\right)^k \quad \nu(z) = \nu \qquad (3)$$

where

$$E_{cm} = E_c - E_m , \ \alpha_{cm} = \alpha_c - \alpha_m . \qquad (4)$$

It is evident that $E = E_c, \alpha = \alpha_c$ at $z = h/2$ and $E = E_m, \alpha = \alpha_m$ at $z = -h/2$.

3. Basic equations

In the present study, the classical shell theory is used to obtain the equilibrium and compatibility equations as well as expressions of buckling loads and postbuckling load-deflection paths of FGM cylindrical shells.

The strains across the shell thickness at a distance z from the middle surface are

$$\varepsilon_x = \varepsilon_{xm} + zk_x , \ \varepsilon_y = \varepsilon_{ym} + zk_y ,$$
$$\gamma_{xy} = \gamma_{xym} + zk_{xy} \qquad (5)$$

where ε_{xm} and ε_{ym} are the normal strains, γ_{xym} is the shear strain at the middle surface of the shell and k_x, k_y, k_{xy} are the curvatures and twist.

Within the framework of the Donnell shell theory, the strains at the middle surface and the curvatures, twist are related to the displacement components u, v, w in the x, y, z coordinate directions, respectively, as [1]

$$\varepsilon_{xm} = u_{,x} + \frac{1}{2}w_{,x}^2, \varepsilon_{ym} = v_{,y} - \frac{w}{R} + \frac{1}{2}w_{,y}^2,$$
$$\gamma_{xym} = u_{,y} + v_{,x} + w_{,x}w_{,y} ,$$
$$k_x = -w_{,xx} , \ k_y = -w_{,yy} , \ k_{xy} = -w_{,xy} \qquad (6)$$

where $y = R\theta$ and subscript $(,)$ indicates the partial derivative. Hooke law for a functionally graded cylindrical shell including temperature effects is defined as

$$(\sigma_x, \sigma_y) = \frac{E}{1-\nu^2}\Big[(\varepsilon_x, \varepsilon_y) + \nu(\varepsilon_y, \varepsilon_x)$$
$$-(1+\nu)\alpha\Delta T(1,1)\Big], \ \sigma_{xy} = \frac{E}{2(1+\nu)}\gamma_{xy}, (7)$$

where ΔT is change of environment temperature from stress free initial state or temperature difference between inner and outer surfaces of the shell.

The force and moment resultants of a shell are expressed in terms of the stress components through the thickness as

$$\left(N_{ij}, M_{ij}\right) = \int\limits_{-h/2}^{h/2} \sigma_{ij}\left(1,z\right)dz, \quad ij = x, y, xy$$
(8)

Substituting Eqs. (3), (5) and (7) into Eqs. (8) gives the constitutive relations as

$$(N_x, M_x) = \frac{\left(E_1, E_2\right)}{1-v^2}\left(\varepsilon_{xm} + v\varepsilon_{ym}\right)$$
$$+ \frac{\left(E_2, E_3\right)}{1-v^2}\left(k_x + vk_y\right) - \frac{\left(\Phi_m, \Phi_b\right)}{1-v} \; ,$$

$$(N_y, M_y) = \frac{\left(E_1, E_2\right)}{1-v^2}\left(\varepsilon_{ym} + v\varepsilon_{xm}\right)$$
$$+ \frac{\left(E_2, E_3\right)}{1-v^2}\left(k_y + vk_x\right) - \frac{\left(\Phi_m, \Phi_b\right)}{1-v} \; ,(9)$$

$$(N_{xy}, M_{xy}) = \frac{\left(E_1, E_2\right)}{2(1+v)}\gamma_{xym} + \frac{\left(E_2, E_3\right)}{1+v}k_{xy} \; ,$$

where

$$E_1 = E_m h + E_{cm} h/(k+1) \; ,$$
$$E_2 = E_{cm} h^2 \left[1/(k+2) - 1/(2k+2)\right] \; ,$$
$$E_3 = E_m h^3/12 + E_{cm} h^3 \left[1/(k+3)\right.$$
$$\left. - 1/(k+2) + 1/(4k+4)\right] \; , \quad (10)$$

$$\left(\Phi_m, \Phi_b\right) = \int\limits_{-h/2}^{h/2}\left[E_m + E_{cm}\left(\frac{2z+h}{2h}\right)^k\right]\times$$

$$\left[\alpha_m + \alpha_{cm}\left(\frac{2z+h}{2h}\right)^k\right]\Delta T(1,z)dz \; .$$

Nonlinear equilibrium equation of an imperfect FGM cylindrical shell based on the classical shell theory is given as [26]

$$D\nabla^4 w - f_{,xx}/R - f_{,yy}\left(w_{,xx} + w^*_{,xx}\right)$$
$$+ 2f_{,xy}\left(w_{,xy} + w^*_{,xy}\right) - f_{,xx}\left(w_{,yy} + w^*_{,yy}\right) - q = 0$$
(11)

where $\nabla^2 = \partial^2/\partial x^2 + \partial^2/\partial y^2$, q is uniform lateral pressure, and

$$D = \frac{E_1 E_3 - E_2^2}{E_1(1-v^2)}.$$
(12)

In Eq. (11), $w^*(x,y)$ denotes a known small imperfection representing a small initial deviation of the shell surface from a circular cylindrical shape. Also, $f(x,y)$ is a stress function defined as

$$N_x = f_{,yy} \; , \; N_y = f_{,xx} \; , \; N_{xy} = -f_{,xy} \; . \; (13)$$

The compatibility equation of an imperfect FGM cylindrical shell may be established as follows [26]

$$\nabla^4 f - E_1(w^2_{,xy} - w_{,xx}w_{,yy} - w_{,xx}/R + 2w_{,xy}w^*_{,xy}$$
$$- w_{,xx}w^*_{,yy} - w_{,yy}w^*_{,xx}) = 0 . \; (14)$$

Eqs. (11) and (14) are basic equations used to investigate the stability of functionally graded cylindrical shells.

4. Stability analysis

In this section, an analytical approach is used to investigate the nonlinear stability of FGM cylindrical shells under mechanical and thermal loads. Depending on the in-plane behavior at two ends, two cases of boundary conditions, labelled Cases (1) and (2) will be considered.

Case (1). Two ends are simply supported and freely movable (FM). The associated boundary conditions are

$$w = M_{xx} = N_{xy} = 0 \; , \; N_x = N_{x0}, x = 0, L \; .$$
(15)

Case (2). Two ends are simply supported and immovable (IM). For this case, the boundary conditions are

$$w = u = M_{xx} = 0 \; , \; N_x = N_{x0}, x = 0, \; L$$
.
(16)

where N_{x0} is prebuckling force resultant in axial direction for Case (1) and is fictitious compressive edge load making the edges immovable for Case (2). To solve two Eqs. (11) and (14) for unknowns w and f , and with consideration of the boundary conditions (15), (16), we assume the following approximate solutions

$$(w, w^*) = (W, \mu h) \sin \lambda_m x \sin \mu_n y$$

$$f = A_1 \cos 2\lambda_m x + A_2 \cos 2\mu_n y + A_3 \sin \lambda_m x \sin \mu_n y$$

$$+ A_4 \cos 2\lambda_m x \cos 2\mu_n y + \frac{1}{2} N_{x0} y^2 \qquad (17)$$

where $\lambda_m = m\pi / L$, $\mu_n = n/R$, $m = 1, 2, 3, \ldots$ are number of half waves and waves in x and y directions, respectively, and W is amplitude of deflection. Also, parameter μ represents the size of imperfection and $A_i (i = 1 \div 4)$ are coefficients to be determined.

Substituting Eq. (17) into Eq. (14), the coefficients A_i are determined as

$$A_1 = \frac{E_1 \mu_n^2}{32 \lambda_m^2} W(W + 2\mu h),$$

$$A_2 = \frac{E_1 \lambda_m^2}{32 \mu_n^2} W(W + 2\mu h),$$

$$A_3 = \frac{E_1 \lambda_m^2}{R(\lambda_m^2 + \mu_n^2)^2} W \quad , \quad A_4 = 0. \qquad (18)$$

Introduction of Eqs. (17) into Eq. (11) and applying Galerkin method for the resulting equation yield

$$\left[D\left(\lambda_m^2 + \mu_n^2\right)^2 + \frac{E_1 \lambda_m^4}{R^2 \left(\lambda_m^2 + \mu_n^2\right)^2} \right] W$$

$$- \frac{32 E_1 \lambda_m^4 \mu_n^2}{3mn\pi^2 R \left(\lambda_m^2 + \mu_n^2\right)^2} W(W + \mu h)$$

$$- \frac{2 E_1 \mu_n^2}{3mn\pi^2 R} W(W + 2\mu h) + \frac{E_1 \left(\lambda_m^4 + \mu_n^4\right)}{16} \times$$

$$W(W + \mu h)(W + 2\mu h) + \lambda_m^2 N_{x0}(W + \mu h)$$

$$- \frac{16q}{mn\pi^2} = 0. \qquad (19)$$

Eq. (19), derived for odd values of m, n, will be used to determine buckling loads and nonlinear postbuckling paths of FGM cylindrical shells under mechanical and thermal loads.

4.1. Mechanical stability analysis

A simply supported FGM cylindrical shell with freely movable edges (that is, Case (1)) is assumed to be subjected to axial compressive load P_x (in Pascals), uniformly acted on the two ends in the absence of lateral pressure and temperature conditions. In this case, $N_{x0} = -P_x h$, $q = 0$ and Eq. (19) leads to

$$P_x = \left[\frac{\bar{D}\left(m^2\pi^2 + n^2 L_R^2\right)^2}{m^2\pi^2 R_h^2 L_R^2} + \frac{\bar{E}_1 m^2\pi^2 L_R^2}{\left(m^2\pi^2 + n^2 L_R^2\right)^2} \right] \times$$

$$\frac{\bar{W}}{\bar{W} + \mu} - \frac{2\bar{E}_1 n L_R^2}{3m^3\pi^4 R_h} \frac{\bar{W}(\bar{W} + 2\mu)}{\bar{W} + \mu}$$

$$- \frac{32mn\bar{E}_1 L_R^2}{3R_h \left(m^2\pi^2 + n^2 L_R^2\right)^2} \bar{W}$$

$$+ \frac{\bar{E}_1 \left(m^4\pi^4 + n^4 L_R^4\right)}{16 m^2\pi^2 R_h^2 L_R^2} \bar{W}(\bar{W} + 2\mu) \qquad (20)$$

where

$$R_h = R/h, \ L_R = L/R, \ \bar{D} = D/h^3,$$

$$\bar{E}_1 = E_1/h, \ \bar{W} = W/h. \ (21)$$

For a perfect FGM cylindrical shell, i.e. $\mu = 0$, Eq. (20) gives equation from which bifurcation-type buckling compressive load P_{xb} may be obtained at $\bar{W} = 0$ as

$$P_{xb} = \frac{\bar{D}\left(m^2\pi^2 + n^2 L_R^2\right)^2}{m^2\pi^2 R_h^2 L_R^2} + \frac{\bar{E}_1 m^2\pi^2 L_R^2}{\left(m^2\pi^2 + n^2 L_R^2\right)^2}. \qquad (22)$$

Specialization of Eq. (22) for isotropic cylindrical shells, i.e. $E_c = E_m = E$, yieds

$$P_{xb}^{iso} = \frac{E\left(m^2\pi^2 + n^2 L_R^2\right)^2}{12(1 - v^2)m^2\pi^2 R_h^2 L_R^2} + \frac{E m^2\pi^2 L_R^2}{\left(m^2\pi^2 + n^2 L_R^2\right)^2} \qquad (23)$$

Eq. (23) has been derived by Brush and Almroth [1] when they analyzed the linear buckling of axially compressed isotropic

cylindrical shells by using adjacent equilibrium criterion.

In case of $\mu \neq 0$, $P_x(\bar{W})$ curves start from original point and Eq. (20) shows initial imperfection sensitivity of axially compressed FGM cylindrical shells.

4.2. Thermal stability analysis

A simply supported FGM cylindrical shell with immovable edges (that is, Case (2)) subjected to thermal loads in the absence of lateral pressure is considered. The condition expressing the immovability on two edges, i.e. $u = 0$ on $x = 0, L$, is fulfilled on the average sense as

$$\int_0^{2\pi R} \int_0^L \frac{\partial u}{\partial x} dx dy = 0 \qquad (24)$$

From Eqs. (6) and (9) one can obtain the following relation in which Eq. (13) and imperfection have been included

$$\frac{\partial u}{\partial x} = \frac{1}{E_1}\left(f_{,yy} - \nu f_{,xx}\right) + \frac{E_2}{E_1} w_{,xx} - \frac{1}{2} w_{,x}^2$$

$$- w_{,x} w_{,x}^* + \frac{\Phi_m}{E_1}. \qquad (25)$$

Substituting Eqs. (17) into Eq. (25) and then introduction of the result into Eq.(24) give

$$N_{x0} = -\Phi_m + \frac{4\lambda_m^2}{mn\pi^2}\left[E_2 - \frac{E_1(\nu\lambda_m^2 - \mu_n^2)}{R(\lambda_m^2 + \mu_n^2)^2}\right] W$$

$$+ \frac{E_1\lambda_m^2}{8} W(W + 2\mu h), \qquad (26)$$

which represents the compressive stresses making edges immovable.

In this report, environment temperature is assumed to be uniformly raised from initial value T_i to final one T_f and temperature difference $\Delta T = T_f - T_i$ is a constant.

The thermal parameter Φ_m can be expressed in terms of the ΔT from Eqs. (10).

Subsequently, employing this expression of Φ_m in Eq. (26) and then introduction of the result into Eq. (19) with $q = 0$ yield

$$\Delta T = \left[\frac{\bar{D}\left(m^2\pi^2 + n^2 L_R^2\right)^2}{Pm^2\pi^2 R_h^2 L_R^2}\right.$$

$$+ \frac{\bar{E}_1 m^2\pi^2 L_R^2}{P\left(m^2\pi^2 + n^2 L_R^2\right)^2}\right]\frac{\bar{W}}{\bar{W} + \mu}$$

$$+ \left\{\frac{4m}{nP}\left[\frac{\bar{E}_2}{R_h^2 L_R^2} - \frac{\bar{E}_1\left(\nu m^2\pi^2 - n^2 L_R^2\right)}{R_h\left(m^2\pi^2 + n^2 L_R^2\right)^2}\right]\right.$$

$$\left. - \frac{32\bar{E}_1 mn L_R^2}{3R_h P\left(m^2\pi^2 + n^2 L_R^2\right)^2}\right\}\bar{W}$$

$$- \frac{2\bar{E}_1 n L_R^2}{3m^3\pi^4 R_h P}\frac{\bar{W}(\bar{W} + 2\mu)}{\bar{W} + \mu} +$$

$$\left[\frac{\bar{E}_1\left(m^4\pi^4 + n^4 L_R^4\right)}{16Pm^2\pi^2 R_h^2 L_R^2}\right.$$

$$\left. + \frac{\bar{E}_1 m^2\pi^2}{8PR_h^2 L_R^2}\right]\bar{W}(\bar{W} + 2\mu) \qquad (27)$$

where

$$P = E_m\alpha_m + \frac{E_m\alpha_{cm} + E_{cm}\alpha_m}{k+1}$$

$$+ \frac{E_{cm}\alpha_{cm}}{2k+1}, \quad \bar{E}_2 = E_2/h^2. \qquad (28)$$

Eq. (27) expresses nonlinear relation between uniform temperature rise and the deflection of perfect and imperfect FGM cylindrical shells. The buckling temperature difference of perfect cylindrical shells may be obtained from Eq. (27) as

$$\Delta T_b = \frac{\bar{D}\left(m^2\pi^2 + n^2 L_R^2\right)^2}{Pm^2\pi^2 R_h^2 L_R^2} + \frac{\bar{E}_1 m^2\pi^2 L_R^2}{P\left(m^2\pi^2 + n^2 L_R^2\right)^2}$$

$$(29)$$

5. Results and discussion

To illustrate the proposed approach, we consider a ceramic-metal functionally graded cylindrical shell that consist of alumina and aluminum with the following properties.

$$E_m = 70\,GPa, \quad \alpha_m = 23 \times 10^{-6o}\,C^{-1} \quad (30)$$

$$E_c = 380\,GPa, \quad \alpha_c = 7.4 \times 10^{-6o}\,C^{-1}, v = 0.3\,.$$

Fig. 2 shows the effects of the volume fraction index $k\,(= 0,\,1)$ on the postbuckling behavior of FGM cylindrical shells under axial uniform compression. As can be seen, both buckling loads and postbuckling loading carrying capacity of FGM shells are considerably reduced when k increases. This is expected because the volume percentage of ceramic constituent, which has higher modulus of elasticity, is decreased with increasing values of k. This figure also indicates that with only one half wave in the axial direction axially compressed cylindrical shells experience a snap-through behavior and exhibit an initial imperfection sensitivity.

Fig.3 shows effect of buckling mode on the postbuckling behavior of FGM cylindrical shells under axial compressive load. As can be observed, when number of half waves in the axial direction differ from one, i.e. $m \neq 1$, there is no snap-through phenomenon occurs for compressed FGM cylindrical shells and postbuckling load-deflection paths are stable.
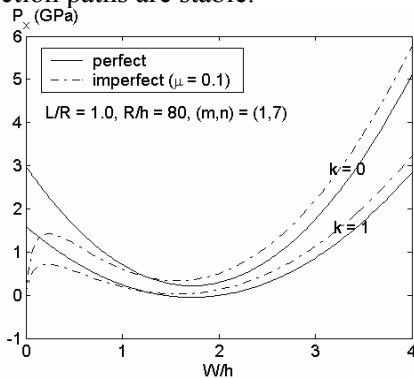
Figure.2. Effect of k index on the postbuckling behavior of FGM cylindrical shells under compression $(m,n) = (1,7)$.
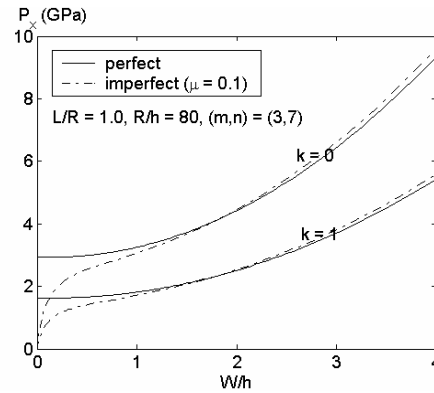
Figure.3. Effect of k index on the postbuckling behavior of FGM cylindrical shells under compression $(m,n) = (3,7)$.

Fig. 4 shows the effects of radius to thickness $R/h\,(= 60,\,80$ and $100)$ ratio on the postbuckling behavior of FGM cylindrical shells under axial compression. As can be seen, the capacity of loading carrying of FGM cylindrical shells is remarkably reduced when R/h ratio is enhanced. Moreover, the postbuckling equilibrium paths of FGM cylindrical shells become less stability with higher values of R/h ratio.
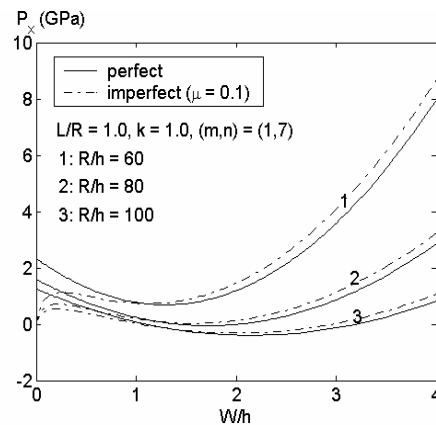
Figure.4. Effect of R/h ratio on the postbuckling behavior of FGM cylindrical shells under compression.

Finally, Fig. 5 illustrates the effects of the volume fraction index k on the postbuckling behavior of FGM cylindrical shells subjected to uniform temperature rise. Obviously, both buckling temperatures and postbuckling

curves of FGM cylindrical shells are decreased when k is increased. Furthermore, snap-through phenomenon of heated FGM cylindrical shells is relatively benign in comparison with that of axially compressed FGM cylindrical shells, and postbuckling temperature-deflection paths of FGM cylindrical shells under thermal loading are comparatively stable.
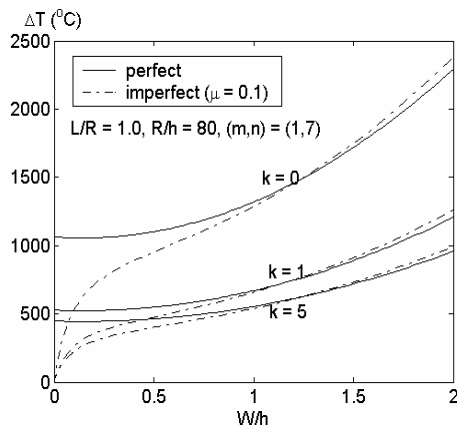
Figure.5. Effect of k index on the postbuckling behavior of FGM cylindrical shells under uniform temperature rise.

6. Concluding remarks

This report investigates the buckling and postbuckling behaviors of FGM cylindrical shells under axial compressive and thermal loads by an analytical approach. Basic equations are derived within the framework of the classical shell theory with both geometrical nonlinearity and initial geometrical imperfection are incorporated. Approxiamte solutions are chosen to satisfy simply supported boundary conditions and explicit expressions of buckling loads and postbuckling paths are determined by Galerkin method. The results shows that material and geometrical properties have great influence on the buckling loads and the capacity of postbuckling loading bearing. The study also reveal that initial imperfection and buckling mode have significant effects on the response of FGM cylindrical shells.

References

[1]. D. O. Brush, B. O. Almroth (1975), *Buckling of Bars, Plates and Shells*, McGraw-Hill, New York.

[2]. R. Javaheri, M. R. Eslami (2002), Buckling of functionally graded plates under in-plane compressive loading, *ZAMM Journal*, Vol. 82, No. 4, pp. 277-283.

[3]. R. Javaheri, M. R. Eslami (2002), Thermal buckling of functionally graded plates, *AIAA Journal*, Vol. 40, No. 1, pp. 162-169.

[4]. R. Javaheri, M. R. Eslami (2002), Thermal buckling of functionally graded plates based on higher order theory, *Journal of Thermal Stresses* , Vol. 25, No. 1, pp. 603-625.

[5]. B.A. Samsam Shariat, M.R. Eslami (2007), Buckling of thick functionally graded plates under mechanical and thermal loads, *Composite Structures*, Vol. 78, pp. 433-439.

[6]. Wu Lanhe (2004), Thermal buckling of a simply supported moderately thick rectangular FGM plate, *Composite Structures*, Vol. 64, pp. 211-218.

[7]. B.A.Samsam Shariat R. Javaheri, M.R.Eslami (2005), Buckling of imperfect functionally graded plates under in-plane compressive loading, *Thin-Walled Structures*, Vol. 43, pp. 1020-1036.

[8]. B. A. Samsam Shariat, M. R. Eslami (2006), Thermal buckling of imperfect functionally graded plates, *International Journal of Solids and Structures*, Vol. 43, pp. 4082-4096.

[9]. Hyung-Su Na, Ji-Huwan Kim (2006), Three-dimensional thermomechanical buckling analysis for functionally graded composite plates, *Composite Structures*, Vol. 73, pp. 413-422.

[10].J. N. Reddy, C. D. Chin (1998), Thermomechanical analysis of functionally graded cylinders and plates, *Journal of Thermal Stresses*, Vol. 21, pp. 593-626.

[11]. R. Shahsiah, M. R. Eslami (2003), Thermal buckling of functionally graded cylindrical shell, *Journal of Thermal Stresses*, Vol. 26, No. 3, pp. 277-294.

[12]. Lanhe Wu, Zhiqing Jiang, Jun Liu (2005), Thermoelastic stability of functionally graded cylindrical shells, *Composite Structures*, Vol. 70, pp. 60-68.

[13]. T. L. Wu, K.K.Shukla, J.H.Huang (2007), Post-buckling analysis functionally graded plates, *Composite Structures*, Vol. 81, pp. 1-10.

[14]. K. M. Liew, J. Yang, S. Kitipornchai (2004), Thermal post-buckling of laminated plates comprising functionally graded materials, *J. Applied Mechanics*, Vol. 71, pp. 839-850.

[15]. K. M. Liew, J. Yang, S. Kitipornchai (2003), Postbuckling of piezoelectric FGM plates subjected to thermo-electro-mechanical loading, *International Journal of Solids and Structures*, Vol. 40, pp. 3859-3892.

[16]. X. Zhao, K.M. Liew (2009), Geometrically nonlinear analysis of functionally graded plates using the element-free kp-Ritz method, *Computational Methods in Applied Mechanics and Engineering*, Vol. 195, pp. 2796-2811.

[17]. H.S. Shen (2005), Postbuckling of FGM plates with piezoelectric actuators under thermo-electro-mechanical loadings, *International Journal of Solids and Structures*, Vol. 42, pp. 6101-6121.

[18]. H.S. Shen (2007), Thermal postbuckling behavior of shear deformable FGM plates with temperature-dependent properties, *International Journal of mechanical sciences*, Vol. 49, pp. 466-478.

[19]. H.S.Shen (2004), Thermal postbuckling behavior of functionally graded cylindrical shells with temperature-dependent properties, *International Journal of Solids and Structures*, Vol. 41, pp. 1961-1974.

[20]. H.S.Shen, N. Noda (2005), Postbuckling of FGM cylindrical shells under combined axial and radial mechanical loads in thermal environments, *International Journal of Solids and Structures*, Vol. 42, pp. 4641-4662.

[21]. H.S.Shen (2005), Postbuckling of axially loaded FGM hybrid cylindrical shells in thermal environments, *Composite Sciences and Technology*, Vol. 65, pp. 1675-1690.

[22]. H.S.Shen, N. Noda (2007), Postbuckling of pressure-loaded FGM hybrid cylindrical shells in thermal environments, *Composite Structures*, Vol. 77, pp. 546-560.

[23]. H. Huang, Q. Han (2009), Nonlinear elastic buckling and postbuckling of axially compressed functionally graded cylindrical shells, *International Journal of mechanical sciences*, Vol. 51, pp. 500-507.

[24]. H. Huang, Q. Han (2009), Nonlinear buckling and postbuckling of heated functionally graded cylindrical shells under combined axial compression and radial pressure, *International Journal of Non-Linear Mechanics*, Vol. 44, pp. 209-218.

[25]. H.V. Tung, N.D. Duc (2010), Nonlinear analysis of stability for functionally graded plates under mechanical and thermal loads, *Composite Structures*, Vol. 92, pp. 1184-1191.

[26]. N.D. Duc, H.V. Tung (2010), Nonlinear response of pressure-loaded functionally graded cylindrical panels with temperature effects, *Composite Structures*, Vol. 92, pp. 1664-1672.

Evaluating possibility of water wetting and calculating water film thickness in horizontal and slightly inclined oil–water pipelines based on three-layer liquid-liquid model

Nguyen The Duc[a], Bui Dinh Tri[b], Phan Ngoc Trung[c]

a Vietnam Petroleum Institute, ducnt@vpi.pvn.vn
b Institute of Mechanics, bdtri@imech.ac.vn
c Vietnam Petroleum Institute, trungpn@vpi.pvn.vn

Abstract

The oil-water flow in pipeline is a common occurrence in petroleum industry. As the water cut increase, the regime of stratified flow with separate layers of water and oil phases may occur. The existence of water layer at the pipe bottom may increase possibility of internal corrosion and decrease transport capacity of pipelines. The paper presents a tool for predicting possibility of water wetting and evaluating thickness of water film. Prediction of water wetting possibility is based on calculation of the critical velocity for water entrainment. If all the water is not entrained by the flowing oil phase, a free water layer are formed and it is important to predict water film thickness, in-situ water cut, water velocity and water wetted pipe area for this layer. Method for evaluating these parameters is developed using a two-phase liquid-liquid three-layer model. This model for oil-water flow is developed from solution of mass and momentum equations for three layers: pure water, pure oil and water-oil mixture. The prediction methods are tested by comparing the calculated results with experimental data. Effects of important flow parameters are also analyzed from simulated results.

Key Words: water entrainment, water wetting, critical velocity, oil-water flow, three-layer model

1. Introduction

The simultaneous flow of oil and water in pipelines is a common occurrence in the petroleum industry. A significant amount of water is often present with oil from the well perforations to the final stage of oil separation. The water phase contains dissolved corrosive gases such as CO_2 or H_2S, therefore the water is corrosive. At low water volume fraction, the water is entrained by the flowing oil, consequently oil wets the pipe and the corrosion is negligible. As the volume fraction of water increases, the water "break out" may appear, the bottom of the pipe is wetted by water, and corrosion occurs (Phan Ngoc Trung, 1986).

Because corrosion mainly occurs when a water film exists and pipe flow in the stratified regime. It is important to predict

possibility of water wetting and to evaluate thickness of water film. Three-dimensional CFD (Computational Fluid Dynamics) model can be used for simulating two-phase flow (Nguyen The Duc et al, 2009). However, this model is difficult to use for long pipes because it requires very large computing time. On other hand, the applicability of gas-liquid prediction models has been proven to be inadequate for oil-water flow (Taitel et al, 1976; Arirachakaran et al, 1986; Trallelo et al, 1996; Bratlan et al, 2009). The developments of better prediction methods are necessary.

The paper presents a method for predicting possibility of water wetting and evaluating thickness of water film. Prediction of water wetting possibility is based on calculation of the critical velocity for water entrainment. Method for evaluating water film thickness is based on a two-phase liquid-liquid three-layer model. The prediction methods are tested available experimental data. Effects of important flow parameters are also discussed using simulated results.

2. Method for evaluation of water entrainment

To distinguish between fully dispersed and stratified flows, we use the method developed by Barnea (1987) and Brauner (2001). A critical velocity for water entrainment is used as the criterion for forming stable water-in-oil dispersed flow. Two main physical properties are compared to deduce the criterion:

1. Maximum droplet size $d_{\max}$ related to breakup and coalescence.
2. Critical droplet size d_{crit} related to settling and separation.

Under favorable condition, water is entrained by the flowing oil phase in the form of fine droplets, it is necessary to know the maximum droplet size $d_{\max}$ that can sustain by the flow without further breakup.

In the dilute water-in-oil dispersion, value of $d_{\max}$ is related to the balance between the turbulent kinetic energy and the droplet surface energy. Brauner (2001) shows that this relation can be written as,

$$\left(\frac{d_{\max}}{D}\right)_{dilute} = 1.88\left[\frac{\rho_o(1-\varepsilon_w)}{\rho_m}\right]^{-0.4} We_o^{-0.6} \, \text{Re}_o^{0.08} \quad (1)$$

where

$$\text{Re}_o = \frac{\rho_o D U_c}{\eta_o} \; ; \; We_o = \frac{\rho_o D U_c^2}{\sigma}$$

with D is the pipe diameter (m), ε_w is the in-situ water cut, ρ denotes the densities ($kg.m^{-3}$). The subscripts o, m and w denote oil phase, oil-water mixture and water phases respectively. The subscript *dilute* denotes dilute dispersion. U_c is the velocity of continuous (oil) phase (ms^{-1}). η_o is the viscosity of oil phase ($Pa.s$) and σ is the interfacial tension of oil phase (Nm^{-1}).

It is noted that this equation can be only valid in the dilute dispersion that means it satisfies the following condition:

$$(1-\varepsilon_w)\frac{\rho_o}{\rho_m} \cong 1 \qquad (2)$$

In the condition of dense dispersions, droplet coalescence takes place. Equation (1) can not be used in this case. Under this condition, the flow rate of oil phase Q_o should carry sufficient turbulent energy to disrupt the coalescing tendency of the water droplets flowing at a rate Q_w. This requirement means that the rate of surface energy production in the coalescing water phase is proportional to the rate of turbulent energy supply by the flowing oil phase. From this condition, Brauner (2001) obtained the following equation for determining the maximum droplet size in the case of dense water-in-oil dispersion:

$$\left(\frac{d_{max}}{D}\right)_{dense} = 2.22 C_H^{0.6} \cdot \left(\frac{\rho_o U_c^2 D}{\sigma}\right)\left(\frac{\varepsilon_w}{1-\varepsilon_w}\right)^{0.6}$$
$$\times \left[\frac{\rho_m}{\rho_o(1-\varepsilon_w)}\right]^{-0.4} \quad (3)$$

where C_H is a constant of the order of 1. The subscript *dense* denotes the dense oil-in-water dispersion. f is the friction factor:

$$f \cong 0.046/\text{Re}_o^{0.2} \quad (4)$$

Therefore, with a given oil-water system, the maximum droplet size that can be sustained is the larger of the two values obtained via (1) and (3), which can be considered as the worst case for a given oil-water system,

$$\frac{d_{max}}{D} = \max\left[\left(\frac{d_{max}}{D}\right)_{dilute}, \left(\frac{d_{max}}{D}\right)_{dense}\right] \quad (5)$$

Along with determination of maximum droplet size d_{max} that can be sustained by the flow without further breakup, it is essential to evaluate a critical droplet size d_{crit}. Droplet larger than a critical droplet size d_{crit} will separate out from the two-phase flow dispersion either due to gravity forces in horizontal flow, or due to deformation and creaming in vertical flow (Barnea, 1987).

Critical droplet diameter d_{cb} above which separation of droplets due to gravity takes place can be found via a balance of gravity and turbulent forces as:

$$\frac{d_{cb}}{D} = \frac{3}{8}\frac{\rho_o}{|\Delta\rho|}\frac{fU_c^2}{Dg\cos(\theta)} = \frac{3}{8}\frac{\rho_o}{|\Delta\rho|}Fr_o \quad (6)$$

Where θ is the pipe inclination, the Froude number is:

$$Fr_o = \frac{fU_c^2}{Dg\cos(\theta)}$$

and

$$\Delta\rho = \rho_o - \rho_w$$

This effect is common at low pipe inclination i.e. in horizontal and near horizontal flows.

In vertical and near-vertical flows, critical droplet diameter $d_{c\sigma}$ above which drops are deformed and creamed leading to migration of the droplets towards the pipe walls can be calculated by following equation (Brodkey, 1969):

$$\frac{d_{c\sigma}}{D} = \frac{0.5\sigma}{|\Delta\rho|gD^2\cos(\beta)} \quad (7)$$

with

$$\beta = \begin{cases} |\theta| & khi \quad |\theta| < 45^o \\ 90-|\theta| & khi \quad |\theta| > 45^o \end{cases}$$

Then the critical diameter d_{crit} can be estimated for any pipe inclination (Barnea, 1987):

$$\frac{d_{crit}}{D} = Min\left(\frac{d_{cb}}{D}, \frac{d_{c\sigma}}{D}\right) \quad (8)$$

Finally, the criterion for water entrainment can be formulated. The transition from stratified flow to stable water–in-oil dispersed one takes place when the oil phase turbulence is intense enough to maintain the water phase broken out into droplets not larger than d_{max} which has to be smaller than a critical droplet size d_{crit} causing droplet separation. The final criterion is then (Brauner, 2001):

$$d_{max} \leq d_{crit} \quad (9)$$

where d_{max} and d_{crit} are calculated from equations (1)-(8).

By using equations (5), (8) and (9), we can determine the critical velocity u_{crit} above which the flow is fully dispersed.

3. Three-layer two-phase liquid-liquid model for stratified flow

The above mentioned method can predict whether the water phase is not entirely

entrained and flows separated from oil phase. In the case of stratified flows, for corrosion calculations it is crucial to predict the in-situ water cut, water velocity, water film thickness and water wetted pipe cross-section area. Multi-layer segregated flow model is suitable for above requirement. A three-layer segregated flow model was proposed by Neogi et al (1994) and Taitel et al (1995) to calculate the thickness of water layer for gas-water-oil three-phase stratified flow. Vendapuri (1997) developed a three-layer segregated flow model to calculate the thickness of water layer and in-situ water cut for oil-water flows. This model for developed water-oil flow considers water, oil and a mixed layer in between as three different phases with their own distinct properties. The existence of mixed layer is confirmed from visualization experiments. Assume that the interface between the pure water layer and mixed layer and the interface between the mixed layer and pure oil layer are flat. The modeling representation of the flow can be seen in Figure 1.
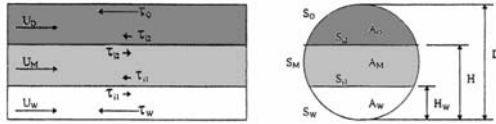
Figure 1: Schematic representation of the three-phase segregated oil-water flow

Using the notations in Figure 1, the momentum balance for each phase can be written as follows:

For pure oil layer:

$$-A_o\left(\frac{dp}{dx}\right)-\tau_o S_o-\tau_{i2}S_{i2}-\rho_o A_o g\sin\alpha \quad (10)$$

For oil-water mixed layer:

$$-A_m\left(\frac{dp}{dx}\right)-\tau_m S_m-\tau_{i1}S_{i1}+\tau_{i2}S_{i2}-\rho_m A_m g\sin\alpha$$
$$(11)$$

For pure water layer:

$$-A_w\left(\frac{dp}{dx}\right)-\tau_w S_w+\tau_{i1}S_{i1}-\rho_w A_w g\sin\alpha \quad (12)$$

where,

The subscripts o, m and w denote the pure oil layer, the oil-water mixed layer and the pure water layer, respectively. The subscript $i1$ and $i2$ represent the interface between layer as shown in Figure 1.

A_o, A_m, A_w - cross-sectional areas.

S_o, S_m, S_w - wetted perimeters.

S_{i1}, S_{i2} - interfacial perimeter.

α - pipe inclination (α is positive for upward flow)

ρ_o, ρ_m, ρ_w - density of different phases (kg/m^3)

τ_o, τ_m, τ_w - wall shear stress (N/m^2)

τ_{i1}, τ_{i2} - interfacial shear stress (N/m^2)

$\frac{dp}{dx}$ - pressure gradient (N/m^2)

It is assumed that pressure gradient is the same in the three regions. The equations are combined to remove this term.

From equations (10) and (11), elimination of the pressure term gives,

$$\tau_o\frac{S_o}{A_o}-\tau_m\frac{S_m}{A_m}-\tau_{i1}\frac{S_{i1}}{A_m}+\tau_{i2}\left(\frac{S_{i2}}{A_o}+\frac{S_{i2}}{A_m}\right)$$
$$+\left(\rho_o-\rho_m\right)g\sin\alpha=0 \quad (13)$$

By eliminating the pressure term from equation (11) and (12), we have,

$$\tau_m\frac{S_m}{A_m}-\tau_w\frac{S_w}{A_w}-\tau_{i2}\frac{S_{i2}}{A_m}+\tau_{i1}\left(\frac{S_{i1}}{A_m}+\frac{S_{i1}}{A_w}\right)$$
$$+\left(\rho_m-\rho_w\right)g\sin\alpha=0 \quad (14)$$

The shear stresses can be evaluated using Blasius type relation (Taitel and Ducker, 1976):

$$\tau_o=f_o\frac{\rho_o U_o^2}{2}\ ;\ \tau_m=f_m\frac{\rho_m U_m^2}{2}\ ;\ \tau_w=f_w\frac{\rho_w U_w^2}{2}$$

$$\tau_{i1}=f_{i1}\frac{\rho_{i1}\left(U_m-U_w\right)|U_m-U_w|}{2}$$

$$\tau_{i2} = f_{i2} \frac{\rho_{i2}(U_o - U_m)|U_o - U_m|}{2} \qquad (15)$$

where:

U_m, U_o, U_w - in-situ velocities of the different phases.

f_o, f_m, f_w - friction factors.

f_{i1}, f_{i2} - interfacial friction factors.

ρ_{i1}, ρ_{i2} - densities at the interfaces.

The density at the interface is set to the larger of two densities of interfacing layers:

$$\rho_{i1} = \max(\rho_m, \rho_w)$$

$$\rho_{i2} = \max(\rho_o, \rho_m)$$

The friction factors are evaluated using a method similar to Brauner et al (1992):

$$f_o = C_o \left(\frac{\rho_o D_o |U_o|}{\mu_o} \right)^{-N_o}$$

$$f_m = C_m \left(\frac{\rho_m D_m |U_m|}{\mu_o} \right)^{-N_m} \qquad (16)$$

$$f_w = C_w \left(\frac{\rho_w D_w |U_w|}{\mu_w} \right)^{-N_w}$$

with D_o, D_m and D_w are layer hydraulic diameters:

$$D_o = \begin{cases} \dfrac{4A_o}{S_o} & if \quad U_o \le U_m \\[2ex] \dfrac{4A_o}{S_o + S_{i2}} & if \quad U_o > U_m \end{cases}$$

$$D_m = \begin{cases} \dfrac{4A_m}{S_m} & if \quad U_m \le U_o \,\&\, U_m \le U_w \\[2ex] \dfrac{4A_m}{S_m + S_{i2}} & if \quad U_m > U_o \,\&\, U_m \le U_w \\[2ex] \dfrac{4A_m}{S_m + S_{i1}} & if \quad U_m \le U_o \,\&\, U_m > U_w \\[2ex] \dfrac{4A_m}{S_m + S_{i1} + S_{i2}} & if \quad U_m > U_o \,\&\, U_m > U_w \end{cases}$$

$$D_w = \begin{cases} \dfrac{4A_w}{S_w} & if \quad U_w \le U_m \\[2ex] \dfrac{4A_o}{S_w + S_{i1}} & if \quad U_w > U_m \end{cases} \qquad (17)$$

and μ_o, μ_m, μ_w denote the phase viscosities.

The values of C_k and N_k ($k = o, m, w$) are depended whether the flow condition is turbulent or laminar:

- $C_k = 0.046$ and $N_k = 0.2$ in turbulent flows.

- $C_k = 16$ and $N_k = 1$ in laminar flows.

Turbulent or laminar flow conditions in each phase are identified by calculating the Reynold number for each phase:

$$\text{Re}_k = \frac{4U_k A_k \rho_k}{S_k \mu_k} \quad \text{with } k = o, m, w \qquad (18)$$

Laminar flow is assumed for $\text{Re}_k \ge 2300$ and flow is turbulent for $\text{Re}_k < 2300$.

Friction factor of the interface is assigned to the larger among the two wall friction factors of the interfacing layers.

Figure 2 shows a schematic diagram of the mixing phenomena in oil-water flows. It can be seen that the two known parameters are the volumetric flow rate of oil and of the water. Usually, the analysis of the oil-water flows requires knowledge of the superficial velocities of the three phases-pure oil, pure water, and oil-water mixture:

$$U_{so} = \frac{Q_o}{A} \; ; \; U_{sm} = \frac{Q_m}{A} \; ; \; U_{sw} = \frac{Q_w}{A} \qquad (19)$$

with Q_o, Q_m and Q_w are the volumetric flow rates of the pure oil, pure water, and oil-water mixture phases respectively (m^3/s).
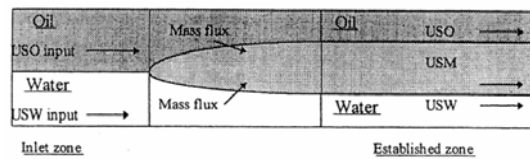
Figure 2: Schematic representation of the mixing phenomena in oil-water flows

From Figure 2, it can be seen that the mass balance can be written as follows:

$$Q_{w,input} = Q_w + C_{ml}Q_m \qquad (20)$$

$$Q_{o,input} = Q_o + (1 - C_{ml})Q_m \qquad (21)$$

where:

$Q_{w,input}$ - Input water volumetric flow rate, m^3/s.

$Q_{o,input}$ - Input oil volumetric flow rate, m^3/s.

C_{ml} - Water fraction within mixture layer.

From above mass balance equations, the relations between the superficial velocities can be written as follows:

$$U_{sw,input} = U_{sw} + C_{ml}U_{sm} \qquad (22)$$

$$U_{so,input} = U_{so} + (1 - C_{ml})U_{sm} \qquad (23)$$

where:

$U_{sw,input}$ - Input superficial velocity of the water layer, m/s.

$U_{so,input}$ - Input superficial velocity of the oil layer, m/s.

U_{sw} - In situ superficial velocity of water layer, m/s.

U_{sm} - In situ superficial velocity of mixture layer, m/s.

U_{so} - In situ superficial velocity of oil layer, m/s.

The momentum and the mass balance equations need to be solved simultaneously. However, there are only four equations containing six unknowns. These unknowns are U_{sw}, U_{sm}, U_{so}, C_{ml}, A_w and A_m. Therefore, two more equations have to be added.

In this model, the additional relations are determined from the experimental observations related to the composition and velocity of mixture layer [12]. The first relation is that the in situ velocity of the mixture layer is approximately 1.2 times the input mixture velocity. The second relation is also defined from the measurements. It was seen that in most cases studies, the water percentage of the mixture layer was very close to the input water cut. Therefore, the closure equations can be written as follows:

$$U_m = 1.2 * U_{in} \qquad (24)$$

$$C_{ml} = \frac{Q_{w,input}}{Q_{o,input} + Q_{w,input}} \qquad (25)$$

4. Description of computation program

Using above mentioned mathematical model, a computer program have been developed. The program was written in Fortran 90.

The input of the program includes the fluid properties, the total mixture velocity and water cut, and the pipe diameter and inclination. The water fraction of the mixture layer is then set to the input water cut. Initially, the in situ superficial velocity of mixture layer is set to a very low value. Using equations (22) and (23), the in situ superficial velocities of oil and water layers can be calculated. At this time, the superficial velocities and the properties of three layers are available. Equations (13) and (14) are then solved to predict the height H_W, which is the film thickness of the water layer, and the height H, which is the sum of the film thickness of the water and mixture layers. After the film thicknesses are calculated, the in situ velocities of three phases are calculated. A check for convergence is made by comparing the in situ mixture layer. If the criterion is not satisfied, U_{sm} is modified by the bisection algorithm [14].

5. Calculated results

5.1. Experimental validation

The model is validated by comparing its predicted results with experimental data of

Shi et al [15] for the pure layer thickness at input water cuts from 20% to 80%. All the experiments were conducted at the temperature of 25° C in a 200'' long, 4'' (0.1016 m) internal diameter pipeline. The properties of used oil at 25° C were: ρ_o =820 kg/m^3 and μ_o =2 cP. The seawater was used with the following properties: ρ_w =1024 kg/m^3 and μ_w =1 cP. The oil water surface tension was σ =0.029 N/m.

The comparison between measurement and prediction for the pure water layer thickness at input water cut of 20% is shown in Figure 3. Similarly, figures 4-6 present the comparison at water cuts of 40%, 60% and 80% respectively. From the figures, it is found the reasonable agreements between the experimental and the predicted data are achieved, especially for lower water cut.
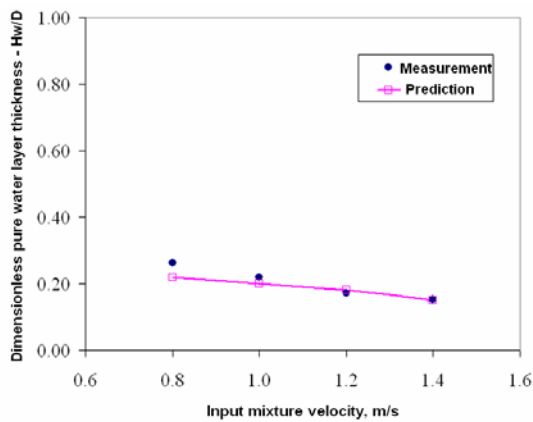
Figure 3: Comparison between measurement and prediction for the pure water layer thickness at input water cut of 20%.
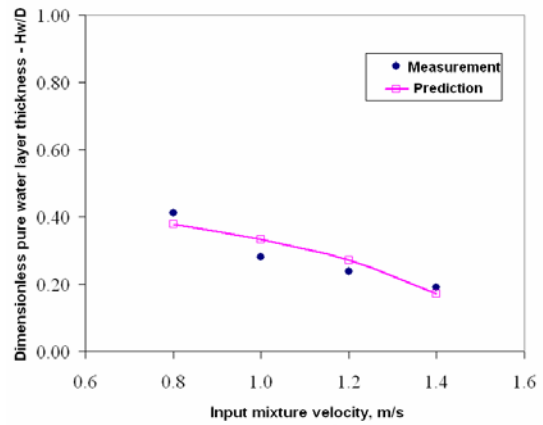
Figure 4: Comparison between measurement and prediction for the pure water layer thickness at input water cut of 40%.
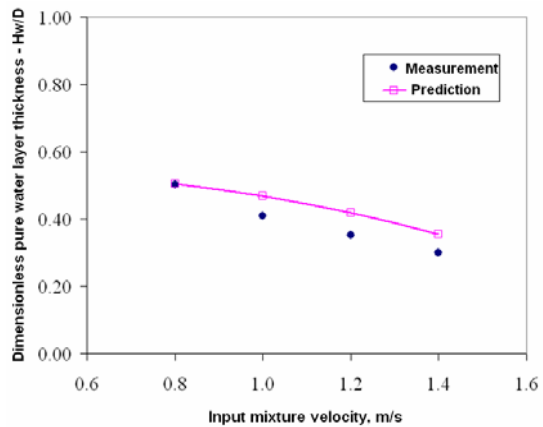
Figure 5: Comparison between measurement and prediction for the pure water layer thickness at input water cut of 60%.
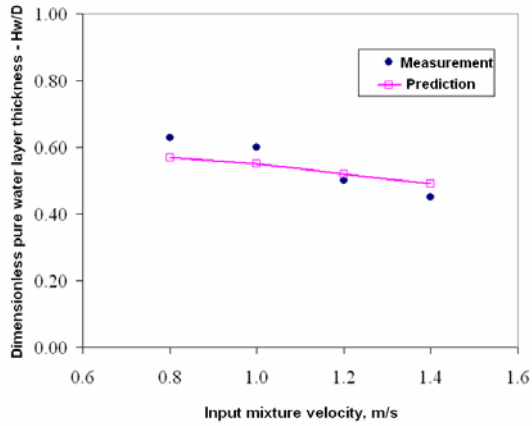
Figure 6: Comparison between measurement and prediction for the pure water layer thickness at input water cut of 80%.

5.2. Effect of flow parameters on critical velocity

The model is used to investigate effect of flow parameter on the critical velocity.

Figure 7 shows the effect of water cut on critical velocity for the case of ρ_o =820 kg/m^3, μ_o =2 cP, d =0.1016 m and σ =0.029 N/m. From the figure, it can be seen that increasing water cut leads to higher critical velocity.
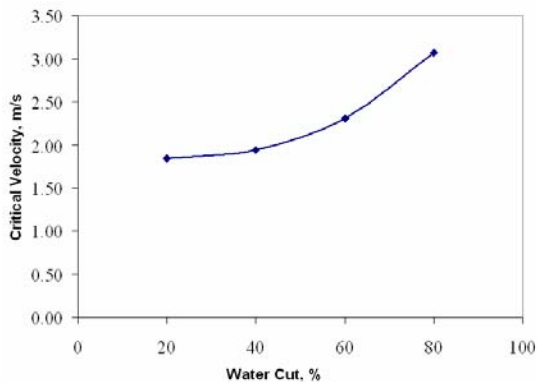
Figure 7: Effect of water cut on critical velocity at ρ_o =820 kg/m^3, μ_o =2 cP, d =0.1016 m and σ =0.029 N/m.

Figure 8 shows the effect of the pipe diameter on the critical velocity for the case of ρ_o =820 kg/m^3, μ_o =2 cP, water cut=

20% and σ =0.029 N/m. Larger pipe diameter is associated with larger critical velocity. However, it can be seen that the relation is not really linear.
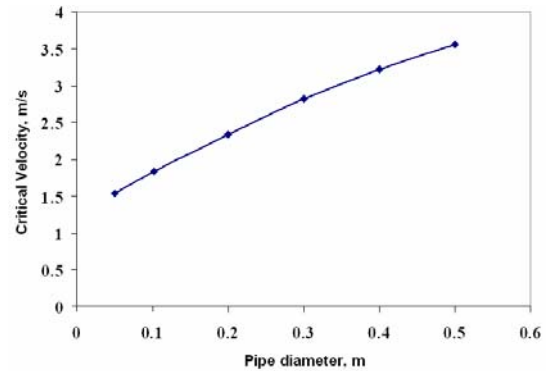
Figure 8: Effect of pipe diameter on critical velocity at ρ_o =820 kg/m^3, μ_o =2 cP, water cut = 20% and σ =0.029 N/m.

The effect of oil density on the critical velocity is show in Figure 9 for the case of d =0.1016 m, μ_o =2 cP, water cut=20% and σ =0.029 N/m. Increasing oil density decreases the critical velocity. The reason of this phenomenon is that when the oil density increases, the miscibility between oil and water increase. The momentum and mass exchange between them is much easier so that water can be much easier entrained and suspended by heavier oil phase.
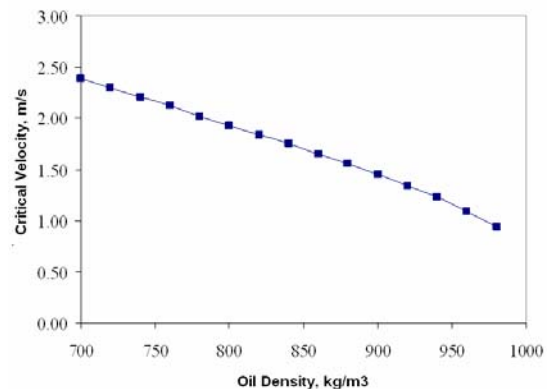
Figure 9: Effect of oil density on critical velocity at d =0.1016 m, μ_o =2 cP, water cut = 20% and σ =0.029 N/m.

Figure 10 shows the effects of oil surface tension on the critical velocity. The figure shows that higher surface tension corresponds to higher critical velocity. It can be explained that higher surface tension correspond to higher surface energy of droplets. This means that higher flow rate of the flowing oil phase is need to deform and break the droplets.
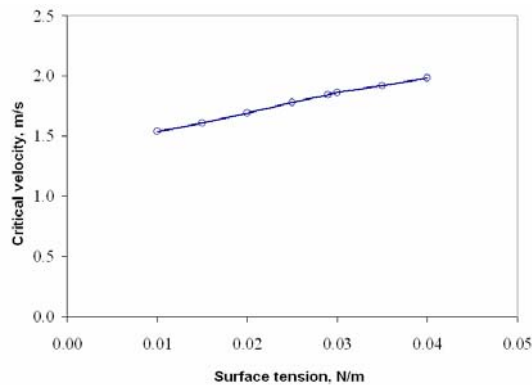
Figure 10: Effect of surface tension on critical velocity at d =0.1016 m, μ_o =2 cP, water cut = 20% and ρ_o =820 kg/m^3.

Figure 11 shows the effect of oil viscosity on the critical velocity. It can be seen that the effect is relatively small. The oils with high viscosities have a slightly higher tendency to form stable oil-water emulsion. One water droplets are entrained in the flowing oil phase; they will be stabilized and suspended as droplets in the oil phase because the coalescence of droplets decreases with increasing the oil viscosity. In this case, lower coalescence at higher oil viscosity leads to a lower critical velocity to form stable water-in-oil dispersed flow.
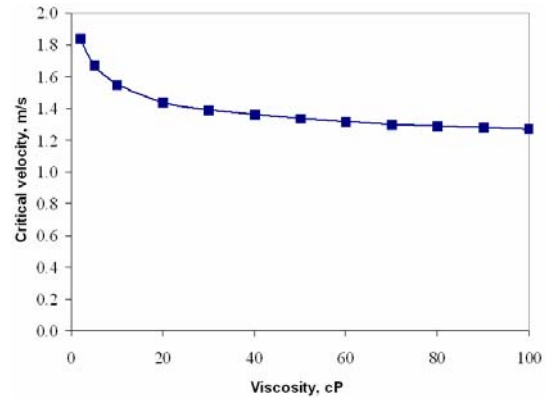
Figure 11: Effect of viscosity on critical velocity at d =0.1016 m, μ_o =2 cP, water cut = 20%, ρ_o =820 kg/m^3 and σ =0.029 N/m.

Conclusion

−   The paper presents a method for evaluating possibility of water wetting and calculating water film thickness in horizontal and nearly horizontal pipelines.
−   The prediction of water wetting possibility is based on the calculation of the critical velocity for water entrainment.
−   The calculation of water film thickness along with in situ water cut, water velocity is carried out by using a two-phase liquid-liquid three-layer model.
−   The validation of the method was performed by using available published experimental data.
−   The effect of input water cut, pipe diameter, oil density, oil-water surface tension and oil viscosity on the critical velocity were evaluated and discussed.

References

Arirachakaran, S., K. D., Oglesby, M. S., Malinovsky, M.S., Shoham, O., and J.P. Brill (1989), An Analysis of Oil-Water Flow Phenomena in Horizontal Pipes, *SPE paper 18836*, 155-167.

Barnea, D. (1987), A Unified Model for Predicting Flow Pattern Transitions for the Whole Range of Pipe Inclinations, *Int. J. of Multiphase Flow*, Vol.11, pp. 1~12.

Bratland O. (2009), Update on Commercially Available Flow Assurance Software Tools: What they can and can not do?, *PetroMin Pipeliner*, Jan-Mar 2009, pp. 32-40.

Brauner, N. (2001), The Prediction of Dispersed Flows Boundaries in Liquid-Liquid and Gas-liquid Systems, *Int. J. of Multiphase Flow*, Vol.27, pp. 885~910.

Brauner, N., Moalem Maron (1992), Flow Pattern Transitions in Two-phase Liquid-liquid Horizontal Tubes, *Int. J. of Multiphase Flow*, Vol.18, pp. 123~140.

Brodkey, R. S. (1969), *The Phenomena of Fluid Motions*, Addison-Wesley, Reading, M. A., 1969.

Neogi, S., Lee, A.H. and Jepson, W.P. (1994), A Model for Multiphase (Gas-Water-Oil) Stratified Flow in Horizontal Pipelines, *SPE 28799*, pp.553-561.

Nguyen The Duc, Phan Ngoc Trung, Bui Dinh Tri (2009), Simulation of Oil-Water Flow in Tube using RANS Model for Multiphase Mixture, *Proceeding of International Workshop "Thermal Hydrodynamics of Multiphase Flow and Application"*, Ha Noi, May 5-6, pp. 127-134.

Фан Нгок Чунг (1986). *Исследование процесса накопления и разработка мероприятий по выносу воды в процессах нефтедобычи.* Диссертация на соискание ученой степени кандидата технических наук. Баку.

Press W.H., Teukolsky S. A., Vetterling W. T., Flannery B. P. (1996), *Numerical Recipes in Fortran 90: The Art of Parallel Scientific Computing, Volume 2 of Fortran Numerical Recipes*, Second Edition, New York, Cambridge University Press, 1996.

Shi. H., Wang H. and Jepson W. P. (2002), Prediction of water film thickness and velocity for corrosion rate calculation in oil-water flows, *NACE 2002*, Paper No. 02500, pp. 1-18.

Taitel, Y., and Dukler, A.E. (1976), A Model for Prediction Flow Regime Transitions in Horizontal and Near Horizontal Gas-Liquid Flows, *AIChE J.*, Vol. 22, No.l, pp. 47-55.

Taitel, Y., Barnea, D. and Brill, J.P. (1995), Stratified Three-phase Flow in Pipes, *Int. J. Multiphase Flow*, Vol. 21, No.1, pp. 53-60.

Trallero, J. L, Sarica, C and J. P. Brill (1996), A Study of Oil-Water Flow Patterns in Horizontal Pipes, *SPE Paper No. 36609*, 363-375.

Vedapuri, D., Bessette, D. and Jepson, W. P. (1997). A Segregated Flow Model to Predict Water Layer Thickness in Oil-Water Flows in Horizontal and Slightly Inclined Pipes, *Multiphase 97*, 75-105.

On an efficient method for improving the accuracy of the inverse kinematics of robotic manipulators

Nguyen Van Khang[*], Nguyen Quang Hoang[*], Tran Hoang Nam[**]

[*] *Hanoi University of Technology*

1. Dai Co Viet, Hanoi

[**] *Technical Pedagogical College of Vinhlong*

nvankhang@mail.hut.edu.vn, hoangnq-dam@mail.hut.edu.vn

Abstract

The inverse kinematics plays an important role in the trajectory planning and the control of industrial robots. The solutions of this problem have an important influence on the motion quality of end-effectors. This paper presents an improved method based on a combination of Taylor development and Newton-Raphson method. By using this method, the accuracy of the solution of inverse kinematics for redundant manipulators is improved. Besides, one of the advantages of redundant manipulators is exploited to avoid impact on joint limitations. Numerical simulations in software Matlab are carried out to verify the efficiencies of the proposed method.

Keywords: redundant manipulator, inverse kinematics, numerical simulation.

1. Introduction

The problem of inverse kinematics plays an important role in the trajectory planning and the motion control of industrial manipulators. This inverse problem should be solved as high accuracy as possible.

The forward kinematics has been solved effectively by several methods such as Denavit-Hartenberg parameters, homogeneous transformation matrix, and e.g. And the results are analytical formulae giving out the relationship of position and orientation of the end-effector in depending on joint coordinates [1-6]. On the contrary, there are not available general methods for solving the inverse kinematics of industrial manipulators. Solution of inverse kinematics in closed form can be obtained in some special cases. In other cases, the numerical methods are a useful tool. Normally, this kind of method based on the jacobian matrix that gives the linear relationship between the velocities of the end-effector and the derivatives of joint coordinates respect to time [9-13]. The joint coordinates can be obtained by integrating its derivatives, which is the solution of linear equations. Simplicity is one of the advantages of this method.

However, error may appear during the integration process due to rounding and integral method. This error is accumulated and therefore the end-effector does not track the desired trajectory. In order to reduce the accumulated error, several researchers use this error as a feedback [4].

This paper presents a novel method based on a combination Taylor development and Newton-Raphson method to improve the accuracy of the solution of the inverse problem.

This paper is organized as follows: section 2 presents a method for inverse kinematics of a redundant manipulator. Some numerical simulations are shown in section 3. Finally, the conclusion is given in section 4.

2. Background of inverse kinematics

2.1 Problem formulation and some formulae

Consider a n DOF robot, let $q \in \mathbb{R}^n$ is a vector containing joint variables. The robot's end-effector is operated in the work space, let $x \in \mathbb{R}^m$ is a vector containing position and orientation variables in the operational space $\mathbb{R}^m$ ($m \leq 6$). The result of forward kinematics yields

$$x = f(q), \qquad x, f \in \mathbb{R}^m, q \in \mathbb{R}^n. \qquad (1)$$

The manipulators are redundant, if $m < n$, the number of DOFs is greater than the required numbers to determine the position and orientation of the end-effector.

Differentiating (1) with respect to time, one obtains

$$\dot{x} = \frac{\partial f}{\partial q}\dot{q} = J(q)\dot{q}, \qquad (2)$$

where

$$J(q) = \frac{\partial f}{\partial q} = \begin{vmatrix} \dfrac{\partial f_1}{\partial q_1} & \dfrac{\partial f_1}{\partial q_2} & \cdots & \dfrac{\partial f_1}{\partial q_n} \\ \cdots & \cdots & \cdots & \cdots \\ \dfrac{\partial f_m}{\partial q_1} & \dfrac{\partial f_m}{\partial q_2} & \cdots & \dfrac{\partial f_m}{\partial q_n} \end{vmatrix}. \qquad (3)$$

Assuming that the jacobian $m \times n$-matrix $J(q)$ has a rank of m. If x and q are known, equation (2) is a set of m linear algebraic equations with n unknown, which is a vector of joint velocity $\dot{q}$. In the set of infinite solutions satisfying (2), we find a solution with a minimal magnitude. In order to find this solution, a quadratic cost functional of joint velocities is introduced

$$J = \tfrac{1}{2}\dot{q}^T W \dot{q}, \qquad (4)$$

where W is a suitable ($n \times n$) symmetric positive definite weighting matrix. This problem can be solved with the method of Lagrangian multipliers. Considering the modified cost functional

$$\mathcal{L}(\dot{q}, \lambda) = \tfrac{1}{2}\dot{q}^T W \dot{q} + \lambda^T[\dot{x} - J(q)\dot{q}], \qquad (5)$$

differentiating $\mathcal{L}$ with respect to $\dot{q}$ one yields

$$\frac{\partial}{\partial \dot{q}}\mathcal{L}(\dot{q}, \lambda) = W\dot{q} - J^T(q)\lambda = 0$$

Solving for $\dot{q}$ one yields

$$\dot{q} = W^{-1}J^T(q)\lambda \qquad (6)$$

which, substituted into (2), gives the sought optimal solution

$$\dot{x} = J(q)\dot{q} = J(q)W^{-1}J(q)^T \lambda. \qquad (7)$$

With the assumption that $J(q)W^{-1}J(q)^T$ is non-singular, solving for λ yields

$$\lambda = [J(q)W^{-1}J(q)^T]^{-1}\dot{x}. \qquad (8)$$

So we get an optimal solution for $\dot{q}$ as

$$\begin{aligned} \dot{q} &= W^{-1}J^T(q)[J(q)W^{-1}J^T(q)]^{-1}\dot{x} \\ &\hat{=} J(q)_W^+\dot{x}. \end{aligned} \qquad (9)$$

The matrix

$$J(q)_W^+ = W^{-1}J^T(q)[J(q)W^{-1}J^T(q)]^{-1} \qquad (10)$$

is called as the weighting pseudo-inverse of $J(q)$ [7,14]. In particular cases, if the weighting matrix W is chosen to be the identity matrix, one obtains.

$$J(q)^+ = J^T(q)[J(q)J^T(q)]^{-1} \qquad (11)$$

Matrix $J^+(q)$ is pseudo-inverse of $J(q)$ and

$$\dot{q} = J^+(q)\dot{x}. \qquad (12)$$

Integrating $\dot{q}$ one gets

$$q(t) = q(0) + \int_0^t \dot{q}(\tau)d\tau \qquad (13)$$

Joint acceleration $\ddot{q}$ can be determined directly by differentiating (12) with respect to time

$$\ddot{q} = J^+(q)\ddot{x} + \dot{J}^+(q)\dot{x} \qquad (14)$$

with $\dot{J}^+(q) = \dfrac{d}{dt}J^+(q)$.

Mathematically, it can differentiate directly pseudo inverse matrix $J^+(q)$ respect to time. But

this work costs burden of calculation. From equation (11) one gets

$$J^+(q)[J(q)J^T(q)] = J^T(q). \qquad (15)$$

By differentiating (16) with respect to time one obtains

$$\dot{J}^+(q)[J(q)J^T(q)] + J^+(q)[\dot{J}(q)J^T(q)]$$
$$+ J^+(q)[J(q)\dot{J}^T(q)] = \dot{J}^T(q). \qquad (16)$$

So we get

$$\dot{J}^+(q) = \{\dot{J}^T(q) - J^+(q)[\dot{J}(q)J^T(q)]$$
$$- J^+(q)[J(q)\dot{J}^T(q)]\}[J(q)J^T(q)]^{-1}. \qquad (17)$$

Substituting (17) into (14) yields

$$\ddot{q} = J^+(q)\ddot{x} + \{\dot{J}^T(q) - J^+(q)[\dot{J}(q)J^T(q)]$$
$$- J^+(q)[J(q)\dot{J}^T(q)]\}[J(q)J^T(q)]^{-1}\dot{x} \qquad (18)$$

The equations (12) and (18) show that the vector of generalized velocity $\dot{q}(t)$ and acceleration $\ddot{q}(t)$ can be determined at time t, if the vector of joint variable $q(t)$ is known. The following section presents a method to get joint variables.

2.2 Determination joint variables by Taylor expand

Assuming that at time t_k, joint coordinates $q_k = q(t_k)$ are known. These joint variables at the time $t_{k+1} = t_k + \Delta t$ will be found. Using Taylor development $q(t)$ around $t = t_k$ as

$$q(t) = q(t_k + \Delta t)$$
$$= q(t_k) + \dot{q}(t_k)\Delta t + \tfrac{1}{2}\ddot{q}(t_k)\Delta t^2 + ... \qquad (19)$$

If taking only two first terms, and putting (5) into (12) one gets

$$q(t) = q(t_k + \Delta t)$$
$$= q(t_k) + J^+(q)\dot{x}(t_k)\Delta t. \qquad (20)$$

If taking three first terms, and putting (12) and (18) into (19) one gets

$$q(t) = q(t_k + \Delta t) = q(t_k) + J^+(q)\dot{x}(t_k)\Delta t$$
$$+ \tfrac{1}{2}[J^+(q)\ddot{x} + \dot{J}^+(q)\dot{x}]_{(t_k)}\Delta t^2. \qquad (21)$$

Thus, the generalized coordinates are determined by equations (20) or (21). With the formulae (20) the calculation is simple but by using formula (21), the precision is better but it costs a burden of calculation. In this paper, the formula (20) is used with an adjustion to get the solution with higher accuracy.

2.3 Determination joint variables by error adjustion

a) Error adjustion at beginning time t_o

At time $t = t_o$, a good approximation $\tilde{q}_o$ of q_o corresponding to $x_o = x(t_o)$ is chosen. The better solution will be found as follows

$$\tilde{q}_0 := \tilde{q}_0 + \Delta q_0 \qquad (22)$$

where Δq_0 is an error required to find. Putting (22) into equation (1), and applying Taylor expansion, we get

$$x_o = f(q_o) = f(\tilde{q}_o + \Delta q_o)$$
$$= f(\tilde{q}_o) + J(\tilde{q}_o)\Delta q_o + ... \qquad (23)$$

Taking only two first terms in (23) one obtains

$$J(\tilde{q}_o)\Delta q_o = x_o - f(\tilde{q}_o). \qquad (24)$$

Solving this set of linear equations for Δq_o yields

$$\Delta q_o = J^+(\tilde{q}_o)[x_o - f(\tilde{q}_o)].$$

Taking $\tilde{q}_0 := \tilde{q}_0 + \Delta q_0$ to be new approximation of q_o. Checking the condition, if $\|x(0) - f(\tilde{q}_0)\| > \varepsilon$, ε is an allowable error, then repeat the solving (24) until $\|x(0) - f(\tilde{q}_0)\| < \varepsilon$.

The generalized velocities $\dot{q}_o$ and accelerator $\ddot{q}_o$ at time t_o are obtained by putting the initial values of q_o into (12) and (14).

b) Error adjustion at time t_{k+1}

Firstly, taking $\tilde{q}_{k+1}$ to be a good approximation of q_{k+1} that is found by (20)

$$\tilde{q}(t_{k+1}) = q(t_k) + J^+(q_k)\dot{x}(t_k)\Delta t \qquad (24)$$

Then, the better approximation of q_{k+1} will be determined by

$$q(t_{k+1}) = \tilde{q}(t_k) + \Delta q_{k+1}, \qquad (25)$$

with Δq_{k+1} is the error needed to be found.

Putting (25) into equation (1) then using taylor expansion

$$\boldsymbol{x}_{k+1} = \boldsymbol{f}(\boldsymbol{q}_{k+1}) = \boldsymbol{f}(\tilde{\boldsymbol{q}}_{k+1} + \Delta \boldsymbol{q}_{k+1})$$
$$= \boldsymbol{f}(\tilde{\boldsymbol{q}}_{k+1}) + \boldsymbol{J}(\tilde{\boldsymbol{q}}_{k+1})\Delta \boldsymbol{q}_{k+1} + ...$$

Taking two first terms in the expansion, the linear equation for $\Delta \boldsymbol{q}_{k+1}$ is given as

$$\boldsymbol{J}(\tilde{\boldsymbol{q}}_{k+1})\Delta \boldsymbol{q}_{k+1} = \boldsymbol{x}_{k+1} - \boldsymbol{f}(\tilde{\boldsymbol{q}}_{k+1}) \,. \qquad (26)$$

Similarly to (24), equation (26) has several solutions, here we take the one with smallest norm as follows:

$$\Delta \boldsymbol{q}_{k+1} = \boldsymbol{J}^+(\tilde{\boldsymbol{q}}_{k+1})[\boldsymbol{x}_{k+1} - \boldsymbol{f}(\tilde{\boldsymbol{q}}_{k+1})] \,. \qquad (27)$$

Taking $\tilde{\boldsymbol{q}}_{k+1} := \tilde{\boldsymbol{q}}_{k+1} + \Delta \boldsymbol{q}_{k+1}$ to be the new approximation of $\boldsymbol{q}_{k+1}$, then cheking condition, if $\left\| \boldsymbol{x}_{k+1} - \boldsymbol{f}(\tilde{\boldsymbol{q}}_{k+1}) \right\| > \varepsilon$, then repeating of solving (26) until $\left\| \boldsymbol{x}_{k+1} - \boldsymbol{f}(\tilde{\boldsymbol{q}}_{k+1}) \right\| \leq \varepsilon$ is satisfied. Putting the obtained value $\boldsymbol{q}_{k+1}$ into (12) and (14) we get $\dot{\boldsymbol{q}}_{k+1}$ and $\ddot{\boldsymbol{q}}_{k+1}$. The block diagram of the algorithm is shown in Fig. 1.

Considering the nullspace of the jacobian matrix $\boldsymbol{J}(\boldsymbol{q})$, the solution of linear equation (2) can be written in the following form:

$$\dot{\boldsymbol{q}} = \boldsymbol{J}^+(\boldsymbol{q})\dot{\boldsymbol{x}} + [\boldsymbol{E} - \boldsymbol{J}^+(\boldsymbol{q})\boldsymbol{J}(\boldsymbol{q})]\boldsymbol{z}_o \qquad (28)$$

where $\boldsymbol{z}_0 \in \mathbb{R}^n$ is an arbitrary vector and $\boldsymbol{E} \in \mathbb{R}^{n \times n}$ is a unit matrix.

By choosing vector $\boldsymbol{z}_0$ advantages of the redundancy are exploited (avoiding obtacles, singularities in configuration, impact with joint limitation). In this paper, the vector $\boldsymbol{z}_0$ is chosen as

$$\boldsymbol{z}_0 = -\alpha \frac{\partial \phi(\boldsymbol{q})}{\partial \boldsymbol{q}} \qquad (29)$$

with constant α and

$$\phi(\boldsymbol{q}) = \frac{1}{2} \sum_{i=1}^{n} c_i \left(\frac{q_i - \overline{q}_i}{q_{iM} - q_{im}} \right)^2, \qquad (30)$$

where q_{iM}, q_{im} and $\overline{q}_i$ are maximal, minimal and average values of joint variables respectively; $c_i > 0$ are weighting coefficients.

Differentiating (28) with respect to time one obtains

$$\ddot{\boldsymbol{q}} = \boldsymbol{J}^+(\boldsymbol{q})\ddot{\boldsymbol{x}} + \dot{\boldsymbol{J}}^+(\boldsymbol{q})\dot{\boldsymbol{x}} +$$
$$[\boldsymbol{E} - \boldsymbol{J}^+(\boldsymbol{q})\boldsymbol{J}(\boldsymbol{q})]\dot{\boldsymbol{z}}_o - \frac{d}{dt}[\boldsymbol{J}^+(\boldsymbol{q})\boldsymbol{J}(\boldsymbol{q})]\boldsymbol{z}_o \qquad (31)$$
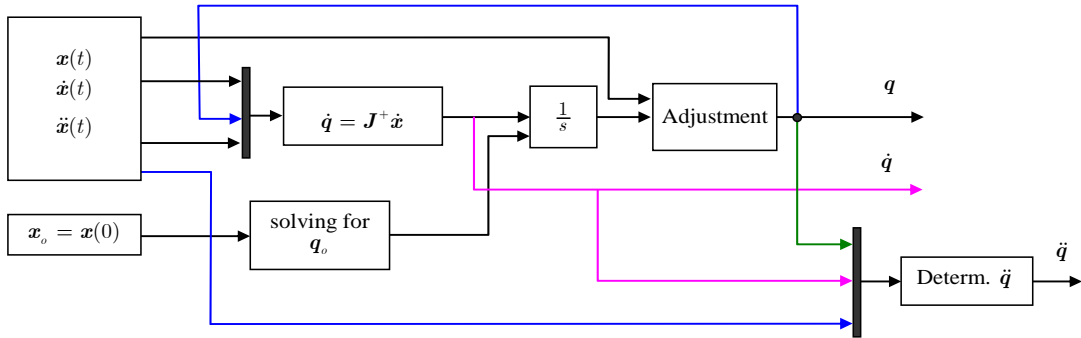
Fig. 1. Block diagram of the algorithm

3. Numerical Simulations

3.1 Case of planar manipulator

In this section, some simulations in universal software Matlab is implemented to illustrate the presented algorithm. Let us consider a 5-DOF planar manipulator moving in the vertical plane. The ith link has a length of l_i. The model of the

manipulator and its parameters are shown in Fig. 2 and Table 1.

Table 1. Some parameters of the manipulator

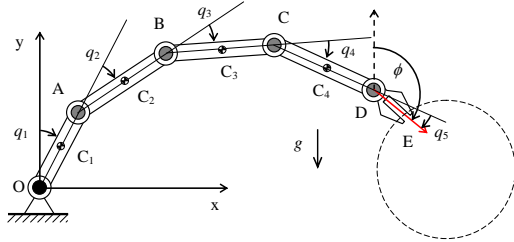| Link i	1	2	3	4	5
l [m]	0.55	0.50	0.45	0.40	0.20

Fig. 2. A 5-DOF planar manipulator

In this simulation, the end-effector (link 5) will be forced to move at the velocity of 0.5 m/s along a circular trajectory, while its orientation is constant, $\phi = 1.0$ rad. The trajectory has a center at $(x_C,\ y_C) = (0.8,\ 0.5)$ m and radius of $R = 0.3$ m.

The result of the forward kinematics, one yields

$$x = f(q),$$

$$f(q) = \begin{bmatrix} \sum_{k=1}^{5} L_k \sin(\sum_{i=1}^{k} q_i) \\ \sum_{k=1}^{5} L_k \cos(\sum_{i=1}^{k} q_i) \\ \sum_{i=1}^{5} q_i \end{bmatrix},$$

where $x = \begin{bmatrix} x & y & \phi \end{bmatrix}^T$ is a vector containing position $(x,\ y)$ and orientation ϕ of the end-effector; $q = \begin{bmatrix} q_1 & q_2 & q_3 & q_4 & q_5 \end{bmatrix}^T$ is a vector of joint angles.

A. Without consideration of joint limitations

In case the vector z_0 is chosen to be a null-vector, it means the limitation of joint variables is not taken into account. The simulation results are shown in figures 3 and 4. Fig. 3 shows the joint variable and its derivatives. And fig. 4 shows the error of position and orientation of the end-effectors.
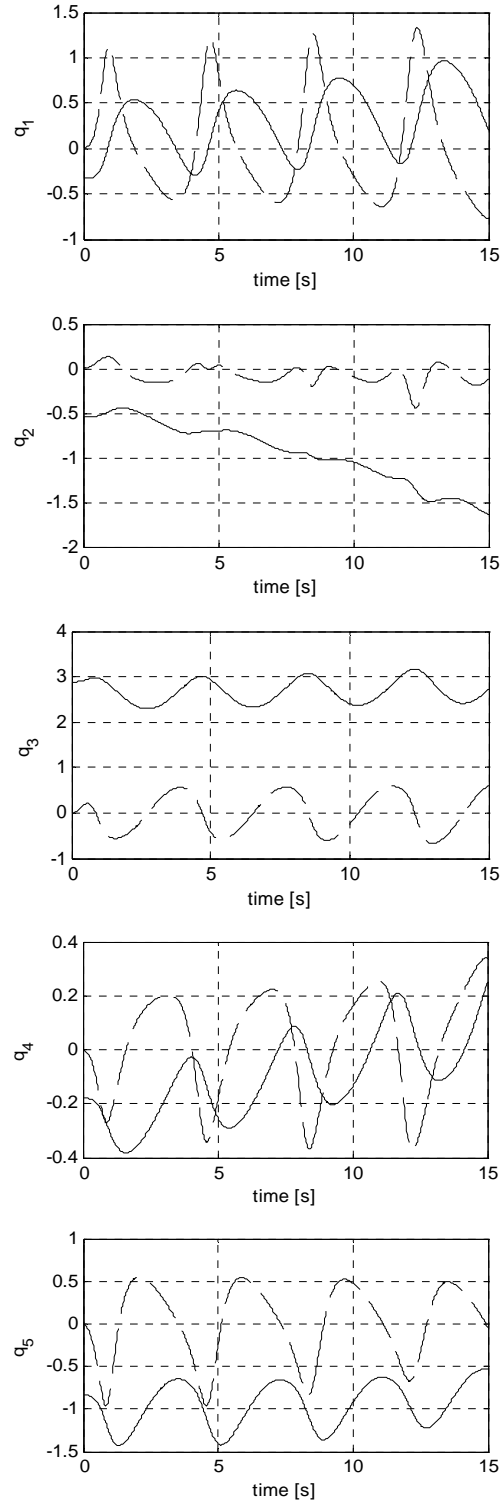
Fig. 3. Time history of joint variables and its derivatievs: $q_i(t)$ (continuous lines) and $\dot{q}_i(t)$ (dashed lines) [$i = 1,...,5$]
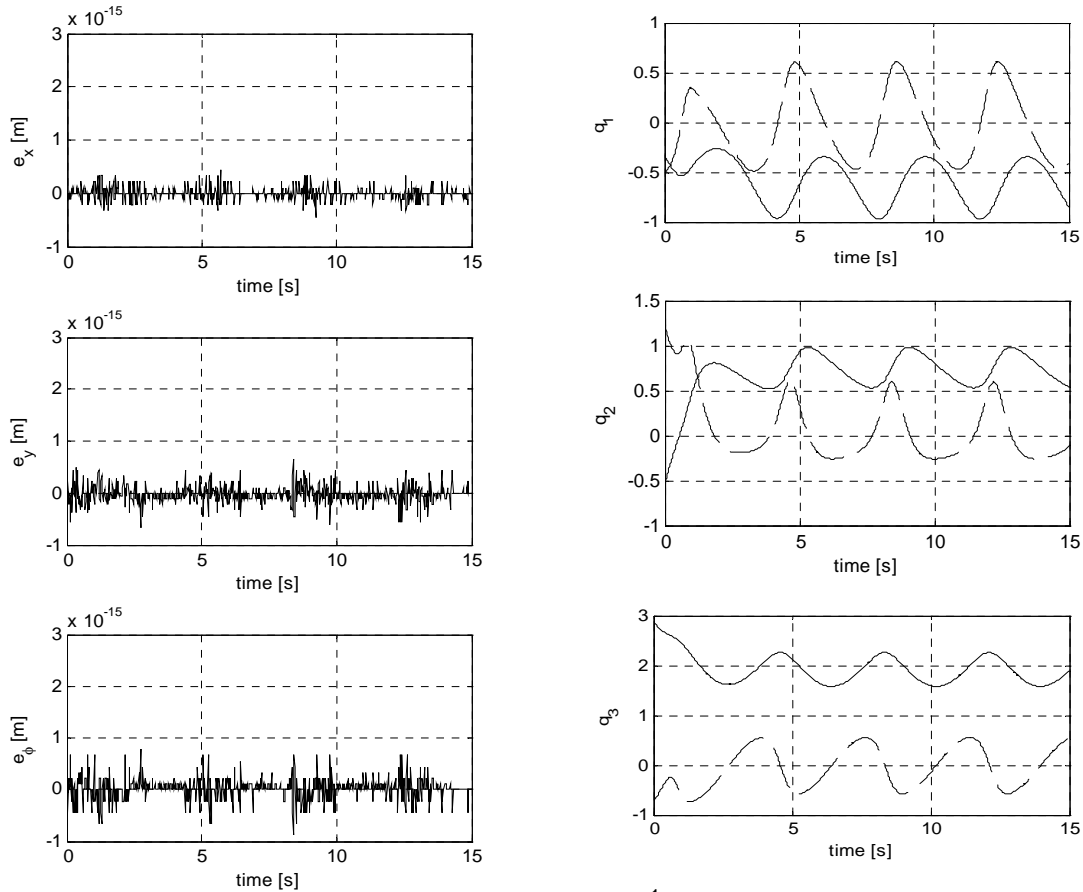
Fig. 4. Position and orientation errors

The results show that although the motion of the end-effector is periodic and repeated serveral times, but joint variables are changed to increase or decrease after each period. If working time is longer, these joint variables may exceed their limitations. The position and orientation error are very small.

B. Consideration of joint limitations

We consider the case, in wich the limitation of joint variables is taken into account with $q_{iM} = 2.5$ rad, $q_{im} = -2.5$ rad, $\overline{q}_i = 0$. In this simulation we chose coefficients $c_i = 1$, $k = -50$ ($i = 1,...,5$). The simulation results are shown in figures 5 and 6. Fig. 5 shows the joint variable and its derivatives. Fig. 6 shows the error of position and orientation of the end-effectors.
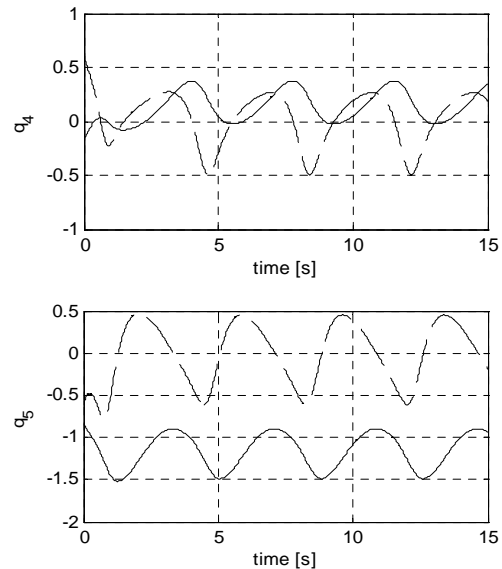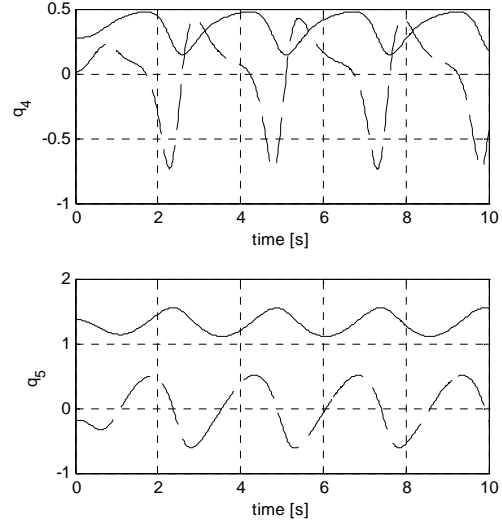

Fig. 5. Time history of joint variables and its derivatievs: $q_i(t)$ (continuous lines) and $\dot{q}_i(t)$ (dashed lines) [$i = 1,...,5$]

Fig. 4. Position and orientation errors
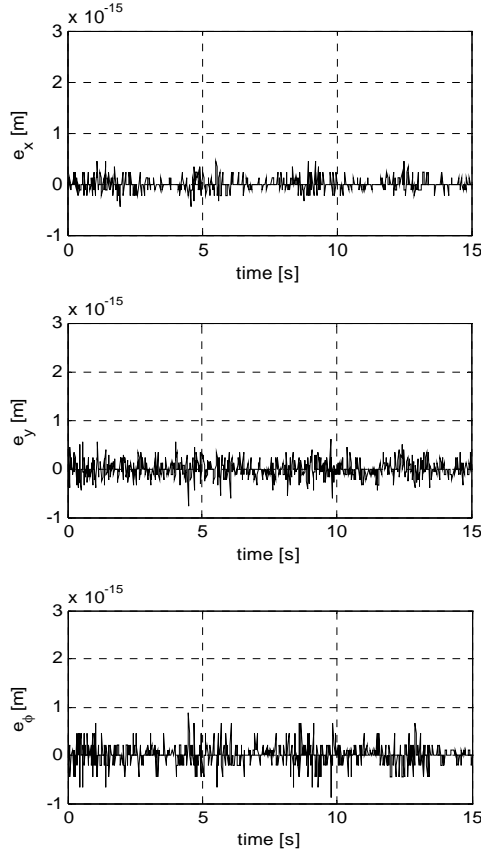
Fig. 7. Manipulator in three dimensions

Similar to the previous case, the position and orientation error are very small. But the considerable feature in this case is that the joint variables are changed and repeats periodically within its limitations.

3.2 Case of spatial manipulator

Let us consider a 5-DOF spatial manipulator. The ith link has a length of L_i. The model of the manipulator and its parameters are shown in Fig. 7 and Table 2.

Table 2. Some parameters of the manipulator

Link i	Length	Values (m)
1	l_1	0.60
2	l_2	0.50
3	l_3	0.25
4	l_4	0.25
5	l_5	0.35

Table 3. Denavit-Hartenberg parameters

Link i	θ_i	d_i	a_i	α_i
1	q_1	l_1	0	$\frac{1}{2}\pi$
2	$\frac{1}{2}\pi + q_2$	0	l_2	0
3	$-(q_3 - \frac{1}{2}\pi)$	0	0	$\frac{1}{2}\pi$
4	q_4	$l_3 + l_4$	0	$-\frac{1}{2}\pi$
5	$\frac{3}{2}\pi - q_5$	0	l_5	0

Joint limitations:

$$q_{iM} = 2.5\,\text{rad},\ q_{iM} = -2.5\,\text{rad},\ \overline{q}_i = 0\,,$$

$$i = 1,...,5$$

In order to obtain the coordinates of the end-effector depending on joint variables the Denavit-Hartenberg convention is applied. With the parameters shown in Table 3, the position of end-effector in the fixed frame are determined as

$$\begin{aligned}
x_E = &-cq_1 sq_2 l_2 + (cq_1 cq_2 sq_3 - cq_1 sq_2 cq_3)l_3 \\
&+ (cq_1 cq_2 sq_3 - cq_1 sq_2 cq_3)l_4 \\
&+ (sq_5 cq_4 cq_1 sq_2 sq_3 + sq_2 cq_4 cq_1 cq_2 cq_3 \\
&- sq_5 sq_1 sq_4 \\
&- cq_5 cq_1 sq_2 cq_3 + cq_5 cq_1 cq_2 sq_3)l_5
\end{aligned}$$

$$y_E = -sq_1sq_2l_2 + (sq_1cq_2sq_3 - sq_1sq_2cq_3)l_3$$
$$+(sq_1cq_2sq_3 - sq_1sq_2cq_3)l_4$$
$$+(sq_5cq_4sq_1sq_2sq_3 + sq_5cq_4sq_1cq_2cq_3$$
$$+sq_5cq_1sq_4$$
$$-cq_5sq_1sq_2cq_3 + cq_5sq_1cq_2sq_3)l_5$$
$$z_E = l_1 + cq_2l_2 + (cq_2cq_3 + sq_2sq_3)l_3$$
$$+(cq_2cq_3 + sq_2sq_3)l_4$$
$$+(cq_4sq_5sq_2cq_3 - cq_4sq_5cq_2sq_3$$
$$+cq_5cq_2cq_3 + cq_5sq_2sq_3)l_5$$

In this simulation, the end-effector (point E) will be forced to move at the velocity of 0.5 m/s along a circular trajectory. The trajectory has a center at $(x_C, y_C) = (0.0, 0.4, 0.5)$ m and radius of $R = 0.2$ m.

The simulation results are shown in figures 8 and 9. Fig. 8 shows the joint variable and its derivatives. And fig. 9 shows the error of position and orientation of the end-effectors.

Fig. 8. Time history of joint variables and its derivatievs: $q_i(t)$ (continuous lines) and $\dot{q}_i(t)$ (dashed lines) [$i = 1,...,5$]
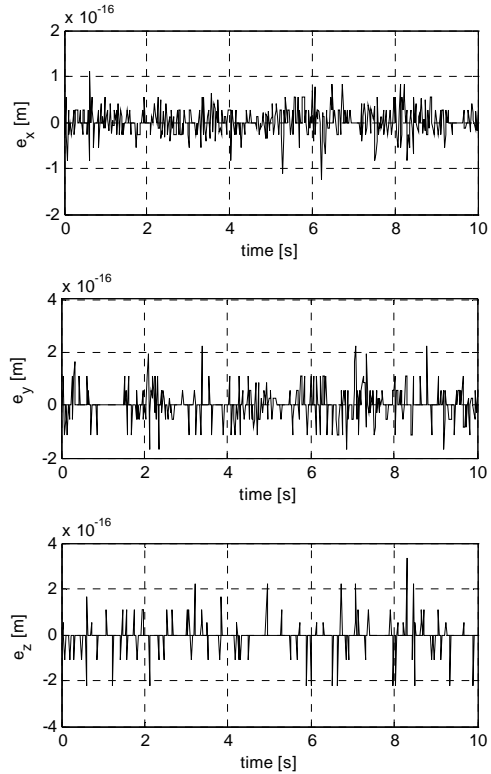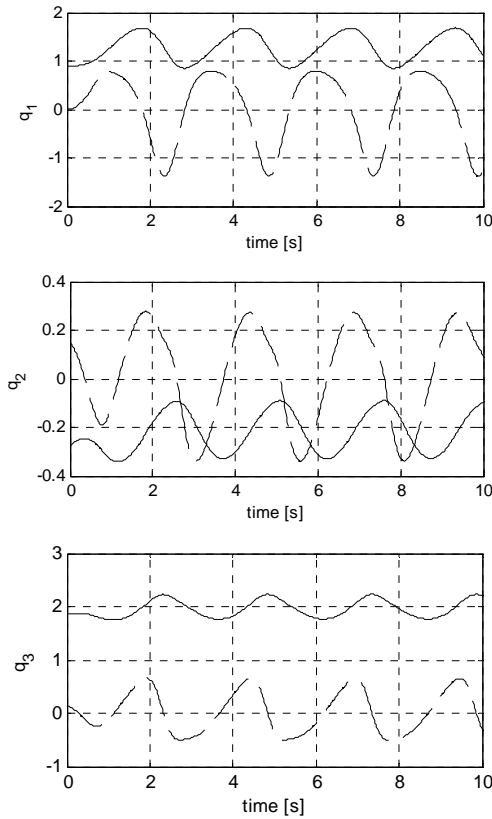
Fig. 9. Position error

The results show that although the relation between x and q - the function $f(x,q)$ - is very complicated but the obtained results have a high accuracy at about 10^{-16} and the diagrams of the joint variables have periodic form within their limitations. Hence, the impact with joint limits can be avoided.

4. Conclusion

This paper presents a new algorithm to solve the inverse kinematics of redundant manipulators, in which the joint variables have been adjusted to improve the accuracy of the solutions. The effectiveness of the proposed method is demonstrated by means of numerical experiments with the redundant planar manipulator as well as the spatial one.

Acknowledgement

References

[1]   Nguyen Van Khang. *Dynamics of mutibody systems*. Science and Technology Publishing House, Hanoi, 2007. (in Vietnamese)

[2]   Nguyen Thien Phuc: *Industrial Robots*. Science and Technology Publishing House, Hanoi, 2002. (in Vietnamese).

[3]   M. W. Spong, S. Hutchinson, and M. Vidyasagar. *Robot Modeling and Control*. John Wiley & Sons, New York, 2006.

[4]   L. Sciavicco, B. Siciliano. *Modelling and Control of Robot Manipulators, 2nd Edition*, Springer-Verlag, London, UK, 2000.

[5]   Murray, R.M. ; Li, Z. ; Sastry, S.S.: *A Mathematical Introduction to Robotic Manipulation*. CRC Press, Boca Raton, Fla. [u.a.], 1994.

[6]   Angeles J.: *Fundamentals of robotics Mechanical Systems* (2. Edition), Springer Verlag, New York, 2003.

[7]   Y. Nakamura. *Advanced Robotics/ Redundancy and Optimization*. Addison-Wesley Publishing Company, Reading 1991.

[8]   R. V. Patel, F. Shadpey: *Control of redundant robot manipulators*. Springer-Verlag, Berlin 2005.

[9]   Nguyen Van Khang, Do Anh Tuan, Nguyen Phong Dien, Tran Hoang Nam: Influence of Trajectories on the Joint Torques of kinematically Redundant Manipulators. Vietnam Journal of Mechanics, Vol. 29 (2007), No.2, pp. 65-72.

[10] Nguyen Van Khang, Le Duc Dat, Tran Hoang Nam. *On an algorithm for solving the inverse kinematics of serial manipulator*. Proceedings of the 8th National Conf. on Mechanics, Vol. 1, pp. 250-259, Hanoi 2008 (in Vietnamese).

[11] Nguyen V. K., Nguyen Q. H., Le D. D., and Tran H. N.. On an algorithm of sliding mode control of redundant manipulators. Journal of Competer Science and Cybernetics. Vol. 4, No. 3 (2008), pp. 269-280. (in Vietnamese).

[12] Nguyen Quang Hoang, Nguyen Van Khang, Tran Hoang Nam: On kinematic inverse of redundant manipulators under consideration of jammed joint. Proceedings of National Conf. on Mechanics (anniversary 30 years Institute of Mechanics and Vietnam Journal of Mechanics), Hanoi 2009. (in Vietnamese).

[13] Nguyen Quang Hoang, Nguyen Van Khang: *On kinematic inverse and control of redundant manipulators under consideration of jammed joint*. Proceedings of the 1st Int. Symp. on Robotics and Mechatronics, Hanoi, 2009, pp.201-207.

[14] C. Radhakrishna Rao and Sujit Kumar Mitra. *Generalized Inverse of Matrices and its Applications*, John Wiley & Sons New York, 1971.

A Proposed Technique for on-Orbit Structural Health Monitoring of the Mechanical Structure of a Satellite under Thermal Loading

Khoa V. Nguyen[a] and Robert H. Bishop[b]

[a] *Institute of Mechanics, Vietnam Academy of Science and Technology*
[b]*Department of Aerospace Engineering & Mechanical Engineering,
University of Texas at Austin, USA.*

Abstract

The spatial strain and displacement of a cracked solar panel of a satellite subjected to thermal loading is investigated in this paper. The purpose is to reveal the distortion of the spatial strain when there is a crack existence. A cracked solar panel is modelled by Finite Element Method (FEM) using ALGOR™ software. When the solar panel is exposed to the sun, one side of the panel is heated by the sun and the other side is in the shadow. Thus, there is a temperature difference between the two sides leading to the bending of the solar panel. The temperature profile of the panel is calculated by Steady State Heat Transfer Analysis and the bending of the panel is analyzed by Static Analysis of ALGOR™. When there is a crack, the strain distribution across the crack can be distorted at the crack area. However, the distortion of the strain caused by a small crack is usually small and difficult to detect visually. In order to detect such small distortion, Wavelet Transform with its capacity of local analysis is used. Simulation results obtained from FEM and data processing technique using Wavelet Transform are promising. It is shown that the wavelet-based method for early crack detection can be used for on-orbit structural health monitoring of satellite structures subjected to thermal loading.

1. Introduction

The mechanical structure of a satellite plays an important role in ensuring reliable operation in space of certain process such as separation from the launcher, deployment and orientation of solar panels, precise pointing of satellite antennae, operation of rotating part and so on. In general, a satellite is facing to the launching as well as working conditions on its orbit. During the launch phase, the satellite structure is acted on by high accelerations and vibrations. When working on the orbit it can be subjected to collision with micrometeorites, space junk, and charged particles floating in space. In addition, some parts of the satellite structure exposed to the sun, such as antennae or solar panels, are suffered to thermal cycles throughout its lifetime. The temperatures can be several hundred degrees Celsius on the side facing the sun and several tens of degrees below zero degrees Celsius on the shaded side. This temperature difference leads to the different thermal expansions of

the two sides. As a result, there is a distortion of the structure. This distortion is repeated during the lifetime of the structure. All the above harsh conditions can result in damages in the form of cracks in the mechanical structure of the satellite. If there are cracks in the parts exposed to the sun, the development of these cracks due to further repeated loading can lead to structural failure. Therefore, online monitoring and assessing the integrity of the mechanical structure of the satellite needs to be carried out.

There are several works carried out on satellite structural analysis under thermal loading. Shin, Kim, Hong, Lee [2] studied the thermal expansion of graphite/epoxy composite materials to predict the failure thermal cycles of composite laminates exposed to attack of low-earth orbit environment. In other work [3], these authors presented transient analyzes to predict the thermal distortion of the Korea Multi-Purposes Satellite solar array on its orbit. In their work, the temperature distribution and thermal distortion of the solar array were calculated to evaluate the degradation effect of the composite facesheets in the low-earth orbit. Abdelal G. et al [4, 5] used finite difference and finite element methods to analyze the thermal fatigue of a small-satellite structure. The temperature profile of the structure was first calculated by finite difference analysis and then, thermal fatigue analysis is performed applying finite-element analysis to calculate the resultant damage due to on-orbit cyclic stresses, and structure deformations at the payload and attitude determination and control subsystem equipments seats, and solar panel structures. Recently, Liua Y., Li G., Jiang L. [6] developed a thermal network model for studying the temperature variation of complicated structure satellite surfaces. The solar incident areas were simulated by means of Monte Carlo ray tracing method. The non-uniformity and the instability of solar radiation were investigated for analysis variation of antenna temperature fields in

detail. Their results showed non-uniformity irradiation effects are greater than those of instability for this kind of geometry sheltering structure. However, as the best knowledge of the authors of this paper, research on damage detection techniques based on thermal loading applied for on orbit satellite structural health monitoring are almost void.

There are different analytical techniques based on different structural response signals which may be applied for the purpose of damage detection such as: vibration response, static response, acoustic response, etc. In these techniques the damage can be detected by using the changes in frequency mode shape, mode shape curvatures, flexibility matrix, or using damage index, artificial neural networks, and wavelet transform. Many authors applied successfully these methods for structural damage detection [7, 8, 9, 10, 11, 12]. However, most of the current works on damage detection are applied for earth-based structures under mechanical excitation forces, not thermal loading.

In the last decade, the wavelet transform has emerged as an efficient tool for signal processing due to its flexibility and precision in time and frequency resolution. Some authors have applied spatial wavelet transform for crack detection of structures subjected to static loads [13, 14, 15, 16]. The spatially distributed structural response measurements have been used in order to extract the crack position using wavelet transform. The minor localized damage induced significant changes of the wavelet coefficients at the location of the damage. In other works [17, 18, 19, 20], wavelet-based approaches were applied to investigate the crack using dynamic responses of cracked structures under external excitations. Cracks were detected by using wavelet analysis of deflections or mode shapes of the cracked structures. Recently [21], the author of this paper proposed a wavelet based method for

crack detection by analyzing the time history signals of a breathing crack of structures.

From the above reviews, the aim of the work is to extend the state of the art of structural health monitoring by applying wavelet based technique for crack detection of satellite structures subjected to thermal loading. In this work, strain signals of an on-orbit mechanical cracked solar panel of a satellite subjected to thermal loading will be simulated by FEM and investigated by wavelet analysis to detect the crack.

2. Continuous Wavelet Transform background

Wavelet transform analysis uses little wavelike function known as *wavelet*. A more accurate description is that a wavelet is a function which has local wavelike properties. The continuous wavelet transform (CWT) is defined as follows [22]:

$$W(a,b) = \frac{1}{\sqrt{a}} \int_{-\infty}^{+\infty} f(t)\psi^*\left(\frac{t-b}{a}\right)dt \quad (1)$$

Where, a is a real number called scale or dilation, b is a real number called position, W(a,b) are wavelet coefficients at scale a and position b, f(t) is input signal, $\psi\left(\frac{t-b}{a}\right)$ is wavelet function, and $\psi^*\left(\frac{t-b}{a}\right)$ is complex conjugate of $\psi\left(\frac{t-b}{a}\right)$.

If denote $\psi_{a,b}(t) = \frac{1}{\sqrt{a}}\psi^*\left(\frac{t-b}{a}\right)$, the wavelet transform (5.1) can be simplified as:

$$W(a,b) = \int_{-\infty}^{+\infty} f(t)\psi_{a,b}dt \quad (2)$$

In order to be classified as a wavelet, a function must satisfy certain mathematical criteria, they are:

1) A wavelet must have finite energy:

$$E = \int_{-\infty}^{+\infty} |\psi(t)|^2 dt < \infty \quad (3)$$

2) If $\hat{\psi}(\omega)$ is Fourier transform of $\psi(t)$, i.e.

$$\hat{\psi}(\omega) = \int_{-\infty}^{+\infty} \psi(t)e^{-i\omega t} dt \quad (4)$$

then the following condition must be satisfied:

$$C_g = \int_0^\infty \frac{|\hat{\psi}(\omega)|^2}{\omega} d\omega < \infty \quad (5)$$

This implies that the wavelet has no zero frequency component: $\hat{\psi}(0) = 0$,

$$\int_{-\infty}^{+\infty} \psi(t)e^{-j\omega t} dt = 0 \quad when \, \omega = 0 \quad (6)$$

or in other words, the wavelet must have a zero mean:

$$\int_{-\infty}^{+\infty} \psi(t)dt = 0 \quad (7)$$

3) An additional criterion is that, for complex wavelets, the Fourier transform must both be real and vanish for negative frequencies.

Inverse wavelet transform

Wavelet transform has its inverse transform:

$$f(t) = C_g^{-1} \int_{-\infty}^{+\infty}\int_{-\infty}^{+\infty} W(a,b)\psi_{a,b}db\frac{da}{a^2} \quad (8)$$

where

$$C_g = 2\pi \int_{-\infty}^{\infty} \frac{|\hat{\psi}(\xi)|^2}{|\xi|} d\xi < \infty \quad (9)$$

Equation (28) can be rewritten as follows:

$$f(t) = C_g^{-1} \int_{-\infty}^{+\infty} a^{-2}\left[\int_{-\infty}^{+\infty} W(a,b)\psi_{a,b}db\right]da \quad (10)$$

3. Simulation of an on-orbit cracked solar panel subjected to thermal loading using ALGOR

When the satellite just comes out of the shadow of the earth, one side of the solar panel of is heated by sun and other side is shadowed by the panel itself. This leads to the difference of temperatures on the two surfaces of the solar panel and this difference continuously varies along the orbit until the satellite enters the earth's shadow. The difference of temperatures and their changes on two sides of a solar panel moving on orbit were investigated by Shin et al [3]. In their work, the temperatures on the two sides of the solar panel were calculated from the environment conditions on low earth orbit and they concluded that the maximum temperature on the panel is about 60 ^{o}C, and the maximum difference of temperatures on the two sides is about 5 ^{o}C. In our work, the calculation of temperatures on the surfaces of the panel is not the objective, thus some extrem scenarios (see Table 1) of temperatures of the solar panel taken from [3] will be used as the input for calculating the temperature profile of the panel. From this, the thermal expansion and bending of the panel will be analyzed. In this work, the temperature profile of the panel is calculated by Steady State Heat Transfer Analysis and the thermal expansion and bending of the panel is analyzed by Static Analysis of ALGOR™.

In this paper, the simulation is carried out for the solar panel of a satellite made in the Department of Aerospace Engineering and Engineering Mechanics, the University of Texas at Austin, US (see Fig. 1). The structure of the solar panel is honeycomb with the dimensions of 300 x 217 x 6.35 mm. The material parameters of honeycomb are given in Table 2.
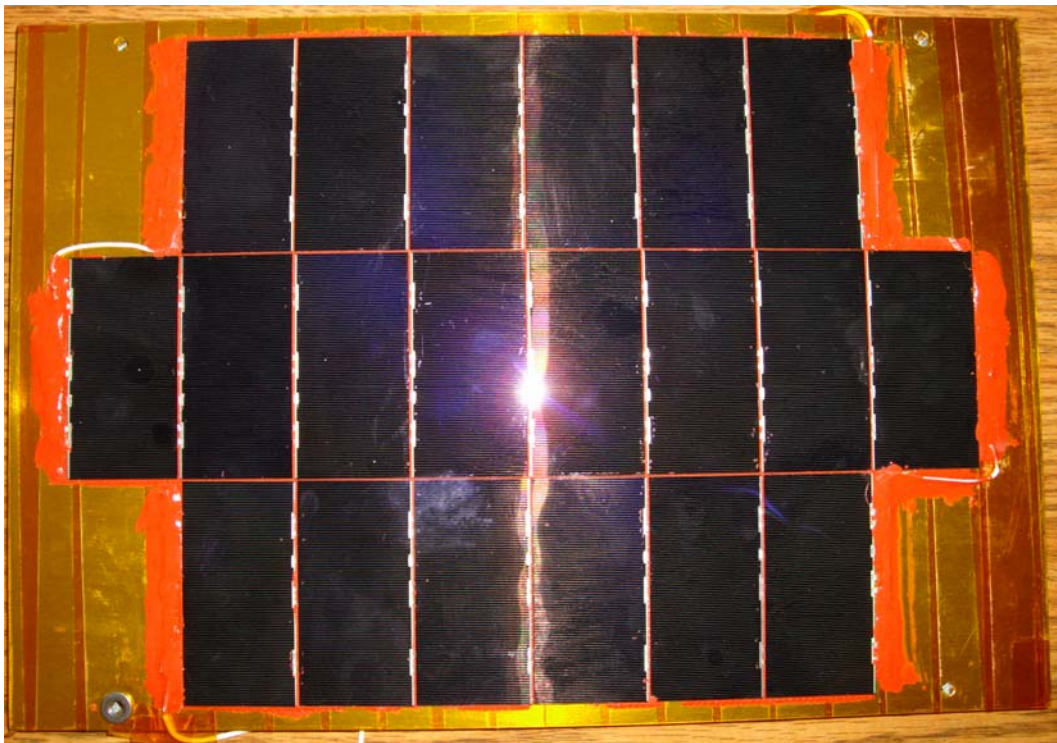
Fig. 1. A honeycomb solar panel

A Proposed Technique for on-Orbit Structural Health Monitoring
of the Mechanical Structure of a Satellite under Thermal Loading

201

A crack with the length of 100mm is made at the middle of the panel. Four levels of the crack from zero to 5% have been applied. These five cases are numbered as in Table 3. The finite element mesh of the cracked panel and the closed up crack are showed in Figs 2 and 3.

Table 1. Scenarios of temperatures on the two surfaces of the panel

Scenario	Temperature on heated side (^{o}C)	Temperature on shade side (^{o}C)
1	60	59
2	60	55
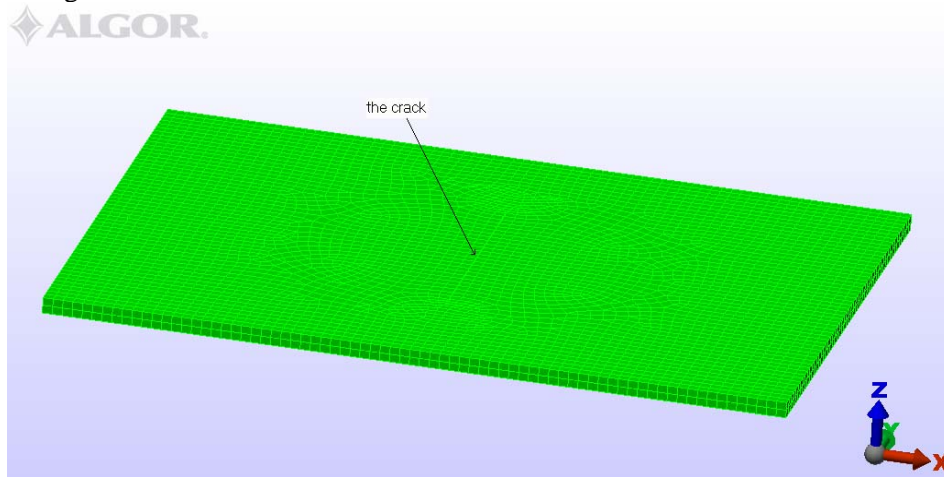
Fig. 2. Finite element model of the cracked solar panel
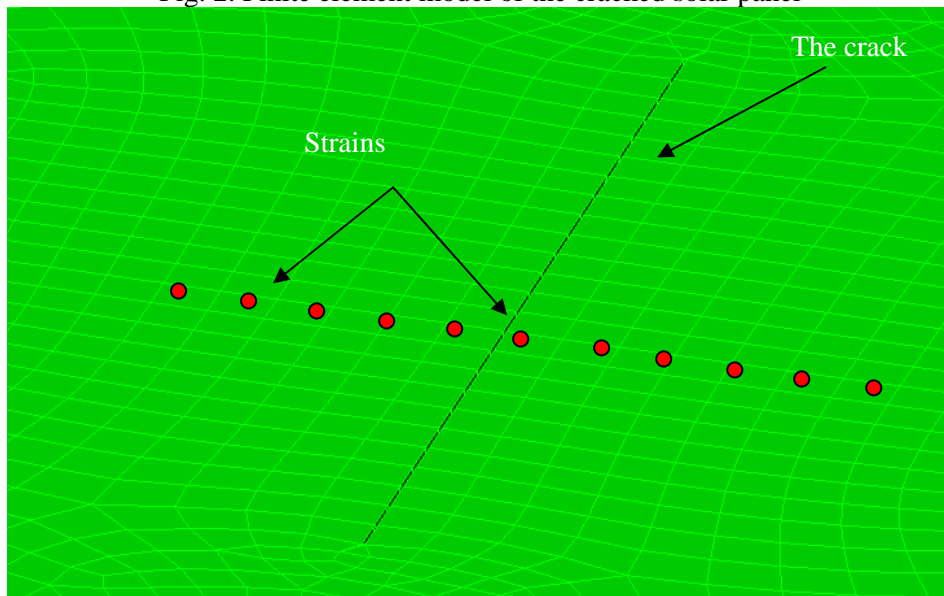
Fig. 3. Closed up crack

Table 2. Material properties of the panel

Density (kg/m^3)	Specific heat (J/kg K)	Thermal conductivity (W/m K)	Thermal expansion coefficient (10^{-6}m/m K)	Poisson's coefficient	Module of elasticity (GPa)		
					E_{11}	E_{22}	G_{12}
48	921	2.1	23.76	0.3	0.41	0.24	0.15

Table 3. Four cases with cracks of varying depths

Case	Crack depth (%)
1	0
2	1
3	2
4	5

4. Crack detection

4.1. Crack detection by noise free signals

In this paper, the crack detection is investigated with both cases, noise free and polluted signals. The noise free signal is first analyzed. When the panel is expanded and bent, the strain distributions along the panel may have a sudden change or distortion at the location of the crack. In general, when the crack is small, the distortion of the strain is small that it can not be detected visually. In such a case, the wavelet transform is applied to analyze this local distortion. In this study, the strain distribution across the crack (see Fig. 3) obtained from finite element analysis will be used to investigate the distortion caused by the crack. The continuous wavelet coefficient extracted at level 2 with wavelet function "Db2" was found suitable for the purpose of crack detection.

As can be seen in Fig. 4, the strain (upper graph) and its wavelet coefficients (lower graph) are quite smooth when there is no crack on the panel. In other words, when there is no crack, the strain distribution and its wavelet transform present no distortions.
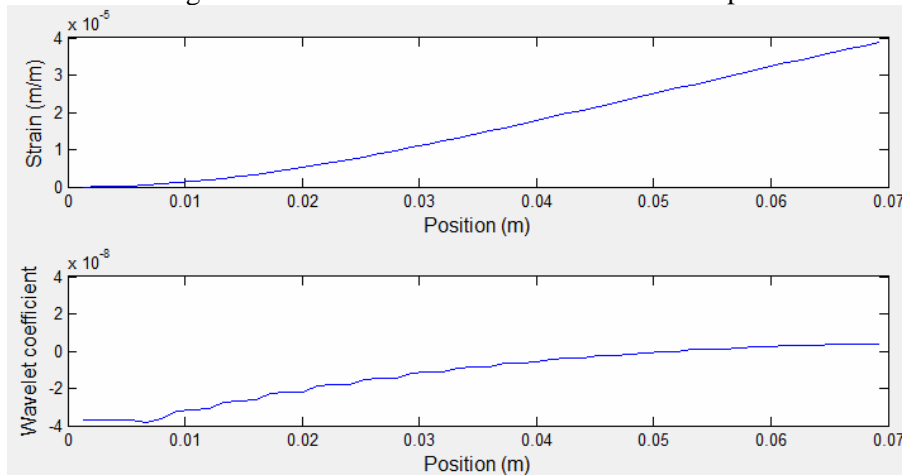
Fig. 4. Strain distribution and its wavelet transform. Crack depth is 0%, temperature difference is 5 $^{\circ}$C

However, when there is a crack, there are distortions at the crack position in strain distribution and its wavelet transform. When the crack depth is small, (1% and 2% of the thickness of the panel), there are distortions in the strain distributions (see upper graphs in Figs. from 5 to 8). However, these distortions are so small that it is difficult to observe the level of the distortions as well as to pinpoint the position of the crack. Meanwhile, in the lower graphs of these figures, the distortions of the strain distributions are amplified clearly by significant peaks in the wavelet transforms, and these peaks point out exactly the position of the crack.

When the crack depth is 5% of the thickness, the distortions of the strain distributions of two scenarios 1 and 2 are presented visually as peaks in upper graphs of Figs. 9 and 10. The locations of these peaks are the same with the crack location. In the lower graphs, the significant peaks of the wavelet transforms of these strain

A Proposed Technique for on-Orbit Structural Health Monitoring
of the Mechanical Structure of a Satellite under Thermal Loading

203

distributions are presented and their positions are at the same positions of the peaks in the strain distributions. These imply that, we can detect the distortions in strain distribution as well as its wavelet transform when the crack depth is large up to 5% of the thickness.
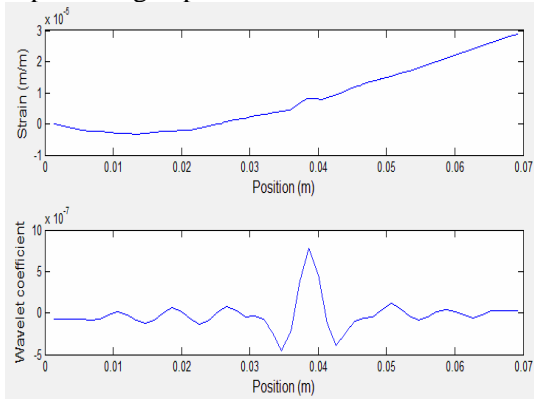
Fig. 5. Crack depth is 1%, temperature difference is 1 ^{o}C
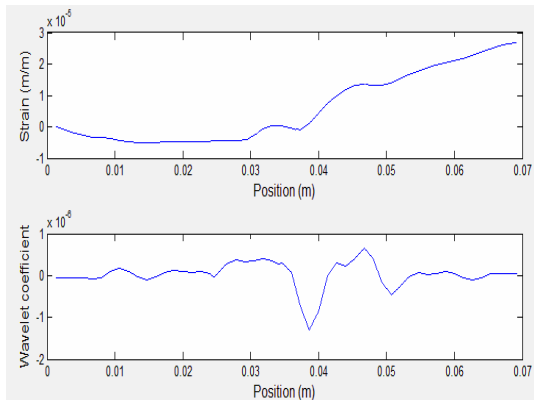
Fig. 6. Crack depth is 1%, temperature difference is 5 ^{o}C
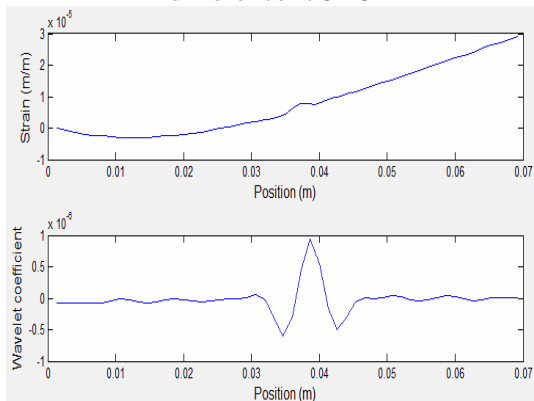
Fig. 7. Crack depth is 2%, temperature difference is 1 ^{o}C
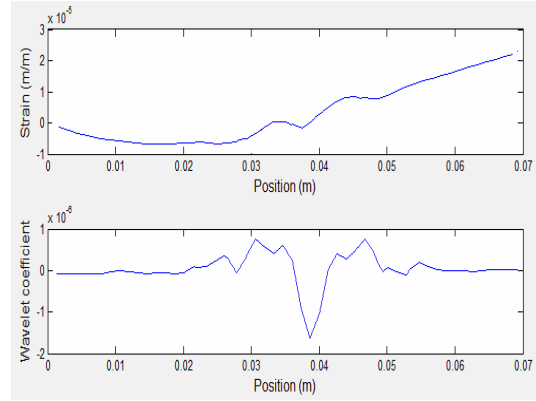
Fig. 8. Crack depth is 2%, temperature difference is 5 ^{o}C
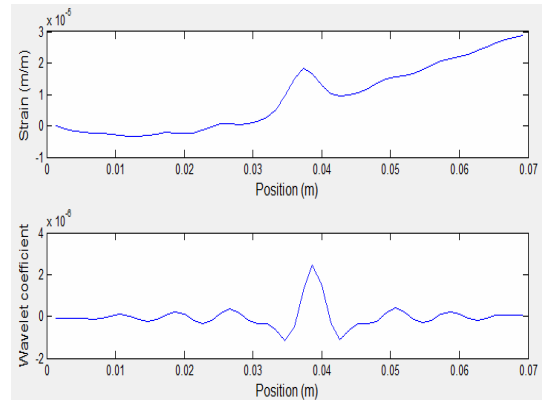
Fig. 9. Crack depth is 5%, temperature difference is 1 ^{o}C
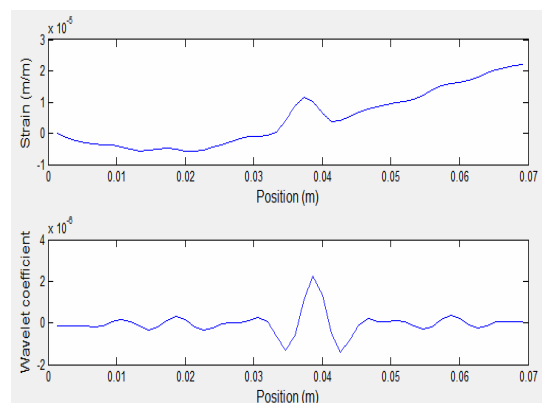
Fig. 10. Crack depth is 5%, temperature difference is 5 ^{o}C

4. 1. Influence of the noise

The influence of the noise on the method was also carried out in this work. In order to

simulate the polluted measurements, the white noise is added to the calculated responses of the beam. The noisy strain is calculated as following formula:

$$\varepsilon_{noisy} = \varepsilon + E_p N \sigma(\varepsilon) \qquad (11)$$

where ε_{noisy} is the noisy displacement. E_p is the noise level and N is a standard normal distribution vector with zero mean value and unit standard deviation. ε is the strain distribution obtained from the numerical simulation, and $\sigma(\varepsilon)$ is its standard deviation

Figs. from 10 to 13 show the strain distribution and their wavelet transforms with 5% noise for the crack depths of 1% and 5% subjected to the temperature difference between two sides of the panel of 1 ^{o}C and 5 ^{o}C, respectively.
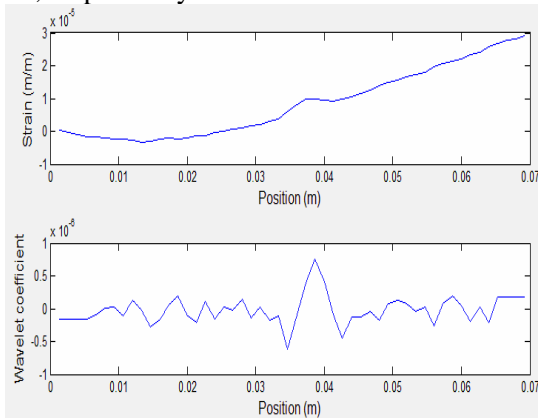
Fig. 11. Crack depth is 1%, temperature difference is 1 ^{o}C, 5% white noise
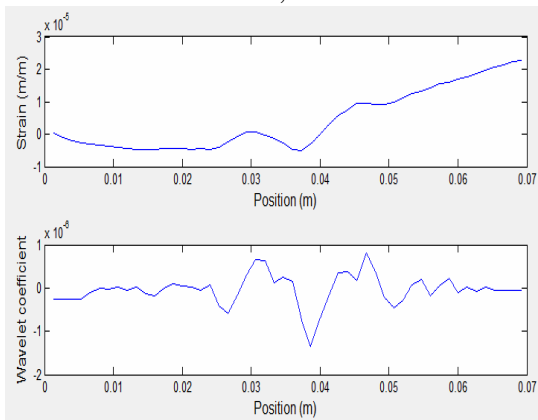
Fig. 12. Crack depth is 1%, temperature difference is 5 ^{o}C, 5% white noise
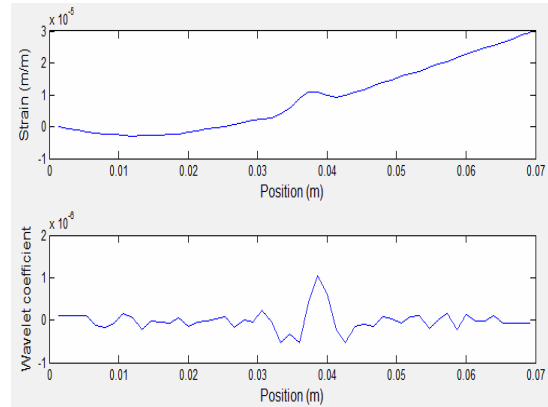
Fig. 13. Crack depth is 2%, temperature difference is 1 ^{o}C, 5% white noise
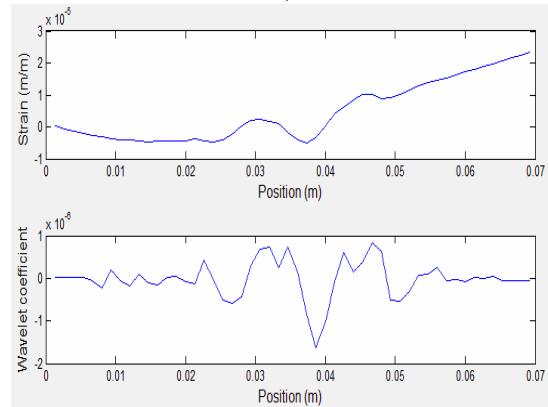
Fig. 14. Crack depth is 2%, temperature difference is 5 ^{o}C, 5% white noise
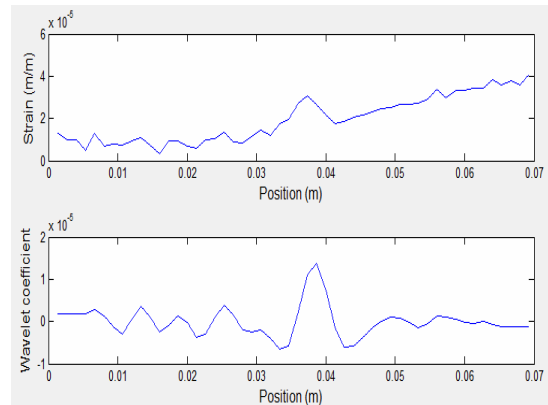
Fig. 15. Crack depth is 5%, temperature difference is 1 ^{o}C, 15% white noise

Figs. 14 and 15 present similar results for the crack depth of 5%. From these results it is concluded that for the crack depth as small as 1%, the proposed method can be applied for the strain signals with 5% noise. When

the crack depth is larger, the method can be applied for the strain signals polluted up to 15% noise.
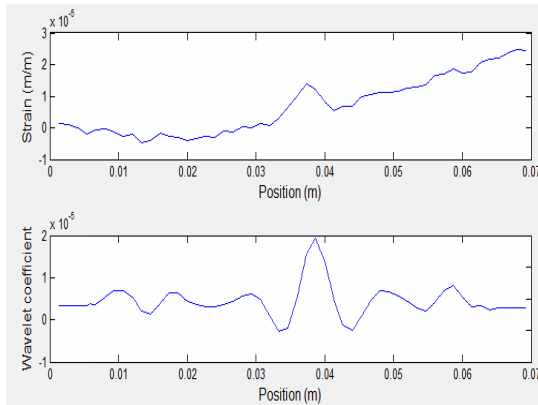

Fig. 16. Crack depth is 5%, temperature difference is 5 $^{\circ}$C, 15% white noise

5. Conclusions

A technique for on-orbit structural health monitoring of the mechanical structure of a satellite under thermal loading based on wavelet transform is presented. The simulation results of the case studies with thermal load are promising. The conclusion remarks are as follows:

− The existence of the crack can be detected from the strain distribution and its wavelet transform.
− When the crack size is small, the distortion of the strain distribution at the crack position is small and difficult to be detected visually. The wavelet transform is needed for crack detection and it showed good results.
− When the crack size is large, the distortions of strains can be detected visually. In this case, both strain and its wavelet transform can be used to detect the crack.
− The proposed method can be applied for the polluted signals with up to 15% noise for a crack depth as small as 5%.

The advantage of the method is that no information of the intact structure is needed. The method exploits the natural thermal load from the satellite environment, thus it does not need to apply any load on the satellite structure. The proposed technique is very sensitive to the crack depth since it can detect the crack as small as 1%.

To validate the method presented herein, experimental testing needs to be carried out at a future date.

Acknowledgements

References

[1] Anil K. Maini, Varsha Agrawal. *Satellite Technology: Principle and Applications*. 2007. John Wiley & Sons Ltd.

[2] Shin K., Kim C., Hong C., Lee H., *Prediction of failure thermal cycles in graphite/epoxy composite materials under simulated low earth orbit environments*. Composite: Part B 31 (2000), 223-235.

[3] Shin K., Kim C., Hong C., Lee H., *Thermal Distortion Analysis of Orbiting Solar Array Including Degradation Effects of Composite Materials*. Composite: Part B 32 (2001), 271-285.

[4] Abdelal G., Abuelfoutouh N., Hamdy A., Ayman Atef A., *Thermal Fatigue Analysis of Small-Satellite Structure*. Int J Mech Mater Des 3 (2006), 145–159;

[5] Farouk G., Abdelal A., *Thermal fatigue analysis of solar panel structure for micro-satellite applications*. Int J Mech Mater Des 4 (2008), 53–62.

[6] Liua Y., Li G., Jiang L., *Numerical Simulation on Antenna Temperature Field of Complex Structure Satellite in Solar Simulator*. Acta Astronautica, accepted 5 March 2009.

[7] Pandey A. K., Biswas M. and Samman M. M., *Damage Detection from Changes in Curvature*

Mode Shapes. Journal of Sound and Vibration 1991, Vol. 145 (2), pp. 321-332.

[8] Chondros T.G., Dimarogonas A. D., and Yao J., *Vibration of a Beam with a Breathing Crack.* Journal of Sound and Vibration 2001, Vol. 239, pp. 57-67

[9] Verboven P., Parloo E., Guillaume P. and Overmeire M. V., *Autonomous Structural Health Monitoring - Part I: Modal Parameter Estimation and Tracking*. Mechanical Systems and Signal Processing 2002, Vol. 16(4), pp. 637-657.

[10] Shinha J. K. and Friswell M. I., *Simulation of the Dynamic Response of a Cracked Beam*. Computers and Structures 2002, Vol. 80, pp. 1473-1475.

[11] Reda Taha M.M. and Lucero J., *Damage Identification for Structural Health Monitoring using Fuzzy Pattern Recognition*. Engineering Structures 2005, Vol. 27, pp. 1774-1783.

[12] Loutridis S., Doubka E., and Hadjileontiadis L. J., *Forced Vibration Behaviour and Crack Detection of Cracked Beams Using Instantaneous Frequency*. NDT&E International 2005, Vol. 38(5), pp. 411-419.

[13] Wang Q. and Deng X., *Damage Detection with Spatial Wavelets*. International Journal of Solids and Structures 1999, Vol. 36, pp. 3443-3468.

[14] Hong J.-C., Kim Y.Y., Lee H.C., and Lee Y.W., *Damage Detection Using the Lipschitz Exponent Estimated by the Wavelet Transform: Applications to Vibration Modes of a Beam*. International Journal of Solids and Structures 2002, Vol. 39, pp. 1803-1816.

[15] Rucka M. and Wilde K., *Crack Identification Using Wavelets on Experimental Static Deflection Profiles*. Engineering Structures 2006, Vol. 28, pp. 279-288.

[16] Ovanesova A.V. and Suarez L.E., *Application of Wavelet Transform to Damage Detection in Frame Structures*. Journal of Engineering Structure 2004, Vol. 26, pp. 39-49.

[17] Gentile A. and Messina A. *On the Continuous Wavelet Transforms Applied to Discrete Vibration Data for Detecting Open Cracks in Damaged Beams*. International Journal of Solids and Structures 2003, Vol. 40, pp. 295-315.

[18] Loutridis S., Douka E., and Trochidis A., *Crack Identification in Double-cracked Beam Using Wavelet Analysis*. Journal of Sound and Vibration 2004, Vol. 277, pp. 1025–1039.

[19] Poudel P. and Fu_ G., and Ye J., *Structural Damage Detection Using Digital Video Imaging Technique and Wavelet Transformation*. Journal of Sound and Vibration 2005, Vol. 286, pp. 869–895.

[20] Castro E., Garcia-Hernandez M. T., Gallego A., *Damage Detection in Rods by Means of the Wavelet Analysis of Vibration: Influence of the Mode Order*. Journal of Sound and Vibration 2006, Vol. 296, pp. 1028-1038.

[21] Nguyen K. V., Olatunbosun O. A., *A Proposed Method for Fatigue Crack Detection and Monitoring Using the Breathing Crack Phenomenon and Wavelet Analysis*. Journal of Mechanics of Materials and Structures 2007, Vol 2 No 3, p. 400-420.

[22] Daubechies I., *Ten Lectures on Wavelets*. SIAM, Philadelphia 1992.

Influence of the road surface unevenness on the multi-crack detection of a beam-like structure subjected to moving vehicle

Khoa Viet Nguyen, Hai Thanh Tran and Dung Dinh Nguyen

Institute of Mechanics, Vietnam Academy of Sciences

Abstract

The influence of the road unevenness on the dynamic response of a moving vehicle as well as the method for detecting a multi-cracked beam-like structure is presented in this report. According to the principle of Saint-Venant, the stress field of a cracked structure is only affected in the region adjacent to the crack. Therefore, the dynamic response of the bridge-vehicle system is distorted at the moments when the vehicle is passing by crack regions. In general, distortions in the dynamic response caused by the cracks are small and difficult to detect visually. A method for detecting these small distortions is proposed based on the wavelet transform which has recently been applied widely for crack detection problem. When the road unevenness is taken in to account, it will influence the dynamic response of the system and the crack detection result in comparison with the case when the road unevenness is not presented. Numerical results show in this report that the wavelet based method for crack detection of the cracked beam-like structure can still be applied regarded to the road roughness. The proposed method can successfully be applied with the surface irregularity depth up to 0.5m, and with the random different angular phase of the road unevenness function up to 4%.

Keywords: Crack detection, damage detection, moving vehicle, moving load, wavelet transform, wavelet-based method, road unevenness, road surface roughness.

I. Introduction

Many methods for crack detection problem in mechanical structures has been investigated and developed widely in the last two decades as reviewed by Dimarogonas [1], Salawu [2] and Doebling et al. [3]. In the crack detection problem, non-destructive methods based on the changes in the dynamic properties of the structure (frequencies, mode shapes, transfer functions) has been attracted many researchers. Hu and Liang [4] proposed an integrated approach to detect cracks using the knowledge of changes in natural frequencies. In their work, the spring model and continuum damage model were combined to calculate crack locations and crack depths. Based on this approach, Patil and Maiti [5] developed a technique for detection of multiple cracks in slender beams which extends the scope of the method given in [4] from a single segment beam to multi-segment beams and eliminates the symbolic computation to determine the uncracked

beam mode shapes. Pandey et al [6] proposed the application of mode shape curvature in detecting damage. The reduction in cross section caused by the damage tends to increase the curvature of the mode shapes in the vicinity of the damage. Khoo et al [7] presented modal analysis techniques to monitor a wooden wall structure. The significant changes in natural frequencies were used to detect the existence of damage and to identify modes that are sensitive to damage. The damage location was determined by comparison of the deformation of identified mode shapes before and after damage.

Recently, the wavelet transform has emerged as an efficient tool for signal processing due to its flexibility and precision in time and frequency resolution. The effectiveness of the continuous wavelet transform (CWT) in terms of its capability to estimate the Lipschitz exponent was studied by Hong et al [7]. In their study, the magnitude of the Lipschitz exponent was used as an indicator of damage severity when studying bending mode shapes of a cracked beam. Lu and Hsu [8] proposed a method based on the wavelet transform for detection of structural damage. The minor localized damage induced significant changes of the wavelet coefficients at the location of the damage. Ovanesova and Suarez [9] used wavelet transform to analyse the deflection of an open cracked beam. The position of the crack was found using bior6.8 wavelet. These authors have also developed the method for application to frame structures and obtained satisfactory results. Loutridis et al [10] presented a wavelet based method to detect cracks in a double-cracked beam. The fundamental vibration mode of a double-cracked cantilever beam was investigated using CWT. The crack locations were determined by the sudden changes in the spatial variation of the transformed response. The author of this paper and his co-author [11] presented a method for remote monitoring the cracked structure using the

breathing crack phenomenon and wavelet transform. In this study the crack is detected by analyzing the discontinuity of the dynamic response obtained from only one measurement point.

The analysis of continuous elastic systems subjected to moving subsystems has been a topic of interest for well over a century. Parhi and Behera [12] presented an analytical method along with the experimental verification to study the dynamic behavior of a cracked beam under a moving mass. The differential equations involved in analyzing the dynamic deflection of the cantilever beam were solved by the Runge–Kutta algorism. Lee et al. [13] proposed a procedure consisting of identification of the operational modal properties and the assessment of damage locations and severities. The modal parameters were identified from the free-decay signals extracted using the random decrement method. The damage was assessed based on the estimated modal parameters using the neural networks technique. Bilello and Bergman [14] studied damaged beams under a moving load. The damages were modeled by rotational springs whose compliance is evaluated using linear elastic fracture mechanics. Recently, Zhu and Law [15] analyzed the operational deflection time history of the bridge subjected to a moving vehicular load based on CWT. Baeza and Ouyang [16] studied the vibration of a truss structure composed of a number of rigidly connected Timoshenko beams. The excitation is provided by a moving oscillator of an unsprung mass that supports another mass through a spring (oscillator) and moves on top of the truss structure. Most of the current methods apply dynamic responses obtained from points on the bridge for crack detection.

This study presents the influence of the road surface unevenness on the wavelet based technique for crack detection using dynamic response of a cracked beam-like

structure measured directly on the moving vehicle.

II. Vibration of a beam-like structure under moving vehicle

II.1. Intact beam

$$\begin{bmatrix} I_0 & 0 & 0 & 0 \\ 0 & m_0 & 0 & 0 \\ 0 & 0 & m_1 & 0 \\ 0 & 0 & 0 & m_2 \end{bmatrix} \begin{Bmatrix} \ddot{d}_1 \\ \ddot{d}_2 \\ \ddot{d}_3 \\ \ddot{d}_4 \end{Bmatrix} + \begin{bmatrix} b_1^2 c_1 + b_2^2 c_2 & b_1 c_1 - b_2 c_2 & -b_1 c_1 & b_2 c_2 \\ b_1 c_1 - b_2 c_2 & c_1 + c_2 & -c_1 & -c_2 \\ -b_1 c & -c_1 & c_1 + c_3 & 0 \\ b_2 c_2 & -c_2 & 0 & c_2 + c_4 \end{bmatrix} \begin{Bmatrix} \dot{d}_1 \\ \dot{d}_2 \\ \dot{d}_3 \\ \dot{d}_4 \end{Bmatrix}$$

$$+ \begin{bmatrix} k_1 b_1^2 + k_2 b_2^2 & k_1 b_1 - k_2 b_2 & -k_1 b_1 & k_2 b_2 \\ k_1 b_1 - k_2 b_2 & k_1 + k_2 & -k_1 & -k_2 \\ -k_1 b_1 & -k_1 & k_1 + k_3 & 0 \\ k_2 b_2 & -k_2 & 0 & k_2 + k_4 \end{bmatrix} \begin{Bmatrix} d_1 \\ d_2 \\ d_3 \\ d_4 \end{Bmatrix} = \begin{Bmatrix} 0 \\ 0 \\ k_3[u_1 + r(x_1)] + c_3 \dot{u}_1 \\ k_4[u_2 + r(x_2)] + c_4 \dot{u}_2 \end{Bmatrix} \quad (1)$$

Consider the bridge–vehicle system as shown in Fig. 1. The half -vehicle model is adopted in this investigation. The bridge is modelled as an Euler–Bernoulli beam. Regarding to the surface unevenness of the bridge, the governing equation of motion for the bridge–vehicle system can be derived as follows:
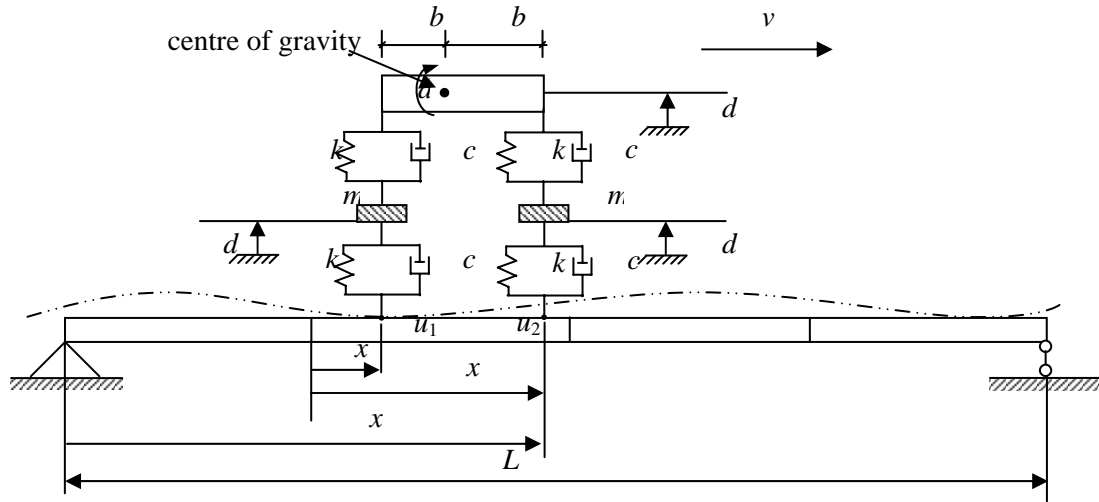
Fig 1. A beam-like bridge under moving vehicle

$$\mathbf{M\ddot{D}} + \mathbf{C\dot{D}} + \mathbf{KD} = \mathbf{N_1^T} f_1 + \mathbf{N_2^T} f_2 \quad (2)$$

where the displacements underneath the tyres are given:

$$y_1 = u_1(x,t) + r(x_1) \quad (3)$$

$$y_2 = u_2(x,t) + r(x_2) \quad (4)$$

with $r(x) = \dfrac{\bar{d}}{2}\left[1 - \cos\left(\dfrac{2\pi x}{\bar{l}}\right)\right] \quad (5)$

and the interaction forces between the vehicle and the bridge can be written as:

$$f_1 = -m_1 g - m_1 \ddot{d}_3 - \frac{m_0 g b_2}{b_1 + b_2} - \frac{I_0 \ddot{d}_1 + m_0 b_2 \ddot{d}_2}{b_1 + b_2}$$

$$f_2 = -m_2 g - m_2 \ddot{d}_4 - \frac{m_0 g b_1}{b_1 + b_2} - \frac{I_0 \ddot{d}_1 + m_0 b_1 \ddot{d}_2}{b_1 + b_2}$$

(7)

Here I_0, b_1, b_2, m_0, m_1, m_2, k_1, k_2, k_3, k_4, c_1, c_2, c_3, c_4 are vehicle parameters as shown in

Fig. 1; d_1, d_2, d_3, d_4 denote the vehicle degrees of freedom; v is the vehicle velocity; u_1, u_2 are the vertical displacements of the contact points and equal to the vertical displacement of the beam at the contact positions; where d_m and $\bar{l}$ are the surface irregularity depth and length, respectively. $\mathbf{M}$, $\mathbf{C}$ and $\mathbf{K}$ are structural mass, damping and stiffness matrices; f_1 and f_2 are the interaction forces acting on the beam for contact points 1 and 2; g is gravitational acceleration; $\mathbf{N}^T$ is the transposition of the shape functions at the position x of the interaction force; d is the nodal displacement

of the beam. The displacement of the beam u at the arbitrary position x can be obtained from the shape functions $\mathbf{N}$ and the nodal displacement - column matrix $\mathbf{D}$ as [17]:

$$u = \mathbf{ND} \tag{8}$$

The shape function of an element can be obtained as:

$$\mathbf{N} = \begin{bmatrix} N_1 & N_2 & N_3 & N_4 \end{bmatrix} \tag{9}$$

Substituting (8) and (9) into equations (1) and (2) yields:

$$\begin{bmatrix} M & \sum_{i=1}^{2} N_i^T f_{\theta i} & \sum_{i=1}^{2} N_i^T f_{yi} & m_1 N_1^T & m_2 N_2^T \\ 0 & I_0 & 0 & 0 & 0 \\ 0 & 0 & m_0 & 0 & 0 \\ 0 & 0 & 0 & m_1 & 0 \\ 0 & 0 & 0 & 0 & m_2 \end{bmatrix} \begin{pmatrix} \ddot{\mathbf{D}} \\ \ddot{d}_1 \\ \ddot{d}_2 \\ \ddot{d}_3 \\ \ddot{d}_4 \end{pmatrix} +$$

$$+ \begin{bmatrix} C & \{0\} & \{0\} & \{0\} & \{0\} \\ 0 & b_1^2 c_1 + b_2^2 c_2 & b_1 c_1 - b_2 c_2 & -b_1 c_1 & b_2 c_2 \\ [0] & b_1 c_1 - b_2 c_2 & c_1 + c_2 & -c_1 & -c_2 \\ -c_3 N_1 & -b_1 c_1 & -c_1 & c_1 + c_3 & 0 \\ -c_4 N_2 & b_2 c_2 & -c_2 & 0 & c_2 + c_4 \end{bmatrix} \begin{pmatrix} \dot{\mathbf{D}} \\ \dot{d}_1 \\ \dot{d}_2 \\ \dot{d}_3 \\ \dot{d}_4 \end{pmatrix} +$$

$$+ \begin{bmatrix} K & 0 & 0 & 0 & 0 \\ 0 & k_1 b_1^2 + k_2 b_2^2 & k_1 b_1 - k_2 b_2 & -k_1 b_1 & -k_2 b_2 \\ 0 & k_1 b_1 - k_2 b_2 & k_1 + k_2 & -k_1 & -k_2 \\ -k_3 N_1 - c_3 N_{1x} \dot{x}_1 & -k_1 b_1 & -k_1 & k_1 + k_3 & 0 \\ -k_4 N_2 - c_4 N_{2x} \dot{x}_2 & -k_2 b_2 & -k_2 & 0 & k_2 + k_4 \end{bmatrix} \begin{pmatrix} \mathbf{D} \\ d_1 \\ d_2 \\ d_3 \\ d_4 \end{pmatrix} = \begin{pmatrix} \sum_{i=1}^{2} N_i^T \hat{f}_i \\ 0 \\ 0 \\ k_3 r(x_1) \\ k_4 r(x_2) \end{pmatrix}$$

$$\tag{10}$$

where:

$$f_{\theta 1} = \frac{1}{b_1 + b_2} I_0, \quad f_{\theta 2} = -\frac{1}{b_1 + b_2} I_0,$$

$$f_{y1} = \frac{b_2}{b_1 + b_2} m_0, \quad f_{y2} = \frac{b_1}{b_1 + b_2} m_0, \tag{11}$$

$$\hat{f}_1 = -\frac{b_2}{b_1 + b_2} m_0 g - m_1 g,$$

$$\hat{f}_2 = -\frac{b_1}{b_1 + b_2} m_0 g - m_2 g \tag{12}$$

where the subscript x implies the differentiation with respect to x.

Influence of the road surface unevenness on the multi-crack detection of a beam-like structure subjected to moving vehicle

211

II.2. Multi-cracked beam like structure

Fig. 2 shows a uniform beam-like structure divided into Q elements with R cracks situated in R different elements. It is assumed that the cracks only affect the stiffness, while the mass and damping coefficient of the beam remain constant. According to the principle of Saint-Venant, the stress field is only affected in the region adjacent to the crack. Therefore, the element stiffness matrices of intact elements can be considered unchanged under certain limitations of element sizes, thus only the element stiffness matrices of cracked elements are changed. An element stiffness matrix of a cracked element can be obtained as follows [18]: Neglecting shear action, the strain energy of an element without a crack can be written as:

$$W^{(o)} = \frac{1}{2EI}\left(M^2 l + MPl^2 + \frac{P^2 l^3}{3} \right) \quad (13)$$

where P and M are the shear and bending internal forces at the right node of the element (Fig. 2). The additional stress energy of a crack has been calculated from fracture mechanics and the flexibility coefficients are obtained by a stress intensity factor in the linear elastic range, using Castigliano's theorem. For a rectangular beam with the thickness h, the width b, and the additional energy due to the crack can be written as

$$W^{(1)} = b \int_0^a \left(\frac{\left(K_I^2 + K_{II}^2\right)}{E'} + \frac{(1+v)K_{III}^2}{E} \right) da \quad (14)$$

where $E' = E$ for plane stress, $E' = \dfrac{E}{1 - v^2}$ for plane strain and a is the crack depth, and K_I, K_{II}, K_{III} are stress intensity factor for opening type, sliding type and tearing type cracks, respectively.

The generic component of the flexibility matrix $\widetilde{C}$ of the intact element can be calculated as

$$\widetilde{c}_{ij}^{(o)} = \frac{\partial^2 W^{(o)}}{\partial P_i \partial P_j}; \quad i, j = 1,2 ; \quad (15)$$
$$P_1 = P; \ P_2 = M$$

The additional flexibility coefficient is

$$\widetilde{c}_{ij}^{(1)} = \frac{\partial^2 W^{(1)}}{\partial P_i \partial P_j}; \quad i, j = 1,2 ; \quad (16)$$
$$P_1 = P; \ P_2 = M$$

Therefore, the total flexibility coefficient is:

$$\widetilde{c}_{ij} = \widetilde{c}_{ij}^{(o)} + \widetilde{c}_{ij}^{(1)} \quad (17)$$

By the principle of virtual work the stiffness matrix of the cracked element can be expressed as:

$$\mathbf{K_c} = \mathbf{T^T \widetilde{C}^{-1} T} \quad (18)$$

where

$$\mathbf{T} = \begin{pmatrix} -1 & -L & 1 & 0 \\ 0 & -1 & 0 & 1 \end{pmatrix}^{\mathbf{T}} \quad (19)$$

Substituting global matrices $\mathbf{M}$, $\mathbf{C}$, and $\mathbf{K}$ of the cracked beam into equation (10) and solving this equation by the Newmark method, the dynamic responses of the vehicle and the beam will be obtained.

III. Wavelet transform

The continuous wavelet transform is defined as follows [19]:

$$W(a,b) = \frac{1}{\sqrt{a}} \int_{-\infty}^{+\infty} f(t)\psi^*\left(\frac{t-b}{a}\right) dt \quad (20)$$

where a is a real number called scale or dilation, b is a real number called position, $W(a,b)$ are wavelet coefficients at scale a and position b, $f(t)$ is input signal, $\psi(t - b/a)$ is wavelet function and $\psi^*(t - b/a)$ is complex conjugate of $\psi(t - b/a)$. In order

to simplify the expression of the wavelet transform, denote

$$\psi_{a,b}(t) = \frac{1}{\sqrt{a}}\psi^*(t-b/a),$$

the wavelet transform (20) can be written:

$$W(a,b) = \int_{-\infty}^{+\infty} f(t)\psi_{a,b}dt \qquad (21)$$

IV. Case study

The numerical simulation is carried out for a beam with two cracks at locations of $Lc_1=L/3$ and $Lc_2=2L/3$ is analyzed. In this study, the crack depths of the two cracks are identical. Parameters of the beam are as follows: Mass density is 7855 kg/m^3; modulus of elasticity E=2.1x10^{11} N/m^2; L=50 m; b=1 m; h=2 m. Modal damping ratios for all modes are equal to 0.01. Vehicle parameters are described as follows: m_0=12404 kg; m_1=m_2=725.4 kg; k_1=1969034 N/m; k_2=727812 N/m; k_3=4735000 N/m; k_4=1972900 N/m; c_1=7181.8 Ns/m; c_2=2189.6 Ns/m; c_3=c_4=0 Ns/m; I_0=172160 kg.m^2; b_1=b_2=3 m. The displacement-time history of the moving vehicle is obtained to investigate the influence of the road surface unevenness on the crack detection. When the beam is cracked, the local distortions caused by the cracks are well detected by the CWT.

When the road surface roughness is taken into account, although the peaks caused by the cracks are less clear, they can still be used to detect the cracks up to the road irregularity depth of 0.5 m.

IV.1. Influence of the surface irregularity depth

In order to detect local distortions in the dynamic response of the vehicle due to the presence of cracks, the wavelet transform is applied. The velocity of the vehicle is v=1 m/s. Fig. 2 shows the vertical displacement of the vehicle and its wavelet transform for the crack depth of 30 % and 50 % of the beam height. As can be seen in this graphs, regardless to the road surface roughness, the wavelet transforms clearly show four peaks at t=10.6 s, 16.6 s, 27.4 s, and 33.4 s. The peaks at t=10.6 s and t=16.6 s correspond to the moments when the first leg and the second leg of the vehicle pass by the location of $L/3$ of the beam, while the peaks at t=27.4 s and t=33.4 s correspond to that of 2L/3. The peaks of the wavelet transforms imply that there are distortions in the dynamic response of the vehicle at moments when the two legs pass by the crack positions. Therefore, the peaks in the wavelet transform indicate the existence of the cracks. The crack locations can be easily ascertained from the positions of the peaks and the velocity of the vehicle.
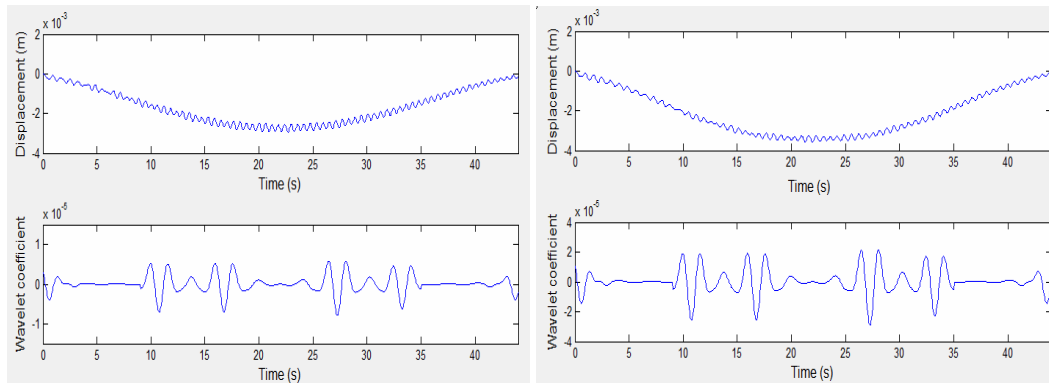

Fig. 2. Displacement and its wavelet transform: d_m =0; crack depth: a) 30%; b) 50%

When the road surface unevenness is taken into account, these peaks in the wavelet

transforms become less clear. As can be seen in Fig. 3 and 4, when the surface irregularity

depth is 0.3 m and 0.5 m, the peaks at moments *t*=16.6 s and 27.4 s become smaller. However, the cracks are still be detected by

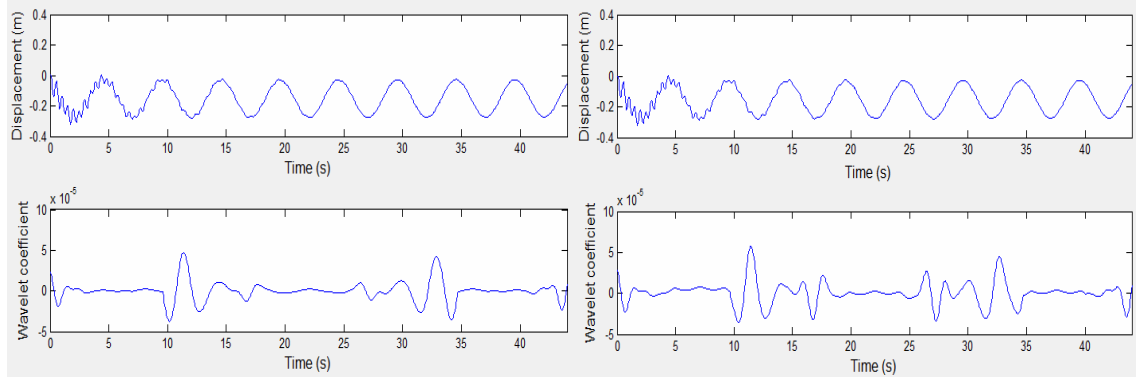significant peaks at t=10.6 s and 33.4 s with the irregularity depth up to 0.5m.

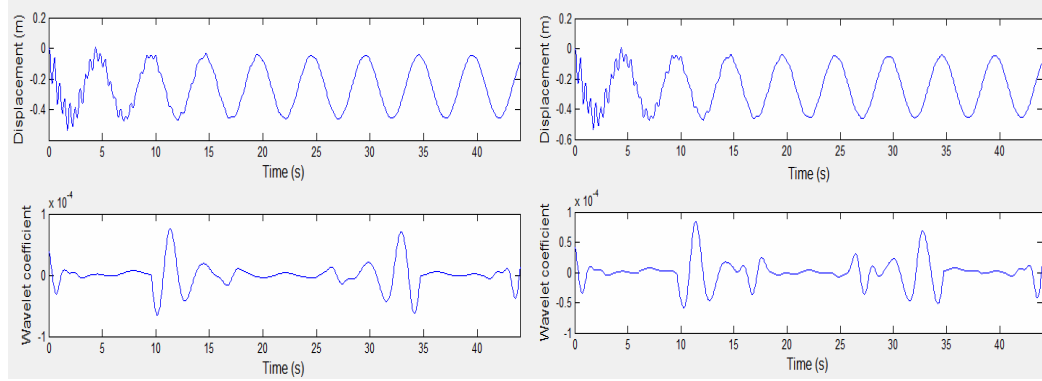Fig. 3. Displacement and its wavelet transform: d_m=0.3; crack depth: a) 30%; b) 50%

Fig. 4. Displacement and its wavelet transform: d_m=0.5m; crack depth: a) 30%; b) 50%

IV.2. Influence of the noise

In order to simulate the influence of the noisy measurements, white noise is added to the dynamic responses of the vehicle as following formula:

$$d_{2noisy} = d_2 + E_p N\sigma(d_2) \qquad (22)$$

where d_2 is the vehicle dynamic displacement obtained from the numerical simulation. E_p is the noise level and N is a standard normal distribution vector with zero mean value and unit standard deviation. d_{2noisy} is the polluted displacement, and $\sigma(d_2)$ is standard deviation of d_2.

Fig. 5 and 6 show the polluted displacements in four cases d_m=0.025 m, 0.05 m, 0.075 m and 0.1 m and their wavelet transforms of the vehicle moving on the beam with the crack depth of 50 % and the velocity of the vehicle at 1 m/s. When the measured signals are noisy, the proposed method for crack detection is still efficient but the road surface irregularity depth d_m is limited to 0.1 m and the noise level is limited to 4 %.
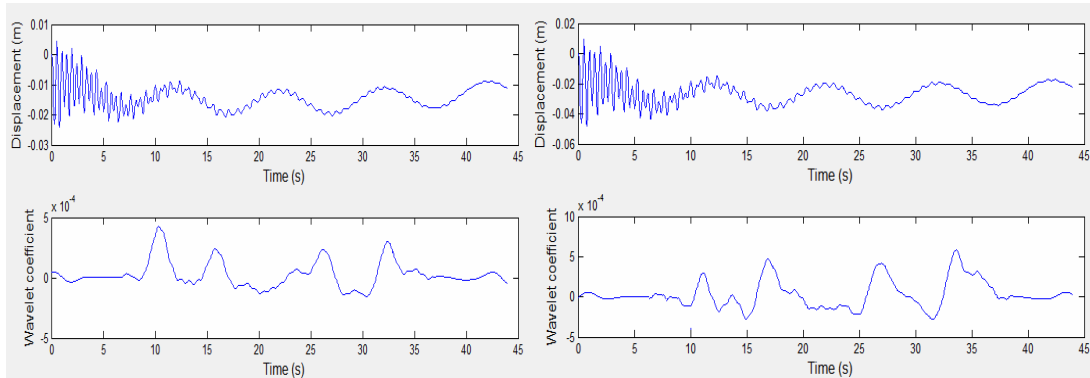
Fig. 5. Displacement and its wavelet transform: 4 % noise Crack depth:
a) d_m =0.025 m; b) d_m =0.05 m
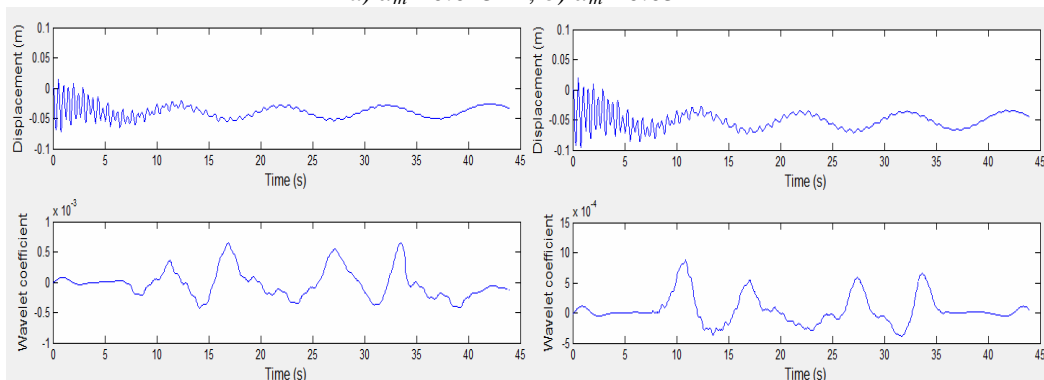
Fig. 6. Displacement and its wavelet transform: 4 % noiseCrack depth:
a) d_m =0.075 m; b) d_m =0.1 m

V. Conclusions

A wavelet based technique for detecting a multi-cracked beam-like structure using the dynamic response measured from a moving vehicle is promising. Conclusion remarks can be drawn from the numerical simulations as follows:

- The existence of the cracks results in significant peaks in the wavelet transform of the dynamic response. The positions of the cracks can be calculated from the locations of the peaks in the wavelet transform and the vehicle velocity.

- There is no need to select the positions to install sensors on the deck of the bridge since the dynamic response of the bridge-vehicle system is measured directly from the moving vehicle.

- It is a simple method since it uses only one vibration transducer attached to the vehicle.

- No information of the intact structure is needed for the crack detection.

- Without noise, the proposed method can be applied for the road with the depth of unevenness up to 0.5m

- The method can be applied for the depth of unevenness up to 0.1 m with the noise up to 4%

- To validate the presented method, experimental testing needs to be carried out at a future date.

References

[1] Dimarogonas A. D., *Vibration of cracked structures-a state of the art review*. Engineering Fracture Mechanics 1996, Vol. 5, 831-857.

[2] Salawu O.S. *Detection of structural damage through changes in frequency: a review*.

Influence of the road surface unevenness on the multi-crack detection
of a beam-like structure subjected to moving vehicle

215

Engineering Structures 1997, Vol. 19 (9), 718–723.

[3] Doebling S.W., Farrar C.R., Prime M.B. *A summary review of vibration-based damage identification methods*. The Shock and Vibration Digest 1998, Vol. 30 (2), 91–105.

[4] Hu J.; Liang R.Y., *An integrated approach to detection of cracks using vibration characteristics*. Journal of the Franklin Institute 1993, Vol. 330(5), 841-853.

[5] Patil D.P., Maiti S.K., *Detection of multiple cracks using frequency measurements.* Engineering Fracture Mechanics 2003, Vol. 70, 1553-1572.

[6] Pandey A. K., Biswas M. and Samman M. M., *Damage detection from changes in curvature mode shapes*. Journal of Sound and Vibration 1991, Vol. 145(2), 321-332.

[7] Khoo L. M., Mantena P. R., and Jadhav P., *Structural damage assessment using vibration modal analysis*. Structural Health Monitoring 2004, Vol. 3(2), 177-194.

[8] Hong J.-C., Kim Y.Y., Lee H.C., and Lee Y.W., *Damage detection using the Lipschitz exponent estimated by the wavelet transform: Applications to vibration modes of a beam*. International Journal of Solids and Structures 2002, Vol. 39, 1803-1816.

[9] Lu CJ. and Hsu YT., *Vibration analysis of an inhomogeneous string for damage detection by wavelet transform*. International Journal of Mechanical Science 2002, Vol. 44, 745-754.

[10] Ovanesova A.V. and Suarez L.E., *Application of wavelet transform to damage detection in frame structures*. Journal of Engineering Structure 2004, Vol. 26, p. 39-49.

[11] Nguyen K. V. and Olatunbosun O. A., *A proposed method for fatigue crack detection and monitoring using the breathing crack phenomenon and wavelet analysis*. Journal of Mechanics of Materials and Structures 2007, Vol. 2 No 3, 400-420.

[12] Parhi D. R. and Behera A. K. *Dynamic deflection of a cracked beam with moving mass.* Proc Instn Mech Engrs 1997, Vol. 211 Part C, 77-87.

[13] Lee J.W., Kim J.D., Yun C.B., Yi J.H., Shim J.M. *Health-monitoring method for bridges under ordinary traffic loadings*. Journal of Sound and Vibration 2002, Vol. 257 (2), 247–264.

[14] Bilello C., Bergman L.A. *Vibration of damaged beams under a moving mass: Theory and Experimental Validation.* Journal of Sound and Vibration 2004, Vol. 274, 567–582.

[15] Zhu X.Q., Law S.S. *Wavelet-based crack identification of bridge beam from operational deflection time history*. International Journal of Solids and Structures 2006, Vol. 43, 2299–2317.

[16] Baeza L., Ouyang H., *Vibration of a truss structure excited by a moving oscillator.* Journal of Sound and Vibration 2009, Vol. 321, p. 721–734

[17] Lin Y. H. and Trethewey M. W., *Finite Element Analysis of Elastic Beams Subjected to Moving Dynamic Loads*. Journal of Sound and Vibration 1989, Vol. 136 (2), 323-342.

[18] Qian G. L., Gu S. N. and Jiang J. S., *The dynamic behaviour and crack detection of a beam with a crack*. Journal of Sound and Vibration 1990, Vol. 138 (2), 233-243.

[19] Daubechies I., *Ten lectures on wavelets*. CBMS-NSF Conference series, 61. Philadelphia, PA: SISAM, 1992.

Experimental and Numerical Studies on Composite Tubes for the Energy Absorber of Korean Tilting Train Express (TTX)

Cao-Son Nguyen[a], Chun-Gon Kim[b]

[a] *Faculty of Engineering Mechanics and Automation, Hanoi University of Engineering and Technology, VNU*
[b] *Department of Aerospace Engineering, KAIST, Daejeon, South Korea*

Abstract

This paper presents an experimental and numerical study on composite tubes for the energy absorber of the Korean TTX(tilting train express). The purpose of the experimental study is to find out which lay-up is the best lay-up for the energy absorber. Four lay-ups were tested using quasi static method: $[0/45/90/-45]_4$, $[0]_{16}$, $[0/90]_8$, $[0/30/-30]_5$. Two triggering methods were used to create initial damage and guarantee the progressive collapse mode: bevel edge and notch edge. As a result, $[0/45/90/-45]_4$ lay-up was find out the best lay-up among the laminates being tested. In the numerical study, a parametric analysis was done to find out the most proper way to simulate the quasi static test of a composite tube using LS DYNA program. A single composite tube was modeled to be crashed by a moving wall. Comparison between simulation and experiment was done. Reasonable agreement between experiment and analysis was obtained. Dealing with parameter TFAIL and the mass scaling factor, this parametric study shows the ability and the limitation of LS DYNA in modeling the quasi static test for the composite tube.

Key Words: Composite tubes, Energy absorption, LS DYNA, Quasi static test

1. Introduction

The Korean TTX is a tilting train that can tilt itself to a maximum angle of 8^0 at the corner to maintain high speed during operating time [1]. The information of this train is given in Table 1. Compare to other high speed trains in the world, the Korean TTX is more light weight and has lower operating speed. During the operating time, the crash worthiness is very important to any vehicle. Based on the crash worthiness standards for the high speed trains from the United Kingdom and USA [2,3,4,5], a requirement for energy absorption of the driving car of the Korean TTX is suggested as in Table 2.

The main method for energy absorption of vehicles is using tubular structure. In the past metal is often used but nowadays, composite is being used more and more as the material for the energy absorption mechanism of vehicles, thank to its high energy absorption (EA) and specific energy absorption (E_S, tens to hundreds kJ/kg). This paper will study the

carbon/epoxy composite tubes for the Korean TTX's energy absorber experimentally and numerically.

Table 1. Information of Korean TTX.

Maximum design speed (km/h)	200	Length (m)	143
Maximum design speed (km/h)	180	N_o of seats	346
N_o of cars	6	N_o of motors	16
Weight (ton)	344	Tilting angle	8^0

Table 2. Suggested crash worthiness requirement for the Korean TTX's driving car.

Energy absorption	2MJ
Peak load	< 2MN
Stroke	75 cm
Deceleration	< 5g

When a collision occurs, the energy absorption and specific energy absorption of the tube can be calculated by the following equations:

$$EA = \int F.dx \qquad E_S = \frac{EA}{\rho AS_b}$$

Where F is the longitudinal force, x is the crush distance, S_b is the final crush distance, A is the cross section of the composite tube, ρ is the density of the material. A composite laminate can be failed in 4 modes: fragmentation crushing, splaying crushing, brittle fracturing crushing and progressive folding crushing [6]. The factors that have effect on the energy absorption of a carbon fiber reinforcement polymer (CFRP) composite laminate are: fiber type, matrix type, fiber direction, specimen geometry, process conditions, fiber volume fraction, and test speed. A study by Farley [7] shows that increase in the fiber strain to failure causes smaller energy absorption. For matrix, the same trend happens in the case of ductile CFRP composite, but in the case of brittle CFRP composite, the contrary occurs.

Another study by Farley [8] on the effect of fiber orientation for $[0\pm\theta]_4$ carbon/epoxy composite showed that E_S decreases when increasing θ up to 45^0 and remains constant when θ is above 45^0. Thornton and Edwards [9] studied the geometrical effects in energy absorption of composite material and concluded that, for a given fiber lay-up and tube geometry, E_S follows the order: circular > square > rectangle > triangle. Besides, the energy absorption will be a decreasing nonlinear function of the diameter to thickness ratio (D/t). The processing conditions also affect the crashworthiness. During making process, if vacuum is applied, it will reduce the matrix volume fraction and improve consolation, thus provide higher EA and E_S [10]. The effect of fiber volume fraction is more complicated. It is not always true that an increase of the fiber volume fraction will improve E_S. At low fiber volume fraction, increase in fiber volume fraction can lead to increase in energy absorption. But at high level of volume fraction (>40%), the contrary will occur [6]. Different test speeds can lead to different collapse modes of the composite laminate, thus different energy absorptions. The two methods for the crash test are impact test and quasi static test. While impact test is a true crash simulation since it applies high test speed which is similar to the real crash and takes into account the strain rate, quasi static test is not a true crash simulation since it applies a very low and constant test speed. For both test methods, triggers should be used to provide the initial damage and guarantee the progressive collapse mode. The common triggering methods are: bevel, notch, steeple, flange and plug.
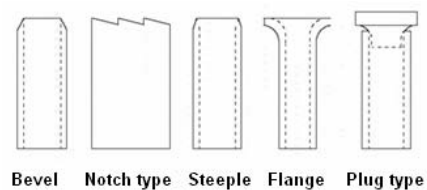

Fig.1   Triggering methods.

2. Experimental study

The specimens were fabricated using the material CU125NS, whose mechanical properties are provided in Table 3. Totally 4 different lay-ups were tested using quasi static method to find out the best lay-up for the energy absorber: $[0/45/90/-45]_4$, $[0/90]_8$, $[0]_{16}$, and $[0/30/-30]_5$. The specimens' dimensions are given in Table 4. Two triggering methods were used to provide the initial damage and ensure the progressive collapse: bevel edge and notch edge. The angle of the bevel is 45^0, and the notch edge was cut to create a slope of 5^0.

Table 3. Material's properties for CU125NS.

Properties	Symbol	Value
Density (kg/m^3)	ρ	1570
Elastic modulus in fiber direction (GPa)	E_1	135.4
Elastic modulus in transverse direction (GPa)	E_2, E_3	9.6
Shear modulus in 1-2 and 1-3 direction (GPa)	G_{12}, G_{13}	4.8
Shear modulus in 2-3 direction (GPa)	G_{23}	3.2
Poisson's ratio	υ_{12}, υ_{13}	0.31
	υ_{23}	0.52
Tensile strength in fiber direction (MPa)	X_T	1933
Compressive strength in fiber direction (MPa)	X_C	1051
Tensile strength in transverse direction (MPa)	Y_T	51
Compressive strength in transverse direction (MPa)	Y_C	141
Shear strength (MPa)	S	61

Table 4. The specimens' dimensions.

	Length (mm)	Outer diameter (mm)	Thickness (mm)
$[0/45/90/-45]_4$	160	100	1.8
$[0/90]_8$	115	100	1.8
$[0]_{16}$	115	100	1.8
$[0/30/-30]_5$	115	100	1.7

After a laminate was made using an inner mold of cylindrical shape, this mold is removed and the laminate is placed in a metal mold. Then the vacuum bag is applied and the specimen is cured in the autoclave while pressure is applied from the inner space. Fig.3 shows the curing cycles for the specimens. After curing, the outer skin of the specimen is perfectly smooth, but its inner side has some corrugation in the horizontal direction. This may due to the compression of the peel plies and bleeders during the curing process. Improvement in skill and stacking method will help to reduce this unexpected phenomenon.
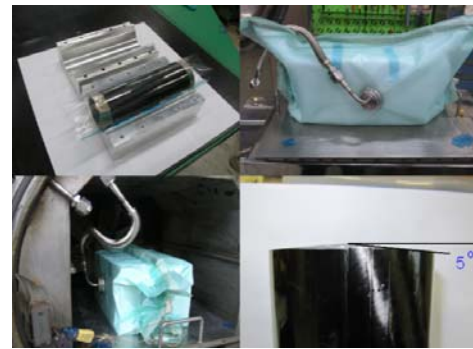
Fig.2. The making of the specimens.
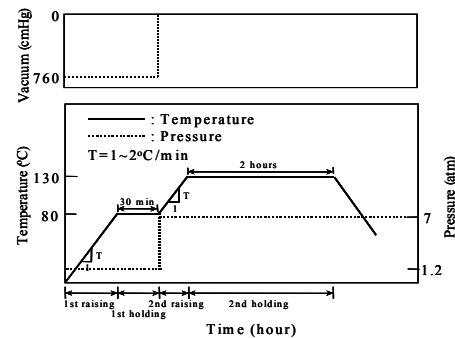
Fig.3. Curing cycle of the specimens.

The quasi static tests were carried out using the Universal Tester 4482. The test load is 100kN, the test speed is 2mm/min. The specimen was placed on a flat plate while being crashed from the upper side by a moving plate. No clamping or any other constrains were used. Observation during the

tests confirms that there was no slide between the specimen and the lower plate.

Fig.4. Quasi static tests set up and results.

The energy absorption and mean force are calculated by the following equations

$$EA = \int F.dx \quad F_{mean} = \frac{EA}{CrushLength}$$

F is the plate's force, and x is the plate's displacement.

Fig.5 plots the Force vs. Crush distance curve of the upper plate for all lay-ups of the notch edge case for a crush distance of 34mm. Summary of the crashworthiness parameters are shown in Table 5. The $[0]_{16}$ lay-up fails right after the initial damage. The $[0/45/90/-45]_4$ lay-up has the highest EA and E_S.
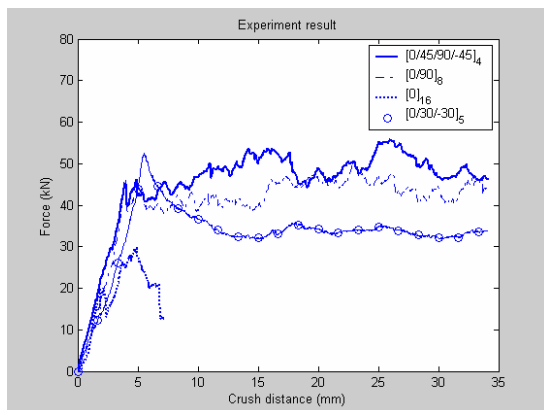
Fig.5. Force vs. Crush distance curve for experiment.

The comparisons of the two triggering types in the cases of $[0/90]_8$ and $[0/30/-30]_5$

lay-ups are shown in Fig.6. In the Force – Crush displacement curve, the difference at the beginning in the case of $[0/30/-30]_5$ lay-up may due to the difference in triggering methods. But in both cases, after the initial damage, there is no large difference between the two triggering methods. This can lead to a more general conclusion: in the quasi static test, triggering method only affects the initial damage of the tube. This may not happens in the impact test, where the high test speed can lead to some unstable collapse and the progressive mode cannot be obtained.

Table 5. Summary of test result.

Lay up	1st peak load (kN)	Mean load (kN)	EA (kJ)	E_S (kJ/kg)
$[0/45/90/-45]_4$	45.18	45.19	1.54	51.83
$[0/90]_8$	46.49	40.31	1.37	46.23
$[0/30/-30]_5$	52.48	32.84	1.12	39.85
$[0]_{16}$	-	-	-	-

From the experiment results, among the different laminates were tested, the $[0/45/90/-45]_4$ lay-up has the highest energy absorption and specific energy absorption (EA= 1.54kJ for a crush distance of 34mm, E_S = 51.83kJ/kg). In order to absorb 2MN of collision energy, if using this lay-up, the Energy Absorber of the Korean TTX will consist of totally 64 quasi-isotropic tubes of 70cm length.
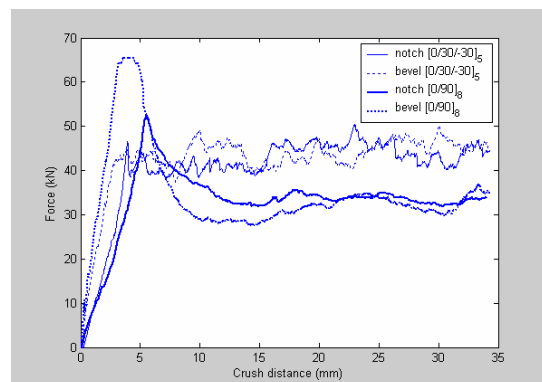
Fig.6. Comparison of triggering methods.

3. Numerical study

A parametric study was done in order to find out the most proper method to simulate the quasi static test of composite tubes using LS DYNA. LS DYNA is the program which is often used for the simulation of the crash test in the literature [11,12,13]. It is a finite element code which uses the Lagrangian formulation. It obtain a stable solution by integrating the equation of motion every small time step. These small time steps are suitable for the impact and crash simulation. The code also has a large material library for metals and composites and efficient contact algorithms. The simulation was done for the notch edge cases of and compared to the experiment's results. This study was done with a Intel(R) Core(TM) 2Quad core CPU 2.66GHz, 3.25 GB RAM computer. Reasonable agreement between the simulation's result and test's result was obtained. Base on this, a further parametric study can be carried out to determine the optimal design for the Energy Absorber used for the TTX.

3.1. Material for the model

In this study, a crash model was set up using the material model used was ENHANCED_COMPOSITE_DAMAGE MAT55, which was found to be the most proper LS DYNA's material model for the unidirectional fiber composite [11,12,13] . The failure criterion of this material model is the Tsai-Wu criterion. This criterion includes 3 modes that the composite model can fail: tensile fiber mode, compressive fiber mode, and tensile and compressive matrix mode. These modes are given as below [14].

Tensile fiber mode:

$$\sigma_{aa} > 0 \quad \text{then} \quad e_f^2 = \left(\frac{\sigma_{aa}}{X_t}\right)^2 + \beta \left(\frac{\sigma_{ab}}{S_c}\right)^2 - 1 \quad \begin{cases} \geq 0 \to \textit{failed} \\ < 0 \to \textit{elastic} \end{cases}$$

$E_a = E_b = G_{ab} = \upsilon_{ba} = \upsilon_{ab} = 0$

Compressive fiber mode

$$\sigma_{aa} < 0 \quad \text{then} \quad e_c^2 = \left(\frac{\sigma_{aa}}{X_c}\right)^2 - 1 \quad \begin{cases} \geq 0 \to \textit{failed} \\ < 0 \to \textit{elastic} \end{cases}$$

$E_a = \upsilon_{ba} = \upsilon_{ab} = 0$

Tensile and compressive matrix mode

$$e_{md}^2 = \frac{\sigma_{bb}^2}{Y_c Y_t} + \left(\frac{\sigma_{ab}}{S_c}\right)^2 + \frac{(Y_c - Y_t)\sigma_{bb}}{Y_c Y_t} - 1 \quad \begin{cases} \geq 0 \to \textit{failed} \\ < 0 \to \textit{elastic} \end{cases}$$

For β=1, the original criteria of Hashin of 1980 is obtained in the tensile fiber direction, while for β=0 we get the Maximum Stress Criterion which is found to compare better to experiments. In this study, β=0 was chosen.

Through the tube's thickness of 1.8mm, there are 16 integration points which are placed equally in each layer (15 points for the case of [0/30/-30]₅). The material properties are defined for each layer using by β angle in the local ordinate system of each element. In this local ordinate system, x-direction is the longitudinal direction of the tube, z-direction is the normal direction of the element, and y-direction is defined by the cross product of vector x and z.
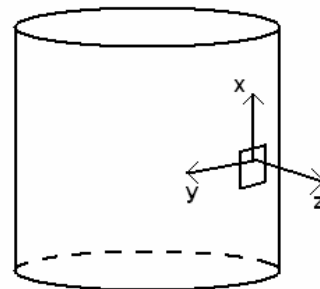

Fig.7.Local ordinate system of an element.

MAT55 also allows eliminating elements if the strain exceeds a limit value, or when a time step of the analysis decreases to a very small value, this is to prevent the large scale folding and avoid the ductile behavior of the model. This eliminating elements method can be controlled using the time step failure parameter TFAIL. This parameter allows us to keep the brittle behavior of the model, and maintain the level of time step to save the

computer time. Varying in the range from 0.1 to 1, low TFAIL provides ductile material, while high TFAIL provides brittle behavior. There is no default value for TFAIL for every material model, so in the simulation the user should test this parameter and choose the most proper value for it which provides the most appropriate behavior compared to real material.

A preliminary study was carried out with several value of TFAIL, and the value of 0.4 was found to be the most proper for this simulation, since it provides the best agreement of the Force-Crush distance curve between analysis and experiment.
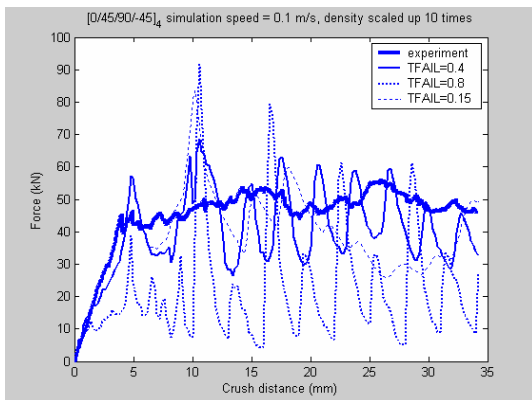
Fig.8. Result of preliminary study for TFAIL.

3.2 Mesh the model

After a preliminary study of convergence, 5700 elements were used for a tube having length of 115mm and outer diameter of 100mm. The size of the element is 3.14×2 mm.
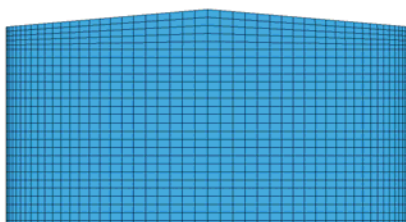
Fig.9 The elements at the top of the tube**.**

The element type is Belytschko-Lin-Tsay quadrilateral shell. At the top of the tube, where has the notch edge, refinement in meshing was made to improve the accuracy.

3.3 Contact and boundary condition

Since the observation during the experiments confirm no large slide between the tube and the lower plate, in the simulation the tube's bottom was modeled to be fixed. The moving plate was modeled using a RIGIDWALL_GEOMETRY_FLAT _MOTION. The friction coefficient of the wall's surface is 0.4.
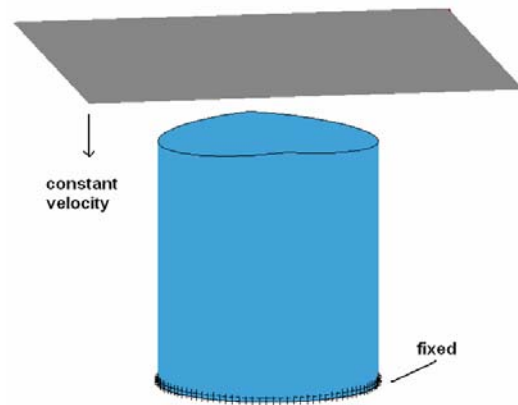
Fig.10 Test set up in the numerical study.

3.4 The quasi static condition

To guarantee the quasi static condition, the kinetic energy should be very small during the analysis. Thus low speed should be applied to the moving wall in the simulation. The best case is that the simulation has the same speed with the experiment. But this will require huge amount of computer time. So, higher speed and mass scaling method are needed to save the computer time.

At first a speed of 1m/s was applied to the moving wall in the case of [0/45/90/-45]₄ lay-up. This level of speed is also used in the literature papers [11,12,13] for the quasi static test. The simulation shown good agreement compared to the experiment (Fig.11). Computer time is 54 minutes.
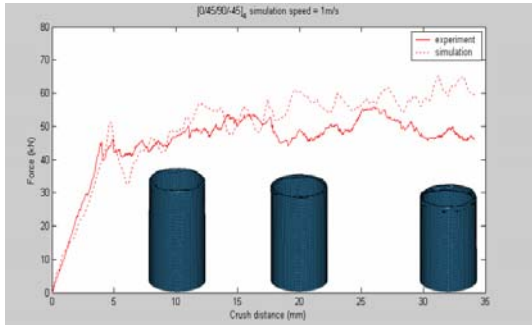
Fig.11. Simulation result for [0/45/90/-45]$_4$ lay-up, test speed = 1m/s.

Table.6   Simulation result for [0/45/90/-45]$_4$ lay-up, test speed = 1m/s.

	Experiment	Simulation	Difference
Crush distance	34.14 mm	34.2 mm	
1st peak load (kN)	45.70	51.16	12.8%
Mean load (kN)	45.486	49.556	9.67%
EA (kJ)	1.54	1.69	9.74%
E$_S$ (kJ/kg)	51.83	56.84	9.67%

$$Difference = \frac{|Simulation - Experiment|}{Experiment} \times 100\%$$

Then the same speed was applied to the case of [0/90]$_8$ lay-up. During the simulation, the tube had some remarkable buckling and the Force vs. Crush distance curve showed large difference compared to the experiment (Fig.12). This means lower simulation speed should be used to guarantee the quasi static condition.

Then a speed of 0.1m/s was chosen for this lay-up. At this speed, using the real density of the material costs huge computer time, so mass scaling method is applied to save the computer time. A parametric study was done to test the accuracy and efficiency of mass scaling method. The density of the tube is scaled up 10, 100 and 1000 times, respectively. The more we scale up the

material's density, the larger the kinetic energy will be, and so will the error. Fig.13 shows the result of this parametric study. Scaling up the density 10 times provides the largest computer time but smallest error between simulation and experiment.
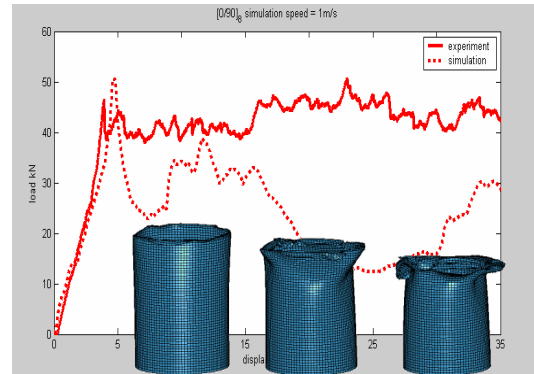
Fig.12. Simulation result for [0/90]$_8$ lay-up, test speed = 1m/s.
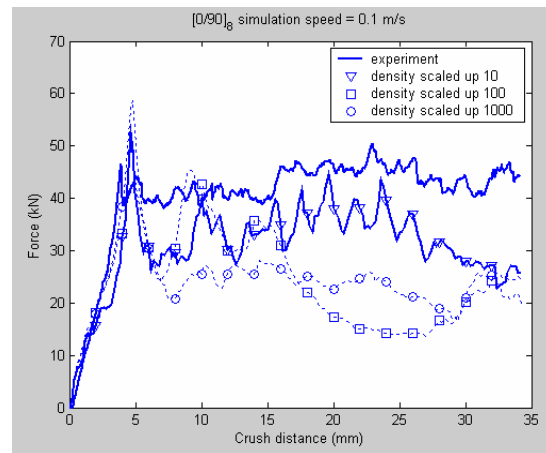
Fig.13 Results for different density scale factors.

Computer time
1000 times: 55 minutes
100 times: 3 hours
10 times: 10 hours

Then the same test speed (0.1m/s) and scale up factor (10 times) were applied for all the other lay-ups. The simulation showed reasonable agreement with the experiment. The simulations' results are shown as follows.

3.5 Final simulations' results

Fig.14 Final stage of the specimens (S: notch, B: bevel).
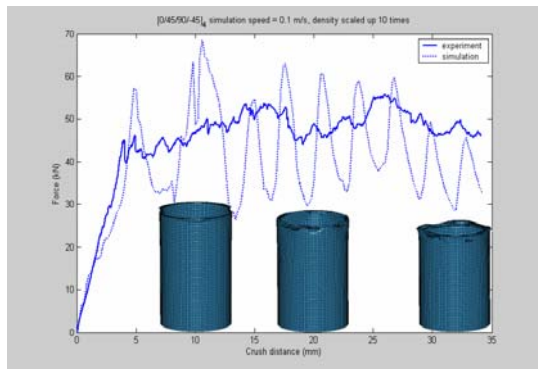
Fig.15 Simulation result for $[0/45/90/-45]_4$ lay-up.

Table.7. Simulation result for $[0/45/90/-45]_4$ lay-up, test speed = 0.1m/s.

	Experiment	Simulation	Difference
Crush distance	34.14 mm	34.2 mm	
1st peak load (kN)	45.18	57.15	26.5%
Mean load (kN)	45.19	40.14	11.2%
EA (kJ)	1.54	1.37	11%
E_S (kJ/kg)	51.83	46.04	11.2%
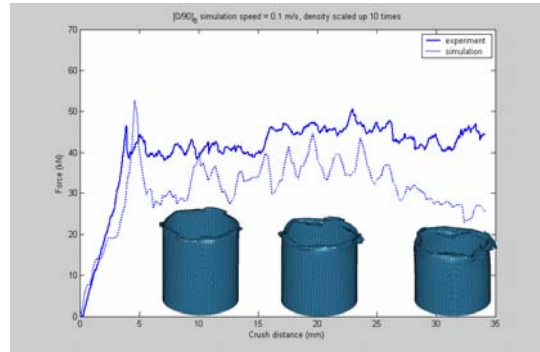
Fig.16 Simulation result for $[0/90]_8$ lay-up.

Table.8. Simulation result for $[0/90]_8$ lay-up, test speed = 0.1m/s.

	Experiment	Simulation	Difference
Crush distance	34.15 mm	34.2 mm	
1st peak load (kN)	46.49	52.72	13.4%
Mean load (kN)	40.31	30.93	23.27%
EA (kJ)	1.37	1.06	23.1%
E_S (kJ/kg)	46.23	35.48	23.25%
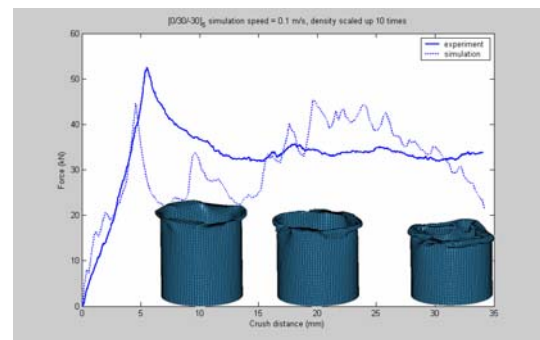
Fig.17 Simulation result for $[0/30/-30]_5$ lay-up.

Table.7 Simulation result for $[0/30/-30]_5$ lay-up, test speed = 0.1m/s.

	Experiment	Simulation	Difference
Crush distance	34.07 mm	34.2 mm	
1st peak load (kN)	52.48	44.6	15%

Mean load (kN)	32.84	30.93	5.82%
EA (kJ)	11.19	10.58	5.45%
E_S (kJ/kg)	39.85	37.53	5.81%
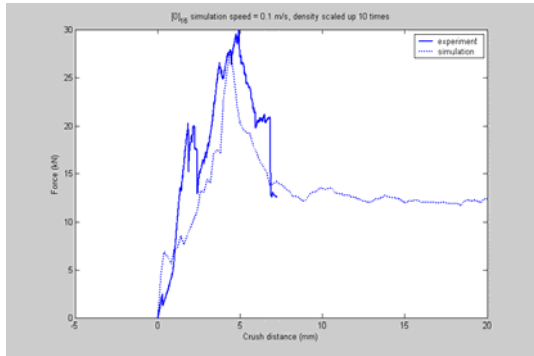
Fig.18 Simulation result for $[0]_{16}$ lay-up.

3.6 Discussion

Though a same test set up was used for all the lay-ups, but the analysis shows different error in each case. $[0/45/90/-45]_4$ has the largest error in EA and E_S (23%), while $[0/30/-30]_5$ has the smallest error (6%).

Only the $[0/45/90/-45]_4$ lay-up show no buckling in the tube's wall and perfect progressive collapse was obtained. In all the other cases, there was buckling and the collapse mode was not exactly the same as the experiment.

In the experiment, the $[0]_{16}$ lay-up fails right after the initial damage, but the simulation cannot provide the same behavior.

In the experiment, after the initial damage, the Force of the upper plate is quite constant during the progressive collapse for all lay-ups. But in the simulation, different behaviors of the Force are obtained, and this lead to different deviations of the simulation compared to the experiment.

This may due to the capacity of the program LS DYNA. Further study can be done with different material model, contact algorithm, and meshing method to improve the simulation.

4. Conclusion and further study

Experimental and numerical studies were done to test the composite material for the Energy Absorber of the Korean TTX. The crashworthiness of the composite tube was tested using quasi static test.

In the experimental study, single composite tubes made of composite material CU125NS were set to be crashed by a moving wall having a constant velocity of 2mm/min. Totally 4 lay-ups were tested to find out the best lay-up for the Energy Absorber: $[0/45/90/-45]_4$, $[0]_{16}$, $[0/90]_8$, $[0/30/-30]_5$. Two triggering methods were used to provide initial damage and guarantee progressive collapse mode: bevel edge and notch edge. Comparison of the triggering methods for the same lay-up shows no large difference after the initial damage. From this result we can make a more conclusion for the quasi static test: triggering method only affects the initial damage of the tube but not the progressive collapse after that. This may not happens in the case of impact test, where some unstable collapse can occur due to high test speed. Comparison of the crashworthiness shows that $[0/45/90/-45]_4$ is the best lay-up among the laminates being tested since it has the highest energy absorption and specific energy absorption ((EA= 1.54kJ for a crush distance of 34mm, E_S = 51.83kJ/kg).

In the numerical study using LS DYNA program, a single composite tube was modeled using ENHANCED_COMPOSITE_DAMAGE MAT55 and 5700 Belytschko-Lin-Tsay quadrilateral shell elements of 3.14 x 2mm size. This tube is crashed by a moving wall at the speed of 1m/s and 0.1m/s. A study on parameter TFAIL and the mass scaling factor was done to find out the most proper method for the quasi static test. The higher test speed has good agreement between simulation and experiment for one lay-up, but large error for the others; while the lower test speed shows reasonable agreement between simulation and

experiment. Still, the simulations have some large buckling, which doesn't occur in the experiment; and the analysis cannot provide the same behavior for the $[0]_{16}$ lay-up, which failed right after the initial damage.

Based on this research, further study can be done to determine the optimal design for the Energy Absorber of the Korean TTX. The experimental study can concern with the thickness/diameter ratio, other triggering methods…The numerical study at this stage shows different Force's behaviors for different lay-up after the initial triggering, which should be quite constant for all lay-ups as in the experiment. Further improvement concerning with the material parameters in the model and the layers of the tube should be made to eliminate this limitation.

5. References

[1]. Kim.J.S (2005) Fatigue assessment of tilting bogie frame for Korean tilting train: Analysis and static test. *Engineering Failure Analysis.*

[2]. UK Structural requirement for railway vehicles, GM/RT2100, 2000

[3]. US Code of Federal Regulations, 49 CRF-Part 238.

[4]. Tyrell.D.C (2001). *US Rail Equipment Crashworthiness Standards.* What can we realistically expect from crashworthiness? Improving train design to withstand future accidents, London, England.

[5]. *UK Report RSSB T118T118.* Whole train dynamic behavior in collisions and improving crashworthiness, 2006.

[6]. Jacob.G.C, Fellers.J.F (2002). Energy Absorption in Polymer Composites for automotive crashworthiness. *Journal of Composite Material*, Vol.36, No 07/2002.

[7]. Farley.G.L (1986) Effect of fiber and matrix maximum strain on the energy absorption of composite materials, *J. Comp. Mater.* Vol.20 pp. 322–334.

[8]. Farley.G.L. Energy absorption of composite material and structures. *Proceedings of the 43rd American Helicopter Society Annual Forum.* St. Louis, USA. pp. 613–627.

[9]. Thornton.P.H. and Edwards.P.J. Energy absorption in composite tubes. *Composite Materials*, Vol.16, pp.521–545.

[10].Melo.J.D.J, Silva.A.L.S, Villena.E.V (2008). The effect of processing conditions on the energy absorption capability of composite tubes. *Composite structures*, Vol. 82, pp.622-628.

[11].Bisagni.C, Di Pietro.G, Fraschini.L, Terletti.D (2005). Progressive crushing of fiber-reinforced composite structural components of a Formula One racing car. *Composite Structures*, Vol.68 pp.491-503.

[12].Kakogianis.D, Van Hemelrijck.D, Wastiels.J (2008). Experimental and numerical study of the energy absorption capacity of pultruded composite tubes. *13th European conference on composite materials, ECCM.*

[13].Mamalis.A.G, Manolakos.D.E, Loannidis.M, Papapostolou.D.P (2006). The static and dynamic axial collapse of CFRP square tubes: Finite element modeling. *Composite Structures*, Vol.74 pp.213-225

[14].LS DYNA keyword manual, version 971.

Maximum Power Point Tracking for Solar System

Thanh Tuan Nguyen [a] and Huy Thuy Nguyen [b]

[a] Mechatronics engineer, Aerospace Dynamics and Precision Mechatronics Department., Space Technology Institute (STI), Vietnam Academy of Science and Technology (VAST),Viet Nam, nttuan@sti.vast.ac.vn or thanhtuan.cn@gmail.com
[b] Mechatronics master, Mechatronics Department, Kyungnam University, Masan City, Korea, nhuythuy@gmail.com

Abstract

Optimizing the operation efficiency of solar panel is very important in using solar energy. One of the methods using to optimize solar efficiency is maximum power point tracking (MPPT). In this paper, the practical implementation of maximum power point tracking method (MPPT) for a solar system is presented. This implementation is done with view to proving that MPPT theories can be executed in practice exactly. The solar system usually consists of a solar panel that converts solar energy into electrical energy, a DC/DC converter that used to control the operating voltage of solar panel at maximum power point voltage and load. The MPPT method that is used in this paper is Incremental Conductance method. This is one of the popular MPPT methods and is easy to implement. The controller is Microchip microcontroller, PIC 16F877A. The tests of algorithm implementation were executed in the laboratory with a 1500W halogen lamp. Finally, the practical results are demonstrated in charts.

Key Words: Solar panel, Solar system, Maximum Power Point Tracking, MPPT, Incremental Conductance, IncCond, Microcontroller, PIC

1. Instruction

Recently, according to the development of society, the demands for electrical energy are increasing fast. Fossil energy sources are becoming exhausted. Furthermore, using fossil fuel produces carbon dioxide (CO_2), the main factor of Greenhouse Effect. So, renewable energy sources such as solar energy are acquiring more significant. Solar energy is considered to be one of the most useful natural energy sources because it is free, abundant, pure and most widely distributed. To use solar energy, the solar panel is required. As known, at a PV (Power - Voltage) curve of a solar panel, there is an optimum operating point such that the solar panel delivers the maximum possible power to the load. PV curve of solar panel changes with solar irradiation, cell temperature and the load. Therefore, at each operating condition, it's essential to track the maximum power point of solar panel. This increases the using efficiency of solar panel. A variety of maximum power point tracking methods are developed such as: perturb and observe (P & O), incremental conductance

(InCond), Parasitic Capacitance and Constant Voltage and Current, etc. In MPPT, InCond is the most popular algorithm because of its high tracking efficiency and it's easy to implement. In this paper, InCond algorithm is presented. In figure 1, a solar system with MPPT is shown.
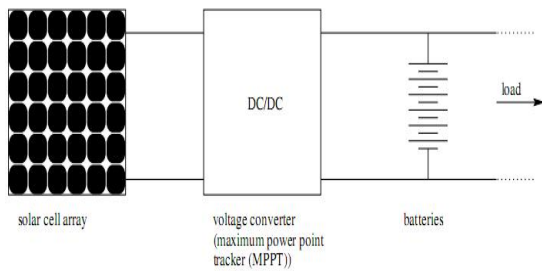

Figure 1. Solar system with MPPT

2. The solar panel

In MPPT, it's essential to understand the characteristics of solar panel because it significantly influences the design of converter and control system. Solar panel is a semiconductor device that operates according to the photoelectric effect. The equivalent circuit of solar panel is shown in Figure 2. When solar panel is illuminated, a direct current is generated. This generated current is dependent of operating condition such as: irradiation, temperature and can be calculated by the following equation:

$$I = I_{sc} - I_0 \left\{ epx \left[\frac{q(V + R_s I)}{nkT_k} \right] - 1 \right\} - \frac{V + R_s I}{R_{sh}}$$

where:

- V and I represent the output voltage and current of the solar panel.

- R_s and R_{sh} represent the series and shunt resistance of the solar panel.

- q is the electronic charge.

- I_{sc} is the light – generated current.

- I_0 is the reverse saturation current.

- n is a dimension factor.

- k is the Boltzmann constant.

- T_k is the temperature in $^{\circ}$K.
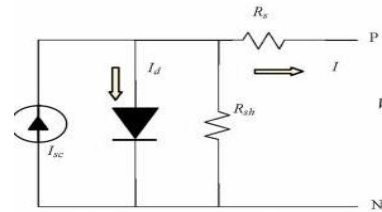
Figure 2. Equivalent circuit of solar cell

Figure 3 shows the electrical characteristic of solar panel. This figure shows that the V-I curve of solar panel is non-linear and changes with irradiation, temperature and load condition. Moreover, when output voltage of solar panel is equal to V_{max}, the solar panel delivers the maximum power to the load.
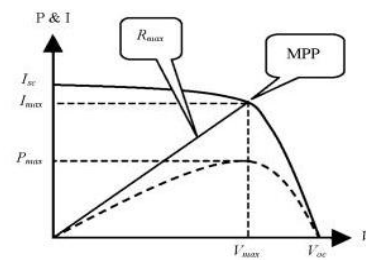
Figure 3. Solar panel characteristic

On the other hand, power of solar panel can be calculated by P = V.I. So, when V, I change, power of solar panel changes correctly. By any way, the solar output voltage can be changed, the solar output power changes. To obtain the maximum power from solar panel, the output voltage must be regulated at V_{max}.

3. DC/DC converter

To regulate solar output voltage, is a dc/dc converter is required such as: buck converter, boost converter or buck-boost converter. In this paper, buck converter is used. Buck converter is a step-down DC to DC converter. It consists of a MOSFET, a

diode, an inductor and a capacitor. Figure 4 show the buck converter circuit.
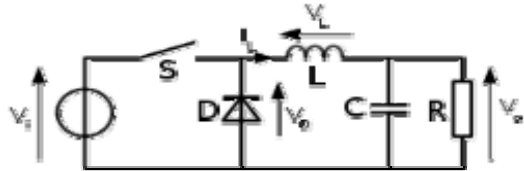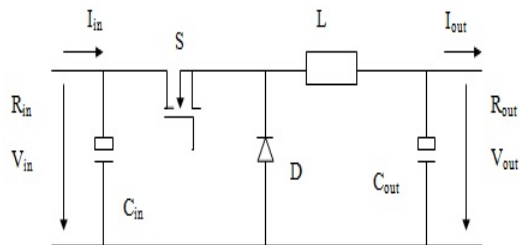
The characteristic of buck converter is:

$$V_o = D.V_i$$

Figure 4. Buck converter

where:

- V_o is the output voltage of buck converter

- V_i is the input voltage of buck converter

- D is duty cycle of switch frequency of S switch.

In this paper, buck converter is used in continuous mode.

Assuming buck converter is ideal (efficiency is 100%), so $P_o=P_i$. And R_i of buck depends on R_o (load) as the following equation:

$$R_i = \frac{1}{D^2}R_o$$

when the load is constant, a change of D causes the change of R_i.

4. Maximum Power Point Tracking

As known, Maximum Power Point Tracking (MPPT) is a method to optimize the efficiency of solar panel. In this paper, one of MPPT methods, incremental conductance (InCond), is presented. InCond algorithm is

developed base on a particular property of P-V curve of solar panel. At maximum power point (MPP) the ratio $\frac{dP}{dV} = 0$, on the left of MPP $\frac{dP}{dV} > 0$ and $\frac{dP}{dV} < 0$ on the right of MPP.
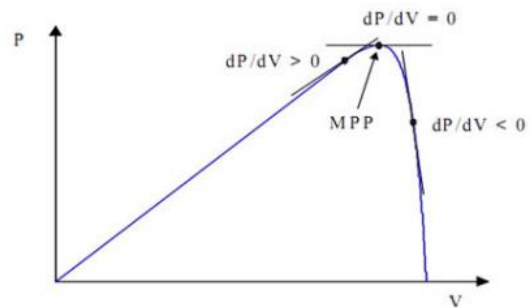
Figure 5. P-V characteristic

P can be calculated by P = V.I, so:

$$\frac{dP}{dV} = \frac{d(VI)}{dV} = I + V\frac{dI}{dV} = 0$$

Finally,

$$\frac{dI}{dV} = -\frac{I}{V} \text{ , at MPP.}$$

$$\frac{dI}{dV} > -\frac{I}{V} \text{ , left of MPP.}$$

$$\frac{dI}{dV} < -\frac{I}{V} \text{ , right of MPP.}$$

where:

dI(k) ≈ dI(k) – dI(k-1);

dV(k) ≈ dV(k) – dV(k-1);

Base on the characteristics at MPP, flow chart of InCond algorithm is shown in Figure 6. The algorithm is implemented by measuring the incremental and instantaneous panel conductance ($\frac{dI}{dV}$ and $\frac{I}{V}$, respectively). Depending on the correlation between $\frac{dI}{dV}$ and $\frac{I}{V}$, the operating voltage of solar panel is adjusted accordingly. The

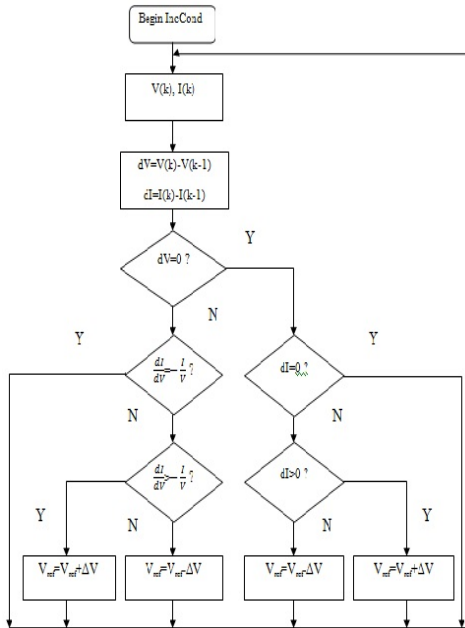advantage of this algorithm is when operating at MPP, the operating voltage is static. So it decreases the power loss.

Figure 6. IncCond algorithm

Tracking efficiency of InCond algorithm η_T can be calculated by:

$$\eta_T = \frac{\int_{t_1}^{t_2} P\,dt}{\int_{t_1}^{t_2} P_{max}\,dt}$$

where:

- t_1 is start-up time of the system.
- t_2 is close-down time of the system.
- P is the solar panel output power.
- P_{max} is the theoretical maximum solar panel power.

The tracking efficiency of this algorithm is above 80%.

5. MPPT system development

The practical circuit of the proposed solar system is shown in Figure 5. It contains a solar panel, a buck converter, a load and a control unit.

5.1. The characteristics of solar panel are:

- Maximum power: 150W
- Short circuit current: 8.9A
- Open circuit voltage: 21.6V
- Maximum power current: 8.7A
- Maximum power voltage: 17.3V
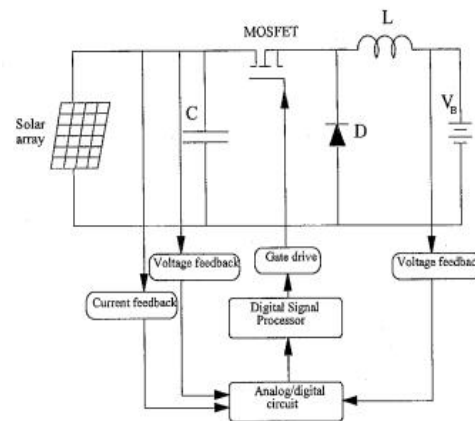
Figure 7. System circuit

Figure 8. Solar panel

5.2. Control unit

Control unit is the brain of this solar system. It controls all operations of system such as: measuring the voltage and current of solar panel, processing data feedback, implementing algorithm, transmitting the control signals to buck converter. These operations have to be implemented exactly and effectively. Because of control unit's

importance, it's necessary to select a suitable control unit. The selected control unit is PIC 16F877A. This is a microcontroller produced by Microchip Technology Inc. PIC 16F877A is 8-bit microcontroller. It has 10-bit ADC and PWM module that integrated.
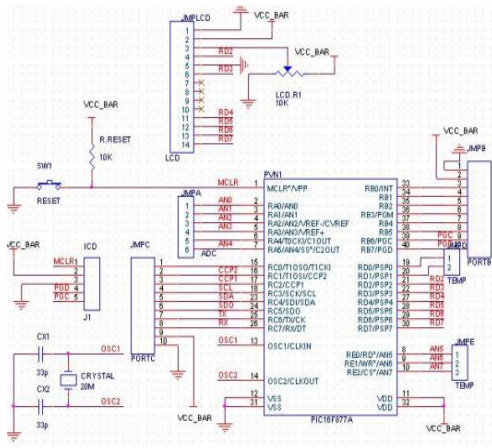
Figure 9 show the practical circuit of control unit.

Figure 9. Control Unit

The voltage and current of solar panel is measured through ADC (Analog – Digital converter) module. Control signal is sent through CCP pin by PWM module.

5.3. Buck converter

Buck converter is used as power processing unit. By adjusting duty cycle of switching frequency, the operating voltage of solar panel increases or decreases accordingly. Circuit of buck converter is shown in Figure 10.
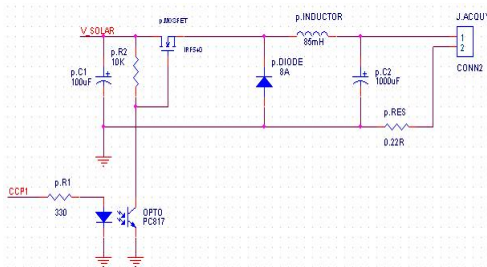
Figure 10. Buck converter

Selecting value of buck's components:

Inductor selection:

Inductance of the inductor can be calculated by:

$$L = (V_{inmax} - V_{out}) \times \frac{V_{out}}{V_{inmax}} \times \frac{1}{f_{sw}} \times \frac{1}{\Delta I_{inductor}}$$

$$= (18 - 10) \times \frac{10}{18} \times \frac{1}{25.10^3} \times \frac{1}{2,1} = 84,7 \mu H$$

where:

- V_{inmax} = 18V;

- V_{out} = 10V;

- I_{outmax} = 7A so $I_{inductor}$ = 0,3*7 = 2,1 A;

- f_{sw} = 25 kHz;

    Choose the inductor L: 85 μH

Output capacitor selection:

Voltage and current at output of buck oscillate continuously. So output capacitance is required to minimize the overshoot and ripple at the output of buck converter. The capacitance can be calculated by the following equation:

$$C_{out} = \frac{L I_{peak}^2}{(\Delta V + V_{out})^2 - V_{out}^2}$$

where: C_{out} is output capacitance.

- ΔV is maximum output voltage overshoot. Commonly, ΔV is equal 5% value of buck's output voltage.

- I_{peak} is inductor's peak operating current (I_{peak} = 8.05A).

    So:

$$C_{out} = \frac{85 \mu H \times (8,05A)^2}{(0.5 + 10)^2 - 10^2} = 537 \mu F$$

To decrease the buck output voltage overshoot and ripple, the capacitance usually is chosen larger than the calculated value. But if the chosen capacitance is too larger than the calculated value, it causes the significant delay of the output voltage.

So, the chosen output capacitor is 1000μF/25V.

MOSFET selection:

As known, the switch frequency is 25 kHz, the solar panel maximum voltage is 21.3V and the maximum current is 8.9A. So the switch must be satisfied with these requirements. To satisfy these requirements, the MOSFET IRF540 is selected. This is N-channel MOSFET that suitable with high frequency. It is also suitable with maximum voltage is 100V and maximum current is 8.9A.
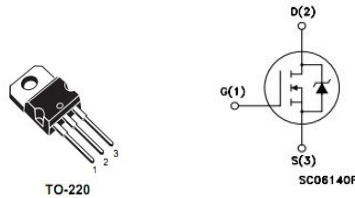

Figure 11. IRF540 MOSFET

Diode selection:

Choosing diode is dependent of power dissipation. Power dissipation can be calculated by:

$$P_{Diode} = \left(1 - \frac{V_{out}}{V_{in}}\right) I_{outmax} \, V_D$$

$$P_{Diode} = \left(1 - \frac{10}{18}\right) \times 7 \times 0.7 = 2.1 \, W$$

where: V_D is the voltage drop across the diode at the given output current I_{outmax}. The selected diode has to be able to dissipate that much power. Commonly, the reverse-repetitive maximum voltage of diode must be greater than the maximum input voltage ($V_{rrm} > V_{inmax}$). The diode's forward-current specification must meet or exceed the maximum output current ($I_{fc} > I_{outmax}$).

5.4. Voltage and current measurement

Figure 12 shows the details of feedback measurement circuit.

Voltage measurement:

Because output voltage of solar panel is larger than 5V (the limitation of ADC's voltage input), voltage feedback is applied to

ADC pin of PIC 16F877A through a resistor voltage divider that has 4 ratio. A voltage loop circuit also is used to isolate ADC pin from power unit. Figure 12 shows the detail of voltage measurement circuit.
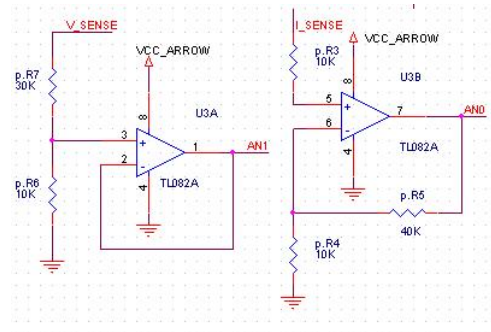

Figure 12. Feedback measurement unit

Current measurement:

Using Ohm's Law, we have:

$$I = \frac{V}{R}$$

So, current of solar panel can be measure by measuring the voltage drop through a 0.22R power resistor. This voltage is quite small, so it is amplified 5 times by using a non-inverter operational amplifier as shown in Figure 12.
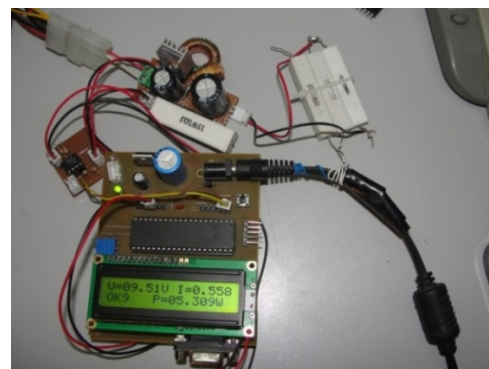
The final circuit is shown in Figure 13.

Figure 13. The practical solar system

6. Implementation of InCond algorithm

As discussed in the later sections, the output power of solar panel depends on its

output voltage. So, by adjusting the solar output voltage, the output power can be adjusted. To adjust the solar output voltage, the microcontroller changes the duty cycle of buck converter switching frequency.

Because of circuit design, when duty cycle D increases, the solar output voltage increases accordingly and vice versa. Base on InCond algorithm and this conclusion, when the operating point is on the left of MPP, the microcontroller increases duty cycle D of switching frequency to reach the MPP. When the operating point is on the right of MPP, the microcontroller decreases duty cycle D.

In practice, condition $\frac{dI}{dV} = -\frac{I}{V}$ doesn't happen. So, it's more practical to choose a ε constant that small enough as long as:

$$\left| \frac{dI}{dV} + \frac{I}{V} \right| < \varepsilon$$

By practice, ε is chosen as 0.0002.

Control program is coded by C language for microcontroller. Using C language helps implement the algorithm easier.

7. Result

This result is tested in static condition: room temperature (24°C); light source is a 1500W halogen lamp; load is a 2.2Ω power resistor.

When changing the output voltage of the solar panel, the output power changes accordingly. From 7V to 16.2V, when the operating voltage is increased, the output power is increased. At 16.2V, the output power is 11.5W. When the operating voltage is increased larger than 16.2V, the output power is decreased. The output power is equal 0W when the operating voltage is approximate the open-circuit voltage.
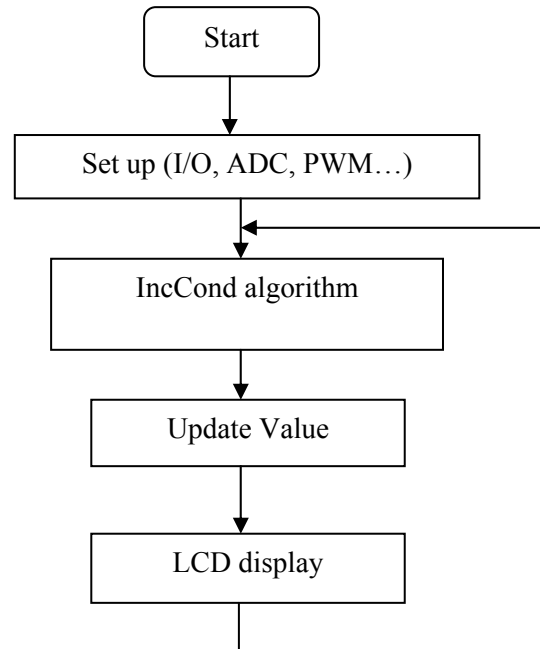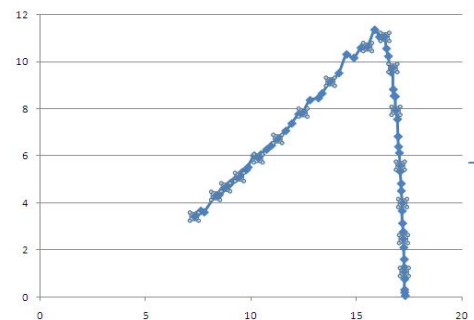

Figure 14. Flowchart of control program

Figure 15. P-V curve without MPPT

At this test condition, MPP is at 16.2V operating voltage and P_{max}=11.5W. Figure 15 is the P-V curve of solar panel without MPPT method. Figure 16 is P-V curve of solar panel with MPPT in the same test condition. Tracking process increases the output power regularly. When the process matches the MPP, the operating voltage is hold at V_{max}. The output power, depending on operating voltage, is hold at $P = P_{max}$. If there is any change in operating condition, InCond algorithm will calculate and transmit a suitable control signal to adjust the operating voltage at V_{max}.

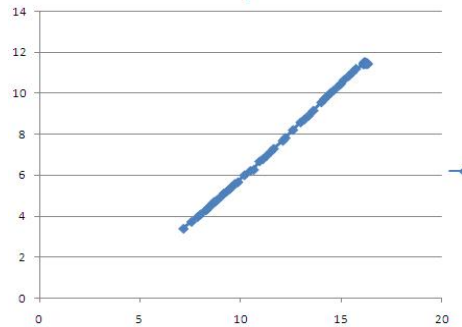Therefore, solar panel will deliver the maximum power to the load.

Figure 16. P-V curve using MPPT

8. Conclusion

This paper introduces about MPPT theory and proves that MPPT can be implemented in practice. MPPT theories were tested exactly and showed expected results in practice. All of the tests were implemented in laboratory but they can be improved to apply in daily life. In advance, this solar system can be upgraded with solar panel attitude control module to force the panel rotate according to sunlight direction. MPPT algorithm can be improved to obtain a larger efficiency and more flexibility.

9. Reference

[1]   Eric Anderson, Chris Dohan, Aaron Sikora. Solar Panel Peak Power Tracking System. Worcester Polytechnic Institute, 2003.

[2]   Liping Guo. Implementation of Digital PID controllers for DC/DC converters using Digital Signal Processors. Electrical & Information Engineering Technology Department of Industrial Technology, University of Northem Iowa, USA, IEEE EIT 2007, tr. 306 – 311.

[3]   Chihchiang Hua and Chihming Shen. Study of Maximum Power Tracking Techniques and Control of DC/DC converter for Photovoltaic Power System. Department of Electrical Engineering, National Yunlin University of Science and Technology Toulin, Yunlin 640, Taiwan, IEEE 1998, tr. 86 - 93.

[4]   Joe Air Jiang, Tsong Liang Huang, Ying Tung Hsiao and Chia Hong Chen. Maximum Power Tracking for Photovoltaic Power System. Department of Bio-Industrial Mechatronics Engineering, National Taiwan University Taipei, Taiwan, 2005.

[5]   Hannes Knopf. Analysis, Simulation, and Evaluation of maximum power point tracking (MPPT) methods for a solar powered vehicle. Master thesis, Portland State University, 1999.

[6]   J. Kouta, A. El-Ali, N. Moubayed and R. Outbib. Improving the incremental conductance control method of a solar energy conversion system. Department of Engineering Faculty of Engineering – Lebanese University, Lebanese.

[7]   Donald Schelle and Jorge Castorena (2006). Buck Converter Design Demystified. Technical Staff, Maxim Integrated Products, Sunnyvale, Calif, pages. 46 - 53.

[8]   International Rectifier, Datasheet IRF540

[9]   Microchip, Datasheet PIC 16F87XA

Điều Khiển Robot Di Động Qua Mạng Internet Sử Dụng Kiến Trúc Truyền Thông CORBA

Phùng Mạnh Dương[a], Quách Công Hoàng[b], Vũ Xuân Quang[c], Trần Quang Vinh[d]

[a] *Bộ môn Điện tử và Kỹ thuật Máy tính, trường Đại học Công nghệ, Đại học Quốc gia Hà Nội.*
Email: duongpm@vnu.edu.vn
[b] *Khoa Điện tử Viễn thông, trường Đại học Công nghệ, Đại học Quốc gia Hà Nội.*
Email: quachconghoang89@gmail.com
[c] *Khoa Điện tử Viễn thông, trường Đại học Công nghệ, Đại học Quốc gia Hà Nội.*
Email: xuanquang110289@yahoo.com.vn
[d] *Bộ môn Điện tử và Kỹ thuật Máy tính, trường Đại học Công nghệ, Đại học Quốc gia Hà Nội.*
Email: vinhtq@vnu.edu.vn

Abstract

Giám sát và điều khiển các hệ thống thời gian thực qua mạng Internet là vấn đề đang nhận được nhiều sự quan tâm nghiên cứu gần đây nhờ khả năng mở ra những ứng dụng mới cho cuộc sống hiện đại như phòng thí nghiệm ảo, hệ thống y tế từ xa, hệ thống điều khiển các thiết bị từ xa... Trong bài báo này, chúng tôi trình bày một hệ thống phân tán sử dụng kiến trúc truyền thông CORBA (Common Object Request Broker Architecture) cho phép chương trình khách có thể triệu gọi các lệnh điều khiển một robot di động qua mạng Internet mà không cần phải quan tâm các lệnh đó được cài đặt ở đâu, bằng ngôn ngữ lập trình gì và trên hệ điều hành nào. Điều này giúp khắc phục nhược điểm của đa số hệ thống điều khiển qua mạng Internet hiện nay thường chỉ tương thích với một ngôn ngữ lập trình và hệ điều hành nhất định. Hệ thống cũng cung cấp các dữ liệu phản hồi theo thời gian thực về môi trường ở xa tới người điều khiển như dữ liệu hình ảnh, dữ liệu siêu âm, dữ liệu hồng ngoại, vị trí và tốc độ hiện tại của robot… Các phép thực nghiệm cho thấy hệ thống có thể hoạt động ổn định và hiệu quả trên môi trường không biết trước trong ứng dụng giám sát an ninh tòa nhà.

Key Words: robot di động, robot từ xa, mạng Internet, kiến trúc CORBA, điều khiển phân tán, điều khiển robot qua mạng Internet

1. Mở đầu

Giám sát và điều khiển các hệ thống thời gian thực qua mạng Internet là vấn đề đang nhận được nhiều sự quan tâm nghiên cứu gần đây nhờ khả năng mở ra những ứng dụng mới cho cuộc sống hiện đại như phòng thí nghiệm ảo, hệ thống y tế từ xa, hệ thống điều khiển thiết bị tòa nhà từ xa... Có thể nhận thấy rằng, độ trì trễ (time delay), độ thăng giáng (delay

jitter) và băng thông truyền không thể dự đoán trước của mạng Internet chính là khó khăn và thách thức lớn nhất với bài toán điều khiển robot qua mạng máy tính nói chung và mạng Internet nói riêng [4]. Để khắc phục vấn đề này, có hai phương pháp tiếp cận chủ yếu là phương pháp phát triển các giải thuật điều khiển từ xa cải tiến kết hợp với kỹ thuật xây dựng giao diện [5]-[9] và phương pháp xây dựng các giao thức truyền tải thời gian thực [4][10].

Phương pháp phát triển các giải thuật điều khiển từ xa cải tiến kết hợp với kỹ thuật xây dựng giao diện không can thiệp vào vấn đề truyền tải dữ liệu qua mạng máy tính mà tập trung xây dựng các thuật toán để dự đoán và bù trừ những tham số ngẫu nhiên gây ra bởi mạng máy tính như độ trì trễ, độ thăng giáng và băng thông cho phép. Trong [11], Kuk-Hyun Han đã phát triển một hệ thống điều khiển robot qua mạng Internet dựa trên những dự đoán về thời gian trì trễ và vị trí của robot để từ đó xây dựng một bộ lọc lệnh (command filter) cho phép điều chỉnh các tín hiệu điều khiển robot. Hình 1 trình bày sơ đồ khối hệ thống. Theo sơ đồ này, một bản đồ ảo đã được xây dựng ở phía người dùng cho phép mô phỏng chuyển động của robot cũng như tọa độ và vị trí sắp tới. Nhờ đó, người dùng có thể dễ dàng quan sát và ra lệnh điều khiển robot. Để khắc phục độ trì trễ do mạng gây ra, Kuk-Hyun Han đã đề xuất công thức dự đoán thời gian trì trễ:

$$T_d(k) = \sum_{i=1}^{n}\left[\frac{I_I}{c} + t_I^R + t_i^L(k) + \frac{M}{b_i}\right]$$

$$= \sum_{i=1}^{n}\left(\frac{I_I}{c} + t_I^R + \frac{M}{b_i}\right) + \sum_{i=0}^{n} t_i^L(k) \qquad (1)$$

$$= d_N + d_L(k)$$

trong đó, $T_d(k)$ là độ trì trễ tại thời điểm k, l_i là chiều dài của liên kết thứ i, C là tốc độ ánh sáng, t_i^R là tốc độ định tuyến của nút mạng thứ i, $t_i^L(k)$ là độ trễ gây ra bởi tải của nút mạng thứ i, M là lượng dữ liệu, và b_i là băng thông của liên kết thứ i. d_N là tham số độc lập

với thời gian, và $d_L(k)$ là tham số phụ thuộc thời gian. Từ thời gian trì trễ dự đoán này, tác giả xây dựng một bộ lọc lệnh trước khi gửi tín hiệu đó tới điều khiển trực tiếp robot.

Trong một nghiên cứu khác [12], thay vì cố gắng bù trừ thời gian trì trễ, Dawei Wang đã phát triển các thuật toán tránh vật cản và cơ chế an toàn cho phép robot có thể phản ứng được với những tình huống không mong đợi do sự trì trễ gây ra. Các thuật toán này về cơ bản dựa trên các thuật toán tránh vật phổ biến như thuật toán trường thế hay thuật toán sử dụng logic mờ nhưng được cải tiến cho phù hợp với bài toán điều khiển qua mạng. Một môi trường ảo cũng được xây dựng ở phía người dùng nhằm dự đoán quỹ đạo robot và trợ giúp điều khiển.

Như vậy, có thể nhận thấy rằng hướng tiếp cận này không cố gắng làm giảm các tham số ngẫu nhiễn do mạng gây ra như độ trì trễ, độ thăng giáng mà tập trung vào vấn đề giảm thiểu ảnh hưởng và phản ứng lại với các yếu tố đó.

Phương pháp xây dựng các giao thức truyền tải thời gian thực tập trung xây dựng các giao thức lớp truyền tải (transport layer) phù hợp với các ứng dụng thời gian thực như giảm độ trì trễ, độ thăng giáng, tận dụng tối đa băng thông cho phép… Điển hình theo hướng tiếp cận này, Peter X. Liu đã đề xuất giao thức truyền tải thời gian thực Trinomial. Giao thức này cải tiến cơ chế điều khiển luồng dựa trên tốc độ truyền tải dữ liệu (rate-based flow control) để giảm độ thăng giáng và tận dụng nhiều hơn băng thông cho phép. Công thức cho sự thay đổi tốc độ truyền dữ liệu được Peter X. Liu đưa ra như sau:

$$\text{increase}: S_t = S_0 + \left(\frac{t}{\alpha}\right)^{\gamma}, \quad \alpha \geq 1, \gamma \geq 0$$

$$\text{decrease}: S_{t+} = (1-\beta)S_t, \quad 0 < \beta < 1 \qquad (2)$$

trong đó, t là chỉ số thời gian; S_t là tốc độ truyền tại thời điểm t ; S_0 là tốc độ truyền sau lần giảm gần nhất; S_{t+} là tốc độ truyền ngay sau thời điểm t; α, β và γ là những hằng số

không âm. Các kết quả mô phỏng và thực nghiệm, Peter X. Liu đã chứng tỏ giao thức do tác giả đề xuất cho kết quả tốt hơn các giao thức đang dùng hiện tại như TCP và UDP về mặt băng thông và độ thăng giáng.

Trong một nghiên cứu khác, tác giả LI Ling đề xuất giao thức IRTP cải tiến từ giao thức RTP để tối ưu hóa cho ứng dụng thời gian thực. Trong giao thức IRTP, tiêu đề của mỗi gói tin được rút gọn xuống 9 byte thay vì 40 byte như của RTP và do đó tăng được hiệu suất truyền tin hơn 10% so với giao thức RTP.
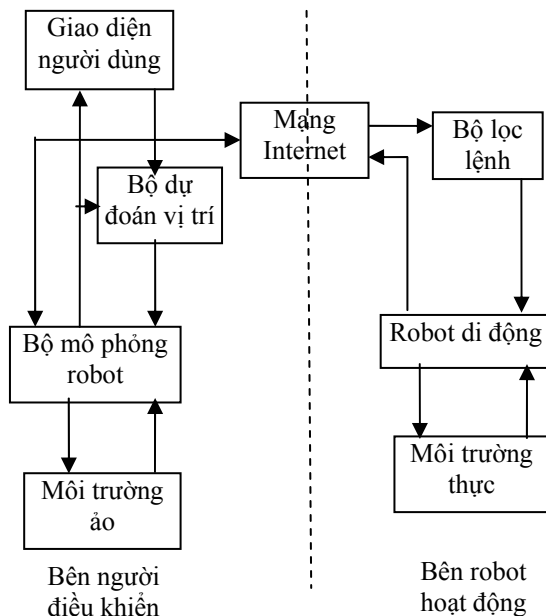
Hình 1. Sơ đồ điều khiển robot qua mạng
sử dụng bộ lọc lệnh

Trong bài báo này, chúng tôi trình bày một hệ thống phân tán sử dụng kiến trúc truyền thông CORBA (Common Object Request Broker Architecture) cho phép chương trình khách có thể triệu gọi các lệnh điều khiển một robot di động qua mạng Internet mà không cần phải quan tâm các lệnh đó được cài đặt ở đâu, bằng ngôn ngữ lập trình gì và trên hệ điều hành nào. Điều này giúp khắc phục nhược điểm của cả hai phương pháp đã nêu thường chỉ tương thích với một ngôn ngữ lập trình và hệ điều hành nhất định. Hệ thống cũng cung cấp các dữ liệu phản hồi theo thời

gian thực về môi trường ở xa tới người điều khiển như dữ liệu hình ảnh, dữ liệu siêu âm, dữ liệu hồng ngoại, vị trí và tốc độ hiện tại của robot… Các phép thực nghiệm cho thấy hệ thống có thể hoạt động ổn định và hiệu quả trên môi trường không biết trước trong ứng dụng giám sát an ninh tòa nhà.

2. Kiến trúc CORBA

CORBA (Common Object Request Broker Architecture) là một chuẩn công nghiệp cho phép gọi các phương thức từ xa và nhận kết quả trả về [13]. Nó có thể được sử dụng khi bên phía gọi và bên phía phương thức được gọi có thể sử dụng các ngôn ngữ lập trình khác nhau, trên nền tảng hệ điều hành khác nhau. Về cơ bản, CORBA bao gồm ba thành phần chính là ngôn ngữ đặc tả giao tiếp IDL (Interface Description Language), trình chuyển tiếp yêu cầu của các đối tượng ORB (Object Request Broker) và Giao thức IIOP (Internet Interoperability Protocol).

Ngôn ngữ đặc tả giao tiếp IDL (Interface Description Language) qui định một tập các mô tả hàm, kiểu dữ liệu và các khai báo cho phép đặc tả đối tượng. Đặc tả đối tượng ở đây mô tả chức năng của đối tượng thông qua hàm, phương thức, thuộc tính… và không có cài đặt mã lệnh trong ngôn ngữ đặc tả.

Trình chuyển tiếp yêu cầu của các đối tượng ORB (Object Request Broker) hoạt động như một dịch vụ cho phép phiên dịch yêu cầu của các đối tượng viết bằng ngôn ngữ khác nhau thành lời gọi theo một quy tắc chung. Hình 2 trình bày cơ chế triệu gọi lẫn nhau của các đối tượng viết bằng C++, Delphi, Java thông qua ORB. Trong quá trình hoạt động, ORB hoàn toàn trong suốt đối với người thiết kế và các lệnh triệu gọi đối tượng của Java trong C++ hay Delphi hoàn toàn theo cách tự nhiên như khi triệu gọi đối tượng được xây dựng từ chính ngôn ngữ gốc.

Giao thức IIOP (Internet Interoperability Protocol) cho phép liên lạc giữa nhiều tiến trình. Giao thức này do tổ chức CORBA đề

xướng và nó làm nền tảng cho tất cả các đối tượng có thể giao tiếp được với nhau trên mạng Internet một cách dễ dàng.
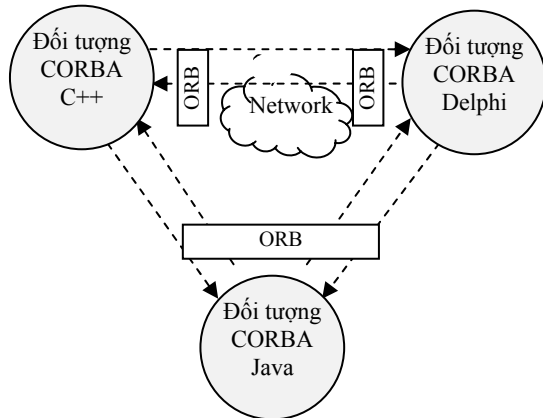
Hình 2. Triệu gọi đối tượng CORBA thông qua ORB

Trong bài báo này, chúng tôi đã sử dụng ưu điểm của CORBA là cho phép triệu gọi đối tượng giữa các ngôn ngữ khác nhau để xây dựng hệ thống điều khiển robot qua mạng Internet.

3. Thiết kế hệ thống điều khiển robot qua mạng Internet sử dụng kiến trúc CORBA

Từ những nghiên cứu lý thuyết nêu trên, tác giả đã xây dựng thực nghiệm một hệ thống điều khiển robot qua mạng Internet sử dụng kiến trúc truyền thông CORBA.

3.1 Thiết kế phần cứng

Hình 3 trình bày cấu trúc phần cứng của hệ thống bao gồm ba thành phần chính: robot di động DrRobot, máy tính trung tâm và máy tính Client.

Trong hệ thống, robot di động được sử dụng là robot Sputnik của hãng DrRobot [9] bao gồm các thành phần cơ bản sau: sáu cảm biến hồng ngoại gắn xung quanh robot; ba cảm biến siêu âm lần lượt gắn ở phía trước, bên phải và bên trái của robot; hai camera màu cho kích cỡ ảnh 353x288 với tốc độ lấy

mẫu 15 khung hình/giây; hai cảm biến phát hiện sự chuyển động của người HMS (Human Motion Sensor) trong khoảng 150 cm; và bốn động cơ điều khiển điều khiển toàn bộ chuyển động của robot. Ngoài ra, robot có thể kết nối với mô đun trung tâm qua mạng cục bộ không dây Wireless LAN hoặc trực tiếp với mạng Internet qua mô đun không dây wi-fi 802.11. Máy tính trung tâm và máy tính Client là các máy tính PC thông thường được cài đặt chương trình phần mềm điều khiển dựa trên CORBA.

3.2 Chương trình phần mềm

Hình 4 trình bày thiết kế phần mềm hệ thống sử dụng CORBA bao gồm hai mô đun Client và Server.

- Mô đun Client có chức năng cung cấp giao diện người dùng (GUI) và truyền các lệnh điều khiển tới robot bằng cách triệu gọi đối tượng điều khiển trên Server. Client đồng thời cũng nhận dữ liệu phản hồi từ robot về vị trí, tốc độ, trạng thái và hiển thị cho người điều khiển. Client được viết bằng ngôn ngữ Visual Basic.

- Mô đun Server được viết bằng ngôn ngữ Java bao gồm các cài đặt đối tượng điều khiển robot như quay trái, quay phải, tiến, lùi, đọc sensor… Các đối tượng này tuân theo chuẩn CORBA và có thể được triệu gọi từ xa từ bất kỳ Client nào. Khi được triệu gọi, đối tượng sẽ điều khiển robot và gửi phản hồi về cho Client.
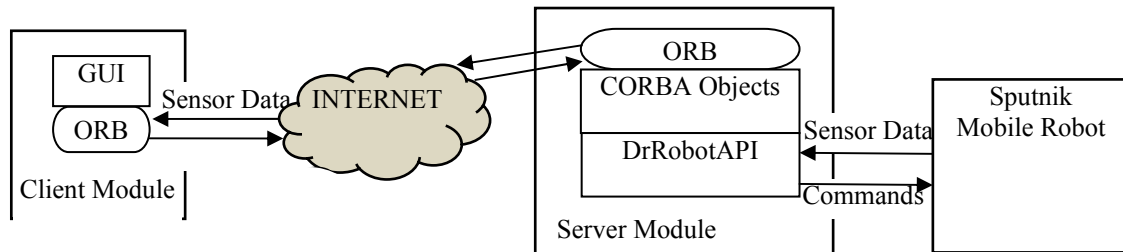
4. Kết quả thực nghiệm

Để đánh giá hoạt động của hệ thống điều khiển robot sử dụng CORBA, nhiều thực nghiệm đã được chúng tôi tiến hành tại tầng 3 tòa nhà G2 thuộc Khoa Điện tử - Viễn thông, trường Đại học Công nghệ, Đại học Quốc gia Hà Nội ở các thời điểm khác nhau, trong những điều kiện khác nhau và với nhiều tình huống giả định có thể xảy ra.

Trong các thực nghiệm, bằng việc sử dụng giao diện GUI đã thiết kế, người dùng, ở vị trí cách xa 15km, đã điều khiển thành công r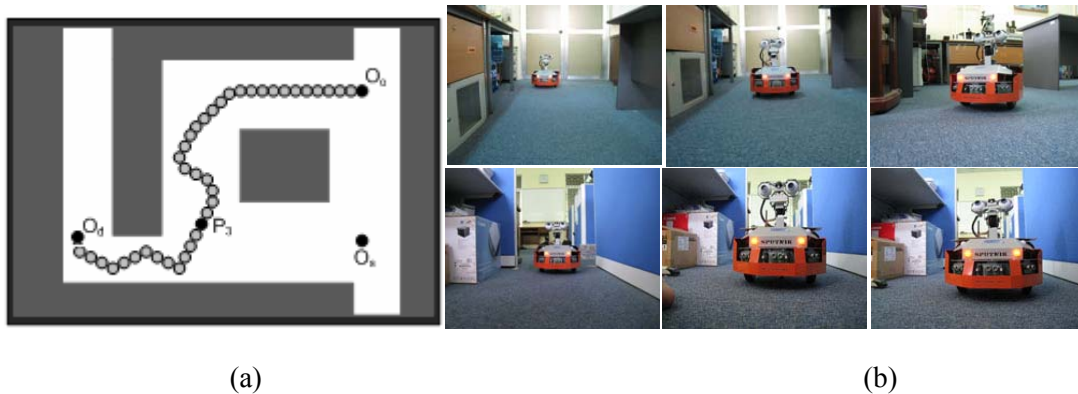obot di chuyển từ điểm xuất phát O_o đến điểm đích $O_đ$ qua mạng Internet (Hình 5a). Hình 5b trình bày một chuỗi hình ảnh của robot được ghi lại trong qua trình điều khiển trên.
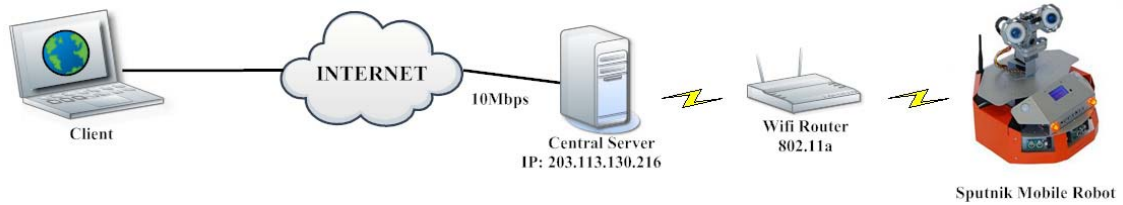
Hình 3. Cấu trúc phần cứng hệ thống

Hình 4. Sơ đồ phần mềm hệ thống

(a)   (b)

Hình 5. Kết quả thực nghiệm hệ thống điều khiển robot qua mạng máy tính:
(a) Đường đi của robot trong quá trình điều khiển từ điểm đầu đến điểm đích
(b) Một chuỗi hình ảnh của robot trong quá trình điều khiển

5. Kết luận

Trong đề tài này, chúng tôi đã xây dựng thành công một hệ thống cho phép điều khiển robot qua mạng Internet mà không cần phải quan tâm các đối tượng điều khiển được cài đặt ở đâu, bằng ngôn ngữ lập trình gì và trên hệ điều hành nào. Điều này giúp khắc phục nhược điểm của đa số hệ thống điều khiển robot qua mạng máy Internet hiện nay thường chỉ tương thích với một nền tảng ngôn ngữ nhất định. Nhiều phép thực nghiệm được tiến hành đã chứng minh tính khả thi và thành công của hệ thống trong bài toán điều khiển robot nói riêng và các hệ thống thời gian thực nói chung qua mạng máy tính.

Tài liệu tham khảo

[1] Laurent A. Nguyen et. al., Virtual Reality Inter-faces for Visualization and Control of Remote Vehicles. Autonomous Robots, Kluwer Academic Publishers, manufactured in The Netherlands, p.59-68, 11 (2001).

[2] Joseph Alex et. al., A virtual reality tele-operator interface for assembly of hybrid MEMS prototypes. Proceeding of Design Engineering Technical Conference DETC'98, Atlanta, GA (1998).

[3] Kuk-Hyun Han, Sinn Kim, Yong-Jae Kim and Jong-Hwan Kim. Internet Control Architecture for Internet-Based Personal Robot. Dept. of Electrical Engineering, Korea Advanced Institute of Science and Technology, Kusong-dong, Yousong-gu, Taejon-shi, 305-701, Republic of Korea.

[4] Peter X. Liu, Max Q.-H. Meng, Polley R. Liu, and Simon X. Yang, "An End-to-End Transmission Architecture for the Remote Control of Robots Over IP Networks," IEEE/ASME transactions on mechatronics, Vol. 10, No. 5, October 2005.

[5] R. C. Luo and T. M. Chen, "Development of a multi-behavior based mobile robot for remote supervisory control through the Internet," IEEE/ASME Trans. Mechatronics, vol. 5, no. 4, pp. 376–385, Dec. 2000.

[6] K. Goldberg et al., "Desktop teleoperation via the world wide web," in Proc. IEEE Int. Conf. Robotics and Automation, Nagoya, Japan, 1995, pp. 654–659.

[7] K. Taylor and B. Dalton, "Issues in Internet telerobotics," in Proc. Int. Conf. Field and Service Robotics, Canberra, Australia, 1997, pp. 151–157.

[8] C. Sayers, "Remote control robotics," New York: Springer Verlag, 1998.

[9] T. Fong and C. Thorpe, "Vehicle teleoperation interfaces," Autonomous Robots, vol. 11, no. 1, pp. 9–18, Jul. 2001.

[10] P. Li, W. Lu, and Z. Sun, "Transport layer protocol reconfiguration for network-based robot control system", IEEE Networking, Sensing and Control, ICNSC2005 - Proceedings 2005, pp. 1049-1053, 2005.

[11] Kuk-Hyun Han, Sinn Kim, Yong-Jae Kim and Jong- Hwan Kim, "Internet Control Architecture for Internet-Based Personal Robot," Journal ò Autonomous Robots 10, 135–147, 2001

[12] Dawei Wang, Jianqiang Yi, Dongbin Zhao, Guosheng Yang, "Teleoperation System of the Internet-based Omni-directional Mobile Robot with A Mounted Manipulator," Proceedings of the 2007 IEEE International Conference on Mechatronics and Automation August 5 - 8, 2007, Harbin, China.

[13] Markus Aleksy, Axel Korthaus, Martin Schader, "Implementing Distributed Systems with Java and CORBA," Springer Berlin Heidelberg Pub, January, 2010.

2D- Numerical Model of contaminant transmission in water

Tran Thu Ha

Institute of Mechanics

Summary:

In this paper the 2D- mathematical model simulating transmission processes of some contaminant substances in a lake of Hanoi is studied. The finite volume method is used in model. The actions between the combination of 6 substances in water are considered and the simulation results are compared with the measurements.

Introduction

Nowadays, water quality is one of the most important problems. Water quality is influenced directly to health of people. In this paper the 2D hydraulic and pollution models are used to simulate the transmissions of the pollution substances. In [5] the linear 2D water pollution water is studied by semi group method. In [1] the nonlinear 2D-Imech water contaminant model has begun establishing in 2005 by the group of Ass. Prof. Hoang Van Lai. In this paper this model is developed to simulate transmission of the combination including of 6 contaminant substances acting each with others in water. In order to get good simulation results of these contaminant substances the coefficients in contaminant water equations are changing and depending on not only the substances but also the element positions.

1. Formulation of the contaminant water problem

2D Contamitant water model is consisted of hydraulic model and transmission – diffusion of pollution substances. The system of equations and boundary conditions are written as follows:

$$\frac{\partial z}{\partial t} + \frac{\partial}{\partial x}(uh) + \frac{\partial}{\partial y}(vh) = 0 \ (\text{in } \Omega) \quad (1.1)$$

$$\frac{\partial u}{\partial t} + u\frac{\partial u}{\partial x} + v\frac{\partial u}{\partial y} + g\frac{\partial z}{\partial x} =$$
$$\qquad\qquad\qquad\qquad (\text{in } \Omega) \quad (1.2)$$
$$-\frac{gu(u^2 + v^2)^{1/2}}{K_x^2 h^{4/3}}$$

$$\frac{\partial v}{\partial t} + u\frac{\partial v}{\partial x} + v\frac{\partial v}{\partial y} + g\frac{\partial z}{\partial y} =$$
$$\qquad\qquad\qquad\qquad (\text{in } \Omega) \quad (1.3)$$
$$-\frac{gv(u^2 + v^2)^{1/2}}{K_y^2 h^{4/3}}$$

$$\frac{\partial C_i}{\partial t} + \frac{\partial}{\partial x} uC_i + \frac{\partial}{\partial y} vC_i$$
$$\qquad\qquad\qquad\qquad (\text{in } \quad \Omega),$$
$$= f_i + D_i(\frac{\partial^2}{\partial x^2}C_i + \frac{\partial^2}{\partial y^2}C_i)$$

$$(i=1,..m) \qquad\qquad\qquad (1.4)$$

The boundary and initial conditions of Saint - Vernant and water pollution equations are:

$$U(x, y).\vec{n}\big|_{\Gamma} = \overline{U}(t),$$

where $\vec{n}$ is the normal out orthogonal vector onto the perimeter of the region Ω

$$U(x, y, 0) = U_o(x, y)$$

$$z(x, y, 0) = z_o(x, y)$$

$$z\big|_{\Gamma} = \overline{z}(t)$$

$$C_i(x, y, 0) = C_{i,0}(x, y)$$

$$C_i(x, y, t)\big|_{(x,y)\in\Gamma_1} = \overline{C}_i(t)$$

and $\dfrac{\partial C_i}{\partial n}\bigg|_{\Gamma_2} = 0$, $\Gamma = \Gamma_1 \cup \Gamma_2$

Here: m- the number of substances dissolved in water; Ω - is a bounded domain of R^2 with a boundary Γ; z is the free surface elevation; h is the water height; u is the average velocity by x direction, v is the average velocity by y direction, g is the gravity acceleration; K_x is the Strickler coefficient by x direction; K_y is the Strickler coefficient by y direction, $S_{o,x}$ is the bottom slope by x direction; $S_{o,y}$ is the bottom slope by y direction; C_i is the concentration of i-substance; f_i is the pollution source of i-substance; D_i is the diffusion coefficient of i-substance; m is the number of substances in water; U=(u,v) is the water velocity vector.

2. Mathematical algorithm calculated 2d contaminant water

In this model the finite Volume Method is used with the calculated triangular mesh. In the regions with complicated topography the flows are well simulated by this grid board. In finite volume method the calculated area is divided by the small simple elements as triangles. The triangular mesh is unstructured. The mesh's unstructured

properties are represented that the numbering of grids and elements are considered by any rule.

To apply the finite volume the equations (1.1)-(1.3) are rewritten as follows:

$$\frac{\partial V}{\partial t} + \frac{\partial A}{\partial x} + \frac{\partial B}{\partial y} = F \qquad (2.1)$$

In the equation (2.1)

$$V = \begin{pmatrix} z \\ q_x \\ q_y \end{pmatrix}, A = \begin{pmatrix} q_x \\ \dfrac{1}{2}u^2 + gz \\ uv \end{pmatrix},$$

$$B = \begin{pmatrix} q_x \\ uv \\ \dfrac{1}{2}v^2 + gz \end{pmatrix}$$

$$F = \begin{pmatrix} 0 \\ -gu\dfrac{\sqrt{u^2 + v^2}}{K_y^2 h^{4/3}} + u\dfrac{\partial v}{\partial y} \\ -gv\dfrac{\sqrt{u^2 + v^2}}{K_y^2 h^{4/3}} + v\dfrac{\partial u}{\partial x} \end{pmatrix}$$

Integrating two sides of equation system(2.1) by small element S we have the formula:

$$\int_S \frac{\partial V}{\partial t} dS + \int_S \nabla.(A, B)dS = \int_S FdS$$

To approximate these integrals we assume that in small element S the functions z, u, v can be the constants. Therefore, using Green formula the above formula can be rewritten as following:

$$\frac{dV}{dt}S + \oint_{\partial S}(A, B).\vec{n}d(\partial S) = \int_S FdS \ (2.2)$$

In formula (2.2), S is the area of element. In the second term of (2.2) ∂S is the

perimeter of element, n is the out normal orthogonal vector onto ∂S. In the slow changing process problem to calculate the integrals we can use the average values for the functions in S element.

The transmission pollution substance equation (1.4) can be rewritten as follows:

$$\frac{\partial C_i}{\partial t} + u\frac{\partial C_i}{\partial x} + v\frac{\partial C_i}{\partial y}$$

$$-\frac{\partial}{\partial x}\left(D_i \frac{\partial C_i}{\partial x}\right) - \frac{\partial}{\partial y}\left(D_i \frac{\partial C_i}{\partial y}\right) = f_i$$

Table 1. The substances and conversion terms

Variable	Conversion term
SS	$Er - De$
BOD	$Hyd + FastCOxid - R_{ON_{Denitri}} Denitri$ $+ Sed_{BOD} - Sett_{BOD}$
CHL	$Growth_{CHL} - Death_{CHL} - Resp_{CHL} - Settl_{CHL}$
DO	$R_{OC_{CHL}} Growth_{CHL} - R_{OC_{CHL}} Death_{CHL} - SOD$ $- FastCOxid - R_{ON_{NITRI}} Nitri + Re\,aeO_2$
NH₄	$R_{NO_{Hyd}} Hyd - R_{NC_{CHL}} P_{ap} Growth_{CHL}$ $+ R_{NC_{CHL}} Re\,sp_{CHL} - Nitri + Sed_{NH_4}$
NO₃	$Nitri - Denitri$ $- R_{NO_3C_{CHL}} (1 - P_{ap})Growth_{CHL} - Sed_{NO_3}$
C_T	$R_{CC_{FastCOxid}} FastCOxid + R_{CC_{Re\,sp}} Re\,sp_{CHL}$ $- R_{CC_{Growth}} Growth_{CHL} + Re\,ae_{CO_2} + Sed_{CO_2}$ $- Pr\,ep_{CO_3}$
ALK	$R_{ALK,CHL} Re\,sp_{CHL} - (R_{ALK,CHL} P_{ap}$ $- R_{ALK,N} (1 - P_{ap}))Growth_{CHL}$ $- R_{ALK,Nitr} Nitri + R_{ALK,Deni} Denitri$
pH/[H⁺]	$f([H^+])$

In the right of equation (2.3) the combination of substances are considered and represented by the source functions f_i (i=1, m). These functions f_i are called by

Or:

$$\frac{\partial C_i}{\partial t} + UgradC_i - \nabla.D_i gradC_i = f_i \quad (2.3)$$

here U=(u,v)

The pollution process model is depending on the combination of substances and number of them. The following substances and the conversion terms are considered:

conversion terms and written as follows :

$$f_i = \sum_{j=1}^{m} k_{i,j} C_j \quad (i,j=1,m).$$ Here, m is the

number of pollution substances, $k_{i,j}$ (i,

j=1,..,m) are the coefficients depending on temperatures, different substances as well as on the element positions.

Integrating two sides of equation (2.3) by dx and dy we have:

$$\int_S \frac{\partial C_i}{\partial t} dxdy + \int_S (div(UC_i) - C_i divU)dxdy$$

$$- \int_S \nabla(D_i gradC_i)dxdy = \int_S \sum_{j=1}^m k_{i,j} C_j dxdy$$

Using the Green formula for the above equation we have:

$$\int_S \frac{\partial C_i}{\partial t} dxdy + \int_{\partial S} UC_i \vec{n} \partial S - \int_S C_i divU dxdy$$

$$- \oint_{\partial S} D_i gradC_i . \vec{n} \partial S = \int_S \sum_{j=1}^m k_{i,j} C_j dxdy$$

Then the above equation can be discrete by the following equation:

$$C_i = (k_{i,1} C_{i,1} + k_{i,2} C_{2t} + ... + k_{i,n} C_{nt})\Delta t dS$$

$$+ C_{i,t} (\frac{z - z_t}{h\Delta t} + 1)dS -$$

$$- (uC_{it} - D_i \frac{\partial C_{it}}{\partial x})n_x \partial S \Delta t$$

$$- (vC_{it} - D_i \frac{\partial C_{it}}{\partial y})n_y \partial S \Delta t$$

Here the functions are calculated at the center point of element; dS is the area of element; ∂S - the perimeter of element; C_t is the concentration in the last step; $\vec{n} = (n_x, n_y)$ out normal orthogonal vector of element; u, v and z are the values solving from (2.2); z_t the value of z in the previous step.

3. Numerical simulation of contaminant water for thanh nhan lake.

ThanhNhan Lake is located behind Thanhnhan hospital. It's area, water height, water capacity respectively are 8.1 ha, 1.5m-

3m and 162.0000m^3. Waste water flowing into lake is about 2100 m^3 per day-night.

a. Physical hydro properties

− Temperature of lake is oscillated from 23.4 ^{o}C to 23.8^o C in dry season.

− pH level is oscillated from 7.88mg/l - 8.57mg/l

− Muddy level is oscillated from 9mg/l to 34 mg/l.

− Salt level (NaCL) isn't changed in at the stations getting samples 0.01%

− Oxygen concentration dissolved in water is oscillated from 7.9 mg/l to 11.6 mg/l.

b. Chemical hydro properties:

• Organic element group:

− The contents of elements that have the origin Nito such as NO_2, NO_3, and NH_3 having the following development processes:

+ The content of NO_2 is oscillated from 0,055mg to 0.062 mg/l higher than permitted critical value of surface water standard in Vietnam (0.01-0.05mg/l)

+ The content of NO_3 is oscillated from 0.76mg to 0.81 mg/l lower very much than permitted critical value of surface water standard in Vietnam (10-15mg/l).

+ The content of NH_3 is oscillated from 0.51mg to 0.62 mg/l not higher than permitted critical value of surface water standard in Vietnam (1 mg/l).

+ The content of PO_4 dissolved in water is oscillated from 0.44mg/l to 0.46 mg/l

+ The content of salt that has origin SO_4 is oscillated from 25mg/l to 27 mg/l.

+ The content of substances that have origin H_2S is oscillated from 0.116mg/l to 0.151 mg/l.

+ The need of chemical biology oxygen BOD_5 is oscillated from 15.5mg/l to 24.0 mg/l less than Vietnamese critical standard of surface water quality (less than 25 mg/l).

+ The need of chemical oxygen COD is oscillated from 345mg/l to 400 mg/l. Therefore, the chemical oxygen need is higher than Vietnamese critical standard of surface water quality about 10 times (less than 35 mg/l).

• The group of chemical toxin is consisted of some elements that have heavy metals such as catmint, mercury, leaden and mangan. In general, the average contents of elements, that have heavy metals, are less than Vietnamese critical standard of surface water quality (1995).

There are the measurement values of some substances in the lake that are writen in table 2.

Table 2: Measurement of 6 considering substances in Thanhnhan lake in 11/2001

	T16 Gate into the north of lake	T17 Area in the middle of lake	T18 Gate out
Temperature ^0C	23.4	23.8	23.8
NO_3-N (mg/l)	0.81	0.78	0.76
NH_3 (mg/l)	0.52	0.51	0.62
PO4 (mg/l)	0,44	0,46	0,46
COD(mg/l)	400	380	345
$BOD_5 20^oC$(mg/l)	24.0	15.5	17.0
SO_4(mg/l)	27	25	25

c. Geographical data

The geographic data of Thanhnhan Lake are collected on the map 1:5.000 with the correction corresponding to real condition.On the collected data, we establish the input data for the model. The geographical data is divided into the boundary and inside area of lake. These data are divided by the unstructured net with 1964 triangular elements and 1058 nodes. This unstructured net are described as the following figure: We use norms of substances in the model such as BOD_5, NH_4, NO_3 PO_4, COD. These substances have exchanging relation. The chemical process disintegrated pollution substances are described as follows:

$$S_i (BOD_5) = k_{11}.BOD_5$$

$$S_i (NH_3) = k_{21}.BOD_5 + k_{22}.NH_3$$

$$S_i (NO_3) = k_{32}.NH_3 + k_{44}.NO_3$$

$$S_i (PO_4) = k_{51}.BOD$$

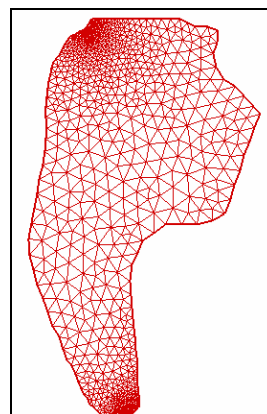$$S_i (COD) = k_{66}COD$$

$$S_i(SO_4) = - k_7 SO4$$

Fig. 1 The unstructured net of the lake

The data of discharges, water height and substance contents in the gate into the lake are as following:

− The discharges in and out of lake are 2100 m^3per day-night.

- The average water height is 4m,
- The content of BOD5 in the gate into lake is equal to the measurement value 24mg/l.
- The content of NH3 in the gate into lake is equal to the measurement value 0.52mg/l.
- The content of PO4 in the gate into lake is equal to the measurement value 0.44 mg/l.
- The content of SO4 in the gate into lake is equal to the measurement value 27 mg/l.
- The content of NO3 in the gate into lake is equal to the measurement value 0.81mg/l.
- The content of COD in the gate into lake is equal to the measurement value 400mg/l.

On the gate out there are the condition of concentration: $\partial C_i / \partial n = 0$ (i=1,..,m) where n is the out orthogonal vector onto the gate out of lake.

The measurement positions are described in the following figure
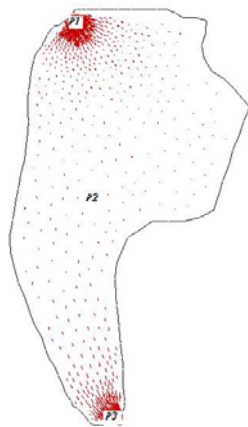
Figure 2. The measurement positions on the lake

With the previous algorithm, the concentration results of BOD_5, NH_3, PO_4, COD, NO_3 , SO_4 are obtained and described in the figures 3-10
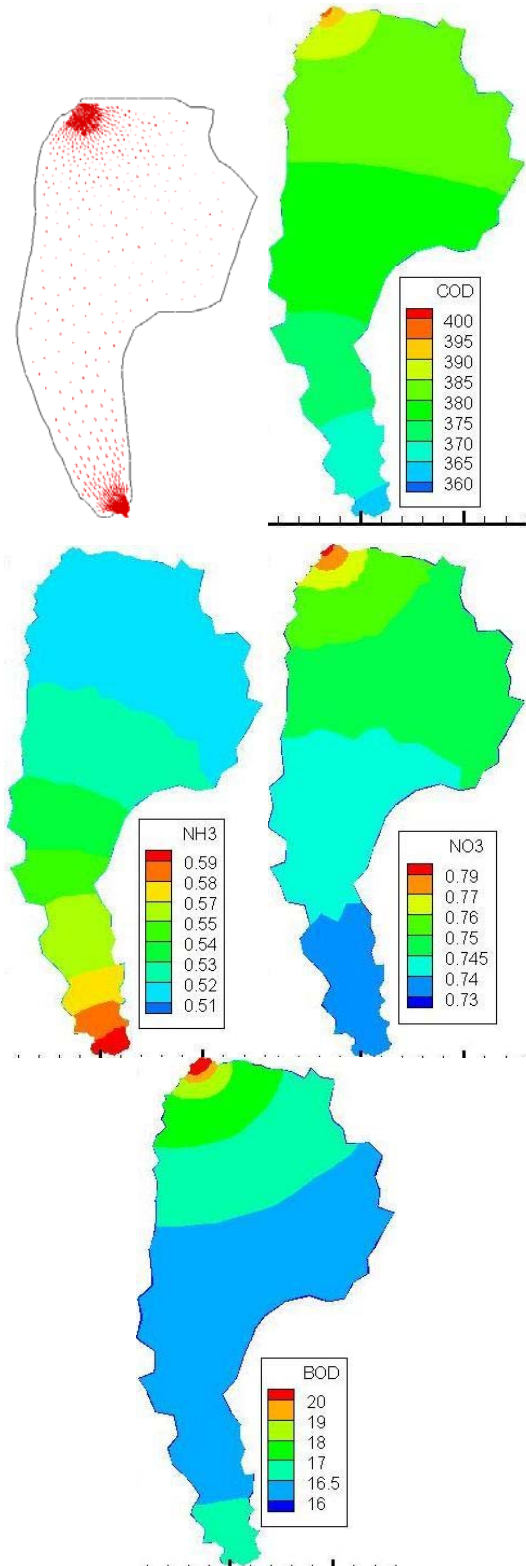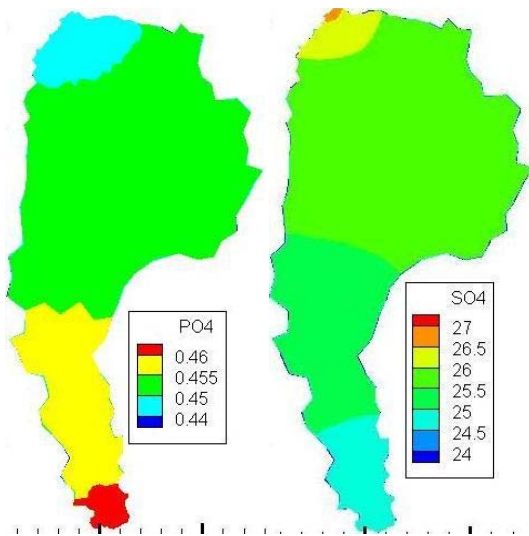
Figure 3. Velocity and substance concentration fields BOD_5, NH_3, PO_4, SO_4, COD and NO_3
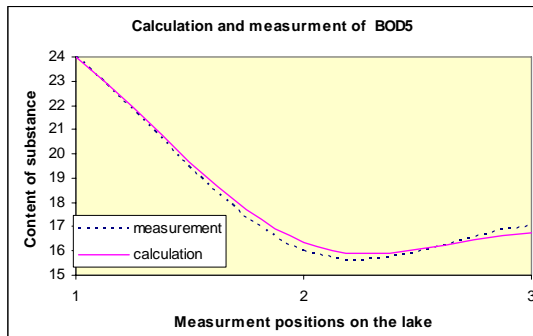
Figure 4. Calculation and measurment of BOD_5 contents at some points on the lake
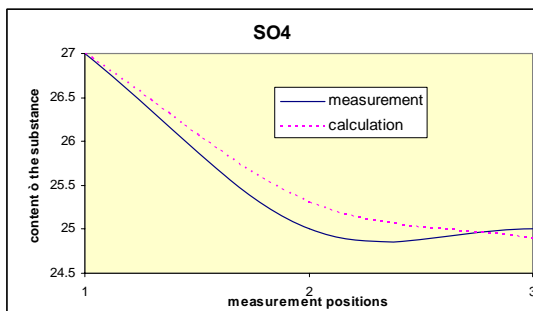
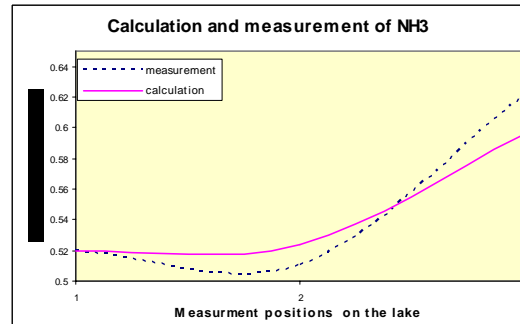Figure 5. Calculation and measurment of SO_4 contents at some points on the lake

Figure 6. Calculation and measurment of NH_3 contents at some points on the lake
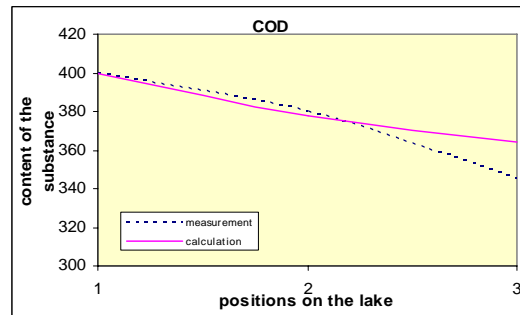

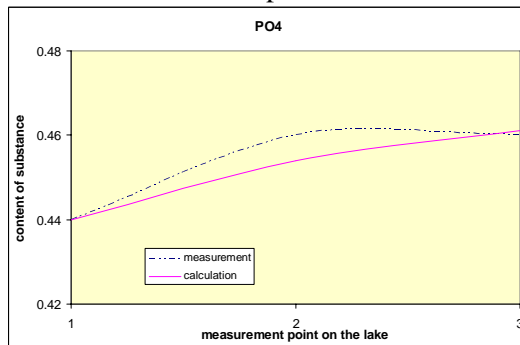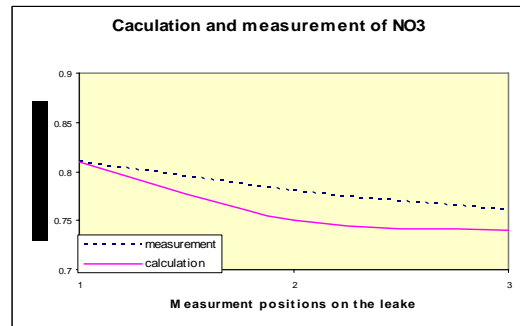Figure 7. Calculation and measurment of COD contents at some points on the lake

Figure 8. Calculation and measurment of PO_4 contents at some points on the lake

Figure 9. Calculation and measurment of NO_3 contents at some points on the lake

Conclusion

From the calculation results described by the transmission pictures of BOD_5, NH_3, NO_3, COD, PO_4 , SO_4 it is easily to see that the calculation contents of these substances are closed to the measurements. In the middle of lake there are some errors between measurements and simulations of BOD_5, NH_3, NO_3, COD, SO_4 and PO_4. These errors can be explained that the contents of pollution substances are also depending on lake's temperatures, alga activates, and sunshine…These influences aren't considered in simulation process. In reality we see in the place near by the gate out of lake we see some dead fishes and garbage. It is can be explained by the direction of flows in the lake. Therefore, in the gate out some the measurements of substance contaminants are higher than in the gate in of lake. The model can be used to simulate the transmission of substance combination in water with unlimited number of them if we have enough data. For the beginning values of coefficients $k_{i, j}$ (i,j=1,…,m) in combination pollution sources f_i (i=1,..,m) from the right side of equation (2.3) we use the experimental results from the Institute of Chemistry with corrections.

In order to improve the model we will apply the new mathematical methods such as Kalman filter to correct the results and Variation Data Assimilation to choose the suitable diffusion and source coefficients D_i, k_{ij} of the contaminant equations. These new mathematical methods applying to this contaminant water problem will be published in the next paper. With the results of simulation, the model can be developed and considered as a supported tool to calculate substance contents and study water quality for the pollution problems.

Acknowledgement

References

1. Doan Xuan Thuy, Hoang Van Lai, Dinh Van Manh, Tran Thu Ha, Nguyen Phu Duc, Le Duy Hung. "Experiment simulation of pollutant transfers on reservoir" Scientific collection, National conference of Fluid and Gas Mechanic Meeting 2007, p. 555-564

2. P.A. Sleigh, P.H. Gaskell, M. Berzins and N.G. Wright: An unstructured Finite Volume Algorithm for predicting Flow in Rivers and Estuaries, Computers & Fluids, Vol. 27, pp 479-508, 1998.

3. Nguyen Tat Dac. "Mathematical model for flows and water quality in river system.". Argiculture publish house. 2004

4. Duong Ngoc Hai ." Some basic problems alaculating air and water pollution National university publish house. 2006.

5. C.Licht, Tran Thu Ha, Quoc phong Vu."On some linearized problems of shallow water flows". Differential and Integral equations. Vol. 22, No 3-4 (2009) 275-283 (USA)

Interfacial Properties of Poly(butylene succinate) Biodegradable Composites Reinforced with Coconut Fibers

Tran Huu Nam[a, b], Shinji Ogihara[b]

[a] *Department of Strength of Materials, Hanoi University of Technology, No. 1- Dai Co Viet road, Hanoi, Vietnam. Email: thnam-vl@mail.hut.edu.vn*
[b] *Department of Mechanical Engineering, Tokyo University of Science, 2641 Yamazaki, Noda, Chiba 278-8510, Japan. Email: ogihara@rs.noda.tus.ac.jp*

Abstract

Natural fiber biodegradable composites made from renewable resources for a wide range of applications are growing due to dwindling petroleum resources, eco-friendly preserving the environment, light weight, energy saving and carbon dioxide reduction and biodegradable characteristics. In the present work, the interfacial shear strength (IFSS) between coconut fiber and poly(butylene succinate) (PBS) matrix was evaluated by single fiber pull-out test. Mean IFSS of native coconut fiber/PBS calculated from debonding force of single fiber pull-out test is low (1.22 MPa), because of the incompatibility between hydrophilic fiber and hydrophobic matrix and existing the impurities on the surface of coconut fibers. Therefore, the surface chemical modification of coconut fibers was carried out to improve the interfacial bonding strength between the fiber and PBS matrix in the composites. Coconut fibers were immersed in aqueous solution NaOH with different concentrations (3%, 5% and 7%) and soaking times (24h, 48h, 72h and 96h). The coconut fibers which were immersed in 5% aqueous solution NaOH for 72h at room temperature showed the best IFSS (2.178 MPa) and 79% higher than that with untreated coconut fibers. The surface morphologies of untreated and alkali-treated coconut fibers were observed by scanning electron microscope (SEM) to show the surface characterization providing the information on the level of interfacial adhesion between coconut fiber and PBS matrix in the biodegradable composite.

Key Words: Natural fiber composite; Coconut fiber; Interfacial strength; Surface treatment

1. Introduction

Natural fiber composites based on petroleum-based thermoplastic or thermoset matrices have been used in various industrial sectors, especially in automobile industry such as door panels, seat backs, headliners, package trays, dashboards, and interior parts (Cheung et al., 2009; Holbery et al., 2001).

However, some of them are not fully environmentally friendly because matrices are non-biodegradable. Therefore, biodegradable composites based on natural fibers and biodegradable polymeric matrix made from cellulose, starch, and other natural resources have been developed to solve the environmental and recycling problems (Liu et at., 2009; Cheng et al.,

2009; Ogihara et al., 2008; Han et al., 2006; Ochi, 2006: Zhang et al., 2005).

The natural fibers such as hemp, jute, kenaf, sisal, flax, bamboo, coir, banana, pineapple, palm, silk, cotton and wood are renewable resources in many developing countries. These fibers offer specific benefits such as low cost, low density, low pollutant emissions, acceptable specific properties, renewable characteristics, enhanced energy recovery, and complete biodegradability (Satyanarayana et al., 2009; Monteiro et al., 2009; Bax and Mussig, 2008; Zhang et al., 2005; Mohanty et al., 2000). They are considered as strong candidates to replace the conventional glass and carbon fibers due to eco-friendless and their advantages. Among the natural fibers, plant fibers which contain strongly polarized hydroxyl groups are hydrophilic in nature leading to poor interfacial adhesion between polar hydrophilic fiber and non-polar hydrophilic thermoplastics, and difficulties in mixing due to poor wetting of the fiber with the matrix (Westerlind et al., 1988). Due to the presence of pendant hydroxyl and polar groups in various constituents of fibers, moisture absorption of fibers is very high that leads to poor interfacial bonding with the hydrophobic matrix polymers. Hence, the interfacial properties can be improved by giving appropriate modifications to the components, which gives rise to changes in physical and chemical interactions at the interface. The most important factor to obtain good fiber reinforced polymer composites is the bonding strength between fiber and polymer matrix. Therefore, in order to develop the composites with better mechanical properties it is necessary to decrease the moisture absorption and hydrophilic character of fibers by suitable surface chemical modification (Islam et al., 2010; John et al., 2008; Rahman et al., 2007; Prasad et al., 1983).

Among the plant fibers, coconut fiber is nowadays extensively used in many industrial applications. Coconut fiber is a versatile lignocellulosic fiber obtained from coconut trees, which grow extensively in tropical countries. Due to hardwearing quality, durability and other advantages, coconut fiber is used for marking a wide variety of floor-furnishing materials, yarn, rope, etc. However, these traditional coir products consume only a small percentage of the potential total world production of coconut husk. Thus, the research and development efforts have been underway to find new use areas for coconut fiber including utilization of coconut fiber as a reinforcement in polymer composites. The structure and properties of coconut fibers were reviewed in Satyanarayana et al. (1981). The mechanical properties of the composites based on polyester and coconut fibers were represented in (Harish et al., 2009; Asasutjarit et al., 2009; Monteiro et al., 2005; Rout et al., 2001).

In order to fabricate a fully natural fiber biodegradable composite it is necessary to reinforce complete biodegradable polymers with natural fibers. Biodegradable polymer is a polymer susceptible to degradation by biological activity with the degradation accompanied by a lowering of its molar mass. Among the complete biodegradable polymers, starch, polylactic acid (PLA) and PBS are of increasing commercial interest (Lee and Wang, 2006). PLA and PBS are biodegradable polymers which aim to replace commodity polymers in the future (Bhatia et al., 2007). The main aim of the present work is to study the IFSS of coconut fiber/PBS system and investigate the effect of alkali treatment on interfacial properties of coconut fiber in the PBS biodegradable composites. Tensile properties of coconut fiber and PBS were also studied. The IFSS of untreated and alkali-treated coconut fiber/PBS was evaluated by single fiber pull-out test. The coconut fiber surface morphology was investigated using SEM providing the information on the level of interfacial adhesion that would exits between the coconut fiber and the matrix.

2. Experimental

2.1. Materials

The golden brown coconut fibers in the present work were supplied from Betrimex, JSC., Bentre, Vietnam. The fiber diameter varies from 100 to 400 μm. Poly(butylene succinate) pellets (PBS, #1001) supplied by Showa High Polymers Ltd. (Tokyo, Japan). The melting temperature of the PBS is about 115°C, the density is 1.26 g/cm^3.

2.2. Fiber and PBS characterization

Tensile properties of coconut fibers were measured using small tensile machine with load cell of 50 N (Figure 1). Gauge length of specimens is 10 mm. The single fiber tensile tests were conducted with a speed of 0.5 mm/min at room temperature. The PBS plates were fabricated in hot press equipment (Imoto corporation, Ltd.., Kyoto, Japan) under 10 MPa pressure for 10 minutes at 150°C and was quenched by ice water. The PBS specimens of 100 x 10 x 1 mm were cut out from the PBS plates to determine their mechanical properties. Tensile tests were performed using Senstar SC-5H tensile machine with a load cell of 5 kN. All the tensile tests were carried out at room temperature with strain rate of 0.5 mm/min.
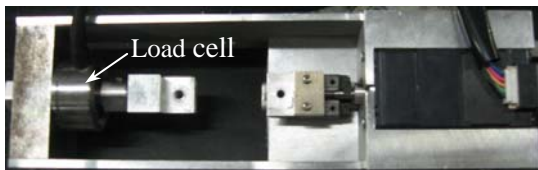

Figure 1. Small tensile testing machine

2.3 Alkali treatment of coconut fibers

Firstly, coconut fibers were treated with 5% NaOH solution for different soaking times (24h, 48h, 72h and 96h), then the fibers were removed from the solution, washed several times with fresh water and subsequently with distilled water until all the sodium hydroxide was eliminated. Finally, the coconut fibers were air-dried for more

than two days. Due to the IFSS between 5% alkali-treated coconut fibers for 72h and PBS matrix showed a higher than that of untreated and other alkali-treated coconut fibers, respectively. Therefore another series of experiments with the same procedure were followed except that the coconut fibers were soaked in various concentrations of NaOH solution (3%, 5% and 7%) for 72h in order to select a best concentration for alkali treatment. The series are designated by 3NX, 5NX and 7NX in which 3N, 5N and 7N corresponding to the soaking in 3%, 5% and 7% NaOH solution, respectively and X corresponding to the soaking time in hours.

2.4. Interfacial characterization

A technique which is most frequently used to measure the IFSS is single fiber pull-out test. In this test, one end of the fiber is embedded in a polymer matrix. Untreated and alkali-treated coconut fibers having length over 120 mm and average diameter from 100 to 300 μm measured by optical microscope were used for preparing pull-out test specimens by pressing individual fiber between two PBS sheets using above hot press equipment. The fiber was kept straight and oriented by fixing its both ends, extending outside the PBS sheets, on the mold using the glue as described by Brahmakumar et al. (2005). Specimens were removed from the mold after cooling in ice water. The desired fiber embedded length in the PBS matrix was obtained by cutting the fiber by punching a hole through the specimen. The free fiber was glued into thin board and clamped with two glass fiber reinforced plastic tabs. The schematic representation of single fiber pull-out specimen was shown in Figure 2, in which d is mean diameter of coconut fiber and L is embedded length. Single fiber pull-out test was performed by using small tensile testing machine with a load cell of 50 N at a speed of 0.5 mm/min. A force is applied to the free end of fiber to pull it out off the matrix while the force is continuously monitored and

recorded. IFSS value (τ) of untreated and alkali-treated coconut fiber/PBS was estimated from the debonding force using following equation (Luo and Netravali, 1999; Valadez et al., 1999):

$$\tau = \frac{F_d}{\pi \times d \times L} \tag{1}$$

where F_d is maximum debonding force.

Firstly the single fiber pull-out test was carried out for untreated, 5N24, 5N48, 5N72 and 5N96 treated fibers to determine the IFSSs for the comparison, then pull-out tests with 3N72 and 7N72 treated coconut fibers were performed to evaluate the effect of alkali treatment on the IFSS and choosing a best concentration of alkali treatment.
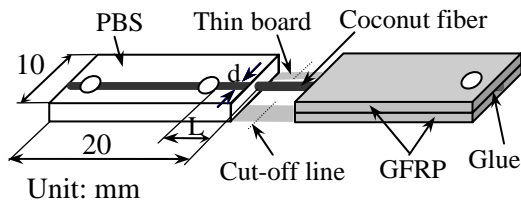
Figure 2. Schematic representation of single fiber pull-out specimen

2.5. Surface morphologies of coconut fibers

The coconut fiber surface morphologies were examined using SEM (VE-7800, Keyence Inc., Osaka, Japan).

3. Results and discussions

3.1. Properties of coconut fiber and PBS

Tensile properties of untreated coconut fiber and PBS are presented in Table 1. The tensile strength of coconut fibers is about from 100 to 150 MPa. The average strength of coconut fiber is low, but the strain at failure is quite high compared with other natural and synthetic fibers such as glass and carbon. However, the strength of coconut fibers is sufficient for their use as a reinforcement in the composites with moderate strength.

Table 1. Tensile properties of fiber and PBS

Materials	Strength (MPa)	Modulus (GPa)	Failure strain (%)
Coir	127.67 ± 17.92	3.0 ± 0.58	27.23 ± 3.29
PBS	33.26 ± 1.26	1.02 ± 0.06	9.70 ± 0.33

3.2 Effect of alkali treatment

Alkali treatment of natural fibers is applied for making high quality fibers. Alkali treatment improves the fiber-matrix adhesion due to the removal of natural and artificial impurities from the fiber surface as well as it change the crystal structure of the cellulose (Valadez et al., 1999). Alkali treatment increases the surface roughness resulting in better mechanical interlocking and the amount of cellulose exposed on the fiber surface (Rahman et al., 2007). Furthermore, alkali treatment reduces fiber diameter and thereby increase the aspect ratio (Satyanarayana et al., 1981). Hence, the development of a rough surface tomography and enhancement in aspect ratio offer better fiber-matrix interfacial adhesion resulting in an increase of mechanical properties.

Figure 3 shows the SEM micrographs of untreated and 5% alkali-treated fibers for different soaking times. Micrograph of untreated coconut fiber shows waxy layer, globular particles and cuticles on the surface (Figure 3a). Almost globular particles which cover the pits on the cell walls are intact in the 5N24 treated fiber surface (Figure 3b). Some of globular particles were intact but at a few isolated places they were removed creating the holes on the surface of 5N48 treated fiber (Figure 3c). When the soaking time was increased to 72h the cell was exposed and a much greater proportion of globular particles appeared to be removed (Figure 3d), hence the roughness of fiber surface increases. However, a micrograph of 5N96 treated fiber shows the fiber surface to be smooth with no fibril exposure (Figure 3e). The smooth surface of 5N96 treated fiber is observed due to removal of the

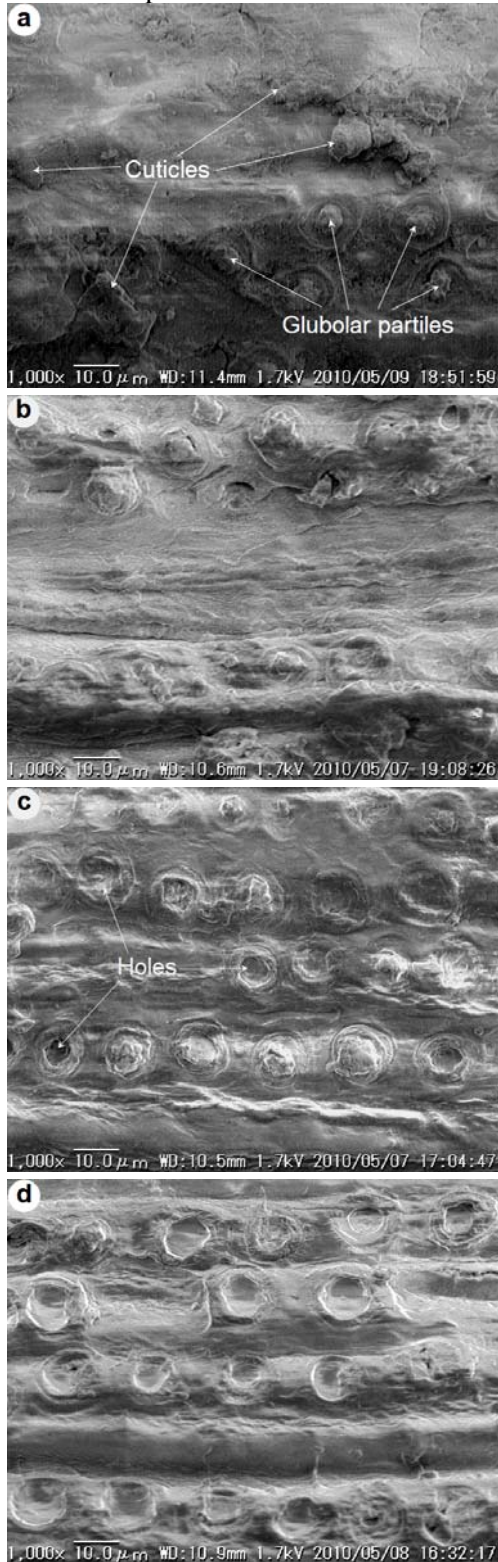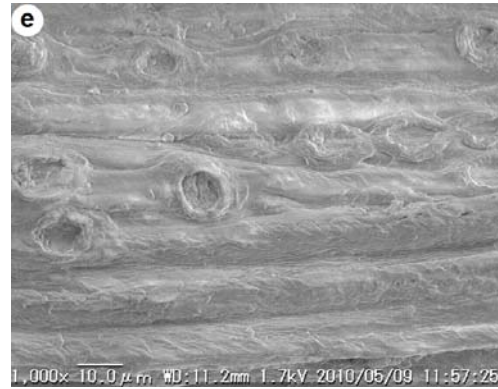substances deposited on the fiber surface.

Figure 3. SEM micrographs of coconut fibers: (a) untreated fiber, (b) 5N24 treated fiber, (c) 5N48 treated fiber, (d) 5N72 treated fiber, (e) 5N96 treated fiber.
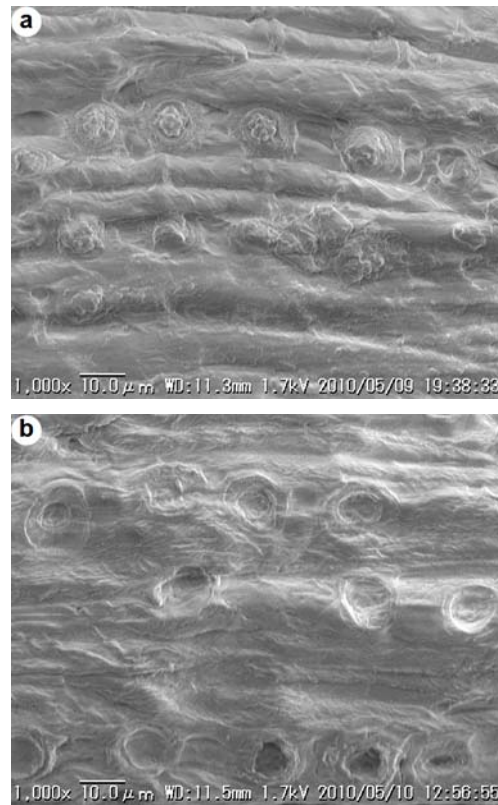
Figure 3.

Figure 4. SEM micrographs of alkali-treated coconut fibers: (a) 3N72 treated fiber, (b) 7N72 treated fiber.

The effect of NaOH concentrations for soaking time of 72h on the coconut fiber surface was shown in Figure 4. For alkali concentration of 3% (Figure 4a) almost

glubolar particles were intact but the surface impurities were removed leading to more smooth compared with untreated fiber surface. When the concentration increases to 7% (Figure 4b) it is observed the removal of the substances and creating the holes on the fiber surface, but the roughness is lower than that of 5N72 treated fiber.

3.3. Interfacial shear strength

The typical force-displacement curves of single fiber pull-out test between untreated and alkali-treated coconut fiber in PBS matrix were shown in Figure 5. These curves are similar in shape compared with several previous predictions (Luo et al., 1999; Valadez et al., 1999). It can be noted that all the curves exhibit non-linear behavior characteristics of a ductile matrix (Desarmont et al., 1991; Pigott et al., 1991; Li, 1994).
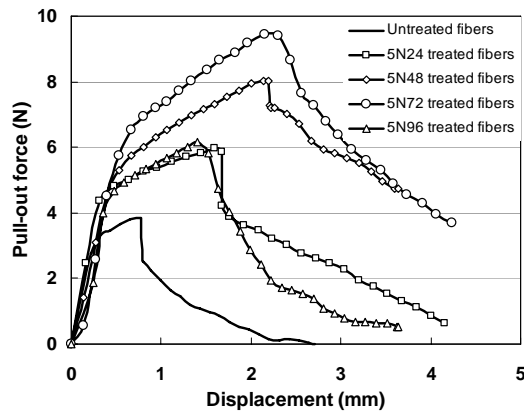

Figure 5. Typical force-displacement curves of single fiber pull-out tests for untreated and alkali-treated coconut fiber/PBS composites

However, once the force reaches its maximum value there are clearly significant differences in the way these curves drop. For the native coconut fiber, it can be seen that the force increases gradually and when it reaches a maximum value, the force suddenly drops to a lower value of the IFSS. Subsequently, the fiber is sliding along the hole-surface until the total embedded length of the fiber is pulled-out from the PBS. This

response agrees well with that one of a poor interface because of the incompatibility between hydrophilic fiber and hydrophobic matrix (Valadez et al., 1999). This behavior shows a slight change in the cases of 5N24 and 5N48 treated fibers due to the higher the roughness of the alkali treated fiber and the better the fiber–matrix mechanical interlocking, therefore the fiber–matrix interaction is improved. In the case of 5N72 treated fiber, the force-displacement curve shows a strongly bonded interphase due to the highest roughness of alkali-treated fiber surface. The force-displacement curve in the case of 5N96 treated fiber depicts a slightly weaker bonded interphase than that for the case of 72h. The force-displacement curves in the pull-out test showed that the behavior of coconut fiber is similar with the one of other natural fibers (Valadez et al. 1999; Stamboulis et al., 1999).

IFSSs between untreated coconut fiber and PBS matrix are shown in Figure 6. Mean IFSS of untreated coconut fiber/PBS system calculated from debonding force of single fiber pull-out tests is low (1.22 MPa), because of the incompatibility between hydrophilic fiber and hydrophobic matrix and existing the impurities on the surface of coconut fiber. Figure 6 also showed the effect of soaking time on the IFSS of 5% alkali-treated coconut fibers/PBS. The IFSS of 5N24, 5N48, 5N72 and 5N96 treated coconut fiber/PBS was 1.613 MPa, 2.089 MPa, 2.178 MPa and 1.665 MPa, respectively. It is observed that with increase of soaking time from 24h to 72h, the IFSS of alkali-treated coconut fibers/PBS increases. This can be explained due to higher fiber surface roughness as shown in Figure 3 resulting in the increase of wettability and interfacial bonding strength with PBS matrix. However, the IFSS of 5N96 treated coconut fiber/PBS is lower than that of 5N72 treated fiber, because its surface is more smooth compared with the one of 5N72 treated fiber as shown in Figure 3d. The results showed that alkali treatment of coconut fibers has

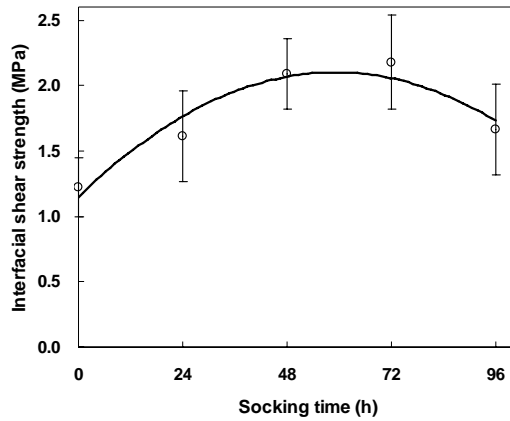increased the IFSS and to be an optimum value at certain alkali treatment.

Figure 6. IFSS between untreated and 5% alkali-treated coconut fiber and PBS matrix
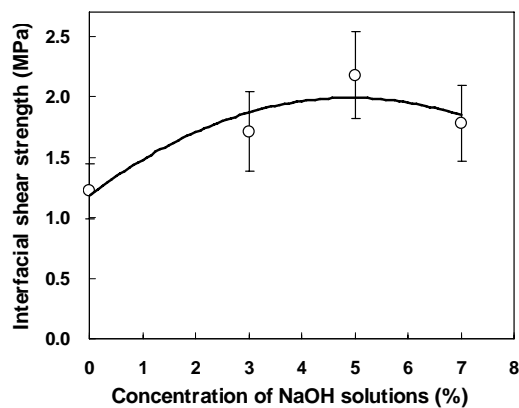

Figure 7. Effect of NaOH concentrations of treated coconut fibers for 72h on the IFSS

Furthermore, the effect of different NaOH concentrations on IFSS between alkali-treated coconut fibers for 72h and PBS matrix was shown in Figure 7. The IFSS of 3N72 and 7N72 treated coconut fiber/PBS are 1.713 MPa and 1.779 MPa, respectively and lower than that of 5N72 treated fiber. This may be explained by the lower fiber surface roughness and the lower IFSS. The surfaces of 3N72 and 7N72 treated coconut fiber as seen in Figure 4 are more smooth compared with the one of 5N72 treated fiber in Figure 3c. Thus, the results show that the highest surface roughness the highest IFSS of alkali-treated coconut fibers/PBS.

On the other hand, Figure 8 shows the relationship between debonding stress and embedded fiber length for untreated and alkali-treated coconut fiber/PBS composite. Strictly speaking, the relationship between debonding stress and embedded fiber length cannot be described by a linear function. This seems to indicate some bond ductility (Pigott et al., 1991; Li, 1994) and the surface treatments increase the fiber–matrix interaction (Desarmont et al., 1991). These curves indicate that fiber-matrix interaction increases in the order untreated, 5N24, 5N96, 5N48 and 5N72 treated fiber.
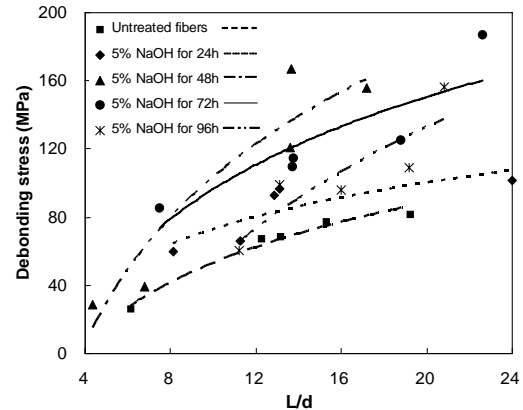

Figure 8. Debonding stress vs. embedded fiber length

4. Conclusions

The mechanical properties of coconut fiber and PBS resin have been investigated and evaluated. Coconut fibers have high variability in their mechanical properties with an average tensile strength of 126.67 MPa and modulus of 3.0 GPa. The IFSS between coconut fiber and PBS matrix was evaluated by single fiber pull-out test The effect of alkali treatment on the IFSS of coconut fiber/PBS biodegradable composite was investigated. The results showed that alkali treatment of coconut fibers has increased the IFSS and to be an optimum value at 5% NaOH concentration for 72h. The IFSS between 5% alkali-treated coconut fibers for 72h and PBS matrix showed

highest value and 79% higher than that of untreated fibers. The fiber surface morphology of coconut fiber soaked in 5% NaOH concentration for 72h showed a highest roughness of fiber surface. As a results, surface modification by alkali treatment can be improved the mechanical properties of the composites.

5. References

Asasutjarit C., S. Charoenvai, J. Hirunlabh, J. Khedari (2009). Materials and mechanical properties of pretreated coir-based green composites. *Composites Part B*, 40, pp. 633-637.

Bax B., J. Mussig (2008). Review impact and tensile properties of PLA/Cordenka and PLA/flax composites. *Compo. Sci. Technol.*, 68, pp. 1601-1607.

Bhatia A., R.K. Gupta, S.N. Bhattacharya, H.J. Choi (2007). Compatibility of biodegradable poly (lactic acid) and poly (butylene succinate) (PBS) blends for packaging application. *Korea-Australia Rheology Journal*, 19, pp. 125-131.

Brahmakumar R., C. Pavithran, R.M. Pillai (2005). Coconut fibre reinforced polyethylene composites: effect of natural waxy surface layer of the fibre on fibre/matrix interfacial bonding and strength of composites. *Comp. Sci. Technol.*, 65, pp. 653-669.

Cheng S., K.T. Lau, T. Liu, Y. Zhao, P.M. Lam, Y. Yin (2009). Mechanical and thermal properties of chicken feather fiber/PLA green composites. *Composites Part B*, 40, pp. 650-654.

Cheung H.Y., M.P. Ho, K.T. Lau, F. Cardona, D. Hui (2009). Natural fibre-reinforced composites for bioengineering and environmental engineering applications. *Composites Part B*, 40, pp. 655-663.

Desarmont G., J.P. Favre (1991). Advances in pull-out testing and data analysis. *Comp. Sci. Technol.*, 42, pp. 151–187.

Han S.O., S.M. Lee, W.H. Park, D. Cho (2006). Mechanical and Thermal Properties of Waste Silk Fiber-Reinforced Poly(butylene succinate) Biocomposites. *J. Appl. Polym. Sci.*, 100, pp. 4972–4980.

Harish S., D.P. Michael, A. Bensely, D.M. Lai, A. Rajadurai (2009). Mechanical property evaluation of natural fiber coir composite. *Materials Characterization*, 60, pp. 44-49.

Holbery J. and D. Houston (2006). Natural Fiber Reinforced Polymer Composites in Automotive Applications. *JOM* 58(11), pp. 80-86.

Islam M.N., M.R. Rahman, M.M. Haque, M.M. Huque (2010). Physico-mechanical properties of chemically treated coir reinforced polypropylene composites. *Composites Part A*, 41, pp. 192-198.

John M.J., B. Francis, K.T. Varughese, S. Thomas (2008). Effect of chemical modification of properties of hybrid fiber biocomposites. *Composites Part A*, 39, pp. 352-363.

John M.J., R.D. Anandjiwala (2008). Recent development in chemical modification and characterization of natural fiber-reinforced composites. *Polym. Compo.*, 29(2), pp. 187-207.

Lee S.H., A. Wang (2006). Biodegradable polymers/ bamboo fiber biocomposite with bio-based coupling agent. *Composites Part A*, 37, pp. 80-91.

Li J.X. (1994). Analysis of the pullout of single fibers from low-density polyethylene. *J. App. Polym. Sci.*, 53, pp. 225-237.

Liu L., J. Yu, L. Cheng, W. Yu (2009). Mechanical properties of poly(butylene succinate) (PBS) biocomposite reinforced with surface modified jute fibre. *Composites Part A*, 40, pp. 669-674.

Luo S., A.N. Netravali (1999). Interfacial and mechanical properties of environment-friendly ''green'' composites made from pineapple fibres and poly(hydroxybutyrate-co-valerate) resin. *J. Mater. Sci.*, 34, pp. 3709-3719.

Mishra S., M. Misra, S.S. Tripathy, S.K. Nayak, A.K. Mohanty (2001). Potentially of pineapple leaf fiber as reinforcement in PALF-polyester composite: surface modification and mechanical performance. *J. Reinf. Plast. Compo.*, 20(4), pp. 321-334.

Mohanty K., M. Misra, G. Hinrichsen (2000). Biofibres, biodegradable polymers and biocomposites: An overview. *Macromol. Mater. Eng.*, 276/277, pp. 1–24.

Monteiro S.N., F.P.D Lopes, A.S. Ferreira, D.C.O. Nascimento (2009). Natural-fiber polymer-matrix composites: cheaper, tougher,

and environmentally friendly. *JOM*, 61(1), pp. 17-22.

Monteiro S.N., L.A.H. Terrones, F.P.D. Lopes, J.R.M. d'Almeida (2005). Mechanical Strength of Polyester Matrix Composites Reinforced with Coconut Fiber Wastes. *Revista Matéria*, 10(4), pp. 571–576.

Ochi S. (2006). Development of high strength biodegradable composites using Manila hemp fiber and starch-based biodegradable resin. *Composites Part A*, 37, pp. 1879-1883.

Ogihara S., A. Okada, S. Kobayashi (2008). Mechanical properties in a bamboo fiber/PBS biodegradable composite. *J. Solid Mech. Mater. Eng.*, 2(3), pp. 291-299.

Pigott M.R., S.R. Dai (1991). Fiber pull-out experiments with thermoplastics. *Polym. Eng. Sci.*, 31, pp. 1246–1249.

Prasad S.V., C. Pavithran, P.K. Rohatgi (1983). Alkali treatment of coir fibers for coir-polyester composites. *J. Mater. Sci.*, 18, pp. 1443-1454.

Rahman M.M., M.A. Khan (2007). Surface treatment of coir (Cocos nucifera) fibers and its influence on the fibers' physico-mechanical properties. *Compo. Sci. Technol.*, 67, pp.2369-76.

Rout J., M. Misra, S.S. Tripathy, S.K. Nayak, A.K. Mohanty (2001). The influence of fibre treatment on the performance of coir-polyester composites. *Compo. Sci. Technol.*, 61, pp. 1303-1310.

Rout J., S.S. Tripathy, S.K. Nayak, M. Misra, A.K. Mohanty (2001). The Influence of Fiber Surface Modification on the Mechanical Properties of Coir-Polyester Composites. *J. App. Polym. Sci.*, 22, pp. 468-476.

Satyanarayana K.G., A.G. Kulkarni, P.K. Rihatgi (1981). Structure and properties of coir fibers. *Proc. Indian Acad. Sci.*, 4, pp. 419-436.

Satyanarayana K.G., G.G.C. Arizaga, F. Wypych (2009). Biodegradable composites based on lignocellulosic fibers – an overview. *Progress in Polym. Sci.*, 34(9), pp. 982-1021.

Stamboulis A., C. Baillie, E. Schulz (1999). Interfacial characterisation of flax fibre-thermoplastic polymer composites by the pull-out test. *Die Angewandte Makromolekulare Chemie*, 272, pp. 117-20.

Valadez-Gonzalez A., J.M. Cervantes-Uc, R. Olayo, P.J. Herrera-Franco (1999). Effect of fiber surface treatment on the fiber–matrix bond strength of natural fiber reinforced composites. *Composites Part B*, 30, pp. 309-320.

Westerlind B.S., J.C. Berg (1988). Surface energy of untreated and surface-modified cellulose fibres. *J. Appl. Polym. Sci.*, 36, pp. 523-534.

Zhang M.Q., M.Z. Rong, X. Lu (2005). Fully biodegradable natural fiber composites from renewable resources: All plant fiber composites. *Compo Sci Technol.*, 65, pp. 2514-2525.

A very Simple Structure of a 3-DOF Piezoresistive Accelerometer

Tran Duc Tan[a,], Chu Duc Trinh[a], Nguyen Thang Long[a] and Nguyen Phu Thuy[a, b]

[a] *MEMS and Microsystems Department, College of Technology, VNUH, VIETNAM tantd@vnu.edu.vn*
[b] *International Training Institute for Materials Science, HUT, VIETNAM, thuynp@vnu.edu.vn*

Abstract

This paper presents the design of a very simple structure of a three-degree of freedom silicon accelerometer. We proposed a flexure configuration in order to meet requirements of small cross-axial acceleration, high and linear sensitivity. The overall chip dimension is $1.5 \times 1.5 \times 0.5$ mm^3 (L$\times$W$\times$T) and the beam size is $500 \times 150 \times 10$ µm^3 (L$\times$W$\times$T). Twelve piezoresistors are diffused on the surface of beam structure. Three simple Wheatstone bridges are formed directly on this sensor by interconnecting these piezoresistors to sense three components of acceleration independently. This sensor is designed to have the bandwidth of 200 Hz with low cross-axis sensitivities.

Key Words: MEMS, piezoresistance, accelerometer

1. Introduction

3-DOF accelerometers are needed for sensing the three dimensional vector of acceleration. There are various kinds of structure of triaxial accelerometer proposed in Tan Duc Tran (2008), Dzung Viet Dao (2004). The most disadvantages of these sensors is the high complexity of structure which lead to failure of fabrication or impairment.

In this paper, a very simple structure of a 3-DOF accelerometer is designed and simulated. The sensor can not only sense the acceleration in three dimensions but also

easy in fabrication or optimization. The overall chip dimension is $1.5 \times 1.5 \times 0.5$ mm^3 (L$\times$W$\times$T) and the beam size is $500 \times 150 \times 10$ µm^3 (L$\times$W$\times$T).

2. Design of the Accelerometer

The 3-D model of the sensor is shown in Fig. 1. The sensing beams are made of Si, with a seismic mass is suspended at the end of the twin beams combined. The p-type silicon piezoresistors are formed by diffusing boron ions at the reasonable places on the surface of the *Si* sensing beams in order to maximize the sensing output and minimize the cross-talk effect. When an external

acceleration is applied to the accelerometer, the seismic mass will be displaced and the twin beams are deformed. Stress will be appeared on the surface of beam that makes the resistance of silicon piezoresistors changed. The variance of resistance will be converted to an output voltage by Wheatstone bridges.
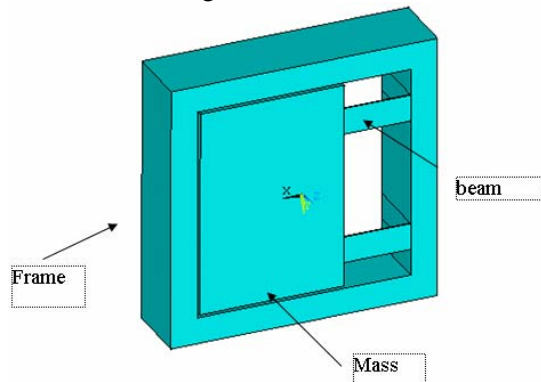

Figure 1. 3-D sensor model

2.1. Structural Analysis

To determine suitable positions to place the piezoresistors on the surface of the twin beams, it is necessary to perform structural analysis. The ANSYS 11.0 software, a finite element method (FEM), has been used to simulate mechanical behaviors of the structure. The FEM model of the accelerometer is shown in Fig. 2. The boundary conditions with non-displacement of beam ends corresponding to anchors is applied.
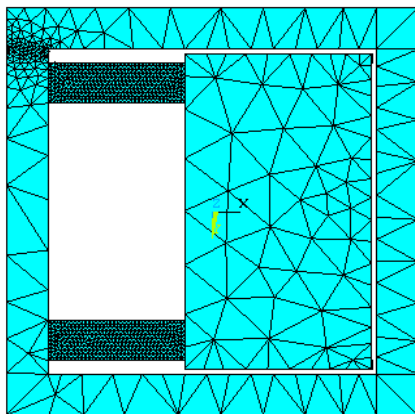
Figure 2. The 3-D meshing model

Natural frequency can reflect the mechanical sensitivity of the accelerometer. To specify the natural frequencies in three directions, the modal analysis has been performed. Table 1 shown the natural frequencies in the first three modes.

Table 1. Natural frequencies

Mode	Frequency (Hz)	Note
1	741	X
2	4247	Y
3	7436	Z

Figures 3 to 9 show the stress distributions on the surface of the twin beams due to application of accelerations. The FEM result shows that the longitudinal stress is a major component, the others can be neglected.
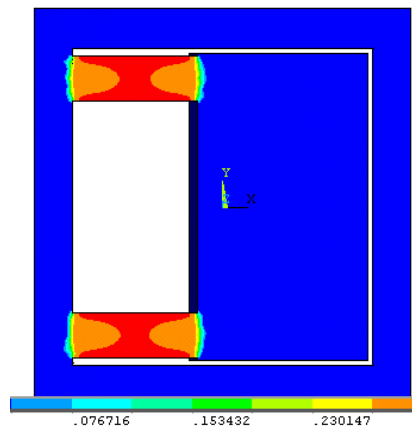

Figure 3. Graphical representation of the stress distribution due to the application of Ax acceleration
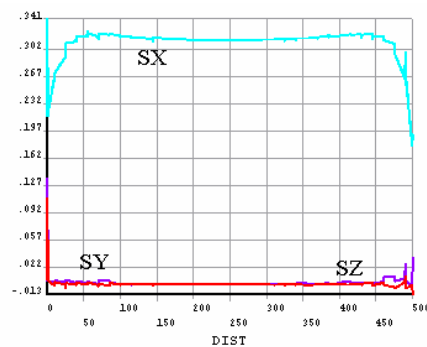

Figure 4. Stress distribution along the first and the second beams due to the application of the Ax acceleration
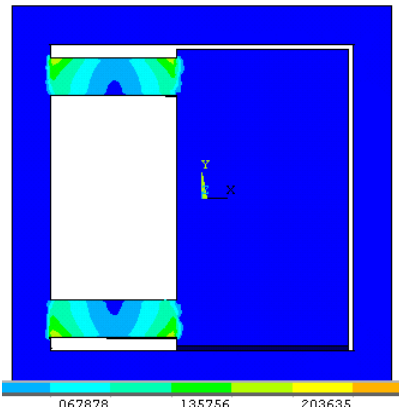
Figure 5. Graphical representation of the stress distribution due to the application of Ay acceleration
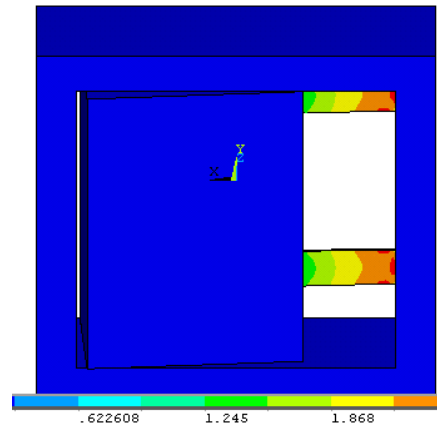

Figure 6. Stress distribution along the first beam due to the application of the Ay acceleration

Figure 7. Stress distribution along the first beam due to the application of the Ay acceleration

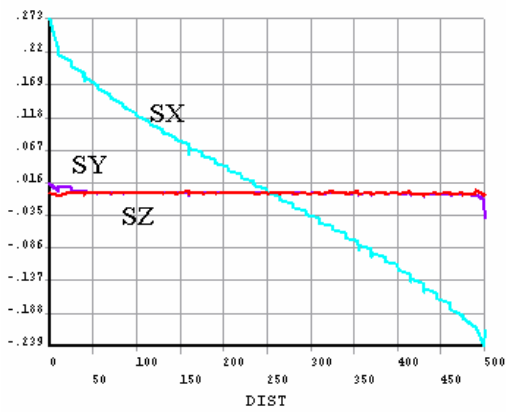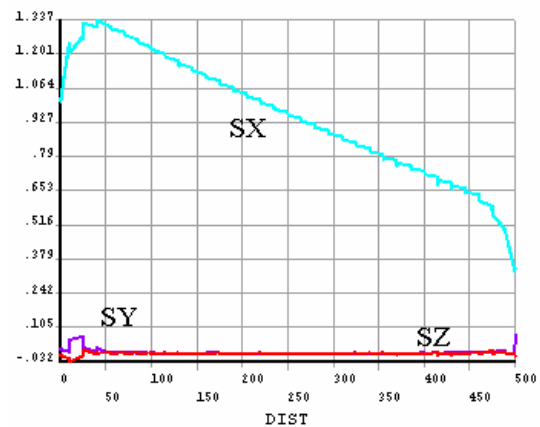Figure 8. Graphical representation of the stress distribution due to the application of Az acceleration

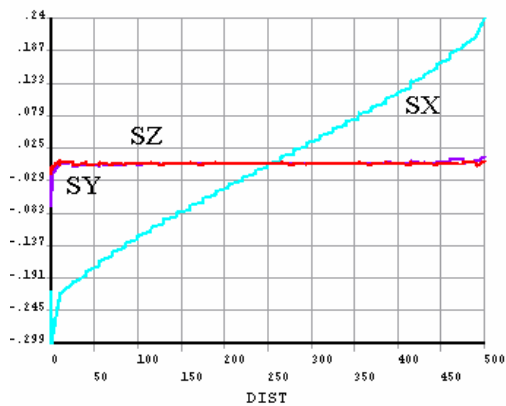Figure 9. Stress distribution along the first and the second beams due to the application of the Az acceleration

3. Piezoresistance effect

The phenomenon that resistance of crystal material is varied when subjected to mechanical stresses is called piezoresistance effect. It caused by the anisotropic characteristics of the energy resolution in crystal space. In silicon material, there are only three independent coefficients π_{11}, π_{12} and π_{44}. The longitudinal piezoresistance coefficient π_l is defined in the case the stress parallels with the direction of the electric filed and current density. Similarly, the

transverse piezoresistance coefficient π_t is defined in the case the stress is perpendicular with the direction of the electric filed and current density. In directions <110> and <1$\overline{1}$0> of n-type silicon (100), we can show these two coefficients thanks to three independent coefficients π_{11}, π_{12} and π_{44} as the following equation:

$$\pi_l = \frac{1}{2}\left(\pi_{11} + \pi_{12} + \pi_{44}\right)$$
$$\pi_t = \frac{1}{2}\left(\pi_{11} + \pi_{12} - \pi_{44}\right)$$
(1)

From simulation results in Fig. 9 (section 3), we found that two normal stresses σ_2 and σ_3 are rather smaller when comparing to σ_1. This phenomenal will affect to the sensitivity of the sensor. To eliminate this effect, we should avoid placing piezoresistors near the fixed end and the start of the beam. Thus, we can calculate the relative change of resistance due to the normal stress as the following equation:

$$\frac{\Delta R}{R} = \pi_l \sigma_l + \pi_t \sigma_t$$
(2)

These p-type piezoresistors were chosen to diffuse on the surface of these four beams because they can provide the maximal resistance variations. These piezoresistors were aligned with the crystal directions <110> and <1$\overline{1}$0> of n-type silicon (100). These piezoresistors were designed to be identical and fabricated by diffusion method. The detail information about piezoresistance phenomena can be found in Yozo Kanda (1981, 1982).

4. Piezoresistors placements

The positions of piezoresistors were chosen by utilizing the stress distribution in order to maximize the sensing output and minimize the cross-talk. Twelve p-type conventional piezoresistors (eight ones on the twin beams and two ones on the sensor

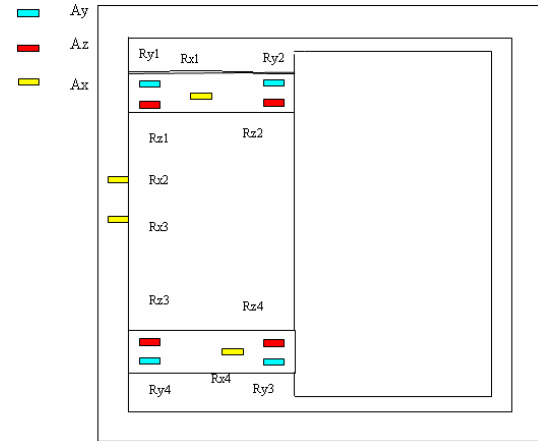frame) are used to form three Wheatstone bridge circuits.

Figure 10. The piezoresistors placement of on the twin-beam and on the sensor frame

Table 2 shows the increase (+), decrease (-), or invariable (0) in resistance of piezoresistors due to application of accelerations.

Table 2. Resistance variations

		Rx				Ry				Rz		
	Rx1	Rx2	Rx3	Rx4	Ry1	Ry2	Ry3	Ry4	Rz1	Rz2	Rz3	Rz4
Az	+	0	0	+	+	-	+	-	+	-	-	+
Ay	+	0	0	+	+	-	-	+	+	+	-	-
Ax	+	0	0	+	+	+	+	+	+	+	+	+

To detect the accelerations in Y and Z directions, piezoresistors are connected to form Wheatstone full bridges (see Fig. 11).
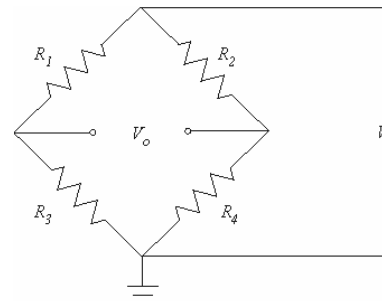

Figure 11. The full Wheatstone bridge circuit

To detect AX acceleration correctly, a specific circuit is design as shown in Fig. 12. Note that resistance values of two

piezoresistors Rx_2 and Rx_3 are constant because they are placed on the outer frame. The output voltage AX can be calculated:

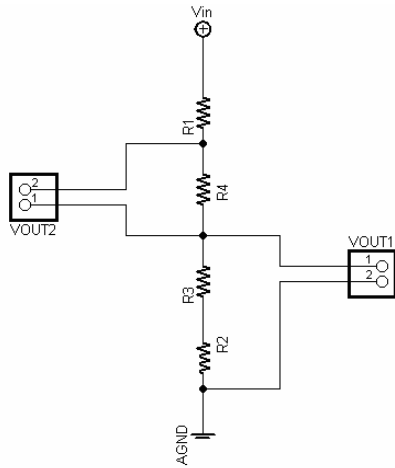$$V_{AX} = V_{out1} - V_{out2} \qquad (3)$$

Figure 12. Calibrated circuit for AX detection

5. Sensor Performance

The sensitivity of the accelerometer is the ratio between the output voltage and the input acceleration. The sensitivities to each components of acceleration Ax, Ay, Az can be summarized in Table 3.

Table 3. Sensor sensitivities

	Sensitivity (mV/V/g)	Note
AX	0.103	X
AY	0.19	Y
AZ	0.24	Z

The Johnson noise plays a main role among noise sources. The *rms* voltage of equivalent acceleration noise in each piezoresistor is:

$$V_i^{Johnson} = \sqrt{4k_B T B_i R} \quad i = X, Y, Z \qquad (4)$$

where k_B= 1.38 x 10^{-23} J/K is Boltzmann's constant, T is temperature in resistors, R is resistance value of the piezoresistor, and B is measured bandwidth.

Resolution is then defined as the noise divided by the sensitivity. The resolutions to each components of acceleration Ax, Ay, Az can be summarized in Table 4.

Table 4. Resolution parameters

	Resolution (mg)	Note
AX	0.36	X
AY	0.85	Y
AZ	1.11	Z

6. Conclusion

In this paper, a very simple structure of a 3-DOF accelerometer is modeled and simulated successfully. The advantage of this sensor is simple, easy to fabricate and optimize while ensuring 3D acceleration detection. The structural analysis utilizing ANSYS plays a major role in determining the positions to place the piezoresistors in order to eliminate cross-axis sensitivities and to maximize the sensitivity to the three acceleration components.

7. References

D. V. Dao, T. Toriyama, S. Sugiyama (2004). Noise and Frequency Analyses of a Miniaturized 3-DOF Accelerometer Utilizing Silicon Nanowire Piezoresistors, Austria, *IEEE Sensor 2004*, pp. 1464-1467.

Tan D. Tran, Dzung V. Dao, Tung T. Bui, Long T. Nguyen, Thuy P. Nguyen, Sugiyama Susumu (2008). Optimum Design Considerations for a 3-DOF Micro Accelerometer Using Nanoscale Piezoresistors, *IEEE-NEMS 2008*, pp. 770-773 .

Yozo Kanda (1981). Piezoresistance Effect of Silicon, *Sensors and Actuators (28)*, pp. 83-91

Yozo Kanda (1982). A graphical representation of the piezoresistance coefficients in silicon. *IEEE Transactions on Electron Devices 29*, pp. 64 – 70.

Optimal design of beams in free bending vibration

Duc-Trung Tran[a] and Hai-Le Bui[b]

[a] Hanoi University of Technology, No. 1 Dai Co Viet Street – Hanoi – Vietnam,
tranductrung-vl@mail.hut.edu.vn.
[b] Hanoi University of Technology, No. 1 Dai Co Viet Street – Hanoi – Vietnam, lebh79@gmail.com.

Abstract

Optimal problems are investigated in the present work in order to determine optimal shape of rectangular and circular beams in free bending vibration. Maier objective functional is used from the multicriteria optimization viewpoint. Necessary conditions for the maximum value of the first natural frequency and the minimum value of the total volume are established by using Pontryagin's Maximum Principle (PMP) to determine the optimal configuration of cross-sectional area along the beam axis.

Key Words: cantilever beam, optimal shape, Pontryagin's Maximum Principle.

1. Introduction

Eigenvalues including natural frequencies, critical load and critical speed are basic and important parameters in the vibration and stability problems of a structure. The PMP has been widely used to investigate the optimal shape of the above-mentioned problems. We mention the works of Tran and Vu (1977), Tran and Nguyen (1979), Szymczak (1983), Szymczak (1984), Tran and Bui (2009), Atanackovic and Simic (1999), Jelicic and Atanackovic (2007), Braun (2008), Atanackovic et al. (2009).

An eigenvalue optimization problem in general and a natural frequency optimization problem of rectangular and circular beams in bending vibration in particular can be solved by numerical methods as a mathematical programming problem (find out the optimal solution in the parameter space - PS) : find $\mathbf{A}$ = $[A_1, A_2, ..., A_n]^\mathrm{T}$ which maximizes $\omega(\mathbf{A})$ and minimizes $[V(\mathbf{A}) - V_0]^2$ (if needed) subjected to the constraints $A_i \in [A_{\min}, A_{\max}]$. Where, the natural frequency $\omega(\mathbf{A})$ and the total volume V can be determined by a direct module (DM), $\mathbf{A}$ is one point in PS, V_0 is a given value, the cross-sectional area of the ith beam segment A_i is a design variable (DV). In order to find out the optimal solution in PS, the total number of feasible solutions (a feasible solution corresponds to one point in PS or one solution of DM) is m^n (assuming that every DV is divided into m values). When increasing m and n, the volume of calculation is very large, especially in global optimal and random algorithms such as Monte Carlo or Genetic ones. These numerical methods can be solved by iteration methods in computer.

The necessary optimality conditions (NOC) obtained from Pontryagin's Maximum Principle (PMP) or variation principles (find out the optimal solution in the state space - SS) allow partially estimating the optimal characteristics before using numerical methods. Like this we can reduce the size of search space namely the *n*-constraint optimal problem can be divided into *n* extremum, single-constraint problems. If $m = 100$ and $n = 100$ then total numbers of feasible solutions in PS and SS are 100^{100} and 100×100, respectively.

Analytical solution can be obtained by using NOC for some cases such as excluding concentrated factors (concentrated masses, TMD,…) or control variables are continuous and unconstrained (Atanackovic et al., 2009; Braun, 2008; Jelicic and Atanackovic, 2007; Atanackovic and Simic, 1999). An analytical – numerical method is needed in other cases.

PMP allows estimating the maximum value of the Hamiltonian function that satisfies the Hamiltonian adjoint equations including original and adjoint state variables (OSVs and ASVs) instead of solving the minimum objective functions directly. An analogy between OSVs and ASVs holds for some cases due to analogy coefficient *k*. The coefficient *k* is often determined by test method.

In this present work, the maximum value of the first natural frequency ω of fixed – free rectangular and circular beams in free bending vibration will be determined using PMP (the solution will be non-trivial although including given total volume or not). Maier functional, which depends on state variables in fixed locations, is used as the objective function. The sign of *k* is determined by a proposition. The constrained values are also established for the control variables A_i.

2. Problem under consideration

We consider a fixed-free beam shown in Figure 1. This beam of length *L* is subdivided into *n*-1 segments (elements). E_i and ρ_i are the elastic modulus and the mass density of beam segment material, respectively. L_i is the length of element *i*. A_i and I_i are the cross-sectional area and the inertial moment of the cross-sectional area of element *i*, respectively. The presentation of A_i and I_i for different cross-sections is shown in Table 1.
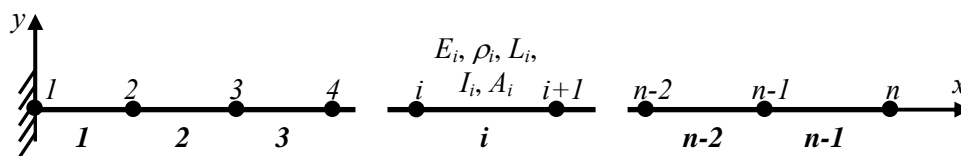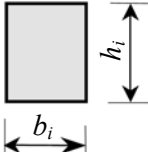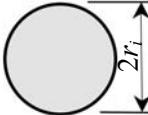

Figure 1. The geometry and FE model of a fixed-free beam.

Table 1. Presentation of A_i and I_i for different cross-sections.

Notation	Cross-Section	Variable parameter	Constant parameter	I_i vs A_i
CS1 (rectangular)		h_i	b_i	$I_i = \dfrac{A_i^3}{12b_i^2}$
CS2 (circular)		r_i		$I_i = \dfrac{A_i^2}{4\pi}$

The finite element model (FEM) of the beam includes n nodes ($1, 2, ..., i, ..., n-1, n$) and ($n$-1) elements ($1, 2, ..., i, ..., n - 2, n - 1$). Each node has two degrees of freedom (DOF) including: transverse displacement v and rotation φ.

According to Nguyen (2005) and Karnovsky and Lebed (2004), state differential equations of a Euler-Bernoulli beam are:

$$\frac{dv}{dx}=\varphi;$$
$$\frac{d\varphi}{dx} = -\frac{M}{EI};$$
$$\frac{dM}{dx} = Q; \qquad (1)$$
$$\frac{dQ}{dx} = -\omega^2 \rho Av.$$

Where, a vector of the state variables consists of the amplitude values of a transverse displacement v, rotation φ, shear force Q and bending moment M.

The fixed-free boundary conditions:

$$v(0) = 0;$$
$$\varphi(0) = 0;$$
$$M(L) = 0; \qquad (2)$$
$$Q(L) = 0.$$

The parameters v, φ, Q and M are calculated via finite element method (see Rao, 2004).

3. Optimization problem

Consider now a fixed-free beam in free bending vibration shown in Figure 1.

PMP (Geering, 2007 and Do, 2007) is used to determine the optimal shape of the beam. Optimization problem is stated as follows: find A_i, $A_i \in [A_{min}, A_{max}]$, which satisfies the objective function F.

$$F = -(1-k_1)\omega + k_1V = \min \qquad (3)$$

Where, ω is the first natural frequency, V is total volume of the beam and k_1 is non-negative weight, $k_1 \in [0, 1]$,. Based on state differential equations (1), objective function (3) as well as boundary conditions (2), the following proposition is needed for solving this problem.

Proposition: with the above-mentioned suppositions, equations (1), (2) and (3), the Hamiltonian function H is maximized (in A), and the analogy coefficient k between adjoint variables and original variables is positive, where:

$$H = \frac{1}{k}\left[-\frac{12M^2}{EI} - \omega^2 \rho Av^2\right] - k_1 A = \max \qquad (4)$$

Proof: The natural frequency ω is here considered as a state variable. It means that the role of ω is equivalent to those of v, φ, Q and M in state equations (1). So, state equations (1) can be rewritten in the form:

$$\dot{v}=\varphi;$$
$$\dot{\varphi} = -\frac{M}{EI};$$
$$\dot{M} = Q; \qquad (5)$$
$$\dot{Q} = -\omega^2 \rho Av;$$
$$\dot{\omega} = 0;$$
$$\dot{V} = A.$$

The objective function (3) can be rewritten in term of the Maier objective functional as follows:

$$F = -(1-k_1)\omega(L) + k_1V(L) = \min \qquad (6)$$

The Hamiltonian function H can be established in the form as follows:

$$H = p_1\varphi - p_2\frac{M}{EI} + p_3Q - p_4\omega^2\rho Av + p_5.0 + p_6A \quad (7)$$

The adjoint equations can be expressed under the following forms:

$$\dot{p}_1 = -\frac{\partial H}{\partial v} = p_4\omega^2 \rho A \qquad (8a)$$

$$\dot{p}_2 = -\frac{\partial H}{\partial \varphi} = -p_1 \qquad (8b)$$

$$\dot{p}_3 = -\frac{\partial H}{\partial M} = \frac{1}{EI} p_2 \qquad (8c)$$

$$\dot{p}_4 = -\frac{\partial H}{\partial Q} = -p_3 \qquad (8d)$$

$$\dot{p}_5 = -\frac{\partial H}{\partial \omega} = 2 p_4 \omega \rho A v \qquad (8e)$$

$$\dot{p}_6 = -\frac{\partial H}{\partial V} = 0 \qquad (8f)$$

The adjoint variables $p_1, p_2, p_3, p_4, p_5, p_6$ are determined as below:

$$\sum_{i=1}^{n} p_i(L)\delta x_i(L) - \sum_{i=1}^{n} p_i(0)\delta x_i(0) + \delta F = 0 \quad (9)$$

Where, x_i, p_i are state and adjoint variables, respectively. Thus,

$p_1(L)\delta v(L) + p_2(L)\delta\varphi(L) + p_3(L)\delta M(L)$
$+ p_4(L)\delta Q(L) + p_5(L)\delta\omega(L) + p_6(L)\delta V(L)$
$- p_1(0)\delta v(0) - p_2(0)\delta\varphi(0) - p_3(0)\delta M(0) -$
$p_4(0)\delta Q(0) - p_5(0)\delta\omega(0) - p_6(0)\delta V(0) -$
$(1 - k_1)\delta\omega(L) + k_1\delta V(L) = 0 \qquad (10)$

Hence,

$p_1(L)\delta v(L) + p_2(L)\delta\varphi(L) + p_3(L)\delta M(L)$
$+ p_4(L)\delta Q(L) + \delta\omega(L)[p_5(L)-(1-k_1)] +$
$\delta V(L)[p_6(L) + k_1] - p_1(0)\delta v(0) -$
$p_2(0)\delta\varphi(0) - p_3(0)\delta M(0) - p_4(0)\delta Q(0) -$
$p_5(0)\delta\omega(0) - p_6(0)\delta V(0) = 0 \qquad (11)$

We obtain:

$p_1(L) = 0$; $p_2(L) = 0$; $p_5(L) = (1 - k_1)$; $p_6(L) = - k_1$; $p_3(0) = 0$; $p_4(0) = 0$; $p_5(0) = 0$. $\qquad (12)$

Assigning:

$$p_1 = -Q_H; p_2 = M_H;$$
$$p_3 = -\varphi_H; p_4 = v_H \qquad (13)$$

We obtain:

$$\dot{v}_H = \varphi_H$$

$$\dot{\varphi}_H = -\frac{M_H}{EI}$$

$$\dot{M}_H = Q_H \qquad (14)$$

$$\dot{Q}_H = -\omega^2 \rho A v_H$$

subjected to

$$v_H(0) = 0;$$
$$\varphi_H(0) = 0;$$
$$M_H(L) = 0; \qquad (15)$$
$$Q_H(L) = 0.$$

It should be emphasized that equations (14) have mathematically similar forms as those of equations (1). Futher, it is noted that the boundary conditions expressed in equations (2) have also similar forms as equations (15) describing the boundary conditions of the adjoint system.

Therefore, it can be concluded that an analogy between the adjoint variables and the original variables is obtained. It allows yielding the following equations:

$$kv_H = v;$$
$$k\varphi_H = \varphi;$$
$$kM_H = M; \qquad (16)$$
$$kQ_H = Q.$$

The sign of k can be determined by integrating equation (8e) with appropriate conditions in equation (12):

$$\int_0^L \dot{p}_5 dx = 1 - k_1 = \frac{1}{k}\omega\rho A \int_0^L v^2 dx > 0 \qquad (17)$$

Thus, the sign of the analogy coefficient k is larger than zero for the case of maximizing ω. It was demonstrated by considering the first natural frequency ω as a state variable. The Hamiltonian function (7) will be maximized if:

$$H = \frac{1}{k}\left[-\frac{12M^2}{EI} - \omega^2 \rho A v^2 \right] - k_1 A = \max \quad (4)$$

Thus, basing on the PMP in optimal control for above-mentioned system's natural frequency, the obtained optimal necessary conditions consist of: the state equations (1), the boundary conditions (2), the control vector $A_i \in [A_{min}, A_{max}]$ and the maximum condition of the Hamiltonian function (4).

From the multicriteria optimization viewpoint, the Pareto front between the criterion (ω, V) is constructed on the basic of the definition 6 in (Coello et al., 2007): A solution $\mathbf{x} \in \Omega$ is said to be Pareto-optimal with respect to Ω if and only if there is no $\mathbf{x'}$ $\in \Omega$ for which $\mathbf{v} = F(\mathbf{x'})=(f_1(\mathbf{x'}),...,f_k(\mathbf{x'}))$ dominates $\mathbf{u} = F(\mathbf{x})=(f_1(\mathbf{x}),...,f_k(\mathbf{x}))$. The phrase **Pareto-optimal** is taken with respect to the entire decision variable space unless otherwise specified. In words, this definition says that $\mathbf{x^*}$ is Pareto-optimal if there exists no feasible vector $\mathbf{x}$ which would decrease some criterion without causing a simultaneous increase in at least one other criterion (assuming minimization).

4. Results and discussion

4.1. Validation of model

In order to verify results obtained in the present work, a fixed – free beam in Nguyen (2005) is studied for validation analysis problem.

The input data include: $n = 20$; $\rho = 8000$ kg/m^3; $E = 2 \times 10^{11}$ N/m^2; $L_i = 0.1$ m; $h_i = 0.02$ m and $b_i = 0.02$ m for CS1; $A_i = 0.0004$ m^2 for CS2; $i = 1…n$-1.

Hence, the total volume of the beam is 0.00076 m^3.

The first natural frequency of the studied beam is shown in Table 2.

It is evident that result obtained in the present work and those in Nguyen (2005) are in good agreement.

Table 2. The first natural frequency ω (rad/s) of the studied beam.

Case	Nguyen (2005) (analytical solution)	Present (FEM solution)
CS1	28.1158	28.1160
CS2	27.4749	27.4751

4.2. Results and discussion for the optimal problems

The optimal problem is described as follows: find out the changing rule of the cross-sectional area $A_i \in [A_{min}, A_{max}]$ which satisfies state differential equations (1); maximizing the first natural frequency ω and minimizing the total volume V. We take $n = 20$; $L_i = 0.1$ m; $b_i = 0.02$ m for CS1; $i = 1...n$-1; $\rho = 8000$ kg/m^3; $E = 2 \times 10^{11}$ N/m^2; $A_{min} = 0.0002$ m^2; $A_{max} = 0.0004$ m^2.

4.2.1. The single criterion optimization problem ($k_1 = 0$)

The results in this subsection include:

- The optimal values of ω: 36.1943 rad/s (for CS1) and 36.1388 rad/s (for CS2).
- The total volumes of the beams: 0.000613 m^3 (for CS1) and 0.000596 m^3 (for CS2).
- The optimal shapes of the beams is shown in Figure 2. Where, l is the distance from the left end of the beams.

It is seen that the first natural frequencies are increased about 29% (for CS1) and 32% (for CS2) whereas the total volumes are decreased about 19% (for CS1) and 22% (for CS2) when comparing the optimal beams in the subsection 4.2.1 with the studied beam in the section 4.1.

4.2.2. The multicriteria optimization problem ($k_1 \neq 0$)

Pareto fronts (or trade-off curves), which include the set of points that bounds the

bottom of the feasible region, are shown in Figure 3.

The Pareto fronts represent the possible trade-off among different objectives (ω, V) and we can evaluate different trade-off levels between ω and V. From Figure 3 it is clear that all objectives can never be simultaneously reached in best possibilities (point O).

4.2.3. Forced vibration

Forced vibration analysis is performed for beam systems to investigate optimal effect on vibration amplitude at free end. Assuming that a harmonic concentrated load $f = F\times\sin(\Omega t)$ is acted at free tip of the beams. F and Ω are taken as 10 N and 25 rad/s, respectively.

The displacement time histories at free tip of the beams (before optimizing – section 4.1 and after optimizing – subsection 4.2.1) are shown in Figure 4 and Figure 5.

From Figure 4 and Figure 5, we can see that optimizing the natural frequency of the beam system leads to reducing vibration amplitude (about 55 % for CS1 and 66 % for CS2 at the free tip).
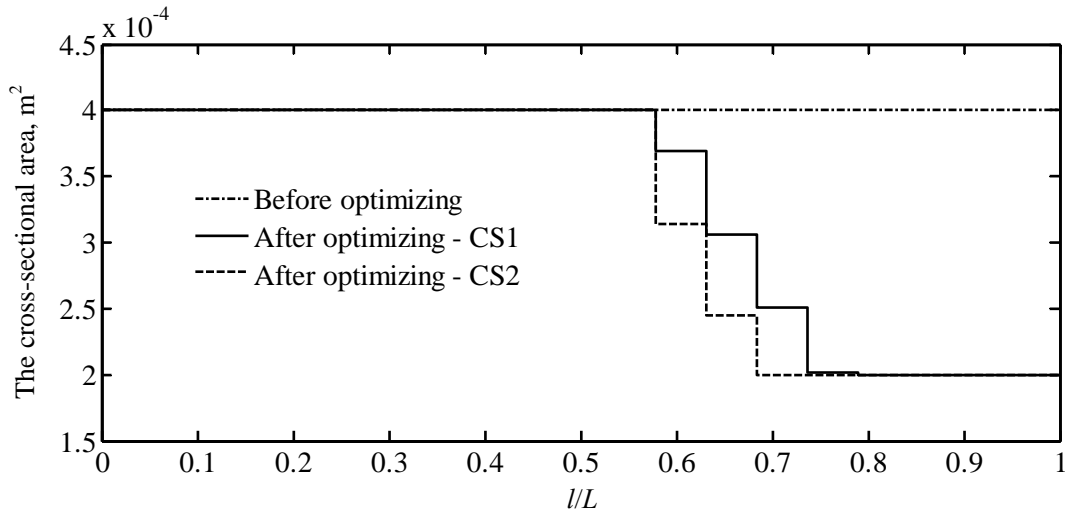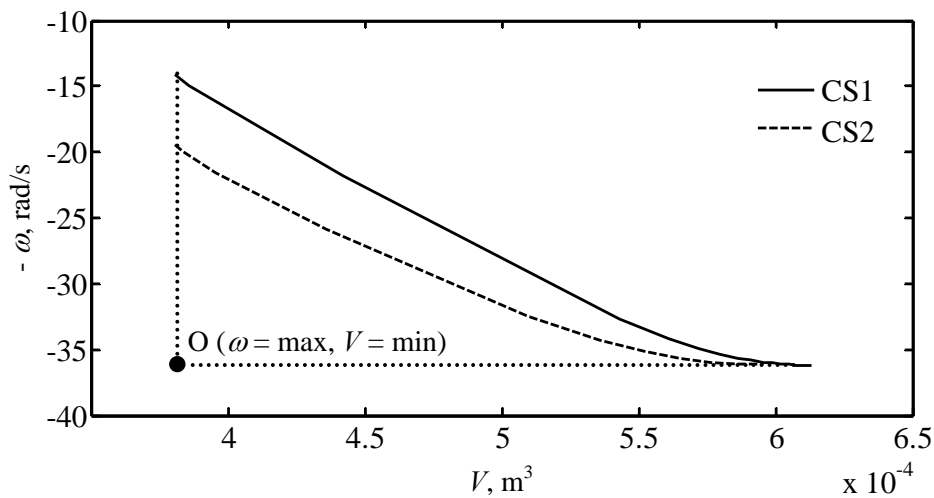

Figure 2. The optimal shapes of the beams.

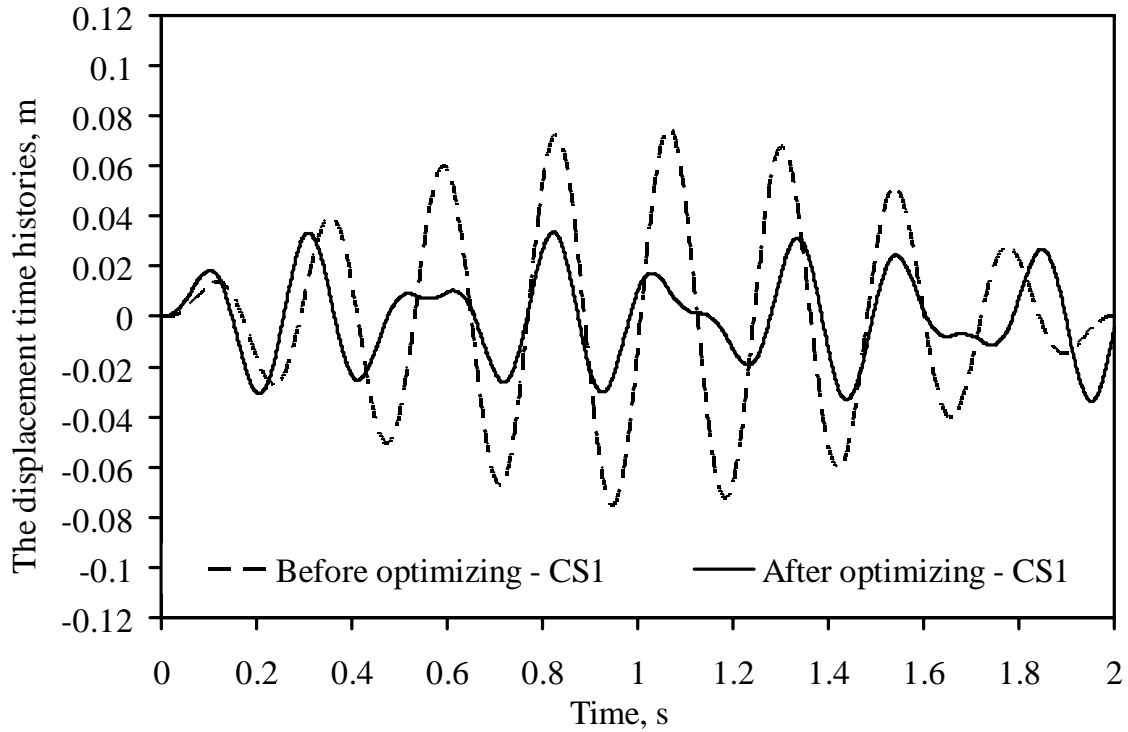Figure 3. The Pareto fronts of the beams.

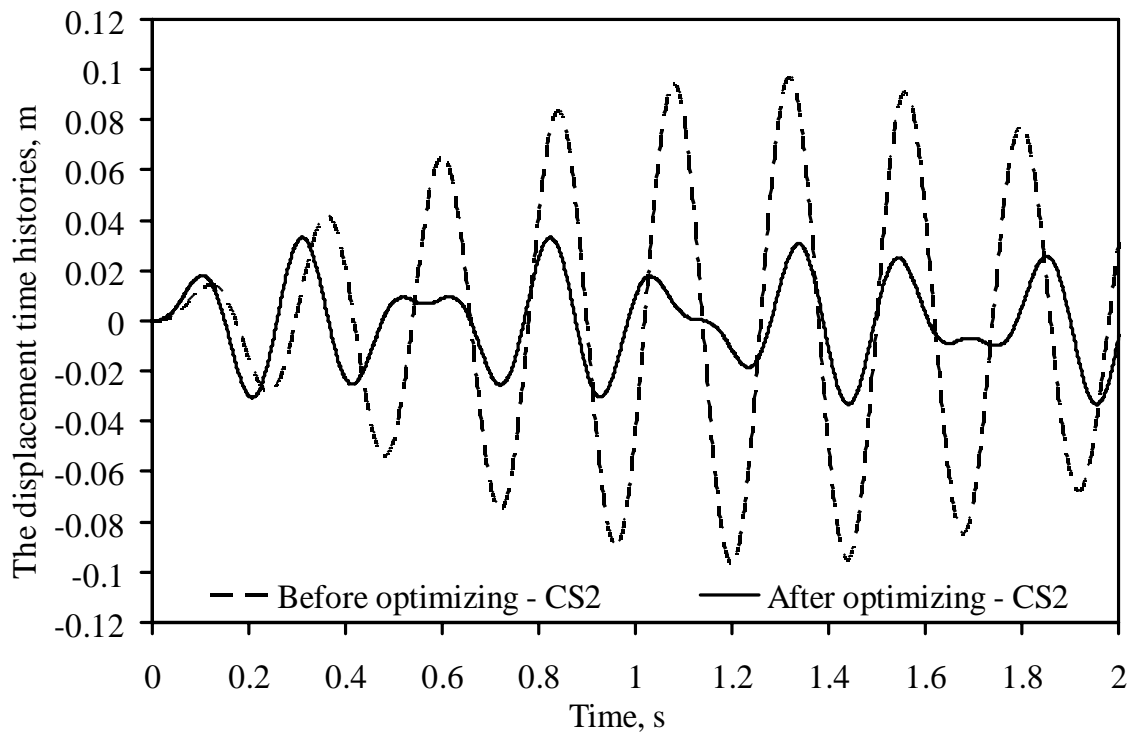Figure 4. The displacement time histories at free tip of the beams – CS1.

Figure 5. The displacement time histories at free tip of the beams – CS2.

5. Conclusions

In the present work, the optimal problem of rectangular and circular beams in free bending vibration was investigated. The main results are summarized as follows:

It is demonstrated that Maier objective functional allows solving multi-objective optimal problems, in which maximizing the first natural frequency ω and minimizing the beam's volume V are simultaneously considered, as a problem of controlling the final state of the objective functional.

The first natural frequency ω is considered as a state variable in order to formulate necessary conditions of the optimal problem by employing the suggested proposition. Using these necessary conditions (equation (4)), multi-objective and multi-constraint optimal problems as shown in subsection 4.2 can be divided into extremum, single-objective and single-constraint problems.

The Pareto front is constructed to evaluate the trade-off level between the objectives (ω, V).

The method proposed in the present work can be developed to eventually control certain natural frequencies by using PMP. Moreover, the above-mentioned optimal design problem could be applied to determine the optimal shape of a structure that is the strongest against buckling.

References

Atanackovic, T. M., Jakovljevic, B. B. and M. R. Petkovic (2009). On the optimal shape of a column with partial elastic foundation. *European Journal of Mechanics A/Solids*, 29(2), pp. 283 – 289.

Atanackovic, T. M., and S. S. Simic (1999). On the optimal shape of a Pflüger column. *European Journal of Mechanics A/Solids*, 18, 903 – 913.

Braun, D. J. (2008). On the optimal shape of compressed rotating rod with shear and extensibility. *International Journal of Non-Linear Mechanics*, 43, 131 – 139.

Coello Coello. C. A., Lamont. G. B. and D. A. Van Veldhuizen (2007). *Evolutionary Algorithms for Solving Multi-Objective Problems*, Springer Press, New York, USA.

Do, S. (2007). *Analytical Mechanics*. Bachkhoa Publishing House, Hanoi, Vietnam (in Vietnamese).

Geering, H. P. (2007). *Optimal Control with Engineering Applications*, Springer Press, Berlin, Germany.

Jelicic, Z. D. and T. M. Atanackovic (2007). Optimal shape of a vertical rotating column. *International Journal of Non-Linear Mechanics*, 42, 172 – 179.

Karnovsky, I. A. and O. I. Lebed (2004). *Formulas for Structural Dynamics*, McGraw-Hill.

Nguyen, V. K. (2005). *Engineering Vibration*. Science and Engineering Publishing House, Hanoi, Vietnam (in Vietnamese).

Rao, S. S. (2004). *The Finite Element Method in Engineering*, Elsevier Science & Technology Books.

Szymczak, C. (1983). Optimal Design of Thin Walled I Beams for Extreme Natural Frequency of Torsional Vibrations. *Journal of Sound and Vibration*, 86(2), 235 – 241.

Szymczak, C. (1984). Optimal Design of Thin Walled I Beams for a Given Natural Frequency of Torsional Vibrations. *Journal of Sound and Vibration*, 97(1), 137 – 144.

Tran, D. T. and H. L. Bui (2009). Optimal control for eigenfrequencies of a torsional shaft system including TMD effect. *Journal of Science and Technology*, 47(4), 37 – 47.

Tran, D. T. and D. Nguyen. (1979). On the optimal axial stiffness of a column. *Journal of Structural mechanics and Design of Structures*, 6, 72 – 74 (ISSN: 0039-2383) (in Russian).

Tran, D. T. and T. B. Vu (1977). Studying influence of a concentrated mass for optimal shape in the problem of longitudinal vibration bar. *Journal of Science and Engineering*, 9 (135), 19 – 25 (in Vietnamese).